Phone : +90 (312) 201 10 00
Fax : +90 (312) 287 91 88
Adress : MTA 06530 - Ankara - TURKEY
www.mta.gov.tr

165

BULLETIN OF THE MINERAL RESEARCH AND EXPLORATION

2021

BULLETIN OF THE MINERAL RESEARCH AND EXPLORATION

Foreign Edition | 2021 | 165 | ISSN : 0026-4563 E-ISSN : 2651-3048

CONTENTS

Research Articles

BULLETIN OF THE MINERAL RESEARCH AND EXPLORATION

Foreign Edition | 2021 | 165 | ISSN : 0026-4563 E-ISSN : 2651-3048

CONTENTS

Research Articles

LOCATION OF MANAGEMENT
Redaksiyon Kurulu Başkanlığı
Maden Tetkik ve Arama Genel Müdürlüğü
Genel Müdürlük Binası (A Block)
Dumlupınar Bulvarı No: 33/A 06530 Çankaya/ANKARA
e-posta: redaksiyon@mta.gov.tr

The translations of Özdemir and Sonel was made by Mustafa Selman ARSAY; Günay was made by Ahmet YILMAZGÖZ; Ergüler, Şahin and Öksüm, Esirtgen and Işık, Çiftçi and Güngör were made by M.Kerem AVCI; Öngen and Ergüler was made by Gülsüm TURGUT; Ulusoy and Kadıoğlu was made by Zehra DEVECİ ARAL.

Bull. Min. Res. Exp. is indexed and abstracted in TR Dizin, Emerging Source Citation Index (ESCI), Scopus, The ICI Journals Master List (Copernicus), Directory of Open Access Journals (DOAJ), Open Academic Journals Index (OAJI), Georef, MIAR, EBSCO and Zoological Record.

The Bulletin of the Mineral Research and Exploration is published in three issues in a year. Each bulletin is printed in Turkish and English languages as two separate issues. The English and Turkish issues of the "Bulletin of the Mineral Research and Exploration" can be obtained from "BDT Department" free of charge, either directly or ordered by adding postage fee from the correspondence address. Typesetting and printing operations are carried out and followed by the Publication Service of the Scientific Documentation and Publicity Department. Typesetting and Print Review: Yaşar Özkan, Tuğba Uğur Aydın e-mail: bdt@mta.gov.tr

The section of "notes to the authors", format, copyright and other information can be obtained from www.mta.gov.tr as PDF files.
Printed Date: 25.08.2021
Printing House: Kuban Matbaacılık - İvedik Organize Sanayi Matbaacılar Sitesi 1514. Sokak No: 20 • Phone: 0312 395 2070 • Fax: 0312 395 3723 • www.kubanmatbaa.com
Periodical
ISSN: 0026-4563
E-ISSN: 2651-3048

Bulletin of the Mineral Research and Exploration

http://bulletin.mta.gov.tr

Metallogenic characteristics of some localities of gold mineralization along shear zones of Elgaab, Dum el Tor and Sodri - Um Bader, (Sudan)

Mohamed Osman ELGIZOULI[a*], Badr El Din KHALIL[b] and Mohammed Y. ABEDELGALIL[b]

[a]*Geological Research Authority of the Sudan, Khartoum, Sudan*
[b]*Al Nileen University, Faculty of Petroleum and Minerals, Khartoum, Sudan*

Research Article

Keywords:
Shear, Related, Gold, Pan - African Orogeny, Metallogeny, Sudan.

ABSTRACT

Study area is located in the eastern sector of Saharan Meta - Craton that includes the western part of Bayuda Terrane and extend southwest to Sodri - Um Badir shear zones. The sector is dominated by metasediments, metavolcanic - sedimentary series represented by chlorite - schist, quartzite, calc - silicate, and marble. Low - grade metamorphic arc - related volcano - sedimentary sequence occurs as thin narrow bands and subjected to tectono - thermal events of Pan - African orogeny during the Late - Proterozoic era (900 - 550 Ma). All these rock sequences have been intruded by syn to Late Orogenic Granitoids and post - orogenic ring - shaped complex and felsic dykes. The intrusions are thought to be the source of hydrothermal fluids that caused the precipitation of gold. Similar characteristics of geological features and tectonic settings support the possibility of the extension of gold mineralization between shear zones. The comparison between the three gold mineralizations reveals variations in minerals assemblages, pathfinders and gold grade. The result of this study defines a new metallogenic province in the west of the River Nile, which occupies a very large area covered by Phanerozoic sediments. Numerous mineral deposits of economic potentiality have been targeted along the shear zones and related fractures and faults. Among those potential deposits, five of them have been chosen as targets for future gold exploration and evaluation.

Received Date: 21.12.2019
Accepted Date: 26.02.2020

1. Introduction

The study area is located in the eastern sector of Saharan meta craton, which is bounded by Uweinat - Salima tectonic belt in northwest Rahib ophiolite Belt in the southwest, and the southwestern boundary is the NE trending Wadi Hawar uplift. Central Africa Fault Zone with deep NE - SW - striking faults extended through the southern side and the western margin of Bayuda desert is bounded eastern side of the study area (Figure 1). The area is relatively flat and cover by thick Phanerozoic sediments. Field observations, geological mapping, and geochemical investigations suggest that study area, dominated by low - grade meta - volcano - sedimentary sequences, has similar litho - tectonic features with North Kurdofan considered by Rahman and Elmahi, (2006) as a possible west continuation of the Upper Proterozoic Pan African Arabian Nubian Shield. The general NE - SW striking of the low - grade Pan - African rocks sequences was parallel to the dominant strike directions all over the Arabian Nubian shield. Gold mineralizations in Elgaab, Hamadi gold mine (Dum el Tor) and Gammama area of Sodri - Um Bader shear zones reveal similar characteristics geological, structural features and tectonic settings.

Citation Info: Elgizouli, M.O., Khalil, B.E.D., Abedelgalil, M.Y. 2021. Metallogenic characteristics of some localities of gold mineralization along shear zones of Elgaab, Dum el Tor and Sodri - Um Bader, (Sudan). Bulletin of the Mineral Research and Exploration 165, 1-12.
https://doi.org/10.19111/bulletinofmre.695138

**Corresponding author: Mohamed Osman ELGIZOULI, mohosmelg111@gmail.com*

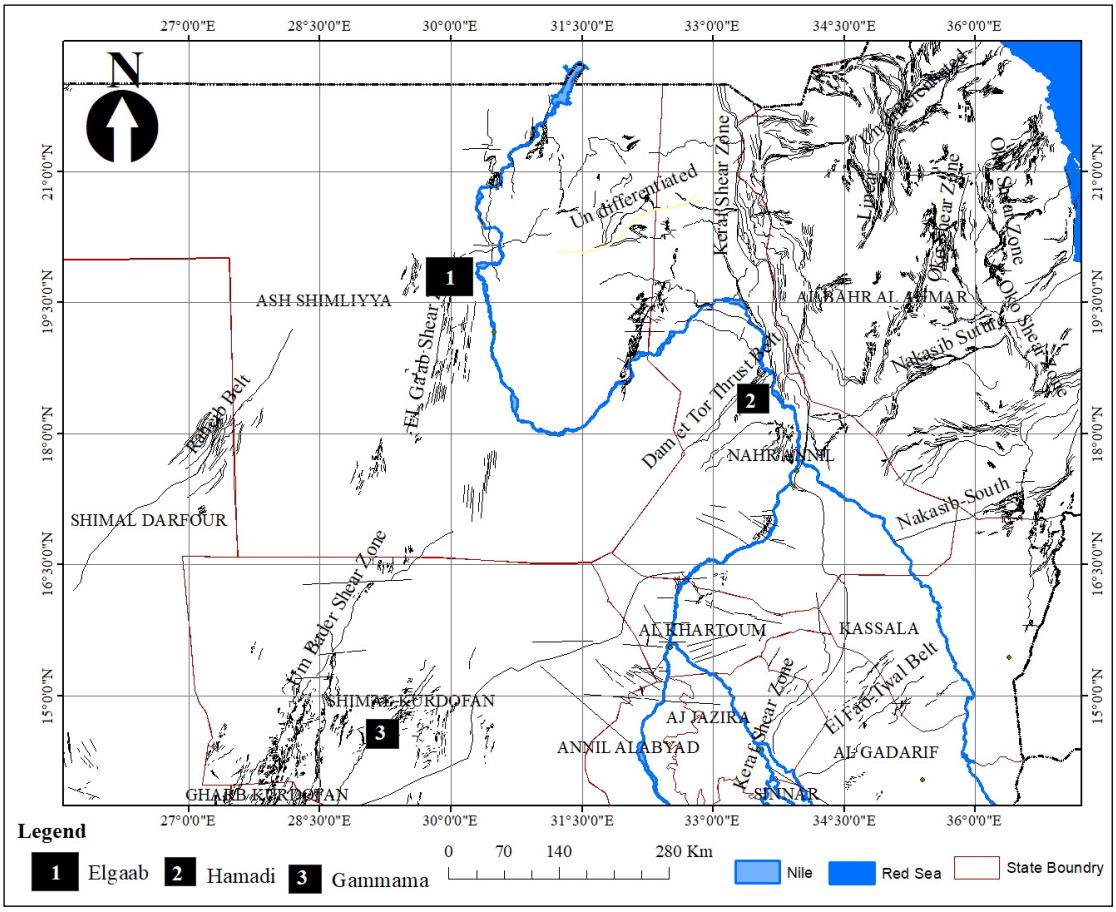

Figure 1- Location map of areas of study.

These characteristics support the possibility of the continuation of gold mineralization between the shear zones.

1.1. Applied Method

A total of 246 samples (25 chips of quartz and rocks, 31 soil, and 190 trenches samples) have been collected and analyzed using X - Ray fluorescence (XRF) method and Atomic Absorption Spectrometry (AAS) XRF analytical method: 10 g of powder sample mix by wax as binder press by pressing machine to make pallets, then read by XRF instrument, calibrated by panalytical stander for all elements (from Be to U). The determined elements depend on the wave length of the elements. AAS, used for analysis of basic elements Co, Ni, Zn, Fe etc.

0.5 g of powder sample adds to mixture of acid hydrofluoric, per chloric and nitric (10 ml, 5ml and 2ml respectively). Dry in hot plate after add 10 ml of HCl 50% then transfer the solution into 50 ml volumetric flask then read it by AAS after calibrated by series of stander solutions. The artisanal gold mining mega-pits and trenches in Elgaab area have helped substantial investigations of the subsurface geology, besides the description of the shapes, features and geometry of the ore body, lithological horizon bearing mineralization since there are no boreholes and geophysical survey conducted in the area. The main aim of the study is to define spreading of the gold mineralization along shear zones beneath thick cover of Phanerozoic sediments. As a result of the study, based on the geological, geochemical and structural features, possible new metallogenic province is defined in the west part of River Nile. In the process, geological, geochemical and structural studies were carried out in the three shear zones.

2. Geological Setting

2.1. Lithology

Metasediments, metavolcano - sedimentary series represented by chlorite - schist, quartzite, calc

- silicate, and marble are dominantly outcropped in the study area. Low - grade metamorphic arc - related volcano - sedimentary sequence occurs as thin narrow bands and subjected to tectono - thermal events of Pan-African orogeny during Late - Proterozoic era (900 - 550 Ma), resulted in low - grade green - schist to lower amphibolite facies, with local high - grade gneiss inlier. All these rock sequences have been intruded by syn to late orogenic granitoids mainly diorite and post - orogenic ring - shaped complex and felsic dykes. The basement rocks of Northern Kurdofan consist of high - grade and low - grade metamorphic assemblage exposed in the foreland of the Arabian - Nubian Shield in the western Nile. Those assemblages are intruded by syn - orogenic granite and post - orogenic granite and dykes. Shear zone related fractures were intruded by intermediate to acidic composition dykes such as quartz porphyry, dacite and trachyte (Figure 2).

2.2. Geotectonic and Local Structures

The continuation of Delgo - Atmur suture in the eastern Nile, were represented by NNE striking Elgaab shear zone, which possible reaches Sodri – Um Badir shear zones in North Kurdofan. Dum el Tor Shear zone which represents the western branch of the Red Sea - Oko shear zone of Nakasib Suture into East Bayuda Desert, and possibly continues westwards. The rifting between East Sahara / Halfa and Bayuda / Kurmut terranes had began before 750 Ma and might have started as early as 830 Ma (Kuster and Liegeois, 2001). Then followed by sea floor spreading and ocean

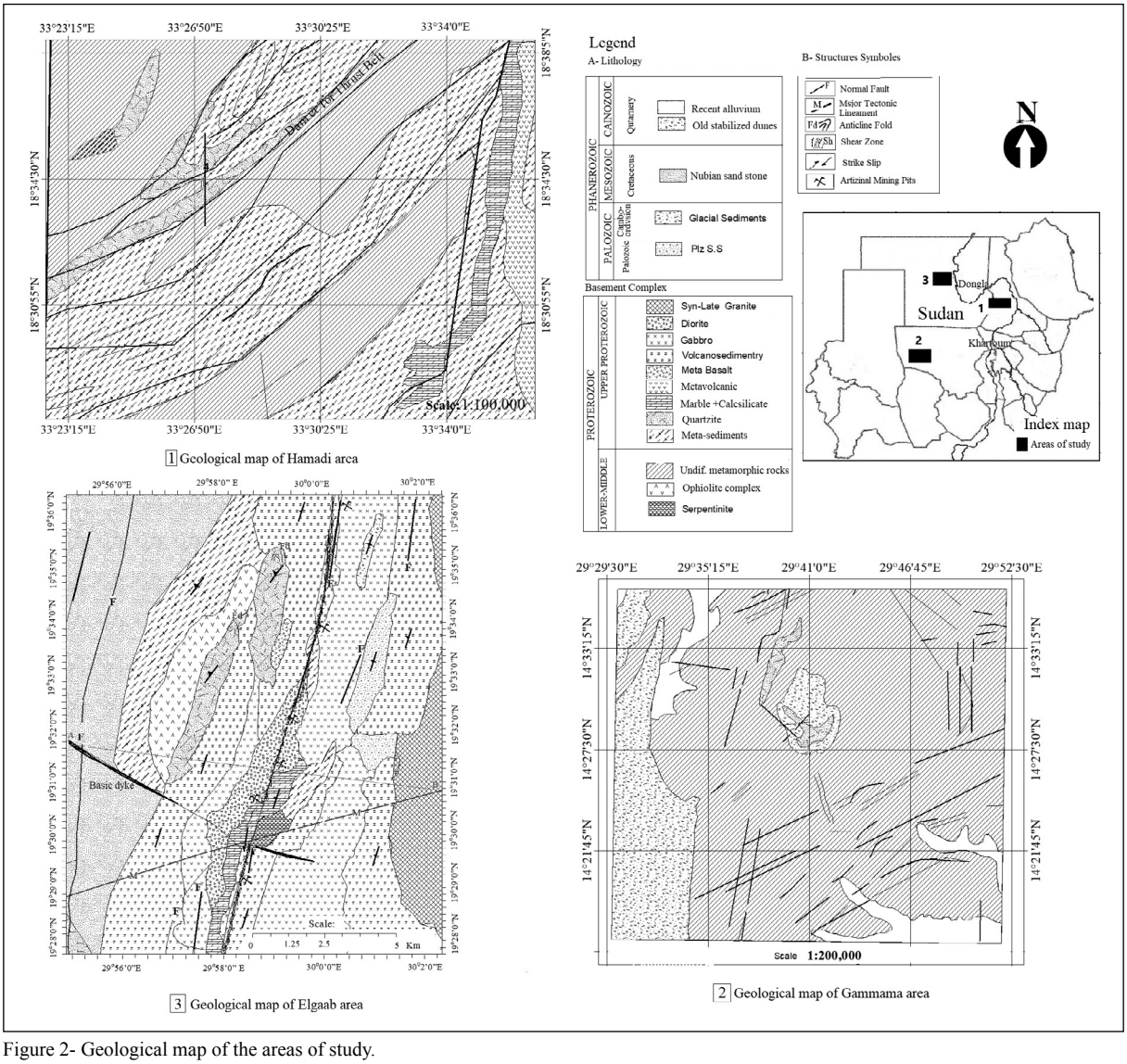

Figure 2- Geological map of the areas of study.

basin formation. Suturing of the terranes was initiated at around 720 Ma, and it was probably completed by 700 Ma (Stern et al., 1994). The Basin closure driven by N - S shortening and collision between Halfa and Bayuda / Kurmut terranes started at southeastern part of the Halfa terrane probably around 750 Ma (Abdelsalam et al.,1995).

The obduction of Atmur-Delgo ophiolite took place ~702 Ma (Harms et al., 1994), and the peak metamorphism were accepted to occur coeval. Collision between Bayuda / Kurmut and Halfa terranes was associated with progressive deformation, granitoid intrusions and metamorphism that continued until 650 Ma. These granitoid intrusions are accepted as the source of hydrothermal fluids that precipitate gold. Data from Jebel Rahib ophiolite within Rahib belt indicates that an ocean was present at ~740 Ma until its closure at ~707 Ma (Harms et al., 1994). Multi - phase deformation has affected the basement rocks in the study area. A pair of anticline - syncline overturn fold system with NE - SW trending axial plane is recognized in the mapped area. The NNE normal faults also deformed the rocks in the study area. Other set of E - W striking fault represent by second order drainage pattern, cutting lithological units and displaced the NE - SW trending lineament (Figure 3). The study area is traversed by NE striking major shear zone and extends several hundred kilometers parallel to Dam El Tor shear zone, suggested earlier as western continuation of Sodri - Um Badir shear zone of Northern Kurdofan (Rahman and Elmahi, 2006). The central part of the shear zone in the area characterized by the present of quartz veins, which are formed in the highly sheared acidic, intermediate and basic meta - volcanic and meta - sediment in Hamadi gold mine area.

More than five phases of deformation have affected the Hamadi gold mine in the East Bayuda area. The first phase is a bedding - parallel schistosity.

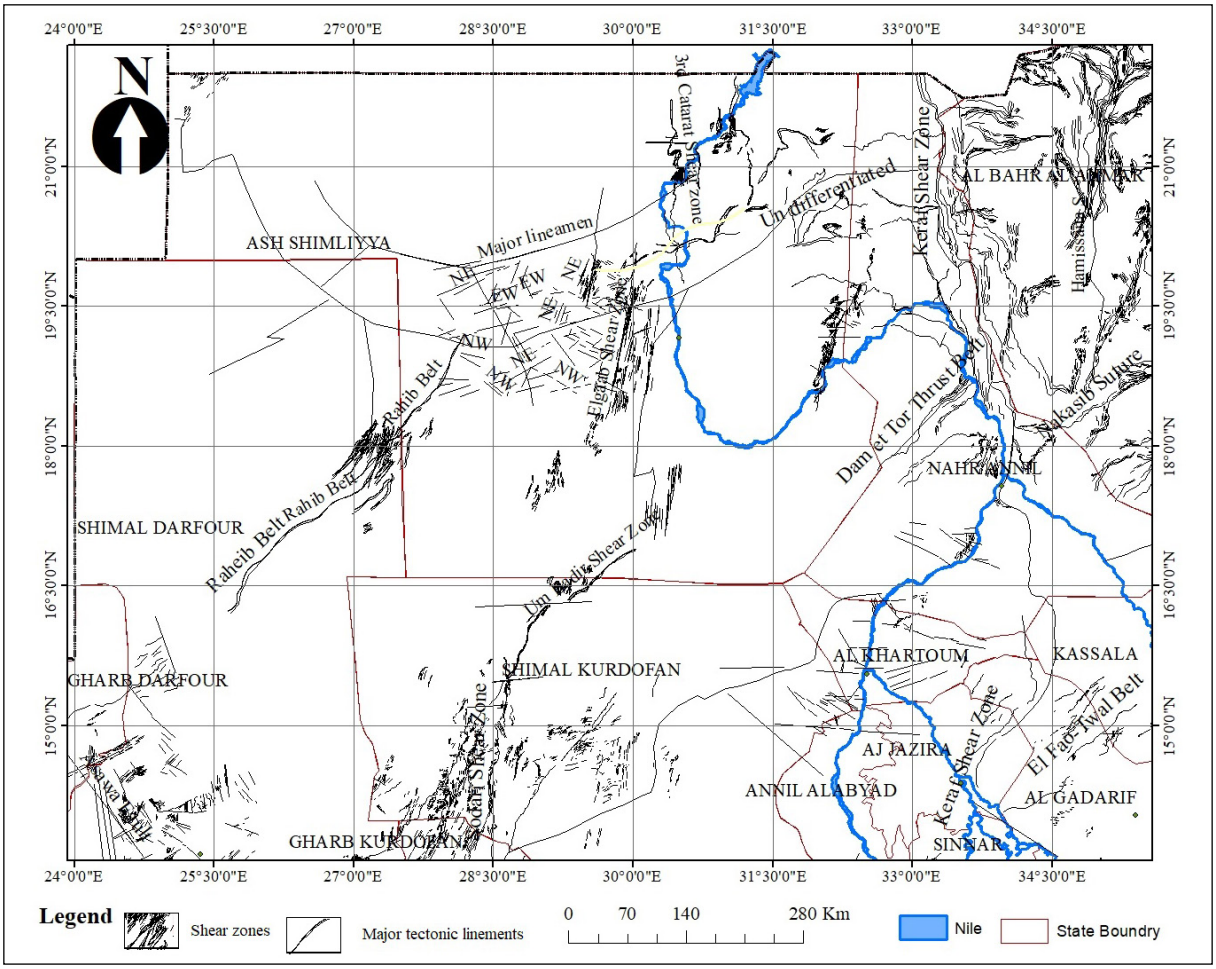

Figure 3- The tectonic map of north and central Sudan modify after tectonic and structural map of Sudan and Rose - Geo (2018) tectonic map of Sudan.

The second phase is related with folding. Dextral shearing is the dominant one and caused the formation of Z - shaped chevron fold from centimeters to hundred meters in size (Figure 4c). As a result of the shearing movement quartz boundinage (pinch - and - swell) structure has formed during the third phase of deformation (Figure 4b). Similarly in Elgaab gold mineralization zone exposed subsurface structures in artisanal gold mining mega pits, shows that at least five phases of deformation have affected the area and represented by: D1; stress pressure (convergent), D2 folding, followed by D3; faults along fold axial-plane, then followed by D4; shears fabrics. D5 corresponds to tension gashes. The complex fabrics are good path ways for fertile hydrothermal fluids to precipitate gold along shear zones (Figure 4).

3. Mineralization

As it is known from the previous geological works in Sudan, many of the vein - type gold deposits are formed along major lineaments, such as the Oko shear zone of Nakasib suture in the Red Sea hills, Dum El Tor shear zone in Bayuda Desert and across Sodari - Umm Badr shear zones in North Kordofan (Schandelmeier and Richter, 1991; Abdel Rahman and Mahi, 2006). Vein - type gold mineralization is also formed along the N - S trending Gabgaba lineament (Keraf shear zone) (Vail, 1985; Kröner et al., 1987; Abdelsalam and Dawoud, 1991; Stern, 1994).

The occurrences of gold - bearing quartz veins along shear zones are controlled by tectonic lineaments with their sub - vertical tension faults (fractures). The gold - bearing quartz veins are mainly developed as fracture filling injected along the foliation planes of greenschist during Pan - African Orogenic event in Late - Proterozoic era. The quartz veins were deformed by the first and second deformation phases (foliation planes). The kink band structures indicate that the veins were subjected to possible several subsequent shearing events, resulted in pinch - and - swell structure. The process and the genesis of gold mineralization may have taken place after the intrusion of granitoid particularly diorite and granodiorite, which are accepted as the source of energy that triggered the initiation of the hydrothermal activity during orogenic events. Heat source during the shearing events is responsible for re-mobilized and re-concentration of gold and associated elements across the study area, which similar processes recognized across the Arabian - Nubian Shield.

Quartz veins are usually thin and stringers are wide - spread. Many types of quartz veins are recognized and recorded; the massive smokey, grey,

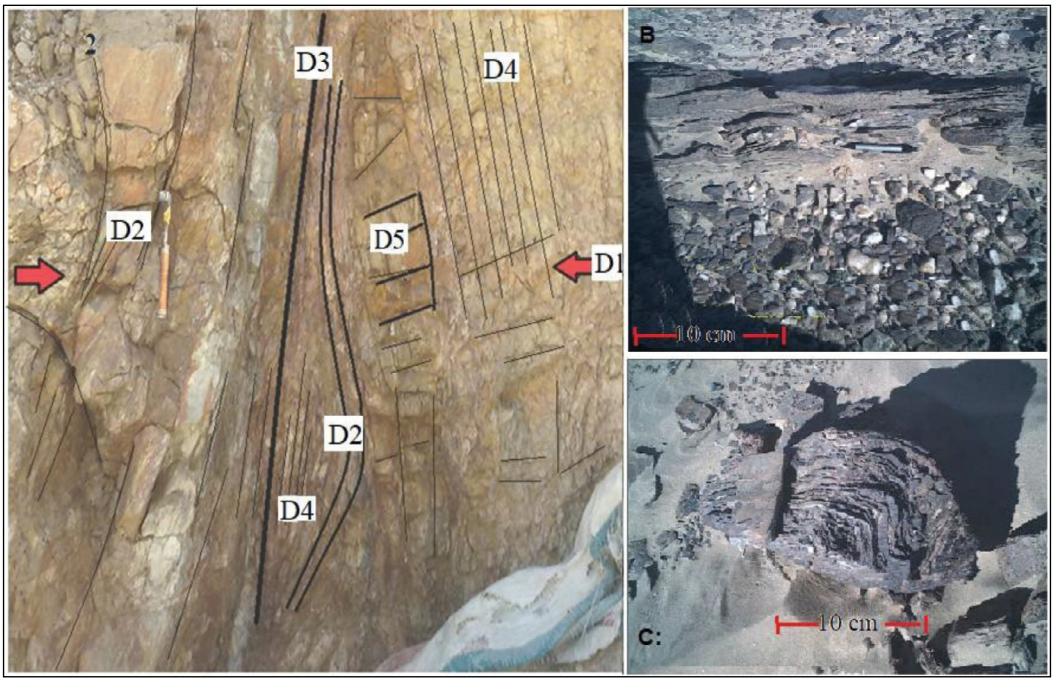

Figure 4- a) Vertical section across artisanal gold mining mega - pits illustrates the subsurface structural features, Elgaab area, b) pench and swelling - Hamadi, c) z - shape chevron fold - Hamadi.

brecciated recrystallized, white to pinkish, and vuggy which are the richest by gold contents. The wall rock alteration is limited and confined to the area adjacent to the quartz veins, generally from 0.7 m to 2.00 m wide. Sericitization, kaolinitization, iron oxides, and iron carbonate are dominant, with rare graphite and chlorite. The gold and associated elements in Elgaab gold mineralization are arsenic, chromite and nickel, with arsenic the main pathfinders. The minerals associated to gold mineralization, based on ore microscopic investigation, are pyrite, magnetite, covellite, and chalcopyrite (Figure 5).

Hamadi gold mineralization associated with anckerite, iron oxides and tourmaline as the pathfinder (Figure 6). In Sodri - Um Badir shear zone gold mineralization in hand spacemen display dark colours, rich in sphelerite, malachite, galena, pyrite and other sulphides mineral. Nuggets of visible gold are often seen around oxidized pyrite or insides the cavities.

Gammama gold mineralization associated with copper, lead and zinc (Figure 7), with no clear pathfinder element. The mineral associated to gold mineralization based on the ore microscopy investigation, are chalcopyrite, pyrite, marcasite, hematite, and magnetite. Adularia, anckerite are indicator minerals (keys elements) and tourmaline could be a pathfinder in prospecting for gold in the study area. Electron Microscope EDS graph shows that the gold is also associated with Pd, Palladium is a precious white metal has price higher than gold (Figure 8).

4. Geochemical Characteristics

4.1. Distribution of Gold and Associated Elements

The assay results of gold and associated elements in Elgaab area Cu, Pb, Zn, As beside Cr and Ni, indicate that the gold content in soil samples shows higher values (0.18 - 8.391 g/t) than those returned by both quartz veins (0.053 up to 2.93) and trenches samples (0.5 to 0.8 g/t). This disparity may be attributed to the secondary gold enrichment. Arsenic display the highest values when compared to the other trace elements. Cu, Pb, Zn, Ni, and Cr show low content and irregular distribution, except for Cr which

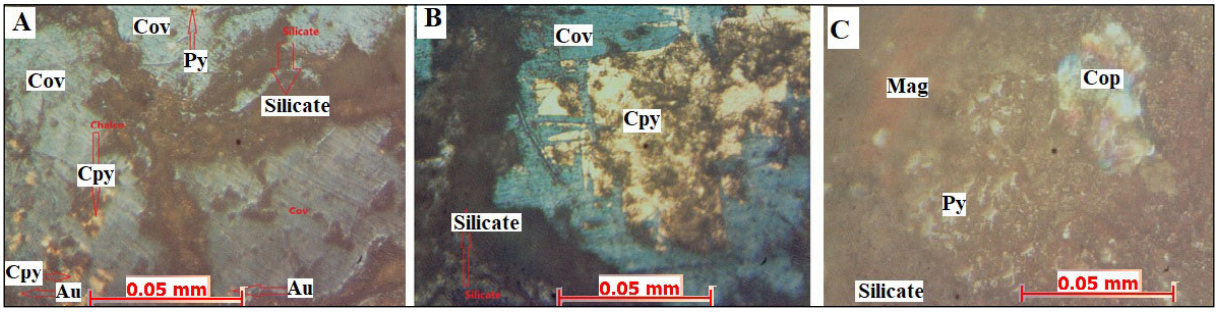

Figure 5- Light reflected microscope views of; a) pyrite (Py), primary chalcopyrite tarnished to yellow (Cpy) replaced by covellite pale blue (Cov), very find grained golden yellowish (Gol) and silicate dark grey (20X), b) primary chalcopyrite yellow (Cpy) replaced by covellite blue (Cov), and silicate dark grey and c) pyrite (Py), multi -colored native copper (cop), pale brown magnetite (Mag) and silicate dark grey (20X) from Elgaab area.

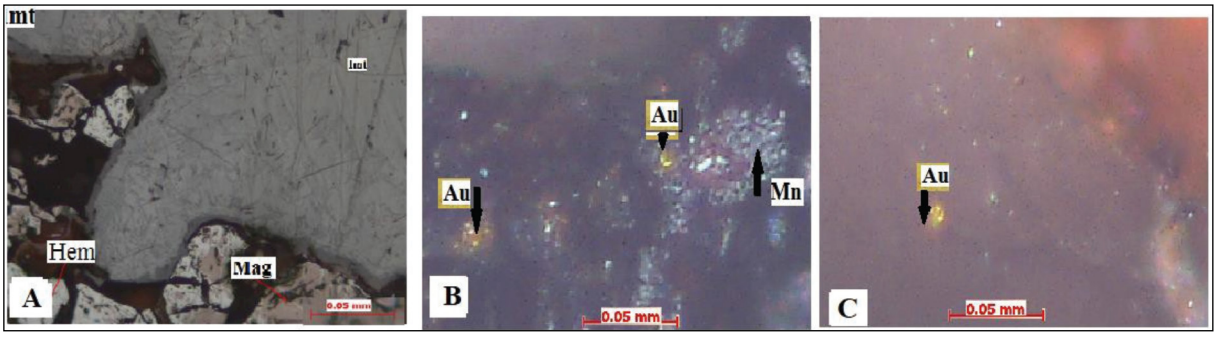

Figure 6- a), b) and c) Shows hematite, magnetite, manganese and pyrite is the most common minerals associated with gold in (Hamadi) Dom el Tor shear zone.

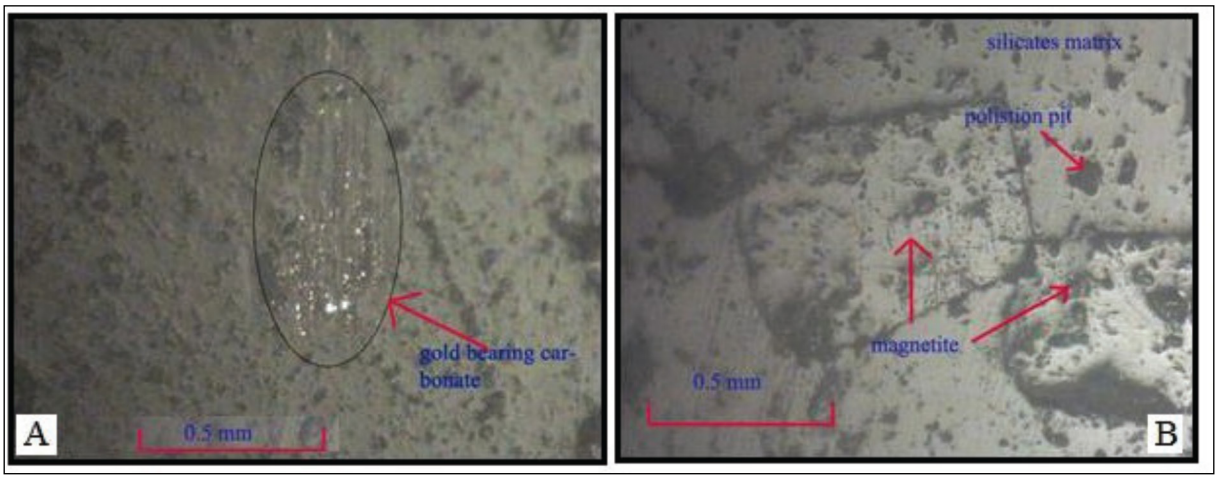

Figure 7- a) Shows gold bearing carbonate, Gammama (Sodari shear zone), b) photomicrograph shows cubic magnetite, Gammama.

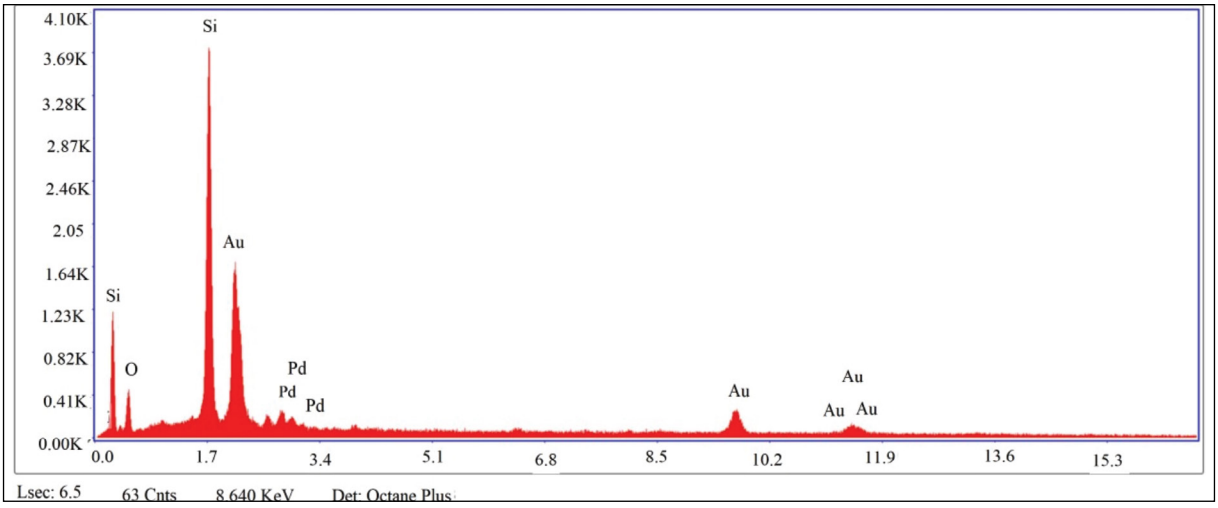

Figure 8- Electron scan microscope graph shows the gold associated with Pd.

has a medium concentration. Arsenic shows irregular but very high content that range between 197 - 17905 ppm. Zn; content range between (16 to 880 ppm). Trace elements Th, Ba, Co, Ga, Mo, Ge, W, V, Nb, Zr, Y, Sc, Rb - Sr, Hf, analysis results obtained from quartz veins samples reveal very low values. Except Ni, Cr, Pb, Zn and Cu shows relatively medium to high values. Cerium (Ce), shows very low value among all samples. Pb content range between (19 to 253 ppm) and (40 to 180 ppm) for quartz veins and soil samples from Elgaab mineralization zone, respectively single elements geochemical mapping "iso - concentrate map" is usually used as an effective tool for assign the areas of anomalous value as well as the trend of mineralization.

It is worth mentioning that, prospecting criteria or evidences for Cu, Pb and Zn, gossans - like and VMS mineralization in Elgaab and Hamadi areas are not recognized during this study. Meanwhile those criteria are recorded in North Kurdofan along Sodri - Umm Badir shear zones. The chemical analysis reveal high Au values ranging between 0.49 and 10.00 g/t, while Ag shows relatively medium values ranging between 3 and 5 ppm. Zn and Pb lead display low concentrations ranging between 8 and 129 ppm and 5 and 79 ppm, respectively. In contrast Cu shows the highest concentration values ranging between 14500 - 77200 ppm. Assay results of quartz veins samples, from Hamadi gold mine, Dom el Tor shear zone, reveal Au content vary between (0.11 to 10.25 g/t). The relative high coefficient of variation of Au

(156.75% - 252.6307%) suggests that Au is inhomogeneously, or irregular distributed in quartz veins when compare to Au content in soil. Cu has highly potential content (14500 - 772000 ppm), which is considered to be highly anomalous in Gammama - Sodri - um Badir shear zone the presence of sulphides, such as pyrite (FeS_2) chalcopyrite ($CuFeS_2$), and galena (PbS), could indicate shear-related massive sulphides mineralization at depth.

The histograms for Au, and associated Cu, Pb, Zn, Ni and Cr for the rocks and quartz veins samples in Elgaab area of study are displaying irregular distributions for the elements described. The histogram of frequencies shows the whole population in the curve of frequencies is bimodal. That means the whole population is split into 2 sub - populations background and anomalous (Figure 9). The high coefficient of variation indicate irregular erratic distribution of gold in quartz veins. While in Hamadi gold mine area the histogram of Au display same population, the Au content range between 0.49 - 10.00 ppm (Figure 10).

In Sodri - Um Badir shear zone gold mineralization histogram for Au, Ag, Zn, Pb and Cu displays irregular symmetrical distribution of Au, Zn, Pb and Cu while Ag shows regular symmetrical distributions (Figure 11).

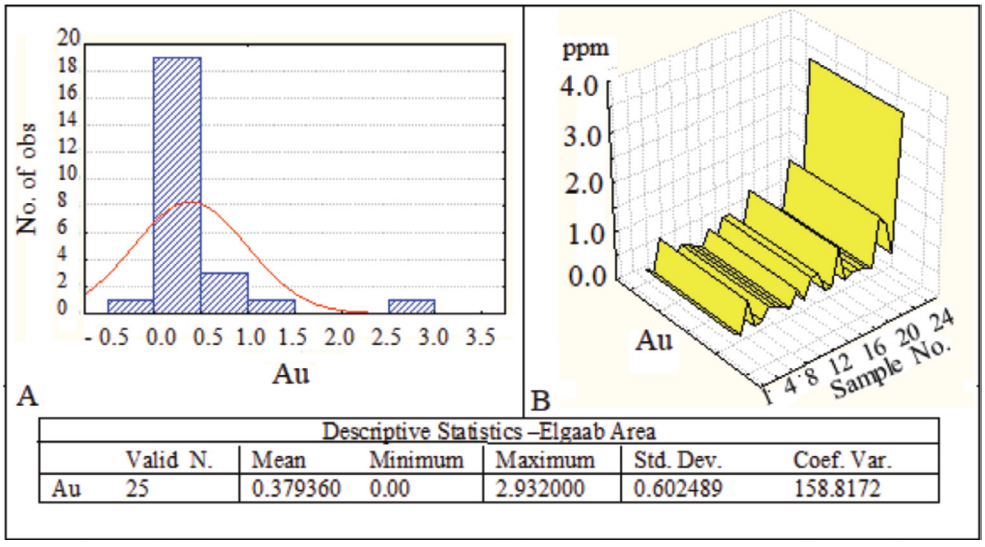

Descriptive Statistics –Elgaab Area

	Valid N.	Mean	Minimum	Maximum	Std. Dev.	Coef. Var.
Au	25	0.379360	0.00	2.932000	0.602489	158.8172

Figure 9- Hamadi area; a) histogram of Au and b) sequential graph.

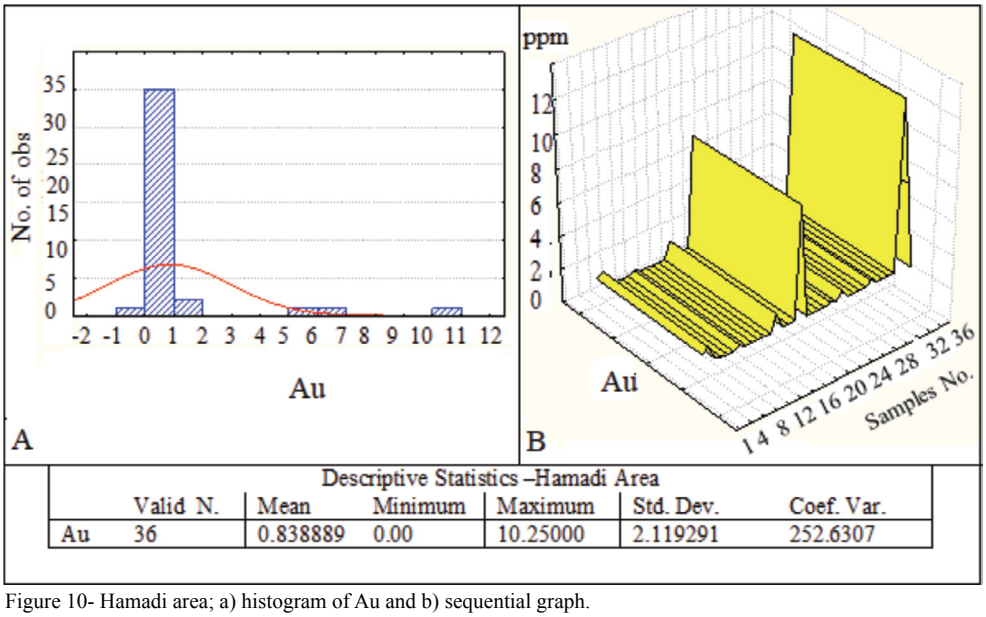

Descriptive Statistics –Hamadi Area

	Valid N.	Mean	Minimum	Maximum	Std. Dev.	Coef. Var.
Au	36	0.838889	0.00	10.25000	2.119291	252.6307

Figure 10- Hamadi area; a) histogram of Au and b) sequential graph.

4.2. Correlation

The proportion of quartz veins samples from Elgaab study area containing gold above the detection limit is 77.4%. Were the detection limit is 0.001 ppm, with mean value 4.416 ppm. The correlation matrix indicate that Cu versus Au show no correlation. Au versus Pb (0.05) and Zn (0.07) show very weak positive correlation. Au versus Cr (-0.02) show negative weak correlation. Au versus Ni (-0.10) show negative correlation. While Au versus As (0.90) shows very strong positive correlation, the correlation matrix display that Au versus Cu (0.45) has perfect correlation. The source of the high Cu content are possibly due to the associating chalcopyrite and malachite observed in auriferous quartz vein in the vicinity of the mineralization zone. Au versus Pb (-0.06) shows negative weak correlation, and Zn (0.49) shows positive perfect correlation, while Pb versus Cr and Ni show positive correlation. Pb versus As show weak positive correlation (Table 1).

The chemical analysis results reveals low values for Pb in both Elgaab and Sodri - Um Badir areas of study. Zn versus Au shows weak positive correlation. On other hand Zn shows no correlation with both Cu and Pb. Zn versus Ni shows weak positive correlation, and versus both Cr and As shows weak negative correlation. The chemical analysis results reveals low values for Zn in Sodri - Um Badir as compared to values obtained for Elgaab area of study. Zn and Pb were detected in hand specimens by their minerals ore sphelerite and galena, respectively. Although the chemical analysis results reveals low values, in Gammama site of Sodri - Um Badir shear zones (Table 2).

Numerous minerals deposit of economic potential have found to be occurring along shear zone and associated gashes and faults. This could be realized by detail exploration using advanced geophysics techniques and deep drilling. In this respect, the study

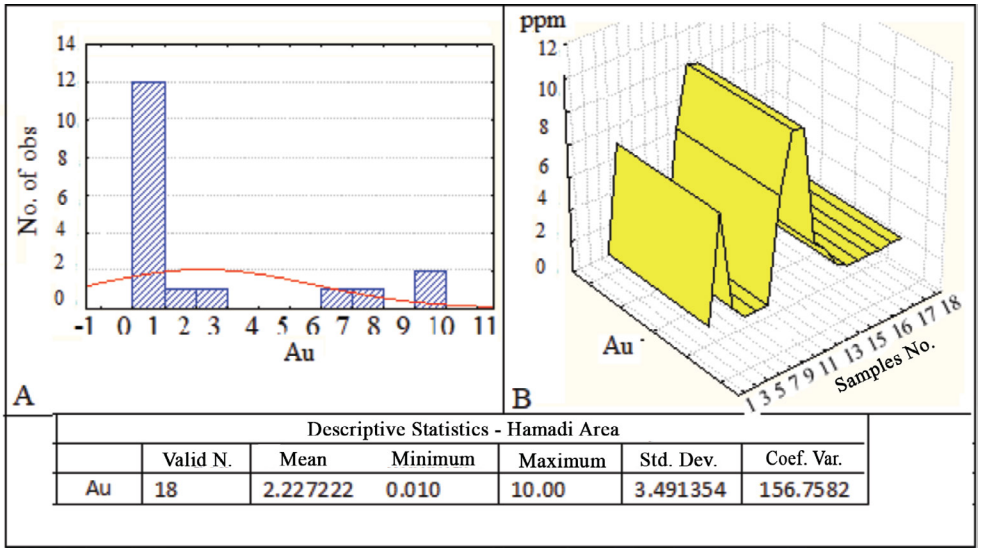

Descriptive Statistics - Hamadi Area

	Valid N.	Mean	Minimum	Maximum	Std. Dev.	Coef. Var.
Au	18	2.227222	0.010	10.00	3.491354	156.7582

Figure 11- Gammama area; a) histogram of Au and b) sequential graph.

Table 1- Correlations matrix (Elgaab) gold and associated elements.

	Au	Cu	Pb	Zn	Ni	Cr	As
Au	1.00						
Cu	-0.00	1.00					
Pb	0.05	-0.01	1.00				
Zn	0.07	0.05	-0.08	1.00			
Ni	-0.10	0.74	0.43	0.14	1.00		
Cr	-0.02	0.05	0.58	-0.21	0.36	1.00	
As	0.90	0.05	0.11	-0.08	-0.01	-0.04	1.00

Table 2- Correlations matrix (Gammama) gold and associated elements.

	Au	Ag	Zn	Pb	Cu
Au	1.00				
Ag	-0.118319	1.00			
Zn	0.49	0.35	1.00		
Pb	-0.06	0.15	0.54	1.00	
Cu	0.45	0.03	0.326	0.33	1.00

points to five selected targets for future gold follow up exploration (Figure 12).

5. Results

The areas of study intersected by three major shear zones namely; Elgaab, Gammama in Sodri - Um Badir and Hamadi mine of Dom el Tor shear zone. All zones constitute huge flat area of sandy sheets covering both Phanerozoic sediments and underlying basement rocks. Volcano - sedimentary sequences of Neo-Proterozoic and partially Meso - Proterozoic granitic gneiss were intruded by syn to late granitoid intrusions, and later by post orogenic granite and felsic dykes. The gold - bearing quartz veins are mainly developed as fracture filling injected along the foliation planes of green-schist rocks, formed at different stages during the Pan - Africa Orogenic events (900 – 550 Ma.).

The geological, lithological, structural criteria and geochemical mapping indicate that the mineralization domains are confined to the NNE shear and related tensional gashes. Thus, Elgaab gold mineralization could be classified as epigenetic shear - related mineralization. The process and the genesis of gold mineralization emplacement may had taken place after the intrusion of batholithic granitoids particularly diorite and granodiorite, which were believed to be the source of energy that triggered the hydrothermal solutions during orogenic events. While the heat generated during the shearing events could be responsible for re-mobilization and re-concentration (enrichment) of gold and associated elements across the area of study, in similar process as documented in Arabian - Nubian Shield.

The assay results of Au and the associated Cu, Pb, Zn, As, Cr and Ni in Elgaab area indicate that the

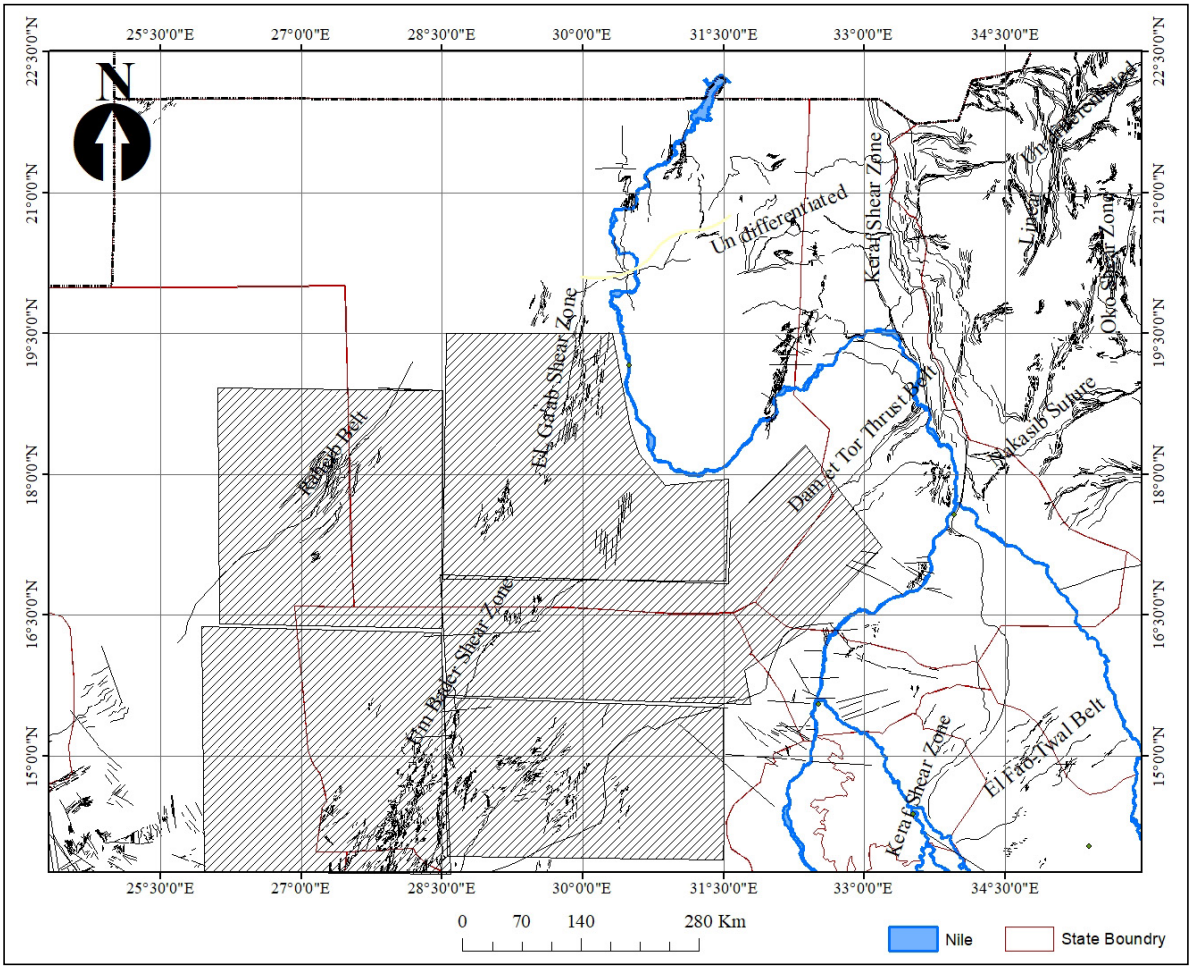

Figure 12- Location map of the selected five prospective areas for future gold exploration.

Au content in the soil samples are of higher values content (0.18 - 8.391 g/t) than those revealed by both primary lodes (0.053 up to 2.93 g/t) and trenches samples (0.5 to 0.8 g/t) respectively. The relative high coefficient of variation of Au (158.8%) suggests that Au is inhomogeneously and irregularly distributed in quartz veins. Assay results of samples from Hamadi gold mine quartz veins reveal that Au content varies between 0.11 and 10.25 g/t. The mineral associated with gold mineralization are chalcopyrite, pyrite, marcasite, hematite, and magnetite. Adularia and ankerite are indicator minerals (keys elements), whereas tourmaline could be a pathfinder. Electron Microscope - Electron dispersion spectrometry (EDS) shows that the Au is also associated with Cu and Pd. The results of analysis of quartz veins samples from Gammama in Sodri - Um Badir shear related - gold mineralization indicate that the elements associated with Au, are Ag, Zn, Pb and Cu. The Au content ranges between 0.49 and 10.00 ppm, while Cu has anomalous values as higher as 77200 ppm. The presence of sulphides, such as pyrite (FeS_2) chalcopyrite ($CuFeS_2$), and galena (PbS), along Sodri - Umm Badir shear zones in North Kurdofan suggests the presence of shear - related massive sulphides mineralization at depth.

Comparison between Elgaab shear zone gold mineralization, Dum el Tor shear - related gold mineralization and Sodri - Um Bader shear mineralization indicates similarities in lithological characteristics of Upper Proterozoic rock assemblages. The NNE - SSW and NE - SW structural grain of Pan African Arabian- Nubian Shield were dominant, as well as the mode of occurrences of the ore bodies, and the grade of metamorphism. Regardless of those similarities there are broad variations in the metallogenic characteristics such as mineral association, pathfinder, and grade of gold content.

The results of this study define new metallogenic province in the region west of the River Nile. West of Dongla the province constitutes a huge sandy area lying between Elgaab, Dam el Tor and Sodri – Umm Badir shear zones cover the Phanerozoic sediments and basement assemblages. Nemours minerals deposit of economic potential have found to be occurring along shear zones and associated gashes and faults. This could be further realized by detailed exploration using advanced techniques and deep drilling. In this respect, the study pointed out five potential targets for future gold exploration and evaluation, according to litho - stratigraphic similarity, geochemical and geotectonic characteristics.

Acknowledgment

This study was completed as a part of thesis submitted for the degree of Doctor of Philosophy (PhD) in Geological Sciences faculty of petroleum and minerals, Alnileen University, Khartoum. I would like to thanks to Professor Badr el Din Khalil and Dr. Mohammed Yahia for their contributions to develop this article.

References

Abdel Rahman, E. M., El Mahi J. E. 2006. A new discovery of base metals - precious metals mineralization in North Kordofan, Sudan: implications for trans - shield mineralized corridors. The 9th Arab Conference for Minerals Resources, Jeddah, Saudi Arabia, 33.

Abdelsalam, M. G., Dawoud, A. S. 1991. The Kabus ophiolite mélange, Sudan, and its bearing in the western boundary of the Nubian Shield. Journal of the Geological Society, London 148, 83-92.

Abdelsalam, M. G., Stern, R. J., Schandelmeier, H., Sudan, M. 1995. Deformational history of the Keraf Zone in NE Sudan. Journal of Geology 103, 475-491.

Harms, U., Darbyshire, D. P. F., Denkler. T., Hengest, M., Schandelmeier, H. 1994. Evolution of the new Proterozoic Delgo suture zone and crustal growth in Northern Sudan: geochemical and radiometric isotope constrain. Geologische Rundschau 83, 591-603.

Kröner, A., Greling, R., Reischmann, T., Husein, I. M., Stern, R. J., Durr, S., Kruger, J., Zimmer, M. 1987. Pan African crustal evaluation in the Nubian segment of the North East Africa. American Geophysical Union Series 17, 235-257.

Kuster, D., Liegeois, J. P. 2001. Sr, Nd isotopes and geochemistry of the Bayuda Deserthigh - grade metamorphic basement (Sudan): an early Pan - African oceanic convergent margin, not the edge of the East Saharan ghost craton. Precambrian Research 109(1-2), 1-23.

Schandelmeier, H., Richter, A. 1991. Brittle shear deformation in Northern Kordofan, Sudan: Late Carboniferous to Triassic reactivation of Precambrian fault systems. Journal of Structural Geology 13(6), 711-720.

Stern, R. G., Reischman, T., Bender, R., Dawoud, A. S. 1994. Precambrian basement around Wadi Halfa; a new prospective of evolution of east Sahara Carton. Geologische Rundschau 83, 564-575.

Rose Geo. 2018. A report submitted to GRAS within the frame work of technical cooperation agreement. GRAS, Report No: 1 (2), Moscow (unpublished).

Vail, J. R. 1985. Pan African (Late Precambrian) tectonic terrains and reconstruction of the Arabian Nubian Shield. Geology 13, 839-842.

Bulletin of the Mineral Research and Exploration

http://bulletin.mta.gov.tr

Evaluation of thermomagnetic properties and geothermal energy potential in parts of Bida Basin, Nigeria, using spectral analysis

Churchill Chukwunonso OKONKWO[a*], Augustine Ifeanyi CHINWUKO[b], Ajana Godwin ONWUEMESI[b], Emmanuel Kenechukwu ANAKWUBA[b], Sunday Okechukwu OKEKE[a] and Ayatu Ojonugwa USMAN[c]

[a]*Federal College of Education Umunze, Department of Physics, Nigeria*
[b]*Nnamdi Azikiwe University, Department of Geological Sciences, Awka, Nigeria*
[c]*Alex Ekwueme Federal University, Department of Physics / Geology / Geophysics, Ndufu - Alike, Ebonyi, Nigeria*

Research Article

Keywords:
Lineament, Rose Diagram, Magnetic Sources, Curie Isotherm, Thermal Properties.

ABSTRACT

Thermomagnetic properties and geothermal energy potential in parts of Bida Basin, Nigeria have been evaluated using spectral analysis of integrated nine aeromagnetic data. The study area covering 27.225 km^2 of aeromagnetic data was examined and construed in order to delineate the thermal properties of the country-rock in the area. The result of the visual inception of the residual map reveals that the area comprises an extremely irregular pattern of magnetic intensities that range from 220 to 240 nT. Two structural features of folding evidence were also delineated in the area namely; uplift and depression. The result of the lineament structures from the shaded relief map and Rose diagram depicts NE-SW as the major trend with the minor trend is NW - SE. Two depths to magnetic sources were distinguished in the area: the shallower bodies which vary from 1.27 to 1.96 km and the deeper bodies that vary from 2.01 to 4.27 km. The result also shows an average depth to the centroid as 12.97 km in the area. The thermomagnetic properties analysis show average values of 23.12 km Curie isotherm, 25.27 °C/km geothermal gradients and 63.17 mWm^2 heat flow in the area. The study concludes that the study area possesses good potential quality for geothermal energy generation and exploration.

Received Date: 16.04.2020
Accepted Date: 17.09.2020

1. Introduction

The major problem threatening the Nigerian economic space is the epileptic power supply situation in the country and gap in accessing information on alternative energy resources. The capacity of Nigeria to adequately cater for the energy demands of its ever growing population is seriously inadequate if further effort is not invested in the search for renewable, sustainable and cleaner energy resources capable of meeting this growing demand. Therefore, there is great need to investigate and harness the geothermal energy potentials for satisfaction of the nations energy needs especially around the fields of lighting, transportation, communication and others.

Accordingly, recent researches have shown that the geothermal energy sources are viable in those regions that were underlain by basement rocks, which comprises metamorphic and igneous rocks that were formed from the interior part of the earth (Chukwu et al., 2017; Abraham et al., 2014; Anakwuba and Chinwuko, 2015). Surprisingly, two-third of Nigeria

Citation Info: Okonkwo, C. C., Chinwuko, A. I., Onwuemesi, A. G., Anakwuba, E. K., Okeke, S. O., Usman, A. O. 2021. Evaluation of thermomagnetic properties and geothermal energy potential in parts of Bida Basin, Nigeria, using spectral analysis. Bulletin of the Mineral Research and Exploration 165, 13-30.
https://doi.org/10.19111/bulletinofmre.796381

**Corresponding author: Churchill Chukwunonso OKONKWO, chukschurchill@yahoo.com*

land mass is covered by these rock types, but little or no attention has been paid to the chase for geothermal energy exploration. As a result, there has been a gap in thermomagnetic properties information within Nigeria and the study area is no exception. Furthermore, considering the environmental impact of petroleum products during and after exploration couple with decline in oil and gas production in our country, it has become imperative for our nation to explore the alternative source of energy called geothermal energy in order to meet our energy needs.

However, thermomagnetism can be defined as the magnetism that originated from the action of heat or caused by the action of heat within the subsurface. Thermomagnetic properties such as Curie isotherm depth, subsurface geothermal gradient and heat flow are essential in exploration of geothermal energy. According to several authors (Burke, 1972; Chinwuko et al., 2012; Okonkwo et al., 2012; Abraham et al., 2014; Abraham et al., 2015; Biswas et al., 2017; Chukwu et al., 2017), the palaeomagnetic signal of rocks (including the thermomagnetic properties) occurs primarily due to the existence of iron - bearing oxide solid solutions with the spinel crystal structure (like titanomagnetites). These authors also established that there are possibilities of these minerals to obtain strong and stable remanent magnetization due to the presence of Curie temperature, saturation magnetization, and remanence properties of the rock based on their fundamental crystal chemical state and microstructure of minerals. Actually, the thermomagnetic properties evaluation is a geophysical method which can serve the purpose of geothermal data in such areas where borehole data are absent or missing, and the study area is no exception (Bhattacharyya and Leu, 1975; Ross et al., 2006; Saibi et al., 2015; Biswas, 2015; Singh and Biswas, 2016; Biswas and Sharma, 2016,).

Consequently, this research focuses on the evaluation of thermomagnetic characteristics of rock units in order to deduce the geothermal energy potential of parts of Southern Bida Basin, Nigeria, through the use of spectral analysis technique. This approach will outline the anomalous bodies across the area through estimation of the depth to magnetic sources, the depth to the centroid and crustal temperature information in the area of study. The study will also ascertain the lineament patterns along with the real view of the Basin. The researchers are optimistic that this research will contribute to the vast potential of Nigeria's untapped, renewable and sustainable energy resources and heat flow information.

1.1. Geographic and Geologic Background

Geographically, the area under investigation lies between latitudes 8º 00 - 9º 30' N and longitudes 5º 30 - 7º 00' E (Figure 1) with an areal extent of 27.225 km^2. Geologically, the area is situated within the Southern Bida Basin, Nigeria and it is associated with sedimentary terrain which comprises alluvium deposits of Cenezoic Era. However, the Basement Complex rock intruded within and around the study area account for the great fracturing observed in the area. According to Adeleye (1974) and Obaje et al. (2013), the Bida Basin sometimes referred to as Nupe Basin can be classified as an intracratonic sedimentary basin that trend in NW - SE direction and it widens from Niger State precisely Kontagora to regions feebly outside Lokoja region of Kogi State in the southern part.

Notwithstanding, the stratigraphic successions of the southern Bida Basin in Figure 1, reveals that the Lokoja Formation being the oldest material is overlain by the Patti Formation which is as well overlain by the Agbaja ironstone Formation (Obaje et al., 2013; Ojo and Akande, 2012). According to some authors, the Campanian Nkporo and Enugu Formations of northern Anambra Basin have some lateral equivalents with the Lokoja Formation (Ojo and Akande, 2012). Also, the Mamu Formation of Anambra Basin possesses some lateral equivalents with three formations of Bida Basin namely; Patti, Bida and Lokoja Formations. More so, the Ajalli sandstones which are member of Ajalli Formation have its laterally equivalent in the Bida Basin as the Patti Formations (Ikumbur et al., 2013; Obaje et al., 2013; Ojo and Akande, 2012).

2. Research Methodology

The method applied in this research involved the use of nine (9) aeromagnetic data sheets: 183 (Egbako), 184 (Bida), 185 (Paiko), 204 (Pategi), 246 (Baro), 206 (Gulu), 225 (Isanlu), 226 (Aiyegunle) and 227 (Kotonkarfi) (Figure 2). These data were obtained from Nigeria Geological Survey Agency (NGSA), which were integrated to generate a total magnetic

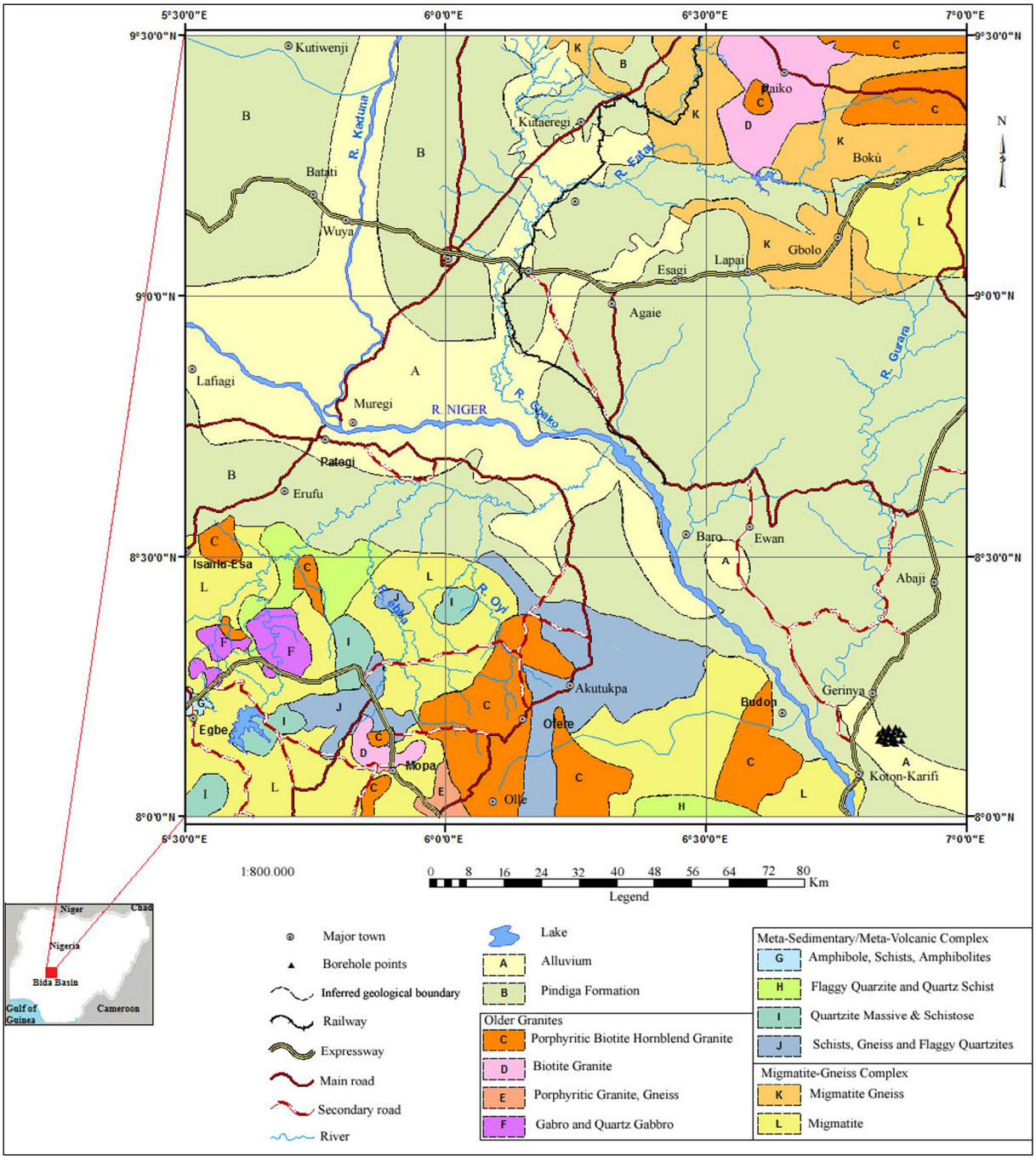

Figure 1- Local geological map of the study area (modified after Obaje et al., 2013 and Petters,1978).

intensity map (Figure 3) and the residual data were analyzed with the aid of spectral analysis. The visual inception analysis was carried out on the magnetic maps based on magnetic closures and lineament delineation through the azimuth direction of the structural lineaments. With the aid of shaded relief maps produced from four different horizontal position light angles - HPLA (0°, 45°, 90°, and 135°) at constant vertical position light angle - VPLA (0°), paved way for perfect delineation of lineament orientation across the area. The result of lineament delineation serves as key parameters that were keyed into the Grapher - 5 software package in order to generate a Rose diagram for the area.

More so, the integrated data which became the total magnetic intensity (TMI) data (Figure 3) were subjected to filtering using a generated linear trend

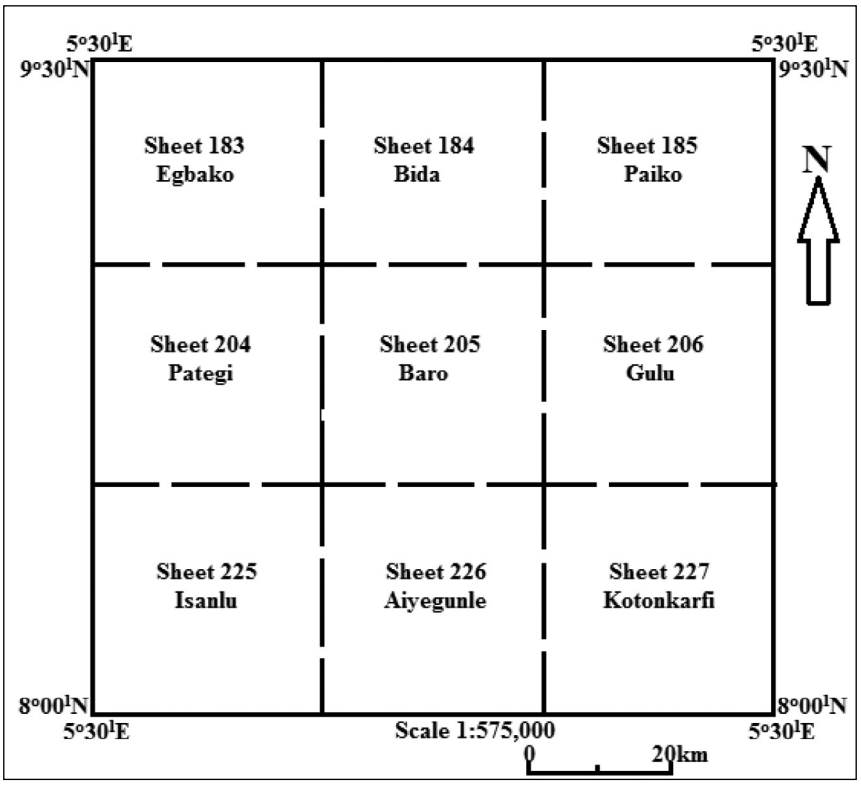

Figure 2- Acquired nine sheets of aeromagnetic data.

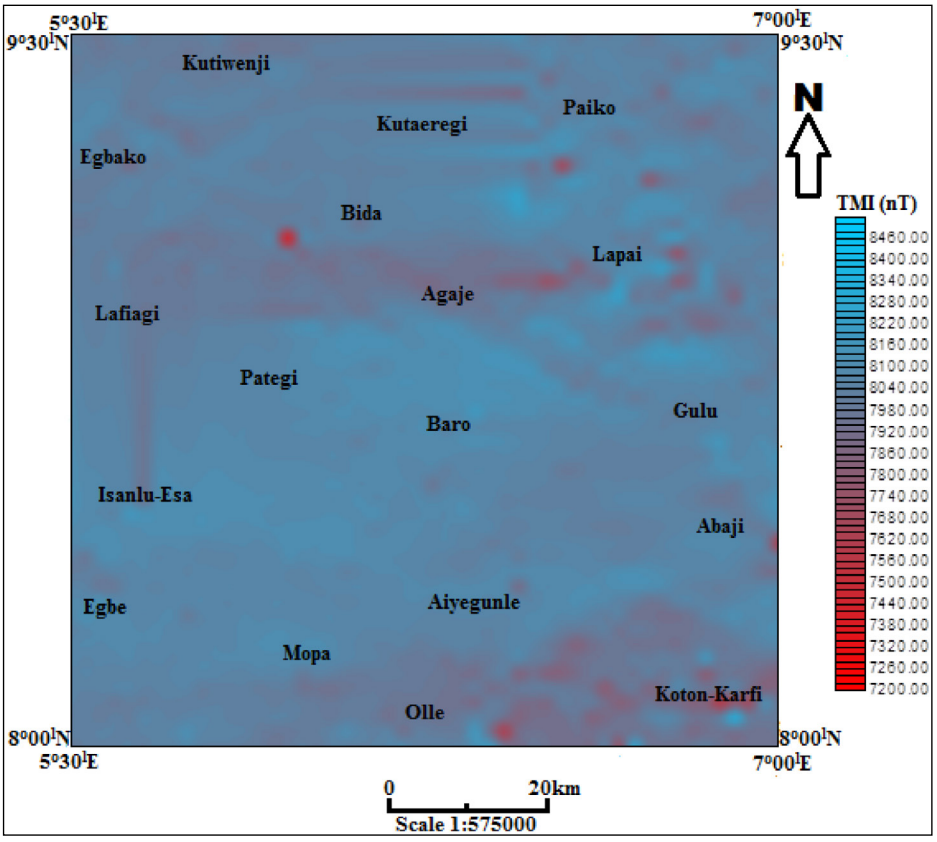

Figure 3- TMI map of Bida and its environments (contour interval ~ 20 nT).

surface (equation 1) of the multiple regression techniques as discussed by previous authors (Spector and Grant, 1970; Chinwuko et al., 2012; Ikumbur et al., 2013; Chinwuko et al., 2014). This filtering was carried out in order to separate both the regional and residual magnetic anomalies.

$$S(a, b) = 1452.07b - 77.08a - 4658.08 \quad (1)$$

Where, S (a, b) = the regional value; a = the latitude and b= the longitude.

In addition, the regional trend surface data obtained were deducted from the total magnetic field intensity data in order to generate the residual magnetic data (Figure 4). Thus, the residual anomaly data were subjected to spectral analysis in order to obtain the depth to magnetic sources and thermal properties within the area. The spectral analysis is a mathematical tool associated with Discrete Fourier Transform method which has been described and used by some many authors such as Spector and Grant (1970), Bhattacharyya and Leu (1975), Onwuemesi (1995), Onwuemesi (1997), Chinwuko et al. (2014), Pamukçu et al. (2014) and others.

Subsequently, the result of the spectral analysis was used to compute depth to the magnetic sources; delineate Curie isotherm depth, geothermal gradient along with mantle heat flow (see equations 2, 3 and 4). Immediately after obtaining the main amplitude, the next was to obtain the gradient of the linear segments of the first and second longest wavelengths of the spectrum as discussed by previous authors (Bhattacharyya, 1966; Bhattacharyya and Leu, 1975; Okubo et al., 1985; Tanaka et al., 1999; Nwankwo and Ekine, 2010; Frashëri et al., 2011; Mandal et al., 2013; Abraham et al., 2015; Singh and Biswas, 2016; Ojonugwa et al., 2018).

Then, the basal depth of the magnetic source or Curie depth (Z_b) was calculated from the equation of Bhattacharyya and Leu, (1975) that contains the depth to centroid (Z_o) and the depth to the top boundary (Z_t) as shown in equation 1 below:

$$Z_b = 2Z_o - Z_t \quad (2)$$

According to Tanaka et al. (1999), Curie temperature (θ) can be obtained from the Curie point depth (Z_b) and the geothermal gradient (dT/dZ) using

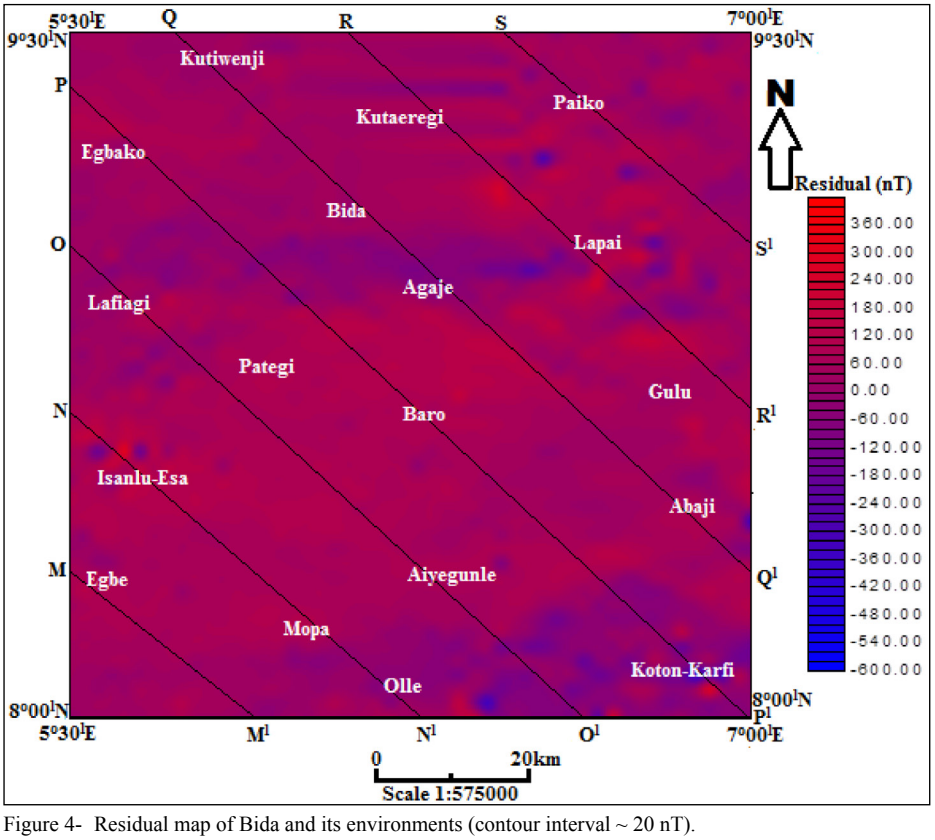

Figure 4- Residual map of Bida and its environments (contour interval ~ 20 nT).

equation 2, provided that there are no heat sources or sinks between the earth's surface and the Curie point depth.

$$\theta = \left[\frac{dT}{dZ}\right] Z_b \quad (3)$$

More so, Tanaka et al. (1999) established a mathematical relationship between the Curie point depth (Z_b) and the heat flow (q) as shown in equation 3:

$$q = \lambda \left[\frac{\theta}{Z_b}\right] \quad (4)$$

In this research, the Curie point temperature (θ) of 580 °C and thermal conductivity (λ) of 2.5 $Wm^{-1}°C^{-1}$ as average for igneous rocks were used as standard according to Nwankwo et al., 2010.

All the results obtained were used to generate distribution maps for all the key parameters in order to delineate the structural configuration within the area. Lastly, areas with geothermal energy potential were delineated using integrated geological and geophysical data.

3. Findings and Interpretation

3.1. Visual Interpretation

The visual assessment of total magnetic intensity and residual anomaly maps in the area depicts that there are complex patterns of magnetic signatures which consist of both small and lengthy wavelengths (Figures 3 and 4). According to Ikumbur et al. (2013), this variation in amplitude of the anomaly within the study area implies that there are evidence of different causative sources which are associated with various magnetic intensities, such as the magnetic intensity in the area which range from 7200 to 8460 nT and -220 to 240 nT respectively. Around Paiko, Kutaeregi, Koton-karfi, Bida, Lapai, Agaje, and Aiyegunle areas, the total magnetic intensity (TMI) and residual anomaly maps depict the underlying basement as having magnetic intensities. There are strong evidences of igneous intrusion when juxtaposed with the geologic map of the area. Indeed, these areas mentioned above possess mostly close - spaced contour lines and this implies that these areas are marked by numerous closed contours, which could serve as an indicative of igneous intrusions which usually contain aggregate of mineral deposits as evident in the study area like Koton - Karfi, Abaji, Bida and Paiko areas.

3.2. Lineament Trend

The major lineament structural trends defined from the shaded relief map (Figure 5) are NE - SW while the minor trends are visible along E - W and NW - SE directions. The lineament trends obtained here is in confirmation with previous studies carried out within the Bida Basin and its surrounding Basement Complex (Ikumbur et al., 2013; Obaje, et al., 2013 and Ojonugwa et al., 2018). Juxtaposing these lineaments on the geological map of the area, it depicts that the lineament orientations are predominately within the area underlain by basement rocks compared with the area covered by sedimentary basin. Hence, the researchers can deduced that there are numerous tectonic activities going on within the area due to high concentration of structural lineaments across the area (Figure 5).

Furthermore, the structural configuration of the study area is also confirmed by the generated Rose diagram (Figure 6), in order ascertain the particular geologic age of rocks in the area as suggested by Anudu et al., (2012). As a result, the Rose diagram (Figure 6) has shown clearly that the prominent trends in the area are NE - SW and NNE - SSW, whereas, the minor trends occur along E - W and NW - SE directions across the area. According to previous works such as, Ikumbur et al. (2013), Obaje et al. (2013), Anakwuba and Chinwuko, (2015) and Ojonugwa et al. (2018), three of the identified trends namely; NE - SW, NNE - SSW and NW - SE within the study area are regarded as Pan - African Orogeny while the E - W might have occurred during the era of Pre - Pan - African Orogeny.

3.3. Identification of Magnetic Anomaly

In order to identify various anomalies across the study area, seven different profiles were taken on the residual anomaly map (Figure 4); M - M^1, N - N^1, O - O^1, P - P^1, Q - Q^1, R - $R^1$and S - S^1. These profiles were taken perpendicular to the direction of the magnetic anomalies. The profile results revealed a total of thirty nine (39) anomalies across the study area (Figure 7). The identified anomalies occur in peak and trough patterns and they are ranked from anomaly 1 - 39 (Figure 7).

3.4. Depth to the Magnetic Sources

The magnetic anomalies were subjected to spectral analysis in order to obtain the depth to the causative

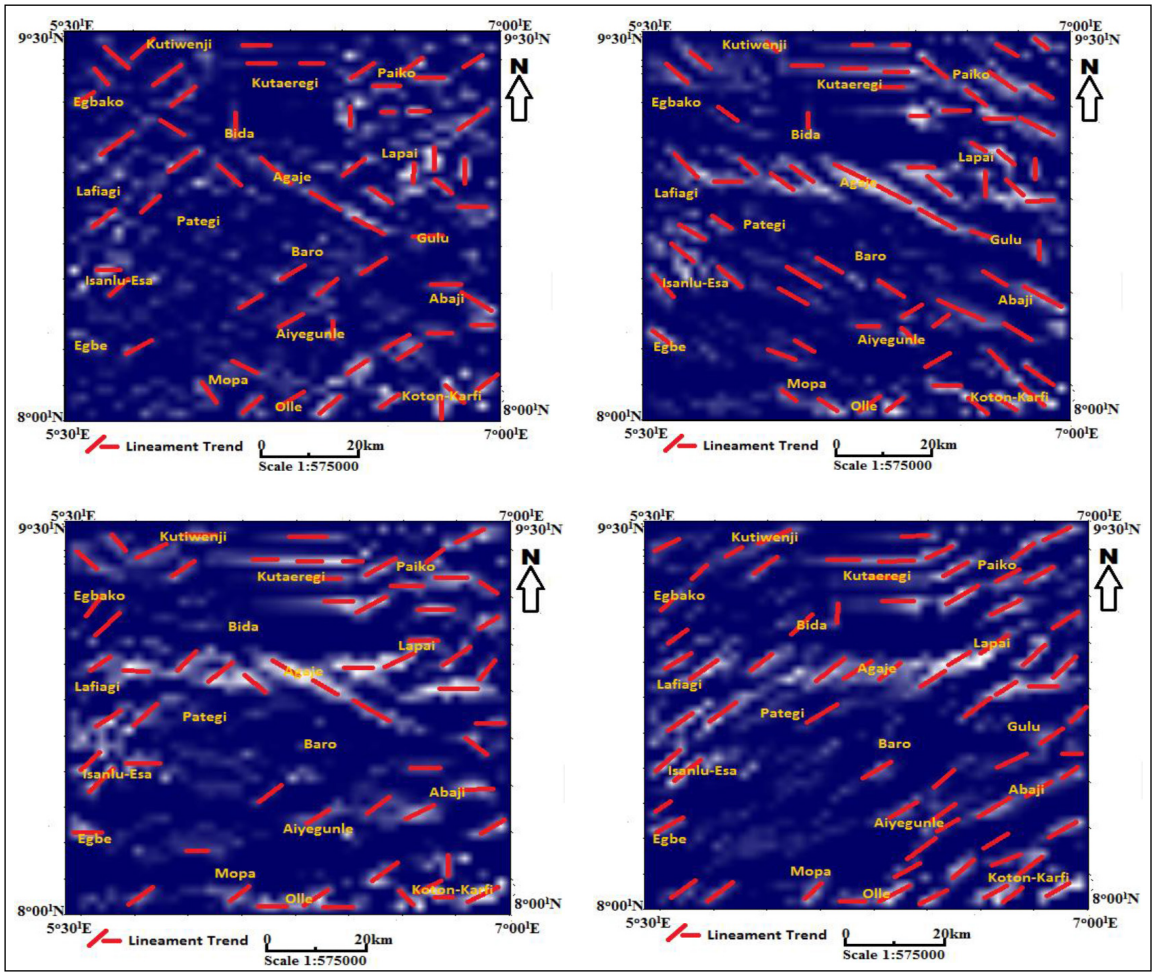

Figure 5- Shaded relief maps showing lineament trend in the area. a) HPLA-0° and VPLA-0°, b) HPLA-45° and VPLA-0°, c) HPLA-90° and VPLA-0°, d) HPLA-135° and VPLA-0 °.

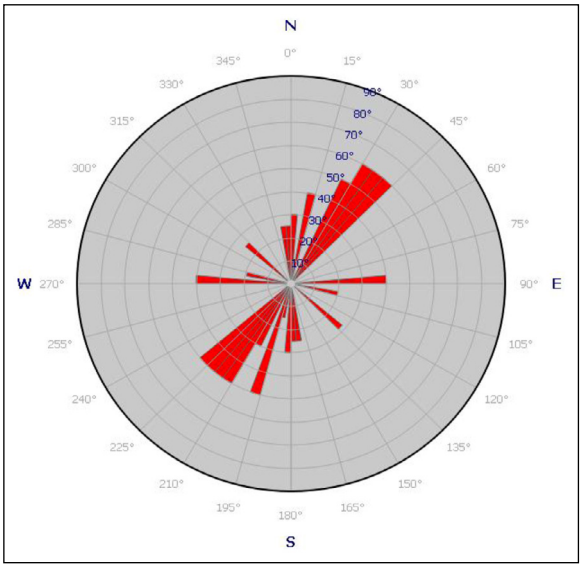

Figure 6- Rose diagram showing lineament trend across the study area.

bodies or magnetic sources around the study area (Figure 8). The spectral analysis result depicts two magnetic sources, namely; the shallower bodies which vary from 1.27 to 1.96 km and the deeper bodies which vary from 2.01 to 4.27 km (Table 1). However, the depth to the centroid obtained through the spectral analysis depicts depth range from 9.79 to 15.75km across the study area (Table 1).

Consequently, a basement relief map of the study area was produced using depth to the top of magnetic sources (Figure 9). The depth of basement is deeper in the southern and central part of the study area trending northwest - southeast direction whereas, at other parts of the area such as Kutawenji, Lafiaji, Koton - Karfi and Lapai areas have shallower sources (Figure 9). More so, the 3 - D surface plot of depth to the top of the magnetic sources shows presence of structural features such as peaks (uplifts) and depressions

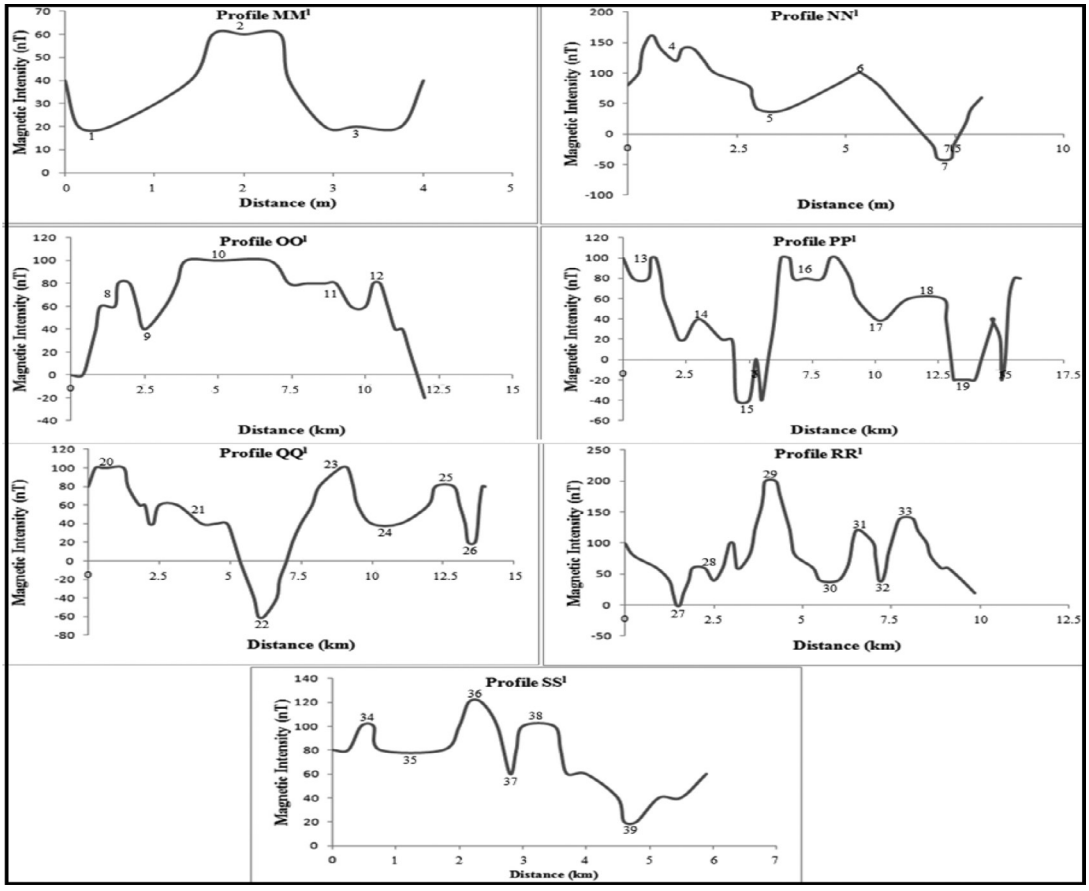

Figure 7- Graphs of profiles within the study area.

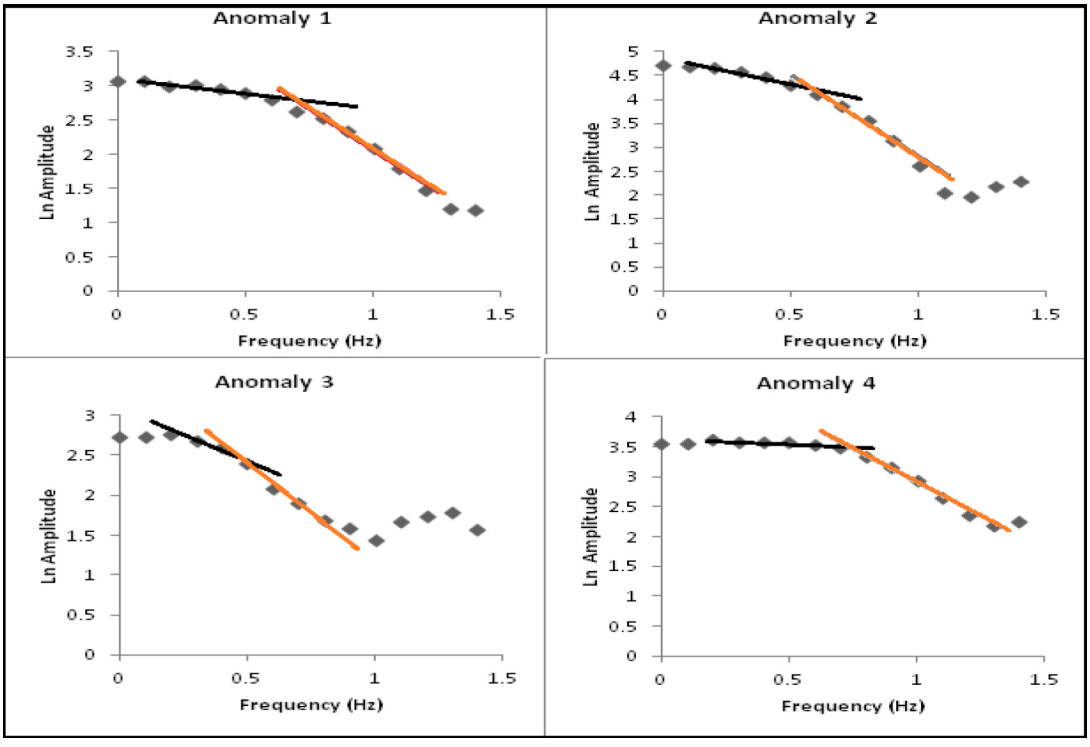

Figure 8- Representative spectral graph in the area.

Table 1- Thermomagnetic parameters estimation from spectral analysis.

	Spectral Analysis				
Anomaly	Depth to the top (km)	Depth to the Centroid (km)	Curie Depth (km)	Geothermal gradient (ºC/km)	Heat flow (mWm2)
1	2.89	13.17	23.45	24.733	61.834
2	3.4	12.04	20.68	28.046	70.116
3	3.53	14.18	24.83	23.359	58.397
4	1.27	12.53	23.79	24.380	60.950
5	3.22	11.88	20.54	28.238	70.594
6	3.47	14.24	25.01	23.191	57.977
7	3.45	13.91	24.37	23.800	59.499
8	2.58	12.36	22.14	26.197	65.492
9	2.84	11.49	20.14	28.798	71.996
10	3.59	15.75	27.91	20.781	51.953
11	3.2	13.18	23.16	25.043	62.608
12	1.96	12.29	22.62	25.641	64.103
13	3.06	14.41	25.76	22.516	56.289
14	3.55	13.98	24.41	23.761	59.402
15	2.16	10.67	19.18	30.240	75.600
16	3.23	11.94	20.65	28.087	70.2179
17	4.09	13.86	23.63	24.545	61.363
18	2.14	12.09	22.04	26.316	65.789
19	4.27	14.21	24.15	24.017	60.041
20	3.88	13.72	23.56	24.618	61.545
21	2.31	12.88	23.45	24.733	61.834
22	2.56	11.96	21.36	27.154	67.884
23	3.89	12.75	21.61	26.839	67.099
24	3.07	13.29	23.51	24.670	61.676
25	3.74	13.15	22.56	25.709	64.273
26	2.18	11.87	21.56	26.902	67.254
27	2.56	14.33	26.1	22.222	55.556
28	1.69	14.04	26.39	21.978	54.945
29	1.73	12.81	23.89	24.278	60.695
30	2.85	13.45	24.05	24.116	60.291
31	2.01	13.21	24.41	23.761	59.402
32	1.32	11.66	22	26.364	65.909
33	2.84	10.79	18.74	30.950	77.375
34	1.86	12.31	22.76	25.483	63.708
35	2.92	13.18	23.44	24.744	61.860
36	2.97	14.07	25.17	23.043	57.608
37	1.73	11.45	21.17	27.397	68.493
38	2.88	13.82	24.76	23.425	58.562
39	3.16	12.99	22.82	25.416	63.541
Average	2.82	12.97	23.12	25.277	63.173

(troughs) within the area. Around Agaje, Egbako, Olle, Mopa and Abaji areas, there are visible linear depressions and these areas reveal higher sediments than the other parts such as Kutaeregi, Paiko, Lapai, Lafiagi, Aiyegunle, and Koton - Karfi areas which have prevalent uplifts (peaks) in conjunction with lower sedimentary thicknesses (Figure 10). The presence of these peaks (uplifts) suggests that there are numerous intrusive bodies around these areas; as a result, they are more tectonically active than the areas associated

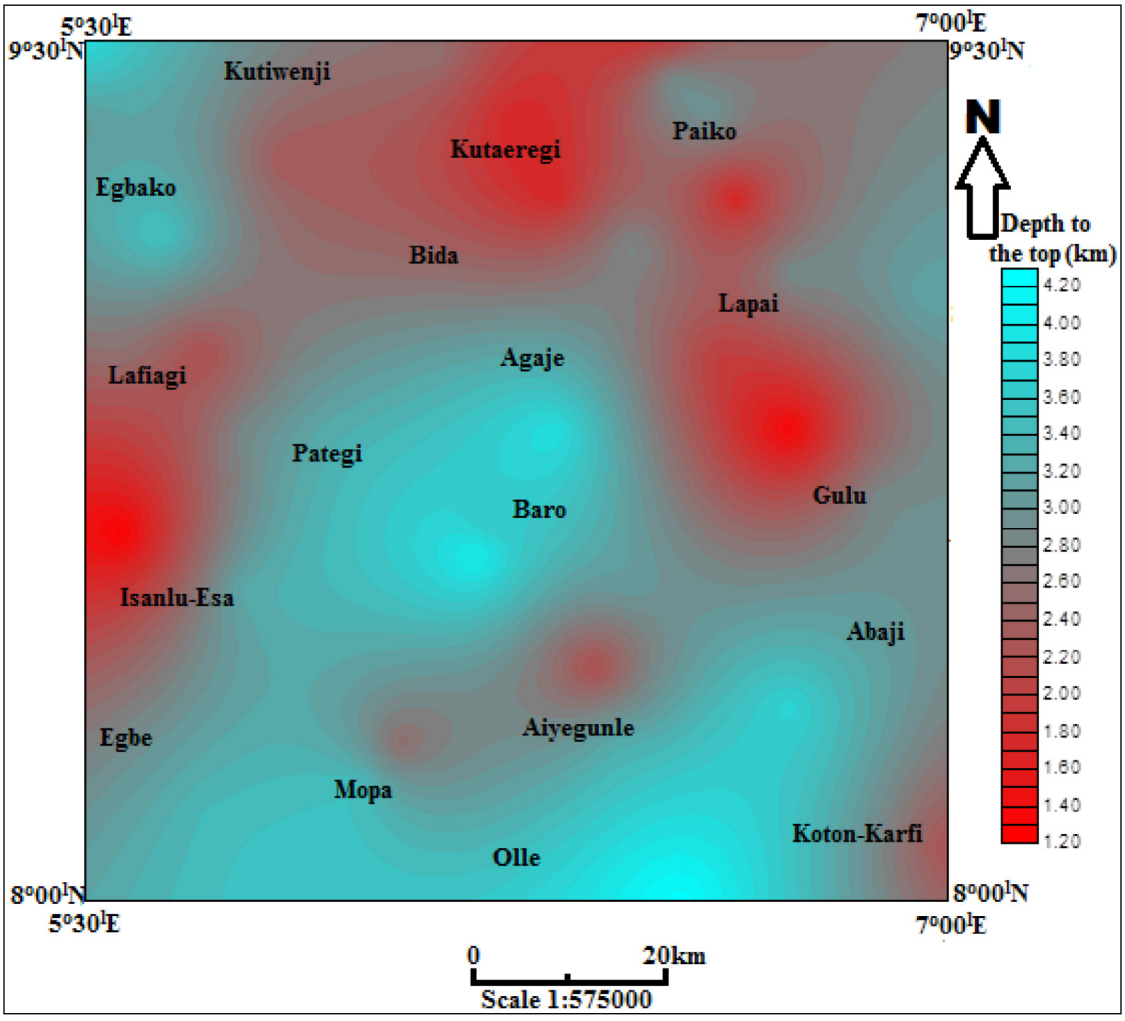

Figure 9- Depth to the top of the magnetic body in the area (contour interval 0.1 m).

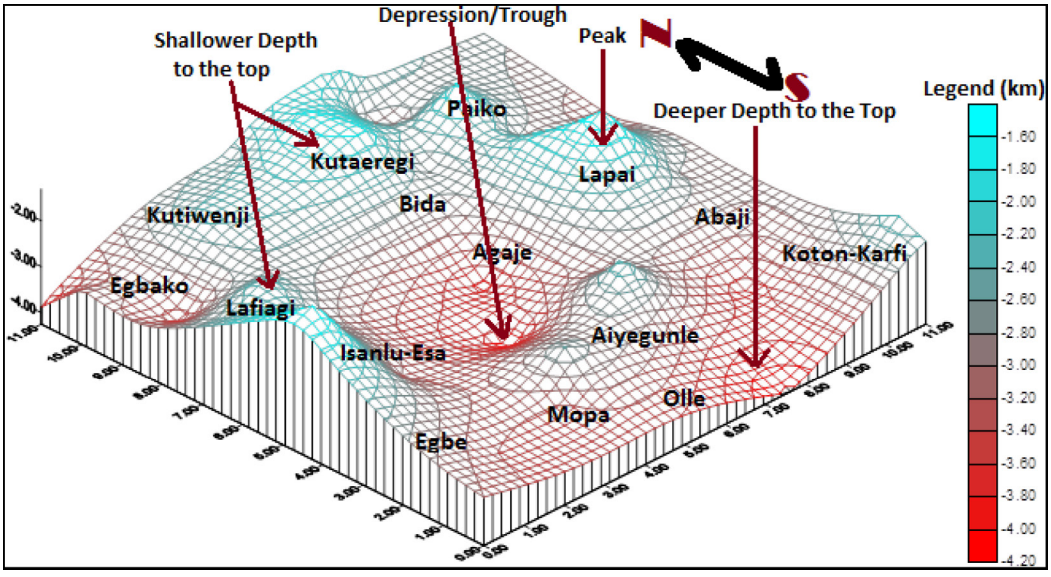

Figure 10- Real view model of depth to the top in the area.

with depressional feature. According to Kogbe (1989), these identified igneous intrusives generally occur as silly and dykes.

3.5. Computation of Thermomagnetic Properties

3.5.1. Curie Isotherm Depth

The Curie isotherm depth result revealed deeper depth at Kutiwenji, Egbako, Lapai, Paiko, Olle, Mapo and Baro areas, ranging from 22.60 to 27.91 km, in other parts, the Curie isotherm depth was shallower and ranged from 19.18 to 22.20 km (Table 1; Figure 11). The average depth to the Curie isotherm in the area is 23.12 km. In addition, the 3 - D surface plot shows presence of uplifts and depressions across the study area (Figure 12). Around Kutiwenji, Egbako, Lapai, Paiko, Baro, Mopa, Agaje, and Olle areas, there are visible linear depressions and these areas reveal higher depth to the Curie point isotherm than the other parts such as Lafiagi, Isanlu - Esa, Gulu and Abaji areas which have prevalent uplifts (peaks) in conjunction with lower values (Figure 12). However, a scattered plot of depth to the top of basement and Curie depth across the study area depicts a direct relationship with a very poor correlation value of 0.1356 (Figure 13).

3.5.2. Geothermal Gradient

The result of the geothermal gradients obtained according to Tanaka et al. (1999) ranges between 21.98 and 30.95 °C/km with an average of 25.27 °C/km across the study area (Table 1). At Lafiagi Isanlu - Esa, Egbe, Abaji and Gulu areas, geothermal gradient have relatively high geothermal gradient ranging between 25.76 and 30.95 °C/km with total average of 25.27 °C/km (Figure 14) which compares favourably with average geothermal gradient of 23.56 °C/km obtained within the Niger Delta by Emujakporue and Ekine (2014). More so, the 3-D surface plot shows

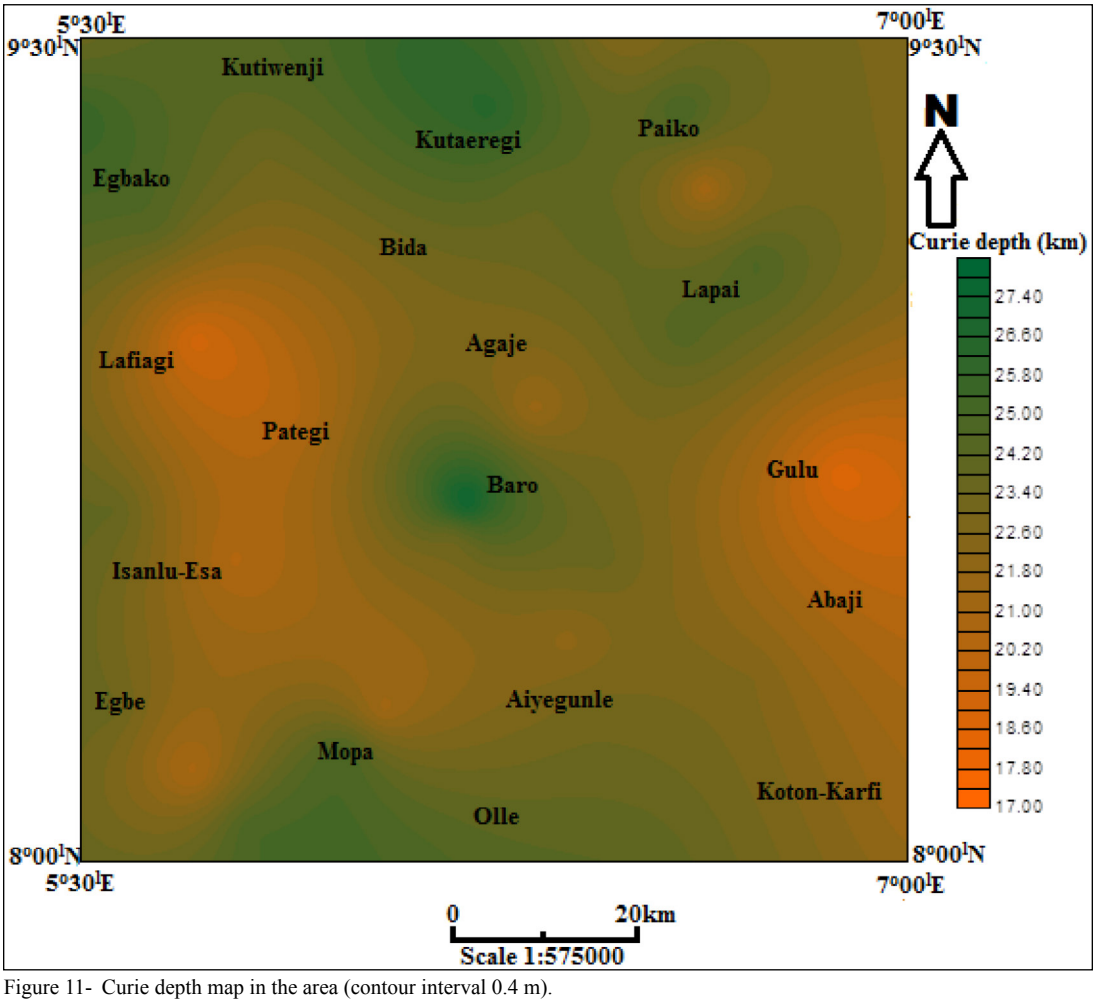

Figure 11- Curie depth map in the area (contour interval 0.4 m).

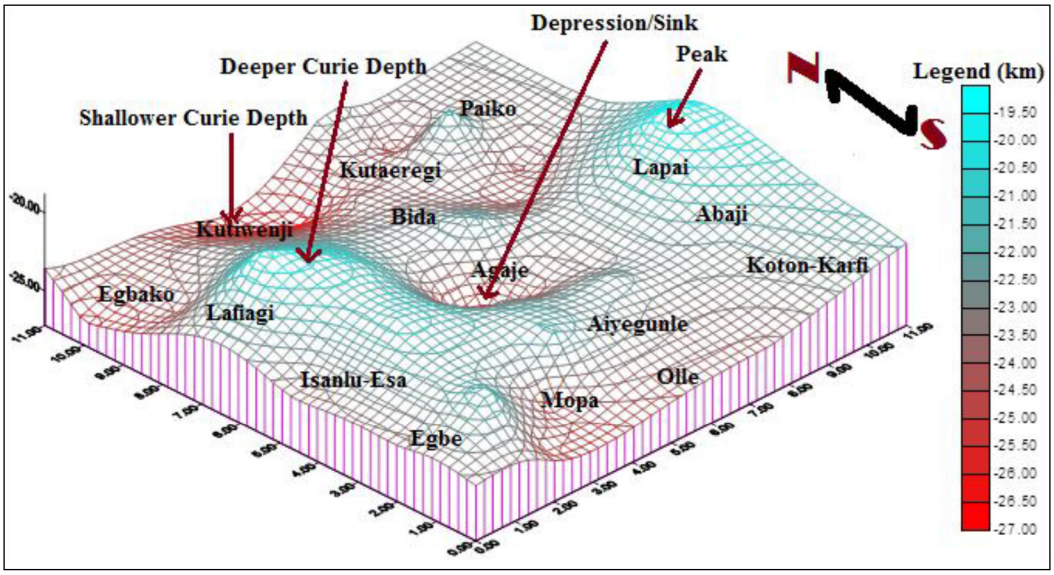

Figure 12- Real view model of Curie depth in the area.

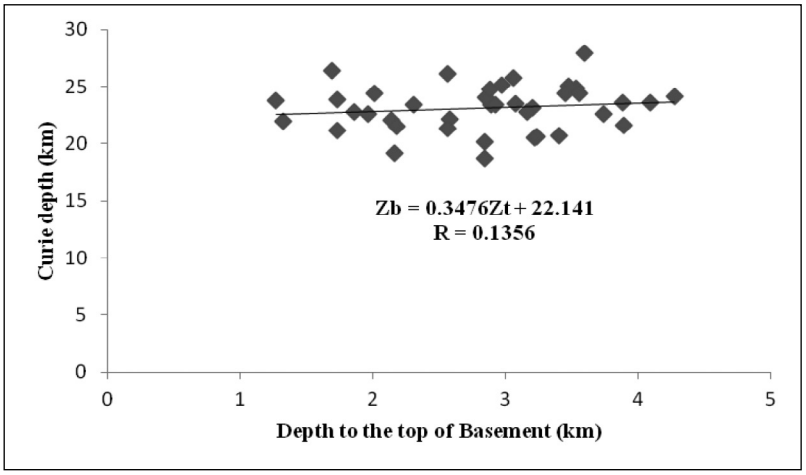

Figure 13- Comparison of basement relief and Curie depth in the area.

presence of uplifts and depressions across the study area (Figure 15).

3.5.3. Heat Flow

The result of the heat flow values obtained according to Tanaka et al. (1999) ranges between 51.95 and 77.37 mWm^2 with an average of 63.17 mWm^2 across the study area (Table 1). The heat flow is lower around the northern and southern parts compared to the other areas within the study area (Figure 16). Furthermore, the 3 - D surface plot of the heat flow shows presence of peaks (uplifts) and depressions across the study area (Figure 17). Around Lafiagi Isanlu - Esa, Egbe, Abaji and Gulu areas, there are visible linear depressions and these areas reveal higher geothermal gradient than the other parts such as Kutiwenji, Kutaeregi, Paiko, Lapai, Egbako, Mapo, and Olle areas which have prevalent uplifts (peaks) in conjunction with lower values (Figure 17).

3.5.4. Correlation Between Curie Depth and Geothermal Gradient

There is an inverse perfect relationship between Curie point isotherm and geothermal gradient across the study area with correlation value as approximately 1 (Figure 18). The designated areas of elevated

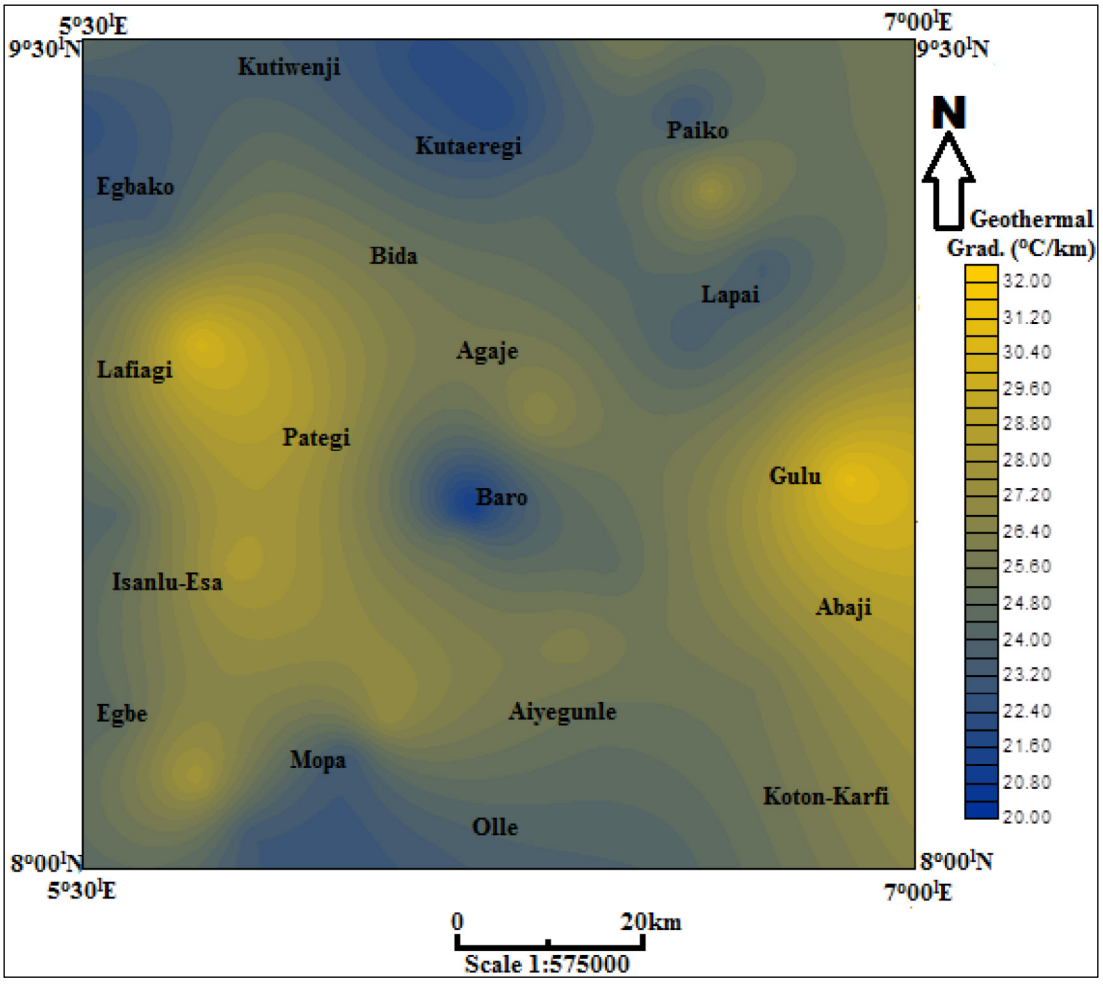

Figure 14- Geothermal gradient map in the area (contour interval ~ 0.4 °C/km).

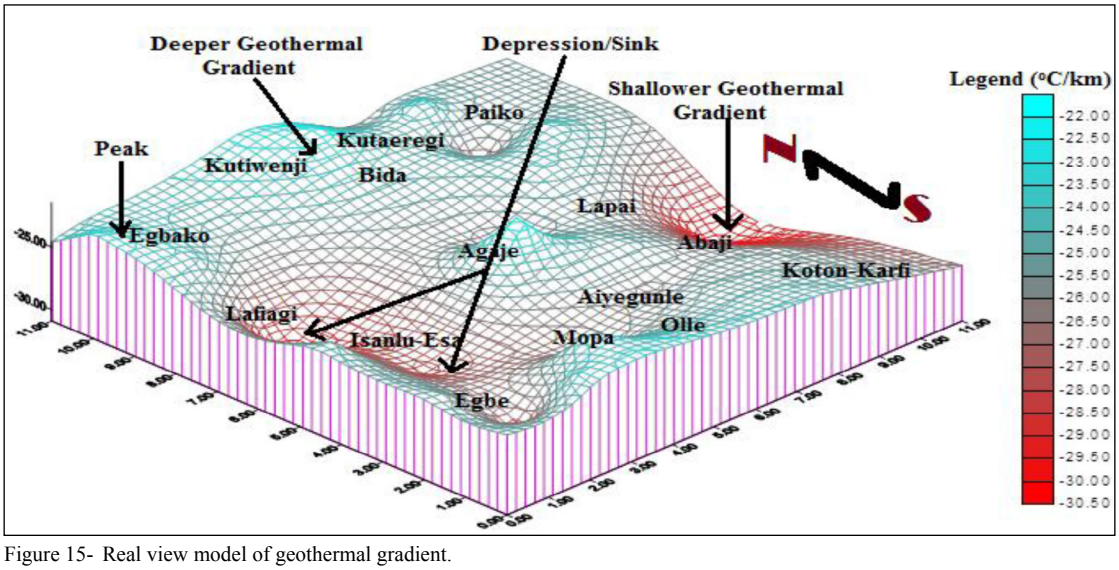

Figure 15- Real view model of geothermal gradient.

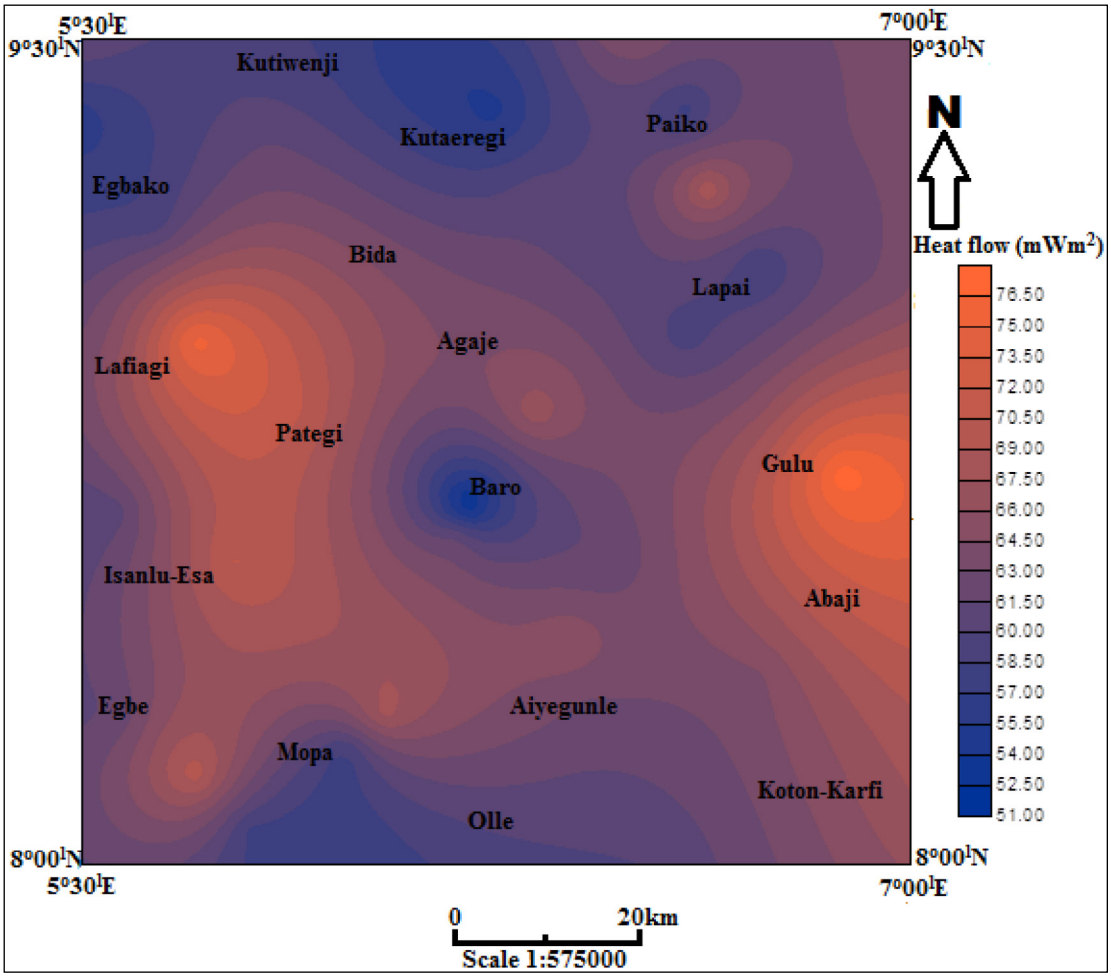

Figure 16- Heat flow map in the area (contour interval ~ 1.5 mWm^2).

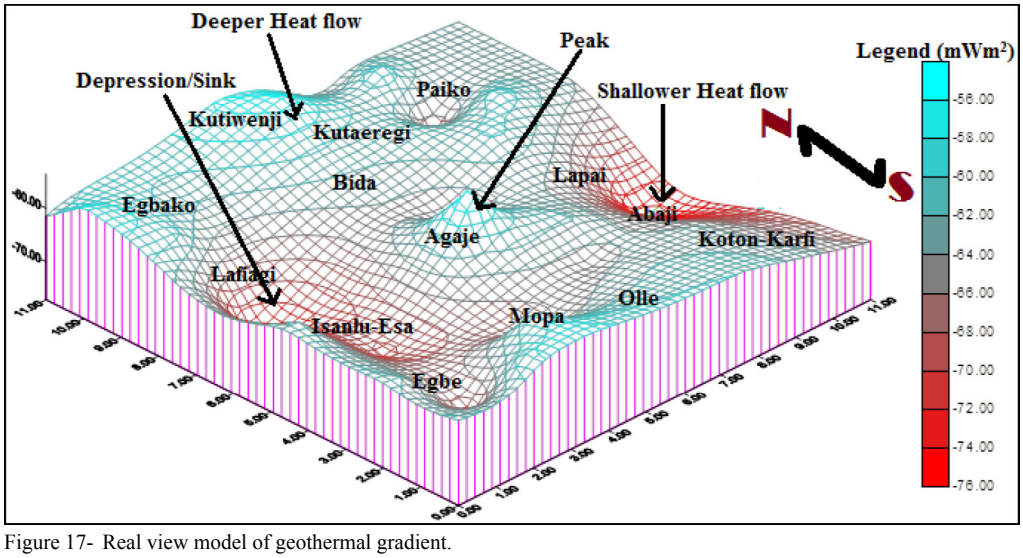

Figure 17- Real view model of geothermal gradient.

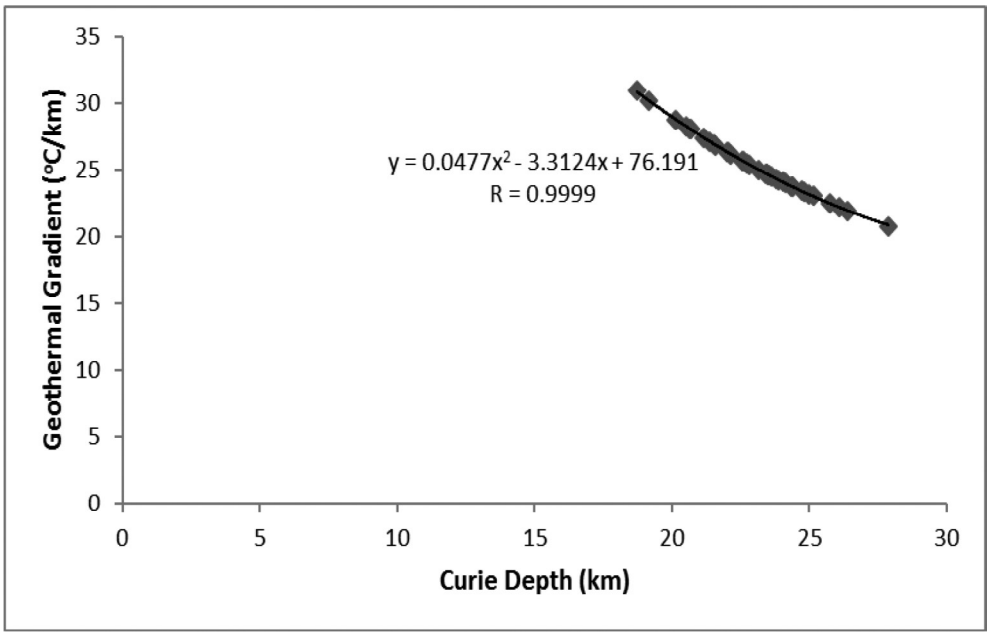

Figure 18- Relationship between Curie depth and geothermal gradient.

Curie point depth show considerable low geothermal gradient (Kutaeregi, Koton - Karfi as well as Baro). These areas have low sedimentary infillings (shallower depth to basement), while areas of low Curie point isotherm depth shows high geothermal gradient (Isanlu - Esa, Pategi and Aiyegunle). Some previous authors such as Nwankwo and Ekine (2010), Ikumbur et al. (2013) and Anakwuba and Chinwuko, (2015), believe that those sediments which were characterized by elevated values of geothermal gradients tend to mature earlier compared to those with low values of geothermal gradient.

4. Discussion

4.1. Geothermal Energy Potentials and Its Implication

The computed thermomagnetic properties according to Tanaka et al. (1999) showed average values of 23.12 km Curie isotherm depth, 25.27 ^{o}C/km geothermal gradients and 63.17 mWm^2 heat flows in the area (Table 1). These values indicated that the geothermal energy was of good quality. The values were used to generate a generalized map for possible area of geothermal energy exploration across the study area.

Moreover, integrating all the results and deductions obtained in this work, it can be deduced that these regions such as Lafiagi, Pategi, Bida, Baro, Koton-Karfi, Egbe, Isanlu - Esa, Abaji, Paiko, and Agaje possess relatively high geothermal gradient and heat flow; which will possibly pave way for high geothermal energy potential in these areas (Figure 19), since at the far northeastern and southwestern parts of the area were covered by Basement rocks. But, there is low geothermal energy potential around Egbako, Kutiwenji, Kutaeregi, Lapai, Mopa, Olle and Aiyegunle (Figure 19). It is good to note that the geothermal energy deduced within the study area may have originated from the formation of the earth and possibly from decay of long - lived isotopes of uranium, thorium and potassium found within the basement complex rocks.

Generally, this study have shown that the geothermal energy sources are viable in those regions that were underlain by basement rocks and it is supported by previous researches conducted by Chukwu et al. (2017), Abraham et al. (2014), and Anakwuba and Chinwuko (2015). Despite this numerous abundance across our country, Nigeria, little or no attention has been paid to the chase for geothermal energy exploration. As a result, there has been a gap in thermomagnetic properties information within Nigeria and the study area is no exception. Furthermore, considering the environmental impact of petroleum products during and after exploration couple with decline in oil and gas production in

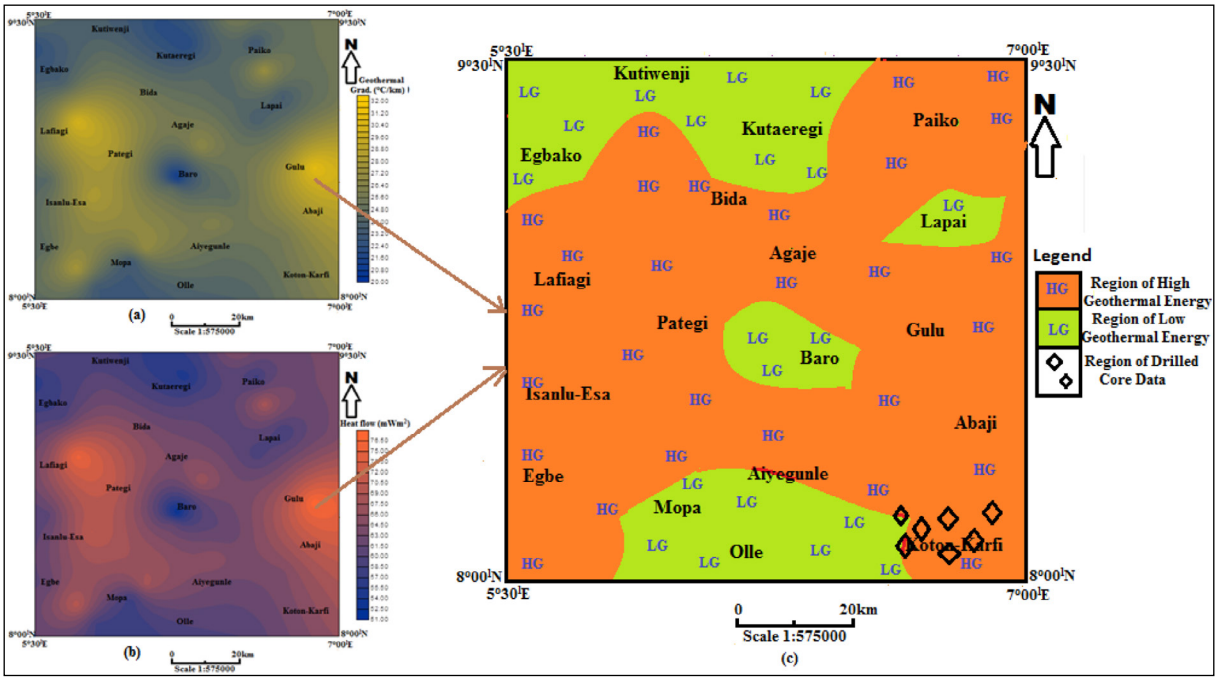

Figure 19- a) Geothermal gradient map in figure 14, b) Heat flow map in figure 16, and c) a potential map for possible geothermal energy across the study area.

our country, it has been necessary to explore this alternative source of energy called geothermal energy in order to meet our energy needs.

5. Results

The following conclusions have been reached after comprehensive analysis of magnetic anomalies:

1. The magnetic anomaly maps depict two prevalent structural features namely; uplift and depression, which are evidence of folding.

2. The lineament maps and Rose diagram produced signify that the study area is extremely faulted with prominent trends in NE - SW, whereas, the minor trends occur along E - W and NW - SE.

3. Two layers depth model were delineated: the shallower bodies varied from 1.27 to 1.96 km; the deeper bodies vary from 2.01 to 4.27 km.

4. The computed thermomagnetic properties showed average values of 23.12 km Curie isotherm depth, 25.27 ^{o}C/km geothermal gradients and 63.17 mWm^{2} heat flows in the area. These values indicated that the geothermal energy was of good quality.

5. The computed results and models provided information on the capabilities of spectral analysis in delineating geothermal energy potentials and as such could be adopted to other areas with similar geologic framework in Nigeria and beyond.

Acknowledgements

The researchers are grateful to the National Geological Survey Agency, Abuja Nigeria, for their kind consent and endorsement to utilize the acquired nine aeromagnetic data for this research. In addition, we acknowledged the management of Federal College of Education Umunze, Nigeria for their permission and motivation during entire period of in this work.

References

Abraham, E. M., Lawal, K. M., Ekwe, A. C., Alile, O., Murana. K. A., Lawal, A. A. 2014. Spectral analysis of aeromagnetic data for geothermal energy investigation of Ikogosi warm Spring - Ekiti state, Southwestern Nigeria. Geothermal Energy 26, 1-21.

Abraham, E. M., Obande, E. G., Mbazor, C., Chibuzo, G. C., Mkpuma, R. O. 2015. Estimating depth to the bottom magnetic sources at Wikki Warm Spring region, northeast Nigeria using fractal distribution

of sources approach. Turkish Journal of Earth Science 24, 1-19.

Adeleye, D. R. 1974. Sedimentology of the fluvial Bida Sandstone (Cretaceous), Nigeria. Elsevier Journals of Sedimentary Geology 12(1), 1-24.

Anakwuba, E. K., Chinwuko, A. I. 2015. One dimensional spectral analysis and Curie depth isotherm of Eastern Chad Basin, Nigeria. Journal of Natural Sciences Research 5(19), 14-22.

Anudu, G. K., Onuba, L. N., Onwuemesi, A.G., Ikpokonte, A.E. 2012. Analysis of aeromagnetic data over Wamba and its adjoining areas in north-central Nigeria. Earth Sciences Research Journal 16(1),25-33.

Burke, K. 1972. Longshore Drift, submarine canyons and submarine fans in development of Niger delta. American Association of Petroleum Geologist Bulletin 56, 1975-1983.

Biswas, A. 2015. Interpretation of residual gravity anomaly caused by a simple shaped body using very fast simulated annealing global optimization. Geosciences Frontiers 6(6), 875-893.

Biswas, A., Sharma, S. P. 2016. Integrated geophysical studies to elicit the structure associated with Uranium mineralization around South Purulia Shear Zone, India: A Review. Ore Geology Reviews 72, 1307-1326.

Biswas, A., Parija, M. P., Kumar, S. 2017. Global nonlinear optimization for the interpretation of source parameters from total gradient of gravity and magnetic anomalies caused by thin dyke. Annals of Geophysics 60(2), 1-17.

Bhattacharyya, B. K. 1966. Continuous spectrum of the magnetic field anomaly due to a rectangular prismatic body. Geophysics 31, 121.

Bhattacharyya, B. K., Leu, L. K. 1975. Spectral analysis of gravity and magnetic anomalies due to dimensional structures. Geophysics 40, 993-1031.

Chinwuko, A. I., Onwuemesi, A. G., Anakwuba, E. K., Onuba, L. N., Nwokeabia, N. C. 2012**.** The interpretation of aeromagnetic anomalies over parts of Upper Benue Trough and southern Chad Basin, Nigeria. Advances in Applied Science Research 3(3), 1757-1766.

Chinwuko, A. I., Usman, A. O., Onwuemesi A. G., Anakwuba, E. K., Okonkwo, C. C., Ikumbur, E. B. 2014. Interpretations of aeromagnetic data over Lokoja and environments, Nigeria. International Journal of Advanced Geosciences 2(2), 66-71.

Chukwu, C. G., Udensi, E. E., Abraham, E. M., Ekwe, A. C., Selemo, A. O. 2017. Geothermal energy potential from analysis of aeromagnetic data of part of the Niger-delta basin, southern Nigeria. Energy 143, 846-853.

Emujakporue, G. O., Ekine, A. S. 2014. Determination of geothermal gradient in the Eastern Niger Delta Sedimentary Basin from bottom hole temperatures, Journal of Earth Sciences and Geotechnical Engineering 4(3), 109-114.

Frashëri, A., Alikaj P., Frashëri, N. 2011. Some survey and interpretation problems on IP method. 6th Congress of Balkan Geophysical Society, Budapest, Hungary, 22.

Ikumbur, E. B., Onwuemesi, A. G., Anakwuba, E. K., Chinwuko, A. I., Usman, A. O., Okonkwo, C. C. 2013. Spectral analysis of aeromagnetic data over part of the southern Bida basin, West-Central Nigeria. International Journal of Fundamental Physical Sciences 3(2), 27-31.

Kogbe, C. A. 1989. The Cretaceous and Paleogene sediments of Southern Nigeria. Geology of Nigeria (2nd Ed.). Rock View Ltd. Nigeria, 538.

Mandal, A., Biswas, A., Mittal, S., Mohanty, W. K., Sharma, S. P. Sengupta, D., Sen, J., Bhatt, A. K. 2013. Geophysical anomalies associated with uranium mineralization from Beldih mine, South Purulia shear zone. Journal Geological Society of India 82(6), 601-606.

Nwankwo, C. N., Ekine, A. S. 2010. Geothermal gradients in the Chad Basin, Nigeria, from bottom hole temperature logs. Scientia Africana 9(1), 37- 45.

Obaje, N. G., Balogu, D. O., Idris - Nda, A., Goro, I. A., Ibrahim, S. I., Musa, M. K. Dantata, S. H., Yusuf I., Mamud- Dadi, N., Kolo I. A. 2013. Preliminary integrated hydrocarbon prospectivity evaluation of the Bida Basin in North Central Nigeria. Petroleum Technology Development Journal 3(2), 36-65.

Ojo, O. J., Akande, S. O. 2012. Sedimentary facies relationships and depositional environments of the Maastrichtian Enagi Formation, Northern Bida Basin, Nigeria. Journal of Geography and Geology 4(1), 136-147.

Ojonugwa, U. A., Ezeh, C. C., Chinwuko, I. A. 2018. Integration of aeromagnetic interpretation and induced polarization methods in delineating mineral deposits and basement configuration within Southern Bida Basin, North-West Nigeria. Journal of Geology and Geophysics 7, 449-454.

Okubo, Y. J., Graf, R., Hansen, R. O., Ogawa, K., Tsu, H. 1985. Curie point depth of the Island of Kyushu and surrounding areas. Japan Geophysics 53, 481-491.

Okonkwo, C. C., Onwuemesi, A. G., Anakwuba, E. K., Chinwuko, A. I., Ikumbur B. E. and Usman, A.O. 2012. Aeromagnetic interpretation over Maiduguri and environments of Southern Chad Basin, Nigeria. Journal of Earth Sciences and Geotechnical Engineering 2(3), 77-93.

Onwuemesi, A. G. 1995. Interpretation of magnetic anomalies from the Anambra Basin of Southeastern Nigeria. Ph.D Thesis, Nnamdi Azikiwe University, Awka, Nigeria.

Onwuemesi, A. G. 1997. One dimensional spectral analysis of aeromagnetic anomalies and curie depth isotherm in the Anambra Basin of Nigeria. Journal of Geodynamics 23(2), 95-107.

Pamukçu, O., Akçığ, Z., Hisarlı, M., Tosun, S. 2014. Curie point depths and heat flow of eastern Anatolia (Turkey). Energy Sources, Part A: Recovery, Utilization, and Environmental Effects 36(24), 2699-2706.

Petters, S. W. 1978. Stratigraphic evolution of the Benue Trough and its implications for the Upper Cretaceous paleogeography of West Africa. Journal of Geology 86, 311-322.

Ross, H. E., Blakely, R. J., Zoback, M. D. 2006. Testing the use of aeromagnetic data for the determination of Curie depth in California. Geophysics 71(5), 51-59.

Saibi, H, Aboud, E., Azizi, M. 2015. Curie point depth map for Western Afghanistan deduced from the analysis of aeromagnetic data, Proceedings World Geothermal Congress 2015, Melbourne, Australia, 19-25.

Singh, A., Biswas, A. 2016. Application of global particle swarm optimization for inversion of residual gravity anomalies over geological bodies with idealized geometries. Natural Resources Research 25(3), 297-314.

Spector, A., Grant, F.S. 1970. Statistical models for interpretation of aeromagnetic data. Geophysics 35, 293-302.

Tanaka, A. Y., Okubo, Y., Matsubayashi, O. 1999. Curie point depth based on spectrum analysis of the magnetic anomaly data in East and Southeast Asia. Tectonophysics 396, 461-470.

Bulletin of the Mineral Research and Exploration

http://bulletin.mta.gov.tr

Geological properties of Güney formation (Ereğli - Ulukışla Basin, Niğde)

Ayfer ÖZDEMİR[a,b*] and Nurettin SONEL[c]

[a]*Helmholtz Centre for Enviromental Research, UFZ Department of Computational Landscape Ecology, 04318, Leipzig, Germany*
[b]*Ministry of Agriculture and Forestry, General Directorate of Water Management, Flood and Drought Department, 06560, Ankara, Turkey*
[c]*Ankara University, Faculty of Engineering, Department of Geological Engineering, Ankara, Turkey*

Research Article

Keywords:
Ereğli - Ulukışla Basin, Güney Formation, Sandstone, Sedimantology, Stratigraphy, Petrography.

Received Date: 13.04.2020
Accepted Date: 06.01.2021

ABSTRACT

The aim of this study to determine stratigraphic, sedimentological and petrographic characteristics of the Upper Paleocene - Lower Eocene Güney formation in the Ereğli - Ulukışla Basin based on the lithological and environmental interpretations related to petroleum source and reservoir rock properties of it. For this purpose, the geological characteristics of the Güney formation and its relations with other units were followed by field observations and the unit was investigated by making a stratigraphic cross section from bottom to top. In addition, during the field studies, four (4) scaled stratigraphic sections (OSK) were formed and fifty - two (52) sandstone samples were taken from these OSKs. The Güney formation starts with conglomerates at the basement and continues as sandstone - shale alternation. The fact that the sand size material is more than the clay size material, the sandstone layers are thick (at least 2 m) around the Kardeşgediği station, the presence of channel fillings, slump structures, and pebbles indicate that the sequence shows convergent turbidite character. However, in the vicinity of Ovacık - Güney village and Tatlıpınar ridges, shales having an average layer thickness of 30 cm (thick) and sandstones up to 3 - 5 cm (thin) and shales are denser than sandstones show the formation has divergent character. The Güney formation transitions laterally and vertically overlies the agglomerate unit of the Ulukışla formation and turbiditic sandstone - shale units of the Halkapınar formation. The Aktoprak formation passes laterally and vertically over the Formation. Petrographic studies show that the formation sandstones are lithic arenite and feldspathic arenite and are deposited in the fore - arc basin.

1. Introduction

The study area is located in the Ereğli - Ulukışla basin, between Ulukışla (Niğde) and Bor (Niğde) districts and İmrahor (Ulukışla) village (Figure 1). The outcrops in the Ereğli - Ulukışla basin have been investigated by many researchers in terms of stratigraphic, sedimentological and structural features. (Okay, 1955; Ketin and Akarsu, 1965; Demirtaşlı et al., 1973; Yoldaş, 1973; Baş et al., 1986; Nazik and Gökçen, 1989, 1992; Gürbüz et al., 2020; Akgün et al., 2020). The geology and petroleum possibilities assessment studies conducted in the Ereğli - Ulukışla basin show that there may be hydrocarbon formation in this basin (Dellaloğlu and Aksu, 1986; Sonel and Sarı, 2004). The Güney formation is transitional in a lateral direction with the Hasangazi formation, which is petroleum source rock and has been proven to be hydrocarbon (Sonel and Sarı, 2004). Although the Güney formation shows petroleum bedrock and reservoir rock characteristics; until now, the lithological features of the formation have not been studied in

Citation Info: Özdemir, A., Sonel, N. 2021. Geological properties of Güney formation (Ereğli - Ulukışla Basin, Niğde). Bulletin of the Mineral Research and Exploration 165, 31-52.
https://doi.org/10.19111/bulletinofmre.855696

**Corresponding author: Ayfer ÖZDEMİR, ozdemir.ayfer@gmail.com*

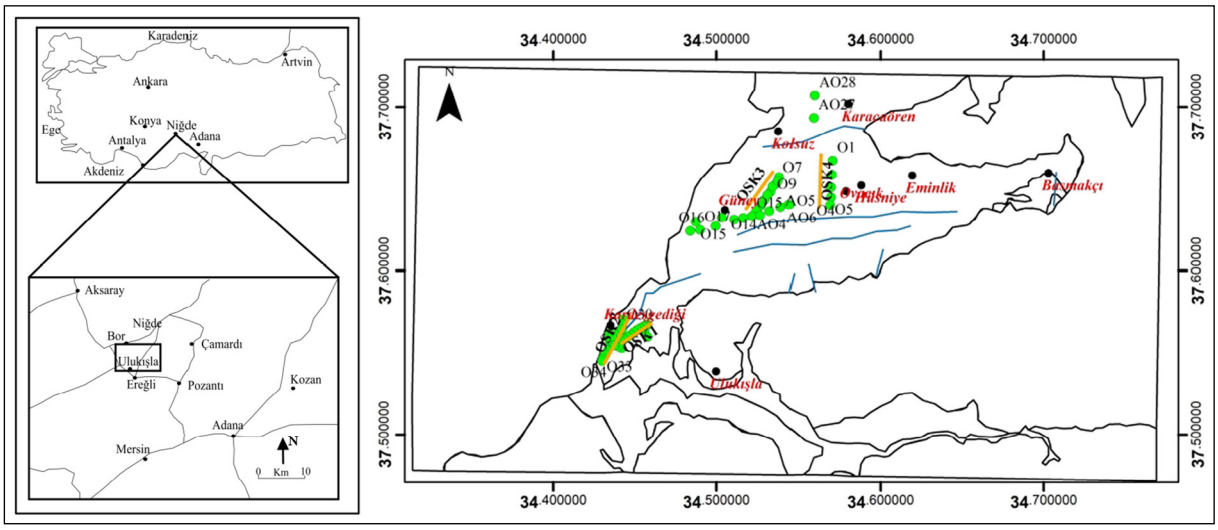

Figure 1- Study area location and sampling map.

detail from a geological perspective. The unit studied as the Güney formation was named Ovacık formation by Dellaloğlu and Aksu (1986) and Güney formation by Oktay (1982). The name given by Oktay (1982) was used because the place where the formation was best observed the Güney village in Ulukışla district. Oktay (1982) studied the Güney formation for the first time at the formation level. The researcher stated that the Güney formation was deposited by turbid currents and that the depositional environment of the formation was inside the volcanic island arc and the deep pits located around it and the slopes connecting the pits to the volcanic islands. In this study, the Early - Middle Eocene aged Serenkaya formation, which was examined within the Ulukışla group by Oktay (1982), was included in the Güney formation and examined as the basal levels of the Güney formation. The Serenkaya formation with the volcanics of the Ulukışla formation forms the transitional facies of the deep marine sediments of the Ovacık formation. In addition, the regions where Serenkaya formation is common are capable of forming reservoir rock for gas. The Ovacık formation contains deep marine shales and thin turbiditic sandstone bands. The areas where the channel fillings on the upper parts of the turbidite fan show reservoir rock features (Dellaloğlu and Aksu, 1986).

In this study, the stratigraphic, sedimentological, and petrographic properties of the Güney formation based on lithological and geological setting interpretations were investigated since the Güney formation shows petroleum source rock and reservoir rock properties. The units named and studied as the Serenkaya formation and Ovacık formation in previous studies were evaluated under the name of Güney formation in this study and the geological characteristics of the Güney formation were investigated by field studies and petrographic investigations.

2. Material and Method

Field and laboratory studies were conducted to determine the geological features of the Late Paleocene - Early Eocene Güney formation. The geological characteristics of the formation and its relations with other units were followed by field observations and the unit was investigated by making a stratigraphic section from bottom to top. In addition, four (4) measured stratigraphic sections (ÖSK) were prepared during the field studies and fifty - two (52) sandstone samples were taken from these ÖSK's. ÖSK study was carried out on the canal fillings surfacing at the Kardeşgediği Station of the Early - Middle Eocene aged Serenkaya formation which was stated to be in the Ulukışla group and the sandstone-shale facies where the typical section location of the Güney by Oktay (1982). Formation located in Tatlıpınar ridges. In addition, ÖSK study was carried out on the sandstone - shale unit defined as Ovacık formation by Dellaloğlu and Aksu (1986) in the north of Ovacık village. In order to define the petrographic characteristics of the sandstones, thin sections were made from fifty - two (52) hand samples (Figure 1) taken from the field and petrographic analyzes (grain

size, roundness, sorting, contact relationship, cement type and porosity type) were made under the optical microscope. Samples were defined according to Folk et al. (1970) classification. Source areas of the Güney formation were determined according to Dickinson et al. (1983). Petrographic examinations were carried out in Ankara University Faculty of Engineering Department of Geological Engineering.

3. Stratigraphy

Ereğli - Ulukışla Basin contains the different origins of geological units (Figures 2, 3). Sedimentary units started to form after ophiolite settlement in the Late Cretaceous period in the basin. The formation of these units took place continuously in the Late Cretaceous - Miocene time interval. The units filling the basin are clastic sediments, volcano - sedimentary units, carbonates, and evaporitic sediments. Lithofacies variations in horizontal and vertical directions are very common between units. In particular, there are lithofacies changes in lateral and vertical directions between Ulukışla, Halkapınar, Hasangazi and Güney formations (Sonel and Sarı, 2004). In order to better understand the stratigraphy of the Güney formation, which is the subject of this study, the stratigraphic characteristics of the formation and it`s under and above units are as follows.

3.1. Ulukışla Formation (KTu)

The formation was described by Demirtaşlı et al. (1973). The majority of the Ulukışla formation consists of agglomerate, andesitic lava flows, tuffs, tuffites and volcanic breccias, pillow lavas. All this volcanic material is interbedded with turbiditic sandstone, shear deposits and rarely limestone and shale.

According to Oktay (1982), The Ulukışla group forms the basis of the Ereğli - Ulukışla region. In this group, it is stated that there are shallow - deep sea sediments, undersea volcanics and dykes or shallow intrusions which have entered them from time to time. The researcher divided the Ulukışla group into Sansartepe formation, Serenkaya formation, Başmakçı limestone, Cehritepe syenite, Köyderesi trachyte, Karatepe limestone, Güney formation, Tayhacı andesite and Dikmendere trachytes.

The contact of the unit with the Halkapınar formation is transitive in lateral and vertical directions. The Ulukışla formation also displays a strong lateral and vertical transition with the Hasangazi formation and Güney formation. Due to the complex magmatic - sedimentary relationships of the formation, the thickness of the formation could not be determined. Its age is thought to be Late Cretaceous - Middle Eocene (Sonel and Sarı, 2004).

3.2. Halkapınar Formation (Th)

The formation was first named by Demirtaşlı et al. (1973). Halkapınar formation, which covers a large area, is the Paleocene - Early Eocene base of the Ereğli - Ulukışla Basin; It consists of marl, ophiolitic olistostrome, and generally Triassic limestone olistoliths including sandstone and agglomerates and syphilitic basalt lava interlayers.

Halkapınar formation covers the Kalkankaya formation concordantly. Halkapınar formation is laterally transitive to the west with Güneydağı formation and is located on the Güneydağı formation in the west of the region. Ulukışla formation is laterally and vertically transitive with Halkapınar formation.

3.3. Hasangazi Formation (Thz)

The unit was named as Koçak f ormation by Ketin and Akarsu (1965) and as Hasangazi formation by Demirtaşlı et al. (1973). Demirtaşlı et al. (1973) studied the formation by dividing it into three members. The formation is the Middle - Late Eocene age. It has a wide distribution and presents typical flysch facies feature in most places. It also contains canal fillings with massive, thick, sandstone - conglomerate lithology. Strong lithofacies changes are observed in the formation both in the lateral and vertical directions. The lateral continuity of sandstone and channel fill is not much. Very thin bedded sandstone - shale alternation in some places shows a flysch type lithology and a mechanism formed by turbiditic flows.

3.4. Güney Formation (Tgü)

Güney formation was named as Ovacık formation by Dellaloğlu and Aksu (1986) and as Güney formation by Oktay (1982). Oktay's (1982) nomenclature is used in this study because the place where the formation is best developed is the Güney village of Ulukışla district. The Early - Middle Eocene Serenkaya formation, which was included in the Ulukışla group by Oktay (1982), was included in the

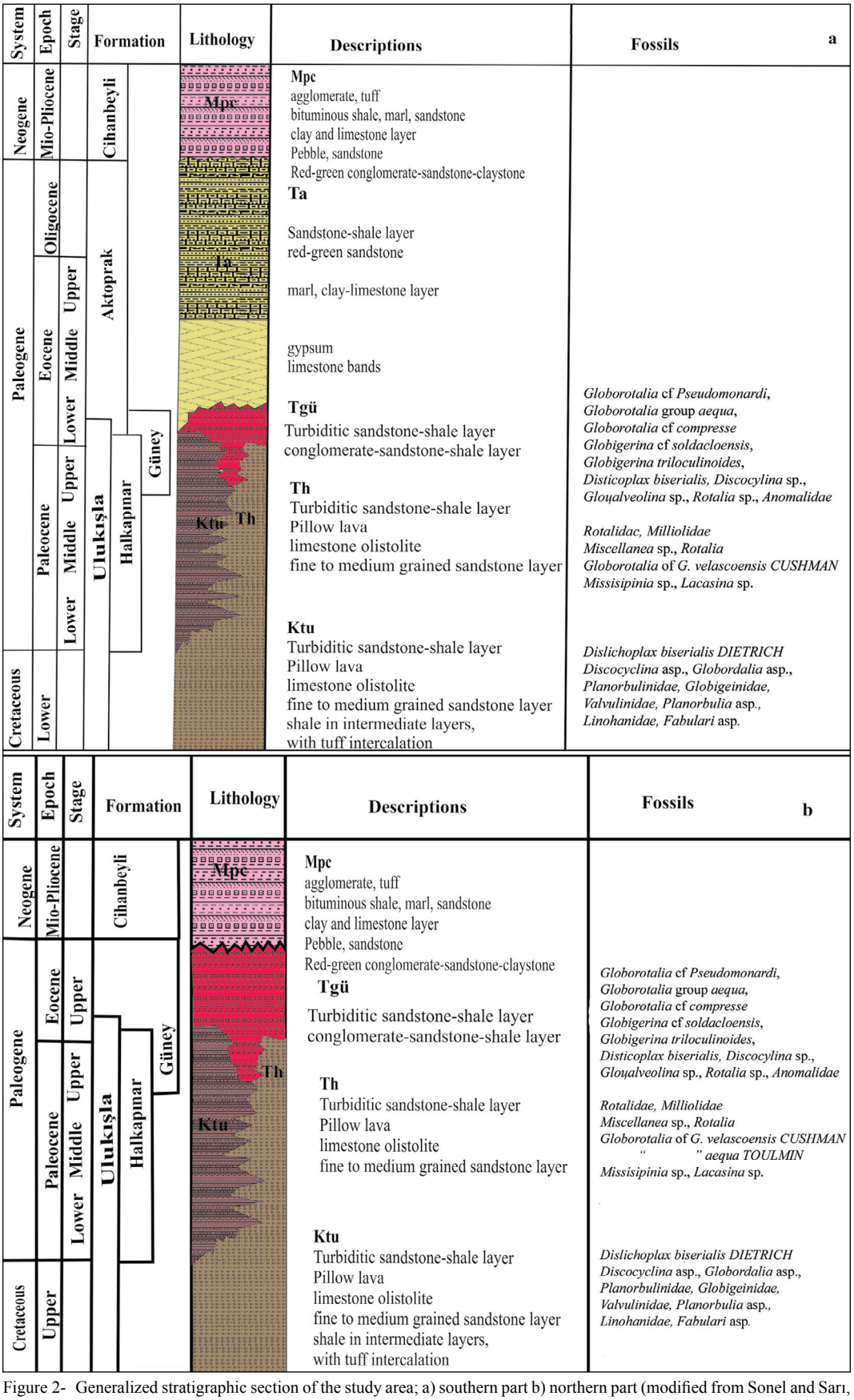

Figure 2- Generalized stratigraphic section of the study area; a) southern part b) northern part (modified from Sonel and Sarı, 2004).

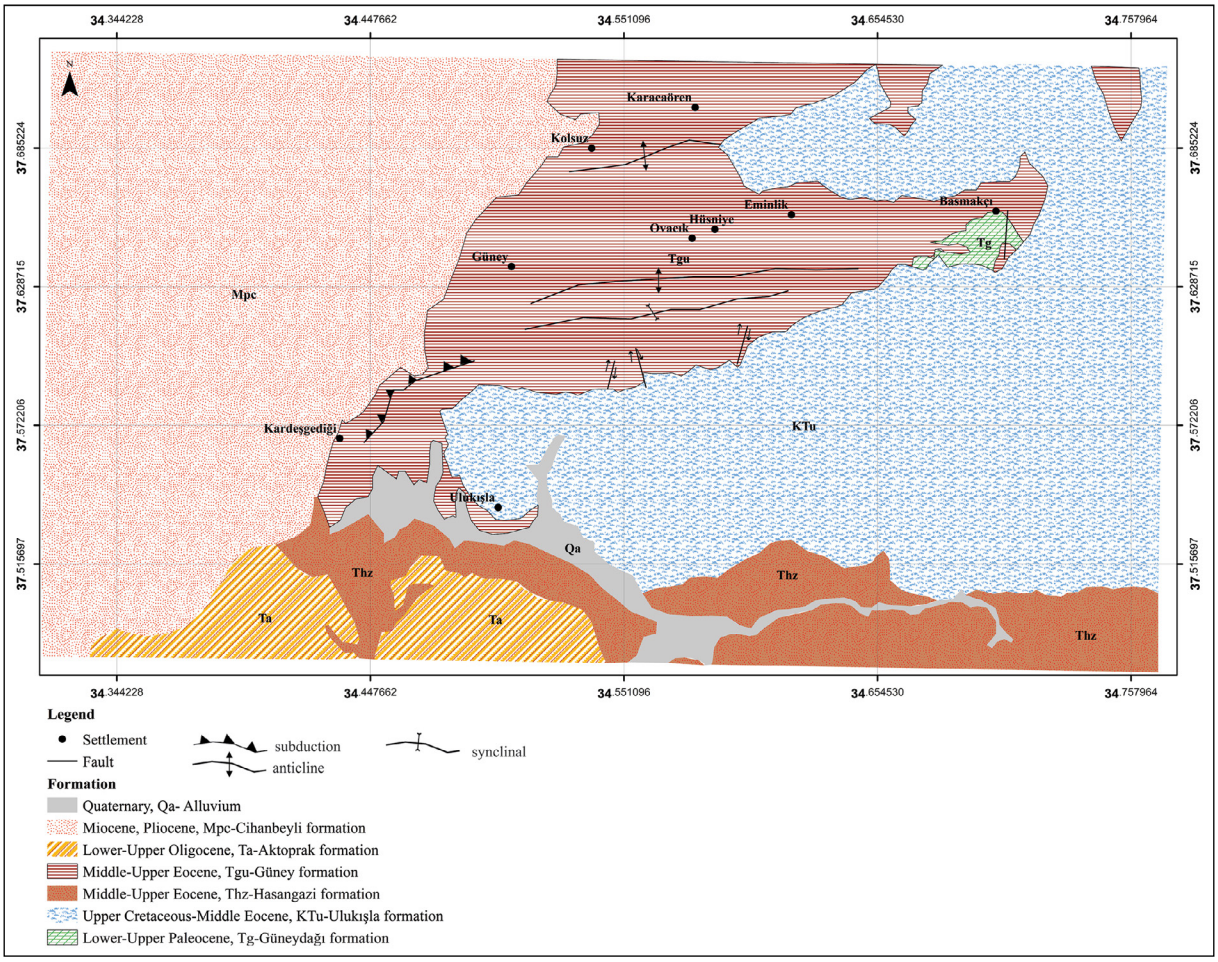

Figure 3- Geological map of the study area (modified from Sonel and Sarı, 2004).

Güney formation in this study, it was studied as the base levels of the Güney formation. It is observed in different facies and ages in typical location and southeast of Ulukışla (Oktay, 1982). Güney formation in typical location, it is composed of lenticular and blocky coarse conglomerate at the bottom and cyclically deposited and graded bedded conglomerate - sandstone - shale sequence at the top. The formation shows great variations in lithology and thickness. The Güney formation consists of a 365 m sandstone-conglomerate sequence around Ulukışla. It consists of a sandstone - conglomerate - shale sequence predominantly 90 m around Porsuk village in the east of Ulukışla and 160 m in the east of Çaykavak pass (on the Ulukışla - Niğde road). The unit is generally developed as a sequence of gray - coarse sandstone and shale and shows a thickness of approximately 800 m. In the north of Ulukışla, all of the material of the Güney formation is derived from volcanic and shallow intrusive type igneous and mostly consists of conglomerates. When the formation is evaluated considering Bouma (1964) turbidite environment interpretation; It is understood that the depth of the depositional environment differs from north to south and is generally deposited by turbiditic flows. Graded stratified channel fillings, shear deposits, and turbiditic sandstone alternations are common in the upper levels of the sequence. The lenticularity, large - scale cross - bedding and lateral rapid lithological changes observed in the coarse - grained clastics especially in the lower part of the sequence indicate a rapid deposition in shallow marine conditions. The change in the thickness and density of the sandstone - shale layers in the upper parts, the erosive - channeled formation of the conglomerate - sandstone - shale sequences in the transition towards each other and the presence of large cavity fill structures, the presence of graded bedding as the common internal structure, and the local sliding structures, the shallow marine deposition conditions over time indicates that the

environment is changing and the environment is deepening. Sandstone and shale densities are equal towards the north in the study area. The lower parts of the stack contain canal fillings. In this area, sandstone density is high, sandstone grains become coarse and shale density decreases. Therefore, the sequence shows convergent turbiditic character in this region.

In the study area, it is laterally and vertically transitive with the Güney formation, the Ulukışla formation and the Halkapınar formation. In the south of Ulukışla, the Güney formation is not encountered, in this area, the Hasangazi formation, which is the same age as the Güney formation, was deposited. The Aktoprak formation transitions laterally and vertically with the Hasangazi formation and the Güney formation and deposited on these units. The Miocene - Pliocene age Cihanbeyli formation sits unconformably over the Aktoprak formation in the south of the study area and on the Güney formation in the north. As a result of the nanoplankton biostratigraphy study conducted by Sınacı (2006) in Güney formation; determined *Discoaster multiradiatus* Zone (Tanesian), *Heliolithus ridelii* Zone (Tanesian), *Heliolithus kleinpellii* Zone (Late Selandian - Early Tanesian), *Fasciculithus tympaniformis* Zone (Late Selandian) Late Paleocene and *Tribrachiatus contortus* Zone (Late Eocene). Therefore, the age of the unit has been determined as Late Paleocene - Early Eocene.

3.5. Aktoprak Formation (Ta)

The formation consisting of evaporite and clastic was first named as Aktoprak formation by Demirtaşlı et al. (1973). The unit defined by Dellaloğlu and Aksu (1986) as Aktoprak is also the gypsiferous series defined by Blumental (1956) and corresponds to the Yalçındere, Emirler, Kurtulmuştepe and Kızılöz formations defined by Ketin and Akarsu (1965). The unit was divided by Demirtaşlı et al. (1973) into the Kurtulmuştepe member consisting of alternation of marl, clayey limestone, sandstone, and a red - green sandstone member. Oktay (1982) defined the unit as Zeyvegediği anhydrite and Kurtulmuştepe Formation. Gypsiferous - anhydrite units called Zeyvegediği anhydrites were shown within the Kabaktepe member of the Hasangazi formation by Demirtaşlı et al. (1973). The formation continues as anhydrites at the base and marl - clayey sandstone alternation upwards and consists of red - green sandstones at the top. The Aktoprak formation covers the Hasangazi formation conformably in the south and southwest of Ulukışla. The unit is not seen in the west and north of Ulukışla. The Güney formation, which is the same age as the Hasangazi formation, comes with lateral and vertical transitions in this region. On the other hand, young sediments of the Miocene - Pliocene age Cihanbeyli formation unconformably cover all units in the region. The age of the unit is Late Eocene - Oligocene (Demirtaşlı et al., 1973).

3.6. Cihanbeyli Formation (MPc)

The formation is named by Dellaloğlu - Aksu (1986). It overlies other old formations with an angular unconformity. It has a wide distribution over the units of both Ereğli - Ulukışla Basin and Tuz Gölü Basin. It starts with the alternation of red - green conglomerate - sandstone - claystone at the base. It then continues as conglomerate - sandstone alternation, consisting of clayey limestone, tuff, agglomerate and lava. The sediments forming the formation mainly consist of stream and lake units. It also contains uneconomic lignite veins and volcanic intercalations. There are bituminous levels with less thickness in some parts of the unit (Sonel et al., 1999). Grain size decreases towards the top and passes into marl and clayey limestones. Large - scale cross - stratification in the formation and lensing in clastics indicate the fluvial environment, while limestone and bituminous marls indicate the presence of a lacustrine environment. The age of the formation is Mio - Pliocene (Dellaloğlu and Aksu, 1986). Some researchers evaluated this unit under the name of Altaylar, Ulukışla, Beştepeler in formation degree (Oktay, 1982).

4. Findings

The Güney formation was measured at different locations in the research area and field observations were made on the sediments. Field observations and measured section data are as follows:

4.1. ÖSK - 1, 2: Kardeşgediği Station

ÖSK - 1 and ÖSK - 2 studies were carried out in the area between 37° 55’ - 37° 57’ north latitude and 34° 43’ - 34° 44’ east longitude around Kardeşgediği station and at an altitude of 1466 m. In this area, lithology is observed in the form of alternation of sandstone - shale - conglomerate - shale. The

sandstone unit is observed in two different lithologies. Fine - grained brown sandstones overlie the coarse - grained green sandstones. The layer thickness and grain size of the sandstones increase in the south - north direction. Green colored sandstones are fed from volcanic material and generally contain serpentine and orthoclase minerals. Coarse - grained pebble - sized serpentine, radiolarite and basalt fragments are observed in the light brown colored sandstone unit. The dark green shale unit with thin lamination lies on top of the sandstone unit. The layer thicknesses of shales vary from thick to thin. As one goes towards the east, the slopes decrease and they become closer to the horizontal. Sandstone shale alternation creates a small scale slump structure, sandstones are dark gray, and shales are dark green - blackish. Conglomerate consists of coarse and blocky at the bottom, lenticular graded at the top, more or less rounded, large and small basalt, andesite, serpentine grains. The lower parts of the conglomerates are serpentine, and the upper parts are basalt. Dark gray (almost black) shales are observed between sandstone - conglomerate units. There is a groove filling structure between the conglomerates and shales overlying the shale unit. Light colored sandstones are layered together with igneous rock composition conglomerates. The diameter of the grain sizes in conglomerates is about 10 - 15 cm and this size decreases to 2 - 3 cm in the west direction. Therefore, the grain size varies from east to west and conglomerates are channel fill (Figure 4). The measured stratigraphic section made in the study area is shown in Figure 5.

According to the petrographic examinations made on thin sections of 20 samples taken from this area (samples between Ö23 and Ö43); light brown in color; The grain size of the fine grained sandstone samples varies between 0.6 - 2.8 mm and the average grain size is 1.6 mm. The cement type between grains is about 4% clay cement and the porosity type is intergranular. Light brown fine grained sandstones, except for Ö29 sample, are moderately sorted and slightly rounded. In the sample Ö29, the sandstones are well sorted and rounded, the grain size varies between 0.2 and 1.2 mm. In this example, the clay cement content is 8%.

Particle size varies between 0.3 and 5.2 mm in samples taken from sandstones containing light green

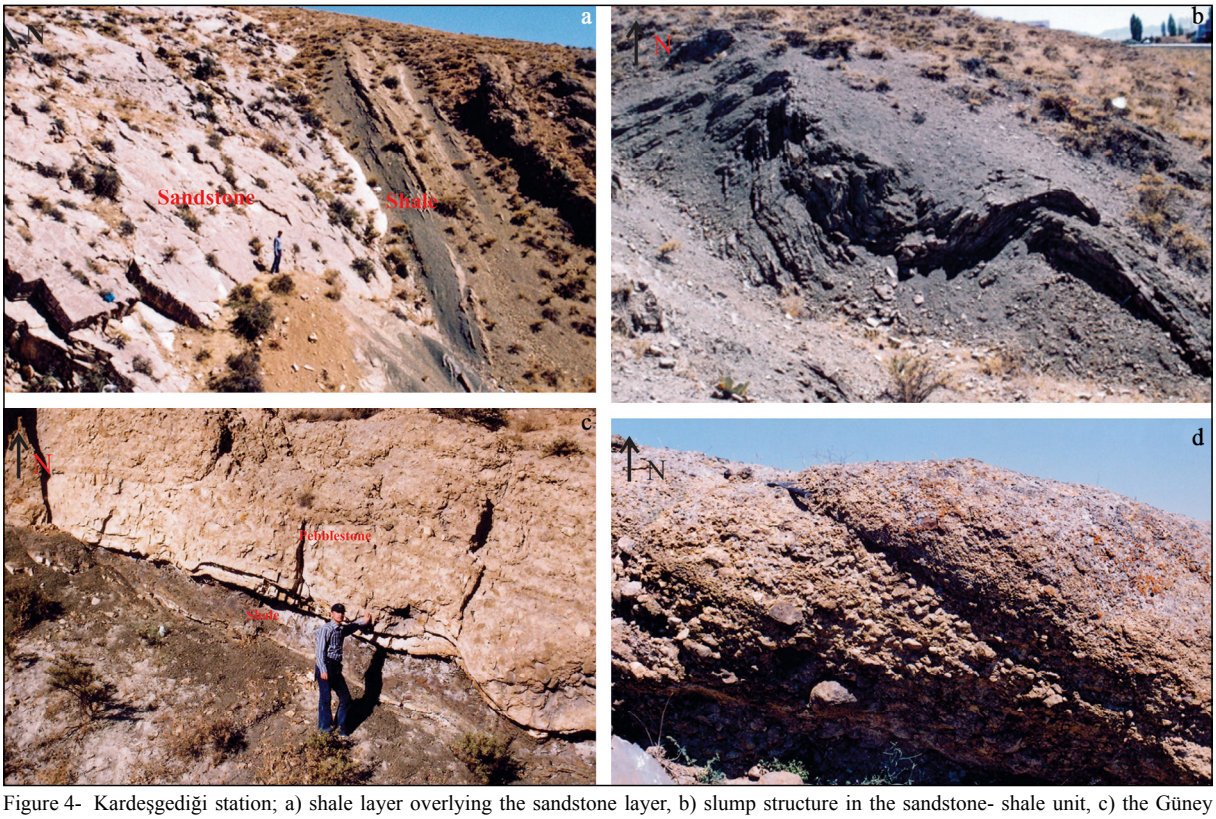

Figure 4- Kardeşgediği station; a) shale layer overlying the sandstone layer, b) slump structure in the sandstone- shale unit, c) the Güney formation channel fill, groove fill structure between two units, d) Güney formation channel fill, normal grading in east - west direction in conglomerates (Özdemir, 2006).

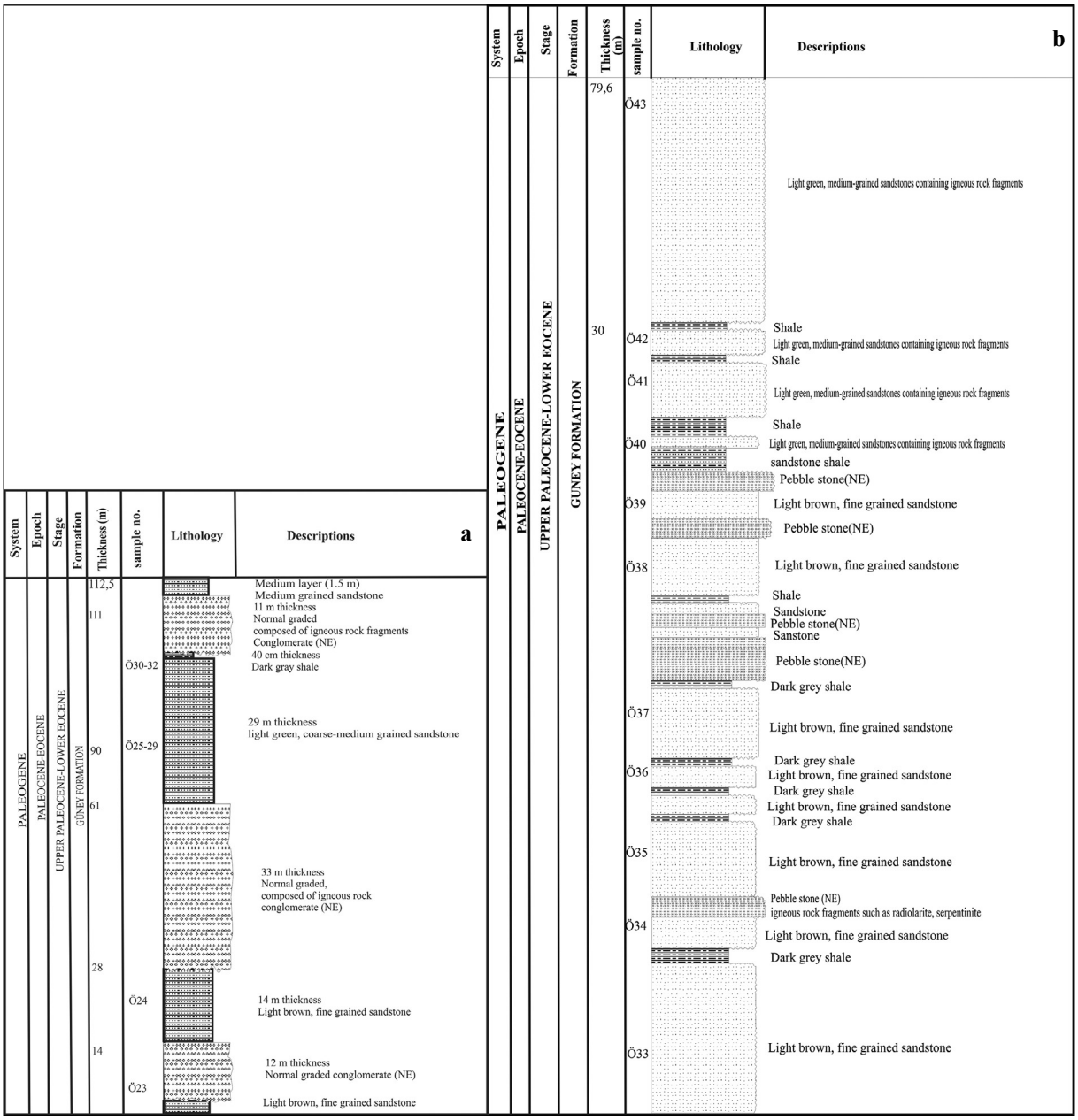

Figure 5- a) Around the Kardeşgediği station: measured stratigrapfic section of the Güney formation (ÖSK - 1), b) south of the Kardeşgediği station: measured stratigraphic section of the Güney formation (ÖSK - 1) (Özdemir, 2006).

medium - grained igneous rock fragments. Sandstones are slightly rounded and medium - poor graded. The samples contain approximately 4% clay cement. The contact relationship between sandstone grains is tangential and the type of porosity is intergranular.

As a result of field observations, OSK studies and petrographic investigations in this area, sand size material is more than clay size, sandstones are slightly rounded and medium - poorly graded, fine - medium grained sandstone layers are thick (at least 2 m), channel fillings, slip (slump) structures and the presence of conglomerates indicate a shallow marine sedimentation environment, indicating that the sequence has convergent turbidite character.

4.2. Around Hantepe

A field study was conducted in the area around Hantepe between 37° 57’ north latitude and 34° 47’ east longitude. In this area, light green, thin laminated shales are observed, and light green shales transition

into light - brown - beige shales. Shale dominance is quite higher compared to sandstones. The upper surfaces of the shales are altered. The transition of thin - bedded shales, which are brown due to ironoxidation, to a light green - colored thick - bedded state indicates the regime change. At the contact between the Güney formation and the Ulukışla formation, the slope of the shales is almost vertical and striking NE. Thickness decreases from bottom to top. The shales of the Güney formation transitions laterally to the agglomerates of the Ulukışla formation. Agglomerates are composed of matrix - supported volcanic material of very coarse size, generally consisting of basalt and andesite grains (Figure 6).

4.3. Near Karalar Station

A field study was conducted in the area around Karalar Station between 37° 62' north latitude and 34°48' east longitude. Sandstones observed in the

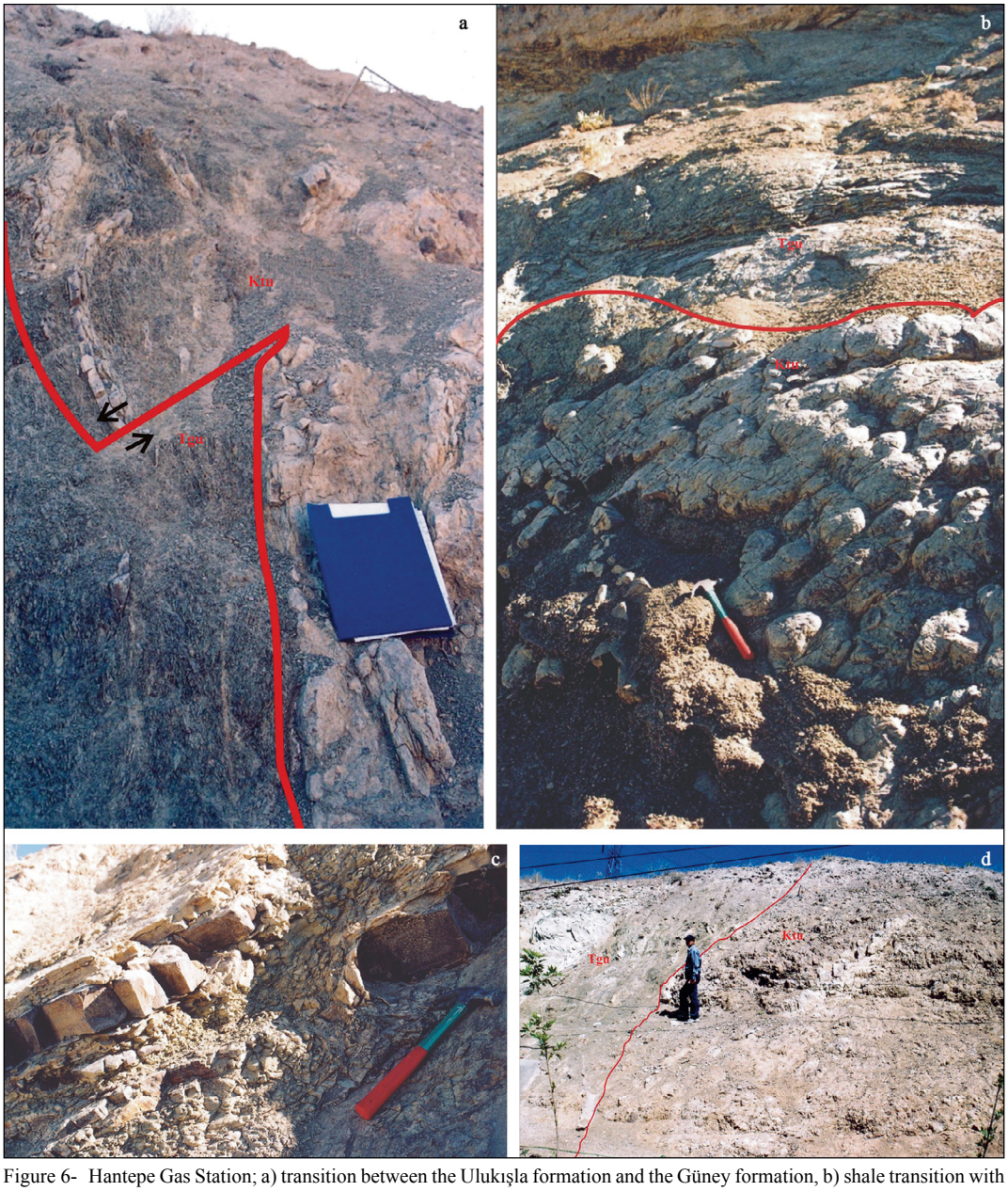

Figure 6- Hantepe Gas Station; a) transition between the Ulukışla formation and the Güney formation, b) shale transition with agglomerate unit at the contact between the Ulukışla formation and the Güney formation, c) close view of shales, d) chale transition with agglomerate unit at the contact between the Ulukışla formation and the Güney formation (KTu: Ulukışla formation, Tgü: Güney formation) (Özdemir, 2006).

area are very fragile, light brown in color, fine grained and their upper surfaces are red - brown due to iron oxidation. Mica and calcite grains are observed in the sandstones. Sandstone layer thicknesses vary from south to north from a thin layer to a thick layer. This thickness difference in the bedding shows the regime change during the storage of sandstones. The depositional environment of the sandstones becomes shallow from south to north.

In the petrographic examinations made on samples Ö16 and Ö17 taken from this area, sandstone sample Ö16 has a grain size between 0.4 and 1.2 mm and shows a slightly rounded medium degree of grading. In this example, the sandstone grains show tangential contact relationship, and the cement type between the grains is clay and is about 12%. Sandstone sample Ö17 has sandstone grain size between 0.2 and 1.2, well sorted and rounded. In this example, the contact relationship between sandstone grains is complete and the clay cement content is 8%. Intergranular pore type was determined in both samples. The Cihanbeyli formation unconformably overlies the Güney formation in the west of the region (Figure 7).

4.4. ÖSK - 3: Tatlıpınar Ridges

ÖSK - 3 study was carried out in the area between 37° 63' - 37° 66' north latitudes and 34° 52' - 34° 54' east longitudes on the hills of Güney village Tatlıpınar, at an altitude of 1523 m. This measured cross-section is on the Güney Village road 2 km inland from the Adana - Niğde Road and Hüsniye junction. An alternation of green shale and brown sandstone is observed in this region. Shale layer density is higher than sandstone layer density. Shale layers are very thinly laminated, sandstones are cracked and brittle as a result of alteration. Calcite veins are seen between the layers. The layer thickness of the shales is 30 cm on average, and the thickness of the sandstone layers varies from approximately 25 - 30 cm to 3 - 5 cm (Figure 8). Sandstone - shale units have formed syncline - anticline - syncline fold structures from north to south. Ovacık syncline is seen in this area. The measured stratigraphic section of the region is presented in Figure 9. Sandstone samples taken from this area are dark green and dark gray, fine to medium grained. Petrographic studies of sandstone samples between AÖ - 1 and AÖ - 6 show that the sandstone grain sizes vary between 0.1 and 1 mm, and the grains have a slightly rounded, medium graded and the intergranular contact relationship is tangential. In these examples, the intergranular cement type contains clay and is approximately 10%. Sandstone samples between Ö6 and Ö15 have grain sizes varying between 0.2 and 1.4 mm. Sandstone samples except for samples Ö11 and Ö15; medium-poorly sorted and slightly rounded. Samples Ö11 and Ö15 are rounded and well sorted.

Figure 7- Transition between the Cihanbeyli formation and the Güney formation (MPc: Cihanbeyli formation, Tgü: Güney formation) (Özdemir, 2006).

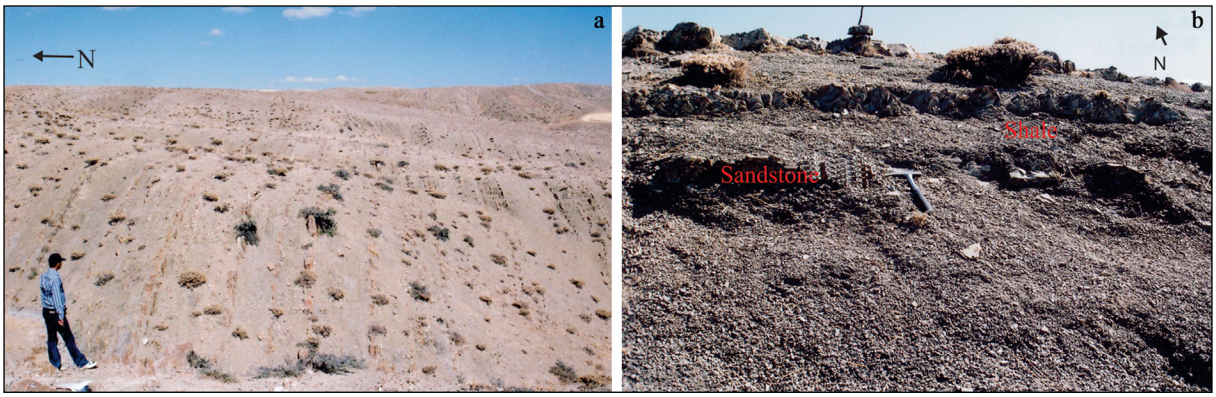

Figure 8- The Güney formation sandstone - shale unit; a) Tatlıpınar ridges, b) North of the Tatlıpınar ridges; sandstone - shale unit close view (Özdemir, 2006).

The clay cement content is lower than other samples and is approximately 4%. Field observations, ÖSK studies, and petrographic investigations in this area show that the deposition environment has deepened and the sequence is divergent turbidite facies.

4.5. ÖSK - 4: Around Ovacık Village

ÖSK - 4 study was carried out in the area between 37° 57' north latitude 34° 47' east longitude around Ovacık Village, at an altitude of 1631 meters. The Güney formation exposed on the slopes in this area consists of sandstone - shale units. Sandstone layers are about 5 cm thick. Shale layers are thicker than sandstone layers. As one goes from the Ovacık village from south to north, the thickness of the sandstone layers increases and the thickness of the shale layers becomes thinner (Figure 10a). This indicates sediment input into the environment together with turbidite currents and indicates that the depositional environment of the unit becomes shallow from south to north. In the north of the area, the transition between Ulukışla formation and Güney formation can be observed (Figure 10b). The measured stratigraphic section made in Ovacık village is shown in Figure 11.

Sandstone grain sizes vary between 0.2 and 1.1 mm in petrographic examinations on sandstone samples taken from this area up to Ö1 - Ö5. Except for the sample Ö5, the sandstones are slightly rounded and medium-poorly sorted. Although samples Ö1 to Ö4 have a clay and iron content of about 10%, the clay cement content of sample Ö5 is about 6%. The pore type of all samples taken from this area is intergranular.

4.6. Adana - Niğde Road

A field study was conducted on the Adana - Niğde road between 37° 69' - 37° 71' north latitudes and 34° 56' east longitudes. Dark brown shale units and light brown sandstone units are observed in this area. The units are in NE direction and their dips are almost vertical. Shales are very fragile, very fine grained, and sandstone units are very hard, thick bedded, coarse grained.

Sandstone - shale - conglomerate units are observed around Taşpınar Gediği, and the slope of these units has increased according to the slope of the units on the previous Adana - Niğde road. There are shale layers between thick bedded, dark gray and medium grained sandstone units. Calcite filling is observed between layers of sandstones. Petrographic studies of sandstone sample AÖ27 taken from this area show that the grain sizes of sandstone varied between 0.5 and 2.2 mm, medium grading, rounded and clay cement content is approximately 10%. The contact relationship between sandstone grains is tangential. In this area, the Cihanbeyli formation comes on the Güney formation. However, the contact border of the Aktoprak formation with the Güney formation is not clear.

Very fine grained, dark gray sandstone and dark gray - blackish shale units are observed at the Karacaören road junction. Sandstone layers are thicker than shale layers. Sandstone thickness decreases towards the upper levels (Figure 12). Petrographic studies on the AÖ28 sample taken from this area show that the grain size of sandstone varied between 0.2 mm and 2.7 mm,

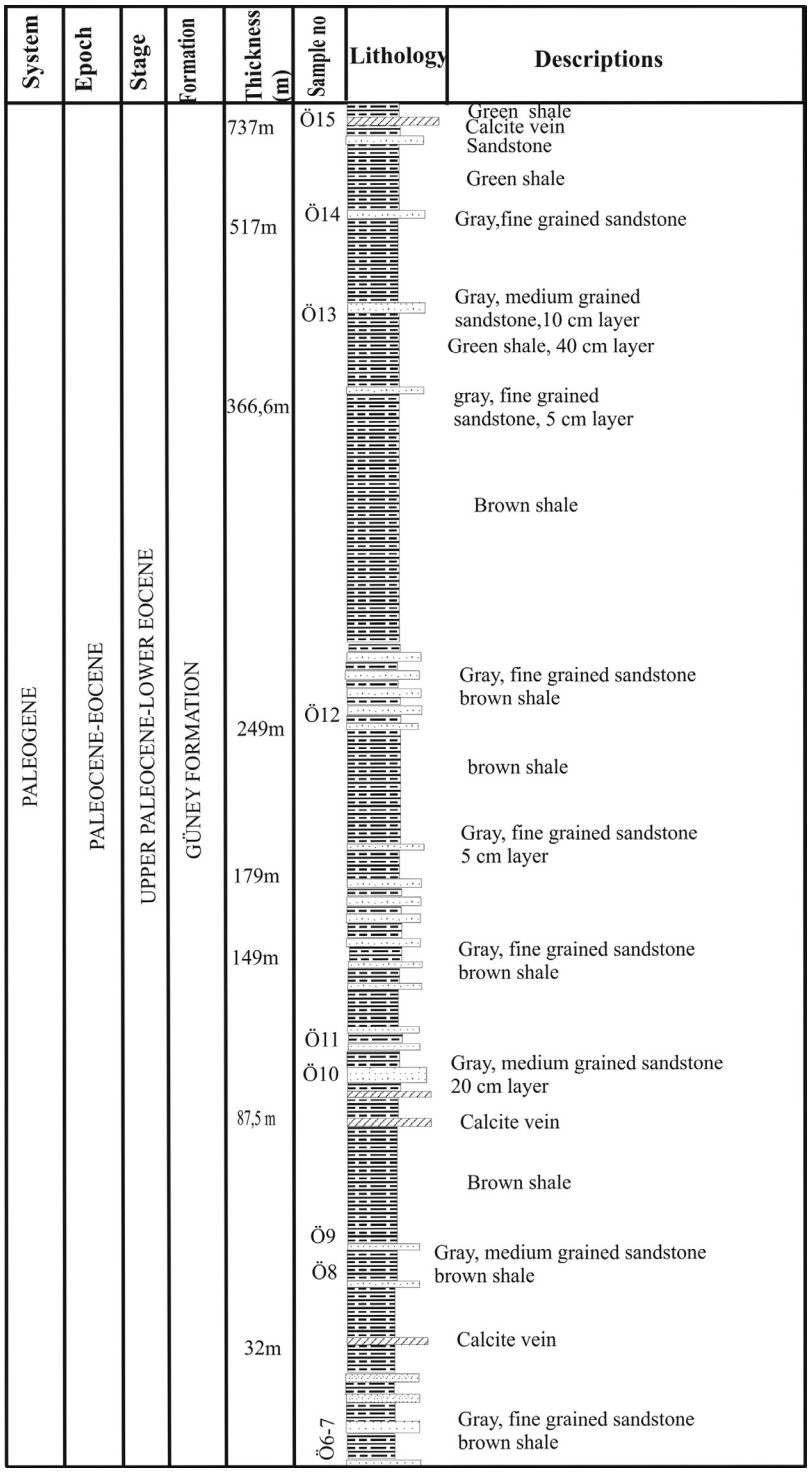

Figure 9- Measured stratigraphic section of Tatlıpınar ridges in the Güney formation (ÖSK - 3) (Özdemir, 2006).

the intergranular contact relationship is tangential, less rolling and medium grading.

The formation shows great variations in lithology and thickness. Lenticularity observed in the coarse - grained clastics in the lower part of the sequence, Large - scale cross - bedding and lateral fast lithological changes indicate a rapid deposition in shallow - deep marine conditions. The change in thickness and density of sandstone - shale layers in the upper parts,

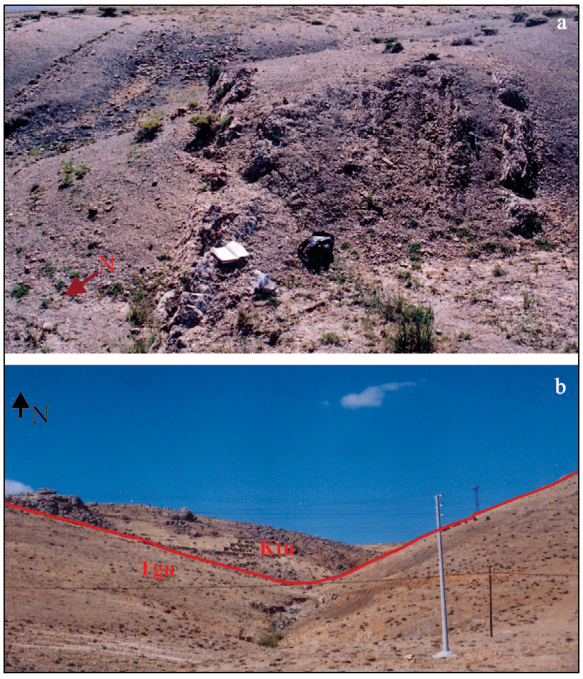

Figure 10- a) Close view of the Güney formation sandstone unit around Ovacık village, b) transition between the Güney formation and the Ulukışla formation (Ktu: Ulukışla formation, Tgü: Güney formation) (Özdemir, 2006).

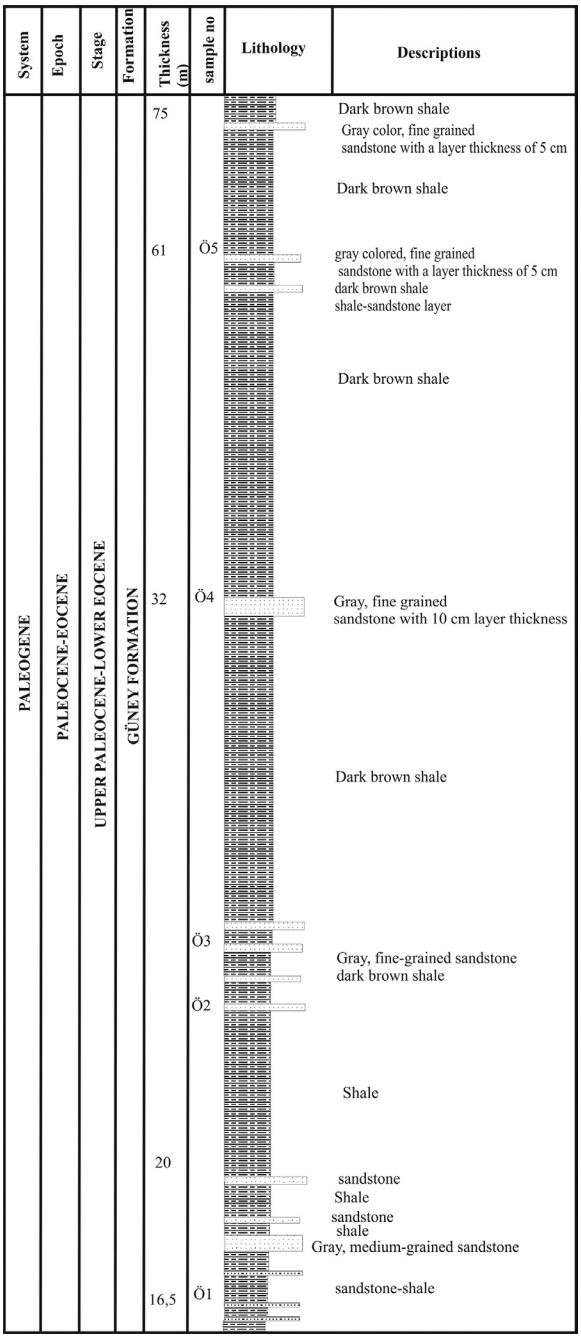

Figure 11- The Güney formation, measured stratigraphic section north of Ovacık village (ÖSK - 3) (Özdemir, 2006).

the erosional - channeled formation of conglomerate-sandstone - shale sequences towards each other and the presence of large hollow fill structures, the presence of gradual bedding as common internal structure and the shallow marine deposition conditions have changed over time, indicates that the environment is getting deeper. The Güney formation consists of a 365 m sandstone - conglomerate sequence around Ulukışla, 90 m thick around Porsuk village in the east of Ulukışla, 160 m sandstone - conglomerate - shale sequence in the east of Çaykavak pass (on the Ulukışla - Niğde road). In the north of Ulukışla, all of the material of the Güney formation is derived from volcanic and shallow intrusive type magmatics and consists mostly of conglomerates. Graded bedded channel fillings, shear deposits, and turbiditic sandstone alternations are common in the upper levels of the sequence.

5. Petrography

Fine sections obtained from fifty - two (52) sandstone hand specimens taken from the formation were petrographically examined under microscope, and their grain size, grain roundness, grading, contact relationship, cement type and porosity type characteristics were determined. The average grain composition was evaluated according to the percentage of feldspar, quartz, rock fragments and secondary mineral content. In petrographical studies, sandstone samples taken from south - north direction in the study area show a grain size distribution from thin to coarse. The sandstones are of medium maturity and medium - poorly sorted texturally. Generally dense textured, partially well sorted, rounded. Matrix generally consists of clay and its content is around

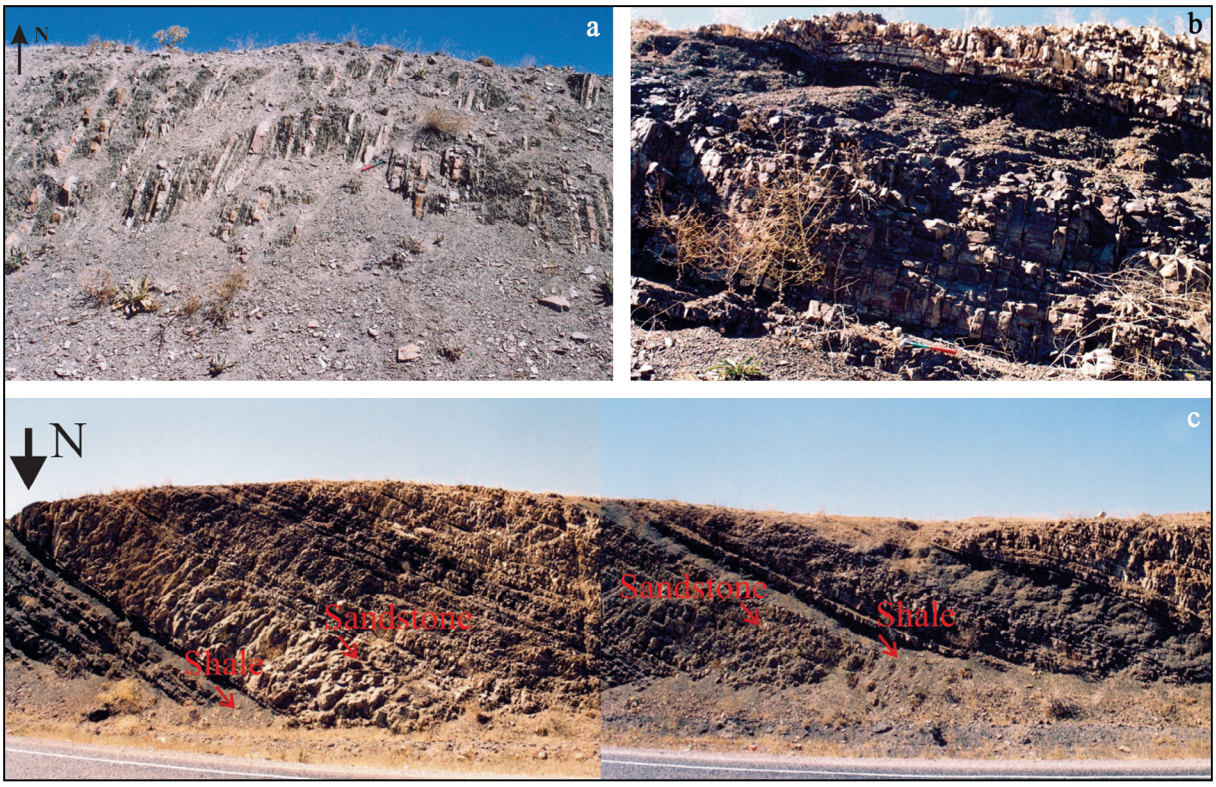

Figure 12- a) Sandstone - shale units of the Adana - Niğde road Güney formation, b) Karacaören road junction, the Güney formation sandstone - shale alternation, c) Karacaören road junction, the Güney formation sandstone - shale alternation (Özdemir, 2006).

10% on average. Clay + Fe matrix content is on average 4%. Iron oxide and carbonate cement were also observed in sandstone thin section samples, and they are found together with clay cement. Tangential growths were observed in quartz grains in sandstone sections (Figure 13).

The Güney formation's average grain composition; Total quartz varies between 11 - 65%, monocrystalline quartz 4 - 45%, polycrystalline quartz 5 - 40%, feldspar 28 - 15%, rock fragments 28 - 85%, secondary mineral content is between 2 and 4%, these are mica and epidote (Table 1). According to the Folk et al. (1970) classification, sandstones are feldspathic lithicarenite and lithicarenite (Figure 14).

6. Source Areas of the Güney formation

Considering the average grain composition of the Güney formation, Dickinson et al. (1983); it occurred in the undissociated arc and regenerated orogenic provenance (Figure 15). According to Dickinson and Suczek (1979), it is between the undivided arc, active island arc and continental crust. Arc ridges are partially eroded. The depositional areas, inside trenches, front of the arc, behind the arc, and local basins in the volcanic belt. These basins indicate that the source area of the Güney formation is an unallocated arc and deposited in front of the arc.

Thrust complexes deform oceanic sediments and lavas, the collision orogen coexists with the continental blocks and the basin in front of the folding - faulting belt. In the arcs in front of the continental block, suture belts occur between the magmatic arc and disappearing arc basins. The regenerated orogenic provenance areas are between trench axes in arc - trench systems and volcanic elevation. Sediments were deposited from the folded - faulting zone towards the fore basin, between the trench and the trench-arc from the thrust complex (Dickinson and Suczek, 1979). The Güney formation, located in the regenerated orogenic provenance resource area, shows that the sandstones were deposited in front of the arc (Figure 16).

An island - arc extending east - west has formed around Ulukışla (Oktay 1982). Ulukışla, Hasangazi and Halkapınar formations were fed from the materials derived from this island arc. These formations formed behind and in front of the island arc (Özdemir, 2006).

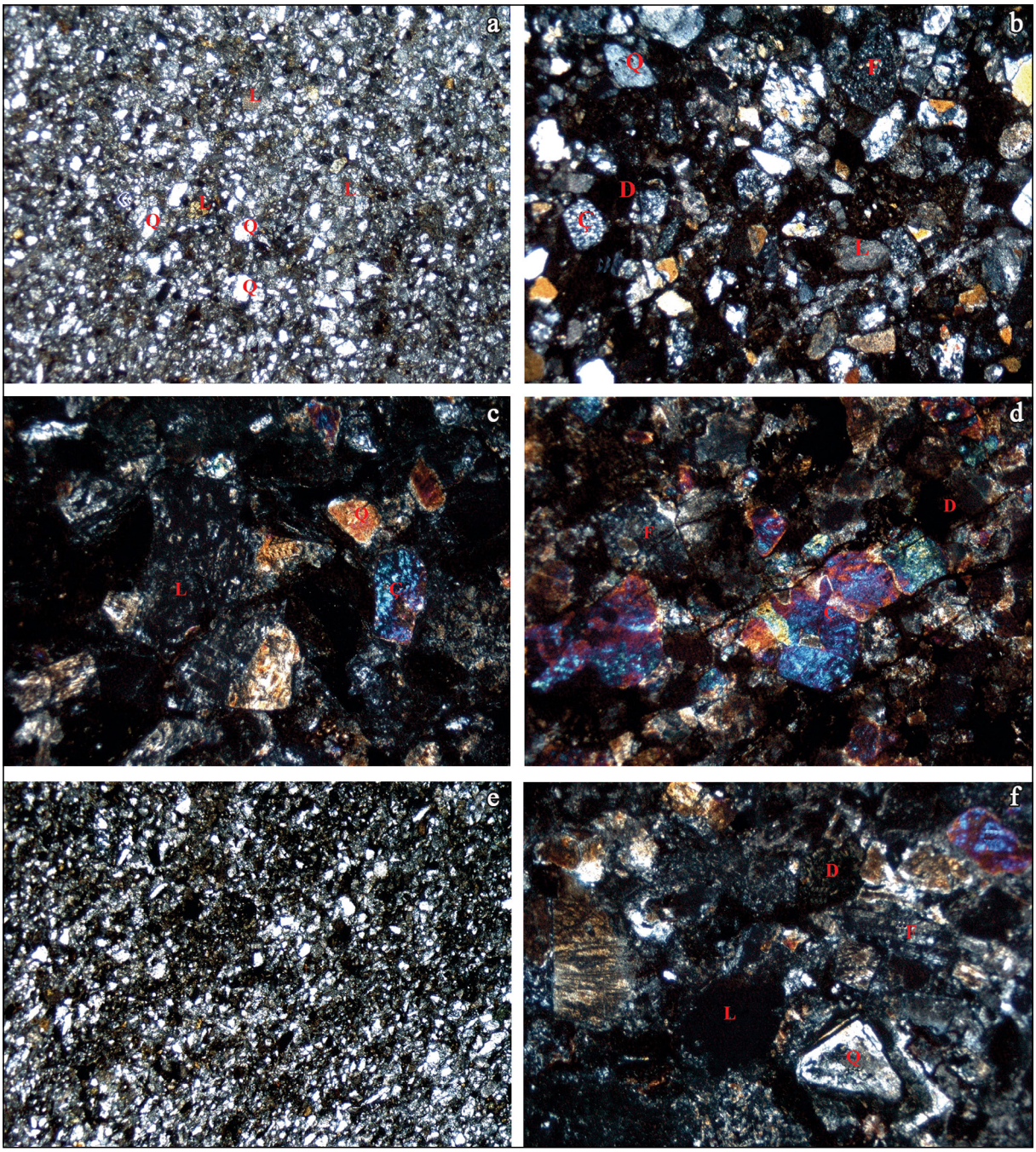

Figure 13- Güney formation sandstone; a) crossed nicols view of thin section of sample Ö5, sandstones are moderately sized and slightly rounded (10X), b) Crossed nicols view of thin section of sample Ö9, sandstones are slightly rounded and medium sorted (10X), c) crossed nicols view of thin section of sample Ö2, sandstones are slightly rounded and poorly sorted (10X), d) sample Ö33, thin section crossed nicols view, sandstones are slightly rounded and poorly sorted (10X), e) Nicol image of sample thin section no Ö5, sandstones rounded and well sorted (10X, f) crossed nicols view of thin section of sample Ö25, tangential growths in quartz grains (10X) (D: iron oxide cement, L: lithic piece, Q: quartz, F: feldspar, Ç: chert) (Özdemir, 2006).

Table 1- Güney formations grain composition (Özdemir, 2006).

Sample No.	%Qt	%Qm	%Qp	%F	%Rock fragments	%Secondary mineral
AÖ-1	60	45	15	8	30	2
AÖ-2	60	45	15	10	30	
AÖ-3	60	45	15	10	30	
AÖ-4	65	50	15	5	28	2
AÖ-5	20	14	6	4	76	
AÖ-6	60	25	30	10	30	
AÖ-7	55	40	15	10	25	
AÖ-8	55	40	15	10	25	
AÖ-9	55	40	15	10	35	
AÖ-10	60	35	25	8	32	
AÖ-11	55	30	40	10	35	
AÖ-12	50	40	10	2	40	
AÖ-15	17	9	8	3	80	
AÖ-16	12	4	8	5	80	
AÖ-17	50	15	35	10	40	
AÖ-18	15	5	10	5	80	
AÖ-19	11	6	5	4	85	
AÖ-20	13	10	8	75	4	
AÖ-21	41	30	11	4	55	
AÖ-22	40	25	15	8	48	4
AÖ-23	45	15	30	5	50	
AÖ-24	50	40	10	10	40	
AÖ-25	30	5	25	5	65	
AÖ-26	30	20	10	15	55	
AÖ-27	60	45	15	10	30	
AÖ-28	60	50	10	8	32	

Sample No.	%Qt	%Qm	%Qp	%F	%Rock fragments	%Secondary mineral
Ö1	55	45	10	10	35	
Ö2	55	45	10	10	35	
Ö3	55	45	10	10	35	
Ö4	55	45	10	10	35	
Ö5	55	45	10	8	35	2
Ö8	60	45	15	10	30	
Ö9	62	40	22	8	30	
Ö10	40	25	15	10	50	
Ö11	40	25	15	10	50	
Ö12	40	25	15	10	50	
Ö15	40	25	15	10	50	
Ö16	20	4	16	5	75	
Ö17	35	30	5	10	55	
Ö22	40	25	15	5	55	
Ö27	30	25	15	10	60	
Ö28	33	18	15	7	60	
Ö29	40	35	5	5	55	
Ö30	30	25	5	10	60	
Ö31	30	25	5	10	60	
Ö32	40	10	6	10	50	
Ö33	40	30	10	8	52	
Ö34	30	25	5	5	65	
Ö35	50	40	10	5	35	
Ö36	50	40	10	5	45	
Ö39	20	13	12	5	75	
Ö40	30	20	10	5	65	
Ö41	20	15	5	5	75	
Ö43	15	10	5	5	80	

7. Discussion

Ketin and Akarsu (1965) and Demirtaşlı et al. (1973) stated that the Ereğli - Ulukışla Basin is in the form of an asymmetrical rift. According to the researchers, the basin burial and rift formation started in the Maestrichtian and Paleocene. In the Late Cretaceous, the function of the subduction zone, which provided ophiolite settlement to the south of the region, ended and a new subduction zone in the basin began to dip towards the north. For this reason, the magmatic function is observed in the basin in the form of submarine volcanism trending east - west in the Late Cretaceous or Early Paleocene. As a result of the submerged plate, its movement throughout the Paleocene, and its partial melting, an island arc developed in an east - west direction around Ulukışla. Some parts of the arc emerged in the form of volcanic islands in the Early Paleocene. These formed two separate belts from Ulukışla to the east, south and north of Eminlik. In the Late Paleocene, especially in the north of the island arc, with the end of magmatism, clastic material started to come from both the islands

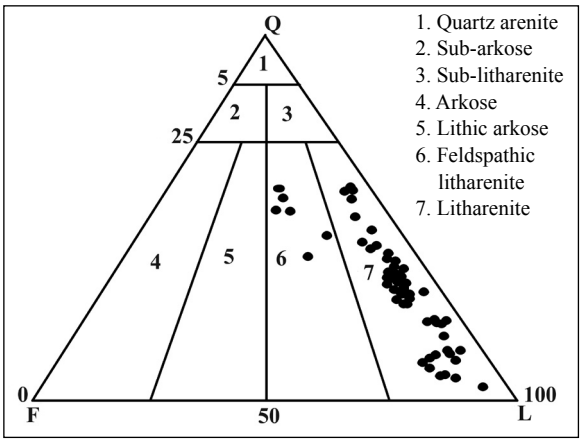

Figure 14- According to Folk et al. (1970) Sandstones Classification (Q - Quartz, F - Feldspar, L - Rock fragment) (Özdemir, 2006).

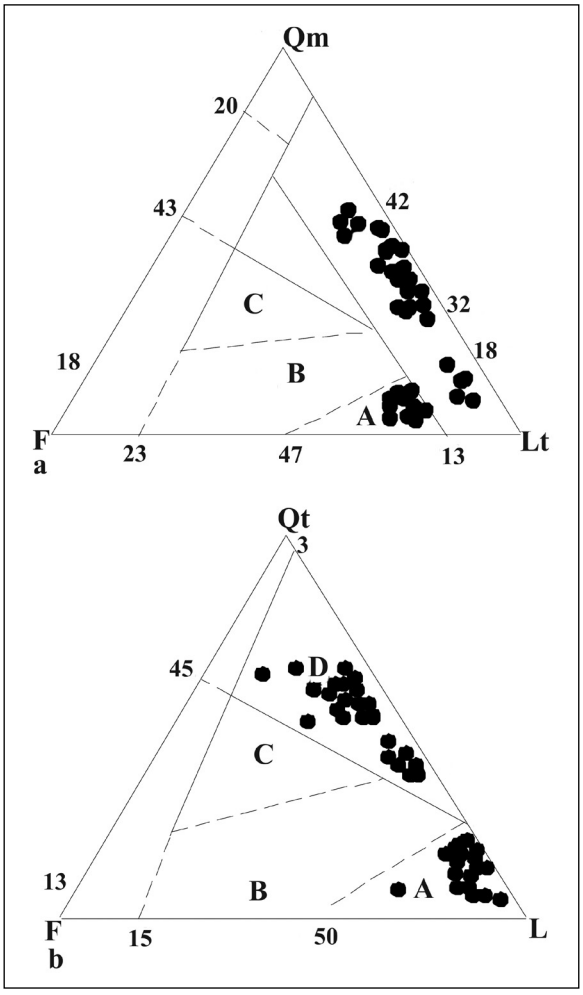

Figure 15- The diagrams which showing the average grain composition of sandstones; a) QmFLt diagram, b) QtFLt diagram (Qm- monocrystalline quartz, Qt- total quartz grains, F - feldspar and Lt - total lithic parts). Provenance (source) areas (Dickinson vd., 1983): A - unallocated arc, B - arc (partially separated). C - separated arc and D - regenerated orogenic provenance (Özdemir, 2006).

above the water and possibly from the western part of the Tuz gölü basin - as well as with turbidite flows. In the Early Eocene, the section north of the island arc of the basin folded into a land. Oktay (1982) stated that this event also caused the end of the volcanic activity in the southern part of the island arc and the Güney formation to begin to deposit, and also stated that the Güney formation was deposited in the deep trenches between Bolkardağı and Ulukışla while the conditions in the region were continuing unchanged in the Middle Eocene. Although Oktay (1982) claims that the depositional environment of the Güney formation is the deep trenches in and around the volcanic island arc and the slopes connecting these trenches to the volcanic islands, as a result of the evaluation made by considering the average grain composition in this study, it is revealed that the deposition environment of the formation is in front of the arc.

Turbidites are observed in two types according to the current density. Sediments formed in high - density flows are generally thicker - bedded, low - graded, coarser - grained, relatively poorly graded, with little internal laminates, and their bottom structures are either undeveloped or slightly developed. Sediments with fine - bedded, fine - grained, well - developed vertical grading and sorting, well - developed laminated, small - scale cross - bedding are formed by the low - density turbid flow. Bouma (1964) divided the ideal layer structure that the regime (energy / power) of a turbid current can create into five structural sections; massive grade gravel (Ta), laminated sand (Tb), cross- laminated sand (Tc), laminated stack (Td), laminated mud (Te). A turbidite stack cannot always have its ideal structure because the energy of each flow is different and the energy is not constant even within the same flow regime. Turbidite deposits accumulated away from the source area (in the direction of the sea) or below the slope are missing from the bottom, Ta; Ta, Tb; Ta is Tb, Tc and Ta, Tb, Tc, Td sections are the missing parts. Top eroded successions are observed as Ta; Ta; Tb; Ta; Tb; Tc, and Ta, Tb, Tc, Td. Tb, Tc, Td, Te; Tc, Td, Te; Td, Te; Te; sections are missing. Such a sequence is a sequence formed by a second turbidite stream eroding a previously deposited turbidite sequence and close to the source of sediment (inland direction). When a complete turbidite sequence is missing from both top and bottom; They are observed as layers missing from the bottom and eroded from the top. These stacks

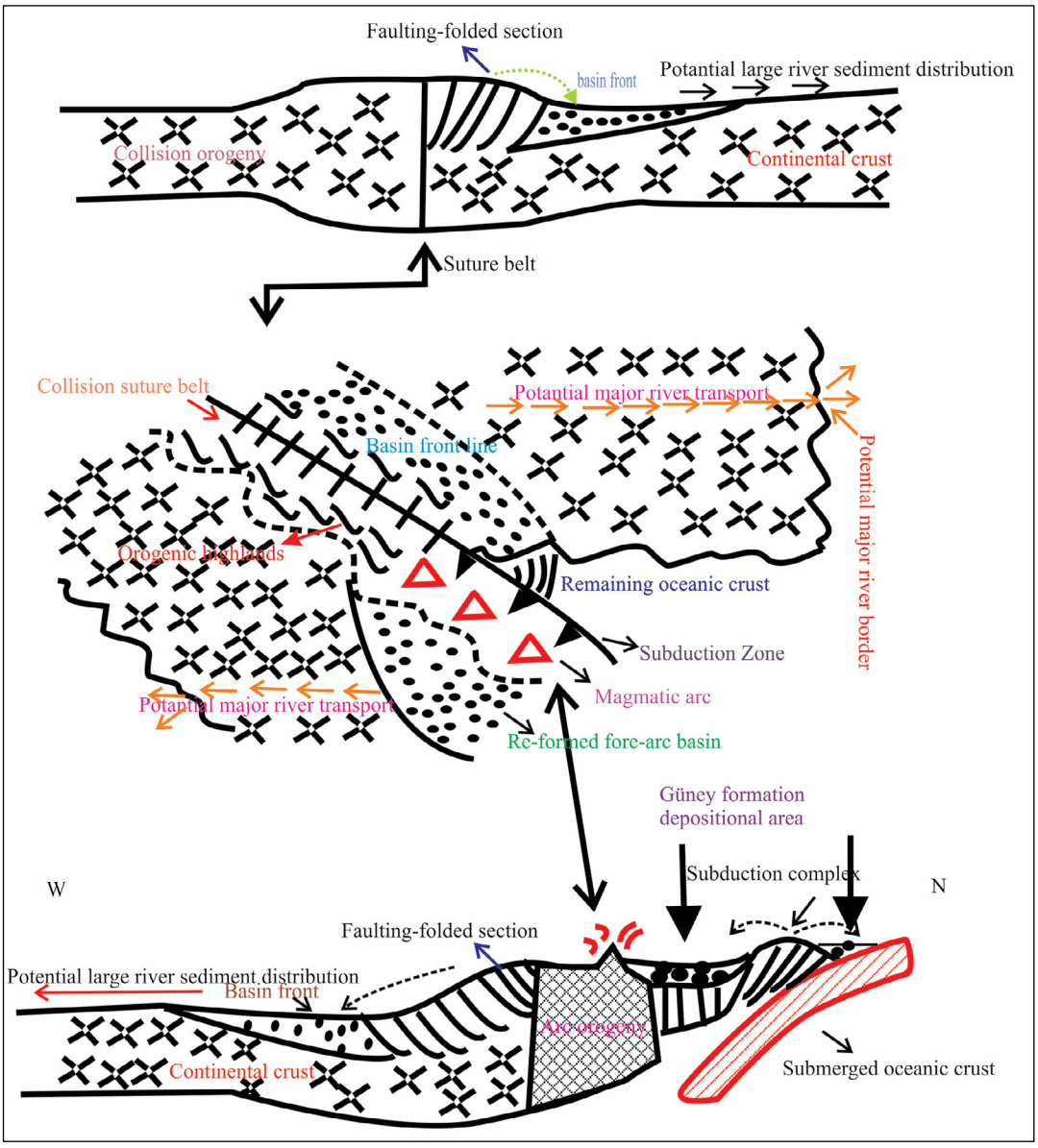

Figure 16- Basins associated with regenerated orogenic provenance. The shape seen at the top; collision orogen, bottom figure; The arc orogen shows the basin and front basin currents, the fore-arc basin and trench are well developed within the active trench system. The areas indicated by arrows at the bottom show the sediment distribution derived from the faulting-folded area and the thrust complex (Dickinson and Suczek, 1979) (N:North, S: South).

can consist of Tb; Tb, Tc; Tb, Tc, Td and Td sections. These sequences can be deposited both near and far from the source of sediment (Mutti, 1992). The ÖSKs prepared as a result of the field studies carried out in the Ovacık village, Tatlıpınar ridges, point to the Bouma succession, which is missing from the bottom and eroded from the top. However, at the Kardeşgediği station, the Güney formation has the Ta and Tb series of the Bouma sequence, and it outcrops here as being sculpted from the top.

According to Walker (1978), the alluvial fans on which the turbiditic facies assemblages are located are divided into three parts, namely inner fan, middle fan and outer fan, according to lithofacies assemblages. Convergent turbidites are deposited in the upper fan. The matrix is in the size of sand. Thick bedded, coarse sandstone, pebbly sandstone and conglomerates are widely observed. Conglomerates are generally well rounded, in quite different sizes and mostly grain supported. Sandstones are generally coarse - grained

and cross - bedding is quite common. Stratified fine-grained sediments are observed in the outer range, where sediments with divergent turbidite character are deposited.

ÖSK - 1, 2, 3 and ÖSK - 4, which are made in the Güney formation and are correlated with each other; (From Hantepe to Ulukışla - Niğde road, along the Karacaören road junction) from bottom to top shale - volcanic rock- added conglomerate - fine grained sandstone - medium grained sandstone - shale - gray, fine - grained sandstone - shale - gray - colored, fine -grained sandstone in the form. The stack is developed in turbidite facies. At the Kardeşgediği Station (ÖSK - 1, ÖSK - 2), the sand size material is more than the clay size material, the sandstone layers are thick (at least 2 m), the channel fillings, slump structures and pebbles show the convergent turbidite character. However, in Tatlıpınar Ridges (ÖSK - 3) and Ovacık-Güney village (ÖSK - 4) shales have an average layer thickness of 30 cm (thick) and sandstones up to 3 - 5 cm (thin). Shales are denser than sandstones, which show divergent turbidite features (Figure 17, 18).

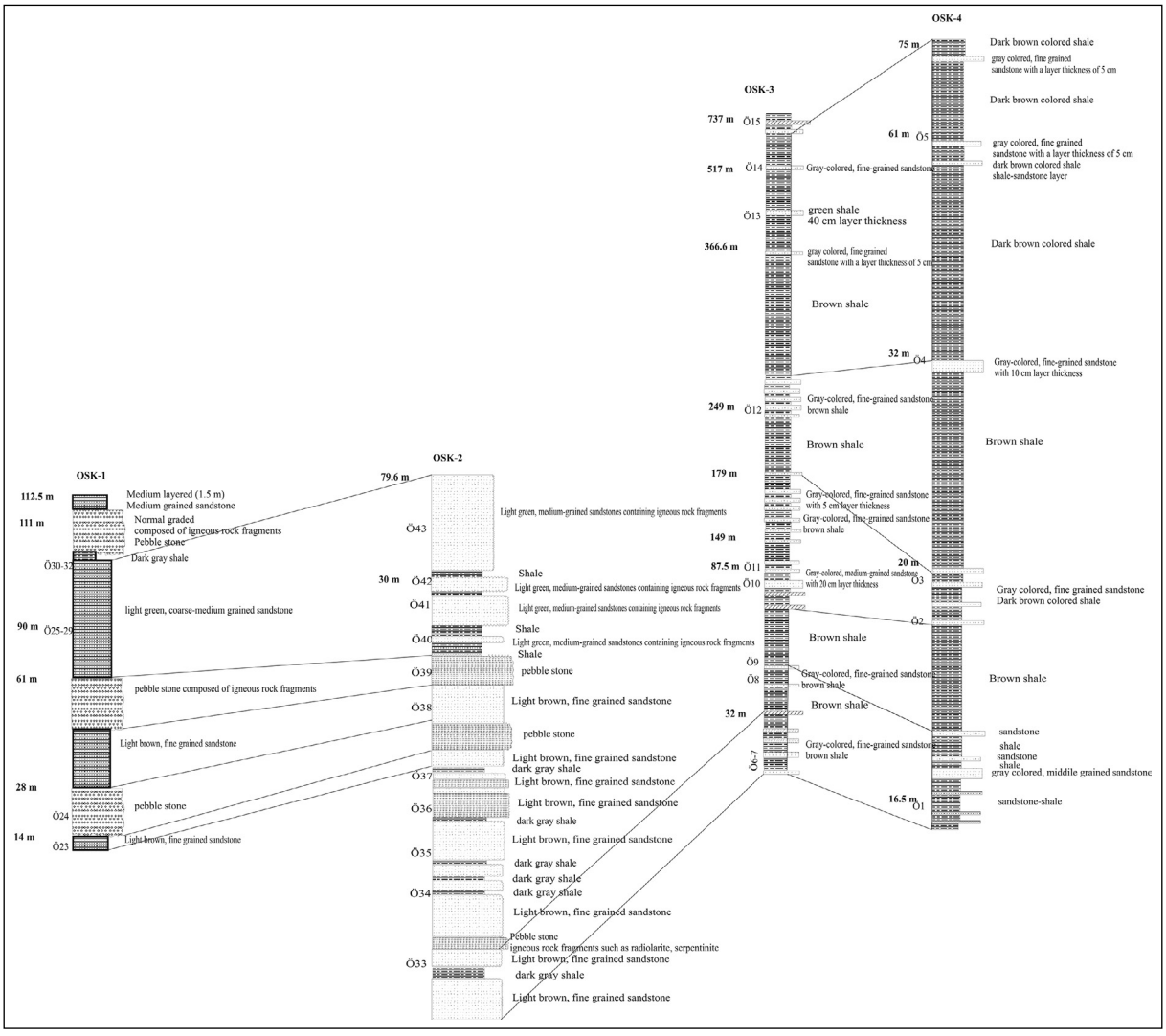

Figure 17- Correlation of ÖSK's in the study area.

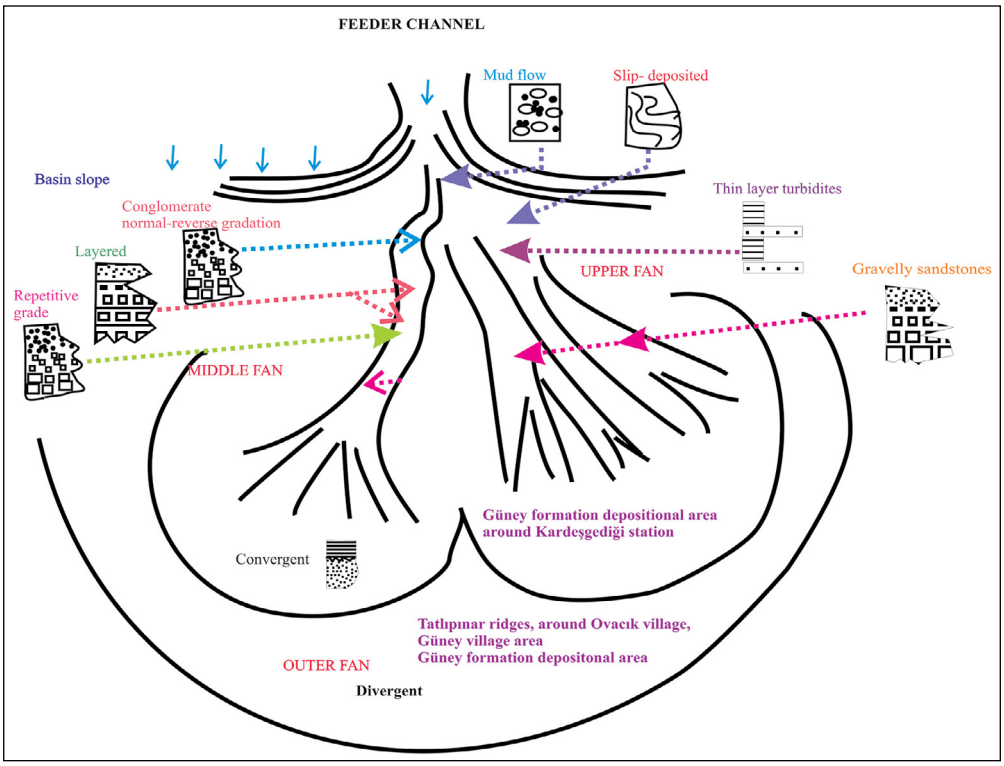

Figure 18- Turbidite fan model (Walker, 1978).

8. Results

In previous studies, the units referred to as Serenkaya and Ovacık formations were investigated under the name of Güney formation considering their distribution and location in the region. It has been observed that the Güney formation starts with lenticular conglomerates at the base and continues as sandstone - shale alternation.

In the study area, there is the Late Cretaceous - Middle Eocene Ulukışla formation at the basement. Paleocene - Early Eocene Halkapınar formation is laterally and vertically transitive with the Ulukışla formation. The Güney formation overlies these formations by transiting laterally and vertically with the Ulukışla and Halkapınar formations observed at the basement. The Late Eocene - Oligocene aged Aktoprak formation comes over the Güney formation by transitioning in lateral and vertical directions. The Miocene - Pliocene aged Cihanbeyli formation overlies these units unconformably.

ÖSK - 1, 2, 3 and ÖSK - 4, which are made in the Güney formation and are correlated with each other; (From Hantepe to Ulukışla - Niğde road, along the Karacaören road junction) from bottom to top shale - volcanic rock - added conglomerate - fine - grained sandstone - medium - grained sandstone - shale - gray, fine - grained sandstone - shale - gray - colored, fine - grained sandstone in the form. The stack has been deposited by turbiditic flows.

The lower parts of the sequence contain channel fillings and the sandstone density is high, so it presents a convergent turbiditic character. Sandstone and shale densities are equal towards the north in the study area. In the upper parts of the sequence, channel fillings are again observed, and the sandstone grains become coarse and their density increases, while shale density decreases. Therefore, the upper levels are seen in the convergent turbiditic character.

The unit is generally developed as a sequence of gray - coarse sandstone and shale, with a thickness of approximately 800 m. Due to the sandstone - shale - conglomerate - shale alternation lithology of the unit as a result of the ÖSK - 1 and ÖSK - 2 study performed at an altitude of 1466 m in the area between 37° 55’ - 37° 57’ north latitude and 34° 43’ - 34° 44’ east

longitudes around Kardeşgediği station, the sequence is in convergent turbidite character in this area. Güney village, on the hills of Tatlıpınar between 37° 63' - 37° 66' north latitudes and 34° 52' - 34° 54'east longitudes, 1523 m high ÖSK - 3, around Ovacık Village, between 37° 57' north latitude and 34° 47' east longitude, 1631 meters high ÖSK - 4 study was carried out. According to the studies of ÖSK - 3 and ÖSK - 4, the Güney formation consists of sandstone-shale units. The sequence reflects the divergent turbidite character in these areas.

Sandstone samples collected from the study area are lythic arenite and feldspathic arenite according to Folk et al. (1970) classification.

According to Dickinson et al. (1983) in the data we obtained from petrographic investigations, the Güney formation sandstones are found in the arc and regenerated orogenic provenance zones, whose source areas are not separated. According to Dickinson and Suczek (1979), these regions show that the Güney formation's depositional area is in front of the island arc.

Acknowledgments

This article is the product of a master's thesis on the geology and petroleum reservoir rock properties of the Ereğli - Ulukışla basin Güney formation. During the master thesis field study, I express my deepest love and respect to my late father Cemil Özdemir, who helped take and carry samples, and Manolya Sınacı, who helped with fossil determinations. I would like to express my gratitude and respect to Prof. Dr. Yusuf Kaan Kadıoğlu, who provided laboratory facilities during petrographic examinations. In addition, I would like to express my gratitude and respect to Prof. Dr. Atike Nazik, who added invaluable contributions and opinions to this article and made an evaluation. Also i would like to express my gratitude and respect to the editor of Bulletin of the Mineral Research and Exploration Prof. Dr. Halim Mutlu, and to the assistant editors.

References

Akgün, F., Kayseri Özer, M.S., Tekin, E., Varol, B., Şen, Ş., Herece, E., Gündoğan, İ., Sözeri, K., Us, S., M. 2020. Late Eocene to Late Miocene palaeoecological and palaeoenvironmental dynamics of the Ereğli - Ulukışla Basin (Southern Central Anatolia). Geological Journal 1-31. https://doi.org/10.1002/gj.4021

Baş, H., Ayhan, A., Atabey, E. 1986. Ulukışla - Çamardı (Niğde) volkanitlerinin bazı petrolojik ve jeokimyasal özellikleri. Türkiye Mühendis ve Mimarlar Odası Birliği Jeoloji Mühendisliği Dergisi 26, 27-34.

Blumental, M. M. 1956. Yüksek Bolkardağının Kuzey Kenar Bölgelerinin ve Batı Uzantılarının Jeolojisi. Maden Tetkik ve Arama Genel Müdürlüğü Yayını, 153.

Bouma, A. 1964. Turbidites. Turbidites Developments in Sedimentology 3, 247-256. doi:10.1016/s0070-4571(08)70967-1

Dellaloğlu, A. A., Aksu, R. 1986. Ereğli (Konya) - Ulukışla-Çiftehan - Çamardı (Niğde) dolayının jeolojisi ve petrol olanakları. Türkiye Petrolleri Anonim Ortaklığı, Rapor No: 2205, 11-15, Ankara.

Demirtaşlı, E., Bilgin, A. Z., Erenler, F., Işılar, S., Sanlı, D., Selim, N., Turhan, N. 1973. Bolkardağlarının jeolojisi. Cumhuriyetin 50. yılı Yerbilimleri Kongresi. Bulletin of Mineral Research and Exploration 12, 42-67.

Dickinson, W. R., Suczek, C. A. 1979. Plate tectonics and sandstone compositions. American Association of Petroleum Geologists Bulletin 63, 2142-2182.

Dickinson, W. R., Beard, L. S., Breakendridge, G. R., Erjavec, L. J., Ferguson, Inman, K. F., Knepp, R. A., Lindberg, F.A., Ryberg, P. T. 1983. Provenance of North American Phanezoic sandstones in relation to tectonic setting. Geogical Society of America Bulletin 94, 222-235.

Folk, R. L., Andrews. P. B., Lewis, D. W. 1970. Detrial sedimentary rock classification and nomenclature for use in New Zeland. Journal of Geology and Geophysics 13(4), 937-968.

Gürbüz, E., Seyitoğlu, G., Güney, A. 2020. Late Cenozoic tectono - sedimantary evolution of the Ulukışla Basin: progressive basin development in south-central Turkey. International Journal of Earth Science (Geologische Rundschau) 109, 345-371. https://doi.org/10.1007/s00531-019-01805-8

Ketin, İ., Akarsu, R. 1965. Ulukışla Tersiyer Havzasının jeolojik etüdü hakkında rapor. Türkiye Petrolleri Anonim Ortaklığı, Rapor No: 339, Ankara.

Mutti, E., Davoli, G. 1992. AGIP Press. Turbidite Sandstones, 275.

Nazik, A., Gökçen, N. 1989. Ulukışla Tersiyer istifinin foraminifer and ostrakod faunasına göre stratigrafik yorumu. Türkiye Jeoloji Kurultayı Bülteni 32, 89-99.

Nazik, A., Gökçen, N. 1992. Ostracoda genus Zonocypris and its species in Kurtulmustepe Formation of Ulukisla Basin (Turkey). Revista Española de Micropaleontologia 24, 63-69.

Okay, A. C. 1955. Niğde - Çamardı ve Ulukışla arasındaki bölgenin jeolojisi. Maden Tetkik ve Arama Genel Müdürlüğü, Rapor No: 2381, Ankara (unpublished).

Oktay, F. Y. 1982. Ulukışla ve çevresinin stratigrafisi ve jeolojik evrimi. Türkiye Jeoloji Kurultayı Bülteni 25, 15-23.

Özdemir, A. 2006. Ereğli - Ulukışla Havzası Güney Formasyonunun Jeolojisi ve Petrol Hazne Kaya Özelliklerinin İncelenmesi. Yüksek Lisans Tezi, Ankara Üniversitesi, Jeoloji Mühendisliği, 93.

Sınacı, M. 2006. Ereğli - Ulukışla Havzası Güney Formasyonu Nannoplankton Biyostratigrafisi. Yüksek Lisans Tezi, Ankara Üniversitesi, Jeoloji Mühendisliği, 130.

Sonel, N., Sarı, A. 2004. Ereğli - Ulukışla (Konya - Niğde) havzasının hidrokarbon potansiyelinin incelenmesi. G. Ü. Mühendislik - Mimarlık Fakültesi Dergisi 19(14), 393-403.

Sonel, N., Sarı, A., Toprak, Ö., Şengüler, İ. 1999. Ulukışla (Niğde) bitümlü şeyllerinin jeokimyasal incelemesi. S. Ü. Mühendislik - Mimarlık Fakültesi Dergisi 14(2), 77-89.

Walker, R. G. 1978. Deep water sandstone facies and ancient submarine fans: model for exploration for stratigraphic traps. American Association of Petroleum Geologists Bulletin 62(6), 932-966.

Yoldaş, R. 1973. Niğde - Ulukışla bitümlü şist alanının jeolojisi ve ekonomik olanakları. Maden Tetkik ve Arama Genel Müdürlüğü, Rapor No: 5050, Ankara (unpublished).

Bulletin of the Mineral Research and Exploration

http://bulletin.mta.gov.tr

Comparison of different approaches of computing the tilt angle of the total horizontal gradient and tilt angle of the analytic signal amplitude for detecting source edges

Luan Thanh PHAM[a*], Erdinç ÖKSÜM[b], Thanh Duc DO[a] and Minh Duc VU[a]

[a]*Vietnam National University,University of Science, Faculty of Physics, Department of Geophysics, Hanoi, Vietnam*
[b]*Süleyman Demirel University, Engineering Faculty, Department of Geophysical Engineering, 32200, Isparta, Turkey*

Research Article

Keywords:
Edge Detection, Horizontal Gradient, Analytic Signal, Tilt Angle, Direct Expression, Frequency Technique.

Received Date: 14.04.2020
Accepted Date: 02.06.2020

ABSTRACT

This paper compares effectiveness of the different approaches of computing the tilt angle of the horizontal gradient amplitude and tilt angle of the analytic signal amplitude such as use of direct expression and frequency domain technique (also called k - function) in terms of their accuracy on the detection of the edges of magnetic and gravity sources. These approaches were performed on both synthetic magnetic and gravity data where the frequency domain technique shows improvements in delineation of the actual edges of the sources compared to the direct expression. Additionally, real magnetic data from Zhurihe (Northeast China), and real gravity data from Tuan Giao (Northwest Vietnam) was considered and the obtained results from applying the different approaches were compared with known geological structures. The results show that the boundaries detected from the use of the frequency domain technique are in accord with the known geological structures.

1. Introduction

The knowledge of the edges of the potential field sources is important for geological interpretation because it could delineate subsurface geological structures such as contacts and faults. Many filters have been developed over the decades to detect the source edges, most of which is based on the computation of vertical or horizontal gradients of the field. Evjen (1936), Cordell and Grauch (1985), Roest et al. (1992), Hsu et al. (1996), Fedi and Florio (2001), Fedi (2002), Cella et al. (2009), and Beiki (2010) provided examples of the use of amplitude-based filters to delineate the source edges. The disadvantage of these filters is that they cannot balance the amplitudes of anomalies generated by the sources located at different depths (Ma et al., 2014; Pham et al., 2018*a*, *b*). Several authors developed phase - based methods to highlight the source horizontal boundaries (Miller and Singh, 1994; Rajagopalan and Milligan, 1995; Wijns et al., 2005; Cooper and Cowan, 2006; Cooper and Cowan, 2008; Li et al., 2012; Ma and Li, 2012). The major advantage of these filters is that they make it possible to equalize anomalies from shallow and deep source bodies (Oruç, 2011; Eldosouky, 2019; Pham et al., 2019*a*). However, the universal disadvantages of these filters are that they bring false edges in the output result or the obtained results depend on the window size used. To solve this problem, Ferreira et al. (2013) suggested using a modified version of the tilt angle, called the tilt angle of the horizontal gradient amplitude. Another modified version of the tilt angle, was also introduced by Cooper (2014*a*),

Citation Info: Pham, L. T., Öksüm, E., Do T. D., Vu, M. D. 2021. Comparison of different approaches of computing the tilt angle of the total horizontal gradient and tilt angle of the analytic signal amplitude for detecting source edges. Bulletin of the Mineral Research and Exploration 165, 53-62.
https://doi.org/10.19111/bulletinofmre.746858

**Corresponding author: Luan Thanh PHAM, luanpt@hus.edu.vn*

called the tilt angle of the amplitude of the analytic signal. Both the TTHG and TAS filters are based on the vertical derivative of the nonharmonic functions (the horizontal gradient amplitude THG and the analytic signal amplitude AS). Florio et al. (2006) showed that the vertical derivative of the analytic signal amplitude calculated from the frequency domain technique can be used to estimate the source depth, but it is not effective in detecting the structural index. Ferreira et al. (2013), Yao et al. (2015), Pham et al. (2019*a*) estimated horizontal boundaries by using the vertical derivative of the horizontal gradient amplitude calculated from the frequency domain technique. Cooper (2014*b*), Pham et al. (2019*b*) used a direct expression for computing the vertical derivative of the analytic signal amplitude. Yan et al. (2016) suggested using the frequency domain technique for computing the vertical derivative of the analytic signal amplitude.

In this paper, we compare the edge detection results of the tilt angle of the horizontal gradient amplitude and the tilt angle of the analytic signal amplitude by using the direct expression and the frequency domain technique. The efficacy of the approaches is tested on both synthetic and real magnetic and gravity data.

2. Methods

The tilt angle of the horizontal gradient amplitude is given by (Ferreira et al., 2013)

$$TTHG = tg^{-1}\frac{\frac{\partial THG}{\partial z}}{\sqrt{\left(\frac{\partial THG}{\partial x}\right)^2+\left(\frac{\partial THG}{\partial y}\right)^2}}, \quad (1)$$

where THG is the horizontal gradient amplitude of the filed F, which is given by

$$THG = \sqrt{\left(\frac{\partial F}{\partial x}\right)^2+\left(\frac{\partial F}{\partial y}\right)^2}. \quad (2)$$

The tilt angle of the amplitude of the analytic signal is calculated using the following equation (Cooper, 2014*a*):

$$TAS = tg^{-1}\frac{\frac{\partial AS}{\partial z}}{\sqrt{\left(\frac{\partial AS}{\partial x}\right)^2+\left(\frac{\partial AS}{\partial y}\right)^2}}, \quad (3)$$

where AS is the analytic signal amplitude of the filed F, and is given by

$$AS = \sqrt{\left(\frac{\partial F}{\partial x}\right)^2+\left(\frac{\partial F}{\partial y}\right)^2+\left(\frac{\partial F}{\partial z}\right)^2}. \quad (4)$$

The vertical derivatives of the horizontal gradient amplitude and the analytic signal amplitude can be easily estimated using the direct expressions (Cooper, 2014*b*), as follows:

$$\frac{\partial THG}{\partial z} = \frac{\frac{\partial F}{\partial x}\frac{\partial^2 F}{\partial x \partial z}+\frac{\partial F}{\partial y}\frac{\partial^2 F}{\partial y \partial z}}{THG} \quad (5)$$

and

$$\frac{\partial AS}{\partial z} = \frac{\frac{\partial F}{\partial x}\frac{\partial^2 F}{\partial x \partial z}+\frac{\partial F}{\partial y}\frac{\partial^2 F}{\partial y \partial z}+\frac{\partial F}{\partial z}\frac{\partial^2 F}{\partial z^2}}{AS} \quad (6)$$

Another approach, based on the vertical derivative operator in frequency domain, also can be used to compute the vertical derivative of the horizontal gradient amplitude and the analytic signal amplitude. The definition of the vertical derivative operator is given by Blakely (1995) as follows:

$$\begin{aligned} F\left[\frac{\partial \phi}{\partial z}\right] &= \lim_{\Delta z \to 0}\frac{F[\phi]-F[\phi]e^{-|k|\Delta z}}{\Delta z} \\ &= \lim_{\Delta z \to 0}\frac{1-e^{-|k|\Delta z}}{\Delta z}F[\phi] \\ &= |k|\,F[\phi] \end{aligned} \quad (7)$$

where F[ ] denotes Fourier transformation, ϕ is the horizontal gradient amplitude or the analytic signal amplitude, e is the exponential function and k is the wavenumber defined as

$$k = \sqrt{k_x^2+k_y^2} \quad (8)$$

where k_x and k_y are the wavenumbers in the x and y directions, respectively. The inverse Fourier transform of Equation (7) provides the vertical derivative of the function ϕ. Note that the horizontal derivatives in Equation (1) and (3) are computed in the space domain using the finite difference method.

3. Theoretical Examples

In this section, we compare the edge detection results of the TTHG and TAS by using the direct expressions with the results obtained by using the frequency domain approach. The first model considered includes three magnetized prisms located at different depths. Figure 1a shows the 3D perspective view of the model. The prismatic sources have the same size of 30×130×5 km. The top of the sources 1A, 1B, and

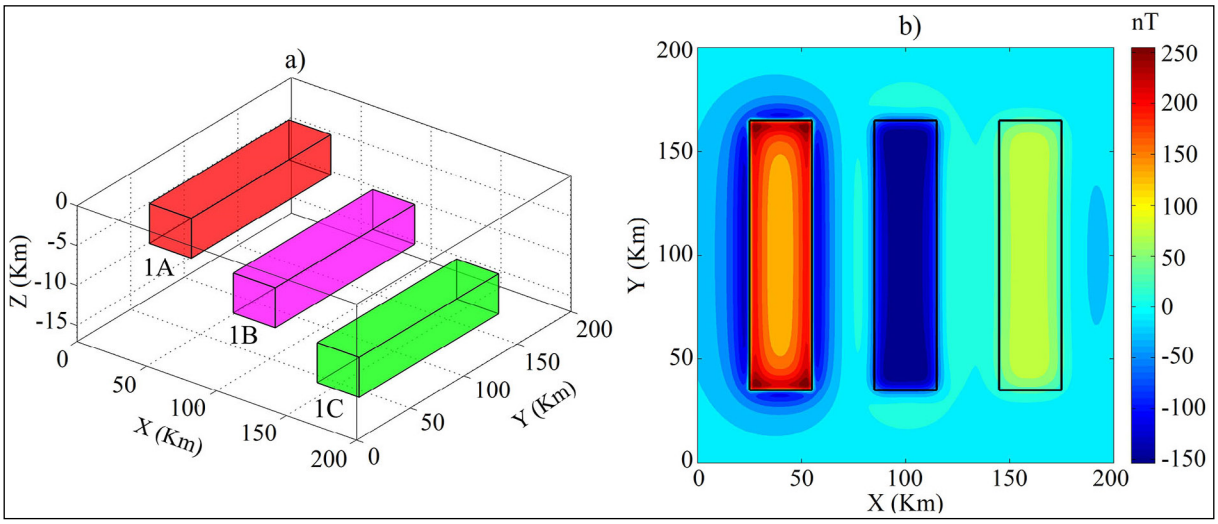

Figure 1- a) Perspective view of the first model, consisting of three magnetic sources (1A, 1B and 1C) with top depths of 1 km, 6 km and 11 km, respectively, b) synthetic magnetic field generated by the model. The black lines show actual edges of the sources.

1C are 1, 6, and 11 km, respectively. The sources have a magnetic declination of 0° and an inclination of 90°. The magnetization magnitudes of the sources 1A, 1B, and 1C are 1, -1.2, and 1 A/m, respectively. We computed the magnetic anomaly produced by these three prismatic sources on a grid of 201×201 points with 1 km spacing. The magnetic anomaly of the model is shown in Figure 1b. Figure 2a shows TTHG result obtained from using the direct expression. As can be seen from this figure, although the use of the direct expression can detect all the source edges, it brings spurious maxima around the prismatic bodies. In addition, this approach also generates maximum values over the sources. Figure 2b shows the TTHG result obtained from using the frequency domain vertical derivative operator. We can see that, in this case, the TTHG cannot only highlight all the source horizontal boundaries, but also can avoid generating spurious boundaries. Figure 2c shows TAS result obtained from using the direct expression. As depicted in this figure, the use of the direct expression can highlight the source horizontal boundaries. However, this approach brings spurious maxima between the sources. Figure 2d shows TAS result obtained from using the frequency domain vertical derivative operator. Clearly, in this case, the TAS can detect all the source edges without any spurious edges.

Since the very complex nature of the geological phenomena, it is necessary to also test the performance of these approaches in a more complex model. Here, we consider a gravity model that includes six prismatic sources. Figure 3a shows the 3D perspective view of the model. The geometric and density parameters are presented in Table 1. The gravity anomaly due to the model is computed on a grid of 201×201 points with 1 km spacing, and is shown in Figure 3b. Figure 4a shows the TTHG result obtained from using the direct expression. As clearly seen from this figure, the TTHG filter can highlight the source horizontal boundaries, but it produces some of the artefacts over source 2C and between sources 2A and 2D. Figure 4b depicts TTHG result by using the frequency domain approach. We can see that, in this case, the TTHG is effective in detecting all the source horizontal boundaries without any other spurious boundaries. Figure 4c and d depict TAS results obtained from using the direct expression and the frequency domain approach, respectively. For both forms of the calculations, the TAS filter cannot highlight the edges of the thin sources (2D and 2E). Moreover, the use of the direct expression also produces a spurious boundary between sources 2A and 2D, and spurious minimum contours around the source 2B and between sources 2D and 2E.

To further test the stability of the approaches, the data in Figure 3b was corrupted with random noise with amplitude equal to 5% of the anomaly amplitude. Figure 5a shows noise - corrupted gravity data. Because the TTHG and TAS filters use second-order derivatives of the field, they are sensitive to noise. To attenuate the noise effect, an upward continuation of 2 km was applied to the noise data prior to calculating the filters. Figure 5b shows the transformed field after

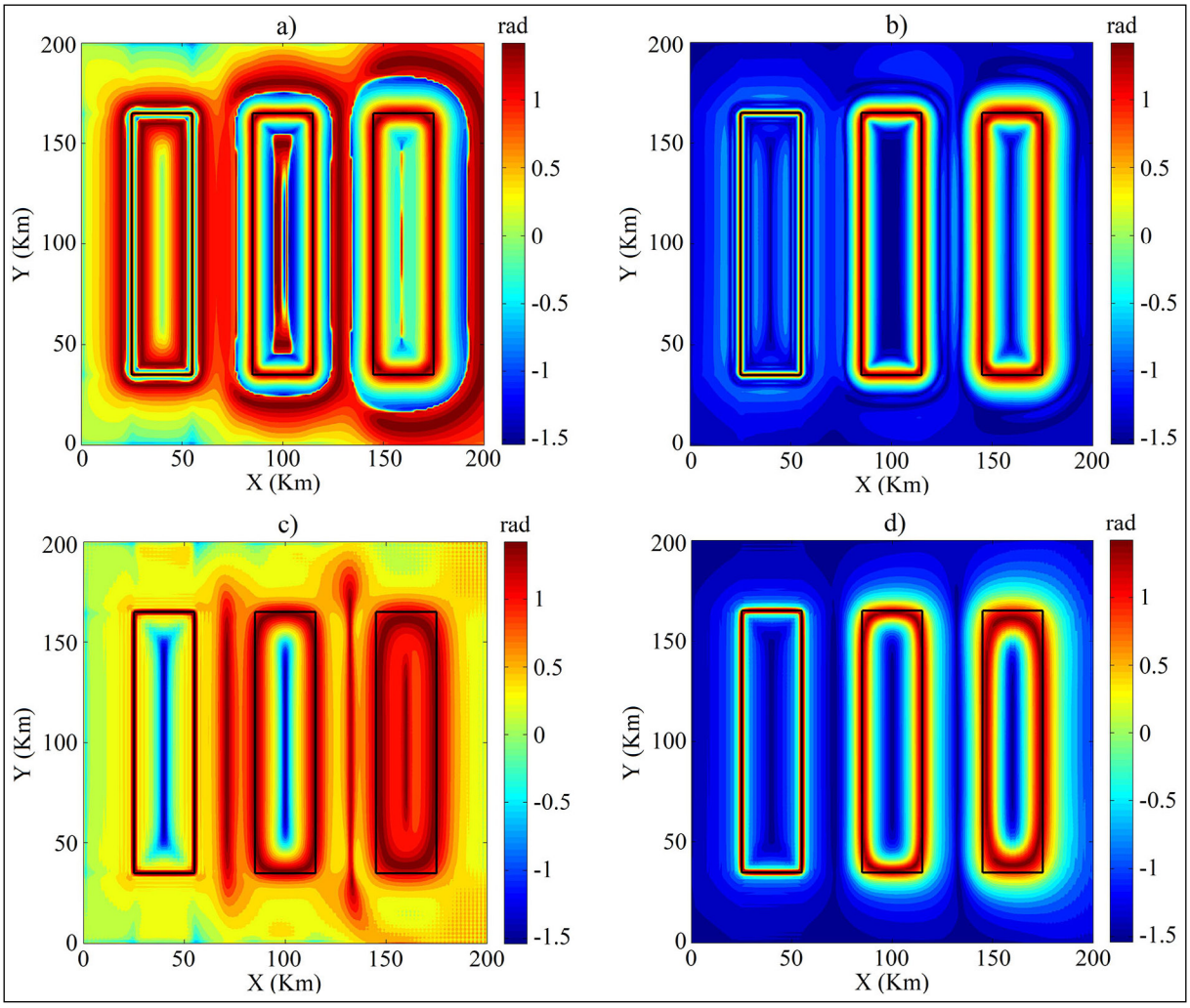

Figure 2- a) TTHG using the direct expression, b) TTHG using the frequency domain approach, c) TAS using the direct expression, d) TAS using the frequency domain. The black lines show actual edges of the sources.

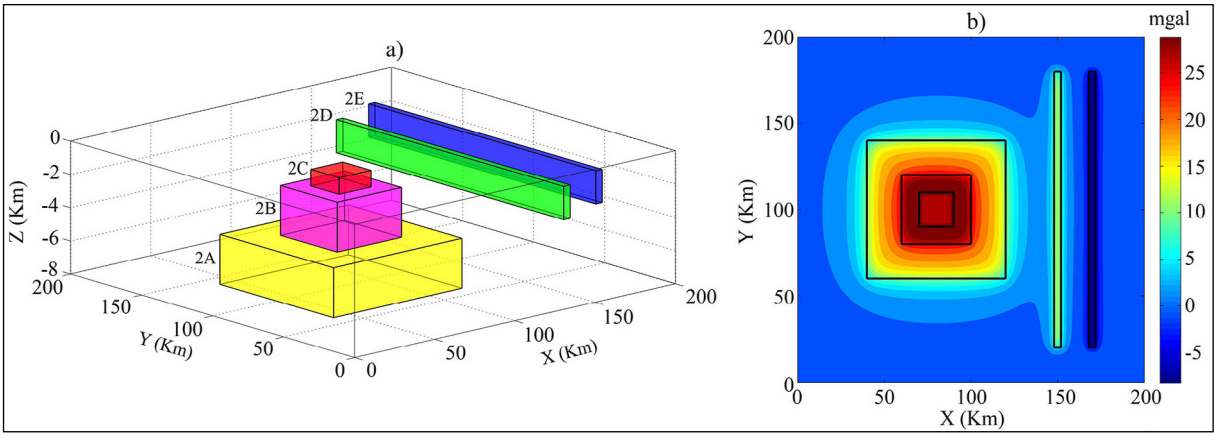

Figure 3- a) Perspective view of the second model; b) synthetic gravity field generated by the model. The black lines show actual edges of the sources.

Table 1- The geometric and density parameters of the second model.

Parameters / Prism ID	2A	2B	2C	2D	2E
x-coordinates of center (km)	80	80	90	150	170
y-coordinates of center (km)	100	100	100	100	100
Width (km)	20	40	80	4	4
Length (km)	20	40	80	160	160
Depth of top (km)	1	2	5	1.5	1
Depth of bottom (km)	2	5	8	3.5	3
Density contrast (g/cm^3)	-0.1	0.1	0.2	0.3	-0.2

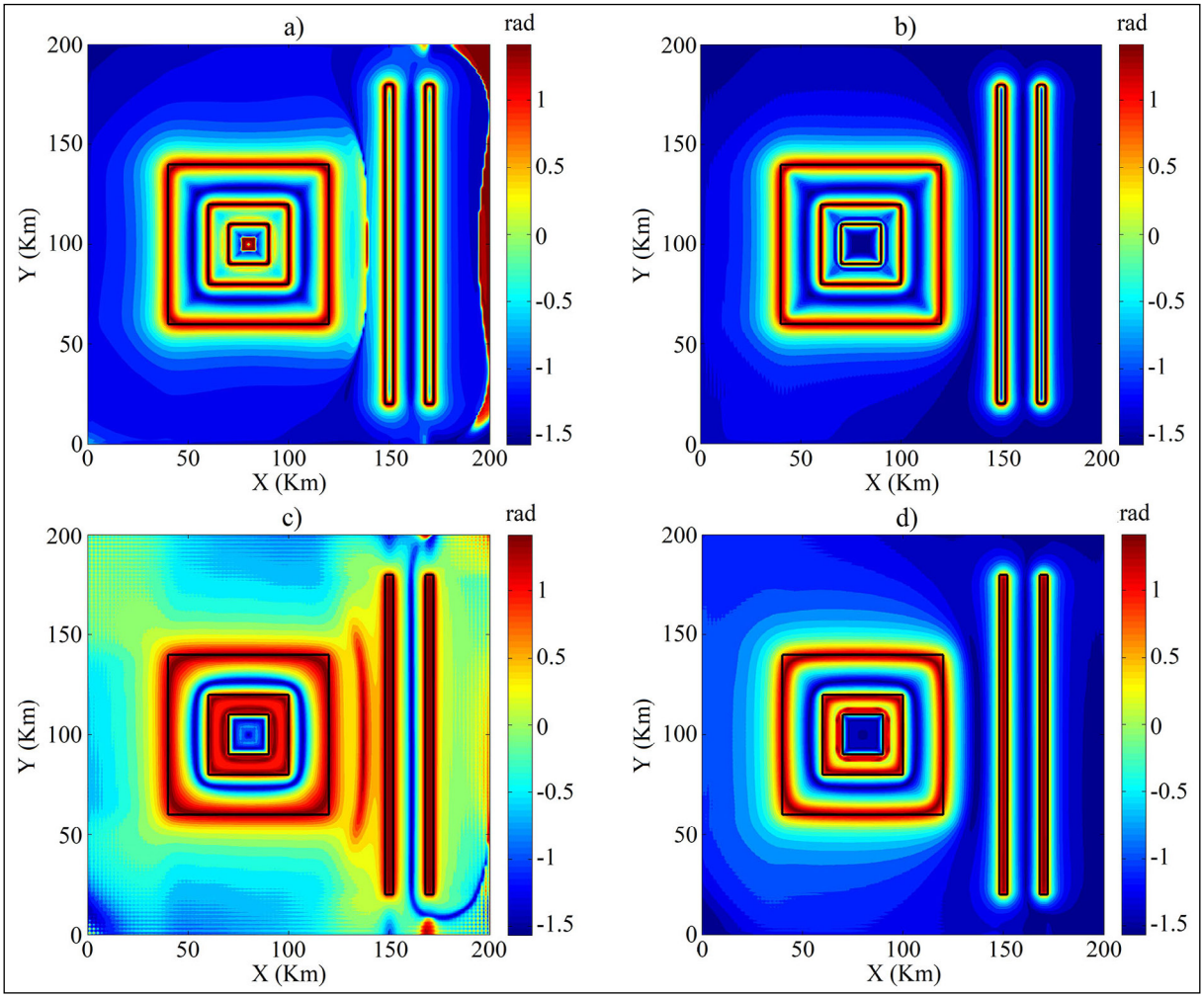

Figure 4- a) TTHG using the direct expression, b) TTHG using the frequency domain approach, c) TAS using the direct expression, d) TAS using the frequency domain. The black lines show actual edges of the sources.

the upward continuation where the effect of the high frequency noise was attenuated somewhat. Figure 6a and b display TTHG results obtained from performing the direct expression and the frequency domain approach, respectively. Clearly, both the approaches can delineate all the source edges, but the use of the direct expression brings some false maxima over the source 2C. Figure 6c and d displays TAS results obtained from using the direct expression and the frequency domain approach, respectively. It can be clearly seen that the edges of the thin sources (2D and 2E) could not be outlined by the TAS filter, and

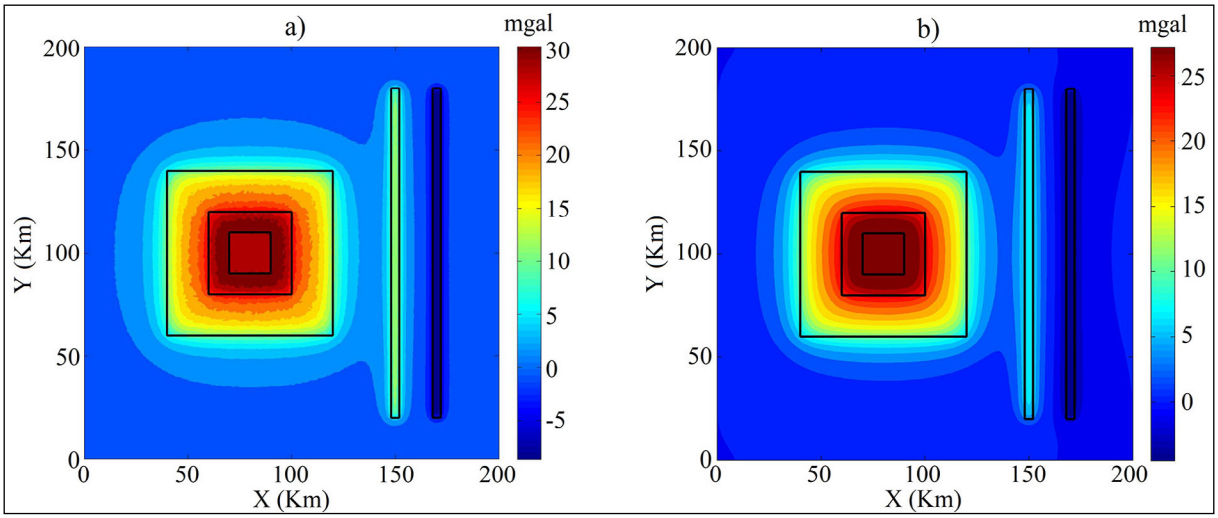

Figure 5- a) Synthetic gravity field generated by the second model with 5% random noise, b) synthetic gravity field after upward continuation of 2 km. The black lines show actual edges of the sources.

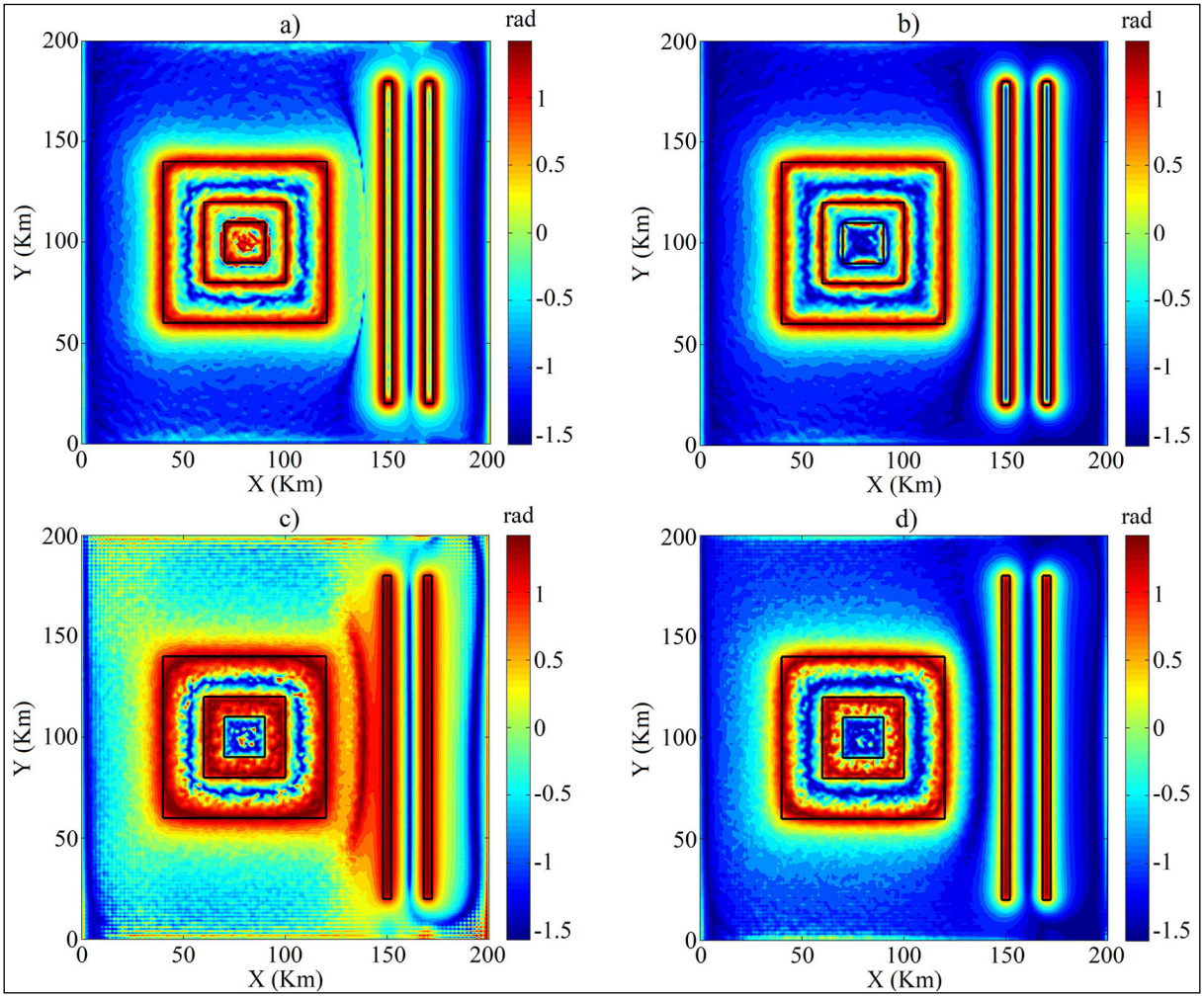

Figure 6- a) TTHG using the direct expression, b) TTHG using the frequency domain approach, c) TAS using the direct expression, d) TAS using the frequency domain. The black lines show actual edges of the sources.

the use of the direct expression produces a spurious edge between sources 2A and 2D. Moreover, the TAS is more sensitive to noise than the TTHG as it uses second-order vertical derivative of the field, whereas the TTHG uses only the first-order vertical derivative.

4. Application to Real Data

In order to test the practical applicability of the approaches, we apply them to real magnetic data from Zhurihe (Northeast China), and real gravity data from Tuan Giao (northwest Vietnam).

Figure 7a shows the magnetic anomaly data reduced to the pole of the Zhurihe area (Yuan and Yu, 2014). The study area is 73×117 km, with an interval of 1 km along the east and north directions. Figure 7b and c show TTHG results obtained from using the direct expression and frequency domain approach, respectively. Figure 7d and e show TAS maps obtained from the use of the direct expression and frequency domain approach, respectively. Figure 7f displays geological map of the area (modified from Ma et al., 2014). The continental sediments cover most of the Zhurihe area, except for some nearly SE - NW trending iron-rich sandstone dykes (Ma et al., 2014, Zhou et al., 2017). As can be observed, the edge maps of the TTHG are consistent with the geology information (Figure 7f). In this case, the TAS is less effective in highlight the geological boundaries, and it is more sensitive to noise than the TTHG. However, it

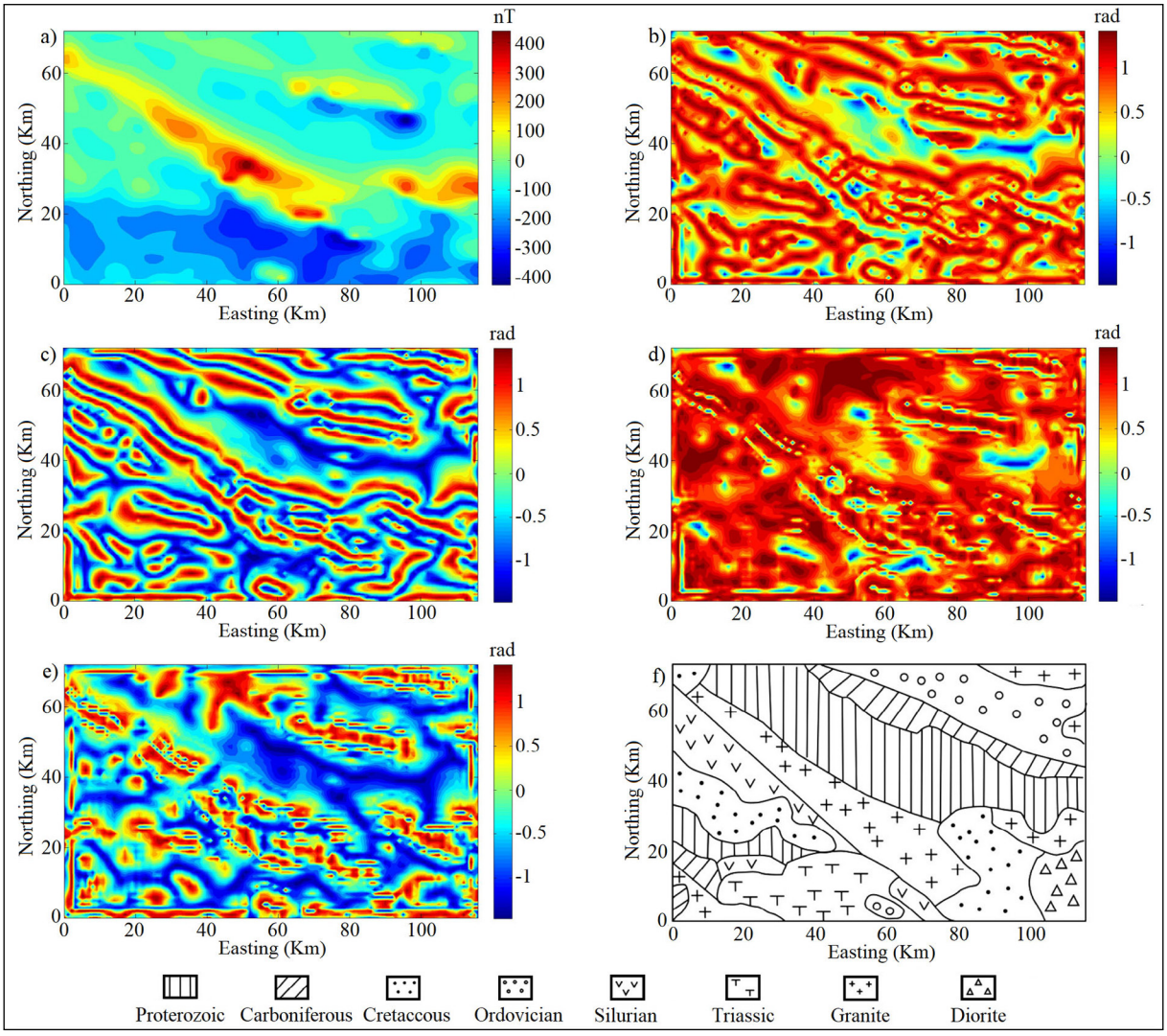

Figure 7- a) Magnetic anomaly data reduced to the pole of the Zhurihe area, b) TTHG using the direct expression, c) TTHG using the frequency domain approach, d) TAS using the direct expression, e) TAS using the frequency domain, f) geological map of the area (Ma et al., 2014).

is worth noting that the use of the frequency domain approach for both the TTHG and TAS filters provides more clearly results, compared to the use of the direct expression.

Figure 8a shows the Bouguer gravity anomaly map of the Tuan Giao area (Pham et al., 2019*a*). The study area is characterized by high seismicity (Roger et al., 2014; Duan and Duong, 2017), covering an area about 116 km × 155 km with an interval of 1.22 km along the east and north directions. Figure 8b and c display TTHG maps obtained from the use of the direct expression and frequency domain approach, respectively. Figure 8d and e display TAS results obtained from using the direct expression and frequency domain approach, respectively. Figure 8f displays geological map of the area (modified from Roger et al., 2012). The Tuan Giao area has complex SE-NW trending geological structures including many faults, sedimentary rocks, magmatic rocks, and volcanoes. We can see that, the horizontal boundaries detected by the TTHG are consistent with the geology information (Figure 8f). In addition, the use of the frequency domain approach for calculating the TTHG shows a more clearly result compared to the use of the direct expression. The TAS results by both approaches are less effective in detecting the geological boundaries compared to those obtained from the TTHG filter. However, similar to the TTHG case, the use of the frequency domain approach for calculating the TAS brings a more clearly result compared to the use of the direct expression.

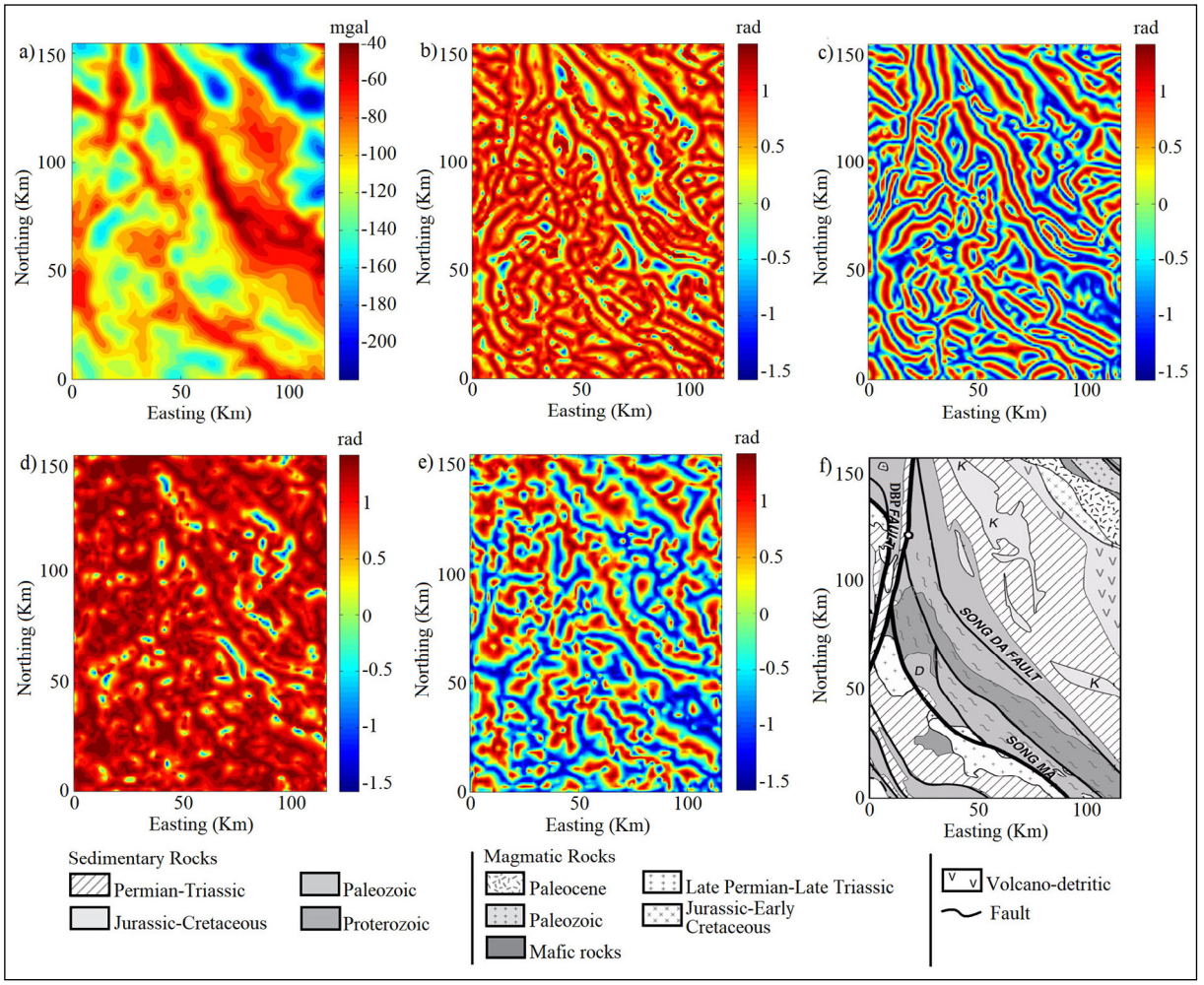

Figure 8- a) Bouguer gravity anomaly of the Tuan Giao area, b) TTHG using the direct expression, c) TTHG using the frequency domain approach, d) TAS using the direct expression, e) TAS using the frequency domain, f) geological map of the area (Roger et al., 2012).

5. Results

We tried to review the effectiveness of the use of the frequency domain approach and direct expression to compute the tilt angle of the total horizontal gradient and tilt angle of the analytic signal amplitude for detecting the source edges. Test studies were performed on a synthetic magnetic data, and also on synthetic gravity data with and without random noise. The obtained results showed that the use of the frequency domain approach is more effective in highlighting the geological boundaries compared to the use of the direct expression. Test studies also were performed on real magnetic data of the Zhurihe area (Northeast China), and real gravity data of the Tuan Giao area (northwest Vietnam), where edges obtained from using the frequency domain approach are in accord with the known geological structures. We also showed that the edges detected from the tilt angle of the total horizontal gradient are more clearly than those from the tilt angle of the analytic signal amplitude.

Acknowledgement

The authors record with pleasure their sincere thanks to the editor and the reviewers for their very constructive suggestions to improve the paper. This research is funded by the Vietnam National University, Hanoi (VNU) under project number QG.20.13.

References

Beiki, M. 2010. Analytic signals of gravity gradient tensor and their application to estimate source location. Geophysics 75 (6), 159-174.

Blakely, R. J. 1995. Potential Theory in Gravity and Magnetic Applications. Cambridge. Cambridge University Press, Cambridge, 326.

Cella, F., Fedi, M., Florio, G. 2009. Toward a full multiscale approach to interpret potential fields. Geophysical Prospecting 57, 543-557.

Cooper, G. R. J. 2014*a*. Reducing the dependence of the analytic signal amplitude of aeromagnetic data on the source vector direction. Geophysics 79, J55-J60.

Cooper, G. R. J. 2014*b*. The automatic determination of the location and depth of contacts and dykes from aeromagnetic data. Pure and Applied Geophysics 171(9), 2417-2423.

Cooper, G. R. J., Cowan, D. R. 2006. Enhancing potential field data using filters based on the local phase. Computers and Geosciences 32, 1585-1591.

Cooper, G. R. J., Cowan, D. R. 2008. Edge enhancement of potential - field data using normalized statistics. Geophysics 73(3), H1-H4.

Cordell, L., Grauch, V. J. S. 1985. Mapping basement magnetization zones from aeromagnetic data in the San Juan Basin, New Mexico, in Hinze, William J. (Ed.), The utility of regional gravity and magnetic anomaly maps: Society of Exploration Geophysicists, Tulsa, Oklahoma, 1985, 181-197.

Duan, B. V., Duong, N. A. 2017. The relation between fault movement potential and seismic activity of major faults in Northwestern Vietnam. Vietnam Journal of Earth Sciences 39(3), 240-255.

Eldosouky, A. M. 2019. Aeromagnetic data for mapping geologic contacts at Samr El-Qaa area, North Eastern Desert, Egypt. Arabian Journal of Geosciences 12, 2.

Evjen, H. M. 1936. The place of the vertical gradient in gravitational interpretations. Geophysics 1(1), 127-136.

Fedi, M. 2002. Multiscale derivative analysis: A new tool to enhance detection of gravity source boundaries at various scales. Geophysical Research Letters 29(2), 1029.

Fedi, M., Florio, G. 2001. Detection of potential fields source boundaries by enhanced horizontal derivative method. Geophysical Prospecting 49(1), 40-58.

Ferreira, F. J. F., de Souza, J., de Bongiolo, A. B. E. S., de Castro, L. G. 2013. Enhancement of the total horizontal gradient of magnetic anomalies using the tilt angle. Geophysics 78(3), J33-J41.

Florio, G., Fedi, M., Pastek, R. 2006. On the application of Euler deconvolution to the analytic signal. Geophysics 71(6), L87-L93.

Hsu, S. K., Coppense, D., Shyu, C. T. 1996. High - resolution detection of geologic boundaries from potential field anomalies: An enhanced analytic signal technique. Geophysics 61, 1947-1957.

Li, L., Ma, G., Du, X. 2012. Edge Detection in Potential-Field Data by Enhanced Mathematical Morphology Filter. Pure and Applied Geophysics 170(4), 645-653.

Ma, G., Li, L. 2012. Edge detection in potential fields with the normalized total horizontal derivative. Computers and Geosciences 41, 83-87.

Ma. G., Liu, C., Li, L. 2014. Balanced horizontal derivative of potential field data to recognize the edges and estimate location parameters of the source. Journal of Applied Geophysics 108, 12-18.

Miller, H. G., Singh, V. 1994. Potential field tilt a new concept for location of potential field sources. Journal of Applied Geophysics 32, 213-217.

Oruç, B. 2011. Edge detection and depth estimation using a tilt angle map from gravity gradient data of the Kozaklı - Central Anatolian Region, Turkey. Pure and Applied Geophysics 168, 1769-1780.

Pham, L.T., Oksum, E., Do, T. D., Le - Huy, M. 2018*a*. New method for edges detection of magnetic sources using logistic function. Geofizichesky Zhurnal 40(6), 127-135.

Pham L. T., Le-Huy M., Oksum, E., Do T. D. 2018*b*. Determination of maximum tilt angle from analytic signal amplitude of magnetic data by the curvature - based method. Vietnam Journal of Earth Sciences 40(4), 354-366.

Pham, L. T., Oksum, E., Do, T. D. 2019*a*. Edge enhancement of potential field data using the logistic function and the total horizontal gradient. Acta Geodaetica et Geophysica 54, 143-155.

Pham, L. T., Oksum, E., Do, T. D., Le - Huy, M., Vu, M. D., Nguyen, V.D. 2019*b*. LAS: a combination of the analytic signal amplitude and the generalised logistic function as a novel edge enhancement of magnetic data. Contributions to Geophysics and Geodesy 49(4), 425-440.

Rajagopalan, S., Milligan, P. 1995. Image enhancement of aeromagnetic data using automatic gain control. Exploration Geophysics 25, 173-178.

Roest, W. R. J., Verhoef, J, Pilkington, M. 1992. Magnetic interpretation using the 3-D analytic signal. Geophysics 57(1), 116-125.

Roger, F., Maluski, H., Lepvrier, C., Tich, V. V., Paquette, J. L. 2012. LA - ICPMS zircons U / Pb dating of Permo - Triassic and Cretaceous magmatisms in Northern Vietnam - geodynamical implications. Journal of Asian Earth Sciences 48, 72-82.

Roger, F., Jolivet, M., Maluski, H., Respaut, J. P., Münch, P., Paquette, J. L., Vu - Van, T., Vu - Van, V. 2014. Emplacement and cooling of the Dien Bien Phu granitic complex: implications for the tectonic evolution of the Dien Bien Phu fault (Truong Son Belt, NW Vietnam). Gondwana Research 26(2), 785-801.

Wijns, C., Perez, C., Kowalczyk, P. 2005. Theta map: edge detection in magnetic data. Geophysics 70, 39-43.

Yan, T. J., Wu, Y. G., Yuan, Y., Chen, L. N. 2016. Edge detection of potential field data using an enhanced analytic signal tilt angle. Chinese Journal of Geophysics 59(4), 341-349.

Yao, Y., Huang, D., Yu, X., Chai, B. 2015. Edge interpretation of potential field data with the normalized enhanced analytic signal. Acta Geodaetica et Geophysica 51(1), 125-136.

Yuan, Y., Yu, Q. 2014. Edge detection in potential-field gradient tensor data by use of improved horizontal analytical signal methods. Pure and Applied Geophysics 172(2), 461-472.

Zhou, S., Huang, D., Jiao, J. 2017. Total horizontal derivatives of potential field three - dimensional structure tensor and their application to detect source edges. Acta Geodaetica et Geophysica 52(3), 317-329.

Bulletin of the Mineral Research and Exploration

http://bulletin.mta.gov.tr

Genesis of the Zebra dolomites and relation to carbonate - hosted Au - Ag - Zn ± Pb deposits in the Maden village (Ulukışla - Niğde), Central Taurides, South Turkey

Asuman KAHYA[a*], Ercan KUŞCU[b] and Firdevs İrem YENİCE[a]

[a]*General Directorate of Mineral Research and Exploration, Ankara, 06800, Turkey*
[b]*Demir Export A.Ş., Ankara, 06800, Turkey*

Research Article

Keywords:
Zebra Dolomite, Carbonate - hosted, Au - Ag - Zn ± Pb Deposits, Bolkar Mountain, Turkey.

ABSTRACT

Zebra dolomites and carbonate - hosted Au - Ag - Zn ± Pb deposits of Maden village is located in the shelf type carbonate rocks of the Bolkar Mountains. The Zebra dolomite (ZD) locally form and there is no evidence for relation between dolomitization and mineralization. Maden village ZD is characterized by parallel light and dark bands that have similar mineralogy and chemistry by petrographic and SEM + EDX investigation. The $\delta^{13}C$ (V - PDB) composition of the Zebra dolomite from 2.59‰ to 2.72‰ and the $\delta^{18}O$ (V - PDB) values of the Zebra dolomite from -11.39 ‰ to -14.88 ‰. These isotopic values show that the source of oxygen and carbon was derived from marine carbonates and freshwater carbonates. Fluid inclusion studies on Zebra dolomite show homogenization temperatures of 80 °C - 180 °C. Based on petrographic, isotope values and fluid inclusion study, we can say that the dolomitization occurred during the late diagentic conditions prior mineralization.

Received Date: 18.04.2020
Accepted Date: 03.02.2021

1. Introduction

Zebra dolomites have been defined as an interesting lithology, characterized by a repetition of mm - scale dark gray (a) and light (b) colored dolomite sheets that make up the abbabba - sequences (Nielsen et al., 1998). The term has differently been described as diagenetic crystallization rhythmites (Levin and Amstutz, 1976; Fontbote, 1981; Fontbote and Amstutz, 1983; Wallace et al., 2018), banded or ribbon ores (Sass Gustkiewicz et al., 1982; Tompkins et al., 1994; Wallace et al., 2018), Zebra rocks or textures (Beales and Hardy, 1980; Wallace et al., 1994; Zeeh, 1995), expansion structure (Beales and Hardy, 1980; Wallace et al., 2018), and Zebra rock / texture / fabric / dolomite (Beales and Hardy, 1980; Wallace et al., 1994; Nielsen at al., 1998; Diehl et al., 2010; Morrow, 2014). The origin of the Zebra texture is uncertain and debated (Wallace et al., 2018 and Nielsen et al., 1998). The interpretations of origin Zebra dolomite vary from synsedimentary (Fontbote and Amstutz, 1983) to epigenetics (Arne and Kissin, 1989). Beales and Hardy (1980) explained that the White Zebra dolomite sheets are pseudomorphs after evaporate minerals. This interpretation was followed by Tompkins et al. (1994) for the rhythmically banded ores at Cadje but (Canning basin, Western Australia), which appear to be laterally porous, gypsiferous laminated limestone. Wallace et al. (1994) proposed that Zebra textures are not always hosted by evaporatic sediments, Zebra fabric is generally associated with sulfides or sulfide associated phases. Some authors stated that Zebra

Citation Info: Kahya, A., Kuşcu, E., Yenice, F., İ. 2021. Genesis of the Zebra dolomites and relation to carbonate - hosted Au - Ag - Zn ± Pb deposits in the Maden village (Ulukışla - Niğde), Central Taurides, South Turkey. Bulletin of the Mineral Research and Exploration 165, 63-75.
https://doi.org/10.19111/bulletinofmre.877977

**Corresponding author: Asuman KAHYA, asuman27@gmail.com*

textures occur in a variety of different geological settings and are associated with both carbonate - hosted ore deposits (Mississippi Valley type mineralization, intrusive - related lead - zinc deposits and Carlin - style gold deposits) and hydrothermal dolomite reservoirs (Fontbote, 1993; Davies and Smith Jr, 2006; Diehl et al., 2010; Morrow, 2014; Hiemstra and Goldstein, 2015; Wallance, 2018). Dolomitization occurs as a result of various geological processes involving evaporatic, normal marine and meteoric water (Morrow, 1998) which including diagenesis of limestone, and hydrothermal alteration (Wilkinson et al., 2005; Zentmyer et al., 2011; Bouabdellah et al., 2012; Gomez - Rivas et al., 2014). Many researchers have been investigated the nature (diagenetic or hydrothermal) and the timing of dolomitization with respect to associated sulfide mineralization in order to define the type of ore deposit (Wilkinson, 2003; Wilkinson et al., 2005; Leach et al., 2006; Johnson et al., 2009; Bouabdellah et al., 2012; Wilkinson, 2014).

The study area is located in the foothills of Bolkar Mountains, which is a part of the Tauride block including Lower Paleozoic to Upper Cretaceous recrystallized limestone, dolomite, marble, and calc-schist (Figure 1; Özgül, 1976; Demirtaşlı et al., 1984; Alan et al., 2007). This belt is one of the major Pb - Zn mining areas in Turkey and is known for hosting carbonate - hosted Pb - Zn deposits (Koptagel et al., 2007). Near the investigated Zebra dolomite, there is a Maden village carbonated hosted Au - Ag - Zn ± Pb deposit which is hosted in the

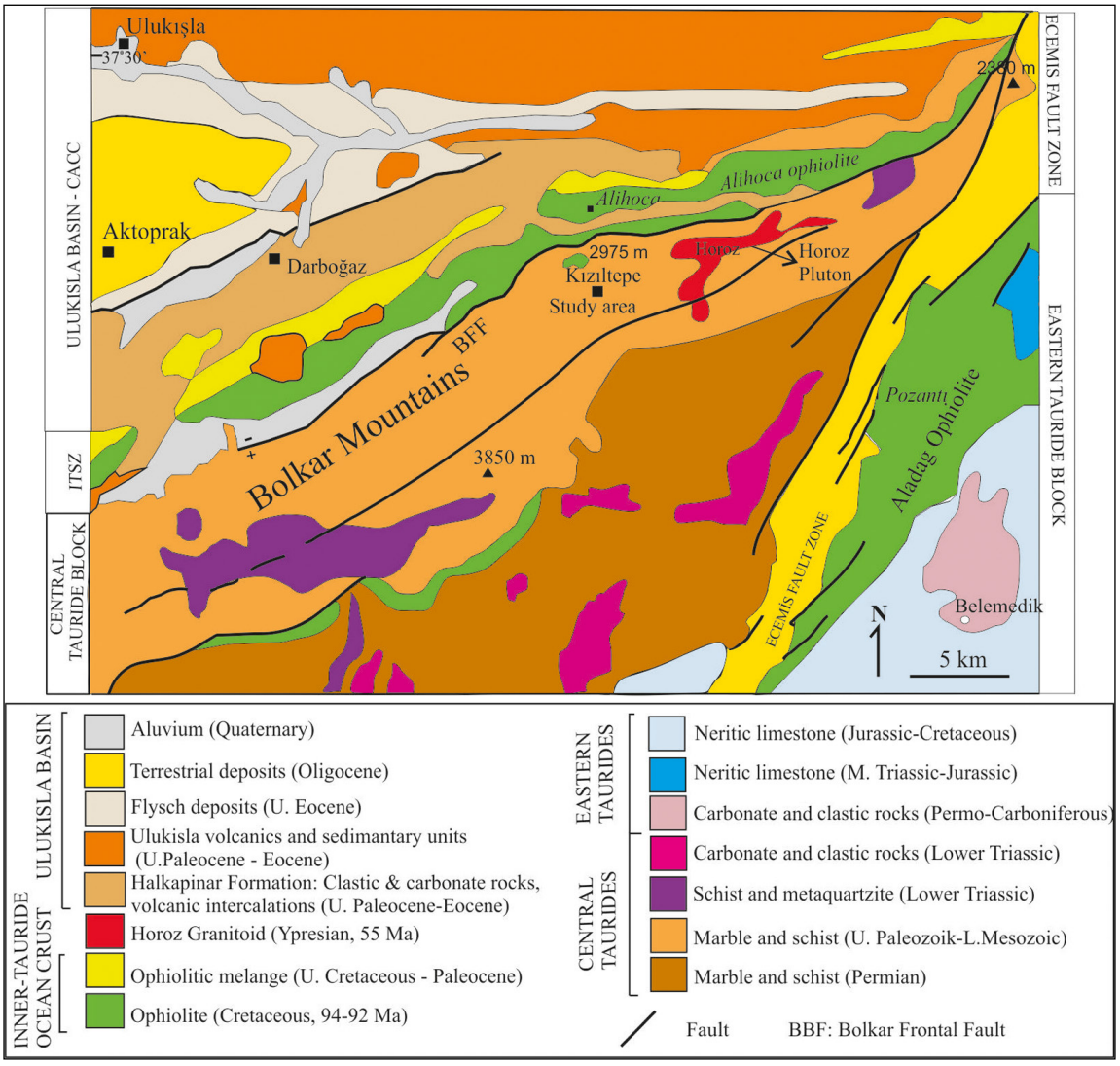

Figure 1- Geologic map of south - central Turkey, showing the distributions of major tectonic units, faults, and the Horoz pluton in the Central Tauride block. BBF, Bolkar Frontal Fault (Kadıoğlu and Dilek, 2010).

Jurassic-Cretaceous marbles of the northern flank of the Bolkar Mountains anticline, mostly close to near vertical E - W and N30°W trending faults. The Maden village deposits, are one of the most important economic sources of Au - Ag - Zn ± Pb in Turkey, with average grades of 7.37 g/t Au, 813.71 g/t Ag, 31.06% Pb, and 5.94% Zn (Gümüştaş Company AŞ, 2014). The mineralization in the study area is placed in Jurassic - Cretaceous recrystallized limestone which both relicts of hypogene and supergene ore are found. The supergene non - sulfide ore occurs in dissolution cavities within marble, mainly along joint planes and fractures (tension gashes). The hypogene sulfide mineralization is a relicts of cave wall / floor, and tectonic contacts between marble and melange. The sulfide mineralization (hypogene) in the area is extensively oxidized as a result of uplift the Tauride block during Oligo - Miocene, progressive erosion of landscape, development of fractures (tension gashes) under extensional conditions, and consequently weathering of the protore (Kahya et al., 2019). Locally occurred Zebra Dolomite (ZD) near the Maden village carbonated hosted ore deposit. So far the ZD has not been studied. Therefore, isotopic data, detailed mineralogic studies, and fluid inclusion studies were used in this study to find the source of dolomitizing fluids and their relationship with the Maden village carbonate - hosted deposits.

2. Material and Method

Mineralogical and petrographical studies were carried out on dolomite. X - ray diffraction (XRD) studies were made on dolomite to determine the mineral contents using XRD analyzer Philips PW 3710 / 1830 in MTA (General Directorate of Mineral Research and Exploration, Turkey). Minerals were determined by optical microscopy at MTA using Leica DM2500P polarizing microscope. Petrographic observations (optical microscopy and scanning electron microscopy (SEM + EDX) of thin sections and fresh samples were used to establish textural properties and to identify mineral species. SEM + EDX analyses used a FEI Quanta 400 MK2 SEM and EDAX Genesis XM4i EDS detector at MTA. Fluid inclusion studies were carried out on the two surface polished thin section of dolomite sample and 14 fluid inclusion analyses were made and measurements were performed with a Linkam MDSG 600 heating - freezing stage mounted on the Leica DM 2500 microscope at MTA. The O and C isotope compositions were measured on 4 clear dolomite samples in the Isotope Geochemistry Laboratory of Arizona University. The $\delta^{18}O$ is given in per mil (‰) V - SMOW (Vienna Standard Mean Ocean Water); $\delta^{13}C$ values are in per mil (‰) V - PDB (Vienna Standard Pee Dee Belemnite). All measured isotopic compositions are given in Table 1. The O and C values of carbonates were measured using an automated carbonate preparation device (KIEL - III) coupled to a gas-ratio mass spectrometer (Finnigan MAT 252). Powdered samples were reacted with dehydrated phosphoric acid under vacuum at 70 °C. The isotope ratio is calibrated using repeated measurements of NBS - 19 and NBS - 18 with precision of ±0.1‰ for $\delta^{18}O$ and ±0.06‰ for $\delta^{13}C$ (1sigma).

3. Regional Geological Setting and Local Geology

The study area belongs to the Bolkar Mountains Units, which are part of the Tauride block south of the ITSZ (Inner - Tauride Suture Zone). The Bolkar Mountains Units comprises carbonate, siliciclastic, and volcanic rocks and their metamorphic equivalents with ages ranging from Upper Permian to Late Cretaceous (Demirtaşlı et al., 1984; Özgül, 1976). This unit is interpreted as a ribbon shaped continent rifted off from Gondwana (Özgül, 1976, 1984; Görür et al., 1998; Garfunkel, 1998). Platform carbonates in the Bolkar Mountains have multiple folds and are imbricated along thrust faults, which caused substantial shortening and crustal thickening

Table 1- Oxygen ($\delta^{18}O$) and carbon ($\delta^{13}C$) isotope analyses of the Zebra Dolomites.

Sample	$\delta^{13}C$ (V - PDB) ‰	$\delta^{18}O$ (V - PDB) ‰	$\delta^{18}O$ (V - SMOW) ‰
WHITE Zebra dolomite	2.60	-14.87	15.58
WHITE Zebra dolomite	2.59	-14.86	15.59
DARK Zebra dolomite	2.72	-11.39	19.17
DARK Zebra dolomite	2.71	-11.38	19.16
Host rock limestone	2.81	-6.58	24.12

within the platform. These contraction structures and the crustal - shortening first developed during the obduction of the ITO (Inner Tauride Ophiolites) from the north in the Late Cretaceous and subsequently during the collision of the Tauride Block with the CACC in the Late Paleocene - Eocene (Dilek et al., 1999*b*; Kadıoğlu and Dilek, 2010). The Tauride Block experienced a gradual uplift in the footwall of a north-dipping frontal normal fault system along its northern edge starting in the Miocene, and it developed a southward - tilted, asymmetric mega - fault block with rugged, Alpine topography (Dilek et al., 1999*b*; Kadıoğlu and Dilek, 2010, Kahya et. al., 2019). These fault system is important for dolomitization. The Horoz Granitoid and quartz porphyries intrude into the Lower Paleozoic - Upper Cretaceous Tauride Block rocks in the Bolkardağ (Dilek and Whitney, 2000; Kadıoğlu and Dilek, 2010). The Horoz Pluton was unroofed by the Early Miocene as a result of both crustal uplift and erosion (Kadıoğlu and Dilek, 2010). The age of the Horoz Granitoid is determined as Paleocene - early Eocene (Alan et al., 2007). The Ulukışla basin formed after the emplacement of the ITO (Inner Tauride Ophiolite) and melanges on the Tauride platform during the Late Cretaceous period and underwent late Eocene emergence, deformation, and onset of Oligo - Miocene non - marine deposition (Blumenthal, 1956; Demirtaşlı et al., 1984; Atabey et al., 1990; Görür et al., 1998; Clarc and Robertson, 2002; Kadıoğlu and Dilek, 2010). The Ulukışla basin filled with Upper Cretaceous to Oligo - Miocene volcanic and sedimentary materials and became part of a larger, shallow intra - continental basin consisting mainly of lacustrine and fluvial deposits that covered much of Central Anatolia throughout the Miocene and Quaternary period (Kadıoğlu and Dilek, 2010).

The study area is located in Maden village, south of the Ulukışla (Niğde) town, in the eastern part of the Central Taurus Mountains of Turkey. In the study area, the Namrun Tectonic Slice, the Bolkar Mountain Unit, the Bozkır Unit, and the Tertiary cover rocks of the Ereğli - Ulukışla basin are exposed (Figure 2). Bolkar Mountains Units forms the basement of the study area. The Middle - Late Triassic Tozlutepe formation is located at the bottom of this. This formation is conformably covered by the Late Triassic Metrisyayla formation which is unconformably overlain by the Jurassic - Cretaceous Koçakkale formation, and consists of recrystallized limestone and dolomite (Alan et al., 2007). The mineralization and studied Zebra Dolomite is located in the recrystallized limestone of the Koçakkale formation reffered to as the Bolkar Mountains Marble by Şişman and Şenocak (1981). The Late Cretaceous Kaledere formation overlies the Koçakkale formation with a transitional contact (Alan et al., 2007). Çiğdemgölü formation of Namrun tectonic zone is overthrusted onto the Bolkardağ unit. The Namrun unit in the study area is composed of the Early Permian Çiğdemgölü formation, the Late Permian Karlığıntepe formation, and the Early - Middle Kocatepe formation. The Kocatepe formation overlies the former units with a transitional contact. The Kızılcadağ Ophiolitic melange and the olistostromes of the Bozkır unit tectonically overlie the Namrun tectonic unit. In the study area, the units are overlain by the units of the Ereğli - Ulukışla basin. The Paleocene - Middle Eocene Halkapınar formation and the Middle Eocene Delimahmut formation are units of the Ereğli Ulukışla basin (Alan et al., 2007, Figure 2). Furthermore, in the region, the Paleocene - Early Eocene Horoz Granitoid crosscuting the pre - Middle Eocene units. All of these units are uncomformably overlain by younger alluvial deposits (Figure 2).

4. Petrography

The study area ZD have been locally occurred. The host rock is recrystallized limestone and contact with the ZD are sharp (Figure 3a). We have been done XRD analysis to determine the ratio of calcite and dolomite as %. Petrographically the ZD is microcrystalline texture and consist of > 90 % dolomite and little calcite (Figure 3c). The ZD has geopatic fabric (Figure 3b) and has been characterized by parallel light and dark bands that occur at a millimeter to centimeter scale. The light and dark bands of the this have similar mineralogy and chemistry by petrographic and SEM investigation results. Gray dolomite commonly lines the base of the white coarsely crystalline dolomite (Figure 3b, c). In thin sections fine grained dolomite crystals in the gray layers are generally fine grained - anhedral, with fitted irregular intercrystalline boundaries. Dolomite crystals in the white layers are medium - coarse grained, subhedral to euhedral with straith intercrystalline boundaries (Figure 3c, d). Geopetal textures are common in the Zebra fabric and show that the horizontal deposition. Cavities and layered mineral fillings within them indicate the fluctuations in chemistry of the dolomitizing solutions during the form of ZD, which alternate between corroding and

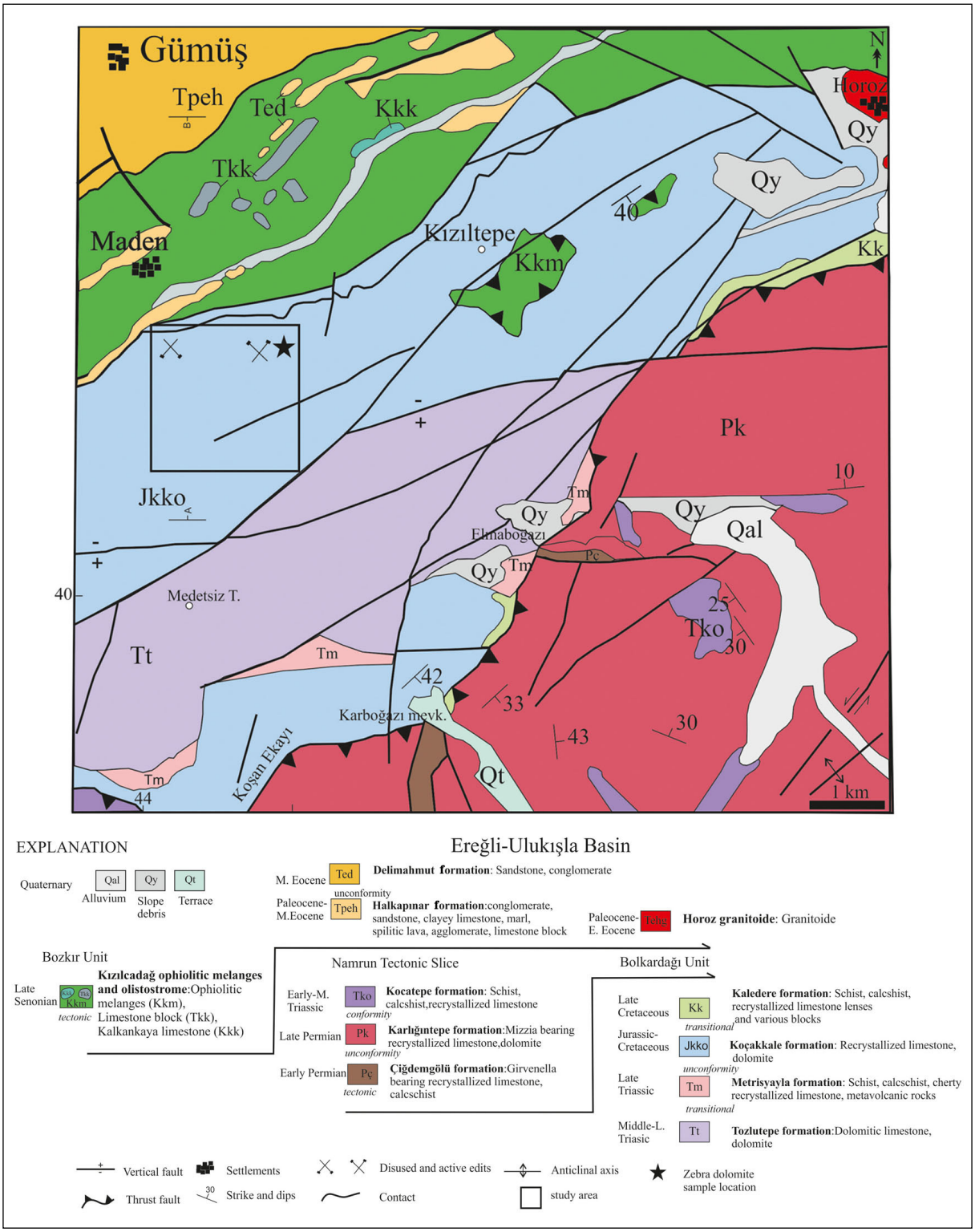

Figure 2- Geologic map of the study area modified from Alan et al. (2007).

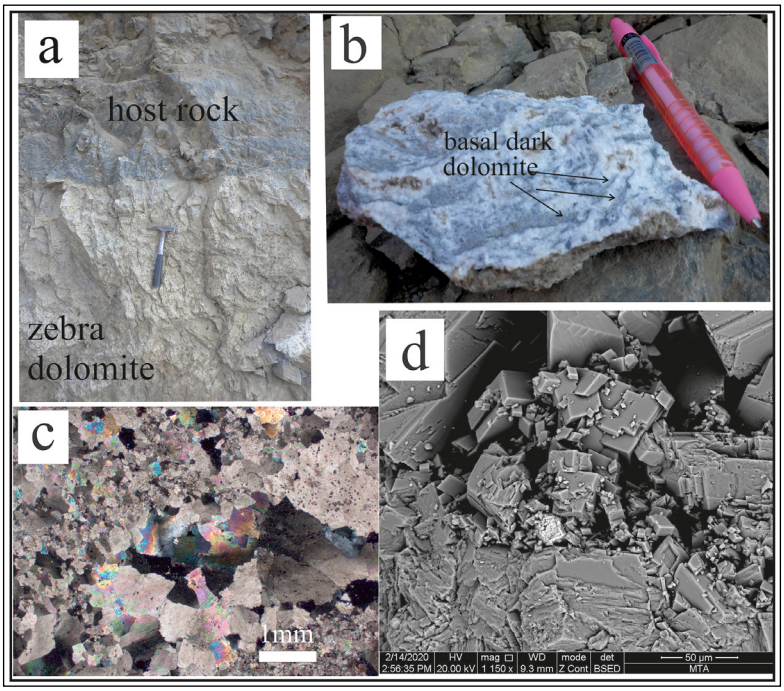

Figure 3- a) Contact between the ZD and limestone, b) Hand spicemen at the study area ZD showing the detailed appearance of the ZD layers. The dark dolomite alternates with light layers, c) Photomicrographs of ZD layer. Coarse grained band between the fine grained dolomite level (dense dolomite, crossed polar), d) SEM image of the fine and coarse grained dolomite.

dissolving, and precipitation and deposition (Bray, 1983).

5. Fluid Inclusion Study

Microtermometric measurement were performed on fluid inclusions in dolomite and primary inclusions were observed. Based on fourteen measurements, homogenization temperatures range from 80 to 180 °C (n=14, all data graphically display in Figure 4). Most of the primary inclusions consist of a single phase (gas) (Figure 5a) or two - phase (liquid + gas) (Figure 5b). Primary origin inclusions are seen generally like square, rectangular, elongated, rod - shaped, tube - shaped, round - shaped and/or irregular shape. The diamensions of the primary inclusions range from <1 to 1 µm (Figure 5). Because the two - phase (liquid

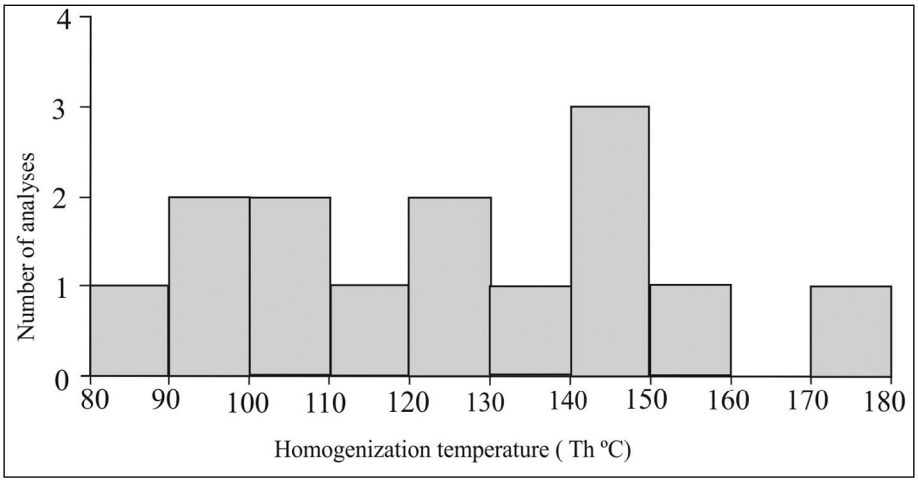

Figure 4- Histogram of the thermometric measurement of fluid inclusions in Zebra Dolomite.

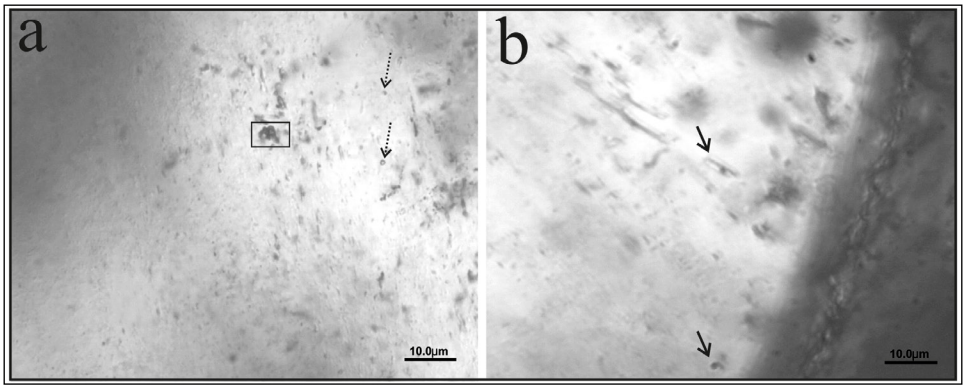

Figure 5- Photomicrographs of typical fluid inclusions; a) dotted arrows highlight primary single - phase aqueous inclusions, most fluid inclusions are submicron in size and vapor bubble (inside rectangle), b) arrows highlight two phase aqueous inclusions (liquid + gas).

+ gas) primary inclusions are very small, phase transitions cannot be clearly detected at a lower temperature (<0 °C).

6. Oxygen and Carbon Isotopes Results

The δ ^{18}O values of the ZD range from -11.39 ‰ and -14.88 ‰ VPDB while the δ ^{13}C values of the ZD range from 2.59‰ and 2.72 ‰ V - PDB (n = 4, Table 1, Figure 6). Figure 7 shows a plot $\delta^{18}O$ versus $\delta^{13}C$ where, the data of the ZD display positive correlation. The light and gray layer of ZD have similar stable isotope data and mineral composition (based on SEM data). The ZD δ ^{13}C values close to the values of the host rocks (host rock δ ^{13}C values is 2.81 V - PDB, Table 1, n = 1).

Equilibrium isotopic composition (the dolomite - water fractionization) of the solution was calculated by the equation $1000In\alpha_{D\text{-}H_2O}=3.06x10^6T^{-2}-3.24$ (Matthews and Katz, 1977) and using the fluid inclusion T° (between 80 °C and 180 °C). Therefore, the $\delta^{18}O$ composition of precipitating fluids of dolomitization was found to be between 1.1 and 1.6 ‰ V - SMOW. According to these values, the source of the solution of precipitating ZD may be similar to marine water. Tucker and Wright (1992) stated that the dolomite $\delta^{18}O$ isotope data between +1.2 and 2.2 ‰ indicate that precipitation from near - normal marine water, rather than hypersaline or brackish water. If the $\delta^{13}C$ is 2 to 4 ‰, well within the field of marine $CaCO_3$ the dolomite replaced, or it is derived from dolomitizing fluids (modified seawater) that have a similar $\delta^{13}C$ values to the seawater from which the $CaCO_3$ grains are precipitated (Tucker and Wright, 1992). It is noted that the source of carbon is typically of marina origin when $\delta^{13}C$ values between 0 and +4 ‰ V - PDB (Irvin et al., 1977). Accordingly, based on the $\delta^{13}C$ and precipitating fluids $\delta^{18}O$ values of the ZD, we can say that the source of dolomitization fluids is derived from marine water.

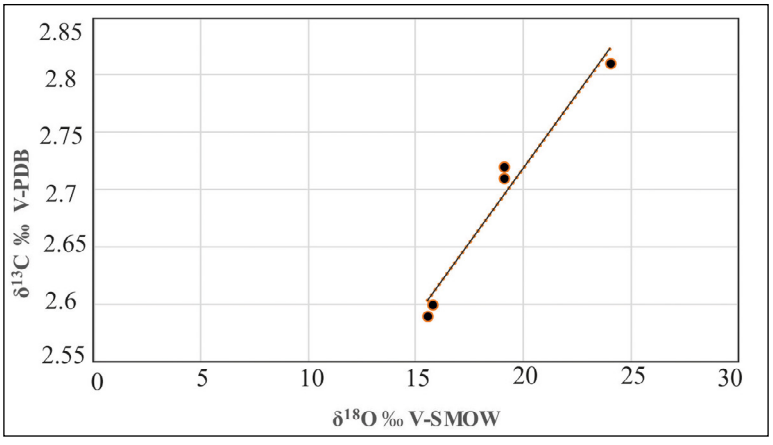

Figure 6- Diagram of $\delta^{18}O$ versus $\delta^{13}C$ (V - PDB) of the study area ZD.

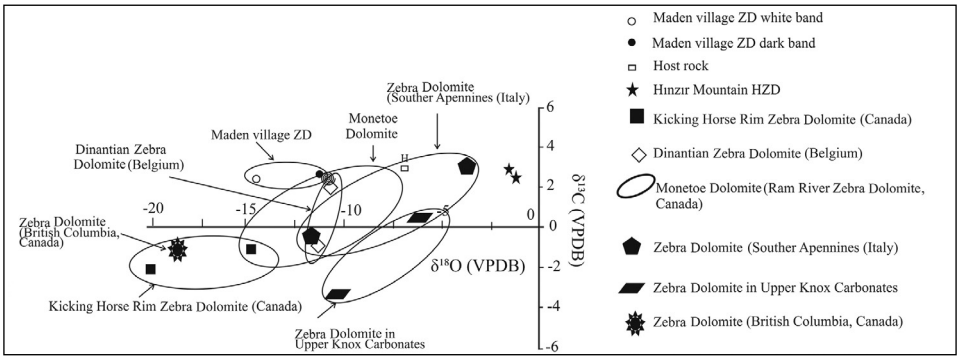

Figure 7- Values $\delta^{13}C$ (V - PDB) and $\delta^{18}O$ (V - SMOW) of the study area and of world Zebra Dolomite occurrences.

7. Discussion

The study area in the Bolkar Mountains Unit of Tauride Block. During the Miocene this area gradually uplifted along the normal faults (i.e. the Bolkar Frontal Fault, as a result of subduction processes), building a southward - tilted asymmetric mega-fault block with a rugged, Alpine topography (Dilek and Whitney, 1997, 2000; Dilek et al., 1999*b*; Kadıoğlu and Dilek, 2010). The fault system and uplifted may be lead to karstic development processes. The fault which is the normal fault, E - W trending and 36 - 45° S-dipping faults in the study area. The mildly acid meteoric water infiltrates and reacted with carbonate host rocks, dissolves the host limestone giving rise to a large karst throughout the Upper Triassic carbonate rock of the Bolkar Mountain (Kahya et. al., 2019). Tectonically deformed and uplifted terrains, characterized by moderate to high vertical and lateral permeabilities, may be the locale of deeply penetrating dilute fluids that mix with formation water or basinal brines (Garven, 1985; Bethke and Marshak, 1990). Therefore investigated dolomitization controlled by the fault. The carbonate - hosted Maden village ore deposits near the investigated ZD are in the same host rock. But the occurrences process are different.

The carbonate - hosted Maden village deposit occurred by supergene oxidation of primary sulfide minerals during complex interactions such as tectonic uplift, karst development (Kahya et.al., 2019), but the ZD may have occurred during the late diagenetic process. But what they have in common is that both of their formations occur after tectonic uplift. At first, we thought that the formation of the ZD was related to the carbonate - hosted Maden village ore deposits.

Based on $\delta^{18}O$ and $\delta\ ^{13}C$ data of the ZD, we determined that the source of oxygen is derived from marine limestone, clastic sediments, metamorphic rocks (Criss, 1999), and that the source of CO_2 is derived from marine limestone, freshwater carbonates, metamorphic CO_2 (Clark and Fritz, 1997). The ZD was formed from formation water derived from underlying and/or adjacent rocks. The $\delta\ ^{13}C$ composition of ZD range from +2.5 to +2.7, a little more positive than $\delta\ ^{13}C$ values of carbonate rocks of marine origin (0 to 2 ‰ PDB; Keith and Weber, 1964). These more positive $\delta\ ^{13}C$ values was explained by Friedman (1987) that subsurface diagenetic system in which the host rock subject to waters having salinities of marine or near marine $\delta\ ^{13}C$ values. Because it was involved in exchange reactions with heavier carbon derived from CO_2 / CH_4 exchange reactions in the host fluid (Mattes and Mountjoy, 1980). Dolomitizing fluids slightly greater than seawater due to slightly modification by water-rock interaction during progressively burial (Wang et al., 2015). The $\delta\ ^{18}O$ composition of the ZD range from -11.38 to -14.87 V - PDB and is highly negative. Very negative $\delta\ ^{18}O$ values were explained by Friedman (1987) as the late diagenetic dolomite occurrences. The $\delta\ ^{18}O$ values versus $\delta\ ^{13}C$ values of the ZD shows a positive correlation (Figure 6) and Tucker and Wright (1992) have explained that mixing-zone dolomitization have pozitive correlation of $\delta\ ^{18}O$ with $\delta\ ^{13}C$ because it consists of a mixture of two water of different isotopic composition. The calculated $\delta\ ^{18}O$ values for dolomitizing solution of the ZD indicate that it is a source of seawater effect (Tucker and Wright,1992; Irvin et al., 1977).

The $\delta^{18}O$ composition of precipitating fluids of studied ZD is between 1.1 and 1.6 ‰ V - SMOW (calculated with this equation 1000InαD-

$H_2O=3.06x10^6T^{-2}$-3.24, Matthews and Katz, 1977), and based on this result, we determined that the source of dolomitization fluids were derived from sea water (Tucker and Wright, 1992; Irvin et al., 1977). The oxygen isotopic composition of dolomite generally reflects the temperature of precipitation and isotopic composition of the dolomitizing fluids (Tucker and Wright, 1992). The next can be influenced by the isotopic composition of the CaO_3 minerals being replaced, however since pore - fluids have rich oxygen, generally precursor minerals solely have an effect in low water / rock ratio or closed diagenetic systems. Under the majority of condition, since dolomitization and recrystallization take place in the presence of water, the dolomite recipitated has a $\delta^{18}O$ value determined by the pore - fluid composition and temperature. On the contrary, the $\delta^{13}C$ value of dolomite is generally severely influenced by that of the precursor. Pore - fluids usually have low carbon contents at first, so that the $\delta^{13}C$ value of $CaCO_3$ being dolomitized is commonly retained by the dolomite (Tucker and Wright, 1992). However, based on the isotope data, in the dolomitiation fluids of the ZD have no meteor effect. Because of this reason the studied ZD formation not related to karstic formation processes. Possible sources for the dolomitizing fluids maybe related to pore waters squeezed out from the surrounding Triassic and Cretaceous formations. The studied ZD occurred locally, surface in a small area, and there is no evidence of hydrothermal origin. Diehl et al. (2010) explained that SEM data in hydrothermal ZD which related to Sedex, MVT Pb - Zn deposits and pluton-related polymetallic replacement deposits that Zn - and Pb - rich growth zones or rims are present (e.g. Blackwater and Queen of Sheba MVT, Death Valley and The Mineral Hill polymetallic vein and replacement deposits, Nevada). Since these mineral contents were not present in the studied ZD (SEM + EDX study), we determined that the ZD formations were not related to Maden village ore deposits.

Hydrothermal dolomitization results from the circulation of fluids with higher temperature than the ambient host rocks, but late diagenetic Saddle dolomite/ZD is formed at temperatures between 60 °C and 160 °C (Davies and Smith, 2006). The studied ZD compared late diagenetic ZD, hydrothermal and MVT-related ZD occurrences in Table 2. The studied ZD homogenization temperature is range of 80 °C to 180 °C and similarities with late diagnetic

Table 2- Isotopic composition and fluid inclusion (Th °C) of ZD in the world.

Name	$\delta^{13}C$ (V - PDB) ‰	$\delta^{18}O$ (V - PDB) ‰	Th °C	Description	References
Zebra Dolomite (Souther Apennines (Italy)	3 to -1	-4 to -12	80 - 120 °C 2 - 6 wt % NaCl eq.	Late Diagenetic	Iannace et al., 2012
Zebra Dolomite in Upper Knox Carbonates (in Southern Appalachian Basin)	-3.8 to +0.9	-11.9 to -5.3	80 - 165 °C 13 - 22 wt % NaCl eq.	Late Diagenetic	Montanez, 1994
Zebra Dolomite (British Columbia, Canada)	-1.35 around	-18.0	80 - 200 °C	Late Diagenetic	Swennen et al., 2003
Kicking Horse Rim Zebra dolomites (Canada)	-2.2 to -0.1	-20 to -14	Th is 130 - 200 °C, with 20 - 30 wt. % $CaCl_2$,	Spatially associated MVT Pb - Zn deposits	Vandeginste et al., 2005
The Dinantian (Belgium) Zebra Dolomite	0.1 to 1.1	-10 to -11	114 to 130 °C 23.8 and 21.2 eq. wt % $CaCl_2$	Spatial relation with MVT type	Nielsen et al., 1998
Manetoe and Presque Dolomite (Ram River Zebra Dolomite)	-1.3 to -1.1	-11.7 to -13.4	153 to 205 °C 11.7 25.8 NaCl eq. wt. %	Hydrothermal	Morrow, 2014
In Turkey, the Hınzır Mountain (Kayseri) Zebra Dolomit	2.4 to 2.7	29.4 to 29.5	-	Origin of the fluids, either surface and / or ocean water, hydrothermal fluids	Aydal et al., 2008
Zebra Dolomite in Great Basin, Nevada	-	-	50 - 150 °C	Hydrothermal	Diehl et al., 2010
Zebra Dolomitization, Irankuh Mining District, Iran	Mean 2.39	Mean - 12.27	170 - 260 °C	Early diagenesis and hydrothermal	Konari and Rastad, 2018

dolomitization. The ZD compared with different formation Zebra Dolomite in the world in terms of $\delta^{18}O$, $\delta^{13}C$, it was determined that the carbon isotope value is slightly different, that is, it contains a slightly positive high value than late diagenetic occurrences (Table 2 and Figure 7). It is similar to the ZD in Iran in terms of carbon isotope value (range from + 0.54 to + 3.51 ‰ by Konari and Rastad, 2018). Konari and Rastad (2018) explained that the the state of these carbon isotopes is mainly influenced by precursor carbonates. The source of Mg^{+2}, which is necessary for zebra dolomite formation, may have originated from schist in the Late Cretaceous units (Kaledere formation) which overlies the Koçakkale formation, or ophiolites which tectonically overlie them. All of these features comply with generally accepted criteria for late diagenetic dolomitization formation (compare with Morrow et al., 1990 and Machel, 2004).

8. Results

The Jurassic - Cretaceous recrystallized limestone of the Bolkar Mountains host the locally occur dolostone bodies showing fabric and petrographic characteristics typical of late diagenetic dolomites displaying zebra like structures. The fluid inclusion of the ZD sample (homogenization temperature range from 80 °C to 180 °C) indicates that similarities with late diagenetic dolomitization from Italy, Canada, Iran (Table 2). The $\delta^{18}O$, $\delta^{13}C$ and calculated $\delta^{18}O$ composition of precipitating fluids of the ZD, in conjunction with fluid inclusions suggest that dolomitization fluids derives from sea water and dolomitization was accomplished by squeezing out of formation water from surrounding formation. Summarizing, the study area ZD occurs late diagenetic processes related to fault associated with the uplift of Tauride Block (in Miocene). Dolomitization may be occurred before secondary mineralization and related fluids derived from the formation fluids.

Acknowledgement

This study is a part of TUBİTAK Project No:112Y144, was supported by Scientific and Technical Research Council of Turkey (TUBİTAK). We acknowledge this fun gratefully.The autors also thanks to Dr. Ebru Kavukcu for fluid inclusions study, Ufuk Kibar for SEM + EDX study, Prof. Dr. Halim Mutlu and the anonymous referee for their constructive and very helpful comments.

References

Alan, I., Sahin, Ş., Keskin, H., Altun, I., Bakırhan, B., Balcı, V., Böke, N., Saçlı, L., Pehlivan, Ş., Kop, A., Haniçili, N., Çelik, Ö. F. 2007. The geodynamic evolution of the intermediate Taurus Zone: Ereğli (Konya) - Ulukışla (Niğde) - Karsantı (Adana) - Namrun (İçel) surroundings. Maden Tetkik ve Arama Genel Müdürlüğü, Rapor No: 11006, Ankara (unpublished).

Arne, D., Kissin, S. 1989, The significance of diagenetic crystallization rhythmites at the Nanisivik Pb-Zn-Ag deposit, Baffin Island, Canada. Mineralium Deposita 24, 230-232.

Atabey, E., Göncüoğlu, M. C., Turhan, N. 1990. 1 / 100000 scale Turkish Geological Map, 33, J19.

Aydal, D., Polat, O., Uslu, A., Uslu, İ. 2008. Locating of the ore bearing Zebra dolomites by using landsat 7 etm + and quickbird satellite data in Hınzır Mountain, Kayseri, Turkey. Third International Conference on the Geology of the Tethys, January 2008, Aswan, 217-226.

Beales, F. W., Hardy, J. W. 1980. Criteria for the recognition of diverse dolomite types with emphasis on the study of host rocks for Mississippi Valley - type ore deposits. Society of Sedimentary Geology Special Publication 28, 197-214.

Bethke C.M., Marshak, S. 1990. Brine migration across North America - the plate tectonics of groundwater. Annual Review Earth and Planetary Sciences 18, 287-315.

Blumenthal, M. 1956. Geology of northern edge and west extension of Bolkar Mountains regions. Mineral Research and Exploration Institute of Turkey (MTA) Publication Special Publication Series 7, 1-53.

Bray, T. D. 1983. Stratabound zinc - lead deposits in the Monte Cristo Limestone, Goodsprings, Nevada. Master Thesis, Dartmouth College, 235, Hanover.

Bouabdellah, M., Sangster, D. F., Leach, D. L., Brown, A.C., Johnson, C., Emsbo, P. 2012. Genesis of the touissit - bou beker Mississippi valley - type district (Morocco - Algeris) and its relationship to the Africa - Europe Collission. Economic Geology 107, 117-146.

Clark, I. D., Fritz, P. 1997. Environmental Isotopes in Hydrogeology. Lewis Publishers, Boca Raton, New York, 328.

Clark, M., Robertson, A. H. F. 2002. The role of the Early Tertiary Ulukisla Basin, Southern Turkey, in suturing of the Mesozoic Tethys ocean. Journal of the Geological Society of London 159, 637-690.

Criss, R. E. 1999. Principles of Stable Isotope Distribution. Oxford University Press, New York, 264.

Davies, G. R., Smith Jr, L. B. 2006. Structurally controlled hydrothermal dolomite reservoir facies: an overview. American Association of Petroleum Geologists Bulletin 90, 1641-1690.

Demirtaşlı, E., Turhan, N., Bilgin, A. Z., Selim, M. 1984. Geology of the Bolkar Mountains, in Tekeli, O., and Göncüoğlu, M. C., eds., Geology of the Taurus Belt. Proceedings of the International Symposium, Mineral Research and Exploration Institue of Turkey (MTA), Ankara, Turkey, 125-141.

Dilek, Y., Whitney, D. L. 1997. Counterclockwise PTt trajectory from the metamorphic sole of a Neo-Tethyan ophiolite (Turkey). Tectonophysics 280, 295-301. doi: 10.1076/50040-1951(97)00038-3

Dilek, Y., Whitney, D. L. 2000. Cenozoic crustal evolution in central Anatolia: extension, magmatism and landscape development. Proceedings of the 3 rd International Conference on the Geology of the Eastern Mediterranean, September 1998, Nicosia, Cyprus, 183-192.

Dilek, Y., Whitney, D. L., Tekeli, O. 1999*b*. Links between tectonic processes and landscape morphology in an Alpine Collision Zone, south - Central Turkey. Annals of Geomorphology 118, 147-164.

Diehl, S. F., Hofstra, A. H., Koenig, A. E., Emsbo, P., Christiansen, W., Johnson, C. 2010. Hydrothermal Zebra Dolomite in the Great Basin, Nevada - attributes and relation to Paleozoic stratigraphy, Tectonics, and ore deposits. Geosphere 6(5), 663-690.

Fontboté, L. 1981. Strata - bound Zn - Pb - F - Ba - deposits in carbonate rocks: new aspects of paleogeographic location, facies factors and diagenetic evolution: (with a comparison of occurences from the Triassic of southern Spain, the Triassic / Liassic of central Perú and other localities). PhD thesis, University of Heidelberg, 192.

Fontbote, L. 1993. Self - organization fabrics in carbonate-hosted ore deposits: the example of diagenetic crystallization rhythmites (DCRs), In Hach - Ali, P. F., Torres - Ruiz, J., and Gervilla, F., eds., Current research in geology applied to ore deposits. Proceedings of the Second Biennial Society for Geology Applied to Mineral Deposits Meeting, Granada, Spain, 11-14.

Fontbote, L., Amstutz, G. C. 1983. Mineral Deposits of the Alps and of the Alpine Epoch in Europe. (Ed H.G. Schneider), Springer, Heidelberg, 347–358.

Friedman, G. M. 1987. Deep - Burial Diagesis: its implications for vertical movements of the crust, uplift of the lithosphere and isostatic unroofing - a review. Sedimentary Geology 50, 67-94.

Garfunkel, Z. 1998. Constraints on the origin and history of the Eastern Mediterranean Basin. Tectonophysics 298, 5-35.

Garven, G. 1985. The role of regional fluid flow in the genesis of the Pine Point deposit, Western Canada sedimentary basin. Ecoomic Geology 80, 307-324.

Gomez Rivas, E., Corbella, M., Martin - Martin, J. D., Stafford, S. L., Teixel, A., Bons, P. D., Griera, A., Cardellach, E. 2014. Reactivity of dolomitizing fluids and Mg source evaluation of fault controlled dolomitization at yhe Benicassim outcrop analogue (Maestrat basin, E Spain). Marine and Petroleum Geology 55, 26-42.

Görür, N., Tüysüz, O., Şengör, A. M. C. 1998. Tectonic evolution of the Central Anatolian Basins. International Geology Review 40, 831-850.

Hiemstra, E. J., Goldstein, R. H. 2015. Repeated injection of hydrothermal fluids into down dip carbonates: a diagenetic and stratigraphic mechanism for localization of reservoir porosity, Indian Basin Field, New Mexico, USA. Geological Society, London, Special Publications 406, 141-177.

Iannace, A., Gasparrini, M., Gabellone, T., Mazzoli, S. 2012. Late dolomitization in basinal limestones of the southern Apennines Fold and Thrust Belt (Italy). Oil and Gas Science and Technology 67 (1), 59-75.

Johnson, A. W., Shelton, K. L., Gregg, J. M., Somerville, I. D., Wright, W. R., Magy, Z. R. 2009. Regional studies of dolomites and their included fluids: Recognizing multiple chemically distinct fluids during the complex diagenetic history of Lower Carboniferous (Mississipian) rocks of the Irish Zn - Pb ore field. Mineralogy and Petrology 96, 1-18.

Kadıoğlu, Y., Dilek, Y. 2010. Structure and geochemistry of the adakitik Horoz granitoid, Bolkar Mountains, south - central Turkey, and its tectonomagmatic evolution. Intertational Geology Review 52, 505-535.

Kahya, A., Kuşcu, E., Cengiz, O., Yıldız, M. 2019. S and Pb Isotope Geochemistry of the carbonate - hosted Au - Ag - Zn ± Pb deposits in the Maden village (Ulukışla - Niğde), Central Taurides, South Turkey. Neuses Jahrbuch für Mineralogie Abhandlungen (Journal of Mineralogy and Geochemistry) 196, 67-88.

Keith, M. L., Weber, J. N. 1964. Isotopic composition and environmental classification of selected limestones and fossils. Geochimica et Cosmochimica Acta 28, 1787-1816.

Koptagel, O., Ulusoy, U., Fallick, A. E. 2007. Sulfur and lead isotope investigations of the carbonate - hosted Pb - Zn deposits in the Yahyalı Region, Kayseri, Southern Turkey. Turkish Journal of Earth Sciences 16(1), 57-76.

Konari, M. B., Rastad, E. 2018. Nature and origin of dolomitization associated with sulphide mineralization: new insights from the Tappehsorkh Zn - Pb (- Ag - Ba) deposit, Irankuh Mining District. Iranian Geological Journal 53, 1-21.

Leach, D. L., MacQuar, J. C., Lagneau, V., Leventhal, J., Emsbo, P., Preemo, W. 2006. Precipitation of lead - zinc ores in the Mississippi Valley type deposit at Treves, Cevennes region of southern France. Geofluids 6, 24-44.

Levin, P., Amstutz, G. C. 1976. Kristallisation und bewegung in erzrhythmiten am beispiel Triassic - Jurassischer lagerstaten in Ostperu. Munstersche Forschungen Zur Geologie und Palaontologie 38(39) , 111-128.

Machel, H. G. 2004. Concepts and models of dolomitization: a critical reappraisal. In: the geometry and petrogenesis of dolomite hydrocarbon reservoirs, Braithwaith, C. J., Rizzi, G., Darke, G. (eds). Geological Society, Special Publications 235, 7-63.

Matthews, A., Katz, A. 1977. Oxygen isotope fractionation during the dolomitization of calcium carbonate. Geochimica et Cosmochimica Acra 41, 1431-1438.

Mattes, B. W., Mountjoy, E. W. 1980. Burial dolomitization of the Upper Devonian Miette buildup, Jasper National Park, Alberta. In: D.H. Zenger, J.B. Dunham and R.L. Ethington. (Editors), Society of Sedimentary Geology, 28.

Morrow, D. 1998. Regional subsurface dolomitization: models and constraints. Geoscience Canada 25 (2), 57-70.

Morrow, D. W. 1990. Dolomite - part: the chemistry of dolomitization and dolomite precipitation. In diagenesis, Mcllreath, I.A., Morrow, D.W. (eds), St. John's (NL), Geoscience Canada, Reprint Series 4, 113-124.

Morrow, D. W. 2014. Zebra and boxwork fabrics in hydrothermal dolomites of northern Canada: indicators for dilational fracturing, dissolution or in situ replacement. Sedimentology 61, 915-951.

Montanez, I. P. 1994. Late diagenetic dolomitization of Lower Ordovician, upper Knox carbonates: a record of the hydrodynamic evolution of the southern appalachian basin. American Association of Petroleum Geologists Bulletin 78 (8), 1210-1239.

Nielsen, P., Swennen, R., Muchez, Ph., Keppens, E. 1998. Origin of dinantian Zebra dolomites south of the Brabant - Wales Massif, Belgium. Sedimentology 45, 727-743.

Oktay, F. Y. 1982. Stratigraphy and geological history of the Ulukışla and its surroundings. Bulletin of the Turkish Geological Society 25, 13-23.

Özgül, N. 1976. Some geological aspect of the Taurus orogenic belt (Turkey). Bulletin of the Geological Society of Turkey 19, 65-78.

Özgül, N. l984. Stratigraphy and tectonic evolution of the Central Taurides, in Tekeli, Proceedings of the International Symposium on the Geology of the Taurus Belt, 77-90.

Şişman, N., Şenocak, H. 1981. Geology and ore deposits around Bolkar Mountains. Mineral Research and Exploration Institute of Turkey (MTA) Publications, Report No: 1790, Ankara.

Sass-Gustkiewicz, M., Dżułyński, S., Ridge, J. D. 1982. The emplacement of zinc - lead sulfide ores in the Upper Silesian District: a contribution to the understanding of Mississippi valley - type deposits.Economic Geology 77, 392-412.

Swennen, R., Ferket, H., Benchilla, L., Roure, F., Ellam, R. 2003. Fluid flow and diagenesis in carbonate dominated Foreland Fold and Thrust Belts: petrographic inferences from field studies of Late - Diagenetic fabrics from Albania, Belgium, Canada, Mexico and Pakistan. Journal of Geochemical Exploration 78-79, 481- 485.

Tompkins, L. A., Rayner, M. J., Groves, D. I., Roche, M. T. 1994. Evaporites; in situ sulfur source for rhythmically banded ore in the Cadjebut Mississippi valley - type Zn - Pb depoist, Western Australia. Economic Geology 89, 467-492.

Tucker, M. E., Wright, V. P. 1992. Carbonate Sedimantology. Blackwell Oxford, 482.

Wallace, M. W., Both, R. A., Ruano, S. M., Hach-Ali, P. F., Lees, T. 1994. Zebra textures from carbonate - hosted sulfide deposits: sheet cavity networks produced by fracture and solution enlargement. Economic Geology 89, 1183-1191.

Wallace, M. W., Hood, A. V. S. 2018. Zebra textures: fracture networks produced by the force of crystallization during replacement reactions. Sedimentary Geology 368, 58-56.

Wang, G., Li, P., Hao, F., Zou, H., Yu, X. 2015. Dolomitization process and its implications for porosity development in dolostones: a case study from the Lower Triassic Feixianguan Formation, Jiannan area, Eastern Sichuan Basin, China. Journal of Petroleum Science and Enginnering 131, 184-199.

Wilkinson, J. J. 2003. On diagenesis, dolomitization and mineralization in the Irish Zn - Pb ore field. Mineralium Deposita 38, 968-983.

Wilkinson, J. J. 2014. Sediment - hosted zinc - lead mineralization: processes and perspectives. In: Treatise on Geochemistry (2nd Edition), 219-249.

Wilkinson, J. J., Eyre, S. L., Boyce, A. J. 2005. Ore - forming processes in irish - type carbonate - hosted Zn - Pb deposits: evidence from mineralogy, chemistry, and isotopic composition of sulphides at the lisheen mine. Economic Geology 100, 63-89.

Vandeginste, V., Swennen, R., Gleeson, S. A., Ellam, R. M., Osadetz, K., Roure, F. 2005. Zebra Dolomitization as a result of focused fluid flow in the rocky mountains fold and thrust belt, Canada. Sedimentology 52, 1067-1095.

Zeeh, S. 1995. Complex replacement of saddle dolomite by fluorite within Zebra Dolomites. Mineral Deposita 30, 469-475.

Zentmyer, R. A., Pufahl, P. K., James, N. P., Hiatt, E. E. 2011. Dolomitization on an evaporitic Paleoproterozic ramp: widespread synsedimentary dolomite in the Denault Formation, Labrador Trough, Canada. Sedimentary Geology 238, 116-131.

Bulletin of the Mineral Research and Exploration

http://bulletin.mta.gov.tr

Geological and geochemical characteristics of Cünür volcanogenic massive sulfide mineralization (Kastamonu, Turkey)

Kurtuluş GÜNAY[a*]

[a]*The General Directorate of Mineral Research and Exploration, Mineral Research and Exploration Department, Ankara, Türkiye*

Research Article

Keywords:
Island arc, Volcanism, Bimodal-mafic, Volcanogenic Massive Sulfide (VMS).

ABSTRACT

Çangaldağ Metamorphic Complex (CMC) in Central Pontides is an accretionary complex consisting of Jurassic units. Mafic, felsic metavolcanics, metamorphic equivalents of deep marine sediments and mafic meta - lava/sill intercalations are the most distinct units of the complex. Cünür Volcanogenic Massive Sulfide (VMS) mineralization is associated with metavolcanic units of CMC. Metavolcanic units in the mineralization area contain volcanic rocks with compositions ranging from sub - alkali basalt to andesite and dacite (50.3 - 74.6 % SiO_2). For 0.1 % Cu cut - off grade, 3,372,000 tons (t) of mineral resource with 0.28 % Cu, 0.50 % Zn and 0.19 ppm Au has been estimated. Ore paragenesis of the Cünür mineralization predominantly consists of pyrite, chalcopyrite and sphalerite, and lesser amounts of magnetite. The main ore textures are massive, semi - massive, disseminated, brecciated and fracture fillings. Pyrite - chalcopyrite grading and preserved silicified clasts within the massive ore indicate that mineralization has developed in relation to replacement processes. The most significant grade intercepts reported for the mineralization are 9 %, 9 %, 0.3 %, 3300 ppb and 79 ppm for Cu, Zn, Pb, Au, Ag, respectively. Cünür mineralization has similarities to bimodal - mafic (Noranda type) Cu - Zn dominated VMS deposits.

Received Date: 03.05.2020
Accepted Date: 22.10.2020

1. Introduction

Volcanogenic massive sulfide deposits (VMS) are one of the main sources of Zn, Cu, Pb, Ag and Au. Typically, VMS deposits occurring at or near the sea floor in submarine volcanic environments in the form of polymetallic massive sulfide lenses are generally classified according to their Au and base metal contents, the tectonic environment in which they were formed, or the host rock lithologies (Galley et al., 2007). Although VMS deposits can occur in many different tectonic settings such as mid - oceanic ridges or back - arc basins, oceanic arc or active continental margin arcs, continental rifting, the common feature of these formations is that all mineralizations occur in environments where extensional tectonics are effective (Galley et al., 2007; Piercey, 2011). Host rocks of VMS mineralizations can be both volcanic and sedimentary. It is a generally accepted that the formation of these ores is resulted from metal - enriched fluids associated with seafloor hydrothermal convection (Franklin et al., 1981; Franklin, 1993; Galley et al., 2007; Piercey, 2011).

Relative and radiometric age (host rock and ore ages) for the formation of VMS mineralizations in the Anatolian geography show the Triassic - Miocene interval (Yiğit, 2009; Eyüboğlu et al., 2014; Revan et al., 2014; Yıldırım et al., 2012*a, b*; Akbulut et al., 2016; Çiftçi, 2019; Günay et al., 2019*a*). The eastern part of the Pontide orogenic belt is an important metallogenic province associated with VMS. Eastern Pontide

Citation Info: Günay, K. 2021. Geological and geochemical characteristics of Cünür volcanogenic massive sulfide mineralization (Kastamonu, Turkey). Bulletin of the Mineral Research and Exploration 165, 77-96. https://doi.org/10.19111/bulletinofmre.820436

**Corresponding author: Kurtuluş GÜNAY, kurtulus.gunay@mta.gov.tr*

VMS mineralizations are associated with felsic calc - alkaline volcanism and clastic rocks and are classified as Kuroko type or Pontide - type. (Çağatay and Boyle, 1977; Akıncı, 1985; Çağatay, 1993; Çiftçi and Hagni, 2005; Abdioğlu and Arslan, 2009; Revan et al., 2013; Eyüboğlu et al., 2014; Köprübaşı et al., 2014; Revan et al., 2014). Central Pontide VMS mineralizations are associated with mafic tholeiitic volcanism and clastic rocks and are classified as Cyprus and Besshi type (Çakır, 1995; Altun et al., 2015; Akbulut et al., 2016; Günay et al., 2018, 2019*b*).

The Cünür VMS mineralization, which is the subject of this study, is the first discovered VMS deposit formed within felsic volcanics of Jurassic arc volcanism in the middle Pontides. The purpose of this study is to explain the geological and geochemical characteristics of the Cünür mineralization, to approach the origin of it, to compare and classify it with other VMS types known in the Pontide Orogenic Belt.

2. Regional Geology

The east - west trending orogenic belt in the north of Anatolia is named as Pontides. The Pontides consist of three tectonic units collocated in the Cretaceous times: the Strandja Massif, Istanbul and Sakarya Zone (Okay and Tüysüz, 1999; Okay, 2008; Göncüoğlu, 2010, Figure 1 - a). The common cover of these units, which include different lithological elements, starts with the Early Jurassic and continues with the Jurassic - Early Cretaceous platform sediments. After the late Cretaceous, flysch type sediments and units of the Inner - Pontide ocean thrust on the younger units (Göncüoğlu, 2010).

Middle Pontides including meta - granitoids and metamorphics have a complex structure. A large area consisting of many tectonic slices with approximately east - west trending and where the basement units are overlain by the Middle Jurassic and Albian - Turonian thrust and accretion complexes, is named as the Central Pontide Super Complex (CPSC, Okay et al., 2013; Aygül et al., 2015) or the Central Pontide Structural Complex (CPSC, Tekin et al., 2012; Çimen et al., 2016, 2017, 2018, Figure 1 - b). This structural complex includes Permo - Carboniferous basement rocks, metamorphosed ophiolite slices, ensimatic arc volcanics, deep - sea metasediments, rocks associated with the continental arc and Cenozoic cover rocks (Dönmez et al., 2014; Gücer et al., 2016; Ustaömer and Robertson, 1999; Çimen et al., 2016, 2017, 2018; Günay et al., 2019*a*). Within this large structural complex, the metamorphic unit consisting of island arc volcanics and clastic rocks is defined as Çangaldağ Metamorphic Complex (CMC) (Dönmez et al., 2014; Çimen et al., 2016; 2017; 2018; Günay et al., 2018, 2019). Mineral exploration studies carried out on CMC revealed that this complex is an important base metal province of middle Pontides. With the metallic mineral exploration projects carried out by the General Directorate of Mineral Research and Exploration (MTA), many Cu - Zn - Au mineralizations associated with both volcanics and clastic rocks were identified in the CMC (Konya, 1988; Dönmez et al., 2014; Günay et al., 2018, 2019*a*). The Hanönü and Zeybek massive sulfide deposits are located in the metaclastic rocks of the CMC. Hanönü mineral deposits are one of the largest VMS deposits in Turkey with a grade of 0.6 - 1% Cu and containing about 30 million tons of reserve. Cünür VMS mineralization is occured within the felsic metavolcanic units of Çangaldağ Metamorphic Complex.

CMC is an allochthonous mass with a length of approximately 50 - 55 km and a width of 1 - 30 km, in which the units coexist with each other in tectonic slices. CMC includes island arc meta - volcanic rocks with mafic and felsic character and metavolcanoclastics; dark gray to black phyllites formed from shale and siltstone and mafic sills or dykes cutting these clastic units, and to a lesser amount serpantininized peridotite as thin slices, pillow basalt and pelagic sedimentary units. Chlorite, epidote and actinolite minerals observed in volcanics of CMC indicate the metamorphism conditions under greenschist facies (Çimen et al., 2016; Günay et al., 2018, 2019). Early Cretaceous metamorphic age has been determined by Ar - Ar dating performed on micas in the phyllite samples associated with this complex (136 ± 4 Ma and 125 ± 1Ma, Okay et al., 2013). Middle Jurassic magmatic ages were obtained by zircon U - Pb dating performed on metadacites in the volcanic sequence (169 ± 2Ma, Okay et al., 2014; metarhyodacite / U - Pb zircon, 176 ± 2Ma, 163 ± 9Ma, Çimen et al., 2018). Geological and geochemical data of the volcanics in the CMC reveal the presence of an oceanic arc existed in the Middle Jurassic. The existence of this magmatic arc called Çangal island arc is accepted as a common view (Ustaömer and Robertson, 1999; Tekin et al., 2012; Okay et al., 2013; Dönmez et al., 2014; Çimen et al., 2018).

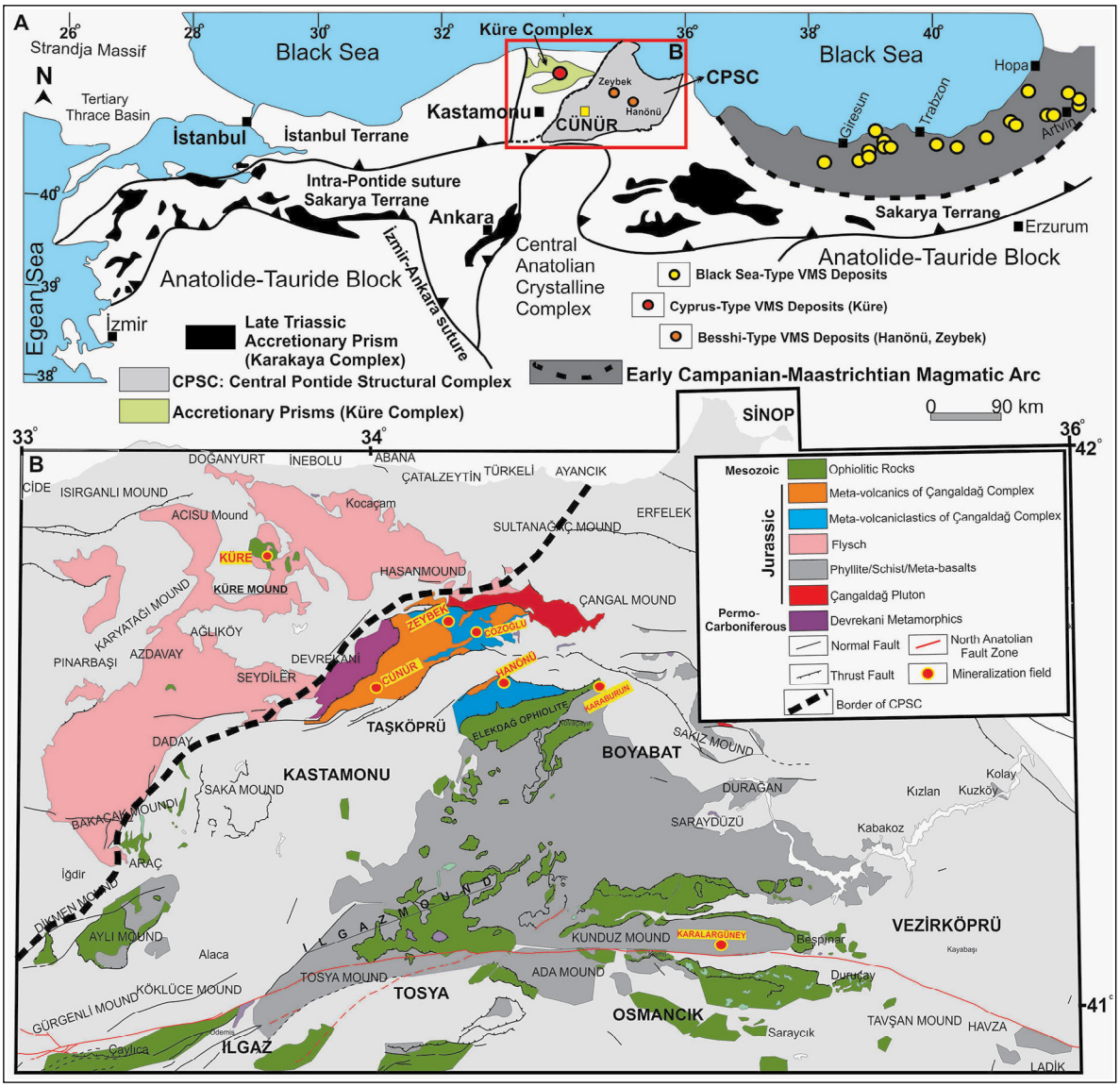

Figure 1- a) North Anatolian tectonic units (Okay and Tüysüz 1999; Göncüoğlu, 2010), the East Pontide magmatic arc and VMS mineralization points (Eyüboğlu et al., 2014), b) Simplified geology map of the Middle Pontides and Çangaldağ Metamorphic Complex (Uğuz et al., 2002), Middle Pontide VMS deposits (Günay et al., 2018, 2019*b*).

3. Material and Method

Analyzes of 50 rock samples and 31 mineralogy - petrography samples taken from the Cünür mineralization area (within the scope of the Mineral Exploration Project in Kastamonu and Surroundings) and 21369 samples for geochemical analysis, 343 mineralogy - petrography samples, 273 polished sections taken from 60 core mine drillings were carried out in MTA (General Directorate of Mineral Research and Exploration) laboratories. Ore containing zones are sampled at one - meter intervals. 2.570 density samples were taken from ore and host rocks and measurements were completed. 200 kg of samples were taken from the ore samples for full technological tests and analyzed in MTA laboratories (Günay, et al., 2019*b*; Archive No: 45892). For the geochemical analysis performed on the samples, the sample preparation methods selected by the sample characters were used and analyzes were performed with ICP - OES (Thermo, Agilint, Spectro brand), ICP - MS (Analytical Jena and Thermo brand), and XRF (Thermo and Axios brand) devices. After the samples were reduced to 1 cm grain size by coarse crushing, they were dried in an oven at 80 °C for about 12 hours

and ground with a disc grinder to have a grain size of fewer than 75 microns. Samples for chemical analysis (XRF, Loss on ignition and major oxide element analysis) were prepared by concentrated ($HClO_4$ + HCI + HNO_3) at a ratio of (1: 2: 2) + 80 - 90 °C water bath (2 hours) + pure water or royal water dissolving (3: 1) ratio concentrated (HCI + HNO_3) + 80 - 90 °C water bath (2 hours) + distilled water process and analyzed. Using the same sample preparation method, trace elements (As, Co, Cu, Mn, Mo, Ni, Pb, Zn) and Ag element analyzes with AAS were performed with ICP - OES. For the Au element, the sample was prepared with (HNO_3 + HCI) + 300 °C Hot Plate method in the ratio of Royal Water (1: 3) and analyzed by ICP - MS. Values above 0.5 gr / ton for Au were analyzed by the Fire Assay method. The UniQuant semi - quantitative analysis method was used in the analyzes. Samples were checked with the appropriate SRMs (JA - 1, JA - 2, JA - 3, G1, JR2, 267, SI - 3, NCS DC 73303). The geochemical analysis results of selected host rock and ore samples associated with the Cünür VMS are given in Table 1 and Table 2.

4. Geological Characteristics of the Cünür VMS Deposit

The Cünür mineralization area within the CMC is represented by the Middle Jurassic metavolcanic rocks (meta - basaltic andesite, meta - dacite, meta - rhyodacite), which have mafic and felsic character, and phyllites (Figures 1 and 2). The presence of chlorite, epidote, albite, actinolite paragenesis and phyllites in mafic rocks both in macro scale and petrography studies indicate that low greenschist facies metamorphism conditions are effective for all rock groups regionally. While mapping lithologies associated with CMC, felsic metavolcanics, which are the host rocks of mineralization, and structurally controlled alteration areas were effectively targeted. The lithologies in the study area have tectonic contact with each other and are often thrust by imbrications and normal faults.

In the study area, meta - basaltic andesites constitute the dominant lithology in the northern and western parts (Figure 2). Chloritization and argillization are common in these rocks with sharp fractured surfaces and dominated by green tones. This unit occasionally exhibits compact aphanitic texture and dominantly has schistosity planes dipping towards (Figure 3a). In metabasaltic andesite, it is observed that mafic minerals and pyrites are altered due to the effect of supergene processes, and limonitization and hematite minerals are observed in fractures. Felsic metavolcanic rocks are composed of metamorphic equivalents of the dacites and rhyodacites. These units are frequently observed as small outcrops within the CMC. The felsic metavolcanites starting from the west of the Kevenlik ridge and extending to the vicinity of Büyük Hill, separated from other units by imbrications and thrusts, contain mineralization areas that constitute the study subject. These units can reach 3 km east - west in places, and north - south extensions up to 500 meters. Felsic metavolcanic rocks exhibit light gray color on weathered surfaces. Least and / or unaltered parts of these rocks are gray in color and have a silicified matrix: Meta - dacites are porphyritic in texture, meta - rhyodacites have generally an aphanitic texture. Porphyric textured metadacites are easily identified in the field with their euhedral - subhedral quartz minerals of 0.1 - 0.5 mm in size, found in a silicified and, partially clayey matrix (Figure 3b, c). On the other hand, meta - rhyodacites have a more glassy, aphanitic texture and contain disseminated pyrite (Figure 3d). Argillization, silicification and limonitization are observed in these felsic metavolcanics. Hematite minerals in felsic metavolcanics appear as fracture - crack fillings. The secondary minerals such as malachite and azurite in silicified zones along the fault planes play an important role in determining the mineralizations (Figure 3e). Phyllites are observed in tectonic contact with metavolcanic units in the southeast of the Kevenlik Ridge and about one kilometer northwest of the Cünür district. Phyllites are clastic units reflecting the low grade metamorphism of black - gray shale and silt stones. These units have very well developed cleavage and micro - folds, with light and dark parts showing a mottled appearance (Figure 3f). The Pliocene aged terrestrial sediments covering the CMC are exposed in the Cünür district and its surroundings. These units are represented by light yellow - beige massive nodular limestone, gray - black colored lacustrine sediments derived from thin - medium bedded silty - clayey material.

The Cünür mineralization has occurred within felsic metavolcanic rocks. These rocks, which are about east - west trending and have tectonic contact with other units, are shifted by an approximately north

Table 1- Representative major oxide (%) and trace element (ppm) compositions of metavolcanic rocks in the area of the Cünür mineralization.

Sample	KG-2	KG-6	KG-7	KG-13	KG-11	KG-12	KG-14	KG-15	KG-16	KG-23	KG-24	KG-26
Rock	Metabasalt		Metabasaltic-andesite		Medium-Felsic Metavolcanics							
SiO_2	55.5	50.3	61.5	69.9	70	69.5	72.10	69	64.7	71	68.7	74.6
TiO_2	2.4	2.4	0.5	0.5	0.3	0.4	0.30	0.4	0.4	0.3	0.3	0.3
Al_2O_3	13.8	13.8	14.9	12.7	15.1	13.4	11.60	15.8	15.6	13.8	12.9	11.1
Fe_2O_{3TOT}	13.8	14.9	8.1	3.6	3.7	3.7	3.80	3.2	4.9	3.2	3.6	1.7
MnO	0.2	0.2	0.2	0.1	0.1	0.09	0.10	0.09	0.1	0.1	0.1	0.09
MgO	3.6	4.5	4	2	2	6.2	1.50	2.1	4.8	1.2	1.3	0.2
CaO	2.9	6.1	2.7	2.2	0.5	0.6	1.00	0.4	1.1	3.1	5.5	3.4
Na_2O	4.4	4.7	4.2	5.9	5.4	1.2	5.60	7.2	6.2	4.2	4	4.9
K_2O	0.09	0.2	0.2	0.1	1	0.8	0.10	0.09	0.09	0.9	0.4	0.1
P_2O_5	0.6	0.2	0.1	0.1	0.1	0.1	0.10	0.1	0.1	0.1	0.1	0.1
LOI	2.55	2.45	3.2	2.2	1.7	3.7	2.20	1.45	2	1.7	2.9	2.45
Sum	99.84	99.75	99.6	99.3	99.9	99.69	98.4	99.83	99.54	99.6	99.8	98.94
Sc	19	22	21.9	1.3	2.5	3.1	2.1	5.2	3.3	0.9	1.1	1.4
V	224	448	224	56	56	56	56	56	56	56	56	56
Cr	45.1	20.2	18.5	137.1	119.4	76.6	268.4	157.6	182.5	111	86.9	252.3
Th	1	1.5	6.6	1.2	0.2	0.6	1.1	0.6	0.3	1.1	1	0.3
Ga	3.2	1.6	15.3	2.2	5.2	3.2	2.3	4.2	6.7	2.3	2.9	0.9
Rb	2.3	4.3	6.9	0.2	13.5	0.5	0.6	2.1	1.9	24.9	8.8	3.4
Sr	25.1	45.1	132.3	78.4	37.6	65.8	44.9	26.1	64.2	9.8	12.6	68
Y	65	32	33	5.9	7.6	4	3.8	6.3	7.7	5.1	18	4.6
Zr	43.2	36.2	48	55.7	77.1	86.4	95.7	106.5	77.9	46.3	46.3	90.2
Nb	4.2	1.4	5.7	1.4	1.6	2	1	2.6	1.6	1.5	1.2	1
Ba	85.2	24.2	20	22.3	308.7	145.8	20.7	30.4	28.1	88.6	48.1	22.2
Cs	2.2	1.2	5.3	<0.1	0.1	<0.1	<0.1	<0.1	<0.1	0.5	0.2	<0.1
La	12	5	11.3	0.8	2.6	0.3	1.3	1.6	0.6	1.6	1.8	1.1
Ce	40	15	17.9	2.5	7.4	0.9	3.2	4.6	1.8	3.9	4.3	3
Pr	7	2	6.4	0.3	1.1	0.2	0.4	0.7	0.3	0.5	0.6	0.4
Nd	35	13	13.8	2.1	5.4	1	1.9	3.4	1.6	1	3	2.4
Sm	11	4	6.8	0.6	1.5	0.4	0.7	1	0.7	0.8	1	0.8
Eu	3	1	1.3	0.2	0.5	0.1	0.1	0.3	0.2	0.2	0.3	0.2
Gd	13	5	7	0.7	1.8	0.6	0.8	1.2	1.1	1	1.6	1.1
Tb	3	1	1.2	0.1	0.3	0.5	0.1	0.2	0.2	0.2	0.3	0.2
Dy	17	7	7.2	0.9	1.7	0.8	0.8	1.3	1.5	1	2	1.1
Ho	3	1	6	0.1	0.3	0.2	0.2	0.3	0.3	0.2	0.5	0.2
Er	9	4	4.8	0.6	0.9	0.5	0.5	0.7	0.8	0.6	1.6	0.5
Tm	1	0.3	0.7	0.1	0.1	0.1	0.1	0.2	0.1	0.1	0.2	0.2
Yb	6	3	3.5	0.4	0.6	0.4	0.3	0.5	0.6	0.6	1.2	0.4
Lu	1.2	0.5	0.4	2	1.2	1.3	0.1	0.1	0.1	0.1	0.2	0.1
Hf	9	2	1.7	1.15	1.2	2.3	2.45	1	1.23	1	2	2
Ta	0.2	0.2	2.3	0.1	0.1	0.2	0.1	0.2	0.2	0.1	0.1	0.08
Pb	2.3	3.1	14.5	5.1	4.2	2.7	6.5	3.9	5	4.3	3.6	4
U	0.1	0.2	4.9	0.3	0.2	0.1	0.2	0.1	0.3	0.3	0.1	0.1
Cd	0.2	0.1	<0.1	<0.1	<0.1	<0.1	<0.1	<0.1	<0.1	<0.1	<0.1	<0.1
Tl	0.2	1	1.2	0.3	0.3	0.2	0.2	0.1	0.3	0.3	0.2	0.3
$(La/Yb)_N$	1.43	1.20	2.32	1.43	3.11	0.54	3.11	2.30	0.72	1.91	1.08	1.97

Table 2- Representative geochemical analysis results of Cu-rich zones in the Cünür mineralization.

Sample	Ag ppm	As ppm	Au ppb	Bi ppm	Co ppm	Cu ppm	Mo ppm	Ni ppm	Pb ppm	Sb ppm	V ppm	Zn ppm
KCS-1-98	79	11	150	18	<5	10.000	8	7	156	<5	<5	9.540
KCS-2/ J159	2.2	15	<20	<5	<5	10.000	5	11	57	<5	22	662
KCS-2/ J160	1.7	9	<20	<5	<5	10.000	<5	9	40	<5	41	2.110
KCS-5-J14	20.1	66	1300	<5	10	10.000	6	23	520	<5	43	4.100
KCS-5-J17	13.4	71	770	<5	9	12.000	8	15	540	<5	32	6.100
KCS-5-J18	8	36	350	<5	<5	10.000	<5	9	370	<5	18	2.600
KCS-5-J20	22.2	120	1.100	17	15	10.000	17	16	690	<5	37	8.000
KCS-5-J23	23.5	130	9.4	19	14	12.000	11	18	650	<5	45	6.600
KCS-5-J26	26.1	130	1.100	6	12	10.000	20	16	920	<5	32	11.000
KCS-5-J65	23.9	130	1.300	<5	10	15.000	35	8	760	9	19	15.000
KCS-5-J66	31.5	120	1.700	<5	10	10.000	31	10	1.500	12	21	17.000
KCS-5-J83	26.5	240	3.300	23	12	50.000	36	26	1.600	17	11	19.000
KCS-8-J330	2.7	99	85	<5	<5	13.170	32	<5	28	6	<5	2.198
KCS-8-J331	2.2	89	70	<5	<5	10.828	36	<5	32	6	<5	1.511
KCS-8-J333	3.3	98	95	<5	<5	11.766	31	6	57	6	<5	4.021
KCS-8-J334	3.2	133	85	<5	<5	12.994	43	<5	35	5	<5	3.991
KCS-8-J335	3.4	100	75	<5	<5	17.299	43	<5	48	6	<5	1.898
KCS-13-J289	4.6	369	150	7	<5	16.141	34	6	74	11	<5	9.298
KCS-13-J306	2	26	25	<5	<5	10.409	18	<5	108	<5	<5	322
KCS-21-J307	2.9	170	40	<5	<5	11.610	88	<5	53	<5	<5	2.268
KCS-21-J312	4.9	268	165	<5	<5	10.810	78	11	66	<5	<5	6.134
KCS-24-J266	39.8	967	685	71	8	92.652	67	5	160	49	<5	7.586
KCS-24-J267	8.5	580	135	24	6	19.266	19	6	39	31	<5	776
KCS-24-J268	26.5	1.369	660	68	7	41.609	51	<5	168	85	<5	2.260
KCS-24-J269	36.7	335	925	73	8	85.458	50	<5	86	32	<5	2.253
KCS-24-J272	36.9	416	1.750	65	9	89.320	43	<5	272	30	<5	941
KCS-27-J164	40.3	107	640	14	11	17.574	23	7	3.412	11	17	90.461
KCS-27-J174	37.1	113	930	13	11	17.376	34	8	2.857	12	17	91.679
KCS-39-J206	15	25	260	<5	<5	22.687	21	<5	276	<5	10	830
KCS-39-J210	9.6	39	180	<5	<5	13.205	30	<5	778	<5	6	16.220
KCS-52-J27	3.8	24	<20	15	<5	15.832	21	6	47	<5	5	182
KCS-59-J128	27.6	95	545	<5	<5	10.166	34	8	2.283	10	6	23.100
KCS-59-J129	11.5	216	890	18	<5	10.203	58	10	214	11	<5	2.339
KCS-59-J130	11.6	225	475	<5	<5	51.500	75	12	293	35	6	7.675
KCS-59-J132	15.8	408	575	<5	<5	54.500	118	14	225	41	6	10.643
KCS-59-J133	10.4	220	335	<5	<5	62.000	94	12	249	15	8	7.433
KCS-59-J134	9.5	142	285	<5	5	53.000	143	10	288	25	<5	9.026

- south trending left strike - slip fault passing through the western slope of Büyükdoruk Hill (Figure 2). The lines where mineralization is observed are generally located in the sections where felsic metavolcanic rocks are observed to be imbricated with other units. Starting from the east, there are silicified, hematitized and argillized alterations with pyrite - limonite, around the Horozbiçtigi Hill, Ahmetolduğu Hill, Kure Stream and Karabay Hill. These alterations are structurally controlled and occasionally appear as small slices of imbrication 5 - 30 meters wide. Quartz, sericite and pyrite mineral assemblages are observed on the northeastern and southwestern slopes of the Kure Stream. In these alteration zones, malachite, azurite, to a lesser extent bornite and covellite minerals, as well as local alunitizations are found.

Mineralization areas that may be of economic importance have been identified in two different areas. These are located in the Ahmetoldugu Hill (ZONE - 1) in the northeastern part of the Kure Stream and the extension of the Kevenlik Ridge and around the Karabay Hill (ZONE - 2). The Cünür mineralization has massive – semi - massive ore structure. The thickness of the largest massive sulfide lens consisting of massive ore in the field was determined as 22 m.

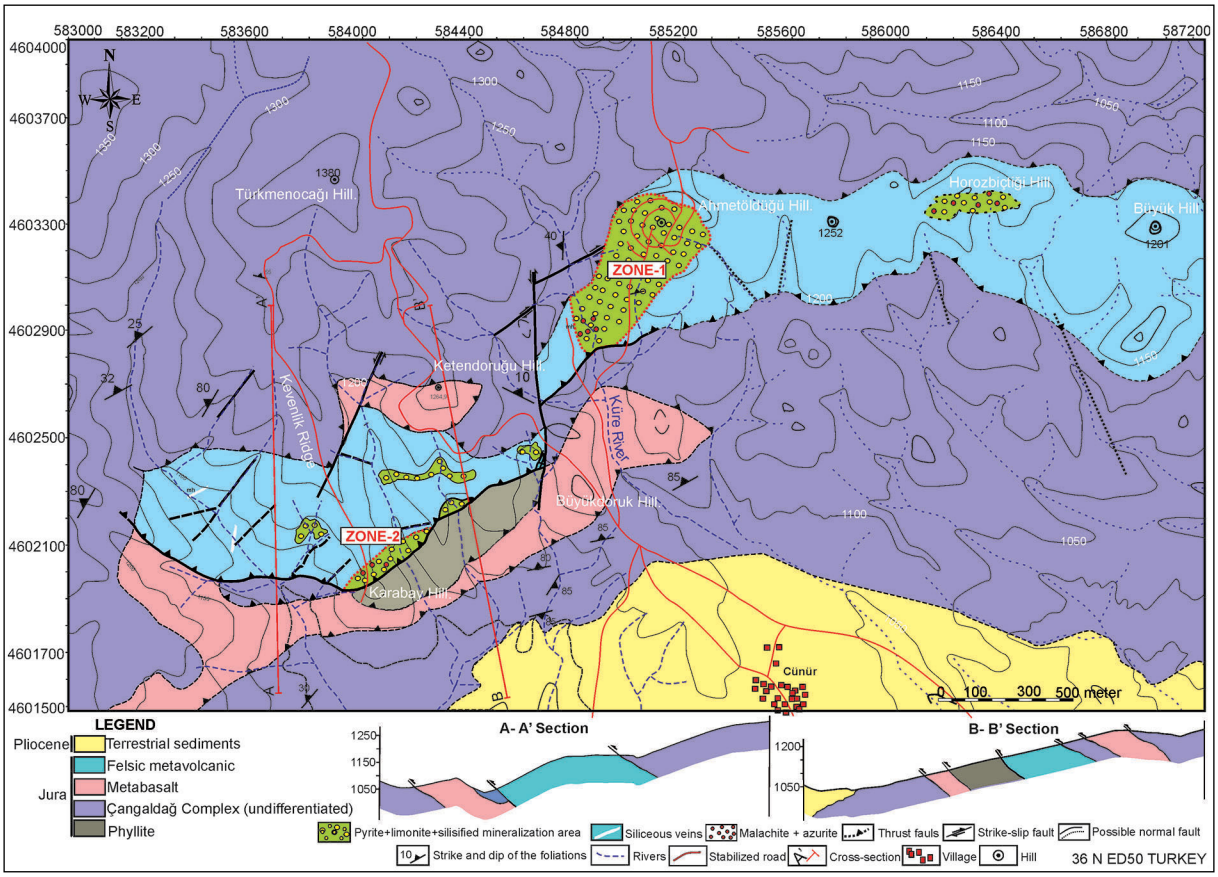

Figure 2- Cünür VMS mineralization and geological map of its surroundings.

Apart from this massive sulfide lens, which lateral continuity reaches 400 meters with decreasing thickness, many small - sized massive ore zones with a thickness of 1 - 15 meters have been identified by core drilling. The ores are found irregularly in the 50 - 370 meters elevation range throughout the field. Massive ores consist of sulfide ore, which is defined as pyritic masses of about 60% (Figure 4a, e). Massive sulfide masses in felsic metavolcanic rocks usually begin with crushed, argillized (montmorillonite, illite) zones and end with crushed, argillized zones (Figures 4a, b). These zones in the mineralization localise the mineralization, correspond to the imbrications. The observation of graded enrichments by pyrite - chalcopyrite minerals in massive sulfide bodies and the fact that the ore contains silicified rock fragments in places may indicate that mineralization has developed in relation to substitution. In felsic metavolcanic rocks, breccia fill and fracture - crack fill which have a continuity of meters and developed in metamorphism and tectonic processes and pyrite formations as veinlets, which include rarely chalcopyrite and sphalerite, are observed (Figure 4c, g). The presence of pyrite - chalcopyrite minerals in secondary siliceous zones as well as coarse (1 - 5 mm) pyrite crystall formations in fracture - crack deposits may indicate remobilization that develops in post - mineralization processes.

4.1. Rocks and Mineralogical - Petrographic Characteristics of Ore in the Cünür Mineralization Area

Mafic metavolcanic rocks, which constitute the dominant lithology in the study area, have intersertal - hypohyaline texture and can mostly be defined as metabasaltic andesite or metabasite. The mineral paragenesis of these rocks consists of amphibole (actinolite), plagioclase, quartz, chlorite, epidote and lesser amounts of opaque minerals (Figures 5a and b). Amphibole minerals are reticular - fibrous, prismatic in places, small - grained and hypidiomorph plagioclase crystals are predominantly sericitized. Platy chlorite and epidote minerals in clusters, in addition small amounts of fine - grained, semi - euhedral quartz and

Figure 3- Field photographs of lithological units in the mineralization area. a) Metabasaltic andesite, b) limonitized altered metadacite, c) altered metadacite with semi-euhedral quartz minerals, d) aphanitic textured, silicified metariodacite containing disseminated pyrite, e) fractured zones containing azurite and malachite, f) phyllite (view direction north).

carbonate minerals are generally found as fracture - fillings. The mineral assemblage of albite, chlorite, and epidote in basaltic andesites indicates metamorphism under greenschist facies conditions at low temperature and moderate pressure.

Felsic metavolcanites are predominantly hypocrystalline porphyritic in texture and contain feldspar, quartz and opaque mineral (pyrite) phenocrysts in a felsic matrix composed of feldspar and quartz (Figure 5 c, d). Feldspars are in the form

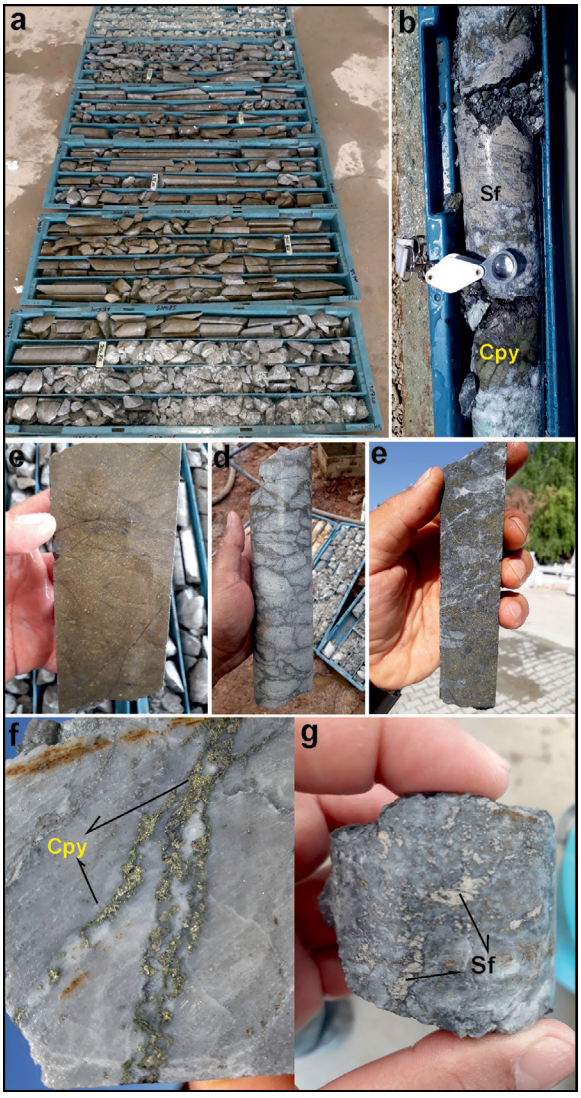

Figure 4- Core photographs associated with the Cünür mineralization. a) Massive sulfide ore with a thickness of 22 meters, consisting of massive ore, b) the appearance of zones rich in chalcopyrite and sphalerite minerals, c) the close view of the massive ore d) tectonic breccia fill secondary pyrite mineralization developed over silicified metariodacite, e) Substitution texture containing siliceous zones in semi-massive ores f) and g) appearance of chalcopyrite and sphalerite minerals filled with fractures and cracks in the silicified host rock.

of fine - grained hypidiomorphic crystals and are predominantly argillized and sericitized. Generally, absorbed quartz and opaque minerals are observed as euhedral, subhedral forms. In these rocks, opaque minerals consisting of euhedral - subhedral pyrites are found as disseminated at a rate of 10 - 20%. Secondary calcite fillings, small amounts of chlorite, epidote, hematite minerals are observed along the fractures in felsic metavolcanic rocks, and predominantly argillisation is observed (Figure 5 c, d). The presence of fine grained epidote minerals in thin sections may indicate that these rocks contain mafic phenocrystals. The change in MgO contents of 0.2 - 6.2% in the geochemistry analysis results of felsic metavolcanic rocks supports the presence of mafic phenocrystals in these rocks.

Black - gray colored and very fine - grained phyllites are seen in lepidogranoblastic texture. These rocks have very fine - grained plagioclase and quartz as main minerals as well as secondary mineral paragenesis of calcite, mica (sericite flakes), and chlorite (Figure 5 e, f).

Pyrite, chalcopyrite and sphalerite are the main mineral paragenesis of the Cünür sulfide mineralization. Apart from magnetite and galena minerals which are rarely seen, bornite, digenite, covellite, chalcocite are found in small amounts as secondary minerals. Quartz is the main gangue mineral and calcite formations are observed in veins and pockets. Pyrites, the most common sulfide mineral, form the first phase in the paragenetic sequence of ore minerals in the Cünür mineralization (Figure 6). The second widespread ore phase is composed of chalcopyrite and sphalerite minerals as anhedral fillings between pyrite grains. Generally, chalcopyrite coexisting with sphalerite is rarely seen as inclusions within sphalerite. Intergrowth textures indicate that a phase with chalcopyrite and sphalerite developed following the early sulfide phase in which pyrite was formed.

In massive ores, the grain size of pyrite minerals is much smaller than semi - massive and other formations, and the ratio of chalcopyrite is much higher. Pyrite crystals in massive ores have a grain size of approximately 5 - 800 µm and appear in euhedral, subhedral, and mostly anhedral forms (Figure 7 a). Pyrites recrystallized in fractures and cracks of the host rocks, on the other hand, have grain sizes in the range of 1 - 5 mm macroscopically in places. Chalcopyrite and sphalerite are found, filling the voids after pyrite crystallization, settling in the fracture - cracks of pyrites and surrounding them, and rarely, chalcopyrite inclusions are observed in sphalerite (Figure 7 b - d). Bornite minerals found in the fractures and cracks of pyrites are transformed into digenite, covelline, and chalcosine. In polished sections dominated by anhedral pyrite minerals, there are rarely galena

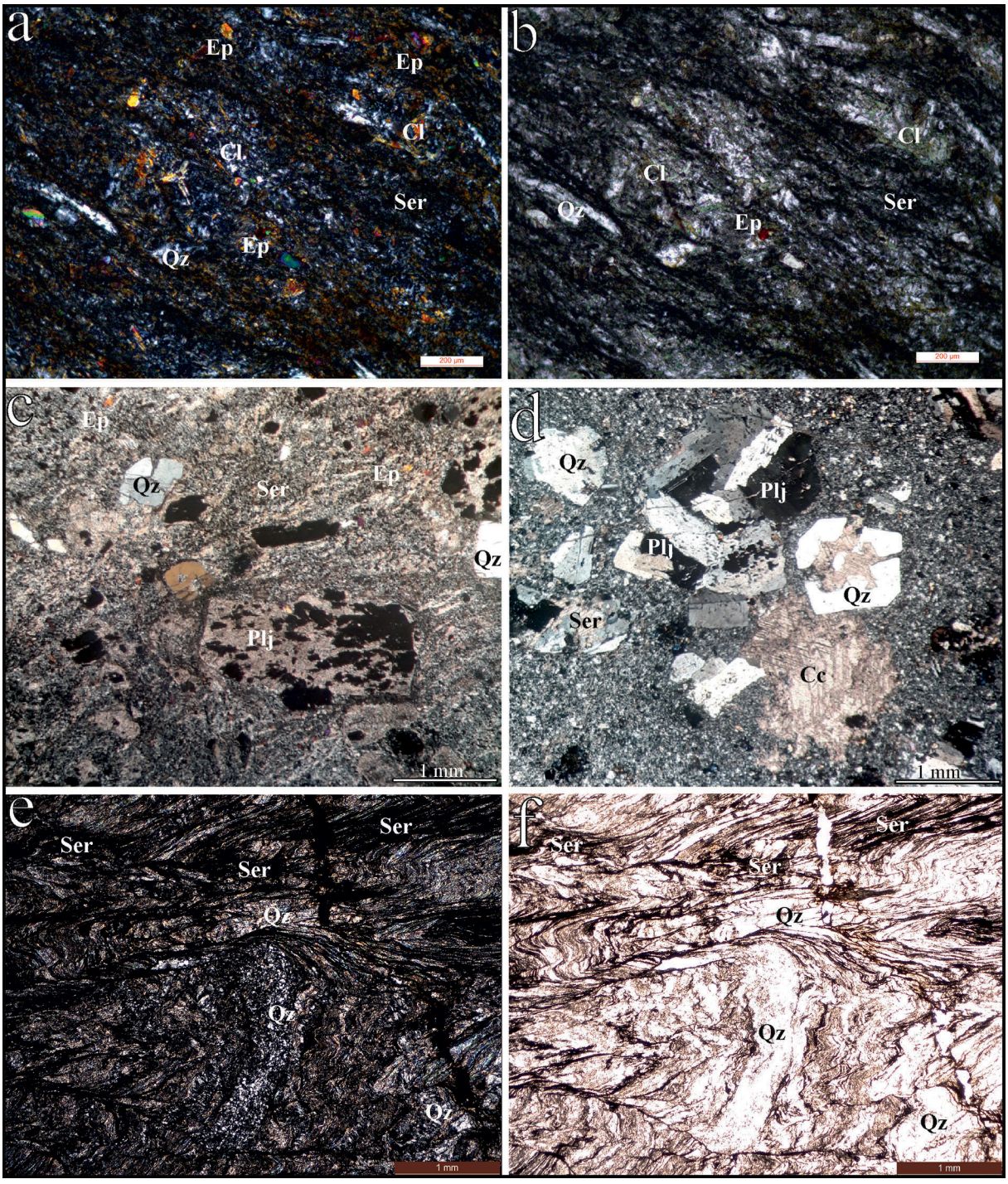

Figure 5- In the Cünür mineralization area, the thin-section images of the chloritized, epidotized, and silicified mafic metavolcanic rocks. a) Cross polarized light, b) plane polarized light); clayed, carbonated, and silicified felsic metavolcanic rocks, c) cross polarized light, d) plane polarized light); phyllite, e) cross polarized light, f) plane polarized light) (Cc-calcite, Cl-Chlorite, Ep-epidote, Ser-sericite, Qz-quartz, Plj-plagioclase).

minerals settled in fractures of pyrite minerals (Figure 7 e). Magnetites are generally in the form of small accumulations, sometimes as disseminated grains. Fine - grained anhedral and sometimes sub - euhedral magnetites of 15 - 60 µm grain size are seen in the spaces of pyrite minerals (Figure 7 f). Pyrite minerals in areas where secondary silicification associated with mineralization are coarse - grained, sharp - angular,

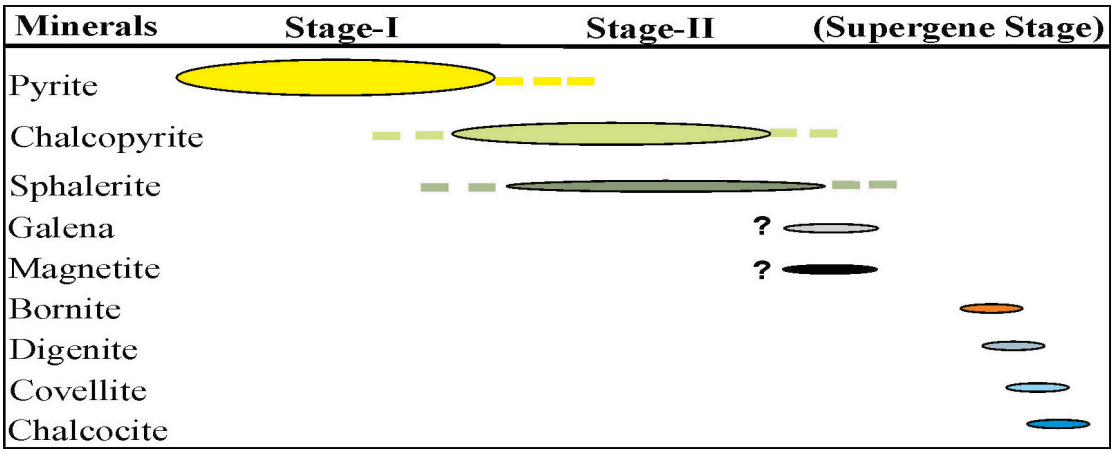

Figure 6- The Cünür mineralization paragenetic sequence table.

fractured and cracked, and chalcopyrite, in addition, sphalerite and chalcopyrite minerals are observed to be developed in their fractures (Figures 7 g, h). This indicates that remobilization has developed in the post - primary mineralization processes.

4.2. Geochemical Characteristics of Metavolcanic Rocks

For the geochemical classifications of metavolcanic rocks outcropping in the Cünür mineralization area, those with loss on ignition values were used, and the major oxide and trace element contents of these rocks are given in Table 1. The loss on ignition of the samples ranged from 1.7% to 3.7%. Samples include volcanic rocks with a composition ranging from partially hydrothermally altered sub - alkaline basalt to andesite and dacite (50.3 - 74.6% SiO_2). This situation indicates that the rocks may have been affected by hydrothermal alteration, low - grade metamorphism or seafloor hydrothermal alteration. Although loss on ignition is partially low, it has been observed that rocks are affected by hydrothermal alteration and metamorphism and partially lost their original textural and mineralogical characteristics. With the effect of hydrothermal alterations, most major elements and LIL (large ion lithophile, excluding Th) elements behave mobile, while HFS and RE (high field strength and Rare earth) elements behave mostly immobile or less mobile (Winchester and Floyd, 1977).

In order to make a more accurate classification approach for metavolcanic rocks in the study area, the Nb / Y - Zr / TiO_2 variation diagram of Winchester and Floyd (1977) was used (Figure 8a). In this diagram, it is seen that the samples have a composition ranging from sub - alkaline basalt series to andesite and dacite. Metavolcanic samples plot within the calc - alkali and island arc tholeiites fields on the Hf / 3 - Th - Ta tectonic discrimination diagram of Wood (1980) (Figure 8b).

N - MORB - normalized spidergram (Figure 9a) demonstrate that samples are generally enriched in LILE (excluding Sr), HFSE and REE relative to N - MORB (Normal Mid - Ocean Ridge Basalts). HFS elements (Nb, Ta, Zr, Hf) are typical with their relative tendency to be depleted relative to LIL and LRE elements. The greater enrichment of LIL and LRE elements than basaltic samples in the transition from sub - alkaline basaltic samples to more evolved andesitic and dacitic samples typically can be corresponded to the fractional crystallization processes in their evolution.

Chondrite - normalized (Sun and McDonough, 1989) REE spidergrams are presented in Figure 8b. There is no enrichment or depletion in these diagrams, the samples show a near - flat trend from LREEs to HREEs (La / YbN = 0.5 - 3.1), typically showing a trend in line with MORB and island arc tholeiite values. In addition, the REE patterns of andesite and dacite samples, which evolved as in the multi - element spider diagrams (Figure 9a), show enrichment in rare earth elements according to the patterns of the sub - related basaltic samples, thus indicating that felsic volcanics are typically derived by fractional crystallization processes.

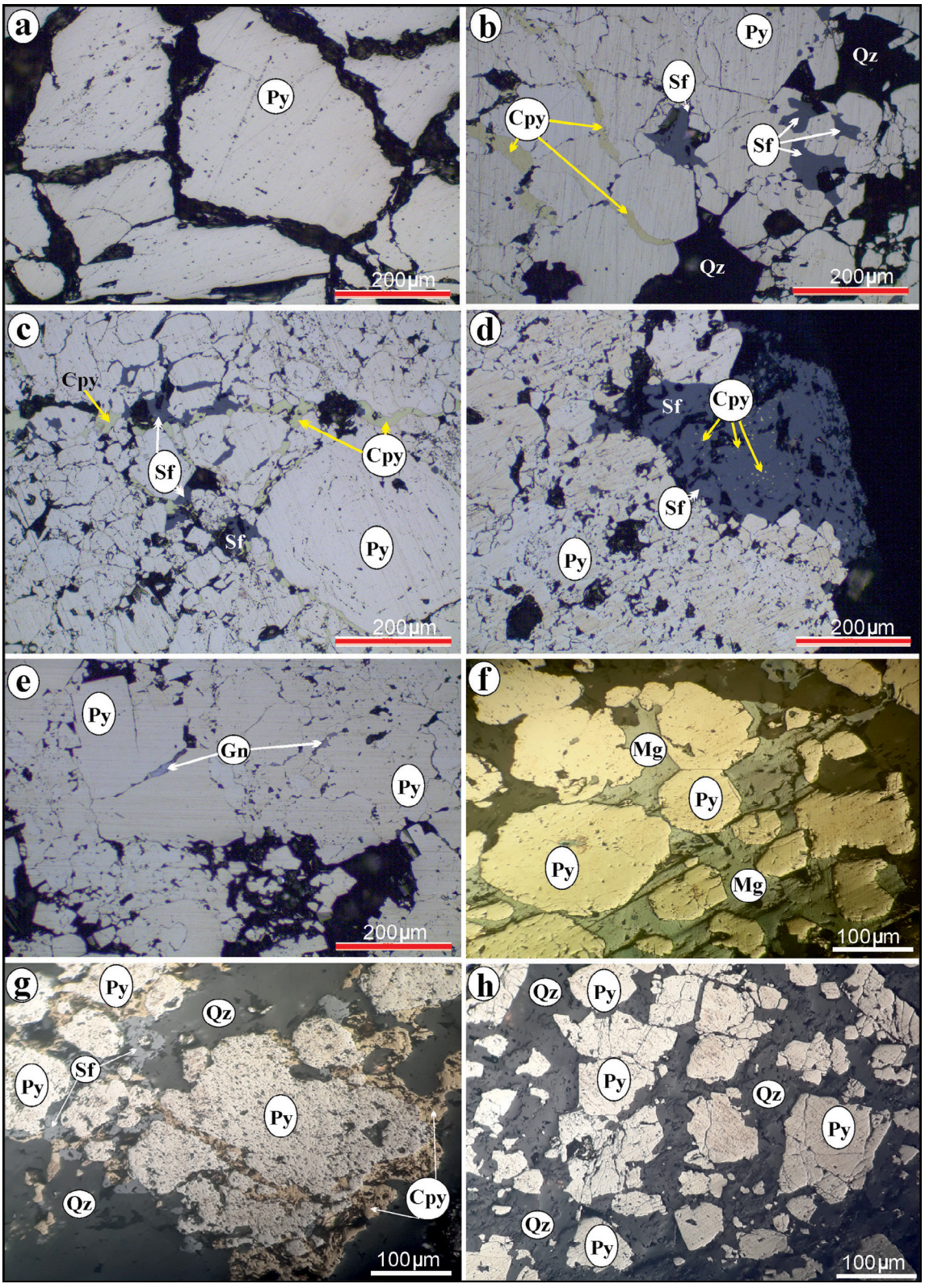

Figure 7- The polished sections images of the Cünür mineralization; a) coarse crystalline fractured pyrite minerals, b) and c) in massive ore rich in chalcopyrite, chalcopyrite and sphalerite minerals that filled fractures-spaces between subhedral and anhedral pyrites and replaced pyrites, d) chalcopyrite inclusions in sphalerite, e) galena minerals seen in anhedral pyrite mineral fractures, f) in zones of pyritic massive ore, euhedral-subhedral pyrite and magnetite minerals filling its spaces, g) and h) in siliceous zones, chalcopyrite-sphalerite filling the gaps of pyrites and pyrites (Cpy- chalcopyrite, Mg- magnetite, Py- pyrite, Sphalerite, Gn- Galen).

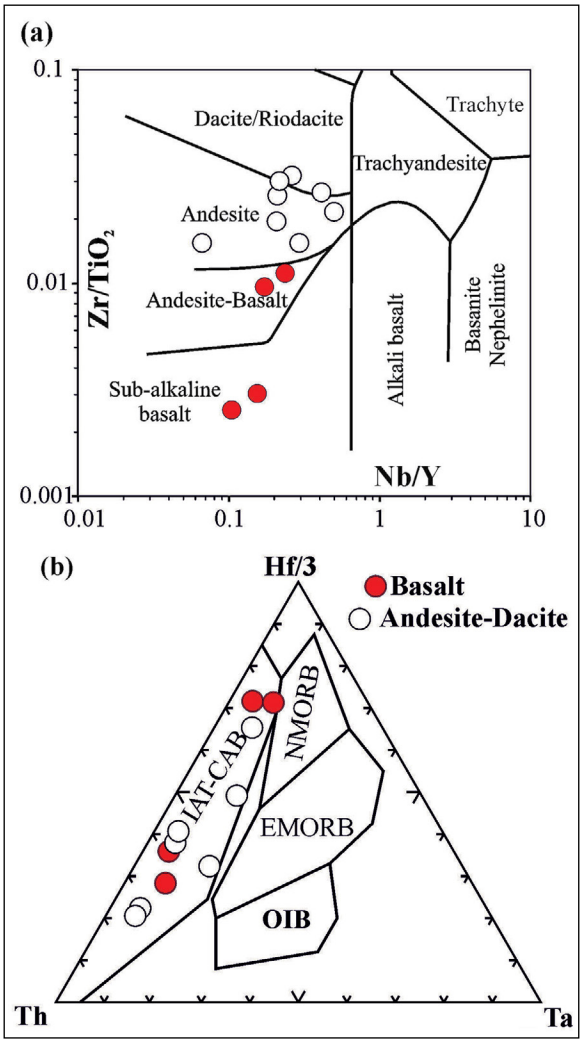

Figure 8- In the Cünür mineralization area, a) Zr/TiO_2 versus Nb/Y classification diagram of metavolcanic rocks (Winchester and Floyd, 1977), b) classification of metavolcanic rocks in Th-Ta-Hf/3 paleotectonic discrimination diagrams (Wood, 1980).

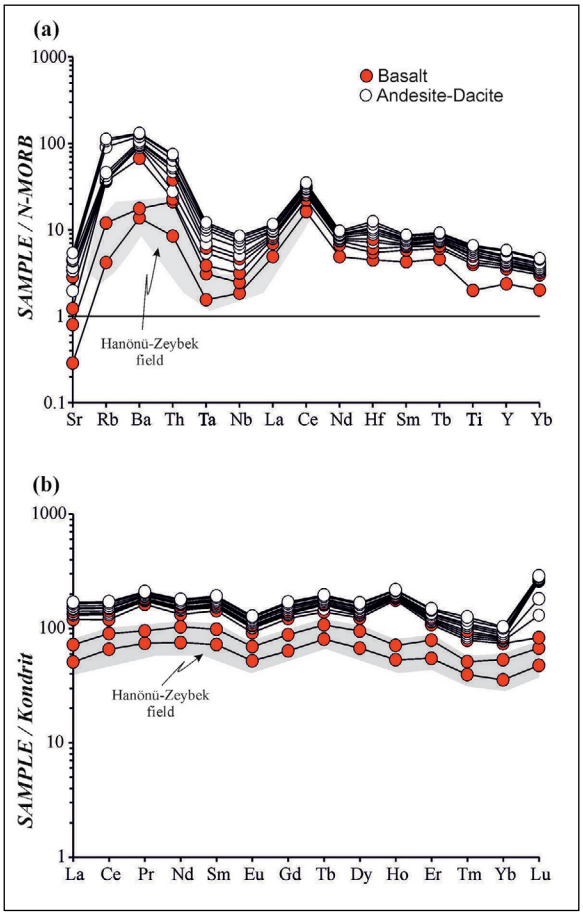

Figure 9- The spider diagrams of metavolcanic rocks normalized to a) N-MORB and b) chondrites (normalized values are taken from Sun and McDonough, 1989).

4.3. Ore geochemistry

In this study, ore samples, which geochemistry was used, were taken from parts of the massive ores where the effects of textural and petrographic alteration and recrystallization processes were not observed. Samples with Cu values higher than 1% of the Cünür mineralization are presented in Table 2. The highest values obtained for base and precious metals were determined as 9% for Cu and Zn, 0.3% for Pb, 3,300 ppb for Au and 79 ppm for Ag. The Cünür mineralization has the highest values of 15 ppm for Co, 143 ppm for Mo, 26 ppm for Ni, 85 ppm for Sb and 45 ppm for V. 227 samples taken from the ore zones in the cores of the drillings made in the field of Cünür mineralization and analyzed have an average of 8,860 ppm Zn, 6,231 ppm Cu, 335 ppm Pb, 24 ppm Ag and 299 ppb Au metal content. With the geochemical data obtained from the core drillings in the Cünür mineralization area, 3,372,000 tons of 0.28% Cu, 0.50% Zn, and 0.19 ppm Au content, with a Cu cut off grade 0.1%, were determined (Günay et al., 2019*b*).

5. Discussion

5.1. Petrogenetic Indicators of Volcanic Rocks in the Cünür Mineralization Area

The unstable trace element trends (Figure 9a), normalized to the MORB (mid - ocean ridge basalts) values of the most mafic sub - alkaline basaltic samples found in the Cünür mineralization area, typically indicate subduction - enriched mantle source areas. The tendency of Nb and Ta elements to be

depleted relative to neighboring LIL and LREE (light rare earth elements) elements indicate mantle source areas metasomatized with subduction component. In contrast, the same trend in rocks of the andesitic and dacitic composition suggests that these rocks have underwent evolutionary processes in magma chambers from sub - alkaline basaltic volcanism, associated with processes of fractional crystallization and / or assimilation and crustal contamination (AFC processes).

Th / Yb versus Nb / Yb diagram is used to reveal the source characteristics of metavolcanic rocks (Figure 10). Nb and Th elements can be used as a normalization factor to reflect the changes in the mantle, while the Yb element can be used as a normalization factor to minimize the effects of fractional crystallization, crystal accumulation, and crustal contamination (Pearce et al., 1984). As can be seen in Figure 10, samples are separated from the EMB - OIB mantle area with Th values rising from sub - alkaline basaltic samples to evolved samples. Increased in Th contents typically represent the presence of subduction component for sub - alkaline basaltic volcanism products, while typically indicate the effects of fractional crystallization for evolved samples. On the diagram, rocks of sub - alkaline basaltic composition associated with the Cünür mineralization cluster in the same / close area with the Hanönü Massive Sulfide (HMS) and Zeybek Massive Sulfide (ZMS) mafic sills and dykes samples (Günay et al., 2018, 2019). This data indicates that the sub - alkaline basalts in the Cünür mineralization area are derived from a mantle source enriched by subduction - zone components, such as rocks of HMS and ZMS. It can be said that the felsic metavolcanics associated with the Cünür mineralization were formed as a result of the evolution of sub - alkali basalts derived from an enriched mantle source.

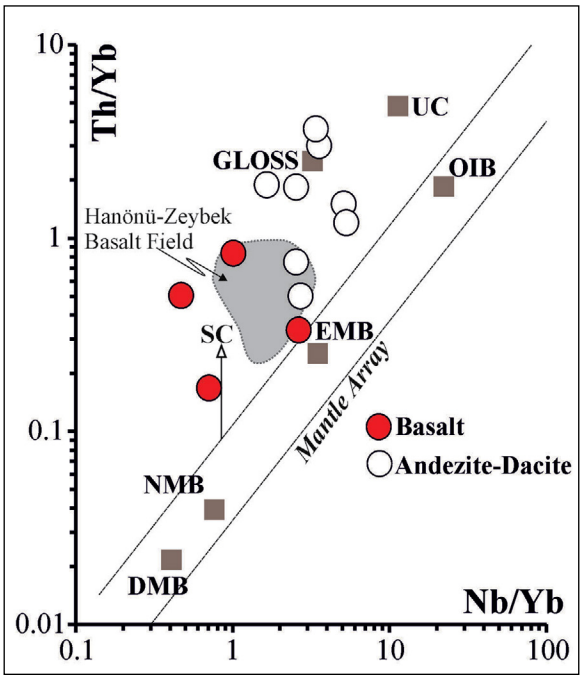

Figure 10- Nb/Yb - Th/Yb binary variation diagram of metavolcanic rocks associated with the Cünür mineralization. NMB (N-type Mid-Ocean Ridge Basalts), EMB (Enriched Mid-Ocean Ridge Basalts), DMM (Depleted Mid-Ocean Ridge Basalts), OIB (Ocean Island Basalts) values were taken from Sun and McDonough (1989), UC-value was taken from Taylor and McLennan (1985). GLOSS values are taken from Plank and Langmuir (1998) and Plank (2014). HMS (Hanonu massive sulfide) and ZMS (Zeybek massive sulfide) data were taken from Günay et al. (2018) and Günay et al. (2019), respectively.

Another approach can be developed over the structural relationships of the Çangaldağ Metamorphic Complex. The members of this metamorphic complex locate with each other in tectonic contact. The members of this complex were formed in two different paleotectonic environments and are present together in accretion. These are mafic volcanics intercalated with deep - sea sediments associated with the Hanönü and Zeybek massive sulfide deposits and an island arc with Jurassic bimodal volcanism products. While the Cünür mineralization takes place within the island arc units associated with bimodal volcanism, this mineralization and mafic volcanics intercalated with deep - sea sediments are found together in tectonic contact. In this context, CMC is an accretionary product in which units formed in two different paleotectonic environments are together.

5.2. Classification of Cünür Mineralization and Status in Other Pontide Belt VMS Formations

Massive sulfide deposits are commonly classified using the Cu - Zn - Pb triangle diagram (Franklin et al., 1981; Franklin et al., 1993; Galley et al., 2007). Relatively higher Cu or Zn content compared to sedimentary exhalative (SEDEX) type mineralizations distinguishes volcanogenic massive sulfide mineralizations from SEDEX type formations. In the Cu - Zn - Pb triangular diagram, Cünür mineralization with high Zn - Cu content is located in the Cu - Zn

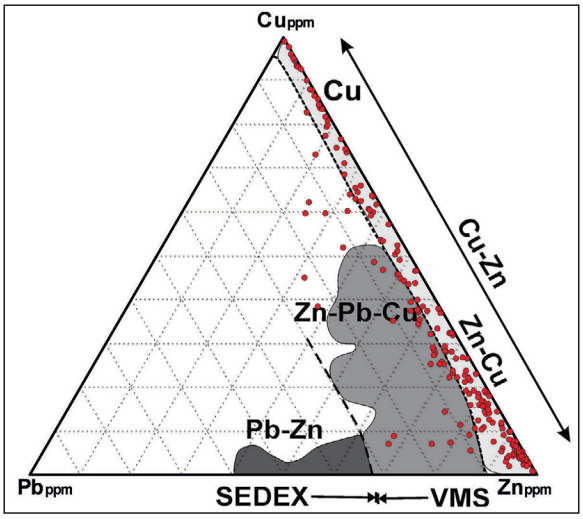

Figure 11- Classification of Volcanogenic Massive Sulfide deposits of the Cünür mineralization according to the Cu-Pb-Zn triangle diagram (Franklin et al., 1981).

group of volcanogenic massive sulfide deposits (Figure 11). SEDEX - type mineralizations with high Pb content are generally found in sedimentary rocks associated with continental rifting. The Cünür mineralization has high Cu - Zn, low Pb content and is a typical VMS formation as the country rocks are the product of bimodal volcanism.

One of the common methods used in the classification of VMS mineralizations is the classification in which paleotectonic environments are taken into consideration. For the Cu - Zn group VMS mineralizations, four different classification criteria have been determined: Noranda type (within mafic - felsic volcanic successions), Mattabi type (similar to Noranda type but with abundant Pb), Cyprus type (within ophiolites), and Besshi type (in sediments in volcanic areas) (Franklin et al., 1981; Franklin, 1993; Lydon, 1984*a, b*). Noranda type VMS mineralizations are located in the lithologies that tholeiitic and calc - alkaline mafic / felsic rocks are dominant. In Noranda type mineralizations, the ore is included in felsic volcanic rocks, while the dominant volcanic rocks in the mineralization area are mafic in character (Franklin, 1993). The Cünür mineralization has characteristics similar to the Noranda type VMS mineralizations with its ore and host rock properties and is different from other VMS formations in the Pontides.

Cu - Pb - Zn content of volcanogenic massive sulfide deposits presents changes according to the relationship of mineralization with the host rock lithologyand the tectonomagmatic settings in which they formed. The VMS deposits are classified into five different groups based on host - rock composition: Mafic, Bimodal - Mafic, Mafic - Siliciclastic, Bimodal - Felsic, Bimodal - Siliciclastic (Barrie and Hannington, 1999). Among these groups, Bimodal - Mafic type VMS mineralizations have host rock lithology that is more than 50% mafic, more than 3% felsic, and a small amount of siliciclastic. In this type of VMS formations, the characteristic of mafic volcanism is tholeiitic. Felsic volcanics are in transition to highly siliceous rhyolites or calc - alkaline rhyolites. Bimodal - mafic type VMS mineralizations are characteristic with high Cu - Zn contents. Considering this new classification based on dominant host rock lithologies for VMS mineralizations, the Cünür mineralization exhibits similar characteristics to bimodal - mafic volcanogenic massive sulfide formations within VMS mineralizations. As in the bimodal - mafic type VMS formations, the host rocks in the Cünür mineralization area are predominantly composed of mafic volcanics. However, the mineralization is within the felsic volcanics and they are accompanied by less silicified volcanoclastic units. It is similar to bimodal - mafic type VMS formations in that the Cünür mineralization has high Cu and Zn content compared to Pb content. However, for volcanogenic massive sulfide mineralizations, this classification criterion alone does not define the tectonomagmatic environment in which mineralization occurs.

The Hanönü and Zeybek VMS mineralizations in CMC (Middle Pontide) were defined as mafic - siliciclastic (Besshi type) type (Günay et al., 2018, 2019*b*). The host - rock lithology of mafic - siliciclastic type VMS mineralizations is mainly composed of mafic volcanic or intrusive rocks and turbiditic silicilastic rocks with lesser or no felsic volcanics. Küre VMS mineralizations exhibiting mafic - siliciclastic type characteristics, have been defined as Cyprus Type VMS formation due to their host rock and paleotectonic setting features (Çakır, 1995; Altun et al., 2015; Akbulut et al., 2016). These VMS deposits known in the Central Pontides have mafic - siliciclastic features and can be defined as Besshi (Hanönü, Zeybek VMS deposits) and Cyprus (Küre VMS deposit) type. Cyprus type mineralizations genetically indicate oceanic rifting, while Besshi type mineralizations indicate continental rifting or divergent sections of

oceanic rifting. The Eastern Pontide VMS deposits are consistent with bimodal - felsic (Kuroko or Eastern Pontide type) type VMS mineralizations according to the relationship of mineralization with the host rock and the tectonomagmatic setting in which they occur (Eyüboğlu et al., 2014; Revan et al., 2014). This type of mineralization has >50% felsic volcanic rocks and <15% siliciclastic rocks, and is defined as VMS mineralizations with widespread barite and the highest Zn and Ag content (Barrie and Hannington, 1999).

Primitive mantle normalized spider diagram of the average metal content of the Central and Eastern Pontide VMS deposits is presented in Figure 12. In this diagram, the metal contents of Bimodal Mafic, Bimodal Felsic, and Mafic Siliciclastic VMS formations are given by normalizing to the primitive mantle (Barrie and Hannington, 1999). The metal contents orientations between the Eastern Pontide VMS deposits and Central Pontide VMS deposits differ significantly. The Eastern Pontide VMS formations are considered between the Bimodal Mafic and Bimodal Felsic VMS formations with their metal contents and high Pb, Zn, Au content is characteristic. The Hanönü and Zeybek VMS mineralizations in the Central Pontides are similar to the Cu metal dominant Mafic - Siliciclastic type VMS mineralizations with metal variations and host rock composition. Although the Küre VMS mineralization exhibits metal variations similar to mafic siliciclastic type VMS formations, it has characteristically high Cu and Au content.

The Cünür VMS mineralization differs from the Central and Eastern Pontide VMS formations in terms of both host rock properties and metal content. Although mafic - intermediate metavolcanic rocks are dominant in the Cünür area, mineralization takes place in felsic metavolcanics, the dominance of Zn metal compared to other mineralizations and the difference of the tectonomagmatic environment in which mineralization host rocks are formed (dominant lithology volcanic rocks with the felsic character) are the most important differences that distinguish the Cünür mineralization from Middle (dominant lithology metaclastic - mafic metavolcanic rocks) and East Pontide VMS (dominant lithology felsic volcanic rocks) mineralizations.

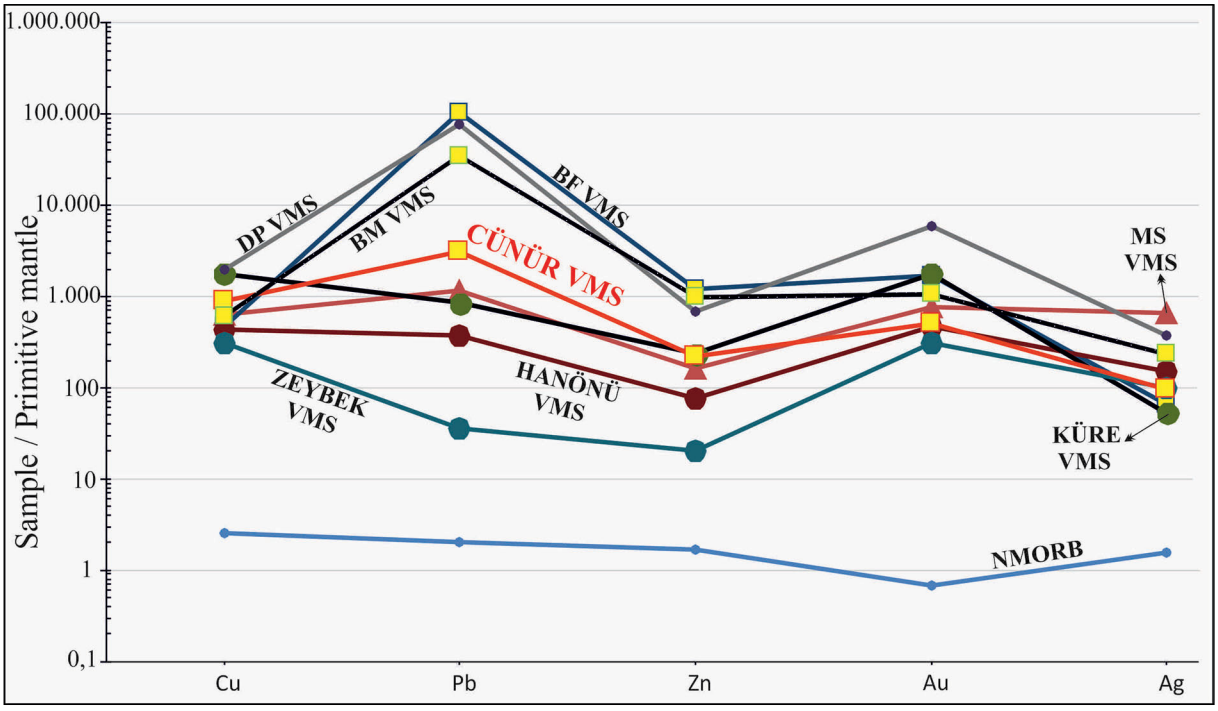

Figure 12- The illustration of metal values of different types of VMS deposits normalized to Primitive mantle in spider diagrams [Primitive mantle values from Wolf and Anders, (1980); Taylor and McLennan, (1985); N-MORB values from Doe, (1994); Keays and Scott, (1976); Hamlyn et al., (1985); Metal contents of Mafic siliciclastic (MS) type VMS beds, Bimodal Mafic (BM) type VMS beds and Bimodal Felsic (BF) type VMS beds from Barrie and Hannington, (1999); Metal contents of the Hanonu and Zeybek VMS deposits from Günay et al. (2018; 2019*b*); the Kure VMS metal contents from Altun et al. (2015); Metal contents of the Eastern Pontide (DP) VMS deposits from Revan et al., 2013)].

The Re / Os data of Küre, Hanönü, and Zeybek Middle Pontide VMS mineralizations indicate that mineralization age is the Middle Jurassic (Küre host rock, 180 Ma, Akbulut et al., 2016; Hanönü - Zeybek ore, 178 My, Günay et al., 2019*a*). The Eastern Pontide VMS formations are younger, and the age data of volcanic units associated with mineralization point to the Late Cretaceous (ore host rock, 91 - 82 Ma, Eyüboğlu et al., 2014). The Cünür mineralization is in the felsic metavolcanics of the Cangaldag Metamorphic Complex. The recent studies for these volcanic rocks indicate the Middle Jurassic age range (metadacite / U - Pb zircon, 169 ± 2My, Okay et al., 2014; metariodacite / U - Pb zircon, 176 ± 2My, 163 ± 9My, Çimen et al., 2018). Although there is no clear syngenetic finding in terms of mineralization host rock relationship, the fact that the mineralization host rock is metavolcanics with felsic character and the mineralization is dominated by Cu - Zn reflects that mineralization developed in relation to the island arc volcanism on the oceanic crust. From this approach, the age of mineralization should be Middle Jurassic, that is the host rock age, or younger.

6. Results

Metavolcanic units in the Cünür mineralization area have compositions ranging from sub - alkaline basalt to andesite and dacite (50.3 - 74.6% SiO_2).

The geochemical characteristics of sub - alkaline basalts in the Cünür mineralization area indicate that these rocks are derived from a mantle source enriched by subduction components. The evolution of sub - alkaline basalts derived from such a source has led to the formation of felsic volcanic rocks associated with the Cünür mineralization.

The Cünür Volcanogenic Massive Sulfide mineralization takes place in the felsic metavolcanic rocks of Çangaldağ Metamorphic Complex.

Geochemical data obtained from 60 core drillings in the Cünür mineralization area revealed the existence of 3,372,000 tons of resources that have 0.28% Cu, 0.50% Zn, and 0.19 ppm Au content with a Cu cut off grade 0.1%.

The highest values obtained for the base and precious metals in dross mineralization are 9% for Cu and Zn, 0.3% for Pb, 3.3 ppm for Au and 79 ppm for Ag, 15 ppm for Co, 143 ppm for Mo, 26 ppm for Ni, 85 ppm for Sb, 45 ppm for V.

The Cünür mineralization is in the Cu - Zn group of volcanogenic massive sulfide deposits, with higher Zn - Cu content compared to Pb content. Considering the ore and host rock properties, the Cünür Cu - Zn mineralization resembles bimodal - mafic type volcanogenic massive sulfide formations.

Paleotectonic environment properties of dominant host rocks and genesis of the Cünür mineralization indicate the Noranda type VMS occurrence within the Cu - Zn group VMS formations. The Cünür mineralization is different from other VMS formations in the Central and Eastern Pontides with its genetic features.

Acknowledgement

This study was carried out within the scope of the "Kastamonu Province and Surrounding Polimetal Mine Searches" project numbered 2011/202032-13-05-01, under the General Directorate of Mineral Research and Exploration, Mineral Research and Exploration Department. I would like to thank Mr. Cahit Dönmez, Head of Mineral Research and Exploration Department, whose confidence I feel in the execution and management of the project at every stage. I would like to thank Assoc. Dr. Vural Oyan, project advisor, for his scientific contributions at every stage of the project.

I would like to thank Prof Dr. Halim Mutlu, who contributed to the development of this article with his criticism and editing, Technical Editor Oğuz Altun and Associate Editor Dr. Hafize Akıllı.

"I would like to thank Geology Engineer Cüneyt Baran, Geology Engineer Kenan Coşkun, Geology Engineer Buğra Çavdar, Dr. Serdar Keskin, Geology Engineer Şenol Şahin and Geology Engineer Aysun Sözcü, who has made great efforts and contributions in the field studies, and Geology Engineer Yusuf Mehmet Erdem who made the reserve calculations. *There is a great team behind all the work carried out in MTA. Thank you wholeheartedly to this great team, whose name is too many to write*".

References

Abdioğlu, E., Arslan, M. 2009. Alteration mineralogy and geochemistry of the hydrothermaly altered rocks of the Kutlular (Sürmene) massive sulfide deposit, NE Turkey. Turkish Journal of Earth Sciences 18, 139-162.

Akbulut, M., Oyman, T., Çiçek, M., Selby, D., Özgenç, İ., Tokçaer, M. 2016. Petrography, mineral chemistry, fluid inclusion microthermometry and Re - Os geochronology of the Küre volcanogenic massive sulfide deposit (Central Pontides, Northern Turkey). Ore Geology Reviews 76, 1-18.

Akıncı, Ö. T. 1985. The Eastern Pontide Volcano-Sedimentary Belt and associated massive sulphide deposits. *In*: Dixon, J.E. and Robertson, A.H.F. (eds), *The Geological Evolution of the Eastern Mediterranean*. Geological Society Publication 17. Blackwell, Oxford, 415-427.

Altun, Y., Yılmaz, H., Şiner, İ., Yazar, F. 2015. The secrets of massive sulfide deposits on mid-ocean ridge and Küre-Mağaradoruk copper deposit. Bulletin of the Mineral Research and Exploration 150, 51-65.

Aygül, M., Okay, A. I., Oberhänslı, R., Ziemann, M. A. 2015. Thermal structure of low- grade accreted Lower Cretaceous distal turbidites, the Central Pontides, Turkey: in- sights for tectonic thickening of an accretionary wedge. Turkish Journal of Earth Sciences 24, 461-474.

Barrie, C. T., Hannington, M. D. 1999. Classification of volcanic-associated massive sulfide deposits based on host - rock composition. In: Barrie, C. T. and Hannington, M. D. (Ed.), Volcanic - associated Massive Sulfide Deposits: Processes and Examples in Modern and Ancient Settings. Rewievs in Economic Geology 8, 1-10.

Çağatay, M. N. 1993. Hydrothermal alteration associated with volcanogenic massive sulfide deposits: examples from Turkey. Economic Geology 85, 606-621.

Çağatay, M. N., Boyle, D. R. 1977. Geochemical prospecting for volcanogenic sulphide deposits in the Eastern Black Sea Ore Province, Turkey. Journal of Geochemical Exploration 8, 49-71.

Çakır, Ü. 1995. Geological characteristics of the Aşıköy - Toykondu (Küre - Kastamonu) massive sulfide deposits. Bulletin of the Mineral Research and Exploration 117, 29-40.

Çiftçi, E. 2019. Volcanogenic Massive Sulfide (VMS) Deposits of Turkey. Pirajno, F., Ünlü, T., Dönmez C., Şahin, B. Mineral Resources of Turkey. Ed., Springer, 427-495.

Çiftçi, E., Hagni, R. D. 2005. Mineralogy of the Lahanos deposit a Kuroko - type volcano - genic massive sulfide deposit from the eastern Pontides (Giresun, NE Turkey). Türkiye Jeoloji Bülteni 48(1), 55-64.

Çimen, O., Göncüoğlu, M. C., Sayit, K. 2016. Geochemistry of the metavolcanic rocks from the Çangaldağ Complex in the Central Pontides: implications for the Middle Jurassic arc - back - arc system in the Neotethyan Intra - Pontide Ocean. Turkish Journal of Earth Sciences 25, 491-512.

Çimen, O., Göncüoğlu, M. C., Simonetti, A., Sayit, K. 2017. Whole rock geochemistry, zircon U - Pb and Hf isotope systematics of the Çangaldağ pluton: evidences for middle Jurassic continental arc magmatism in the Central Pontides, Turkey. Lithos 288-289C, 35-54.

Çimen, O., Göncüoğlu, M. C., Simonetti, A., Sayit, K. 2018. New zircon U - Pb LA - ICP - MS ages and Hf isotope data from the Central Pontides (Turkey): geological and geo - dynamic constraints. The Journal of Geodynamics 116, 23-36.

Doe, B. R. 1994. Zinc, copper, and lead in mid - ocean ridge basalts and the source rock control on Zn / Pb in ocean - ridge hydrothermal deposits. Geochimica et Cosmochimica Acta 58, 2215-2223.

Dönmez, C., Keskin, S., Günay, K., Çolakoğlu, A. O., Çiftci, Y., Uysal, I., Türkel, A., Yıldırım, N. 2014. Chromite and PGE geochemistry of the Elekdag ophiolite (Kastamonu, northern Turkey): implications for deep magmatic processes in a supra - subduction zone setting. Ore Geology Reviews 57, 216-228.

Eyüboğlu, Y., Santosh, M., Keewook, Yi, Tuysuz, N., Korkmaz, S., Akaryalı, E., Dudas, F. O., Bektaş, O. 2014. The Eastern Black Sea - type Volcanogenic Massive Sulfide Deposits: Geochemistry, zircon U - Pb geochronology and an overview of the geody - namics of ore genesis. Ore Geology Reviews 59, 29-54.

Franklin, J. M. 1993. Volcanic - associated massive sulphide deposits, Kirkham, R. V., Sinclair, W. D., Thorpe, R. I., and Duke, J. M., (Ed.), Mineral deposit modeling, Geological Association of Canada Special Paper 40, 315-34.

Franklin, J. M., Lydon, J. W., Sangster, D. F. 1981. Volcanic - associated massive sulfide deposits. Economic Geology, 75th Anniversary vol., 485-627.

Galley, A. G., Hannington, M. D., Jonasson, I. R. 2007. Volcanogenic Massive Sulphide Deposits. Geological Association of Canada, Mineral Deposits Division, 141-161 Special Publication no. 5.

Göncüoğlu, M. C. 2010. Introduction to the Geology of Turkey: Geodynamic evolution of the pre -

alpine and alpine terranes. General Directorate of Mineral Research and Exploration Monography Series. 5-69.

Gücer, M. A., Arslan, M., Sherlock, S., Heaman, L. M. 2016. Permo - Carboniferous grani - toids with Jurassic high temperature metamorphism in Central Pontides, Northern Turkey. Mineralogy and Petrology 110, 943-964.

Günay, K., Dönmez, C., Oyan, V., Yıldırım, N., Çiftçi, E., Yıldız, H., Özkümüş, S. 2018. Geology and geochemistry of sediment - hosted hanönü massive sulfide deposit (Kastamonu - Turkey). Ore Geology Reviews 101, 652-674.

Günay, K., Dönmez, C., Oyan, V., Baran, C., Çiftçi, E., Parlak O., Yıldırım, N., Denge, H.X., Lif, C.,Yıldırım, E., Özkümüş, S. 2019*a*. Geology, geochemistry and Re - Os geochronology of the Jurassic Zeybek volcanogenic massive sulfide deposit (Central Pontides, Turkey). Ore Geology Reviews 111, 102994.

Günay, K., Dönmez, C., Baran, C., Coşkun, K., Akgöz, A., Erdem, Y.M. 2019*b*. Cünür - Sökü (Kastamonu - Devrekâni) Cu - Au - Zn (AR: 201500078 / ER: 3327597) Buluculuk Talebine Esas Maden Jeolojisi ve Kaynak Tahmin Raporu. Maden Tetkik ve Arama Genel Müdürlüğü, Maden Etüt ve Arama Dairesi Başkanlığı, Rapor Arşiv No: 45892, 1-1789, Ankara (unpublished).

Hamlyn, P. R., Keays, R. R., Cameron, W. E., Crawford, A. J., Waldron, H. M. 1985. Precious metals in magnesian low - Ti lavas: implications for metallogenesis and sülfid saturation in primary magmas. Geochimica et Cosmochimica Acta 49, 1797-1811.

Keays, R. R., Scott, R. B. 1976. Precious metals in ocean - ridge basalts; implications for basalts as source rocks for gold mineralization. Economic Geology 71, 705-720.

Konya, S. 1988. Kastamonu Alt Bölgesi (Cu - Pb - Zn) Arama Projesi, Jeokimya Çalışmaları. Maden Tetkik ve Arama Genel Müdürlüğü, Arşiv No:41663 / 11.

Köprübaşı, N., Çiftci, E., Cordan, S., Köprübaşı, N., Özkul, C., Tükel, F. Ş. 2014. Comparative geo - chemical study of soils developed on characteristic black and yellow polymetallic massive sulfide deposits in Eastern Pontides (NE Turkey). Turkish Journal of Earth Sciences 23(2), 129-146.

Lydon, J. W. 1984*a*. Volcanogenic massive sulphide deposits. Part 1. Descriptive model. Geoscience Canada 11, 195-202.

Lydon, J. W. 1984*b*. Some observations on the morphology and ore texture of volcanogenic sulphide deposits of Cyprus. Current Research. Part A.Geological Survey of Canada, vol. 84-1A, 601-610.

Okay, A. I. 2008. Geology of Turkey: A Synopsis. Anschnitt, 21, 19-42.

Okay, A. I., Tüysüz, O. 1999. Tethyan sutures of northern Turkey. In: Durand, B., Jolivet, L., Horvath, F., Seranne, M. (Eds.), The Mediterranean Basins: Tertiary Extension within the Alpine Orogen. Geological Society, London, Special Publication 156, 475-515.

Okay, A. I., Gürsel, S., Sherlock, S., Altıner, D., Tüysüz, O., Kylander - Clark, A. R. C., Aygül, M. 2013. Early Creataceous sedimentation and orogeny on the active margin of Eurasia: Southern Central Pontides, Turkey. Tectonics 32, 1247-1271.

Okay, A. I., Gürsel, S., Tüysüz, O., Sherlock, S., Keskin, M., Kylander - Clark, A. R. C. 2014. Low - pressure - high - temperature metamorphism during extension in a Jurassic magmatic arc, Central Pontides, Turkey. Journal of Metamorphic Geology 32, 49-69.

Pearce, J. A., Harris, N. B. W., Tindle, A. G. W. 1984. Trace element discrimination diagrams for the tectonic interpretation of granitic rocks. Journal of Petrology 25, 956-983.

Piercey, S. J. 2011. The setting, style, and role of magmatism in the formation of volca - nogenic massive sulfide deposits. Mineralium Deposita 46, 449-471.

Plank, T. 2014. The Chemical Composition of Subducting Sediments. Keeling, Ralph, F., Treatise on Geochemistry. Ed., Elsevier, Amsterdam, 607-629.

Plank, T., Langmuir, C. H. 1998. The chemical composition of subducting sediment and its consequences for the crust and mantle. Chemical Geology 145, 325-394.

Revan, M. K., Genç, Y., Maslennikov, V. V., Ünlü, T., Delibaş, O., Hamzacebi, S. 2013. Original findings on the ore - bearing facies of volcanogenic massive sulphide deposits in the eastern Black Sea region (NE Turkey). Bulletin of the Mineral Research and Exploration 147, 73-89.

Revan, M. K., Genç, Y., Maslennikov, V.V., Maslennikova, S.P., Large, R.R., Danyushevsky, L.V. 2014. Mineralogy and trace - element geochemistry of sulfide minerals in hydrothermal chimneys from the Upper - Cretaceous VMS deposits of the Eastern Pontide orogenic belt (NE Turkey). Ore Geology Reviews 63, 129-149.

Sun, S. S., McDonough, W. F. 1989. Chemical and isotopic systematics of oceanic basalts: implications for mantle composition and processes. Saunders, A.D., Norry, M.J., Magmatism in the Ocean Basins Ed., Geological Society of London, Special Publication 42, 45-313.

Taylor, S. R., McLennan, S. M. 1985. The continental crust: its composition and evolution, Geoscience Texts. Blackwell Scientific Publications, London. 312p.

Tekin, U. K., Göncüoğlu, M.C., Pandolfi, L., Marroni, M. 2012. Middle Late Triassic radiolarian cherts from the Arkotdağ melange in northern Turkey: implications for the life span of the northern Neotethyan branch. Geodinamica Acta 25, 305-319.

Uğuz, M. F., Sevin, M., Duru, M. 2002. 1:500.000 ölçekli Türkiye Jeoloji Haritaları Sinop Paftası: Maden Tetkik ve Arama Genel Müdürlüğü, Ankara.

Ustaömer, T., Robertson, A. H. F. 1999. Geochemical evidence used to test alternative plate tectonic models for pre - Upper Jurassic (Palaeotethyan) units in the Central Pontides. Geological Journal 34, 25-53.

Winchester, J. A., Floyd, P. A. 1977. Geochemical discrimination of different magma series and their differentiation products using immobile elements: Chemical Geology, 20, 325-343.

Wolf, R., Anders, E. 1980. Moon and Earth: compositional differences inferred from siderophiles, volatiles, and alkalis in basalts. Geochimica et Cosmochimica Acta 44, 2111-2124.

Wood, D. A. 1980. The application of a Th - Hf / Ta diagram to problems of tectonomagmatic classification and to establishing the nature of crustal contamination of basaltic lavas of the British Tertiary volcanic province. Earth and Planetary Science Letters 50, 11-30.

Yıldırım, N., Dönmez, C., Kang, J., Lee, İ., Pirajno, F., Yıldırım, E., Günay, K., Seo, J.H., Farguhar, J., Chang, S.W. 2012*a*. A magnetite - rich Cyprus - type VMS deposit in Ortaklar: A unique VMS style in the Tethyan metallogenic belt, Gaziantep, Turkey. Ore Geology Reviews 79, 425-442.

Yıldırım, N., İlhan, S., Yıldırım, E., Dönmez, C. 2012*b*. The geology, geochemistry and genetical features of the Ormanbaşı Hill (Sincik, Adıyaman) copper mineralization. Bulletin of the Mineral Research and Exploration 144, 75-104.

Yiğit, Ö. 2009. Mineral Deposits of Turkey in Relation to Tethyan Metallogeny: Implications for Future Mineral Exploration. Economic Geology 104(1), 19-51.

Bulletin of the Mineral Research and Exploration

http://bulletin.mta.gov.tr

The effect of structural properties of Ankara clay on the electrokinetic properties

Güzide KALYONCU ERGÜLER[a]

[a]*General Directorate of Mineral Research and Exploration, Dept. of Environmental Researches, 06530 Çankaya, Ankara, Turkey*

Research Article

Keywords:
Ankara clay, Electrokinetic, SEM, EDS, Zeta potential.

ABSTRACT

The aim of this study is to investigate the effect of structural properties of soil known as Ankara clay, which contains different properties, on its electrokinetic behavior. For this purpose, the 8 disturbed samples from Ankara clay were collected from the different locations of Yüzüncüyıl and Karakusunlar areas, which were observed to contain no excess gravel and carbonate concretions. The electrokinetic behavior of these collected samples were evaluated by using the results of plastic limit, liquid limit, methylene blue, swelling, XRD, XRF, SEM, EDS and BET measurements and analyses as well as zeta potential tests. By these experimental studies, it has been determined that Ankara clay exhibits electrokinetic behavior in line with the whole rock composition since it contains different clay minerals. The monovalent and divalent electrolytes such as NaCl and $CaCl_2$, respectively, increase the zeta potential of Ankara clay negatively. However, in the analyses, it was determined that $FeCl_3$ trivalent electrolyte is the electrolytes determining the zeta potential, tend to convert zeta potential of clays from negative to positive depending on the concentration, and this could be the case with increased concentration.

Received Date: 04.05.2020
Accepted Date: 17.07.2020

1. Introduction

Natural clay minerals are formed by the degradation of the primary minerals forming the rocks by long being exposed to atmospheric conditions and/or alteration by the effect of hydrothermal solutions. When these processes are considered, it is clearly seen that parameters such as the type of primary mineral (bedrock ion content), temperature and pH are very important in the formation behavior of clay minerals. Unlike gravel, sand and silt size soils that are deposited by the effect of gravity, the electrokinetic properties of these minerals come to the fore due to the effect of electrical forces in the formation behavior of clays in the phyllosilicate group. As mentioned in the study of Önalp (2013), the determination of these electrokinetic characteristics of clays is very important in mining applications and projects due to this formation model. The basic structural units in clay minerals are "tetrahedric layer" and "octahedric layer", and the bonding of these basic structural units to each other by forming different layer structures causes the formation of different clay minerals (eg kaolinite, illite, montmorillonite) and therefore exhibit different physico-mechanical behaviors. Therefore, the clays are under the influence of chemical bonding (eg, Van der Waals) forces that form on their surfaces and generate their electrokinetic properties. The crystalline O and OH ions in kaolin mineral of 1: 1 layer type are bonded to each other by H bond and have a low ion-exchange capacity and therefore a low layer charge (x-0). The basic structural units in clay minerals are "tetrahedric layer" and "octahedric layer", and the bonding of these basic structural units

Citation Info: Ergüler Kalyoncu, G. 2021. The effect of structural features of Ankara clay on it's electrokinetic properties. Bulletin of the Mineral Research and Exploration 165, 97-111. https://doi.org/10.19111/bulletinofmre.770990

**Corresponding author: Güzide KALYONCU ERGÜLER, guzidek.erguler@mta.gov.tr*

to each other by forming different layer structures causes the formation of different clay minerals (eg kaolinite, illite, montmorillonite) and therefore exhibit different physico - mechanical behaviors. Therefore, the clays are under the influence of chemical bonding (eg, Van der Waals) forces that form on their surfaces and generate their electrokinetic properties. The crystalline O and OH ions in kaolin mineral of 1: 1 layer type are bonded to each other by H bond and have a low ion - exchange capacity and therefore a low layer charge (x~0). On the other hand, the adjacent interlayer bond in the smectite mineral that has 2: 1 layer structure is the weak Van der Waals bond and has high ion exchange capacity and therefore has a high layer load (x - 0.6) (Moore and Reynolds, 1997).

Angle and Hamza (1989) examined the zeta potentials of the clay mixtures they had prepared in ratios of 70% kaolin and 30% smectite, and stated that H+ and OH- ions had dominant roles in the zeta potential value. Zhao et al. (1989) studied the adsorption velocity and the capacity of polyethylene glycol polymer in different molecular weight of montmorillonite type clays. These researchers determined that the adsorption capacity of clays containing different exchangeable cations was different. Ross et al. (1998) stated in their study by adding sodium electrolyte on montmorillonite clay minerals that thixotropy changes with the electrolyte concentration depending on the surface charges. Benna et al. (1999) investigated rheological and electrokinetic measurements together using three different montmorillonite samples. Besides, the issue of interaction of clay with polymers, surfactants and salts has been extensively studied (Chang et al., 1992; Ece et al., 1999; Alemdar et al., 2000; Pal and Vanjara, 2001; Bergaya and Lagaly, 2001; Güngör et al., 2001; Yalçın et al., 2002; Janek and Lagaly, 2003).

In the evaluation of zeta potentials and electrokinetic behavior of clays until today, certain clay types or samples that are mixed in certain proportions have been used. It was detected that studies consisting of natural clayey soils where swelling and non - swelling clay minerals (smectite and kaolin) coexist in different proportions were found to be quite limited. Therefore, it was needed to investigate its electrokinetic properties, since it contained clay minerals with different crystal structures, which present a complex structure. In order to solve this limitation, the reddish brown, brown clayey units, which contain pebbles in places and lime concretions in their upper parts defined as the "Ankara clay" by Birand (1978) were used. In addition, due to engineering problems such as swelling and settlement observed in the center of Ankara city (Çetinkaya, 1978; Furtun, 1989; Çokça, 1991; Ergüler, 2001; Ergüler and Ulusay, 2003; Avşar, 2003; Avşar et al., 2005; Özgüven, 2014), it was determined that the zeta potential and electrokinetic behavior of the Ankara clay used was not investigated in many studies. Ankara clay causes serious foundation problems with shrinkage in engineering structures as a result of swelling or loss of water depending on the changing water content. Since the behavior of the mineral group constituting Ankara clay is so different that they are called opposite to each other, it is very important to determine the mineral types and thus to reveal the index properties of clayey soils in sense of understanding their mechanical behaviors. On the other hand, it can find wide usage areas such as adsorbents and viscosity because of these properties. Due to its high surface area, especially the activated filtration is also used in paint and paper industry as it shows swelling in water (Akın and Çelik, 1995). Although there have carried out many studies on the mineralogical properties of Ankara clay (Aras et al., 1991; Koçyiğit and Türkmenoğlu, 1991; Met et al., 2005; Sezer et al., 2003), the determination of the physico - chemical properties and Atterberg properties of this clay will contribute to the prevention of damages that may occur during the planning and design phase and afterwards presenting a foresight about the behavior of clay is thought that engineering studies.

Considering the limitations and requirements presented above in summary, the zeta potential and electrokinetic properties of Ankara clay with different physico - mechanical behavior such as kaolinite, illite and smectite (Met et al., 2005) were investigated. For this purpose, the field and sampling studies were carried out in Yüzüncüyıl and Karakusunlar regions. For the determination of parameters such as physical, chemical and mineralogical properties of the samples taken, the Atterberg limits, porosity, methylene blue, swelling, XRD, SEM, Brunauer, Emmett and Teller (BET) gas adsorption method and zeta potential experiments were performed to determine the electrokinetic behavior. The results obtained in these experimental studies were analyzed and interpreted within the scope of this study.

2. Introduction and Geology of the Study Area

The settlement area of Ankara City is located between the North Anatolian Region, which has a rugged mountainous and forested morphological structure, and the arid Konya Plain. Considering the purpose of the study, Yüzüncüyıl and Karakusunlar regions were selected as the study area. This region, which generally has a slightly sloping topography, varies between 848 and 1000 m above sea level. A continental climate prevails in Ankara and its surroundings, similar to the Central Anatolia Region and the rainfalls are intensively observed in winter, spring and autumn. The dry months, which significantly affect the behavior of Ankara clay in the region, are known as June - July - August - September.

As emphasized in previous studies (Chaput, 1931; Erol, 1976; Kasapoğlu, 1980), Lower Paleozoic epimetamorphic schists form the bedrock of geological units outcropping in Ankara and its surroundings. These basic metamorphic units are overlain by the geological units such as greenish - brown and schist interbedded greywackes and metagreywackes which unconformably contain Permo - Carboniferous and Triassic limestone blocks. Liassic red basal conglomerate containing pebbles with granitic mineralogical composition, sandstone, siltstone and fossil calcarenites, and Dogger, Malm and Lower Cretaceous, yellowish - white, ammonitic limestones, siliceous - sandy - clayey limestones, platy and nodular limestones in the upper layers overly these mixed series (Chaput, 1931; Kasapoğlu, 1980; Ergüler, 2001). These units are the overlain by the ophiolitic melange (serpentinite, radiolarite, spilite, basalt, diabase, limestone, sandstone, mudstone, marl, flint and gabbro). The ophiolitic melange is then overlain by a Lower - Upper Cretaceous flysch series containing conglomerate, sandstone, siltstone, marl and olistostromes (Chaput, 1931; Kasapoğlu, 1980; Ergüler, 2001). In the study area, there are conglomerates, sandstone, siltstone, red - green marl and limestones in the Paleocene period, fossilliferous sandy limestones in the Eocene period and sedimentary units formed in lagoon and evaporitic environments in the Oligocene period. As mentioned in previous studies, the rocks such as Miocene siliceous - clayey lacustrine limestones, marls, claystones, conglomerates, andesites, basalts, agglomerates and tuffs are found overly Oligocene units (Chaput, 1931; Kasapoğlu, 1980; Ergüler, 2001). Miocene units are overlain by Upper Pliocene units defined as fluvial and lake deposits (Chaput, 1931; Kasapoğlu, 1980). These Upper Pliocene units with an average thickness of 200 meters in the middle of the basin are composed of pebbly, sandy, silty and clayey levels (Erol, 1976). The typical brown - red clayey formations found in the upper parts of these units, occasionally containing gravel and lime concretions, were named as "Ankara clay" by Birand (1978). Aras (1991), emphasized that these reddish - brown sediments were formed in an alluvial fan environment by making detailed sedimentological evaluation and analysis of these Upper Pliocene sediments. In addition, the same researcher stated that the Ankara clay was formed as a result of the degradation of rocks such as andesite, schist and graywacke in the origin - bedrock study.

3. Material and Method

For the purpose of this study, the Yüzüncüyıl and Karakusunlar regions, where fluvial clayey deposits known as the Ankara clay are heavily exposed, were selected as the study area, and the disturbed samples were taken to be used in pre - planned laboratory experiments in 8 different locations, taking into account the construction excavations and road cuts (Figure 1). A typical cross section in locations where sampling is carried out is presented in Figure 2, and detailed information about the experiments performed on collected samples is explained below.

The particle size of sediments forming clayey units provides preliminary information about the content of possible clay minerals. Considering the effect of the clay particle size ratio on the physicochemical and physicochemical behavior of these units, the particle size distribution graphics of samples were determined by the analyses performed using the method proposed by ASTM (1994) consisting of three different stages such as dry coarse sieve, hydrometer and dry fine sieve. Atterberg limits are frequently used to evaluate the swelling behavior of clayey units and determine the swelling parameters by empirical approaches. Considering the importance of Atterberg limits in determining the behavior of clayey units, the Atterberg limits of the samples collected were similarly determined by considering the standards recommended by ASTM (1994).

The methylene blue test is based on the replacement of methylene blue cations with exchangeable cations

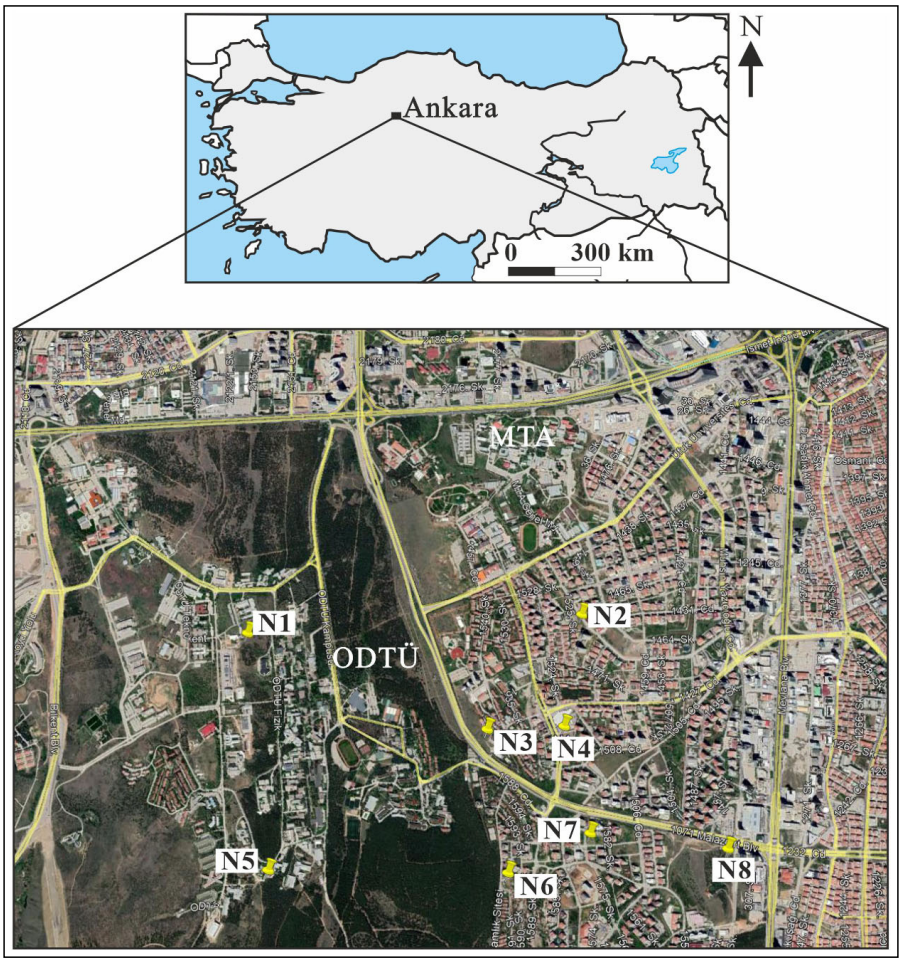

Figure 1- Study area and locations where Ankara clay samples were taken.

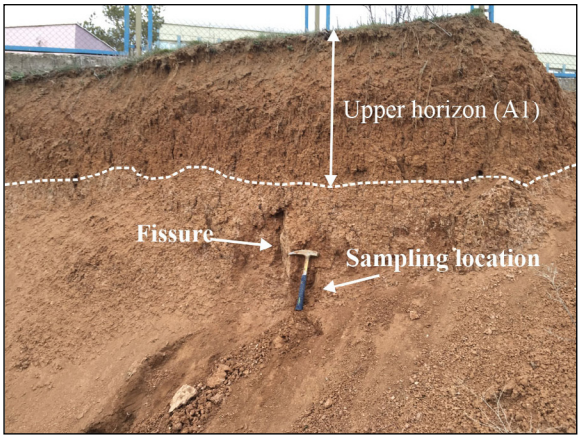

Figure 2- The outcrop where the sampling is made in which the studied clay as a result of the construction foundation excavations is typically observed and sections where plant roots are not present (sample N1; latitude 39.897020° and longitude 32.778787°; look direction NE).

of the clay. Methylene blue is adsorbed as much as the amount of exchangeable cations of the clays during the experimental application phase. After the saturation is reached, the added methylene blue ions are released in the dispersion. Based on the concentration in which methylene blue ions are released, the amount of methylene blue adsorbed by the clay mineral is determined and the cation exchange capacity (CEC) is calculated from the amount of charge they carry. In this study, methylene blue experiments of the samples were carried out in accordance with ASTM C837 (2019) standards.

Many experimental methods have been proposed to determine the swelling parameters of clays. In order to determine the swelling properties of samples collected within the scope of this study, TS 10252 (1992) which is very practical approach was preferred. The samples, which were taken in this swelling behavior determination approach, were powdered until they

reached the size of a particle under 100 microns, then, were poured into the measuring cylinder with a capacity of 100 ml without causing sample loss by taking 2 g from these samples . This prepared water - sample mixture was then left to sedimentation for 24 hours and the resulting volumetric change was determined and recorded.

The BET approach is one of the most used methods in clay definition and classification, as the surface area values vary according to clay types. The BET analysis was used to determine the parameters of surface area, pore volume and pore radius of the collected samples. For this purpose, the surface area and pore size analyzer (Nova 2200e Quantachrome Instruments) was used. For these experiments, 0.2 - 0.5 g of sample was prepared and placed in the chamber of the device. The cell was weighed and placed in the nitrogen container section by filling the liquid nitrogen container with gas to the previously determined level. The desired analysis was drawn considering the pressure sensors, pH, relative pressure graph, adsorption and desorption parameters. During the experiment, the adsorbent pressure in the equilibrium approaches the saturation and the pores are completely filled with the adsorbent. The total pore volume was determined by calculating the adsorbent density with filled pores in the sample.

X - ray diffraction analyses (XRD) were performed in two separate stages, as whole rock (WR) and clay fraction (≤2 μm particle size). For whole rock analyses, the directly powdered Ankara clay samples were used. For clay fraction analyses, a certain amount of powder was put into sample beakers, and then samples were filled with distilled water and mixed in micronized mixers until a homogeneous mixture was obtained. Considering the Stokes' law, the components remaining in suspension were soaked with a pipette and poured on three different glasses. After each glass was dried at room temperature, one sample was made ready for normal shooting, the other one was made ready for retarded shooting kept in ethylene glycol for 2 hours and the remaining sample was made ready for shooting by being kept in an oven at 550° C for 2 hours. The clay fraction shots were carried out in 4 - 30° shooting range. In order to determine the content of exchanging cations (for example, Na^{+}, K^{+}, Ca^{++} and Mg^{++}) in selected samples, the major element analyses of the samples were carried out using the Panalytical Axios XRF Spectrometer device with a relative error margin of ± 3 with 98% accuracy in MTA laboratories. The samples taken for XRF analysis were placed in meter cups and dried in an oven at 105° C for 3 hours. Then, the samples taken from the oven were transferred to the desiccator to cool down and their masses were recorded by weighing after being kept at room temperature for one hour. 3 g of this dry sample was taken and the mixture was prepared by adding 0.9 g of cellulose. In addition to XRD and XRF analyzes of the samples taken from the study area, the scanning electron microscopy (SEM) - EDS analyzes were carried out to take close - up images of the clayey parts, make morphological evaluations and reveal the chemical composition of certain points.

All samples were subjected to size reduction and nano size distribution was obtained before the zeta potential determination. The particle size distributions of the powdered samples were determined by laser. For electrokinetic measurements of clay samples collected within the scope of this study, the pH adjustment was made with NaOH and HCl by taking 1 ml of stock solution. Only the pure water was used in the preparation of samples. The zeta potentials were calculated by measuring movement velocities of the clay particles in the prepared samples at different pH values. In Zeta potential measurements, the Malvern Zetasizer Nano Z device, which can automatically calculate the zeta potential value and considers the voltage and particle velocity, was used. In measurements, approximately 20 readings were taken for each sample whose pH value was adjusted to vary between 3 - 11, and the mean and standard deviation of zeta potential values determined by the device were recorded.

4. Discussion

The engineering problems such as the need for clay raw materials due to the increasing need in ceramic and food industries in our country and the environmental pollution after mining activities clearly reveal the importance of using clay minerals. Today, the electrochemical treatment approach of clay and similar natural materials is widely and effectively used in the treatment of heavy metal pollution of natural resources such as soil contamination after mining activities. In this study, which was carried out by considering the importance of clay minerals today and covering the electrochemical properties of clay, Ankara clay was directly preferred instead of

using kaolin and bentonite or a mixture of these clays prepared in certain proportions like in previous studies. The results obtained from the experiments performed within scope of this study and the evaluations made regarding these results are presented below.

4.1. Physicochemical and Physicomechanical Properties of Ankara Clay

The method proposed by ASTM (1994) to form the particle size distribution curves of unconsolidated soil materials and the results of experiments consisting of three different stages used was combined and presented in Figure 3. Using the graphics given in Figure 3, the clay particle size ratio values of the samples were calculated and presented in Table 1. As can be clearly seen in Figure 3 and Table 1, the clay particle size ratio of these samples is high, varying between 28% and 58% with an average value of about 44%. The results obtained in the Atterberg limit tests are also presented in Table 1. As seen in Table 1, it is seen that a significant portion of the samples taken from Ankara clay are above 50% of the liquid limit values and therefore these clayey units are rich in swelling clay mineral types.

The parameters such as physical properties, surface areas and cation exchange capacity of clayey units, which are generally rich in clay minerals, are controlled by the clay mineralogical composition (Fityus et al., 2000). The methylene blue test is widely used in calculating the amount of exchangeable cations of reactive clays (Çokça and Birand, 1993*a*). Methylene blue dye ($C_{16}H_{18}N_3SCl$) is a large polar organic molecule that adsorbs on the negatively charged surfaces of clay minerals and has a high solubility in water (Yitik, 2006). The CEC values obtained from the methylene blue tests carried out

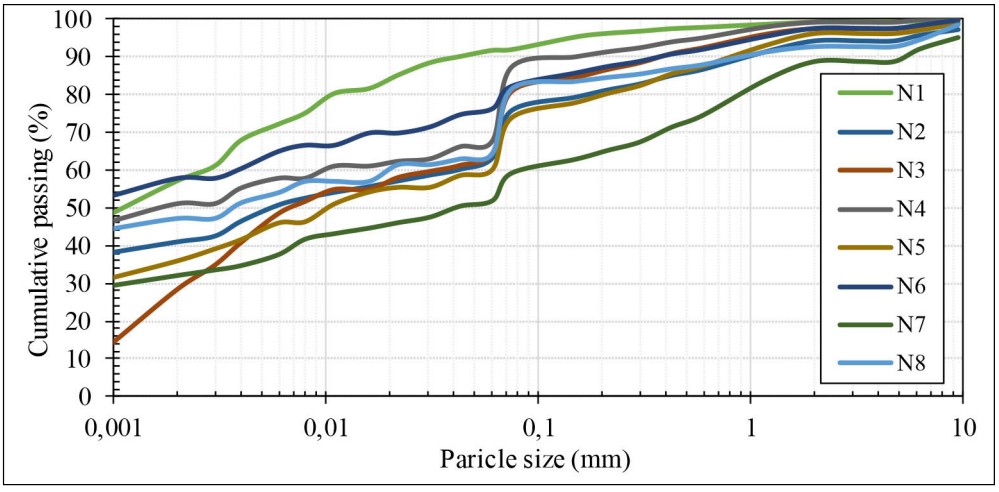

Figure 3- Particle size distribution graphics of the samples.

Table 1- Clay fraction, plastic limit, liquid limit, cation exchange capacity, swelling volume and gelation coefficient values of the samples.

Sample No.	Sample Coordinates		Clay (%)	PL (%)	LL (%)	CEC (meq/100 g)	Swelling Vol. (ml)	Gelation Coeff.
	Lat.	Long.						
N1	39.897020°	32.778787°	57	56	87	4	6	≥8.3
N2	39.897934°	32.800484°	41	31	59	25	2	≥8.3
N3	39.892238°	32.794312°	28	25	50	21	2	≥8.3
N4	39.892390°	32.799248°	51	25	41	48	12	≥8.3
N5	39.885446°	32.780462°	36	38	52	35	10	≥8.3
N6	39.885338°	32.795573°	58	45	72	48	10	≥8.3
N7	39.887212°	32.800795°	32	28	48	24	4	≥8.3
N8	39.886515°	32.809324°	47	23	65	33	8	≥8.3

PL: plastic limit, LL: liquid limit, CEC: cation exchange capacity.

in accordance with ASTM C837 (2019) standards are given in Table 1. As seen in Table 1, the cation exchange capacity values of the samples vary between 4 meq / 100g and 48 meq / 100g with an average value of approximately 30 meq / 100g. These results are consistent with the results obtained from the methylene blue experiments previously performed on Ankara clay (Çokça and Birand, 1993*b*; Ergüler, 2001; Sezer et al., 2003; Met et al., 2005). The CEC values, swelling, plasticity and etc. are important indicators in terms of physical properties. Therefore, the higher these values, the higher the swelling and gelation behavior of the relevant clay sample.

The swelling volume values obtained using the TS 10252 (1992) approach are presented in Table 1. As can be seen in this table, the highest swelling behavior was detected in sample N4. In addition, it was determined that the clay particle size percentage of the sample N4 was detected as 51% compared to the other samples. The gelation coefficients of eight separate samples taken were made according to the TS 5360 (1996) standard, and it was concluded that the samples would not show gelation, since the results obtained (Table 1) were higher or equal than 8.3.

Surface area is an important factor controlling the surface properties and thus the electrokinetic behavior of clay minerals and many approaches have been proposed to determine this parameter of clays. The basic method for measuring surface area from the gas adsorption approach based on the relationship between the volume of gas applied to the samples used in the test and the applied pressure has been widely used in previous studies. As also stated by Santamarina et al. (2002), the surface areas of high surface area materials such as clay minerals can be determined precisely using the BET gas adsorption method. The measured BET surface area of materials that have a microscale hollow texture is calculated from the combination of the adsorption on the surface of the relevant particle and the condensation in micropores (Michot and Villieras, 2006). Considering these evaluations emphasized in previous studies the BET analysis was used in determining the surface area, pore volume and pore radius parameters of the collected samples. Within the scope of this study, the results of detailed BET analysis performed on Ankara clay are given in Table 2. For Ankara clay, it has been determined that the graphs of BET analysis are the most suitable and explanatory type of isotherm since it is linear.

Table 2- Surface area, pore volume and pore radius values of samples taken from Ankara clay.

Parameter	Method	N1	N2	N3	N4	N5	N6	N7	N8
Surface area (m^2/g)	MultiPoint BET	82.800	90.840	59.730	115.100	61.290	89.130	56.680	117.300
	BJH^a	24.020	26.460	19.910	33.340	22.290	34.220	19.360	31.740
	BJH^d	44.170	51.730	35.290	63.820	41.220	61.090	37.390	62.240
	DH^a	24.510	27.020	20.330	34.050	22.760	34.950	19.770	32.420
	DH^d	44.950	52.680	35.940	65.010	42.050	62.300	38.080	63.430
	t^d	55.510	63.980	44.630	81.760	50.340	67.920	49.110	80.990
	t^m	27.290	26.860	15.090	33.380	10.940	21.220	7.567	36.280
Pore Volume (cc/g)	BJH^a	0.071	0.065	0.055	0.074	0.058	0.068	0.048	0.069
	BJH^d	0.079	0.075	0.060	0.087	0.061	0.074	0.053	0.081
	DH^a	0.069	0.063	0.054	0.073	0.057	0.067	0.047	0.068
	DH^d	0.077	0.073	0.059	0.085	0.060	0.072	0.052	0.079
	t^m	0.013	0.013	0.007	0.017	0.005	0.011	0.004	0.019
Pore Radius (µm)	BJH^a	3.357	3.366	3.367	3.384	0.002	0.002	0.002	0.002
	BJH^d	3.769	3.766	3.763	3.755	0.002	0.002	0.002	0.002
	DH^a	3.357	3.366	3.367	3.384	0.002	0.002	0.002	0.002
	DH^d	3.769	3.766	3.763	3.755	0.002	0.002	0.002	0.019

BJH^a: BJH cumulative adsorption; BJH^d: BJH cumulative desorption; DH^a: DH cumulative adsorption; DH^d: DH cumulative desorption; t^d: t-method outer; t^m: t-method micro poreb

4.2. Mineralogical and Chemical Analysis of Ankara Clay

The physico - mechanical behavior of clays versus the change in water content is controlled by the clay mineral type and crystal structure that it contains (Yegorov, 1997). The case that geological units rich in clay minerals to be rich in swelling clay minerals results in increase in plasticity, swelling capacity and compressibility properties (Terzaghi and Peck, 1967). Considering these results obtained in previous studies, XRD analyses were carried out in order to determine the mineralogical composition of the samples. , samples are analyzed in the range of 20 - 70°C 2Θ using nickel filter and copper radiation, and the results obtained are interpreted in accordance with ASTM (1972) standards in qualitative XRD analyzes as a standard. The information obtained from these graphs prepared as a result of XRD analyses was determined qualitatively considering the criteria suggested by ASTM (1972) and presented in Table 3, the data obtained from the diffractograms in this chart are ranked according to the intensity of reflection, and this mineral ranking does not represent any quantitative value. When the normal shooting of clay fraction diffractograms given in Figure 4 is examined, the presence of 14 Å reflection of the smectite mineral is observed. This situation indicates that the exchangeable cation of the smectite group mineral of Ankara clay samples is rich in Ca^{++}.

In addition to the mineralogical composition of clays, physicochemical properties directly affect some engineering properties such as swelling behavior and shear strength of soils (Ergüler, 2001). The values of major elements obtained from the analyses made in the XRF spectrometer are presented in Table 4. Considering the results given in Table 4, it is understood that CaO percentage in Ankara clay are quite high with values varying between 6.7% to 21.2% due to carbonate nodules observed at shallow depths while Na_2O percentage is generally lower than other

Table 3- Minerals detected in the samples as a result of XRD analyses.

Sample No.	Detected minerals
N1	Quartz, Calcite, Smectite, Plagioclase, Chlorite, Kaolinite, Serpentine, Mica
N2	Quartz, Calcite, Smectite, Chlorite, Kaolinite, Mica, İllite
N3	Calcite, Quartz, Plagioclase, Chlorite, Smectite, Mica, İllite, Kaolinite
N4	Quartz, Calcite, Plagioclase, Smectite, Mica, İllite, Chlorite, Kaolinite
N5	Quartz, Calcite, Smectite, Plagioclase, Chlorite, Kaolinite, Mica, İllite
N6	Quartz, Calcite, Smectite, Plagioclase, Chlorite, Kaolinite, Mica, İllite
N7	Quartz, Plagioclase, Montmorillonite, Chlorite, Kaolinite, Mica, İllite, Amorphous material
N8	Calcite, Quartz, Montmorillonite, Plagioclase, Mica, İllite, Serpentine, Chlorite

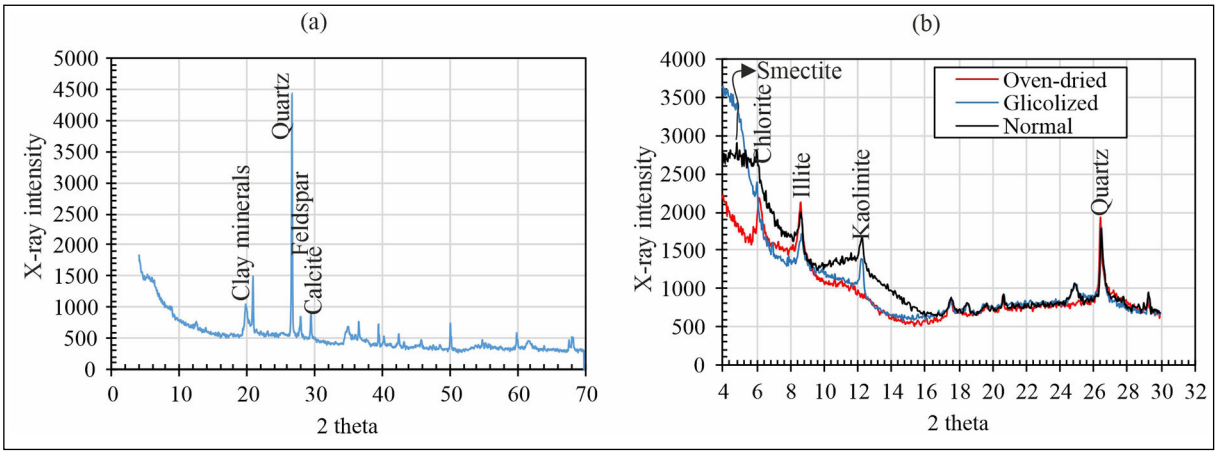

Figure 4- Diffractogram of the whole rock stage of XRD analysis of the sample N4 a) and the diffractograms belonging to the clay fraction of the same sample b).

Table 4- Percentages of major elements obtained from chemical analyses performed on samples (LOI: Loss on Ignition).

Sample No	LOI (%)	Al_2O_3 (%)	BaO (%)	CaO (%)	Cr_2O_3 (%)	Fe_2O_3 (%)	K_2O_3 (%)	MgO (%)	Na_2O (%)	SO_3 (%)	SiO_2 (%)	TiO_2 (%)
N1	14.2	16.9	0.07	10.3	0.02	5.9	1.9	3.9	0.6	0.18	45.3	0.7
N2	13.3	16.9	0.03	9.6	0.02	5.9	1.9	3.0	0.3	0.09	48.3	0.7
N3	19.5	11.7	0.05	21.2	0.02	4.4	1.1	2.8	0.4	0.13	38.1	0.6
N4	10.2	19.1	0.04	3.2	0.02	6.5	2.1	3.2	0.4	0.09	54.4	0.8
N5	16.1	12.9	0.04	15.8	0.02	4.7	1.2	2.7	0.4	0.15	45.5	0.5
N6	11.6	17.4	0.05	6.7	0.02	5.8	1.6	3.0	0.2	0.09	52.8	0.7
N7	13.4	13.7	0.04	13.6	0.02	5.1	1.7	2.7	0.6	0.08	48.5	0.6
N8	19.4	12.7	0.03	19.0	0.02	4.7	1.5	3.0	0.4	0.24	38.4	0.6

major elements with a value varying between 0.2 - 0.6. Abduljauwad (1993) stated that K_2O_3 indicated the presence of illite mineral, while SiO_2, Al_2O_3, Fe_2O_3, MgO and CaO indicated the presence of smectite mineral. When looking at the total percentages of all major elements proposed by Abduljauwad (1993) for smectite, it is concluded that smectite mineral is more than other clay minerals in the studied samples, and this result is consistent with the results obtained in X - ray diffraction analysis.

All results obtained in SEM - EDS analyzes are presented in Table 5. When the SEM images of all samples taken from eight locations within the scope of this study and the EDS analysis results given in Table 5 were examined in order to determine the textural and chemical properties of Ankara clay, no trace of sodium was found in any sample except for the sample N1. It is seen that the sample N2 has more oxygen and relatively less in magnesium than other locations. In general, when the amount of elements in all locations is evaluated in terms of +1, +2 and +3 ion

Table 5- The weight and element percentage amounts of Ankara clay samples obtained from EDS analyses.

Element	Evaluation based on weight							
	N1	N2	N3	N4	N5	N6	N7	N8
O K (%)	43.68	53.86	45.69	33.15	55.56	39.41	49.53	42.92
NaK (%)	1.72	-	-	-	-	-	-	-
MgK (%)	4.01	1.76	2.43	2.15	1.22	2.69	3.35	3.52
AlK (%)	12.62	5.73	9.89	11.31	2.18	14.65	13.48	12.69
SiK (%)	26.70	35.40	28.53	43.71	3.57	29.17	24.85	28.45
K K (%)	2.14	0.80	1.40	2.71	-	2.23	2.12	1.94
CaK (%)	2.74	0.40	6.95	0.62	36.29	3.56	2.48	3.65
TiK (%)	0.21	-	0.27	-	-	-	0.32	1.05
FeK (%)	6.19	2.06	4.85	6.35	1.17	8.29	3.88	5.78
Element	Evaluation based on element							
	N1	N2	N3	N4	N5	N6	N7	N8
O K (%)	59.01	67.62	61.55	47.80	74.55	55.36	64.37	58.62
NaK (%)	1.61	-	-	-		-	-	-
MgK (%)	3.56	1.45	2.15	2.04	1.09	2.49	2.86	3.16
AlK (%)	10.11	4.26	7.90	9.67	1.74	12.20	10.39	10.28
SiK (%)	20.55	25.32	21.89	35.90	2.73	23.34	18.39	22.13
K K (%)	1.18	0.41	0.77	1.60		1.28	1.12	1.08
CaK (%)	1.48	0.20	3.74	0.36	19.44	2.00	1.29	1.99
TiK (%)	0.10	-	0.12	-		-	0.14	0.48
FeK (%)	2.39	0.74	1.87	2.62	0.45	3.33	1.44	2.26

distribution, a close distribution with respect to each other is observed. Considering the Table 1, the lowest and highest values in terms of swelling potential were determined in samples N3 and N4, respectively. In addition, considering the percentage of clay particle size of these samples, it was seen that the samples N4 and N3 had quite different values from each other. Besides, while the ratio of clay fraction of the sample N4 that have high swelling is 51%, the ratio of the clay fraction of the sample N3 with a lower swelling potential is found to be 28%. The results of typical SEM images and EDS analyses of these two locations are given in Figure 5. As can be clearly seen in Figure 5, the SEM image of the sample N4 with a relatively higher swelling volume is detected as more leafy mineral (Figure 5b), however the SEM image of the sample N3 with the lowest swelling volume shows a more granular texture (Figure 5a). Considering the shooting of point where EDS analyzes are made in Figure 5a and the obtained element percentages, it is understood that there is a mineral at this point and it is the clay mineral according to the SEM image given in Figure 5b.

4.3. Electrokinetic Properties of Ankara Clay

The zeta potential (ζ) is defined as the electrical potential that occurs at the boundary surface between the negatively charged colloidal particle and the environment surrounding this particle. The value of this potential varies depending on the amount of surface charge, the type of colloid, pH of the medium and the electrical properties of the solvent. Zeta potential is used to evaluate many important properties such as electrokinetics of colloidal systems with negatively charged surfaces such as clay minerals and determine the electrical charge or potential of particles.

The particle size distribution curves of the powdered samples to be used in Zeta potential experiments are presented in Figure 6. The zeta potential vs pH change graphs obtained from the samples as a result of these experimental activities are presented in Figure 7. As can be seen in the graphs of change in Figure 7, there occurs a decrease in the zeta potential values in all samples depending on certain functions due to increasing ambient pH. When the

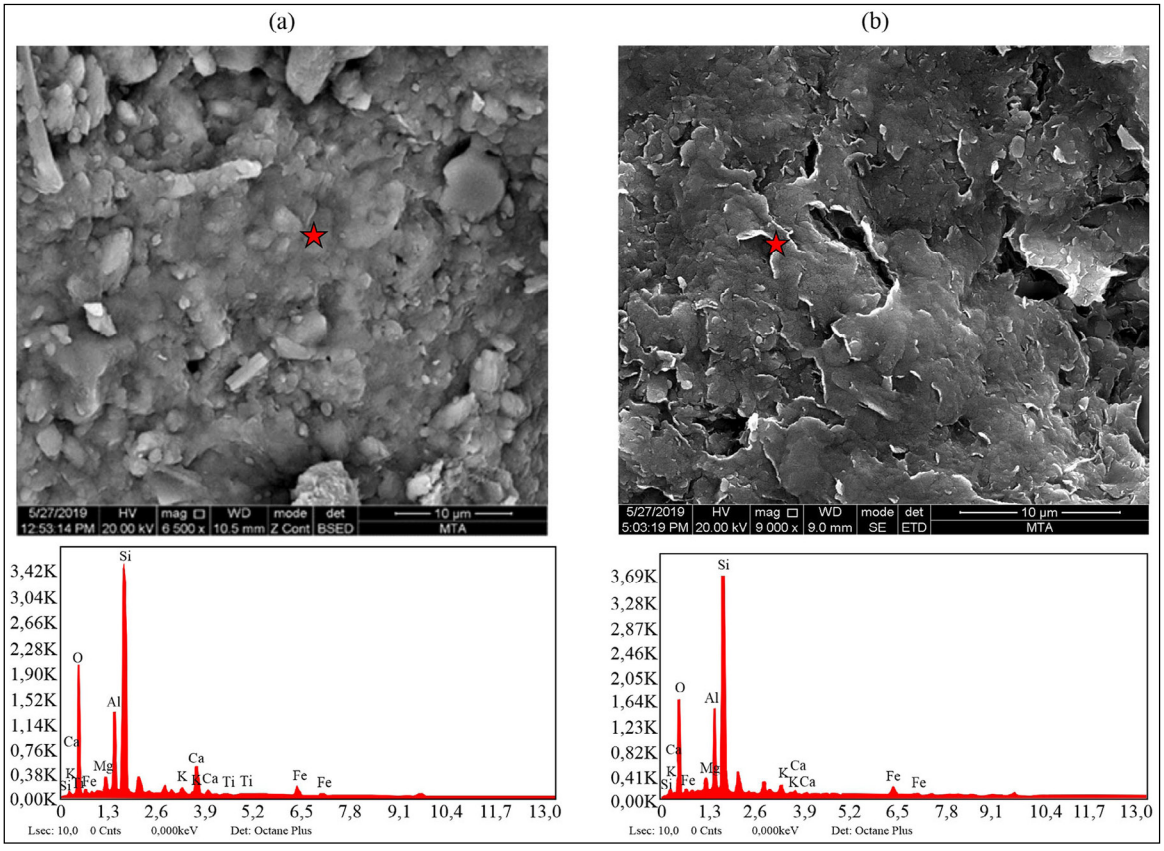

Figure 5- a) SEM image and EDS graph of the sample N3 that has the lowest swelling potential, b) SEM image and EDS graph of the sample N4 that has the highest swelling potential.

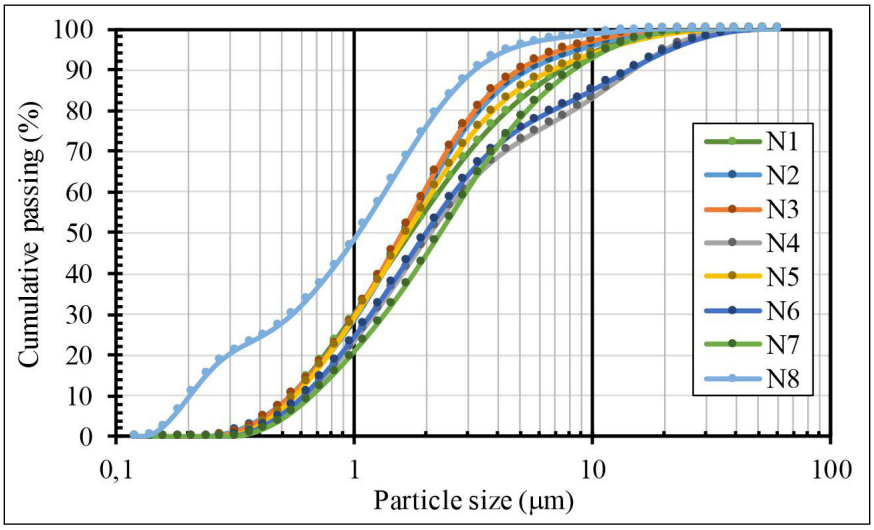

Figure 6- Particle size distribution curves determined by using laser of the samples prepared for zeta potential measurements.

results of zeta potential experiments performe for all samples are taken into consideration, pH values of the clay samples, which also show swelling behavior, vary between 2.03 and 12.10, and the measured zeta potential values vary between -3.56 mV and -51.8 with an average value such as -16.17 mV. Similar results were also obtained in the study conducted by Akın and Çelik (1995) consisting of the electrokinetic behavior of montmorillonitic clay minerals. These researchers emphasized that although they decreased the pH value of the environment to 3, the zeta potentials of the clay mineral they studied remained at negative values and that the zero load point (syn) of the montmorillonite mineral could not be determined. Akın and Çelik (1995) emphasized that they detected similar results for Ünye and Kırka borax montmorillonite minerals. Dikmen et al. (2011) determined the zero load points of Ahırözü and Üçbaşlı kaolin at pH ~4.2 and pH ~3.2, respectively using kaolin type clay in their study. The results obtained from these studies show that the zero load point of clays such as montmorillonite and Ankara clay with swelling capacity could not be found.

In addition to the different ambient pH values of the samples, it was thought that measuring the zeta potentials of the clay solutions in different electrolyte environments by taking the electrolyte type and concentrations into consideration would be useful in understanding the electrokinetic properties of these clayey samples. For this purpose, zeta potential experiments were carried out in single (NaCl), double ($CaCl_2$) and triple ($FeCl_3$) valent electrolyte solutions in concentrations of 0.1 mol L^{-1}, 0.01 mol L^{-1}, 0.001 mol L^{-1} and 0.0001 mol L^{-1}. The results obtained in the experiments performed using pure water at 25° C are presented in Figure 8. As seen in Figure 8, zeta potential values present different exchange functions depending on the type of electrolyte and there occurs a decrease in zeta potential values depending on the increase in concentration. It is seen that the effect of trivalent cations is higher in the decreasing behavior of zeta potential of these clayey units. While cations with +3 ions change zeta potentials from negative to positive in pure clay minerals depending on the concentration, there is only a tendency in Ankara clay and continued at staying in negative value. It was determined that Ankara clay did not have any isoelectric point. While monovalent cations make the zeta potential more and more negative, the exchange of divalent (Ca^{+2}, etc.) cations present in the crystal structure and the univalent (Na^{+}, etc.) cations in the solution has led to the development of a positive charge deficiency on the surface (Dikmen et al., 2011). Dikmen et al. (2011) emphasized that it is expected that the ratio of mineral to water and the intra surface will be replaced by equivalent amounts of cations in order to maintain total electroneutrality since the ion exchange process is basically a stoichiometric reaction. It is also possible that this situation, which is expected in theory, may not be fully realized, and thus, this observed situation caused the clay surface to have a more negative structure.

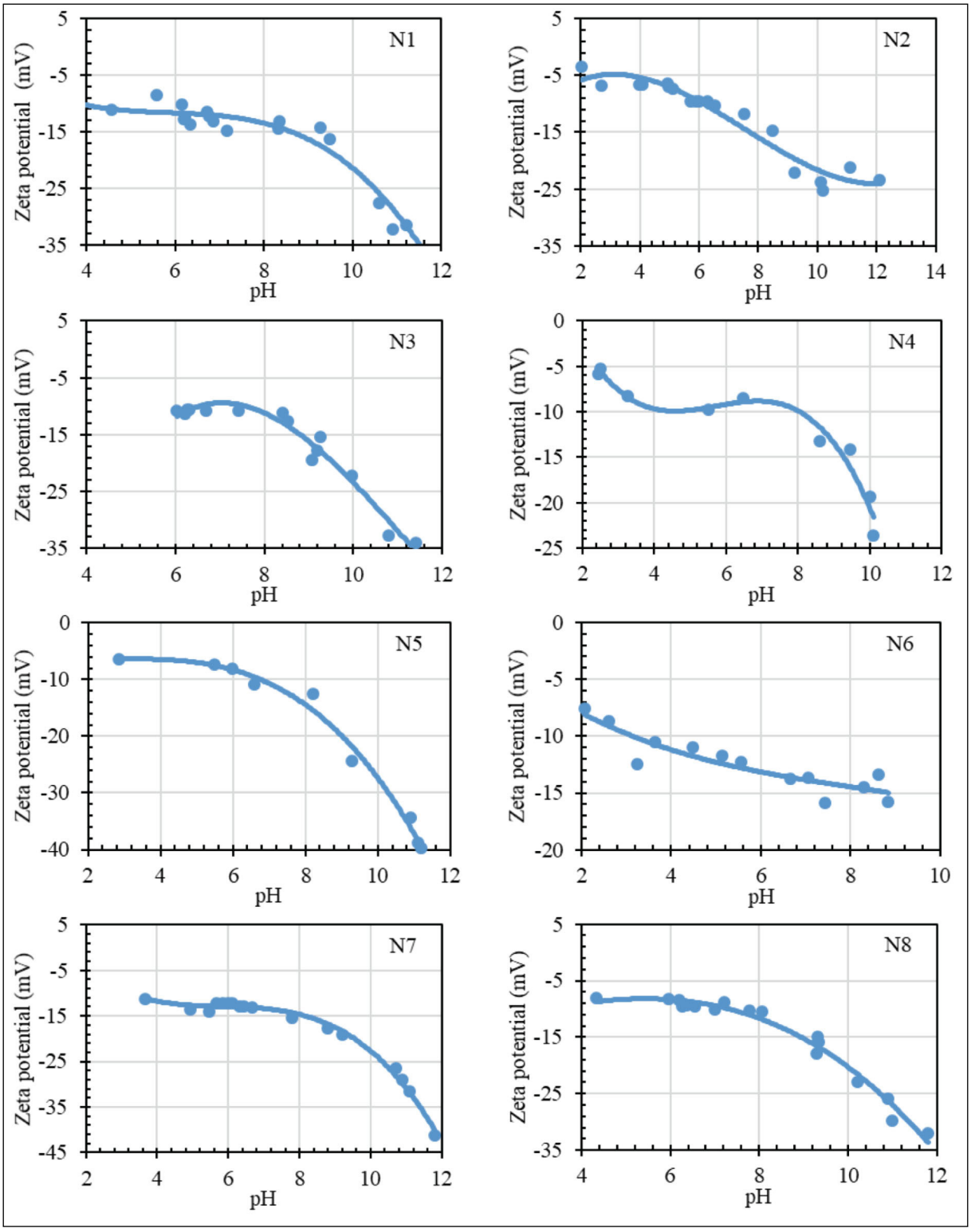

Figure 7- Zeta potential versus pH change graphs of the clay samples.

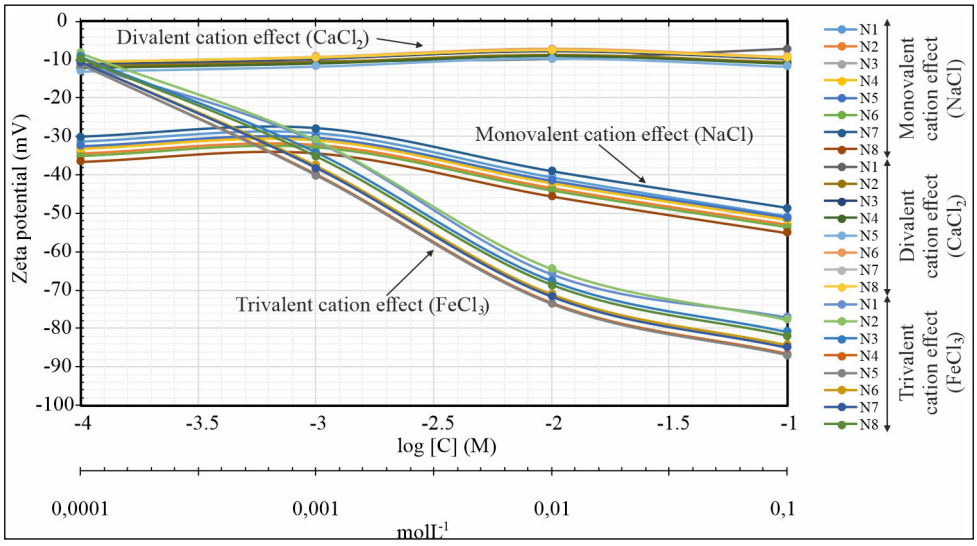

Figure 8- The concentration vs zeta potential variations of Ankara clay in single (NaCl), double ($CaCl_2$) and triple ($FeCl_3$) valence electrolyte solutions.

5. Conclusion

In this study, zeta potential measurements and the structural properties of Ankara clay were examined in detail in order to explain the electrokinetic mechanism. The results obtained are summarized below:

1. It was determined that the mineralogical composition of Ankara clay was generally formed by quartz, calcite, smectite, feldspar, kaolinite, illite and partially by chlorite, serpentine and mica minerals. The presence of swelling type clay minerals such as smectite in its mineralogical composition poses a problem for the light engineering structures of Ankara clay due to the swelling - shrinkage behavior of the region in rainy and dry periods up to a certain base depth.

2. The clay fraction content in Ankara clay reaches as high as 58% with an average value of 44%. The high ratio of clay fraction causes Ankara clay to have high Atterberg limits and therefore to show swelling behavior with the presence of swelling type clay minerals. In the analysis, it was understood that the clay fraction percentage and the liquid limit value are important indicators in understanding the swelling behavior and potential of Ankara clay. Similar swelling potential was also observed in the cation exchange capacity (CEC) results, which were determined in the methylene blue experiments of the samples and consistent with the results obtained in previous methylene blue experiments. Therefore, it was concluded that the CEC parameter was also an important input parameter in the estimation of physical properties of clays such as swelling and plasticity.

3. When MultiPoint BET method is taken as a basis, it was determined that the values of control surface area of the electrokinetic behavior of clay minerals varied between 57 m^2/g - 117 m^2/g with an average value of approximately 84 m^2/g for Ankara clay.

4. It was determined that the zeta potential values of Ankara clay samples, which also showed swelling behavior, varied between -51.8 mV and -3.56 mV with an average value of -16.17 mV, in the experiments performed under ambient pH values of 2.03 and 12.10. Considering the results obtained in all locations, the zeta potential values of all samples increase in negative values due to certain functions depending on the increasing ambient pH. Zero load point could not be determined in Ankara clay.

5. Using the samples taken to investigate the effect of electrolyte type and concentration on the electrokinetic properties of Ankara clay, Zeta potential experiments of single (NaCl), double ($CaCl_2$) and triple ($FeCl_3$) valued electrolyte solutions at concentrations of 0.001 mol L - 1 and 0.0001 mol L - 1 0.1 mol L - 1, 0.01 mol L - 1 were conducted. Monovalent and divalent electrolytes such as NaCl and $CaCl_2$ negatively increased the zeta potential of Ankara clay. However, it is considered that trivalent electrolyte

such as $FeCl_3$ is the electrolyte that determines the zeta potential and that the clay minerals tend to change their zeta potential from negative to positive depending on the concentration.

6. It was determined that Ankara clay, which was rich in different proportions of illite, kaolinite and montmorillonite clay minerals in addition to quartz, feldspar and calcite minerals, did not create any electrokinetic behavior similar with previous studies using minerals such as pure kaolin, montmorillonite, illite and sepiolite.

Acknowledgements

This study was supported by the General Directorate of Mineral Research and Exploration (MTA) within the scope of the project numbered 2020-38-14-01-3, "Uçucu Küllerin Karakteristikleri ve Çevreye Etkilerinin Araştırılması: Sentetik Zeolit Yapımında Kullanılabilirliği" (The Characteristics of Fly Ash and Its Effects on the Environment: Its Usability in Synthetic Zeolite Production).

References

Abduljauwad, S. N. 1993. Study on the performance of calcareous expansive clay. Bulletin of the Association of Engineering Geologists 4, 481-498.

Akın Y., Çelik, M. S. 1995. Montmorillonit tipi killerin elektrokinetik davranışı. Endüstriyel Hammaddeler Sempozyumu, İzmir, 135-142.

Alemdar, A., Atıcı, O., Güngör, N. 2000. The influence of cationic surfactants on rheological properties of bentonit - water systems. Material Letters 43, 57-61.

Angle, C. W., Hamza, H. A. 1989. An electrokinetic study of a natural coal associated mixture of kaolinite and montmorillonite in electrolytes. Applied Clay Science 4, 263-278.

Aras, İ. A. 1991. Clay Mineralogy and Sedimentological Features of The Late Pliocene Sediments in Ankara Area. MSc. Thesis, METU, Ankara 79s.

Aras, İ. A., Hakyemez, H. Y., Türkmenoğlu, A. G. 1991. The mineralogy and depositional environment of Ankara Clay, V. Ulusal Kil Sempozyumu, Bildiriler, A.Ü., Eskişehir, 87-99.

ASTM C837, 2019. Standard Test Method for Methylene Blue Index of Clay, ASTM International, West Conshohocken, PA.

ASTM, 1972. Inorganic index to the powder diffraction file: Joint Committee on Powder Diffraction Standards, Pennsylvania, 1432.

ASTM, 1994. Annual Book of ASTM Standards-Soil and Rock, Building Stones, Section-4, Construction, V. 04.08, ASTM Publication 972.

Avşar, E. 2003. Karbonat yumrularının Ankara kilinin şişme özelliklerine etkisi: Beytepe Kampüsü örneği. Bitirme Projesi. Jeoloji Mühendisliği Bölümü, Ankara, 72 (unpublished).

Avşar, E., Ulusay, R., Ergüler, Z. A. 2005. Swelling properties of Ankara (Turkey) clay with carbonate concretions. Environmental and Engineering Geosciences 11 (1), 73-93.

Benna, M., Kbir- Ariguib, N., Magnin, A., Bergya, F. 1999. Effect of pH on rheological properties of purified sodium bentonite suspensions. Journal of Colloid and Interface Science 218, 242-255.

Bergaya, F., Lagaly, G. 2001. Introduction surface modification of clay minerals, Applied Clay Science 19, 1-9.

Birand, A. A. 1978. Ankara yöresi zeminleri ve jeoteknik sorunlar. Türkiye Jeoloji Kurumu Yerbilimleri Açısından Ankara'nın Sorunları Sempozyumu Bildiriler Kitabı 12-14 Aralık 1978, Ankara, 55-60.

Çetinkaya, A. S. 1978. Preconsolidation pressure and its effects on some properties of METU Campus clay. MSc Thesis, METU, Civil Engineering Department, Ankara, 157 (unpublished).

Chang, H. S., Gupta, K. R., Ryan, M. E. 1992. Effect of the adsorption of polyvinyl alcohol on the rheology and stability of clay suspensions. Journal of Rheology 36. 273-287.

Chaput, E. 1931. Ankara mıntakasının 1/135 000 mikyasında jeoloji haritasına dair izahat (Tercüme eden : H. Nafiz Pamir), İst. Darûlf. Jeol. Enst. Neş. sayı 7, İstanbul.

Çokça, E. 1991. Swelling potential of expansive soils with a critical appraisal of the identification of swelling of Ankara soils by methylene blue tests. PhD Thesis, METU, 323 (unpublished).

Çokça, E., Birand, A. A. 1993*a*. Determination of cation exchange capacity of clayey soils by the methylene blue test. Geotechnical Testing Journal of ASTM 5, 518-524.

Çokça, E., Birand, A. A. 1993*b*. Prediction of swelling potential of Ankara soils by methylene blue test. Doğa -Tr.J. of Engineering and Environmental Sciences 17, 57-63.

Dikmen, S., Ersoy, B., Akpınar, S., Bircan, H., Orhun, Ö. 2011. Eskişehir-Mihalıççık kaolenlerinin elektrokinetik özellikleri. Afyon Kocatepe Üniversitesi Fen Bilimleri Dergisi 11, 9-18.

Ece, O. I., Güngör, N., Alemdar, A. 1999. Influences of electrolytes, polymers and a surfactant on rheological properties of bentonite- water systems. Journal Of Inclusion Phenomena and Molecular Recognition in Chemistry 33, 155-168.

Ergüler, Z. A. 2001. Ankara kilinin şişme davranışının ve örselenmenin şişmeye etkisinin incelenmesi, şişme potansiyelinin görgül yaklaşımlarla belirlenmesi. Yüksek Mühendislik Tezi, Jeoloji Mühendisliği Bölümü, Hacettepe Üniversitesi, Ankara, 125 (unpublished).

Ergüler, Z. A., Ulusay, R. 2003. A simple test and predictive models for assessing swell potential of Ankara (Turkey). Engineering Geology 67, 331-352.

Erol, O. 1976. Ankara Şehri'nin gelişmesinde doğal koşulların etkisi: Ankara: 50. Yıl Konferansları, Ankara Üniversitesi Dil ve Tarih-Coğrafya Fakültesi 257, 45-55.

Fityus, S. G., Smith, D. W., Jennor, A. M. 2000. Surface area using methylene blue adsorption as a measure of soil expansivity. Proc. Int. Conf. on Geotechnical and Geological Engineering, Melbourne, Australia (on CD).

Furtun, U. 1989. An Investigation on Ankara Soils with Regard to Swelling. MSc. Thesis, METU.

Güngör, N., Alemdar, A., Atıcı, O., Ece, I. O. 2001. The effect of SDS surfactant on the flow and zeta potential of bentonit suspensions. Materials Letters 51, 250-254.

Janek, M., Lagaly, G. 2003. Interaction of a cationic surfactant with bentonite: a colloid chemistry study. Colloid Polymer Science 281, 293-301.

Kasapoğlu, K. E. 1980. Ankara Kenti Zeminlerinin Jeo-Mühendislik Özellikleri. Doçentlik Tezi, Hacettepe Üniversitesi Yerbilimleri Enstitüsü, Beytepe-Ankara, 206.

Koçyiğit, A., Türkmenoğlu, A.G. 1991. Geology and mineralogy of the so-called "Ankara Clay" formation: a geologic approach to the "Ankara Clay" problem, V. Ulusal Kil Sempozyumu, Bildiriler, Eskişehir, 112-126.

Met, I., Akgün, H., Türkmenoğlu, A. G. 2005. Environmental geological and geotechnical investigations related to the potential use of Ankara clay as a compacted landfill liner material, Turkey. Envıronmental Geology 47(2), 225-236

Michot, L. J., Villieras, F. 2006. Surface Area and Porosity. Handbook of Clay Science, Ed: F. Bergaya, B.K.G. Theng, G. Lagaly. Elseiver Ltd., 965-978.

Moore, D. M., Reynolds, R. C. 1997. X-ray diffraction and identification and analysis of clay minerals. 2nd Edition, Oxford University Press, New York.

Önalp, A. 2013. Geoteknik bilgisi I zeminler ve mekaniği çözümlü problemlerle. Birsen Yayınevi, İstanbul, 461.

Özgüven, A. 2014. Development of expandability charts for Ankara Kalecik Clay. Applied Clay Science 101, 533-540.

Pal, O. R., Vanjara, A. K. 2001. Removal of malathion and butachlor from aqueous solution by clays and organoclays. Separation Purification Technology 24, 167-172.

Ross, G., De Kretser, Scales, P. J., Boger, D. V. 1998. Surface chemistry-rheology inter-relationships in clay suspensions. Colloids and surfaces 137, 307-318.

Santamarina, J. C., Klein, K. A., Wang, Y. H., Prencke, E. 2002. Specific surface: determination and relevance. Canadian Geotechnical Journal 39, 233-241.

Sezer, G. A., Türkmenoğlu, A.G., Göktürk, E.H. 2003. Mineralogical and sorption characteristics of Ankara clay as a landfill liner. Applied Geochemistry 18, 711-717.

Terzaghi, K., Peck, R. B. 1967. Soil Mechanics in Engineering Practice. John Wiley and Sons, New York, 729.

TS 10252, 1992. Bentonit-İlaç ve Kozmetik Üretiminde Kullanılan, Türk Standartları Enstitüsü, Ankara.

TS 5360, 1996. Döküm Bentoniti, Türk Standartları Enstitüsü, Ankara.

Yalçın, T., Alemdar, A., Ece, I. O., Güngör, N. 2002. The viscosity and zeta potential of bentonite dispersions in presence of anionic surfactants. Materials Letters 53, 211-215.

Yegorov, Y. K. 1997. Swell - shrinkage potential and prediction swell behavior of expansive clays. Proc. of the International Symposium on Engineering Geology and the Environment, Athens 451-455. Greece.

Yitik, H. 2006. İnce tanelerdeki kil içeriğinin metilen mavisi deneyi ile belirlenmesi, Osmangazi Üniversitesi Yüksek Lisans Tezi, Eskişehir.

Zhao, X., Urano, K., Ogasawara, S. 1989. Adsorption of polyethylene glycol from aqueous solution on montmorillonite clays. Colloid and Polymer Science 267, 899-906.

Bulletin of the Mineral Research and Exploration

http: / / bulletin.mta.gov.tr

Geochemistry of Miocene evaporites from the Aşkale (Erzurum, Eastern Turkey) area: constraints for paleo-environment

Emel ABDİOĞLU YAZAR[a*], Mehmet ARSLAN[a], Cahit HELVACI[b], İbrahim GÜNDOĞAN[b], İrfan TEMİZEL[a] and Didem AYDINÇAKIR[a]

[a] *Karadeniz Technical University, Department of Geological Engineering, 61080, Trabzon, Turkey*
[b] *Dokuz Eylül University, Department of Geological Engineering, Buca 35160, İzmir, Turkey*

Research Article

Keywords:
Evaporite, Gypsum, Anhydrite, Geochemistry, Aşkale, Turkey.

ABSTRACT

The Aşkale sub - basin hosts Early Miocene evaporites intercalated with clastic sediments and carbonates. Gypsum - and anhydrite - rich evaporite samples are characterized by high CaO and SO_4 contents, and low Na_2O, K_2O, MgO, and B contents. The Sr contents are 228 - 13100 ppm in evaporite samples, 169 - 992 ppm in claystone, 181 - 60090 ppm in marl, and 15150 ppm in limestone. All the samples are also characterized by enrichment in light rare earth elements (REE) with La_N / Lu_N = 0.667 - 4.243 and have variable Ce_N / Ce* (0.823 - 1.353) ratios. Measured Eu_N / Eu* values of the samples display strong and variable negative and positive Eu anomalies. $\delta^{34}S_{CDT}$ and $\delta^{18}O$ values of gypsum - and anhydrite samples have wide ranges from 21.30 ‰ to 25.62 ‰, and 11.5 ‰ to 19.1 ‰, respectively. Most of these values are heavier than expected Miocene marine gypsum composition and may be resulted from reduction and oxidation reactions of sulfide species in brines. ^{87}Sr / ^{86}Sr ratios range from 0.707475 (Δ_{SW} = −169.8) to 0.708175 (Δ_{SW} = −99.8), close to and / or slightly lower than an Early - Miocene marine isotopic composition. Petrochemical and isotopic data indicate that the Aşkale basin evaporites developed in subtropical conditions via multiple marine transgressions onto a shallow platform or lagoonal environment.

Received Date: 15.05.2020
Accepted Date: 21.07.2020

1. Introduction

Facies analysis combined with mineralogic and petrographic examination of evaporitic units may elucidate the depositional environments and paleo - climatological conditions at the time of formation of these units (Warren and Kendall, 1985; Warren, 2010; Kaspryzk, 2003). In addition, discrimination between marine and non - marine origins for ancient evaporites requires consideration of bulk - rock chemistry and sulfur, oxygen, and strontium isotope data (Toulkeridis et al., 1998; Lu et al., 2003; Palmer et al., 2004).

The stratigraphy, mineralogy, and geochemistry of evaporitic units in Neogene basins in Western and Central Anatolia (Turkey) have been investigated by many researchers (Helvacı and Yağmurlu, 1995; Tekin, 2001; Çiner et al., 2002; Orti et al., 2002; Türkmen, 2004; Gündoğan et al., 2005, 2008; Yeşilova, et al., 2018). Further, sulfur, oxygen, and strontium isotope compositions of Cenozoic evaporites from Turkey were reported in detail by Palmer et al. (2004). In the Eastern Anatolia region, the studies of different basins have revealed valuable

Citation Info: Abdioğlu Yazar, E., Arslan, M., Helvacı, C., Gündoğan, İ., Temizel, İ., Aydınçakır, D. 2021. Geochemistry of Miocene evaporites from the Aşkale (Erzurum, Eastern Turkey) area: constraints for paleo-environment. Bulletin of the Mineral Research and Exploration 165, 113-140.
https://doi.org/10.19111/bulletinofmre.772360

**Corresponding author: Emel ABDİOĞLU YAZAR, abdioglu@ktu.edu.tr*

geochemical data that may explain key tectonic events known to have affected the region, such as closure of the Tethyan Oceans and understanding major climatological changes (Yeşilova, et al., 2018). The Aşkale (Erzurum) sub - basin is located at the border of marine and non - marine evaporitic units (Brinkmann, 1976; Palmer et al., 2004) and exhibits evidence for an active compressional tectonic regime related to collision between the Arabian and Laurasian plates during the Paleocene (?) or Eocene to Lower Miocene (Yılmaz, 1993). Nonetheless, despite this important setting, the evaporitic units in the Aşkale (Erzurum) sub - basin have only been investigated by a few researchers (Sancay, 2005; Abdioğlu et al., 2013, 2015; Aydınçakır, 2013).

The stratigraphy, mineralogy, and depositional environment of evaporitic sequences in the Aşkale (Erzurum) sub - basin in Eastern Anatolia (Turkey) were recently studied in detail by Abdioğlu et al. (2015). In this paper, we expand on this work by presenting the first detailed whole - rock geochemical (major, trace, and rare earth element concentrations) and isotopic ($\delta^{18}O$, $\delta^{34}S_{CDT}$, and $^{87}Sr / ^{86}Sr$) data of the Aşkale evaporites to clarify their mode of origin and time of formation.

2. Geological Setting and Local Geology

Turkey is part of the Alpine - Himalayan orogenic belt, and thus was directly affected by collision between the African - Arabian and Eurasian plates during the Cenozoic. Geologically, it is characterized by four main tectonic units: the Pontides, the Anatolides, the Taurides, and the Border Faults (Ketin, 1966; Figure 1a). From north to south, Eastern Anatolia—where the study area is located—contains three tectonic units: (i) the Pontide unit; (ii) the Eastern Anatolian Accretionary Complex (EAAC), which is covered by Late - Miocene to Quaternary collision - related volcanic units; and (iii) the Bitlis - Pötürge Massif (Şengör, 1980; Keskin, 2003). The EAAC forms part of a large accretionary prism situated between the Pontides and the Bitlis - Pötürge Massif (Şengör, 1980; Şengör et al., 2003). This complex also underlies shallow Eastern - Anatolian Late - Miocene basins that extend in an E - W direction and which formed under N - S - oriented compression (Alptekin, 1973; McKenzi, 1976; Tchalenko, 1977).

The evaporitic units outcropping in the Aşkale (Erzurum) area formed in the Tercan - Aşkale sub - basin, which is one of the shallow Eastern Anatolian basins (Sancay, 2005). Basement rocks in this area comprise Jurassic - Cretaceous volcano - sedimentary and ultramafic rocks, which themselves are overlain by Tertiary basins to the north and northwest (Şahintürk and Kasar, 1970; Tarhan et al., 1992; Şahintürk et al., 1997). The Tertiary sedimentary units—namely the Aşkale formation (Sungurlu, 1971)—exhibit features indicative of a shallow marine depositional environment. In the study area, they comprise a sandstone - mudstone - limestone member, an evaporite member, a gravelstone - sandstone - mudstone member, and a limestone member (Abdioğlu et al., 2015; Figure 1b). The age of the formation was reported as Early to Middle Miocene by Şahintürk (1992) and Middle Miocene by Tekin et al. (2000).

A detailed description of the geology and petrography of the Aşkale evaporites has been made by Abdioğlu et al. (2015). The Aşkale evaporite member mainly contains massive, nodular, nodular - banded, wavy laminated, evenly laminated, laminated - banded, and rare enterolithic and chicken - wire gypsum lithofacies in the form of wedges, pods, and lenses. These are interbedded with gypsum - bearing carbonate and clay - rich strata, implying a sabkha depositional setting within the sub - basin. Petrographically, alabastrine, porphyroblastic, and fibrous textures are common in the evaporites, which are dominated by secondary gypsum alongside minor anhydrite, saponite, illite / smectite, calcite, dolomite, and trace amounts of celestite, epsomite, and lutecite (Abdioğlu et al., 2015).

3. Materials and Methods

Based on stratigraphic, mineralogic, and petrographic characteristics, 58 samples of evaporite, limestone, claystone, and marl collected from various stratigraphic levels of the Aşkale evaporite member (Abdioğlu et al., 2015) were selected for lithochemical studies. Samples were prepared for whole - rock analyses at the Department of Geology, Karadeniz Technical University (Trabzon) by crushing into small fragments using a jaw crusher and then pulverizing using a mild - steel mill to produce rock powders with a grain size of <200 mesh. Evaporitic rocks rich in sulfate minerals were the most difficult to analyze, as

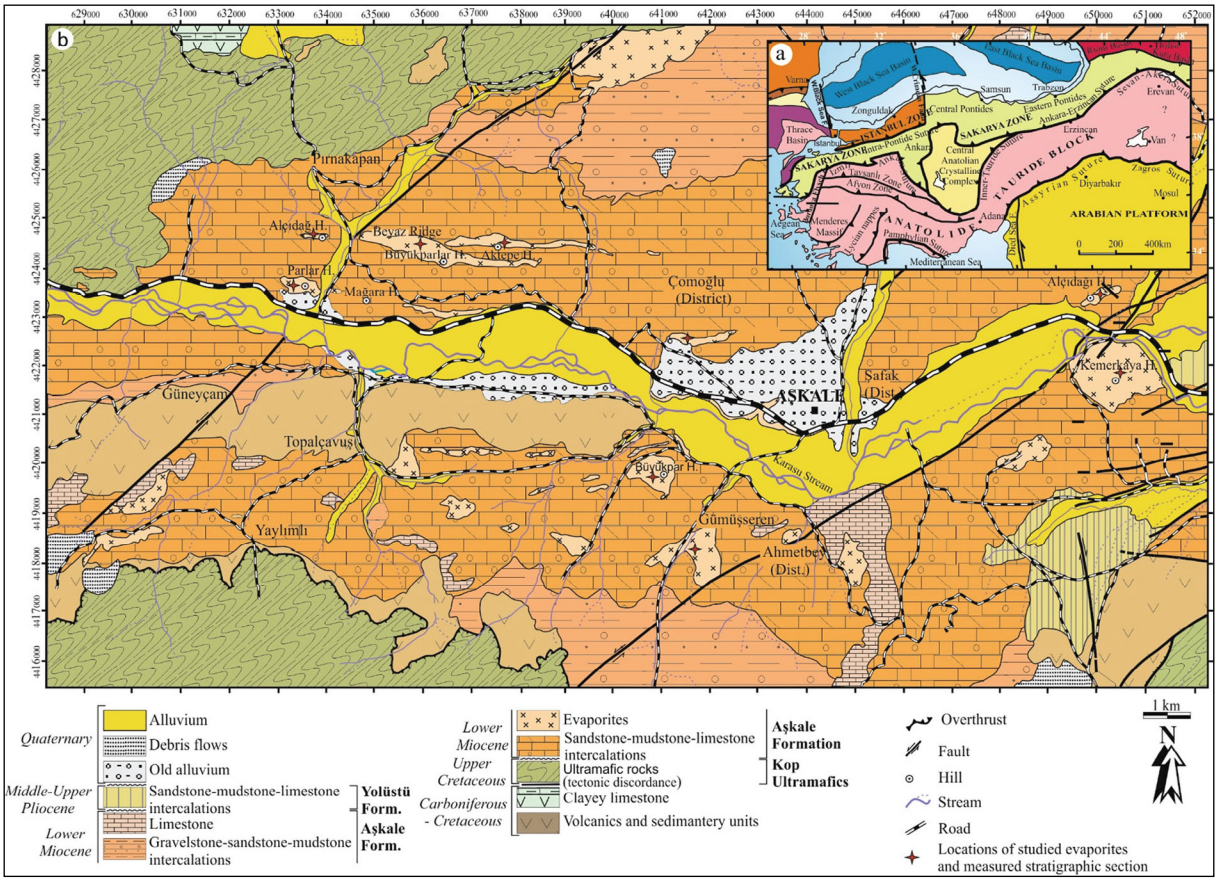

Figure 1- a) Tectonic map of the north-eastern Mediterranean region showing the major sutures and continental blocks (modified after Okay and Tüysüz, 1999). b) Simplified geological map of the Aşkale (Erzurum) sub-basin (modified after Tarhan et al., 1992; Abdioğlu et al., 2015).

each sample had to be ground to 200 mesh to ensure complete fusion of resistant minerals.

Whole - rock analyses were performed at Activation Laboratories Ltd. (Actlabs) in Canada. Whole - rock major, trace, and rare earth element compositions of the 58 samples from different evaporite lithofacies and locations were determined through lithium metaborate / tetraborate fusion with subsequent analysis via inductively coupled plasma optical emission spectrometry (ICP - OES) and mass spectrometry (ICP - MS). Detection limits for major oxides lie within the 0.01 - 0.001 wt. % range. Loss on ignition (LOI) was determined based on weight difference after ignition at 1000 °C. This measured value comprises volatilized H_2O, S, CO_2, organic C, and other weight gains that occur during oxidation of Fe^{2+} to Fe^{3+} but does not include S derived from SO_4 - bearing minerals, as they are non - combustible up to 1050 °C. Detection limits for measured trace and rare earth elements are as follows: 20 ppm for Cr; 5 ppm for V; 2 ppm for Sr and Mo; 1 ppm for Sc, Be, Ba, Ga, and Sn; 0.2 ppm for Sb; 0.5 ppm for Y, Ge, and W; 0.1 ppm for Zr, Rb, In, Bi, Cs, Hf, Co, Ni, Zn, and As; 0.05 ppm for Tl, La, Ce, and Nd; 0.01 ppm for Cu, Pb, Cd, Nb, Ta, Th, Pr, Sm, Gd, Tb, Dy, Ho, Er, and Yb; 0.005 ppm for U and Eu; and 0.002 ppm for Lu and Ag. Analysis of B, Cl, CO_2, and SO_4 contents employed prompt gamma neutron activation (PGNAA), instrumental neutron activation (INAA), infrared (IR), and combustion infrared detection techniques, which have detection limits of 0.5 ppm, 0.01 wt. %, 0.01 wt. %, 0.3 wt. %, respectively.

$\delta^{18}O_{SMOW}$, $\delta^{34}S_{CDT}$ values and ^{87}Sr / ^{86}Sr isotopic ratios were measured in 14 pure gypsum and one anhydrite mineral samples at Activation Laboratories Ltd. (Actlabs) in Canada. The analytical procedures of Kornexl et al. (1999) and Ueda and Krouse (1986) were followed for O and S isotope analysis,

respectively. For Sr isotope ratios, Rb and Sr were separated by extraction chromatography, and then analyzed on a Finnegan MAT 262 multi - collector mass spectrometer. Fifteen simultaneous analyses of SRM - 987 Sr standard runs yielded a weighted average $^{87}Sr / ^{86}Sr$ value of 0.710258 ± 9 (2s). Based on modern sea water $^{87}Sr / ^{86}Sr$ value of 0.709173±3 (Denison et al., 1998), Δ_{SW} is defined as $\Delta_{SW} = (^{87}Sr / ^{86}Sr_{sample} - ^{87}Sr / ^{86}Sr_{\text{modern seawater}}) \times 10^{5}$.

4. Results

All geochemical data and statistical analysis as calculated mean, standard deviation and correlation coefficients for the Aşkale evaporites and associated clastic and carbonate rocks from the Pırnakapan (on the Beyaz Ridge), the Alçıdağ hill, the Gümüşseren, and the Kemerkaya sections (Figure 1b) are presented in Supplementary tables 1 - 3. The additional details of the Pırnakapan, the Alçıdağ hill and the Gümüşseren sections as well as petrographic and depositional features of all samples were presented by Abdioğlu et al. (2015).

4.1. Major and Trace Elements

Major oxide variations within the Aşkale evaporites are mainly expressed in terms of varying CaO contents, which are 29.8 - 33.13 wt. % and 40.23 - 41.85 wt. % in the Pırnakapan section for gypsum - rich and anhydrite rich samples, respectively, and 32.19 - 32.59 wt. % in the Kemerkaya section, 30.83 - 33.45 wt. % in the Alçıdağ hill section, and 31.13 - 33.04 wt. % in the Gümüşseren section for gypsum - rich samples. All sulfate mineral - rich samples are characterized by low Na_2O (0.01 - 0.13 wt. %), K_2O (0.01 - 0.29 wt. %), MgO (0.01 - 2.55 wt. %), and Cl (0.01 - 0.04 wt. %) contents (Supplementary Table 1).

Certain trace elements in evaporites (e.g., Li, Br, and B) provide constraints on their paleo - environment of formation and can be used to discriminate between marine and non - marine origins (Warren, 2010). The B contents of the analyzed Aşkale evaporites are very low, with gypsum - and anhydrite - rich samples having 0.8 - 20.3 ppm, limestone having 13.8 ppm, claystone having 74.9 - 76.6 ppm, and marl having 3.5 - 188 ppm. In all cases, measured Br contents are very close to the detection limits (0.01 - 6 ppm, Supplementary Table 1). Measured Ni, Cr, and Co contents vary from sample to sample, with their concentrations being generally higher in associated clastic sediments. The Aşkale evaporites have Sr contents of 228 - 13100 ppm in gypsum rich samples, 1023 - 1197 ppm in anhydrite rich samples, 169 - 992 ppm in claystone, 181 - 60090 ppm in marl, and 15150 ppm in limestone.

Multi - element spider diagrams normalized to MuQ (Mud of Queensland), which represents the composition of weathered, young, upper - continental crust - derived alluvial sediment (Kamber et al., 2005), show that gypsiferous samples are more depleted than claystone - limestone - marl samples (Figure 2). In addition, all evaporite samples are strongly depleted in Rb, Th, and Zr, but have slight enrichment in Ba and a marked enrichment in Sr.

4.2. Bivariate Plots

Relationships between major oxides and selected trace and rare earth elements in the Aşkale evaporites were quantified using correlation coefficients, which were calculated for a significance level of $p < 0.01$ using the Statistica 10 program (Supplementary Table 3). This analysis shows that most elements have strong positive correlations with each other, except CaO, which generally displays a strong negative correlation, while Sr and Ba display very weak correlations.

Bivariate element variation diagrams have much use in identifying the control of mineralogical variations on the bulk geochemistry of an evaporite. The most important major oxides in the Aşkale evaporites are SiO_2 and CaO, which are significant components in authigenic silicate and sulfate minerals, as well as being able to highlight variations in the proportions of diagenetic and / or clastic minerals. To better understand variations between major oxides and trace elements, variation diagrams for SiO_2 versus other major oxides (Figure 3) and SiO_2 versus trace elements (Figure 4) were plotted. These bivariate plots show positive and negative trends between various components. For example, Al_2O_3, TiO_2, K_2O, Fe_2O_{3total}, MgO, Th, Co, Ba, Ce, As, and Ni have a strong positive correlation with SiO_2, whereas CaO and SO_4 show a weak negative correlation. There appears to be a partly negative (but dispersed) relationship between SiO_2 and Sr.

Figure 5 shows Sr vs. Mg, Na vs. Mg, Sr vs. Na, and Sr vs. B element variation diagrams for gypsum

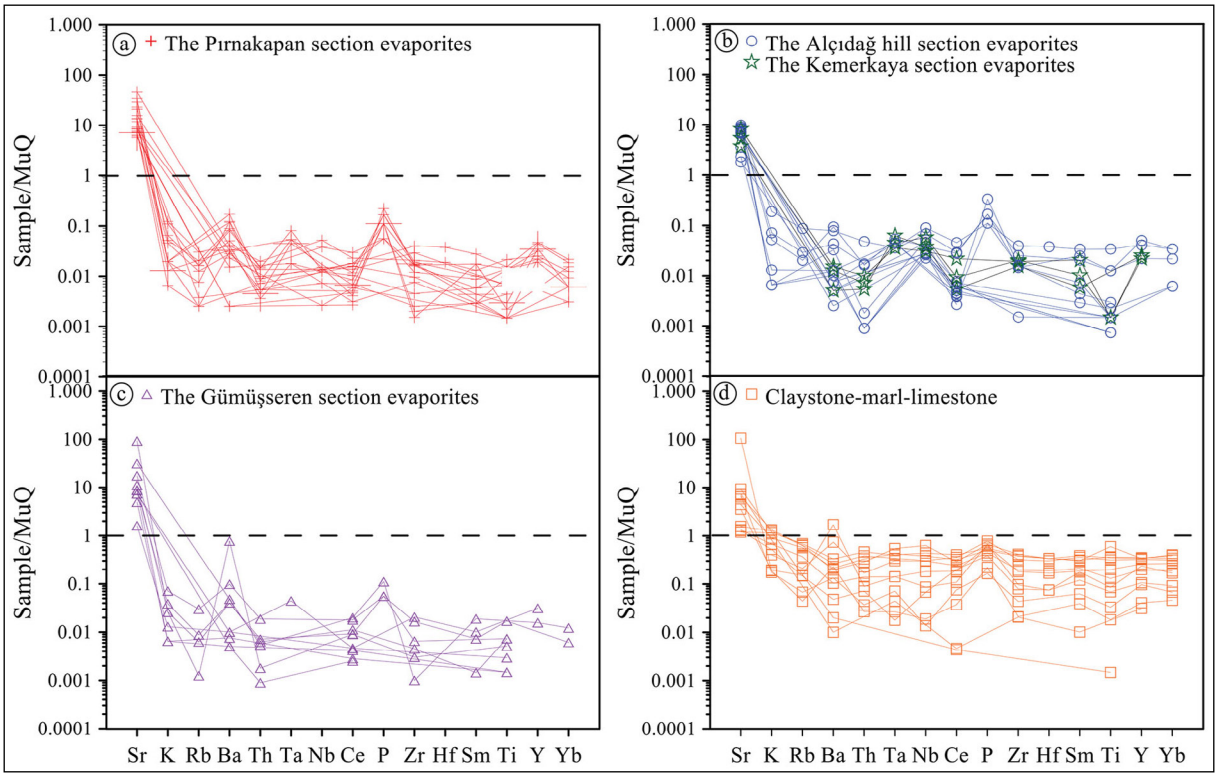

Figure 2- a - d) MuQ-normalized multi-element spider diagrams for the Aşkale evaporites and claystone - marl - limestone. MuQ = Mud of Queensland—an average sediment composition (Kamber et al., 2005).

- anhydrite rich samples from different sections and claystone - limestone - marl samples. These data show that Sr vs. Mg and Sr vs. Na plots have relatively positive trends if claystone - limestone - marl samples not considered but scattered trends in general. Na vs. Mg plot displays a relatively positive trend whereas Sr vs. B plot has a scattered and negative trend (Figure 5).

4.3. Rare Earth Element (REE) Geochemistry

In general, the measured REE contents of the gypsum - anhydrite rich evaporite samples are very low. For example, La contents are in the range 0.08 - 1.97 ppm and Lu contents are in the range 0.002 - 0.019 ppm (Supplementary Table 2). The overall REE concentrations are close to or below their respective detection limits, implying that hydrothermal fluids were not effective during the formation process (Emelyanov and Shimkus, 1986).

All evaporite, claystone, marl, and limestone samples exhibit a generally flat MuQ - normalized REE pattern, with slight enrichment in LREE. La_N / Lu_N ratios are 0.867 - 4.243 for the Pırnakapan section, 2.713 - 4.220 for the Kemerkaya section, 1.349 - 2.488 for the Alçıdağ Hill section, 1.658 for the Gümüşseren section evaporites, and 0.677 - 1.540 for the claystone - marl - limestone samples. All the samples exhibit both positive and negative Ce (0.823 - 1.353) and Eu (0.389 - 2.245) anomalies (Figure 6).

4.4. Isotope Geochemistry

Isotope geochemistry is commonly used to explain the origin, diagenetic conditions, and environment of formation of evaporites. In lithologies containing sulfate minerals, sulfur, oxygen, and strontium isotopes are of critical importance to understand the chemistry and temporal evolution of fluids during precipitation of evaporitic minerals (Müller and Mueller, 1991; Rosell et al., 1998; Ortí and Rosell, 2000; Playà et al., 2000; Palmer et al., 2004; Tekin et al., 2010; Crockford et al., 2019).

Table 1 shows $\delta^{34}S_{CDT}$, $\delta^{18}O$ and ^{87}Sr / ^{86}Sr isotopic ratios for gypsum and anhydrite samples from the Aşkale evaporites. These data highlight that

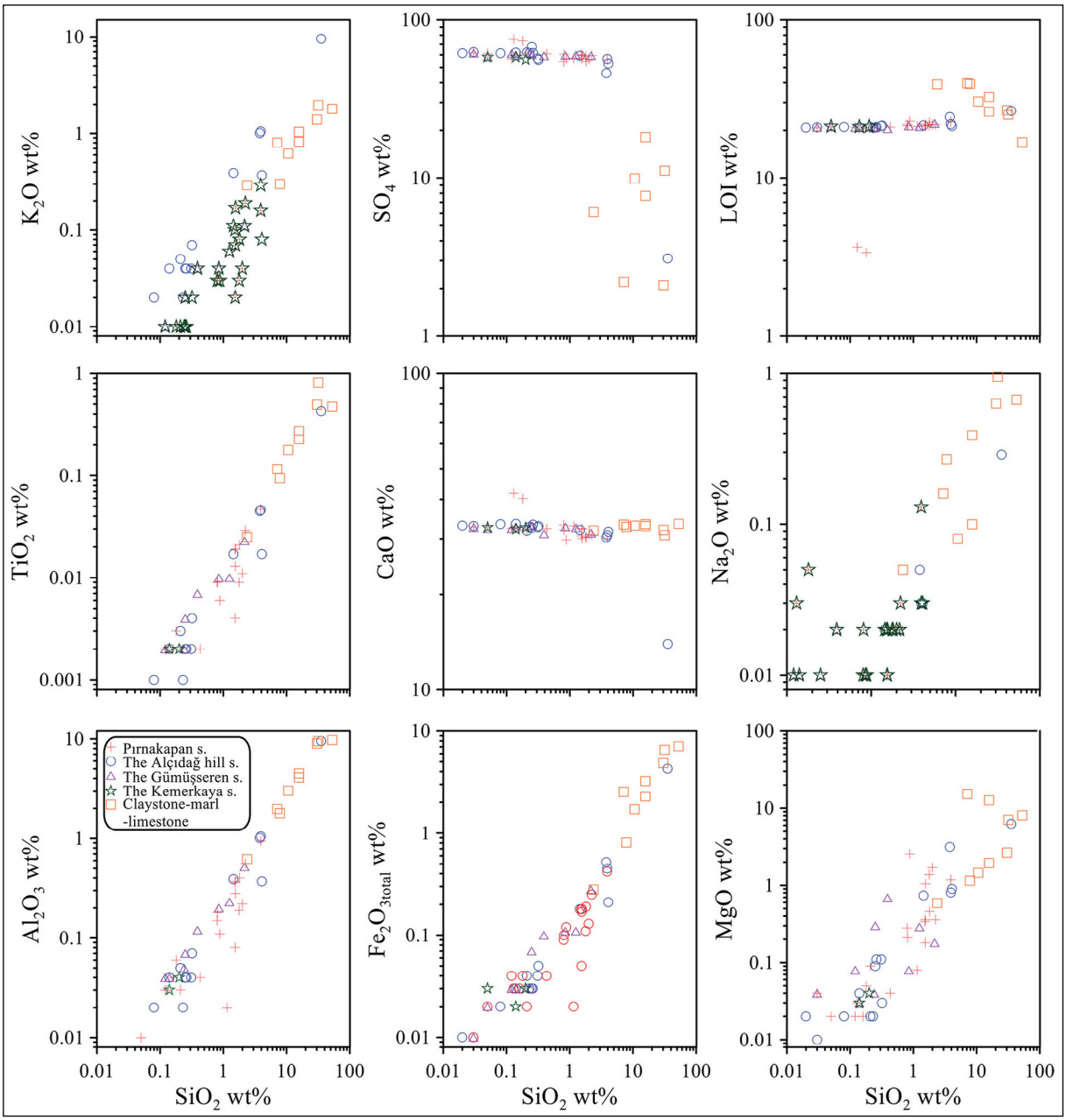

Figure 3- SiO_2 (wt. %) versus selected major element oxide (wt. %) variation plots for the Aşkale evaporites.

the $\delta^{18}O$ isotopic compositions lie within the range 11.5 - 19.1 ‰, with a mean value of 14.67 ‰; the $\delta^{34}S_{CDT}$ isotopic compositions range from 21.3 ‰ to 25.62 ‰, with a mean value of 23.22 ‰; and ^{87}Sr / ^{86}Sr ratios are 0.707475 (Δ_{SW} = −169.8) to 0.708175 (Δ_{SW} = −99.8) (Table 1).

5. Discussion

Determination of the paleo - environment of deposition of the Aşkale evaporites requires combining major, trace, and REE geochemistry with isotopic data. Interpretations of these results are given below.

5.1. Assessment of Whole - Rock Chemical Data

Positive correlations between SiO_2 and other major oxides observed on binary variation diagrams for the Aşkale evaporites (Figure 3, Supplementary Table 1 and 3) indicate that the paleo - depositional environment shallowed due to evaporation, allowing clay or clastic materials to be transported into the

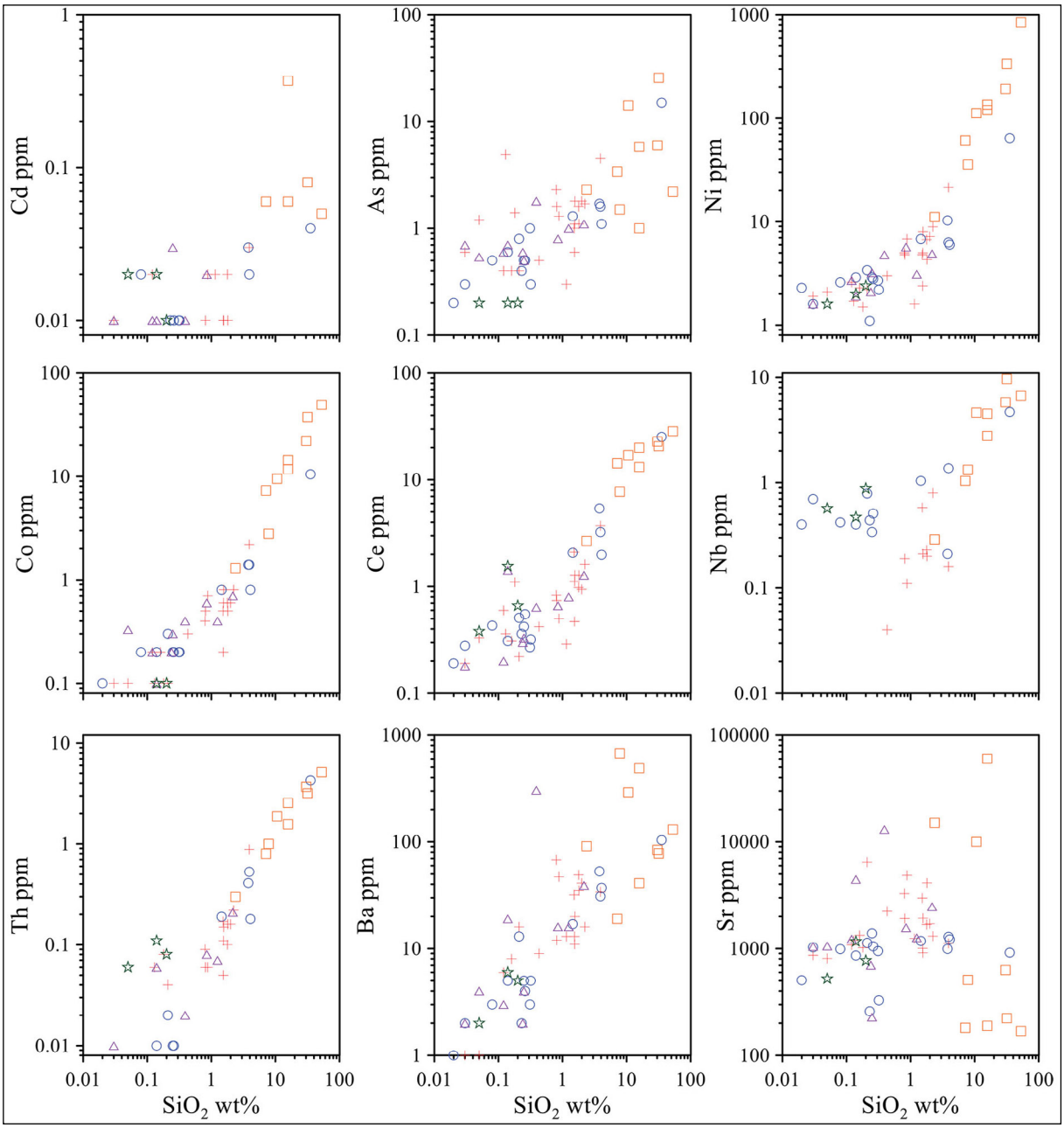

Figure 4- SiO_2 (wt. %) versus selected trace element (ppm) variation plots for the Aşkale evaporites (symbols as in Figure 3).

region from continental sources. Negative SiO_2 - CaO and SiO_2 - SO_4 correlations support this evaporative shallowing hypothesis, as they record reduced precipitation of Ca - sulfate over time (Bahadori et al., 2011). Generally, the poor correlation between SiO_2 and Sr indicates that Sr may have marine source with some continental input. The correlation between SiO_2 and Ba content may be similarly explained via increasing Ba - sulfate and Ba - chloride crystallization during shallowing, likely due to evaporation of the paleo - depositional environment (Bahadori et al., 2011). The low Ba contents of the investigated Aşkale evaporite samples may indicate either input of continental clastic material or, precipitation of barite even under very low Ba concentration (Horner et al., 2017) although barite was never detected by means mineralogical examinations in the Aşkale evaporites.

When binary element variation diagrams are assessed with correlation coefficients (see

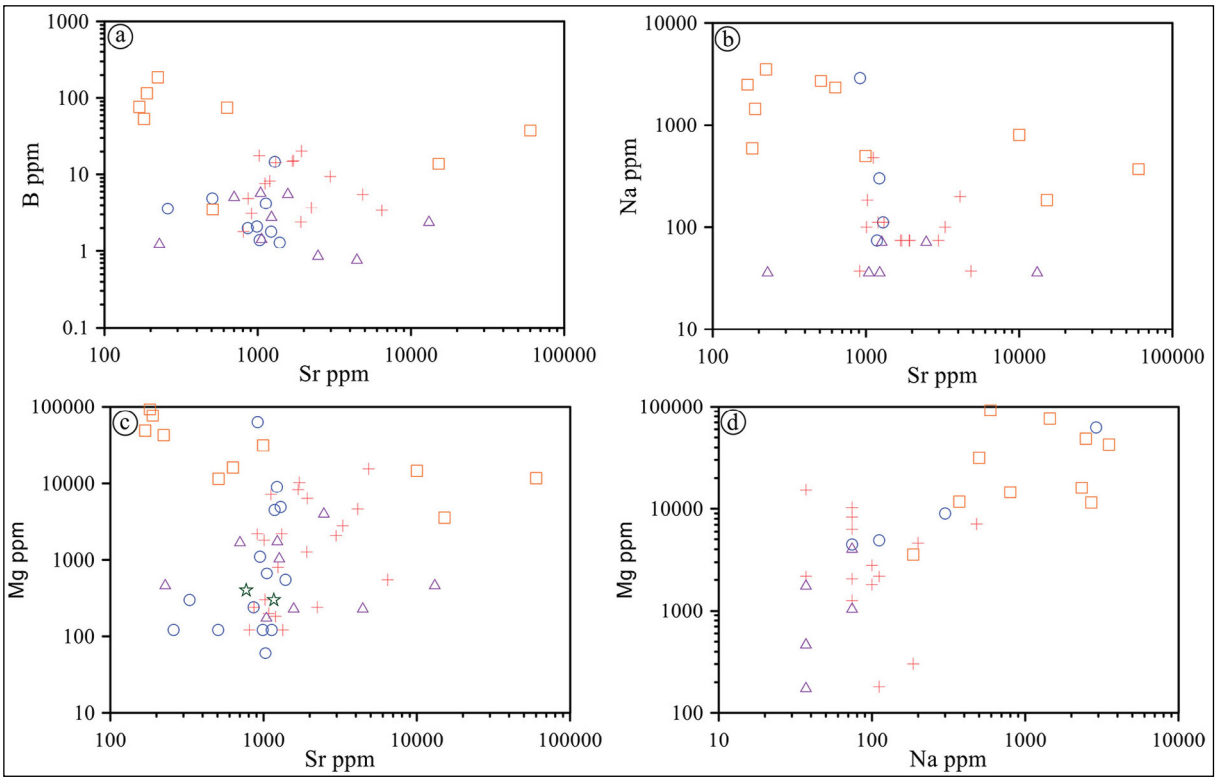

Figure 5- Cross-plots of trace element compositions of the Aşkale evaporites. a) Sr vs. B, b) Sr vs. Na, c) Sr vs. Mg, d) Na vs. Mg (symbols as in Figure 3).

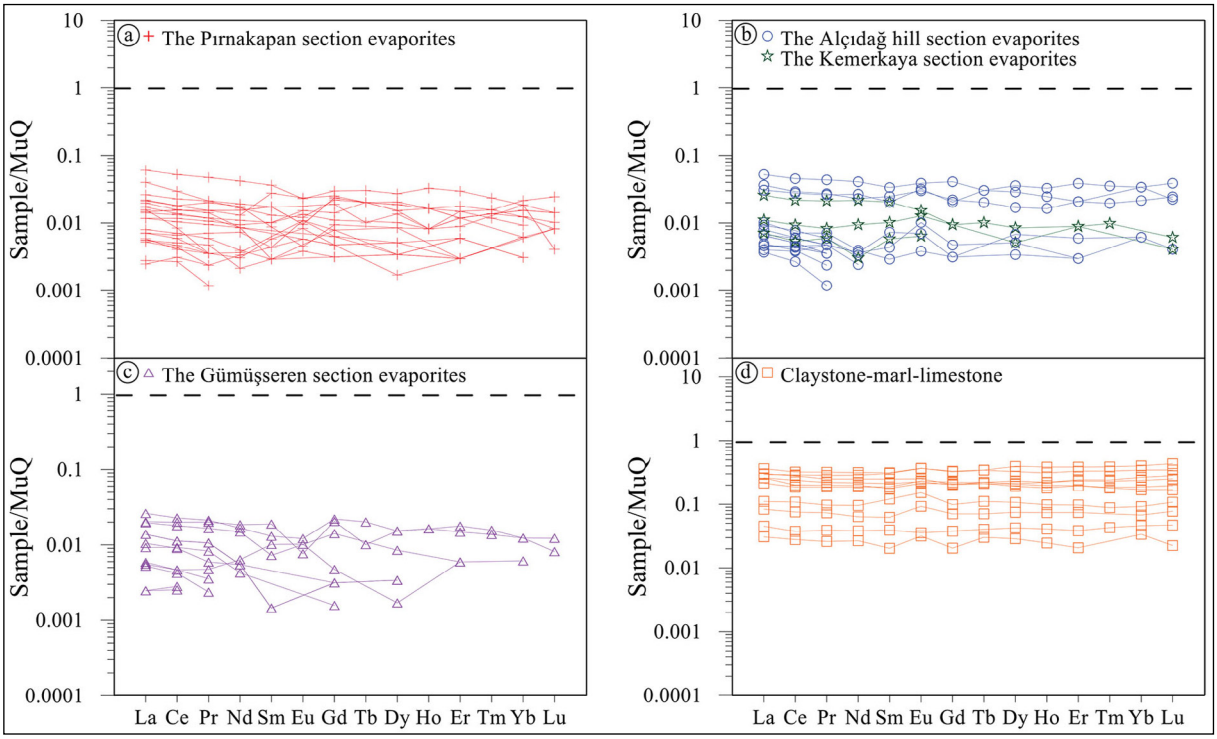

Figure 6- a - d) MuQ-normalized REE patterns for the Aşkale evaporites. MuQ = Mud of Queensland - an average sediment composition (Kamber et al., 2005).

Table 1- $\delta^{18}O_{SMOW}$, $\delta^{34}S_{CDT}$ values, and ^{87}Sr / ^{86}Sr isotopic ratios of gypsum and anhydrite samples from the Aşkale evaporites.

Sample Number	**Section**	**Texture**	**Mineralogy**	**$\delta^{18}O_{SMOW}$** (‰)	**$\delta^{34}S_{CDT}$** (‰)	**^{87}Sr / ^{86}Sr** ±2s	Δ_{SW}
A-1	Alçıdağ hill	nodular	*gypsum*	13.5	22.9	0.707475 ± 4	-169.8
A-6		alabastrine		16.0	23.5	0.707991 ± 5	-118.2
A-11		nodular		12.7	23.4	0.708102 ± 4	-107.1
A-16		alabastrine		13.3	21.3	0.708147 ± 12	-102.6
D1-5	Pırnakapan	laminated		18.0	24.1	0.708076 ± 3	-109.7
D1-28		alabastrine		15.0	22.9	0.708046 ± 4	-112.7
D1-32		alabastrine		14.5	22.9	0.708092 ± 4	-108.1
D3-4		nodular		19.1	23.74	0.707488 ± 8	-168.5
D3-5		laminated		18.8	25.62	0.707480 ± 16	-169.3
K-3	Gümüşseren	alabastrine		14.4	23.6	0.708163 ± 5	-101.0
K-4		alabastrine		11.5	23.23	0.708174± 17	-99.9
K-9		nodular		13.6	22.3	0.708114 ± 5	-105.9
K-14		banded		12.1	22.3	0.708121 ± 3	-105.2
K-25	Kemerkaya	alabastrine		14.1	22.94	0.708175 ± 15	-99.8
D1-22	Pırnakapan	nodular	*anhydrite*	13.5	23.6	0.708144 ± 4	-102.9

Supplementary Table 3), samples containing common sulfate minerals appear to match those with sparse silicate minerals. These silicate minerals are generally accompanied by clay minerals, such as illite and Mg - smectite, and varying proportions of Ni - , Cu - , and Fe - rich minerals. Transportation of clastic material from a continental source region might therefore have occurred in the cycle of evaporite formation, driven by periods of high precipitation that followed dry seasons. This interpretation agrees with constraints imposed by regional geology, as the regression was effective during periods of evaporite formation (Sancay, 2005). Thus, enrichments in Ni, Cu, and Co can be linked to the input of clastic material sourced from the surrounding Kop ultramafic rocks. The positive relationship between SO_4 and CaO results from gypsum and / or anhydrite formation, although SO_4 shows a variably negative correlation with nearly all elements. Importantly, there is no correlation between SO_4 and Sr, as Kushnir (1980, 1982) reported that the increasing evaporation of Sr - rich seawater may drive celestite crystallization simultaneous with gypsum. The presence of epigenetic celestite formed during a late stage of diagenesis was proved by means of petrographical examinations as crack or cavity infillings of micritic limestones and in the secondary gypsum lithofacies accompanying to gypsum and sometimes to lutecite (Abdioğlu et al., 2015). Thus, a high Sr content can be attributed to epigenetic celestite formation.

Figure 5 shows that Sr content has a dispersed and / or negative correlation with B content. Measured B contents in gypsum - rich samples (0.8 - 20.3 ppm), anhydrite - rich samples (8.2 - 17.7 ppm), limestone samples (13.8 ppm), claystone samples (74.9 - 76.6 ppm), and marl samples (3.5 - 188 ppm) show no correlation between it and Sr. In fact, the interpreted increase in clastic material with time appears to relate to a partial increase in B content.

As seawater has a much lower REE concentration than river water (Playà et al., 2007), the REE content of an evaporite is controlled by the input of continental material. Figure 6 shows that regression related Aşkale evaporite samples interpreted to contain clastic material also have high REE contents. Consequently, ultramafic rocks surrounding the paleo - basin should also have high REE contents if they are considered a potential source of detritic material. Clay - rich Aşkale samples have higher REE contents compared to evaporitic samples, and clay and carbonate samples have flat REE distribution patterns, indicating intense chemical differentiation. The REE distributions within evaporite samples are similar in shape but differ in magnitude.

The speciation of Ce and Eu in sedimentary rocks is useful for determining redox states within a depositional environment. Thermodynamic calculations by Sverjensky (1984) indicate that Eu^{2+} is more abundant than Eu^{3+} in high temperature reducing environments. Indeed, minerals precipitating under reducing conditions (Eu^{2+} / Eu^{3+} > 1) generally have a positive Eu anomaly. The Aşkale evaporites have both positive and negative Eu anomalies of varying magnitudes, with Eu_N / Eu* values of 0.389 - 2.245 in gypsum - and anhydrite - rich samples, 0.927 in limestone, 1.045 - 1.396 in claystone, and 1.094 - 1.392 in marl. In Aşkale clastic samples, positive Eu anomalies likely represent the presence of continental sedimentary material. Aşkale samples rich in sulfate minerals show strong negative and positive Eu anomalies, independent of lithofacies, which likely records occasional freshwater input to the depositional environment, with deepening and shallowing periods linked to local climatic and tectonic activity.

Similarly, positive and negative Ce anomalies provide valuable information about the environment of formation. For example, Ce in rocks typically occurs in the 3^+ valence state, but oxidizes over time, and thus enters fluids in the 4^+ valence state. Given that low - temperature seawater - mineral interactions are characterized by high Ce^{4+} / Ce^{3+} ratios in the fluid, rocks affected by such aqueous alteration processes should have a negative Ce anomaly, although if Ce^{4+} is then incorporated into newly formed minerals, rocks should have a positive anomaly (Ludden and Thompson, 1979; Menzies et al., 1979). Thus, the Ce_N / Ce^* values recorded in Aşkale gypsum - and anhydrite - rich samples (0.823 - 1.353), and marl, limestone, and claystone samples (0.873 - 1.045) have both mildly negative and mildly positive Ce anomalies. Such negative Ce anomalies infer the influence of seawater in the paleo - depositional basin.

In evaporites, Sr^{2+} may exchange with Ca^{2+} to form celestite ($SrSO_4$) (Adabi, 2004). Usdowski (1967) indicated that the mean Sr content of seawater that precipitates gypsum is ~1400 ppm, with this value being preserved in the crystals even if gypsum transforms to anhydrite during diagenesis. Evaporites developing in marine environments have a Sr content of 1000 - 3000 ppm (Emelyanov and Shimkus, 1986; Hasselöv et al., 1999), while those developing in continental environments have a Sr content of 50 - 200 ppm (Krauskopf, 1979). Lacustrine Miocene evaporites from north - eastern Spain have Sr contents below 500 ppm with sulfate and chloride ions sourced from adjacent Mesozoic continental salts (Orti et al., 2007). Study of rocks from the East Betik strait, Spain, has shown that normal seawater - derived banded, nodular, and laminated gypsum from Late - Miocene continental and marine evaporites have a Sr content of 800 - 1700 ppm, whereas selenitic and massive gypsum, which form from hydrothermal solutions, have a Sr content of 2400 ppm (Playà et al., 2000). The Aşkale gypsum and anhydrite strata have similar Sr contents to those of strata from the East Betik strait, emphasizing that their constituent minerals formed from seawater (Kushnir, 1980, 1982). In situations where non - marine fluids contribute to evaporite mineral genesis, the compositions of these evaporites may differ significantly from those of evaporites primarily formed from seawater (Usdowski, 1967; Kushnir, 1980, 1982; Rushdi et al., 2000; Symkatz - Kloss and Roy, 2010; Bahadori et al., 2011). The Aşkale evaporites have Sr contents of 228 - 13100 ppm in gypsum - and anhydrite - rich samples and 169 - 60090 ppm in claystone - marl - limestone samples, which most closely resemble marine - sourced evaporites. Gypsum and anhydrite samples with high Sr contents are thought to include Sr^{2+} within their crystal lattices (Tekin, 2001), although high Sr contents are generally thought to denote marine depositional environments. However, it should be considered that simultaneous volcanism around the basin may increase Sr input to environment, resulted in much higher Sr content than normal seawater. Extremely high Sr contents (60090 ppm) are associated with celestite formation, which is very common in carbonate rocks. The source of such enrichment may be related to dissolution of Sr from previously formed gypsum, which may then be precipitated as celestite.

Major and trace element data from evaporites occurred in Neogene basins of Turkey were compared with the gypsum - and anhydrite - rich samples from the Aşkale area (Table 2). The major element contents of the Aşkale evaporites resemble the major oxide values of evaporites from the Ulaş (Sivas) basin (Tekin, 2001) and the Beypazarı and Çankırı - Çorum basins (Gündoğan and Helvacı, 2001; Gündoğan, 2000), but are lower than evaporites in the Central Sakarya basin (Zeybek, 2007) (Table 2). In addition, the Ba, Pb, and Cu contents of the Aşkale evaporites resembles those from evaporites in the Central Sakarya basin but are

much higher than those in evaporites from the Ulaş basin. The Sr contents of the evaporites studied in this work are much higher than those reported by Baysal and Ataman (1980) and Gökçe and Ceyhan (1988) but resemble the results of Tekin (2001) and Zeybek (2007). The Mg content of Aşkale evaporites samples resemble those of Zeybek (2007) but are higher than other studies. As such, the Aşkale evaporites most closely resemble the Ulaş (Sivas) basin evaporites, which are also described as having a marine origin (Tekin, 2001).

5.2. Chemostratigraphic Correlations

The correlation of geochemical variations with stratigraphic level is commonly used to make paleo - climatological interpretations (Bahadori et al., 2011). As such, whole - rock geochemistry was used in combination with measured stratigraphic sections to quantify geochemical variation in the Aşkale evaporites and quantify the types and magnitudes of changes (Figure 7).

Highly soluble ions, such as Na^{+}, Mg^{2+}, and K^{+}, exhibit very different differentiation behaviors compared to stable (insoluble) ions, such as Ti^{4+}, Al^{3+}, and Fe^{3+} (Mason and Moore, 1982). When soluble elements are transported by water, sediments tend to become enriched in insoluble elements. As a result, the relative concentrations of these two ionic groups reflect paleo - environmental conditions (Nesbitt and Young, 1982; Gallet et al., 1996; Roy et al., 2006, 2009). Smykatz - Kloss and Roy (2010) recommended the use of Na_2O / Al_2O_3, Na_2O / Fe_2O_3, Na_2O / TiO_2. and Na_2O / K_2O ratios to decipher the paleo - climatological conditions in which evaporite minerals formed. Of this set, all but Na_2O / K_2O are expected to increase commensurately with an increase in aridity or a reduction in aqueous activity (Bahadori et al., 2011). By contrast, both Na and K are soluble

Table 2- Comparison of major and trace element compositions between some evaporite deposits of Turkey and the Aşkale evaporites.

	Zara-Refahiye Basin	Celali-Karayün-Hafik Basin	Sivas-Ulaş Basin	Beypazarı Basin	Çankırı-Çorum Basin	Middle Sakarya Region	Aşkale Basin
wt%							
SiO_2				0.56 - 3.89	1.14 - 4.97	0.22 - 25.72	0.02 - 3.92
Al_2O_3				0.1 - 0.75	0.26 - 1.15	0.08 -10.72	0.01 -1.05
Fe_2O_3*				0.037 - 0.418	0.135 - 0.693	0.04 - 6.81	0.01 - 0.45
MnO				0.001 - 0.011	0.002 - 0.017	_	0.002 - 0.009
MgO			0.17 - 0.32	0.21 - 7.45	0.14 - 14.73	0.07 - 33.98	0.02 - 2.55
CaO			32.7 - 38.6	2.87 - 39.86	14.13 - 38.62	7.75 - 56.75	29.8 - 41.85
Na2O			0.11 - 0.31	0.004 - 42.38	0 - 0.17	0.06 - 0.27	0.01 - 0.13
K_2O			0.1 - 1.2	0.023 - 0.184	0.051 - 0.315	0.01 - 0.87	0.01 - 0.29
TiO_2				0 - 0.069	0 - 0.069	0.01 - 0.77	0.002 - 0.047
P_2O_5						0.01 - 0.87	0.01 - 0.02
ppm							
Sr	783	2450	2526 - 5368			256.9 - 5270	228-13100
Ba			0.01 -6.5			11.6 - 273.9	1 - 305
Ni						2.2 - 97.1	1.1 - 21.4
B							0.8 - 20.3
Li	2.8	3.1	1.6 - 3				
F	16.1	40	3.4 - 4.8				
Pb			0.14 - 2.5			2 - 20.07	0.04 - 2.12
Cu			0.1 - 2			1 - 43.1	0.41 - 6.07
Mg	3741	6528	3158 - 4768				
Age	Miocene	Miocene	Miocene	Middle-Late Miocene		Miocene	Early Miocene
Environment			Marine	Playa lake		Playa lake	
Reference	Baysal and Ataman (1980)	Gökçe and Ceyhan (1988)	Tekin (2001)	Gündoğan (2000)		Zeybek (2007)	This study

elements, and K is easily adsorbed by sedimentary minerals, such as illite, leading to the formation of new species (Pandarinath et al., 1999). Thus, unless environmental conditions change, the Na_2O / K_2O ratio of an aqueous solution should remain the same (Bahadori et al., 2011).

Figure 7 shows that the Aşkale evaporites have very low Na_2O / Al_2O_3, Na_2O / Fe_2O_3, Na_2O / TiO_2, and Na_2O / K_2O ratios, and there is no significant variation up - section, although Ce_N / Ce^* ratios and Sr contents show minor changes. These data may be explained largely by a non - marine fluid contribution

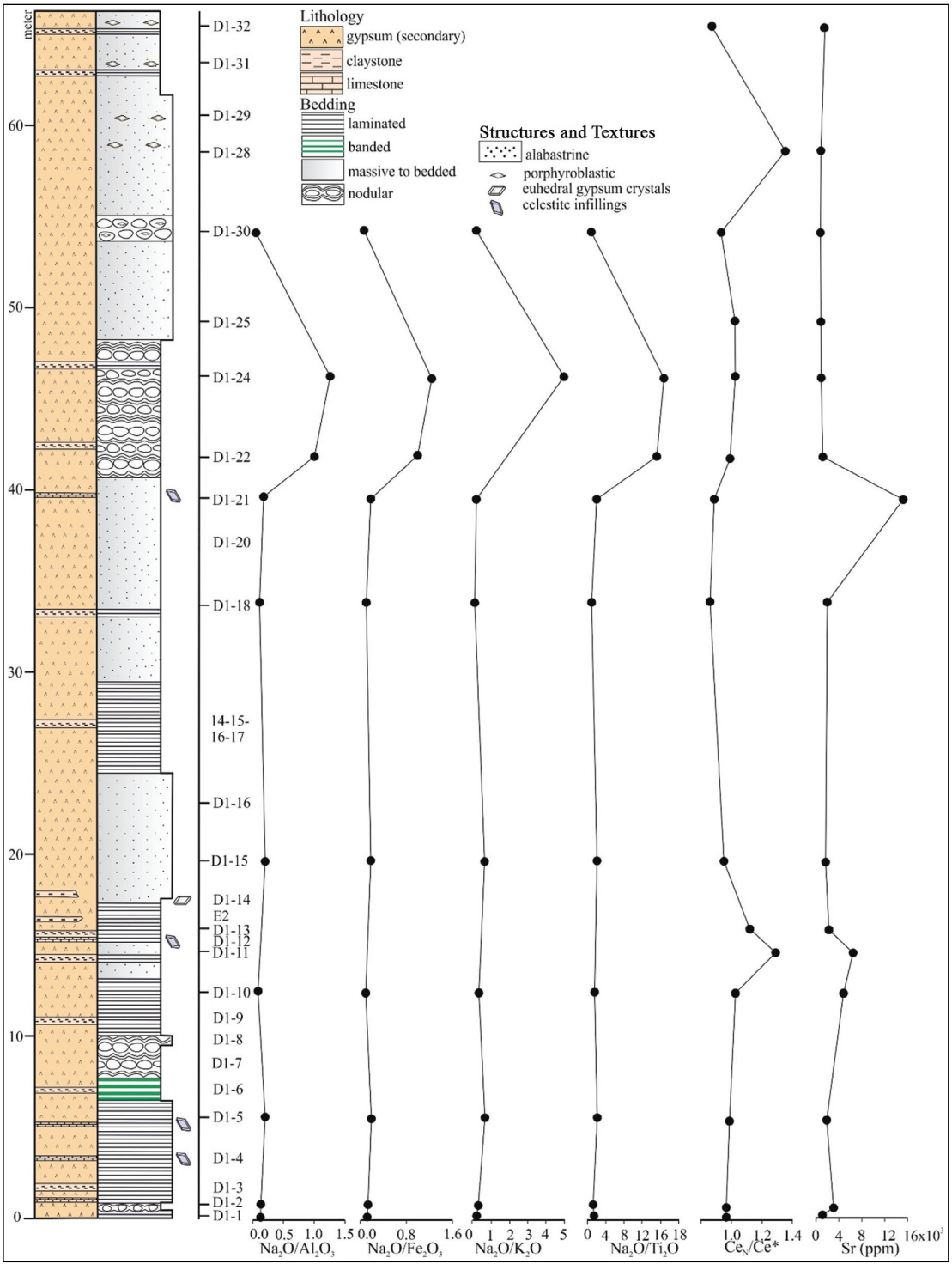

Figure 7- Chemostratigraphic characteristics of the Aşkale evaporites in the Pırnakapan section.

to evaporitic fluids in the paleo - environment of deposition, or else may indicate that seawater was very shallow during evaporite formation; in other words, in an area close to land rather than in the open sea (Bahadori et al., 2011). Additionally, it is noteworthy that despite textural differences in the Aşkale evaporites and the greater abundance of anhydrite, the above - mentioned oxide ratios do not show significant variations (Figure 7). Similarly, Sr contents are significantly higher in stratigraphic horizons with carbonate precipitation, clastic material input, and / or those associated with celestite precipitation.

5.3. Isotopic Characteristics

Sulfur isotope geochemistry and isotopic fractionation patterns can reveal valuable information about the sources of sulfur in a sediment, the mechanisms of sulfate reduction, and the kinetics of formation of sulfate minerals. The present - day seawater $\delta^{34}S$ composition is around 21 ‰ (Rees et al., 1978, Ohmoto, 1986), but this value lies somewhere between 10 ‰ and 30 ‰ for ancient marine evaporites (Garrels and Lerman, 1984).

In modern oceans, the $\delta^{34}S$ value of dissolved sulfate is 19.3 - 21.12 ‰ (Playà et al., 2007). When $\delta^{34}S$ fractionation between gypsum and water is below a mean value of 1.65 ‰ (Playà et al., 2007), fluids that could have formed the Aşkale gypsum and anhydrite would have had a mean $\delta^{34}S_{CDT}$ of 23.22 ‰, which matches normal marine values. While $\delta^{34}S$ ratios are not distinctive enough to be used to distinguish marine and non - marine evaporites in the geological record, the comparison of the frequency distribution of $\delta^{34}S_{CDT}$ values for marine and non - marine evaporites across Turkey (Palmer et al., 2004) with $\delta^{34}S_{CDT}$ values from the Aşkale evaporite samples (Figure 8) suggests that the latter resemble marine evaporites. When $\delta^{34}S_{CDT}$ values obtained from the Aşkale evaporites are compared with $\delta^{34}S$ values from Tertiary marine sulfates forming in other Messinian basins (Lu and Meyers, 2003; Playà et al., 2007; Tekin et al., 2010), they also appear to be similar. For example, the $\delta^{34}S$ values of marine sulfates in the İskenderun - Hatay (Turkey) basin are 20.7 - 25.1 ‰ (Tekin et al., 2010) and are 21.8 - 22.5 ‰ for those in the Gulf of Carpentaria, Australia, (Playà et al., 2007).

Figure 8 compares the frequency distribution of $\delta^{18}O$ values from marine and non - marine evaporites in Turkey (Palmer et al., 2004) with the frequency distribution of $\delta^{18}O$ values for the Aşkale evaporites. Though the Aşkale evaporites resemble both groups, they overlap with marine evaporites. The $\delta^{18}O$ values of sulfate - rich samples do not correlate well with age, as the $\delta^{18}O$ values of sulfate minerals in marine evaporites rise and fall during natural geological processes. For example, $\delta^{18}O$ values were ~17 ‰ in the Precambrian, ~10 ‰ in the Permian, ~16 ‰ in the Triassic, and ~12 - 13 ‰ in the Cenozoic period (Claypool et al., 1980). Considered together, the $\delta^{18}O$ isotopic composition of the Early - Miocene Aşkale evaporites is like that of marine evaporites.

The frequency distribution of Sr isotope values for marine (mean $\Delta_{SW} = -190.2$) and non - marine (mean $\Delta_{SW} = -92$) evaporites of Turkey (Palmer et al., 2004) are shown together with $^{87}Sr / ^{86}Sr$ distributions in Figure 8. Additionally, when the mean $^{87}Sr / ^{86}Sr$ found by Palmer et al. (2004) is considered, marine evaporites have $\Delta_{SW} = -190.2$ (n = 16) and non - marine evaporites have $\Delta_{SW} = -92$ (n = 21). It is not possible to say from these data that $^{87}Sr / ^{86}Sr$ ratios can effectively distinguish between marine and non - marine evaporites; however, the $^{87}Sr / ^{86}Sr$ ratios of the Aşkale evaporites ($\Delta_{SW} = -169.8$ to -99.9) are lower than those of Messinian seawater ($^{87}Sr / ^{86}Sr$ = 0.708825 - 0.708954 and $\Delta_{SW} = -34.8$ to -21.9; Burke et al., 1982; Müller and Mueller, 1991). The $^{87}Sr / ^{86}Sr$ ratio of modern seawater is much higher than the values for the Aşkale evaporites (0.709173 - 0.70920: Denison et al., 1998; Playà et al., 2007). As such, the Aşkale evaporite samples isotopically resemble Messinian seawater, but their lower $^{87}Sr / ^{86}Sr$ values emphasize that continental fluid input and variations in Sr isotopic composition were likely important during the accumulation of Ca - sulfate. The $\delta^{34}S_{CDT}$ and $\delta^{18}O$ isotope values measured in anhydrite and gypsum match those of marine environments, which have 21.3 - 25.62 ‰ and 11.5 - 19.1 ‰, respectively. Similar $^{87}Sr / ^{86}Sr$ and $\delta^{18}O$ values have been reported from other evaporitic basins by Müller (1962), Turekian (1964), Emery and Robinson (1992), Faure and Powell (1972), and Tekin (2001).

As sulfur isotopes cannot identify the source of evaporate - forming fluids, Sr isotopes should be used to provide more reliable constraints on the paleo - environmental conditions (Denison et al., 1998; Playà et al., 2000). On a plot of $\delta^{34}S_{CDT}$ against $^{87}Sr / ^{86}Sr$

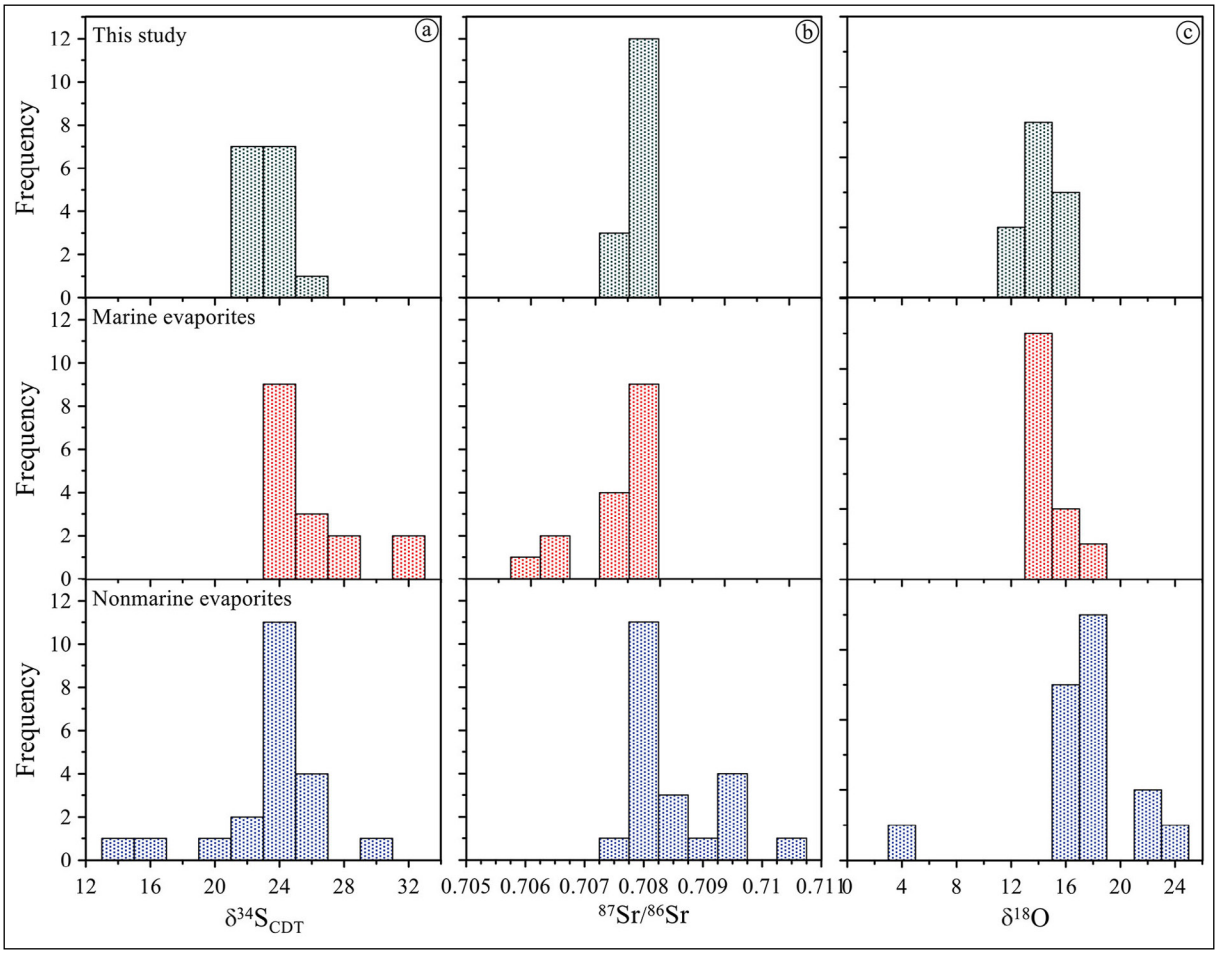

Figure 8- a - c) Histograms showing the distribution of $\delta^{34}S_{CDT}$, ^{87}Sr / ^{86}Sr, and $\delta^{18}O$ values in gypsum and anhydrite from the Aşkale evaporates, compared to those of non-marine and marine evaporites in Turkey (Palmer et al., 2004).

(Figure 9a), Aşkale evaporite samples (apart from nodular gypsum sample A1) have slightly higher ^{87}Sr / ^{86}Sr values than Cenozoic marine evaporites in Turkey. This may be due to the Aşkale evaporites forming in an isolated marine environment (salina: Denison et al., 1988), as shown by Sr isotope ratios, rather than in an open - marine environment, as accepted for the primary formation. On a plot of $\delta^{34}S_{CDT}$ against $\delta^{18}O$ (Figure 9b), the Aşkale gypsum and anhydrite samples have values that overlap with those of marine evaporites (Palmer et al., 2004). Additionally, the positive correlation between $\delta^{34}S_{CDT}$ and $\delta^{18}O$ for the Aşkale gypsum and anhydrite samples (Figure 9b) display similarities with those of sulfate samples precipitated in marine evaporative basins around Mediterranean region (Lu and Meyers, 2003). Obtained $\delta^{34}S_{CDT}$ and $\delta^{18}O$ values have a wide isotope ranges suggesting either a nonmarine contribution or an effective geochemical process to shift isotopic values. These geochemical processes were discussed in detail for the Upper Miocene evaporites from Spain by Lu and Meyers (2003) and summarized as redox reactions or reservoir effects in marine environment. In case of redox processes, dissolved sulfates undergo partial bacterial reduction to sulfides during or before gypsum precipitation and, $\delta^{34}S$ and $\delta^{18}O$ will have relatively higher values in the dissolved sulfate and lower values in sulfides due to preference of light isotopes by sulfate reducing bacteria (Mizutani and Rafter, 1969). Exposing to free oxygen, sulfide would be reoxidized to sulfate. Lu and Meyers (1997) indicate limitations of redox reactions but also imply that these cycling processes led to significantly elevated and variable $\delta^{34}S$ and $\delta^{18}O$. From this perspective, the elevated $\delta^{34}S_{CDT}$ and $\delta^{18}O$ values of the Aşkale gypsum and anhydrite samples may be caused by the reduction and oxidation reactions of sulfides.

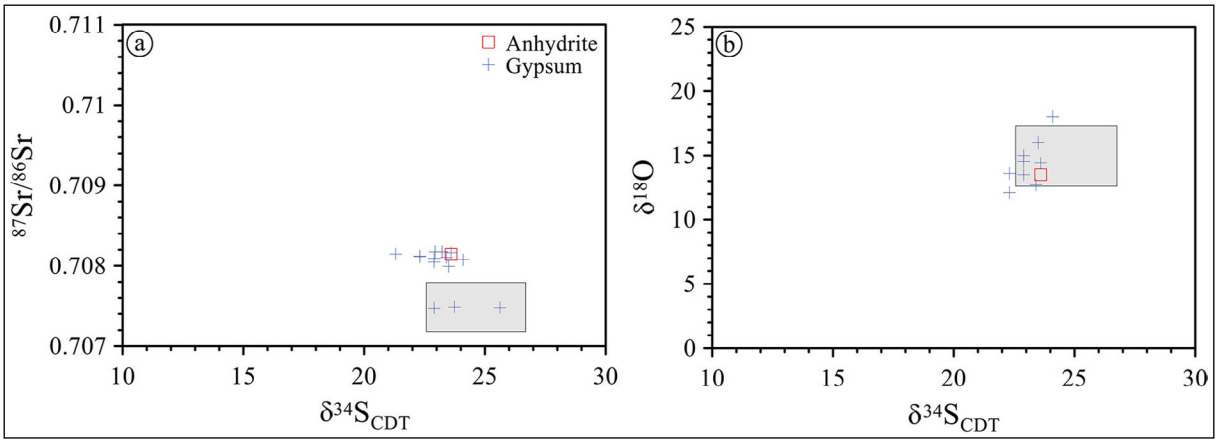

Figure 9- Plots of a) $\delta^{34}S_{CDT}$ versus ^{87}Sr / ^{86}Sr, and b) $\delta^{34}S_{CDT}$ versus $\delta^{18}O$ for the Aşkale evaporites. Gray field refers to gypsum and anhydrite compositions from the Cenozoic marine evaporites in Turkey (Palmer et al., 2004).

Assessing the seawater isotopic composition together with Sr and sulfur isotope results provides important information about the geological history of the Aşkale evaporite sequence. Secular variation in ^{87}Sr / ^{86}Sr and $\delta^{34}S$ (Paytan et al., 1998; McArthur et al., 2001) is shown in Figure 10, and stratigraphic data thus constrain the age of the Aşkale evaporites to be Early Miocene (Tarhan et al., 1992). Based on this interpretation, the mean age for Sr and sulfur isotope data is 19.5 Ma, which lies within the Lower Miocene. As anhydrite ^{87}Sr / ^{86}Sr values do not vary as a result of deformation and recrystallization (Dejonghe et al., 1998), the seawater isotopic composition can be interpreted to have been similar (albeit slightly higher) during deposition of the Aşkale evaporite samples (Figure 10). Additionally, Sr, S, and O isotopic values of the Aşkale evaporites imply formation in a typical marine environment, as $\delta^{34}S$ and $\delta^{18}O$ values for sulfate minerals precipitating from seawater today are around 20.0 ‰ and 9.50 ‰ (Longinelli, 1989), respectively. Fractionation factors associated with precipitation (1.65 ‰ for S and 3.5 ‰ for O: Lloyd, 1968; Thode and Monster, 1965; Céndon et al., 2004) account for this small difference between predicted and measured values. The similarity of isotopic values within the basin show that the Aşkale evaporites are entirely of marine origin, and match values reported for marine evaporites by Claypool et al. (1980).

6. Conclusions

1) Whole - rock major - , trace - , and rare earth - element contents, and ^{87}Sr / ^{86}Sr, $\delta^{34}S$ and $\delta^{18}O$ isotopic data were determined for a suite of Aşkale evaporites. These data reveal that evaporites from different lithofacies show some input of continental

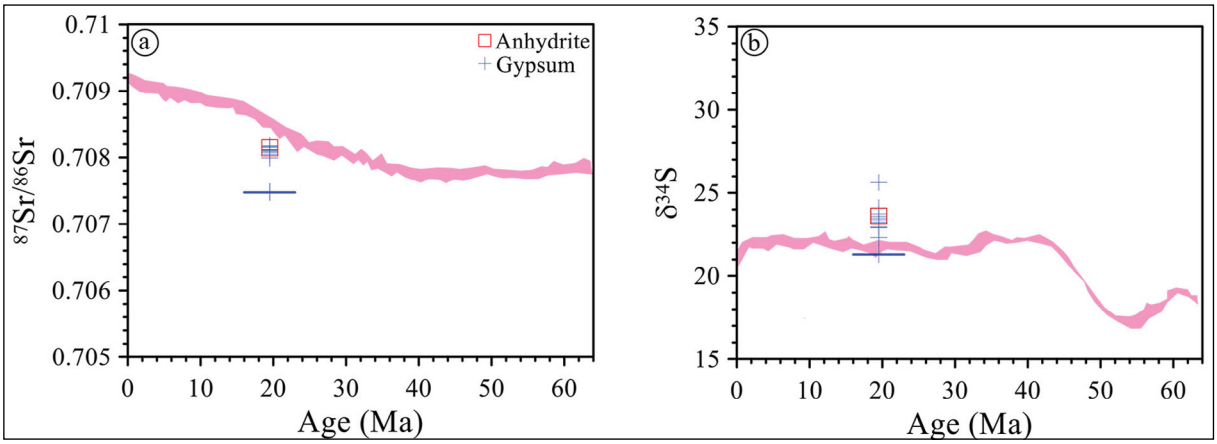

Figure 10- Plots of age (Ma) versus a) ^{87}Sr / ^{86}Sr and b) $\delta^{34}S$ for the Aşkale evaporites. Shaded fields indicate seawater ^{87}Sr / ^{86}Sr (McArthur, 2001) and $\delta^{34}S$ (Paytan et al., 1998) compositions.

detritic material, as indicated by enrichments in light REEs, variable Ce / Ce* ratios, and Ni, Cu, Co, Fe, and Mg contents.

2) In the Aşkale evaporites, strong negative and positive Eu anomalies that are independent of lithofacies transitions in these evaporites record periods of deepening and shallowing of the paleo - environment of deposition, linked to climatic and tectonic activity and the presence of occasional freshwater input. The Sr content of evaporites indicates the importance of marine - sourced Sr; however, especially high Sr contents are associated with the formation of epigenetic celestite and minor volcanic input.

3) ^{87}Sr / ^{86}Sr isotopic ratios, and $\delta^{34}S_{CDT}$ and $\delta^{18}O$ values for the Aşkale gypsum - and anhydrite - samples indicate that these evaporites formed in a marine environment.

4) Examination of the geochemical characteristics of the Aşkale evaporites according to stratigraphic height and vertical lithofacies variations shows that they developed in subtropical conditions, most likely in a shallow platform or lagoonal environment that experienced multiple transgressions.

Acknowledgments

This study was funded by the Turkish Scientific Research Council (TÜBİTAK - ÇAYDAG project no: 110Y023). The authors are grateful to the editor in chief H. Mutlu, reviwers Z.S. Karakaş and O. Ersoy for their constructive comments to improve the paper.

References

Abdioğlu, E., Arslan, M., Gündoğan, İ., Helvacı, C. 2013. Aşkale (Erzurum) Civarındaki Evaporitlerin Mineralojik, Jeokimyasal ve İzotopik Özellikleri, KD Türkiye. TÜBİTAK Projesi, Proje no: 110Y023.

Abdioğlu, E., Arslan, M., Aydınçakır, D., Gündoğan, İ., Helvacı, C. 2015. Stratigraphy, mineralogy and depositional environment of the evaporite unit in the Aşkale (Erzurum) sub - basin, Eastern Anatolia (Turkey). Journal of African Earth Sciences 111, 100-112.

Adabi, M. H. 2004. Sedimentary Geochemistry. Arianzamin Publication, Iran.

Alptekin, Ö. 1973. Focal Mechanism of Earthquakes in Western Turkey and Their Tectonic Implications. PhD Thesis, New Mexico Institute of Mining and Technology, Socorro, USA.

Aydınçakır, D. 2013. Pırnakapan (Aşkale, Erzurum) civarındaki evaporitlerin mineralojik, petrografik ve jeokimyasal incelenmesi. Karadeniz Teknik Üniversitesi, Fen Bilimleri Enstitüsü, Yüksek Lisans Tezi.

Bahadori, A., Carranza, E. J. M., Soleimani, B. 2011. Geochemical analysis of evaporite sedimentation in Gachsaran Formation, Zeloi oil field, southwest Iran. Journal of Geochemical Exploration 111, 97-112.

Baysal, O., Ataman, G. 1980. Sedimentology, mineralogy and geochemistry of a sulphate series (Sivas - Turkey). Sedimentary Geology 25, 67-81.

Brinkmann, R. 1976. Geology of Turkey. Elsevier, Amsterdam.

Burke, W. H., Denison, R. E., Hetherington, E. A., Koepnik, R. B., Nelson, H. F., Otto, J. B. 1982. Variation of seawater ^{87}Sr / ^{86}Sr throughout Phanerozoic time. Geology 10, 516-519.

Cendón, D. I., Chivas, A. R., García, A. 2004. Chemistry of the rivers in the Gulf of Carpentaria drainage division and possible correlations with the sedimentary record during lake phases. 17th Australian Geological Convention. Dynamic Earth: Past, Present and Future. Hobart, Australia, 73, 228.

Claypool, G. E., Holser, W. T., Kaplan, I. R., Sakai, H., Zak, I. 1980. The age curves of sulfur and oxygen isotopes in marine sulfate and their mutual interpretation. Chemical Geology 28, 199-260.

Crockford, P. W., Kunzmann, M., Bekker, A., Hayles, J., Bao, H., Halverson, G. P., Peng, Y., Bui, T. H., Cox, G. M., Gibson, T. M., Wörndle, S., Rainbird, R., Lepland, A., Swanson - Hysell, N. L., Master, S., Sreenivas, B., Kuznetsov, A., Krupenik, V., Wing, B. A. 2019. Claypool continued: Extending the isotopic record of sedimentary sulfate. Chemical Geology 513, 200-225.

Çiner, A., Koşun, E., Deynoux, M. 2002. Fluvial, evaporitic and shallow-marine facies architecture, depositional evolution and cyclicity in the Sivas Basin (Lower to Middle Miocene), Central Turkey. Journal of Asian Earth Sciences 21, 147-165.

Dejonghe, L., Demaiffe, D., Weis, D. 1998. Strontium isotope geochemistry of anhydrites and calcite pseudomorphs after anhydrite from Paleozoic

formations in Belgium. Chemical Geology 144, 63-71.

Denison, R. E., Kırkland, D. W., Ewans, R. 1998. Using strontium isotopes to determine the age and origin of anhydrite and gypsum beds. The Journal of Geology 106, 1-7.

Emelyanov, E. M., Shimkus, K. M. 1986. Geochemistry and Sedimentology of the Mediterranean Sea. Springer, Paris.

Emery, D., Robinson, A. 1992. Inorganic Geochemistry Applications to Petroleum Geology. Blackwell Scientific Publications, Oxford.

Faure, G., Powell, J. L. 1972. Strontium Isotope Geology. Springer-Verlag, New York.

Gallet, S., Jahn, B. M., Torii, M. 1996. Geochemical characterization of the Luochuan loesspaleosol sequence, China, and paleoclimatic implications. Chemical Geology 133, 67-88.

Garrels, R. M., Lerman, A. 1984. Coupling of the sedimentary sulfur and carbon cycles; an improved model. American Journal of Science 284, 989-1007.

Gökçe, A., Ceyhan, F. 1988. Sivas güneydoğusundaki Miyosen yaşlı jipsli çökellerin stratigrafisi, yapısal özellikleri ve oluşumu. Cumhuriyet Earth Science Journal 5, 1, 91-113 (in Turkish).

Gündoğan, İ. 2000. Geology, Mineralogy-Petrography and Economic Potential of the Upper Miocene Evaporites in The Beypazarı and Çankırı - Çorum Basins. PhD Thesis, The Graduate School of Natural and Applied Sciences, DEU.

Gündoğan, İ., Önal, M., Depçi, T. 2005. Sedimentology, petrography and diagenesis of Eocene - Oligocene evaporites: the Tuzhisar Formation, SW Sivas Basin, Turkey. Journal of Asian Earth Sciences 25, 791-803.

Gündoğan, İ., Helvacı, C., Sözbilir, H. 2008. Gypsiferious carbonates at Honaz Dağı (Denizli): First documentation of Triassic gypsum in western Turkey and its tectonic significance. Journal of Asian Earth Sciences 32, 49-65.

Hasselöv, M., Lyvén, D., Haraldsson, C., Sirinawin, W. 1999. Determation of continous size and trace element distribution of field-flow fractionation with ICPMS. Analytical Chemistry 71, 3497-3502.

Helvacı, C. Yağmurlu, F. 1995. Geological setting and economic potential of the lignite and evaporite-bearing Neogene basins of Western Anatolia, Turkey. Israel Journal of Earth Sciences 44, 91-105.

Horner, T. J., Pryer, H. V., Nielsen, S. G., Crockford, P. W., Gauglitz, J. M., Wing, B. A., Ricketts, R. D. 2017. Pelagic barite precipitation at micromolar ambient sulfate, Nature Communications 8, Article number: 1342.

Kamber, B. S., Greig, A., Collerson, K. D. 2005. A new estimate for the composition of weathered young upper contitnental crust from alluvial sediments, Queensland, Australia. Geochimica et Cosmochimica Acta 69, 4, 1041-1058.

Kasprzyk, A. 2003. Sedimentological and diagenetic patterns of anhydrite deposits in the Badenian evaporite basin of the Carpathian Foredeep, southern Poland. Sedimentary Geology 158, 167-194.

Keskin, M. 2003. Magma generation by slab steepening and breakoff beneath a subduction-accretion complex: An alternative model for collision-related volcanism in Eastern Anatolia, Turkey. Geophysical Research Letters 30, 24, 1-4.

Ketin, İ. 1966. Tectonic units of Anatolia (Asia Minor). Bulletin of the Mineral Research and Exploration 66, 23-34.

Kornexl, B. E., Gehre, M., Höfling, R., Werner, R. A. 1999. On-line $\delta^{18}O$ Measurement of organic and inorganic substances. Rapid Communications in Mass Spectrometry 13, 1685-1693.

Krauskopf, K. B. 1979. Introduction to Geochemistry. McGraw-Hill Book Company, New York.

Kushnir, J. 1980. The coprecipitation of strontium, magnesium, sodium, potassium, and chloride ions with gypsum: an experimental study. Geochimica et Cosmochimica Acta 44, 1471-1482.

Kushnir, J. 1982. The partitioning of seawater cations during the transformation of gypsum to anhydrite. Geochimica et Cosmochimica Acta 46, 433-446.

Lloyd, R. M. 1968. Oxygen isotope behavior in the sulphate-water system. Journal of Geophysical Research 73, 6099-6110.

Longinelli, A. 1989. Oxygen-18 and sulphur-34 in dissolved oceanic sulphate and phospate. In: Fritz, P., Fontes, J.C. (Eds.), Handbook of Environmental Isotope Geochemistry. The Marine environment. Elseiver, Amsterdam, 219-255.

Lu, F. H., Meyers, W. J. 1997. Sr, S, O_{SO4} isotopes and quantitative models of Messinian gypsum, the Nijar Basin, Spain (Abstract). International Applied Isotope Geochemistry (AIG-2) Conference, Calgary.

Lu, F. H., Meyers, W.J. 2003. ^{87}Sr / ^{86}Sr, $\delta^{34}S$ and $\delta^{18}O$ (SO_4) isotopes of Messinian evaporites, modeling and environmental significance. Journal of Sedimentary Research 73, 443-449.

Ludden, J. N., Thompson, G. 1979. An evaluation of the behaviour of the REE elements during the weathering of seafloor basalt. Earth and Planetary Science Letters, 43, 85-92.

Mason, B., Moore, C. B. 1982. Principles of Geochemistry. Wiley, New York.

McArthur, J. M., Howarth, R. J., Bailey, T. R. 2001. Strontium isotope stratigraphy: LOWESS version 3: best fit to the marine Sr - isotope curve for 0 - 509 Ma and accompanying look-up table for deriving numerical age. The Journal of Geology 109, 155-170.

McKenzi, D. P. 1976. The East Anatolian Fault: a major structure in Eastern Turkey. Earth and Planetary Science Letters 29, 189-193.

Menzies, M., Seyfried, W., Blanchard, D. 1979. Experimental evidence of rare earth element immobility in Greenstones. Nature 282, 398-399.

Mizutani, Y., Rafter, T.A. 1969. Oxygen isotopic composition of sulfates, 4. Bacterial fractionation of oxygen isotopes in the reduction of sulphate and in the oxidation of sulphur: New Zealand. Journal of Science, 12, 60-68.

Müller, D. W., Mueller, P.A. 1991. Origin and age of the Mediterranean Messinian evaporites; implications from Sr isotopes. Earth and Planetary Science Letters 107, 1-12.

Müller, G. 1962. Zur Geochemie des Strontiums in Ozeanen evaporites unter besonderer Berücksichtigung der sedimentaren Coelestin lagerstatte von Hemmelte-West (Süd Oldenburg). Geologie 11, 1-90.

Nesbitt, H. W., Young, G. M. 1982. Early Proterozoic climates and plate motions inferred from major element chemistry of lutites. Nature 299, 715-717.

Ohmoto, H. 1986. Stable isotope geochemistry of ore deposits. In: Valley, J. W., Taylor J.R., H.P., O'Neil, J.R. (Eds.), Stable Isotopes in High Temperature Geological Processes. Reviews in Mineralogy, Mineralogical Society of America, 16, 491-560.

Okay, A. I., Tüysüz, O. 1999. Tethyan sutures of northern Turkey. In: Durand, B., Jolivet, L., Horváth, F., Séranne M. (Eds.), The Mediterranean Basins: Tertiary Extension within the Alpine Orogen. Geological Society, London, Special Publications 156, 475-515.

Ortí, F., Rosell, L. 2000. Evaporative systems and diagenetic patterns in the Calatayud Basin (Miocene, central Spain). Sedimentology 47, 665-685.

Ortí, F., Gündoğan, İ., Helvacı, C. 2002. Sodium sulphate deposit of Neogene age: the Kirmir Formation, Beypazarı Basin, Turkey. Sedimentary Geology 146, 305-333.

Ortí, F., Rosell, L., Ingles, M., Playà, E. 2007. Depositional models of lacustrine evaporates in the SE margin of the Ebro Basin (Paleogene) NE Spain. Geologica Acta 5, 19-34.

Palmer, M. R., Helvacı, C., Fallick, A. E. 2004. Sulphur, sulphate, oxygen and strontium isotope composition of Cenozoic Turkish evaporates. Chemical Geology 209, 341-356.

Pandarinath, K., Prasad, S., Gupta, S. K. 1999. A 75 ka record of palaeoclimatic changes inferred from crystallinity of illite from Nal Sarovar, Western India. Journal of the Geological Society of India 54, 515-522.

Paytan, A., Kastner, M., Campbell, D., Thiemens, M.H. 1998. Sulphur isotopic composition of Cenozoic seawater sulphate. Science 282, 1459-1462.

Playà, E., Ortí, F., Rosell, L. 2000. Marine to non-marine sedimentation in the Upper Miocene evaporites of the Eastern Betics, SE Spain: sedimentological and geochemical evidence. Sedimentary Geology 133, 135-1666.

Playà, E., Cendon, D. I., Trave, A., Chivas, A. R., Garcia, A. 2007. Using multiple geochemical proxies to trace origin of gypsum (Gulf of Carpentaria, Australia, -70ka). Geogaceta 42, 135-138.

Rees, C. E., Jekins, W.E., Monster, J. 1978. The sulphur isotopic composition of ocean water sulphate. Geochimica et Cosmochimica Acta 42, 377-381.

Rosell, L., Orti, F., Kasprzyk, A., Playa, E., Peryt, T. M. 1998. Strontium geochemistry of Miocene primary gypsum; Messinian of southeastern Spain and Sicily and Badenian of Poland. Journal of Sedimentary Research 68, 63-79.

Roy, P. D., Smykatz-Kloss, W., Sinha, R. 2006. Late Holocene geochemical history inferred from Sambhar and Didwana playa sediments, Thar Desert, India: comparison and synthesis. Quaternary International 144, 84-98.

Roy, P. D., Nagar, Y. C., Juyal, N., Smykatz-Kloss, W., Singhvi, A. K. 2009. Geochemical signatures of Late Holocene paleo - hydrological changes from Phulera and Pokharan saline playas near the eastern and western margins of the Thar Desert,

India. Journal of Asian Earth Sciences 34, 275 - 286.

Rushdi, A. I., McManus, J., Collier, R. W. 2000. Marine barite and celestite saturation in seawater. Marine Chemistry 69, 19-31.

Sancay, R. E. 2005. Palynostratigraphic and Palynofacies Investigation of the Oligocene - Miocene Units in the Kars - Erzurum - Muş Sub-Basins (Eastern Anatolia). PhD Thesis, Middle East Technical University.

Smykatz-Kloss, W., Roy, P. D. 2010. Evaporite mineralogy and major element geochemistry as tools for paleoclimatic investigations in arid regions: a synthesis. Boletin De La Sociedad Geológica Mexicana 62, 3, 379-390.

Sungurlu, O. 1971. İ45a, İ45b, İ46a, İ46b, İ47a, İ47b, paftalarına ait 1 / 50000'lik jeoloji haritaları. TPAO, Ankara.

Sverjensky, D. A. 1984. Europium Redox Equilibria in Aqueous Solution. Earth and Planetary Science Letters 67, 70-78.

Şahintürk, Ö. 1992. Tercan - Çayırlı Basenleri'nin jeolojisi ve hidrokarbon olanakları, TPAO Arama Grubu Rap. No. 3070, Ankara (in Turkish, unpublished).

Şahintürk, Ö., Kasar, S. 1980. Tercan - Çayırlı Baseninin Jeolojisi ve Hidrokarbon Olanakları (Geology and Hydrocarbon Potential of the Tercan-Çayırlı Basin). TPAO Arama Grubu Raporu, no. 1446 (in Turkish, unpublished).

Şahintürk, Ö., Şaroğlu, F., Çaptuğ, A., Temel, Ö., İlleez, H. İ., Tekin, T. 1997. Ağrı Yöresinin Jeolojisi ve Hidrokarbon Olanakları (Geology and Hydrocarbon Potential of the Ağrı Area). TPAO Arama Grubu Rapor No. 3790, Ankara (in Turkish, unpublished).

Şengör, A .M. C. 1980. Türkiye'nin Neotektoniğinin Esasları (Fundamentals of the Neotectonics of Turkey). Publication of Geological Society of Turkey, 2, Ankara (in Turkish).

Şengör, A. M. C., Özeren, S., Zor, E., Genç, T. 2003. East Anatolian high plateau as a mantle-supported, N-S shortened domal structure. Geophysical Research Letters 30, 8044.

Tarhan, N., Deveciler, E., Karabalık, N. N., Akdoğan, E., Çolak, T., Kar, H. 1992. Aşkale - Çat (Erzurum) Dolayının Jeolojisi (Geology of the Aşkale - Çat (Erzurum) area). Maden Tetkik ve Arama Genel Müdürlüğü, Ankara (in Turkish, unpublished).

Tchalenko, J. S. 1977. A reconnaissance of the seismicity and tectonics of the northern border of the Arabian plate (Lake Van Region). Revule de Geographie Physique et de Geologie Dynamiqu 19, 2, 189-208.

Tekin, E. 2001. Stratigraphy, Geochemistry and Depositional Environment of the Celestine - bearing gypsiferous Formations of the Tertiary Ulaş - Sivas Basin, East - Central Anatolia (Turkey). Turkish Journal of Earth Sciences 10, 35-49.

Tekin, E., Varol, B., Ayyıldız, T. 2010. Sedimentology and paleoenvironmental evolution of Messinian evaporates in the İskenderun - Hatay basin complex, Southern Turkey. Sedimentary Geology 229, 4, 282-298.

Tekin, T., Alişan, C., Işık, U., Akça, N., Aras, M., Günal, B. 2000. Aşkale-1 Kuyusu Sonuç Raporu (The Aşkale-1 Final Well Report) TPAO Araştırma Grubu Rapor no: 2514, Ankara (in Turkish, unpublished).

Thode, H. G., Monster, J. 1965. Sulphur isotope geochemistry of petroleum, evaporites and ancient seas. In: Young, A., Galley, J.E. (Ed.), Fluids in Subsurface Environments. American Association of Petroleum Geologists, Tulsa, Oklahoma, USA, 4, 367-377.

Toulkeridis, T., Podwojewski, P., Clauer, N. 1998. Tracing the source of gypsum in New Caledonian soils by REE contents and S - Sr isotopic compositions. Chemical Geology 145, 61-71.

Turekian, K. K. 1964. The marine geochemistry of strontium. Geochimica et Cosmochimica Acta 28, 1479-1496.

Türkmen, İ. 2004. Facies and evaporite genesis of the Kuşçular Formation (Lower Paleocene) saline playa complex, Eastern Turkey. Journal of Asian Earth Science 24, 91-104.

Ueda, A., Krouse, H.R. 1986. Direct Conversion of Sulphide and Sulphate Minerals to SO_2 for Isotope Analysis. Geochemical Journal 20, 209-212.

Usdowski, E. 1967. Der Einbau von Sr in Gips und Anhydrit. Ann. Meet. Deutsche Mineral. Gesell., Berlin.

Warren, J. K. 2010. Evaporites through time: Tectonic, climatic and eustatic controls in marine and nonmarine deposits. Earth Science Reviews 98, 217-268.

Warren, J. K., Kendall, C.G.St.C. 1985. Comparison of marine sabkhas (subaerial) and salina (subaqueous) evaporites: modern and ancient. AAPG Bulletin 69, 1013-1023.

Yeşilova, Ç., Helvacı, C., Carrillo, E. 2018. Evaporitic sedimentation in the Southeastern Anatolian

Foreland Basin: New insights on the Neotethys closure. Sedimentary Geology 369, 13-27.

Yılmaz, Y. 1993. New evidence and model on the evaluation of the southeast Anatolian orogen. Geological Society of America Bulletin 105, 251-271.

Zeybek, B. 2007. Geochemical Studies of Porsuk Formation (Pliocene) Evaporites, Middle Sakarya Region, Central Anatolia, Turkey. MSc thesis, The Graduate School of Natural and Applied Sciences, Ankara University (in Turkish).

Supplementary Table 1- Major (wt%) and trace element (ppm) compositions of the Aşkale evaporites.

	D1-1	D1-2	D1-5	D1-10	D1-11	D1-13	D1-15	D1-18	D1-25	D1-28	D1-30	D1-22	D1-24	D1-21
	The Pırnakapan Section													
	gypsum-rich samples											*anhydrite-rich samples*		*limestone*
SiO_2 wt. %	2.23	1.52	0.81	0.88	0.21	0.43	1.78	1.56	0.05	0.03	1.55	0.13	0.18	2.38
Al_2O_3	0.56	0.36	0.18	0.11	0.03	0.04	0.19	0.37	0.01	< 0.01	0.28	0.03	0.06	0.62
$Fe_2O_3^*$	0.25	0.18	0.1	0.12	0.02	0.04	0.11	0.18	0.02	0.01	0.17	0.03	0.04	0.28
MnO	0.004	0.003	0.002	0.008	0.002	0.002	0.004	0.006	0.002	0.002	0.007	0.002	0.003	0.009
MgO	0.36	0.34	0.21	2.55	0.09	0.04	1.38	1.05	0.02	0.04	0.36	0.03	0.05	0.59
CaO	30.92	30.69	31.99	29.8	31.99	32.3	30.42	30.06	32.98	32.68	32.25	41.85	40.23	48.14
Na_2O	0.03	0.02	0.02	0.01	< 0.01	< 0.01	0.02	0.02	< 0.01	< 0.01	0.01	0.03	0.05	0.05
K_2O	0.19	0.1	0.03	0.03	< 0.01	< 0.01	0.03	0.17	< 0.01	< 0.01	0.07	< 0.01	0.01	0.29
TiO_2	0.029	0.019	0.009	0.006	0.002	0.002	0.009	0.019	< 0.001	< 0.001	0.013	0.002	0.003	0.025
P_2O_5	< 0.01	0.01	< 0.01	< 0.01	< 0.01	< 0.01	< 0.01	0.01	< 0.01	< 0.01	< 0.01	0.02	0.02	0.04
LOI	21.82	21.48	21.38	22.82	20.81	20.93	21.56	21.85	20.99	20.76	21.24	3.65	3.38	39.01
Total	56.39	54.73	54.74	56.34	53.18	53.8	55.51	55.29	54.07	53.54	55.97	45.78	44.03	91.43
Cl wt. %	< 0.01	< 0.01	0.01	0.04	< 0.01	< 0.01	< 0.01	< 0.01	< 0.01	< 0.01	< 0.01	0.03	0.03	< 0.01
CO_2	0.37	0.25	0.22	3.64	0.09	0.18	1.52	1.04	0.07	0.14	0.79	0.06	0.28	38.6
SO_4	59.4	60	60.6	56.9	61.7	60.8	58.6	59.5	61	61.8	59.3	75.5	73.6	6.1
Br ppm	< 0.5	< 0.5	< 0.5	1.6	< 0.5	< 0.5	< 0.5	< 0.5	< 0.5	< 0.5	< 0.5	1.5	2.4	< 0.5
B	14.5	9.4	2.4	5.5	3.4	3.7	15	20.3	1.8	4.9	3.1	8.2	17.7	13.8
V	13	11	9	10	7	8	10	10	7	7	9	8	6	17
Ba	16	32	12	47	16	9	49	20	1	1	11	< 1	< 1	91
Sr	1312	2978	1911	4849	6464	2238	1681	1928	806	865	909	1197	1023	15150
Y	0.8	0.7	< 0.5	< 0.5	< 0.5	< 0.5	< 0.5	0.6	< 0.5	< 0.5	< 0.5	< 0.5	< 0.5	1.3
Zr	4.1	3.3	0.9	0.5	1.5	< 0.1	5.8	2.4	< 0.1	< 0.1	1.9	0.4	0.3	4.2
Ga	< 1	< 1	< 1	< 1	< 1	< 1	< 1	< 1	< 1	< 1	< 1	< 1	< 1	< 1
Ge	< 0.5	< 0.5	< 0.5	< 0.5	< 0.5	< 0.5	< 0.5	< 0.5	< 0.5	< 0.5	< 0.5	< 0.5	< 0.5	< 0.5
As	1.7	1	1.6	1.3	0.4	0.5	1.6	1.8	1.2	0.6	1.1	4.9	1.4	2.3
Rb	2.4	1.3	0.2	< 0.1	< 0.1	< 0.1	0.6	1.3	< 0.1	< 0.1	1	0.3	0.2	3.5
Nb	0.8	0.58	0.19	0.11	< 0.01	0.04	0.23	0.21	< 0.01	< 0.01	< 0.01	< 0.01	< 0.01	0.29
Mo	< 2	< 2	< 2	3	< 2	< 2	< 2	< 2	< 2	< 2	< 2	< 2	< 2	< 2
Ag	< 0.002	0.009	< 0.002	0.004	< 0.002	< 0.002	0.003	< 0.002	0.032	0.009	0.012	0.098	0.02	0.004
In	< 0.1	< 0.1	< 0.1	< 0.1	< 0.1	< 0.1	< 0.1	< 0.1	< 0.1	< 0.1	< 0.1	< 0.1	< 0.1	< 0.1
Sn	< 1	< 1	< 1	< 1	< 1	< 1	< 1	< 1	< 1	< 1	< 1	< 1	< 1	< 1
Sb	< 0.2	< 0.2	< 0.2	< 0.2	< 0.2	< 0.2	< 0.2	< 0.2	< 0.2	< 0.2	< 0.2	< 0.2	< 0.2	< 0.2
Cs	< 0.1	< 0.1	< 0.1	< 0.1	< 0.1	< 0.1	< 0.1	< 0.1	< 0.1	< 0.1	< 0.1	< 0.1	< 0.1	0.3
Hf	0.1	< 0.1	< 0.1	< 0.1	< 0.1	< 0.1	< 0.1	< 0.1	< 0.1	< 0.1	< 0.1	< 0.1	< 0.1	< 0.1
Ta	< 0.01	< 0.01	< 0.01	< 0.01	0.02	< 0.01	< 0.01	< 0.01	< 0.01	< 0.01	< 0.01	< 0.01	< 0.01	0.03
W	< 0.5	< 0.5	< 0.5	< 0.5	< 0.5	< 0.5	< 0.5	< 0.5	< 0.5	< 0.5	< 0.5	< 0.5	< 0.5	< 0.5
Tl	< 0.05	< 0.05	< 0.05	< 0.05	< 0.05	< 0.05	< 0.05	< 0.05	< 0.05	< 0.05	< 0.05	< 0.05	< 0.05	< 0.05
Pb	0.63	0.21	0.1	0.17	0.05	0.04	0.44	0.3	0.06	0.04	0.26	0.11	0.05	0.78
Bi	< 0.1	0.2	< 0.1	< 0.1	< 0.1	< 0.1	< 0.1	< 0.1	< 0.1	< 0.1	< 0.1	< 0.1	< 0.1	< 0.1
Th	0.22	0.17	0.06	0.06	0.04	< 0.01	0.1	0.15	< 0.01	< 0.01	0.11	0.06	0.08	0.3
U	0.163	0.183	0.123	0.254	0.095	0.043	0.084	0.225	< 0.005	< 0.005	0.101	0.045	0.058	2.57
Cd	< 0.01	< 0.01	0.01	0.02	< 0.01	< 0.01	0.02	0.01	< 0.01	0.01	< 0.01	< 0.01	< 0.01	0.05
Cr	< 20	< 20	< 20	< 20	< 20	< 20	< 20	< 20	< 20	< 20	< 20	< 20	< 20	< 20
Co	0.8	0.5	0.5	0.7	0.1	0.3	0.6	0.8	0.1	0.1	0.6	0.1	0.1	1.3
Ni	8.9	4.8	4.8	6.8	2.2	3	6.7	8	2.1	1.9	5	1.7	1.5	11.1
Cu	2.08	2.08	1.23	2.26	0.66	1.16	1.33	1.74	3.24	0.54	1.8	0.93	0.56	2.67
Zn	3.5	2.3	1.4	1.7	1	2.9	2	1.8	2.4	1.5	3	1.8	0.9	3.1

Supplementary Table 1- continue.

	D1-32	D2-4	D3-1	D3-2	D3-5	D3-4	D3-6	28	D2-2	K-22	K-25	K-24
	The Pırnakapan Section									The Kemerkaya Section		
	gypsum-rich samples								*claystone*	*gypsum-rich samples*		
SiO_2 wt. %	0.12	0.16	3.92	2	1.54	1.15	0.8	1.81	30.34	0.2	0.05	0.14
Al_2O_3	0.03	0.04	0.94	0.22	0.08	0.02	0.15	0.4	8.99	0.04	< 0.01	0.03
$Fe_2O_3^*$	0.04	0.03	0.42	0.13	0.05	0.02	0.09	0.19	4.85	0.03	0.03	0.02
MnO	0.004	0.003	0.007	0.005	0.002	0.002	0.004	0.003	0.077	0.002	0.002	0.002
MgO	0.02	0.02	1.18	1.7	0.18	0.08	0.28	0.46	2.66	0.04	< 0.01	0.03
CaO	32.39	32.1	30.2	30.98	32.29	32.92	33.13	30.35	21.57	32.52	32.59	32.19
Na_2O	< 0.01	< 0.01	0.13	0.02	0.01	< 0.01	0.01	0.02	0.63	< 0.01	< 0.01	< 0.01
K_2O	< 0.01	< 0.01	0.16	0.04	0.02	< 0.01	0.03	0.08	1.39	< 0.01	< 0.01	< 0.01
TiO_2	0.002	0.002	0.047	0.011	0.004	< 0.001	0.009	0.021	0.493	0.002	< 0.001	0.002
P_2O_5	0.03	< 0.01	0.02	< 0.01	0.02	0.04	0.03	< 0.01	0.09	< 0.01	< 0.01	< 0.01
LOI	20.94	20.66	22.69	21.76	21.45	21.18	21.75	22.46	26.77	21.1	21.13	21.07
Total	53.58	53.04	59.71	56.88	55.65	55.41	56.28	55.79	97.86	53.93	53.80	53.48
Cl wt. %	< 0.01	< 0.01	< 0.01	< 0.01	< 0.01	< 0.01	< 0.01	< 0.01	0.02	< 0.01	< 0.01	< 0.01
CO_2	0.25	0.38	0.59	2.36	0.28	0.08	1.56	0.09	17.9	0.35	0.03	< 0.01
SO_4	56.4	59.8	56	56.4	56.8	57.1	54.3	54.6	2.1	56	58	58
Br	0.02	< 0.5	< 0.5	< 0.5	0.01	0.02	< 0.01	0,01	< 0.5	< 0.5	< 0.5	< 0.5
B	< 0.5	< 0.5	7.6	15.2	< 0.5	< 0.5	< 0.5	< 0.5	74.9	< 0.5	< 0.5	< 0.5
V	< 5	8	15	10	6	< 5	6	9	98	< 5	6	< 5
Ba	6	8	34	41	13	13	68	35	84	5	2	6
Sr	1081	1334	1118	1710	1008	1242	3286	4111	631	771	523	1168
Y	0.7	< 0.5	1.2	< 0.5	1.1	1	1.4	1.5	11.2	0.8	0.8	0.7
Zr	3.4	< 0.1	8.9	2.1	3.5	3.2	3.8	7.9	75.1	4	3.1	3.8
Ga	< 1	< 1	1	< 1	< 1	< 1	< 1	< 1	10	< 1	< 1	< 1
Ge	< 0.5	< 0.5	< 0.5	< 0.5	< 0.5	< 0.5	< 0.5	< 0.5	0.6	< 0.5	< 0.5	< 0.5
As	0.4	0.4	4.5	1.8	0.6	0.3	2.3	1.1	6	0.2	0.2	0.2
Rb	< 0.1	< 0.1	4.6	1.2	< 0.1	< 0.1	< 0.1	1.6	45.2	< 0.1	< 0.1	< 0.1
Nb	< 0.01	< 0.01	0.16	< 0.01	< 0.01	< 0.01	< 0.01	0.2	5.81	0.88	0.57	0.47
Mo	< 2	< 2	< 2	< 2	< 2	< 2	< 2	< 2	3	< 2	< 2	< 2
Ag	< 0.002	0.011	0.005	0.013	< 0.002	0.005	< 0.002	< 0.002	< 0.002	0.004	< 0.002	0.007
In	< 0.1	< 0.1	< 0.1	< 0.1	< 0.1	< 0.1	< 0.1	< 0.1	< 0.1	< 0.1	< 0.1	< 0.1
Sn	< 1	< 1	< 1	< 1	< 1	< 1	< 1	< 1	< 1	< 1	< 1	< 1
Sb	< 0.2	< 0.2	< 0.2	< 0.2	0.5	0.5	0.7	0.3	< 0.2	0.4	0.3	1.5
Cs	< 0.1	< 0.1	0.1	< 0.1	< 0.1	< 0.1	< 0.1	0.1	3.2	< 0.1	< 0.1	< 0.1
Hf	< 0.1	< 0.1	0.2	< 0.1	< 0.1	< 0.1	< 0.1	0.2	1.8	< 0.1	< 0.1	< 0.1
Ta	0.02	< 0.01	< 0.01	< 0.01	0.05	0.06	0.06	0.09	0.47	0.05	0.07	0.04
W	1.6	< 0.5	< 0.5	< 0.5	1.1	1.5	1.7	0.7	< 0.5	1.5	1.5	1.4
Tl	< 0.05	< 0.05	< 0.05	< 0.05	< 0.05	< 0.05	< 0.05	< 0.05	< 0.05	< 0.05	< 0.05	< 0.05
Pb	0.27	0.07	2.12	0.55	0.06	0.09	0.11	0.16	8.89	0.16	0.01	0.05
Bi	< 0.1	< 0.1	< 0.1	< 0.1	< 0.1	< 0.1	< 0.1	< 0.1	< 0.1	0.1	< 0.1	< 0.1
Th	< 0.01	< 0.01	0.88	0.16	0.05	< 0.01	0.09	0.16	3.69	0.08	0.06	0.11
U	0.097	0.094	0.311	0.128	0.052	0.022	0.087	0.18	3.74	0.031	< 0.005	0.024
Cd	0.02	< 0.01	0.03	< 0.01	0.01	0.02	< 0.01	0.01	0.13	0.01	0.02	0.02
Cr	< 20	< 20	20	< 20	< 20	< 20	< 20	< 20	180	< 20	< 20	< 20
Co	0.2	0.2	2.2	0.6	0.2	< 0.1	0.4	0.5	22.1	0.1	< 0.1	0.1
Ni	2.6	2.3	21.4	7.2	2.4	1.6	5	4.3	192	2.4	1.6	2
Cu	0.71	0.87	3.8	1.61	0.73	0.59	1.2	1.25	27.8	0.56	0.68	0.7
Zn	3	0.8	6.8	2.5	1	0.4	1.5	1.9	110	0.7	0.8	0.6

Supplementary Table 1- continue.

	A-1	A-3	A-5	A-6	A-8	A-10	A-11	A-12	A-15	A-16	A-17	A-19	A-20	A-13	A-2
	The Alçıdağ hill section														
	gypsum-rich samples													*marl*	*claystone*
SiO_2 wt. %	0.21	1.45	3.92	0.03	0.26	0.31	0.14	4.07	0.08	0.32	0.02	0.23	0.25	35.25	3.77
Al_2O_3	0.05	0.39	1.05	< 0.01	0.04	0.04	0.04	0.37	0.02	0.07	< 0.01	0.02	0.04	9.54	1.01
$Fe_2O_3^*$	0.04	0.18	0.45	0.01	0.03	0.04	0.03	0.21	0.02	0.05	0.01	0.03	0.03	4.27	0.52
MnO	0.002	0.009	0.008	0.002	0.002	0.002	0.003	0.011	0.002	0.002	0.002	0.002	0.002	0.097	0.043
MgO	0.02	0.74	0.81	0.01	0.11	0.11	0.04	0.9	0.02	0.03	0.02	0.02	0.09	6.26	3.14
CaO	31.86	32	30.83	32.91	33.25	32.65	33.45	31.57	33.37	32.89	33.02	32.7	32.54	13.95	30.31
Na_2O	< 0.01	0.02	0.03	< 0.01	< 0.01	< 0.01	< 0.01	0.03	< 0.01	< 0.01	< 0.01	< 0.01	< 0.01	0.29	0.05
K_2O	0.01	0.11	0.29	< 0.01	0.01	< 0.01	< 0.01	0.08	< 0.01	0.02	< 0.01	< 0.01	0.01	2.06	0.27
TiO_2	0.003	0.017	0.046	< 0.001	0.002	0.002	0.002	0.017	0.001	0.004	< 0.001	0.001	0.002	0.427	0.045
P_2O_5	< 0.01	0.03	0.02	< 0.01	< 0.01	0.02	< 0.01	0.03	< 0.01	0.06	< 0.01	< 0.01	< 0.01	0.14	0.03
LOI	20.94	21.5	21.89	20.91	20.99	21.27	20.87	21.3	20.99	21.46	20.8	20.74	20.81	26.51	24.26
Total	53.16	56.45	59.34	53.89	54.71	54.44	54.59	58.59	54.52	54.91	53.88	53.77	53.78	98.79	63.45
Cl wt. %	< 0.01	< 0.01	< 0.01	< 0.01	< 0.01	< 0.01	< 0.01	< 0.01	< 0.01	< 0.01	< 0.01	< 0.01	< 0.01	0.03	< 0.01
CO_2	0.05	1.63	1.47	0.03	0.12	< 0.01	0.2	1.95	0.07	0.1	0.16	0.26	0.26	13.3	6.84
SO_4	62.4	59.2	56.5	62.5	61.7	56.9	62.1	52.9	61.4	55.8	61.5	61.8	67.3	3.1	46
Br ppm	1.2	< 0.5	1.4	< 0.5	< 0.5	0.01	< 0.5	0.03	< 0.5	0.01	1.7	< 0.5	1.9	0.04	0.03
B	4.2	< 0.5	14.7	1.4	< 0.5	< 0.5	2	1.8	2.1	< 0.5	4.9	3.6	1.3	< 0.5	< 0.5
V	8	11	18	8	9	7	8	9	9	6	7	8	10	110	15
Ba	13	17	31	2	4	3	5	37	3	5	1	2	5	104	53
Sr	1129	1180	1291	1029	1049	949	860	1221	988	329	506	259	1391	915	992
Y	< 0.5	0.7	1.3	< 0.5	< 0.5	< 0.5	< 0.5	1.6	< 0.5	< 0.5	< 0.5	< 0.5	< 0.5	10.3	3.1
Zr	< 0.1	2.9	7.8	< 0.1	0.3	3.1	< 0.1	5	< 0.1	3.2	< 0.1	< 0.1	< 0.1	63.8	8.7
Ga	< 1	< 1	1	< 1	< 1	< 1	< 1	< 1	< 1	< 1	< 1	< 1	< 1	9	< 1
Ge	< 0.5	< 0.5	< 0.5	< 0.5	< 0.5	< 0.5	< 0.5	< 0.5	< 0.5	< 0.5	< 0.5	< 0.5	< 0.5	0.6	< 0.5
As	0.8	1.3	1.6	0.3	0.5	1	0.6	1.1	0.5	0.3	0.2	0.4	0.5	15.1	1.7
Rb	< 0.1	2.3	6.9	< 0.1	< 0.1	< 0.1	< 0.1	1.6	< 0.1	< 0.1	< 0.1	< 0.1	< 0.1	51.5	5.4
Nb	0.79	1.04	1.37	0.7	0.51	< 0.01	0.4	< 0.01	0.42	< 0.01	0.4	0.44	0.34	4.69	0.21
Mo	< 2	< 2	< 2	< 2	< 2	< 2	< 2	< 2	< 2	< 2	< 2	< 2	< 2	2	< 2
Ag	0.01	0.009	0.008	0.008	0.007	0.003	< 0.002	< 0.002	< 0.002	< 0.002	< 0.002	0.007	0.003	0.006	< 0.002
In	< 0.1	< 0.1	< 0.1	< 0.1	< 0.1	< 0.1	< 0.1	< 0.1	< 0.1	< 0.1	< 0.1	< 0.1	< 0.1	< 0.1	< 0.1
Sn	< 1	< 1	< 1	< 1	< 1	< 1	< 1	< 1	< 1	< 1	< 1	< 1	< 1	< 1	< 1
Sb	< 0.2	< 0.2	< 0.2	< 0.2	< 0.2	0.4	< 0.2	0.5	< 0.2	0.4	< 0.2	< 0.2	< 0.2	0.7	0.3
Cs	< 0.1	< 0.1	0.2	< 0.1	< 0.1	< 0.1	< 0.1	0.1	< 0.1	< 0.1	< 0.1	< 0.1	< 0.1	4.1	0.3
Hf	< 0.1	< 0.1	0.2	< 0.1	< 0.1	< 0.1	< 0.1	< 0.1	< 0.1	< 0.1	< 0.1	< 0.1	< 0.1	1.6	< 0.1
Ta	< 0.01	< 0.01	0.04	< 0.01	< 0.01	0.05	< 0.01	0.06	< 0.01	0.05	< 0.01	< 0.01	< 0.01	0.38	0.08
W	< 0.5	< 0.5	< 0.5	< 0.5	< 0.5	1.1	< 0.5	1.7	< 0.5	1.4	< 0.5	< 0.5	< 0.5	1.1	1.6
Tl	< 0.05	< 0.05	< 0.05	< 0.05	< 0.05	< 0.05	< 0.05	< 0.05	< 0.05	< 0.05	< 0.05	< 0.05	< 0.05	0.18	< 0.05
Pb	0.3	0.38	0.66	0.02	0.34	0.4	0.22	0.35	0.1	0.1	0.02	0.04	0.19	6.73	0.69
Bi	< 0.1	< 0.1	< 0.1	< 0.1	< 0.1	< 0.1	< 0.1	< 0.1	< 0.1	< 0.1	< 0.1	< 0.1	< 0.1	< 0.1	< 0.1
Th	0.02	0.19	0.53	< 0.01	0.01	< 0.01	0.01	0.18	< 0.01	< 0.01	< 0.01	< 0.01	0.01	4.27	0.41
U	0.078	0.148	0.306	< 0.005	0.101	0.651	0.047	0.227	0.027	0.121	< 0.005	0.052	0.361	1.7	0.206
Cd	< 0.01	< 0.01	0.02	< 0.01	0.01	0.01	< 0.01	< 0.01	0.02	0.01	< 0.01	0.01	< 0.01	0.04	0.03
Cr	< 20	< 20	< 20	< 20	< 20	< 20	< 20	< 20	< 20	< 20	< 20	< 20	< 20	60	< 20
Co	0.3	0.8	1.4	< 0.1	0.2	0.2	0.2	0.8	0.2	0.2	0.1	< 0.1	0.2	10.5	1.4
Ni	3.4	6.8	6.3	1.6	2.8	2.7	2.9	6	2.6	2.2	2.3	1.1	2.9	64.4	10.3
Cu	0.99	2.57	6.07	0.48	0.82	0.73	0.83	2.49	0.71	0.83	0.51	0.41	0.93	42.7	5.78
Zn	5.1	2.9	6.6	0.6	1	0.8	1.7	6	1.6	1	1	0.6	1.1	46.4	4.7

Supplementary Table 1- continue.

	K-1	K-3	K-4	K-5	K-9	K-10	K-11	K-12	K-14	K-15	K-7	K-13a	K-13b	K-13c	K-8	K-17	K-19a
	The Gümüşseren section																
		gypsum-rich samples									*marl*						*claystone*
SiO_2 wt. %	0.85	0.03	0.05	0.14	0.24	1.25	2.17	0.39	0.12	0.25	15.75	31.7	15.73	7.16	10.62	7.86	52.95
Al_2O_3	0.2	< 0.01	< 0.01	0.04	0.05	0.23	0.52	0.12	0.04	0.07	4.08	9.49	4.5	1.97	3.01	1.79	9.74
$Fe_2O_3^*$	0.11	0.01	0.02	0.03	0.03	0.11	0.28	0.1	0.03	0.07	2.29	6.54	3.23	2.53	1.71	0.81	7.08
MnO	0.005	0.002	0.002	0.002	0.003	0.004	0.005	0.006	0.003	0.003	0.144	0.085	0.137	0.166	0.11	0.069	0.037
MgO	0.08	0.04	< 0.01	0.03	0.04	0.29	0.18	0.69	0.08	0.3	1.94	7.07	12.64	15.29	1.45	1.15	8.08
CaO	32.68	32.58	32.32	32.76	33	32.54	31.29	31.13	32.29	33.04	28.68	11.22	22.54	28.07	25.29	46.76	2.31
Na_2O	0.01	< 0.01	< 0.01	0.01	< 0.01	< 0.01	0.02	0.02	0.01	0.01	0.1	0.95	0.39	0.16	0.08	0.27	0.67
K_2O	0.04	< 0.01	< 0.01	< 0.01	0.01	0.06	0.11	0.04	0.01	0.02	0.82	1.96	1.04	0.8	0.62	0.3	1.8
TiO_2	0.01	< 0.001	< 0.001	< 0.001	0.002	0.01	0.023	0.007	0.002	0.004	0.227	0.814	0.273	0.116	0.178	0.094	0.473
P_2O_5	0.01	< 0.01	< 0.01	0.02	< 0.01	< 0.01	0.01	< 0.01	< 0.01	< 0.01	0.09	0.12	0.11	0.07	0.08	0.12	0.1
LOI	21.34	20.9	21.11	20.77	20.7	21.16	22.1	20.48	20.86	20.91	26.25	25.15	32.53	39.72	30.38	39.18	16.8
Total	55.33	53.57	53.50	53.81	54.07	55.66	56.71	52.98	53.46	54.7	80.36	95.09	93.11	96.04	73.53	98.40	100
Cl wt. %	0.01	< 0.01	0.02	< 0.01	< 0.01	< 0.01	< 0.01	< 0.01	< 0.01	< 0.01	< 0.01	0.03	0.03	0.04	< 0.01	< 0.01	0.01
CO_2	0.39	0.11	< 0.01	0.18	0.17	0.73	0.32	1.7	0.24	0.85	16.7	12.6	27.8	39.8	22.2	37.1	2.4
SO_4	59.5	61.4	58.1	59.9	61.6	59.7	59.2	59.2	61.2	60.2	18.1	11.1	7.7	2.2	9.9	< 0.3	< 0.3
Br ppm	< 0.5	1.4		< 0.5	< 0.5	< 0.5	< 0.5	< 0.5	< 0.5	< 0.5	< 0.5	4.8	4.2	6	0.41	0.09	< 0.5
B	1.3	5.8	1.5	6	0.8	5.3	< 0.5	0.9	2.5	2.9	37.7	188	115	53.5	< 0.5	3.5	76.6
V	10	7	< 5	7	7	9	13	10	8	9	51	166	68	37	37	25	100
Ba	16	2	4	19	2	16	39	305	3	4	488	78	41	19	292	676	131
Sr	1572	1045	1058	4445	701	1267	2470	13100	1231	228	60090	223	189	181	> 10000	509	169
Y	< 0.5	< 0.5	1	0.5	< 0.5	< 0.5	< 0.5	< 0.5	< 0.5	< 0.5	7.5	10.7	8.3	7.6	6.4	3.4	10.9
Zr	1.3	< 0.1	4.1	0.2	< 0.1	0.9	3.3	0.6	< 0.1	< 0.1	46.5	82.6	36.4	15.8	38.9	19.3	77.4
Ga	< 1	< 1	< 1	< 1	< 1	< 1	< 1	< 1	< 1	< 1	4	11	5	2	4	2	10
Ge	< 0.5	< 0.5	< 0.5	< 0.5	< 0.5	< 0.5	< 0.5	< 0.5	< 0.5	< 0.5	< 0.5	1.2	< 0.5	< 0.5	< 0.5	< 0.5	1.7
As	0.8	0.7	0.2	0.7	0.6	1	1.1	1.8	0.6	0.5	1	25.7	5.8	3.4	14.2	1.5	2.2
Rb	0.5	< 0.1	< 0.1	< 0.1	< 0.1	0.7	2.4	0.1	< 0.1	< 0.1	22.7	49.8	29.1	11.7	16.8	12	54.3
Nb	< 0.01	< 0.01	< 0.01	< 0.01	< 0.01	< 0.01	< 0.01	< 0.01	< 0.01	< 0.01	4.51	9.66	2.79	1.04	4.61	1.33	6.74
Mo	< 2	< 2	< 2	< 2	< 2	< 2	< 2	< 2	< 2	< 2	< 2	25	2	< 2	6	< 2	< 2
Ag	0.01	0.013	< 0.002	0.012	0.011	0.005	0.018	0.016	0.018	0.004	0.019	< 0.002	0.011	0.02	0.013	< 0.002	< 0.002
In	< 0.1	< 0.1	< 0.1	< 0.1	< 0.1	< 0.1	< 0.1	< 0.1	< 0.1	< 0.1	< 0.1	< 0.1	< 0.1	< 0.1	< 0.1	< 0.1	< 0.1
Sn	< 1	< 1	< 1	< 1	< 1	< 1	< 1	< 1	< 1	< 1	< 1	1	< 1	< 1	< 1	< 1	< 1
Sb	< 0.2	< 0.2	0.6	< 0.2	< 0.2	< 0.2	< 0.2	< 0.2	< 0.2	< 0.2	< 0.2	1.9	< 0.2	< 0.2	0.8	0.5	0.7
Cs	< 0.1	< 0.1	< 0.1	< 0.1	< 0.1	< 0.1	< 0.1	< 0.1	< 0.1	< 0.1	1.6	4.1	2.4	0.8	1.3	1.3	3.5
Hf	< 0.1	< 0.1	< 0.1	< 0.1	< 0.1	< 0.1	< 0.1	< 0.1	< 0.1	< 0.1	1.1	1.8	0.9	0.4	1	0.4	1.8
Ta	< 0.01	< 0.01	0.05	< 0.01	< 0.01	< 0.01	< 0.01	< 0.01	< 0.01	< 0.01	0.22	0.61	0.16	0.02	0.34	0.16	0.45
W	< 0.5	< 0.5	1.7	< 0.5	< 0.5	< 0.5	< 0.5	< 0.5	< 0.5	< 0.5	< 0.5	< 0.5	< 0.5	< 0.5	1.5	1.4	1.1
Tl	< 0.05	< 0.05	< 0.05	< 0.05	< 0.05	< 0.05	< 0.05	< 0.05	< 0.05	< 0.05	0.14	0.2	< 0.05	< 0.05	0.13	0.06	0.13
Pb	0.61	0.03	0.03	0.05	0.08	0.2	0.41	0.77	0.2	0.12	7.37	6.48	3.64	2.19	6.42	2.42	8.26
Bi	< 0.1	< 0.1	< 0.1	< 0.1	< 0.1	< 0.1	< 0.1	< 0.1	< 0.1	< 0.1	< 0.1	< 0.1	< 0.1	< 0.1	< 0.1	< 0.1	0.2
Th	0.08	0.01	< 0.01	0.06	< 0.01	0.07	0.21	0.02	< 0.01	< 0.01	2.55	3.18	1.57	0.8	1.88	1	5.15
U	0.091	< 0.005	0.047	0.074	0.023	0.069	0.117	0.419	0.168	0.052	3.82	4.83	2.88	1.08	3.67	1.08	0.948
Cd	0.02	0.01	< 0.01	0.01	< 0.01	< 0.01	< 0.01	0.01	0.01	0.03	0.37	0.08	0.06	0.06	0.41	0.09	0.05
Cr	< 20	< 20	< 20	< 20	< 20	< 20	< 20	< 20	< 20	< 20	50	280	100	50	50	70	630
Co	0.6	< 0.1	< 0.1	0.1	0.2	0.4	0.7	0.4	0.2	0.3	11.8	37.4	14.4	7.3	9.5	2.8	49.4
Ni	5.7	1.6	1.4	1.9	2.1	3.1	4.9	4.8	2.7	3.2	120	337	136	61.2	112	35.7	848
Cu	1.5	0.49	0.54	0.53	0.87	1.45	2.34	1.71	0.74	0.71	16	60.6	33.1	15.5	15.5	7.49	31.9
Zn	2	0.7	0.4	1.4	2.1	2.2	4.3	2.3	1.8	1.8	24.3	43.4	22.5	10.1	33.2	14.2	72.4

All Fe as $Fe_2O_3^*$; LOI is loss on ignition

Supplementary Table 2- Rare earth element (REE, ppm) compositions of the Aşkale evaporites. Normalizing values (MuQ; Mud of Queensland-alluvial sediment composite) from Kamber et al. (2005).

	D1-1	D1-2	D1-5	D1-10	D1-11	D1-13	D1-15	D1-18	D1-25	D1-28	D1-30	D1-22	D1-24	D1-21
	The Pırnakapan Section													
	gypsum-rich samples											*anhydrite-rich samples*		*limestone*
La	0.850	1.300	0.380	0.260	0.080	0.230	0.560	0.710	0.180	0.090	0.640	0.180	0.480	1.470
Ce	1.620	2.100	0.740	0.500	0.220	0.420	0.980	1.280	0.330	0.190	1.120	0.360	1.100	2.680
Pr	0.180	0.180	0.080	0.050	0.020	0.030	0.100	0.170	0.030	0.010	0.120	0.040	0.130	0.330
Nd	0.550	0.630	0.280	0.130	0.110	< 0.05	0.280	0.580	< 0.05	< 0.05	0.280	0.070	0.510	1.260
Sm	0.090	0.120	< 0.01	0.020	< 0.01	< 0.01	< 0.01	0.060	< 0.01	< 0.01	0.020	0.020	0.120	0.270
Eu	0.019	0.028	< 0.005	< 0.005	0.009	< 0.005	< 0.005	0.007	< 0.005	< 0.005	< 0.005	0.006	0.015	0.056
Gd	0.140	0.120	0.040	0.020	0.030	< 0.01	0.030	0.060	< 0.01	< 0.01	0.050	0.020	0.150	0.240
Tb	0.020	0.010	< 0.01	< 0.01	< 0.01	< 0.01	< 0.01	< 0.01	< 0.01	< 0.01	< 0.01	< 0.01	0.020	0.040
Dy	0.090	0.080	0.020	0.020	0.030	< 0.01	0.010	0.050	< 0.01	< 0.01	0.020	0.020	0.110	0.250
Ho	0.020	0.010	< 0.01	< 0.01	< 0.01	< 0.01	< 0.01	0.010	< 0.01	< 0.01	< 0.01	< 0.01	0.020	0.050
Er	0.060	0.050	0.020	0.010	0.020	< 0.01	0.010	0.040	< 0.01	< 0.01	0.020	0.010	0.040	0.130
Tm	0.008	0.006	< 0.005	< 0.005	< 0.005	< 0.005	< 0.005	< 0.005	< 0.005	< 0.005	< 0.005	< 0.005	0.007	0.022
Yb	0.040	0.030	< 0.01	< 0.01	0.010	< 0.01	< 0.01	0.020	< 0.01	< 0.01	0.010	0.020	0.050	0.150
Lu	0.004	< 0.002	< 0.002	< 0.002	< 0.002	< 0.002	< 0.002	< 0.002	< 0.002	< 0.002	< 0.002	< 0.002	0.007	0.023
La_N / Lu_N	3.204	-	-	-	-	-	-	-	-	-	-	-	1.034	0.964
Ce_N / Ce^*	0.961	0.964	0.984	1.011	1.283	1.112	0.949	0.859	1.022	1.353	0.930	0.987	1.027	0.895
Eu_N / Eu^*	0.690	0.982	-	-	-	-	-	0.491	-	-	-	1.263	0.466	0.927

	D1-32	D2-4	D3-1	D3-2	D3-5	D3-4	D3-6	28	D2-2	K-22	K-25	K-24
	The Pırnakapan Section									The Kemerkaya Section		
	gypsum-rich samples								*claystone*	*gypsum-rich samples*		
La	0.51	0.17	1.97	0.46	0.23	0.19	0.38	0.69	11.8	0.36	0.23	0.84
Ce	0.6	0.31	3.71	0.94	0.47	0.29	0.83	1.28	22.8	0.66	0.38	1.55
Pr	0.03	0.02	0.4	0.1	0.06	0.03	0.09	0.13	2.7	0.07	0.05	0.18
Nd	0.12	< 0.05	1.38	0.36	0.24	0.1	0.31	0.43	10.4	0.31	0.1	0.71
Sm	< 0.01	< 0.01	0.25	0.07	0.03	0.04	0.07	0.19	2.16	0.07	0.04	0.14
Eu	0.017	< 0.005	0.036	0.021	0.017	0.013	0.024	0.037	0.58	0.02	0.01	0.024
Gd	0.04	< 0.01	0.19	0.07	0.05	0.03	0.09	0.16	2.06	0.06	< 0.01	0.06
Tb	< 0.01	< 0.01	0.03	< 0.01	< 0.01	< 0.01	0.02	0.02	0.34	< 0.01	< 0.01	0.01
Dy	0.03	< 0.01	0.16	0.06	0.05	0.03	0.09	0.12	1.92	0.03	< 0.01	0.05
Ho	< 0.01	< 0.01	0.04	0.01	< 0.01	< 0.01	0.01	0.02	0.38	< 0.01	< 0.01	< 0.01
Er	0.01	< 0.01	0.1	0.04	0.01	< 0.01	0.03	0.05	1.12	0.03	< 0.01	0.03
Tm	< 0.005	< 0.005	0.012	0.007	< 0.005	< 0.005	< 0.005	0.008	0.17	< 0.005	< 0.005	0.005
Yb	< 0.01	< 0.01	0.06	0.04	0.02	< 0.01	0.06	0.07	1.12	< 0.01	< 0.01	< 0.01
Lu	0.004	< 0.002	0.007	0.005	0.004	< 0.002	0.002	0.012	0.17	0.002	< 0.002	0.003
La_N / Lu_N	1.922	-	4.243	1.387	0.867	-	2.864	0.867	1.047	2.713	-	4.220
Ce_N / Ce^*	0.878	1.148	0.967	1.018	0.933	0.869	1.046	0.984	0.94	0.960	0.823	0.926
Eu_N / Eu^*	-	-	0.693	1.263	1.772	1.573	1.257	0.893	1.158	1.299	-	1.027

Supplementary Table 2- continue.

	A-1	A-3	A-5	A-6	A-8	A-10	A-11	A-12	A-15	A-16	A-17	A-19	A-20	A-13	A-2
	The Alçıdağ hill section														
	gypsum-rich samples													*marl*	*claystone*
La	0.33	1.18	1.7	0.16	0.3	0.13	0.15	1	0.26	0.15	0.12	0.21	0.22	13.2	2.72
Ce	0.51	2.07	3.24	0.28	0.55	0.27	0.31	1.98	0.43	0.32	0.19	0.36	0.42	25.3	5.4
Pr	0.06	0.23	0.37	0.02	0.05	0.04	0.03	0.22	0.04	0.04	0.01	0.03	0.04	2.81	0.62
Nd	0.13	0.76	1.35	< 0.05	0.11	0.12	< 0.05	0.88	< 0.05	0.12	< 0.05	< 0.05	0.08	10.6	2.1
Sm	0.02	0.17	0.23	< 0.01	< 0.01	0.05	< 0.01	0.14	< 0.01	0.03	< 0.01	< 0.01	< 0.01	2.46	0.43
Eu	0.006	0.047	0.061	< 0.005	< 0.005	0.011	< 0.005	0.05	< 0.005	0.016	< 0.005	< 0.005	< 0.005	0.643	0.146
Gd	0.02	0.14	0.26	< 0.01	< 0.01	0.02	< 0.01	0.13	< 0.01	0.03	< 0.01	< 0.01	< 0.01	2.11	0.45
Tb	< 0.01	0.02	0.03	< 0.01	< 0.01	< 0.01	< 0.01	0.03	< 0.01	< 0.01	< 0.01	< 0.01	< 0.01	0.33	0.07
Dy	0.02	0.1	0.21	< 0.01	< 0.01	0.04	< 0.01	0.17	< 0.01	0.03	< 0.01	< 0.01	< 0.01	1.9	0.44
Ho	< 0.01	0.02	0.04	< 0.01	< 0.01	< 0.01	< 0.01	0.03	< 0.01	< 0.01	< 0.01	< 0.01	< 0.01	0.37	0.09
Er	0.01	0.07	0.13	< 0.01	< 0.01	0.02	< 0.01	0.07	< 0.01	0.01	< 0.01	< 0.01	< 0.01	1.05	0.25
Tm	< 0.005	0.01	0.018	< 0.005	< 0.005	< 0.005	< 0.005	< 0.005	< 0.005	< 0.005	< 0.005	< 0.005	< 0.005	0.155	< 0.005
Yb	0.02	0.07	0.11	< 0.01	< 0.01	0.02	< 0.01	0.11	< 0.01	< 0.01	< 0.01	< 0.01	< 0.01	1.02	0.22
Lu	0.002	0.012	0.019	< 0.002	< 0.002	< 0.002	< 0.002	0.011	< 0.002	< 0.002	< 0.002	< 0.002	< 0.002	0.164	0.038
La_N / Lu_N	2.488	1.483	1.349	-	-	-	-	1.370	-	-	-	-	-	1.213	1.079
Ce_N / Ce^*	0.832	0.917	0.949	1.081	1.022	0.870	1.069	0.981	0.95	0.964	1.097	1.012	1.028	0.964	0.968
Eu_N / Eu^*	1.263	1.281	1.046	-	-	1.346	-	1.562	-	2.245	-	-	-	1.188	1.396

	K-1	K-3	K-4	K-5	K-9	K-10	K-11	K-12	K-14	K-15	K-7	K-13a	K-13b	K-13c	K-8	K-17	K-19a
	The Gümüşseren section																
		gypsum-rich samples									*marl*						*claystone*
La	0.3	0.08	0.18	0.66	0.17	0.45	0.64	0.34	0.08	0.19	9.81	9.57	6.96	8.48	8.45	3.62	14.9
Ce	0.66	0.18	0.33	1.42	0.3	0.8	1.28	0.64	0.2	0.33	19.9	20.6	13.2	14.3	17	7.74	28.6
Pr	0.07	< 0.01	0.04	0.17	0.02	0.09	0.14	0.05	< 0.01	0.03	2.11	2.4	1.59	1.69	1.86	0.82	3.3
Nd	0.14	< 0.05	0.21	0.61	< 0.05	0.18	0.49	0.18	< 0.05	< 0.05	8.19	9.43	6.2	6.52	7.15	3.16	12.4
Sm	< 0.01	< 0.01	0.07	0.13	< 0.01	0.01	0.05	< 0.01	< 0.01	< 0.01	1.71	2.1	1.29	1.22	1.46	0.83	2.67
Eu	< 0.005	< 0.005	0.016	0.012	< 0.005	< 0.005	< 0.005	< 0.005	< 0.005	< 0.005	0.393	0.574	0.366	0.336	0.355	0.24	0.628
Gd	0.01	< 0.01	0.03	0.13	< 0.01	0.02	0.09	0.02	< 0.01	< 0.01	1.32	2.11	1.41	1.34	1.28	0.63	2.4
Tb	< 0.01	< 0.01	< 0.01	0.01	< 0.01	< 0.01	< 0.01	< 0.01	< 0.01	< 0.01	0.22	0.34	0.22	0.21	0.21	0.11	0.36
Dy	< 0.01	< 0.01	0.01	0.09	< 0.01	0.02	0.05	< 0.01	< 0.01	< 0.01	1.37	2.33	1.25	1.13	1.22	0.63	2.26
Ho	< 0.01	< 0.01	< 0.01	0.02	< 0.01	< 0.01	< 0.01	< 0.01	< 0.01	< 0.01	0.27	0.47	0.27	0.22	0.24	0.12	0.44
Er	< 0.01	< 0.01	0.02	0.05	< 0.01	< 0.01	0.02	< 0.01	< 0.01	< 0.01	0.79	1.3	0.82	0.66	0.66	0.33	1.24
Tm	< 0.005	< 0.005	< 0.005	0.007	< 0.005	< 0.005	< 0.005	< 0.005	< 0.005	< 0.005	0.118	0.198	0.123	0.092	0.094	0.045	0.191
Yb	< 0.01	< 0.01	< 0.01	0.04	< 0.01	< 0.01	0.02	< 0.01	< 0.01	< 0.01	0.77	1.31	0.86	0.55	0.61	0.3	1.26
Lu	< 0.002	< 0.002	< 0.002	0.006	< 0.002	< 0.002	< 0.002	< 0.002	< 0.002	< 0.002	0.123	0.213	0.138	0.083	0.096	0.053	0.214
La_N / Lu_N	-	-	-	1.658	-	-	-	-	-	-	1.202	0.677	0.76	1.54	1.327	1.029	1.05
Ce_N / Ce^*	1.061	-	0.904	0.989	1.111	0.919	0.994	1.1	-	0.988	1.016	1.002	0.924	0.873	0.997	1.045	0.948
Eu_N / Eu^*	-	-	1.369	0.389	-	-	-	-	-	-	1.098	1.148	1.139	1.103	1.094	1.392	1.045

$Ce_N / Ce^* = Ce_N / ((La_N + Pr_N) / 2)$, $Eu_N / Eu^* = Eu_N / ((Sm_N + Gd_N) / 2)$, Normalizing values (MuQ; Mud of Queensland-alluvial sediment composite) from Kamber et al. (2005).

Supplementary Table 3- Calculated mean, standard deviation, and correlation coefficients of the Aşkale evaporite samples (n=42). Shaded correlation coefficients are significant at p<0.01 value.

	Mean.	Std.Dev.	SiO_2	Al_2O_3	$Fe_2O_3^*$	MnO	MgO	CaO	Na_2O	K_2O	TiO_2	P_2O_5	AK	CO_2	SO_4	B	V	Ba	Sr
SiO_2	4.37	9.99	1.00																
Al_2O_3	1.08	2.47	0.97	1.00															
$Fe_2O_3^*$	1.08	1.55	0.97	0.97	1.00														
MnO	1.08	0.04	0.59	0.66	0.67	1.00													
MgO	1.08	2.94	0.61	0.62	0.71	0.80	1.00												
CaO	1.08	6.69	-0.82	-0.80	-0.82	-0.43	-0.58	1.00											
Na_2O	1.08	0.18	0.88	0.91	0.94	0.56	0.62	-0.70	1.00										
K_2O	1.08	0.49	0.95	0.98	0.97	0.72	0.71	-0.79	0.89	1.00									
TiO_2	1.08	0.15	0.91	0.96	0.96	0.64	0.61	-0.77	0.96	0.95	1.00								
P_2O_5	1.08	0.03	0.81	0.85	0.82	0.81	0.67	-0.52	0.78	0.87	0.82	1.00							
LOI	1.08	5.77	0.21	0.26	0.27	0.60	0.48	-0.04	0.25	0.33	0.26	0.50	1.00						
CO_2	1.08	9.89	0.37	0.43	0.44	0.78	0.63	0.00	0.42	0.49	0.41	0.69	0.82	1.00					
SO_4	1.08	20.75	-0.33	-0.48	-0.44	-0.69	-0.52	0.30	-0.35	-0.54	-0.50	-0.50	-0.55	-0.59	1.00				
B	1.08	31.48	0.67	0.73	0.81	0.58	0.69	-0.61	0.89	0.75	0.85	0.62	0.23	0.41	-0.45	1.00			
V	1.08	37.79	0.64	0.68	0.68	0.43	0.42	-0.57	0.67	0.68	0.71	0.61	0.18	0.25	-0.39	0.58	1.00		
Ba	1.08	117.69	0.31	0.31	0.27	0.51	0.12	0.02	0.26	0.30	0.28	0.57	0.45	0.56	-0.06	0.11	0.13	1.00	
Sr	1.08	8093.36	0.09	0.10	0.08	0.34	-0.02	0.05	-0.04	0.11	0.08	0.17	0.15	0.22	-0.26	0.05	0.02	0.52	1.00
Y	1.08	3.02	0.92	0.95	0.95	0.84	0.76	-0.74	0.86	0.96	0.92	0.90	0.41	0.59	-0.60	0.74	0.66	0.38	0.17
Zr	1.08	20.15	0.95	0.98	0.97	0.70	0.60	-0.78	0.91	0.96	0.97	0.86	0.29	0.45	-0.50	0.75	0.70	0.38	0.17
As	1.08	4.19	0.61	0.72	0.70	0.55	0.46	-0.56	0.72	0.76	0.82	0.67	0.23	0.38	-0.58	0.67	0.55	0.19	-0.07
Rb	1.08	13.42	0.98	1.00	0.98	0.68	0.65	-0.79	0.91	0.99	0.96	0.87	0.28	0.45	-0.47	0.74	0.68	0.33	0.10
Nb	1.08	1.90	0.89	0.93	0.94	0.65	0.54	-0.76	0.90	0.92	0.96	0.80	0.25	0.40	-0.47	0.79	0.69	0.36	0.18
Ag	1.08	0.01	-0.10	-0.09	-0.07	0.05	0.01	0.22	-0.09	-0.07	-0.09	-0.05	-0.39	0.00	0.06	-0.03	-0.14	-0.01	0.09
Hf	1.08	0.45	0.95	0.99	0.96	0.69	0.59	-0.78	0.89	0.96	0.96	0.85	0.27	0.44	-0.50	0.73	0.68	0.37	0.17
Pb	1.08	2.25	0.91	0.93	0.90	0.75	0.55	-0.70	0.81	0.90	0.88	0.84	0.33	0.51	-0.52	0.63	0.60	0.50	0.30
Bi	1.08	0.02	0.44	0.31	0.37	0.00	0.19	-0.42	0.29	0.28	0.23	0.14	-0.10	-0.06	0.25	0.18	0.14	0.05	-0.03
Th	1.08	1.11	0.98	0.98	0.95	0.65	0.58	-0.79	0.84	0.96	0.90	0.84	0.25	0.42	-0.41	0.63	0.63	0.39	0.18
U	1.08	1.11	0.65	0.75	0.74	0.77	0.50	-0.43	0.73	0.76	0.81	0.78	0.50	0.68	-0.74	0.72	0.53	0.48	0.39
Cd	1.08	0.07	0.37	0.41	0.39	0.69	0.20	-0.22	0.27	0.40	0.40	0.53	0.37	0.50	-0.49	0.24	0.24	0.64	0.57
Co	1.08	8.74	0.94	0.90	0.96	0.53	0.61	-0.81	0.92	0.87	0.90	0.71	0.15	0.32	-0.26	0.81	0.63	0.25	0.07
Ni	1.08	122.02	0.87	0.77	0.85	0.37	0.52	-0.76	0.78	0.74	0.73	0.58	0.05	0.20	-0.02	0.64	0.51	0.22	0.04
Cu	1.08	11.53	0.88	0.94	0.94	0.72	0.72	-0.77	0.91	0.97	0.97	0.85	0.32	0.47	-0.57	0.84	0.69	0.26	0.06
Zn	1.08	18.85	0.89	0.91	0.87	0.56	0.46	-0.68	0.83	0.84	0.84	0.72	0.22	0.38	-0.42	0.60	0.57	0.29	0.06
La	1.08	3.60	0.93	0.94	0.94	0.81	0.71	-0.75	0.80	0.95	0.87	0.87	0.38	0.57	-0.53	0.64	0.61	0.42	0.22
Ce	1.08	7.03	0.94	0.95	0.94	0.80	0.69	-0.75	0.82	0.95	0.89	0.88	0.37	0.56	-0.53	0.66	0.62	0.44	0.23

Supplementary Table 3- continue.

	Y	Zr	As	Rb	Nb	Ag	Hf	Pb	Bi	Th	U	Cd	Co	Ni	Cu	Zn	La	Ce
Y	1.00																	
Zr	0.96	1.00																
As	0.69	0.73	1.00															
Rb	0.96	0.98	0.71	1.00														
Nb	0.90	0.96	0.78	0.93	1.00													
Ag	-0.05	-0.09	0.06	-0.08	-0.08	1.00												
Hf	0.96	0.99	0.72	0.98	0.96	-0.06	1.00											
Pb	0.94	0.96	0.65	0.93	0.92	-0.04	0.97	1.00										
Bi	0.24	0.29	-0.03	0.31	0.28	-0.05	0.28	0.26	1.00									
Th	0.94	0.97	0.64	0.98	0.91	-0.07	0.97	0.96	0.37	1.00								
U	0.81	0.82	0.74	0.75	0.84	-0.03	0.81	0.84	0.00	0.72	1.00							
Cd	0.54	0.53	0.40	0.42	0.56	0.05	0.53	0.68	-0.01	0.49	0.74	1.00						
Co	0.86	0.91	0.60	0.90	0.90	-0.08	0.90	0.84	0.47	0.89	0.66	0.35	1.00					
Ni	0.72	0.77	0.38	0.78	0.76	-0.08	0.77	0.73	0.61	0.81	0.46	0.27	0.95	1.00				
Cu	0.92	0.93	0.85	0.95	0.92	-0.06	0.93	0.84	0.19	0.88	0.79	0.38	0.85	0.67	1.00			
Zn	0.87	0.91	0.54	0.90	0.84	-0.08	0.92	0.91	0.29	0.91	0.70	0.45	0.82	0.72	0.76	1.00		
La	0.98	0.95	0.63	0.95	0.89	-0.04	0.95	0.96	0.33	0.97	0.77	0.58	0.85	0.75	0.87	0.87	1.00	
Ce	0.98	0.96	0.66	0.96	0.91	-0.04	0.96	0.97	0.32	0.97	0.79	0.60	0.86	0.75	0.89	0.88	1.00	1.00

Std.Dev., standard deviation; All Fe as $Fe_2O_3^*$; LOI is loss on ignition

Bulletin of the Mineral Research and Exploration

http://bulletin.mta.gov.tr

The relation of seismic velocity and attenuation pattern in the East Anatolian fault zone with earthquake occurrence: Example of January 24, 2020 Sivrice earthquake

Şakir ŞAHİN[a*] and Erdinç ÖKSÜM[a]

[a]*Süleyman Demirel University, Faculty of Engineering, Department of Geophysical Engineering, Isparta, Turkey*

Research Article

Keywords:
EAFZ, Seismic velocity, Attenuation, Tomography.

ABSTRACT

The East Anatolian Fault Zone (EAFZ) is one the main tectonic elements of Turkey, which borders the Anatolian plate from the east. EAFZ, which is NE-SW direction, consists of many fault segments. In the historical and instrumental period, many damaging earthquakes occurred, the largest being 6.8 (Ms) as the 1971 Bingöl earthquake. The last magnitude 6.6 (Ml) (Mw = 6.8) earthquake occurred on January 24, 2020 in Elazığ - Sivrice Hazar - Sincik segment of EAFZ. However, considering the historical and instrumental activity, it is seen that many fault segments are silent. In this study, the silent and active segments, and their seismic velocity (as % Vp and Vp) and attenuation pattern (as Q^{-1}_p) are determined in order to determine the earthquake behavior of EAFZ in the near future. From the results obtained by using the data of the earthquakes that occurred from 2007 to the end of 2019, it was clearly determined that the velocity and attenuation increased on the Hazar - Sincik segment. It has been determined that Vp is 4.08-8.2 km/sec, Q^{-1}_p is ± 0.005 and the frequency dependency varies between 0 - 1.08 along the zone. The variation of velocity and attenuation on the segments where the earthquake occurred and in the silent section were revealed.

Received Date: 23.05.2020
Accepted Date: 09.11.2020

1. Introduction

The East Anatolian Fault Zone (EAFZ) is the largest tectonic member after the North Anatolian Fault Zone in Turkey (NAFZ). The EAFZ, which forms the southern border of the Anatolian Plate with the Arabian plate, joins with the NAFZ in Bingöl - Karlıova. The region where both these tectonic belts join together is the area where the largest stress occur depending on the plate movements in Turkey. The greatest stress occurs here with the pressure exerted by the Arabian plate from south and the Anatolian plate moves westward along the borders of the NAFZ and EAFZ (Allen et al., 2004). In this respect, the EAFZ forms the other border of the Anatolian plate on the land with the NAFZ. The EAFZ, which has a length of 580 km between Karlıova and Hatay, plays a very active role in the geodynamic evolution of the Anatolian block and in the seismicity of Turkey (Arpat and Şaroğlu, 1972; Mc Kenzie, 1976; Taymaz et al., 1991; Herece and Akay, 1992; Şaroğlu et al., 1992; Nalbant et al., 2002; Aksoy et al., 2007; Bulut et al., 2012; Kartal and Kadiroğlu, 2013; Bulut, 2017; Demirtaş and Erkmen, 2019).

In the instrumental period, 1971 Bingöl and 2020 Sivrice earthquakes occurred along the Karlıova - Bingöl and Hazar - Sincik faults respectively with magnitude of 6.5 (Ms) on the EAFZ, which borders the Anatolian Plate from south and consists of many

Citation Info: Şahin, Ş., Öksüm, E. 2021. The relation of seismic velocity and attenuation pattern in the East Anatolian fault zone with earthquake occurrence: Example of January 24, 2020 Sivrice Earthquake. Bulletin of the Mineral Research and Exploration 165, 141-161.
https://doi.org/10.19111/bulletinofmre.824032

**Corresponding author: Şakir ŞAHİN, sakirsahin@sdu.edu.tr*

segments. It was suggested by Demirtaş and Erkmen (2019) that an earthquake should be expected on the parts of Sivrice that continued in the north - east or south - west of the EAFZ, which consists of six fault segments. The very last seismic gaps were formed between the Hazar - Sincik fault and the Bingöl - Karlıova fault after the Sivrice earthquake. In terms of earthquake safety of the cities and large facilities along the EAFZ, it has become important to determine which segments these seismic gaps cover and what kind of earthquake behavior the zone will exhibit in the near future. The seismic velocity change occurring along the zone will help determine the earthquake behavior (Jordan et al., 2011). Considering the ongoing earthquake activity on the EAFZ and finally the 2010 Kovancılar - Elazığ earthquake (Mw = 6.1), it was suggested by Duman and Emre, (2013) that the Pazarcık and Amanos segments had the potential to produce destructive earthquakes in the near future.

Determining the seismic velocity change and attenuation pattern in regions where the earthquake activities are high such as the EAFZ is very important for seismological studies. Seismic velocity diffusion and attenuation within the crust and the mantle are sensitive to heterogeneity in the environment. The seismic attenuation is the decrease in wave energy over time and distance due to the heterogeneity and/or inelastic effects within the crust (Aki and Chouet, 1975; Sato, 1977; Aki, 1980; Pulli, 1984; Sato and Fehler, 1998; Aydın et al., 2020). The transformation of elastic energy into heat or other forms of energy results from the energy dissipation in a heterogeneous environment (Bianco et al., 2002; Abdel - Fattah et al., 2008; Del Pezzo et al., 2006; Sertçelik, 2012). Attenuation studies in time or frequency environments have been performed by various methods using body or surface waves (Pulli, 1984; Ibanez et al., 1990; Mohanty et al., 2009; Mukhopadhyay and Sharma, 2010; Ford et al., 2010; Sharma et al., 2011). The decrease in wave energy depends on the density of the medium and dissipation. The seismic velocity is low and attenuation is high in altered zones and in areas with high volcanic activity, where the fault zones and discontinuities are high. Many studies have been conducted to determine the velocity change and attenuation pattern in the crust in different regions of Anatolia (Akıncı et al., 1994; Akıncı and Eyidoğan, 1996; Eken et al., 2004; Horasan and Boztepe - Güney, 2004; Salah et al., 2007; Sertçelik, 2012; Çağlar, 2019; Demirsıkan et al., 2019; Salah and Şahin, 2019; Aydın et al., 2020).

In this study, the velocity change (%Vp and Vp) and the P wave attenuation (Q_v^{-1}) pattern with the frequency dependency degree (η) according to the characteristics of the environment during the wave propagation were determined the earthquake behavior on the EAFZ January 24, 2020 Sivrice earthquake. The Poisson tomography method was applied for many regions of the world to determine the velocity change and the Coda normalization method was used to determine the seismic attenuation values (Um and Thurber, 1987; Zhao et al., 1992, 1994; Salah et al., 2007; 2011; De Siena et al., 2009; Salah and Şahin, 2019; Demirsıkan et al., 2019; Toker and Şahin, 2019, Şahin and Öksüm, 2020). The elastic wave propagation and attenuation relationships were used to determine these changes. According to the results obtained using the data collected by the end of 2019, it was observed that the %Vp change (Vp values increased) and the attenuation on the Hazar - Sincik fault, where the Sivrice earthquake had occurred, was low. Based on these results, it has been tried to determine what kind of earthquake behavior the other segments on the EAFZ will exhibit.

2. Tectonics and Seismicity of the East Anatolian Fault Zone (EAFZ)

The EAFZ extending between Karlıova in the northeast and Hatay in the southwest, which is approximately 600 km long, consists of 6 different fault segments varying between 50 km to 145 km (Herece, 2003; Demirtaş, 2003; Demirtaş and Erkmen, 2019). These segments, are respectively Türkoğlu - Antakya, Gölbaşı - Türkoğlu, Çelikhan - Gölbaşı, Hazar - Sincik, Palu - Hazar and Karlıova - Bingöl faults as numbered from 1 to 6 in Figure 1. However, the part shown with number 7 not named and it is the intersection of EAFZ fault as shown on the Active Fault Map of Turkey indicated by MTA (2013). On the other hand, the fault shown as number 8 indicates the part where the 2003 Bingöl earthquake occurred (Demirtaş 2003; Demirtaş and Erkmen, 2019). This part is in the same direction with the Yayla Fault (Figure 1).

Structural and geological studies carried out along the EAFZ show that the fault has actively moved in a left - lateral character for the last 3 - 5 million years, with slips around 9 - 40 km (Arpat and Şaroğlu, 1972;

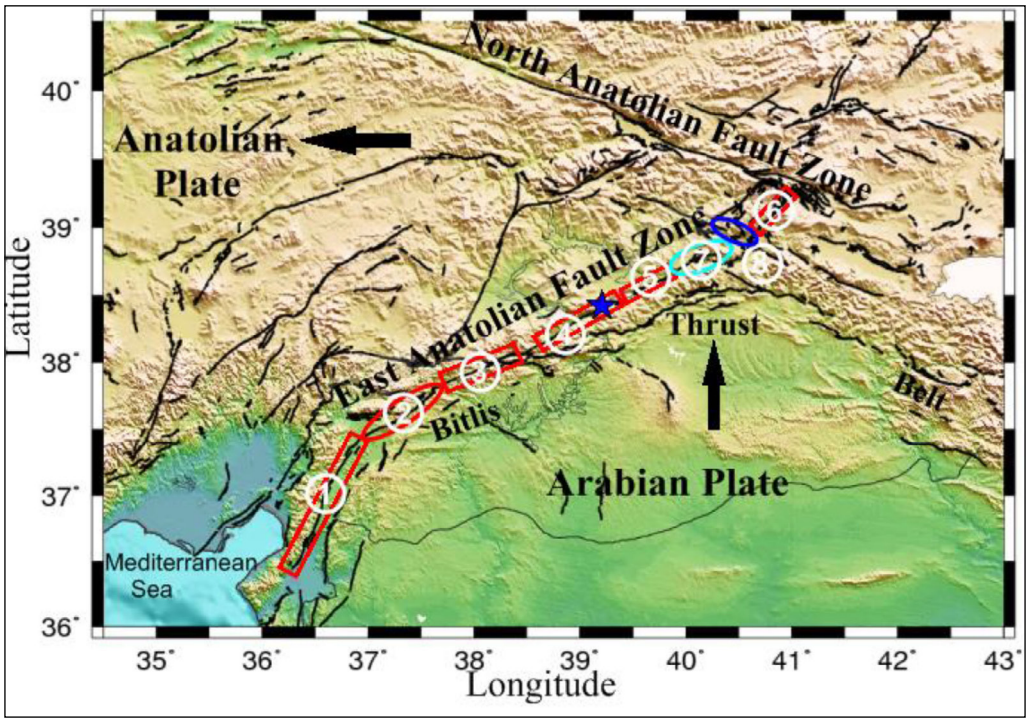

Figure 1- Segments belonging to the Eastern Anatolian Fault Zone (EAFZ) (Demirtaş and Erkmen, 2019) and their tectonic locations. Black arrows show the direction of movement of the plates (Reilinger et al., 2006; Djamour et al., 2011). The segments were shown with red areas, 1. Türkoğlu-Antakya segment, 2. Gölbaşı-Türkoğlu segment, 3. Çelikhan-Gölbaşı segment, 4. Hazar-Sincik segment, 5. Palu-Hazar segment, 6. Karlıova-Bingöl segment. The zone number 7 here is not named, but it is one of the seismic gaps. The number 8 shows the segment where the May 1, 2003 Bingöl earthquake occurred.

Hempton, 1985; Dewey et al., 1986; Allen et al., 2004; Herece and Akay, 1992; Herece, 2003; Aksoy et al., 2007; Demirtaş and Erkmen, 2019). According to the geological data, the age of the EAFZ is expressed as the Upper Pliocene and the average slip rate is 5 - 8 mm/year (Herece, 2003, Demirtaş and Erkmen, 2019). Using the historical earthquake data, it has been determined that there are two seismic gaps between Gölbaşı - Türkoğlu and Palu - Bingöl in EAFZ (Barka and Kadinsky - Cade, 1988; Nalbant et al., 2002; Demirtaş, 2003).

One of the important earthquakes that occurred in the historical period on the segments that form the Eastern Anatolian Fault Zone, numbered as segment 1 above (Figure 1), is the 1822 Antakya Earthquake (Ms = 7.5), which created approximately 200 km of surface rupture (Demirtaş and Erkmen, 2019). The 1866 Karlıova - Bingöl Earthquake (Ms = 7.2), has a surface rupture of approximately 45 km. The May 22, 1971 Bingöl earthquake (Ms = 6.8), took place on the same fault. The historical periods of the earthquakes are respectively; 1872 Amik Lake Earthquake (Ms = 7.2, with approximately 20 km surface rupture) 1874 and 1875 Hazar Lake Earthquakes (Ms = 7.1 and Ms = 6.7 with 45 and 20 km surface ruptures, respectively) and 1893 Malatya Earthquake (Ms = 7.1) (Kartal and Kadiroğlu, 2013; Demirtaş and Erkmen, 2019). The EAFZ, which has a deeper seismogenic zone compared to the NAFZ, produces earthquakes reaching depths of approximately 26 km (Bulut et al., 2012) that started from the NE end of the EAFZ and continued towards SW. The general distribution of historical earthquakes is concentrated in the middle and NE parts of the EAFZ. It is seen that there have not been any devastating earthquakes that formed a surface rupture for the last 500 years on the Gölbaşı - Türkoğlu segment (Figure 1) where the fault folds to the SW.

According to historical records, two damaging earthquakes occurred on the Gölbaşı - Türkoğlu fault in 1114 and 1513 on the EAFZ (segment number 2 in Figure 1). It is stated that after the earthquake that occurred on the segment shown with number 7 in 1789, no significant activity has occurred in this part

(Kartal and Kadiroğlu, 2013; Demirtaş and Erkmen, 2019). After this date, the damaging earthquakes occurred on the Türkoğlu - Antakya fault (segment number 1) in 1822 and 1872, Palu - Hazar (segment number 5) in 1874, Hazar - Sincik in 1875 (segment number 4 where the Sivrice earthquake occurred in 2020), in 1893 and 1905 on the Çelikhan - Gölbaşı segment.

In the instrumental period, damaging earthquakes occurred (Ms = 6.8) on the Karlıova - Bingöl fault (segment number 6) in 1971, in Bingöl (Mw = 6.4) (segment number 8) in 2003 and in Elazığ - Sivrice (Mw = 6.8) on the Hazar - Sincik fault in 2020 (segment number 4) (AFAD, 2020). An earthquake (Mw = 5.2) occurred on the same segment on April 4, 2019. It is observed that earthquakes with Ms = 6.7 and larger occurred along the faults that form the EAFZ in the historical period. The instrumental magnitude of the largest earthquake in the EAFZ in the last century is 6.8 (Ms). If an evaluation is made by considering the mentioned instrumental sizes, it can be said that the middle and NE segment of the EAFZ are more active in the instrumental period. On the other hand, when the historical and instrumental earthquake activities of the EAFZ are assessed together, it is observed that the Gölbaşı - Türkoğlu fault is silent in terms of seismic activity. In addition, the fact that there is no earthquake on segments 2 and 7 (Figure 1) causes that there is a seismically silent phases (Kartal and Kadiroğlu, 2013).

3. Data and Method

In this study, the total of 249,369 P wave arrival time data of 29,687 earthquakes (red circles in Figure 2) was used that had occurred between the latitudes of 35.2 - 41.7 °E and longitudes of 35.9 - 40.1 °N in order to determine the P wave velocity pattern of the Eastern Anatolian Fault Zone. The total of 4,474 digital signals (P phase) of 922 earthquakes (blue circles in Figure 2) was evaluated in order to determine the attenuation pattern that had occurred between the same coordinates. Data were recorded by 40 three - component broadband stations operated by the Kandilli Observatory and Earthquake Research Institute (KOERI) (Figure 3). The location information of stations is given in Table 1. The response function of seismographs in which the earthquakes were recorded is in the range of 0.02 - 100 Hz. The local magnitudes (ML) of the earthquakes used vary between 1 and 6.1 (Figure 2). In determining the attenuation pattern, the signal - to - noise ratio of the earthquake recordings was taken as 1.5 and higher. The beam paths created in determining the beam path distribution velocity values (% Vp and Vp) of the earthquakes used in the study

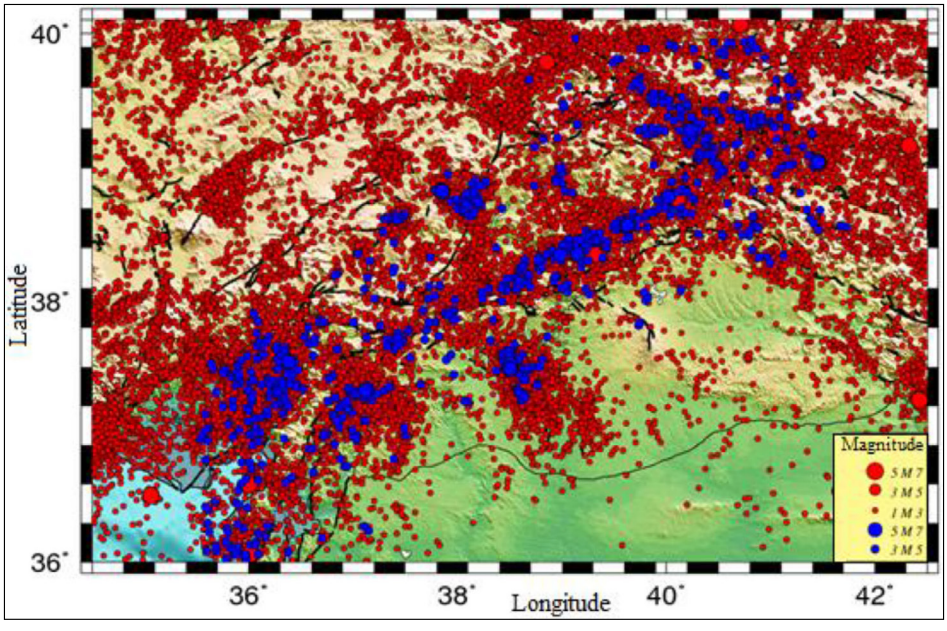

Figure 2- The distribution of earthquakes used in the study. Here, black lines show faults and red circles show the distribution of data used in velocity tomography and blue circles show distribution of earthquakes used in attenuation tomography.

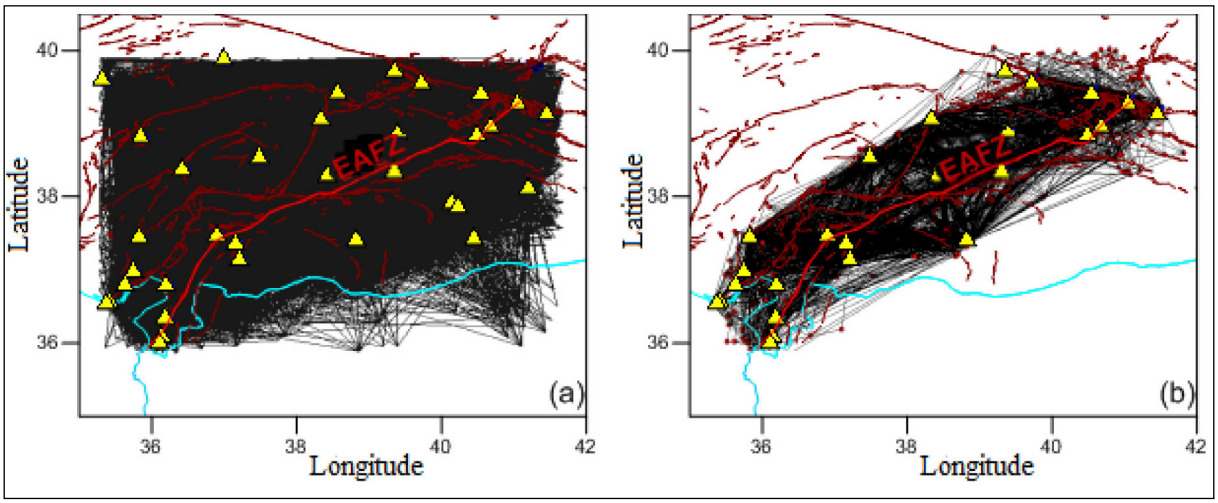

Figure 3- The beam paths created in determining; a) velocity values (% Vp and Vp) and b) attenuation (Q_v^{-1}) values of the earthquakes used in the study. Here, red lines indicate faults (MTA, 2013) and yellow triangles indicate earthquake stations (KOERI, 2020).

Table 1- Location information (KOERI) of the stations where the data used to determine % Vp, Vp and Q_v^{-1} values are recorded.

Station Code	Latitude	Longitude	Height (m)	Station Code	Latitude	Longitude	Height (m)
ARPR*	39.0929	38.3356	1522	BNGB*	38.9913	40.6792	1180
BNN	38.8522	35.8472	1380	CEYT*	37.0107	35.7478	100
DARE*	38.5712	37.4832	1080	DYBB	37.9532	40.1393	657
ERZN*	39.5867	39.7220	1317	GAZ*	37.1722	37.2097	992
ILIC	39.4518	38.5675	1295	KARO*	39.3089	41.0493	1820
KHMN*	37.3916	37.1574	640	KMRS*	37.5053	36.9000	590
KOZT*	37.4805	35.8268	381	KRTD*	36.5934	35.4157	47
KRTS*	36.5730	35.3750	53	MALT*	38.3134	38.4273	1112
MAZI	37.4593	40.4465	1204	PTK*	38.8923	39.3923	1835
SARI	38.4072	36.4182	1673	SVAN	38.1512	41.1985	650
SVRC*	38.3775	39.3060	1680	SVSK	39.9175	36.9925	1630
TAHT*	36.3755	36.1855	278	URFA*	37.4410	38.8213	938
VRTB*	39.1603	41.4558	1498	YEDI*	39.4377	40.5443	1557
YOZ	39.6376	35.3152	1422	BINT*	38.8758	40.4890	1342
BTMT	38.1148	41.2935	854	MYA*	38.3262	38.4253	1050
DIY	37.8958	40.2265	657	EZM	39.9200	41.2800	1870
EZC*	39.7520	39.3535	1500	HTY*	36.1211	36.1378	84
YURE*	36.8258	35.6323	491	DORT*	36.8260	36.1966	27
YAYL*	36.0343	36.1070	1225	ERZM	39.9045	41.3622	23800
ATA5	39.9046	41.2448	18650	EJDE	39.8337	41.3035	29800

*Stations used for attenuation study.

are given in Figure 3a and the beam paths created in determining the attenuation (Q_p^{-1}) values are given in Figure 3b.

The Poisson Tomography method developed by Zhao et al. (1992) was used to determine the seismic velocity pattern of the Eastern Anatolian Fault Zone (EAFZ). In this method, the three - dimensional (3 - D) grid spacing was determined from the inverse solution of the P wave arrival times (Figure 4). The model can be adapted to a general velocity pattern that includes the seismic velocity discontinuities, and 3 - D velocity

changes can be determined throughout the model. The discontinuities represent the known geological boundaries such as Conrad and Moho discontinuities. For this, while defining the initial checkerboard model, the study area was divided into cells (Figure 4), and the velocity distribution in each cell was defined (Figure 5a, b). While the velocity distribution was defined, it was given as the initial velocity model in Table 2 (Kalafat et al., 1987) considering the approximate velocity changes in the study area. Again, Vp / Vs ratio was taken as 1.73 based on in this study. The velocity change at any point in the model is calculated by linear

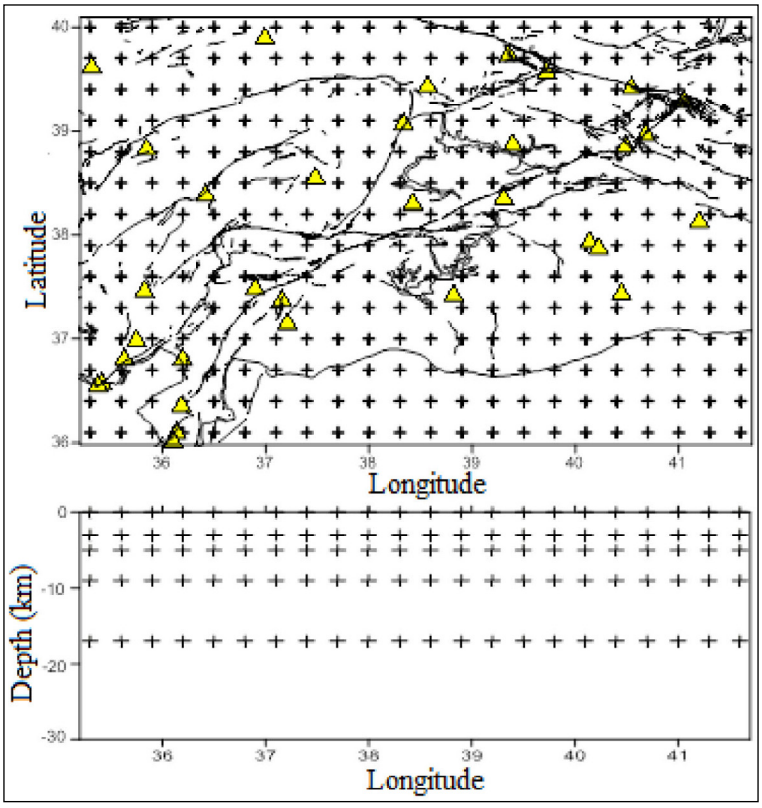

Figure 4- Position of grid spacing in horizontal (top) and vertical (bottom) directions. The grid spacing was taken as 0.3° * 0.3° in the horizontal direction and as -3, -5, -9 and -17 km depths in the vertical direction.

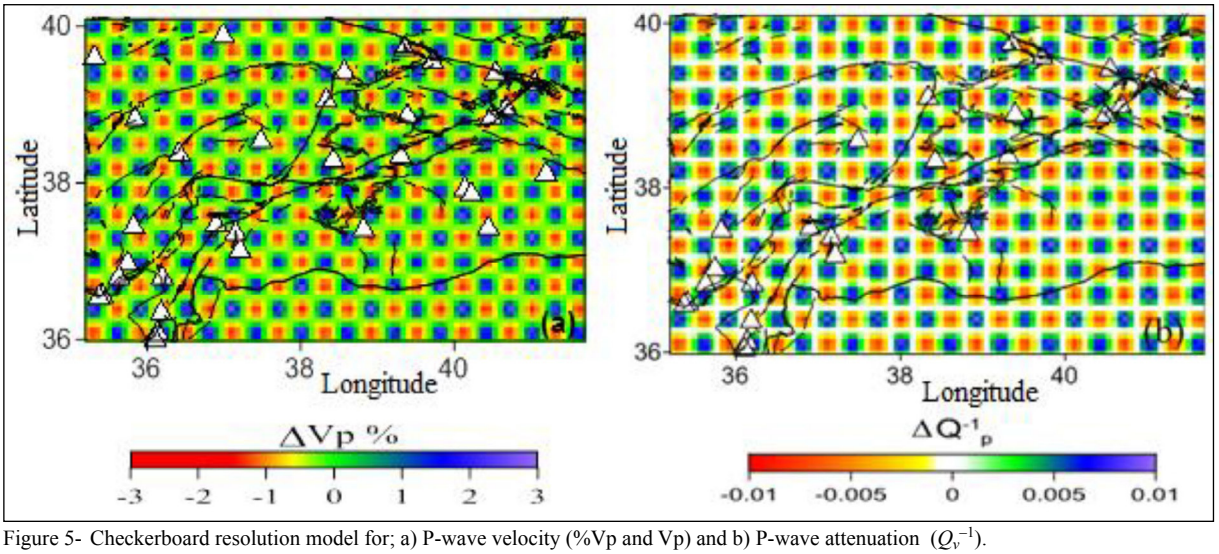

Figure 5- Checkerboard resolution model for; a) P-wave velocity (%Vp and Vp) and b) P-wave attenuation (Q_v^{-1}).

Table 2- Initial velocity model used to determine % Vp, Vp and Q_v^{-1} values (Kalafat et al., 1987).

Depth (km)	Vp (km/sec)	Vs (km/sec)
0	4.50	2.60
5.4	5.91	3.41
31.6	7.80	4.51
89.2	8.30	4.80

interpolation of the velocity changes at eight nodes surrounding that point. The iterative Pseudo Bending technique was used to calculate the arrival times and ray paths, accurately (Um and Thurber, 1987; Zhao et al., 1992). This technique is a three - dimensional ray tracing method. The detection of beam paths is based on Snell's law. In this method, the station heights were also taken into account which is defined as the Poisson tomography.

At the stage of determining the initial model for the checkerboard test (Figure 5a, b), many trials were conducted by changing the horizontal and vertical cell spacing and velocity distributions, considering the width of the study area and the possible velocity changes in the region. As a result of these trials, the study area was gridded at 0.3° * 0.3° in the horizontal direction and as 1 km interval in the vertical direction. The model depth was defined up to 30 km in order to complete the beam paths in the study area. The amplitudes and P wave velocity anomalies for attenuation anomalies were determined as ± 3% and ± 0.01, respectively (Figure 5a, b).

Tomographic methods are based on the inverse analysis of arrival times of seismic waves within the parameters specified above (Zhao et al., 1994). In visualizing the crust and mantle structure, the geometric shape of the structure is taken into account in the model parameterization stage (Thurber, 1987). The TOMOTOOLS (Farouk and Zhao, 2006) software obtained with the interface created for the code of the TOMOG3D (Zhao et al., 1992) software was used to determine the structure of P and S velocities. This software was designed to determine the crust and upper mantle velocity structures from the inverse resolution of arrival times of the recorded local earthquakes. TOMOTOOLS enables the determination of existing complex discontinuities in a realistic model and obtaining 3 - D changes between the velocities.

The vertical component P wave was used to determine the three - dimensional attenuation pattern by tomographic method. For this, the signals that were windowed on the P phase and the noise selected 5 seconds before the 2 second time interval were selected and the spectral amplitudes of the selected signals were determined. The ratio of P wave and noise spectral amplitudes was calculated. The selection of signal and noise is given in Figure 6. The Coda Normalization Method used in the study is based on spectral amplitude ratios. Based on this method, the attenuation patterns were determined with the Matlab - based MuRATv.2 software (De Siena et al., 2016, 2017) developed by De Siena et al. (2009).

This software was developed, which is based on the approach of the coda normalization method model by Del Pezzo et al. (2006), Aki (1980) and Frankel et al. (1990). The method applied is based on the assumption that the average source size and ground amplification calculated from many earthquake data spread in different directions are independent of the source - receiver direction and the average value varies geographically (Aki, 1980). The (Q_p^{-1}) values, which are P wave attenuation parameters, are calculated from the decrease of the P wave amplitude of the crust caused by inelastic conditions at each station (Aki, 1980; Frenkal et al., 1990). For this purpose, 2 - second windows (Δt = 2 seconds) on the P wave and noise were selected and calculated as seen in Figure 6. This process is based on the approach of (Aki, 1980; Frenkal et al., 1990).

$$\langle Ln\{D^{\gamma} * A_P(f)/A_G(f)\}\rangle = a - b * D \quad (1)$$

Here; D is the source - receiver distance, g is the geometric radiation effect, A_p *(f)* is the spectral amplitude of the P wave and A_G*(f)* is the noise spectral amplitude. The coda normalization method is widely used in the calculation of attenuation in the earth crust independent of soil and instrumental transfer function (Aki, 1980; Sato and Fehler, 1998; Şahin and Alptekin, 2003; Aydın et al., 2012).

The P wave attenuation in the EAFZ in Del Pezzo et al., (2006) model was calculated for certain depths along each wave path (Figure 4). The energy reduction relation used for this is given by the formula of;

$$\frac{E_{ij}(f,r)}{E^G(f,t)} r_{ij}^2 = \frac{1}{P(f,t_G)} exp\left[-2\pi f \int \frac{dl}{v(l)Q_P^{ij}(l)}\right] \quad (2)$$

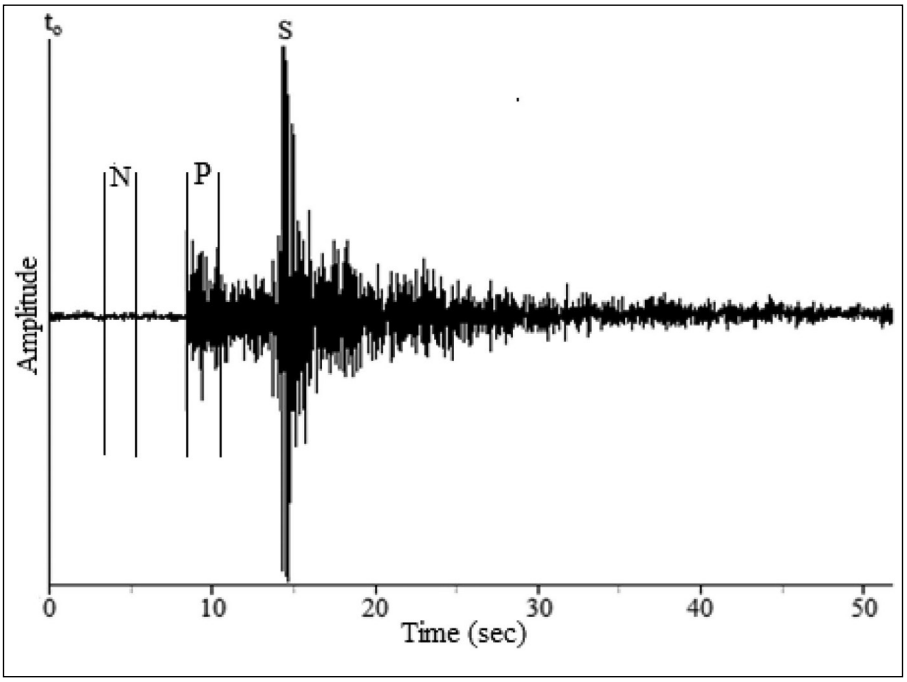

Figure 6- Representation of P and S wave phases on the signal. Here, P and N is the 2-second P wave selected to determine the attenuation parameters, and t_0 indicates the time of occurrence of earthquake.

With the application of linear integral by taking the logarithms of both sides, the following formula is obtained;

$$d_k^G = \frac{1}{2\pi f}\ln\left(\frac{1}{P(f,tc)}\right) - \sum_{b=1}^{N-cell} l_{kb}\, S_b Q_b^{-1} \quad (3)$$

Here the d_K^G value gives the logarithm of the P wave and the noise spectral ratio determined for the beam length and is gridded for the given metric range. The N cells gridded is the total number of blocks traversed by the beam. Here, the S_b attenuation value is the k^{th} beam path length that cuts the block b, which is characterized by the $l_{kb}\,Q$ quality factor, and k is the wave path index between the earthquake focus and the station.

The equation (3) can be rewritten so that the average attenuation value of each b block in the studied area is Q_b^{-1} and increasing dQ_b^{-1}. As a result;

$$\tilde{d}_k^G = \sum_{b=1}^{N-cell} l_{kb}\, S_b \quad Q_b^{-1} \quad (4)$$

From here the following formula is obtained (De Siena et al., 2009).

$$\tilde{d}_k^G = \frac{1}{2\pi f}\ln\left(\frac{1}{P(f,tc)}\right) - \tilde{d}_k^C - Q_P^{-1}\sum_{b=1}^{N-cell} l_{kb}\, S_b \quad (5)$$

From here, Q_p^{-1} values are calculated for a certain frequency value in each cell. In this study, the frequency value was taken as 18 Hz.

With the Coda Normalization Method, the spectral amplitude ratios of the P waves and the noise window are displayed as a function of the distance of earthquakes to the earthquake station, and the attenuation pattern is calculated from the decrease of the amplitude ratio (Aki, 1980; Frenkal et al., 1990). In the last stage, the average Q_v^{-1} wave attenuation parameter for each cell was determined by proportioning the spectral amplitude values of the P wave. In this way, the discontinuities in the crust and the continuity of structures were determined. In the method developed by De Siena et al. (2009) (MuRATv.2), P and S wave attenuation is determined depending on the velocity structure in the environment (De Siena et al., 2016; 2017; Şahin and Öksüm, 2020).

4. Discussion

Checkerboard test was applied to determine the resolution in determining the rate and attenuation pattern on the EAFZ (Figures 7 and 8). Initially, the

checkerboard resolution model was created (Figure 5a, b) and the resolution tests were applied according to the velocity model given in Table 2. The parameters applied for the matrix before the inverse solution are determined according to the station and earthquake distribution, the region examined and the number of rays. For this reason, the special parameterization is made for each study area during the synthetic tests stage and its effects on the results are investigated. The study area in the checkerboard test is divided into square / rectangular prisms of certain sizes (Figure 5a, b). To each of these prisms negative / positive or low / high attenuation values are assigned. Then, the noise is added to the synthetic arrival times considering the phase reading errors and as a result of the inverse solution, it is checked whether these prisms can be synthetically recovered. If the desired resolution is not obtained, then the test is repeated by changing the dimensions of the square / rectangular prism (Özer et al., 2018). In this study, the prism dimensions for the P wave were designed to be 0.3° *0.3°, ± 3% for the DVp% values and ± 0.01 ΔQ_p^{-1} values for the attenuation pattern (Figure 5a, b). It was considered as if the seismic model produced by synthetic arrival times had not been known and the inverse process was performed using a new initial model. In this way, the checkerboard model used in the beginning was tried to be obtained. Checkerboard resolution maps were obtained based on the initial crustal depth and velocity model (Figures 7 and 8). In addition, the resolution sections were taken along the fault zone and perpendicularly (Figures 12, 15 and 18a, d). The resolution level of the designed resolution model at different depths for the P wave velocity and attenuation was examined. According to the results obtained, it was seen that the resolution for the P wave velocity values on the surface could be obtained at 30 km depth, but for P wave attenuation, the resolution could be obtained down to 17 km. In both methods, it was observed that the resolution was low at 2 km depth from the surface, and the resolution increased after 3 km. Based on these results, depth maps were obtained for both methods depending on the resolution at 3, 5, 9 and 17 km. When the map is divided into cells consisting of positive and negative anomalies, it was observed that the results with high resolution were obtained at these

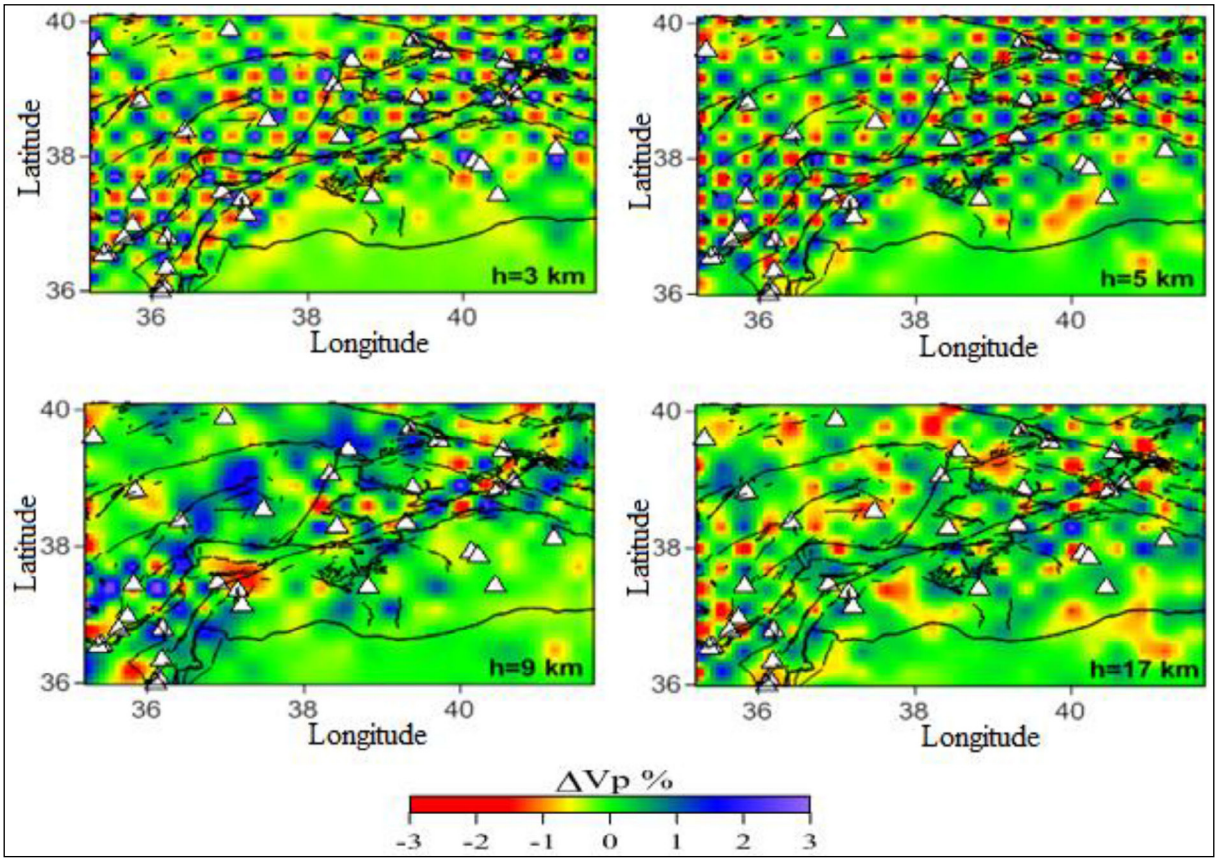

Figure 7- P wave velocity distribution checkerboard test results (% Vp and Vp) at 3km, 5 km, 9 km and 17 km depths.

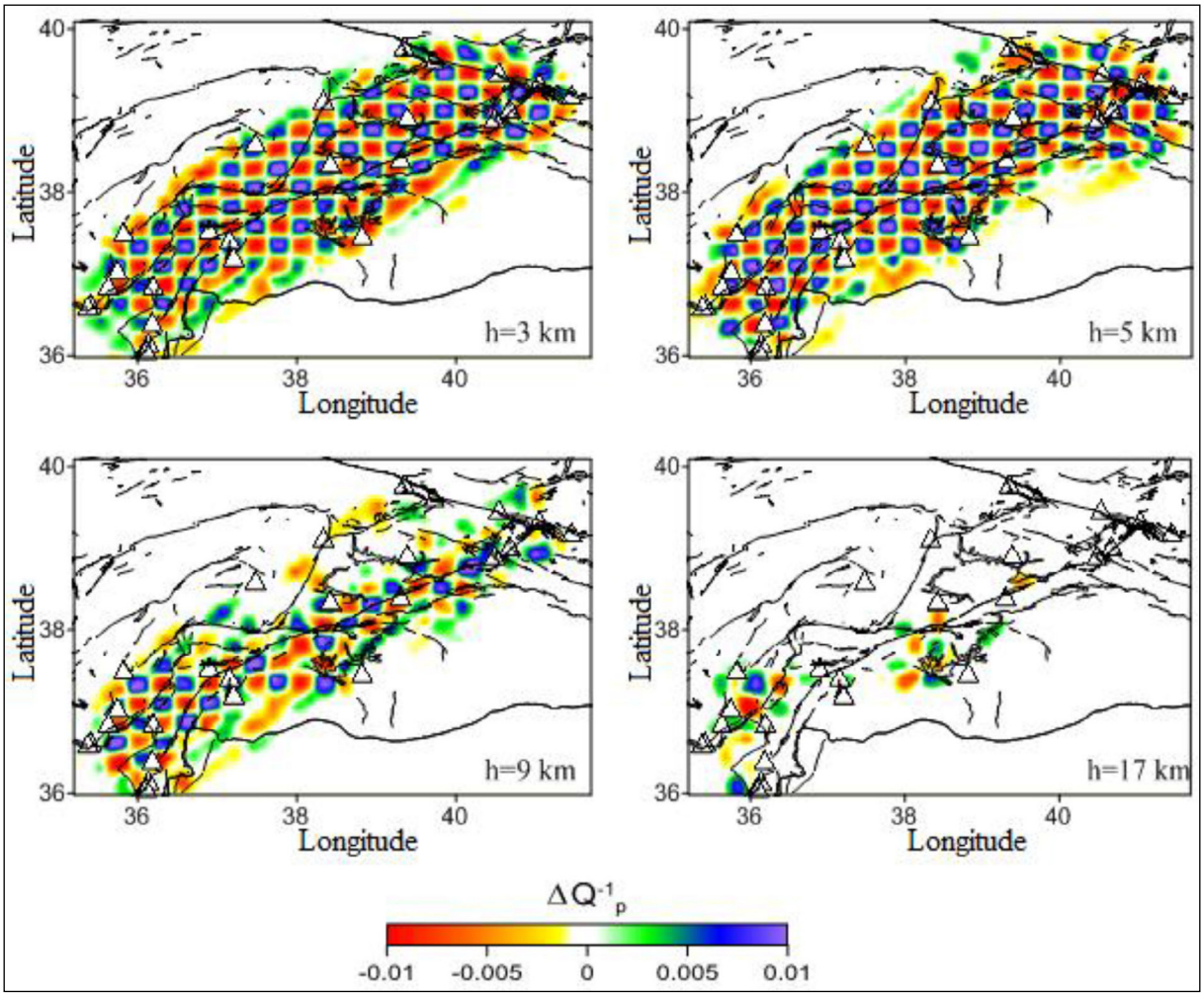

Figure 8- Checkerboard test results for P wave attenuation (ΔQ_v^{-1}) at 3km, 5 km, 9 km and 17 km depths.

depths. According to the checkerboard results, the resolution decreases in the number of rays due to the low number of stations and rare earthquakes, and the low intensity of earthquakes as going towards deeper parts. The resolution changes after 9 km depth for the P wave velocity changes obtained in the checkerboard test results, and after 5 km depth for the attenuation change. The amount of error in depth for determining the change in the P wave velocity is ± 1.24 km and ± 0.9 km for determining the attenuation values. The resolution of the P wave velocity change is higher. Here, the velocity change values were calculated from earthquake data showing both spatial distribution and along the fault, and attenuation values were obtained only from earthquakes occurring along the EAFZ. The deeper adoption of P wave velocity changes in depth sections is due to the long and more beam paths. Therefore, a difference occurs in the deep alignment of the beam path.

By applying the inverse solution to the arrival times of P waves of the earthquakes occurring between longitudes of 35.2° - 41.7° E and latitudes of 35.9° - 40.1° N in the Eastern Anatolian Fault Zone (EAFZ), the three - dimensional velocity changes and the attenuation pattern along the EAFZ were determined (Figures 9-11). The % Vp, Vp and ΔQ_p^{-1} values were correlated with the depth given above and the distribution of earthquakes in the underlying layer (Figures 9-11). According to the results, it was observed that the velocity change and attenuation was low in the Hazar - Sincik segment (segment 4 in Figure 1) where the January 24, 2020 Sivrice earthquake had occurred, and the Vp velocity is the same as the peripheral units down to a depth of 7 - 8 km, but lower in deeper parts with respect to the environment (Figures 9-10).

Although % Vp, Vp and ΔQ_p^{-1} values show regional distribution in parts close to the earth, it is noteworthy

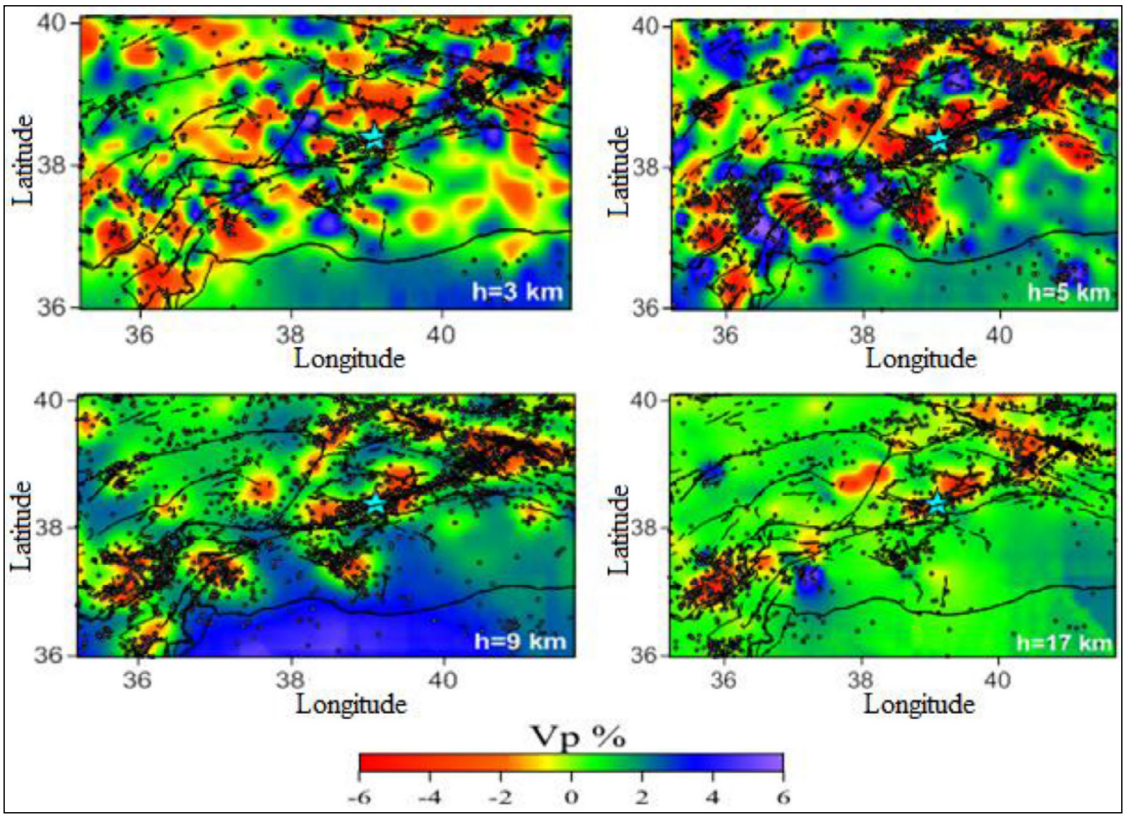

Figure 9- Spatial distribution of P wave velocity change (Vp%) values at 3, 5, 9 and 17 km depths and their relation with the tectonic structure. The points here show the focal distribution of earthquakes at the depths given.

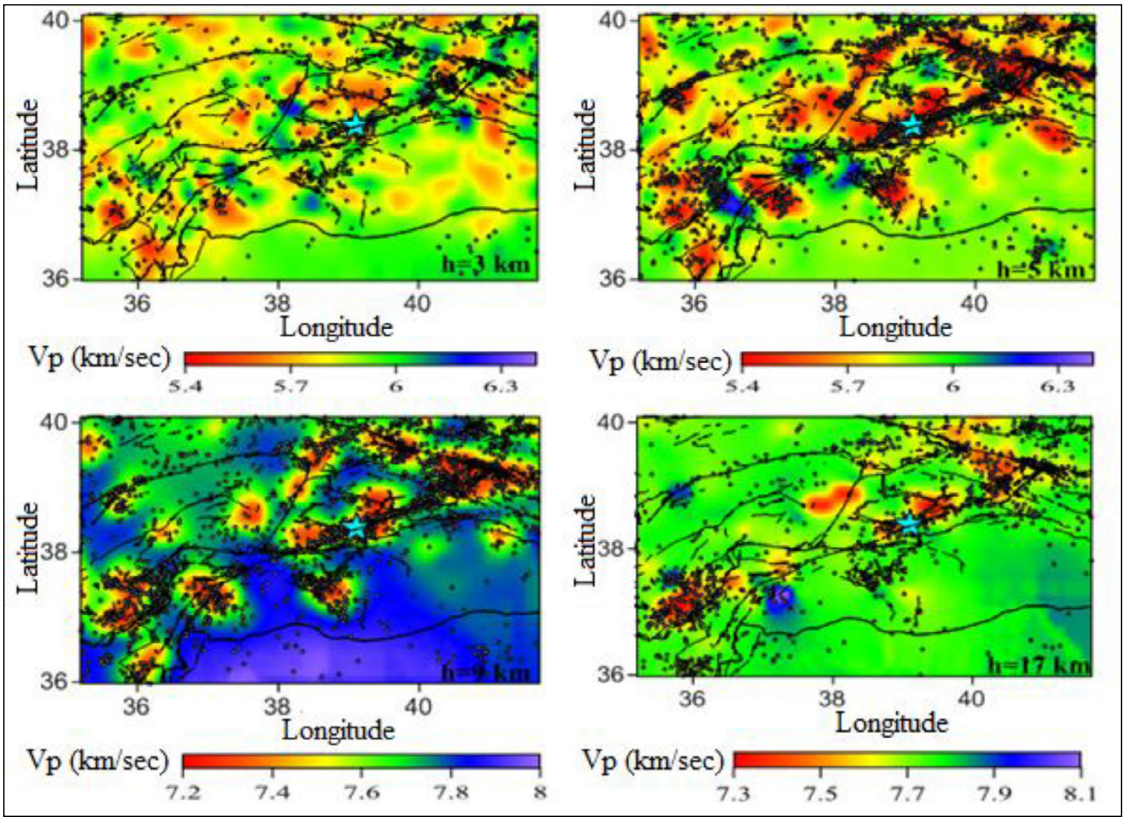

Figure 10- The spatial distribution of P wave velocity (Vp) values at 3, 5, 9 and 17 km depths and their relationship with the tectonic structure. The points here show the focal distribution of earthquakes at the depths given.

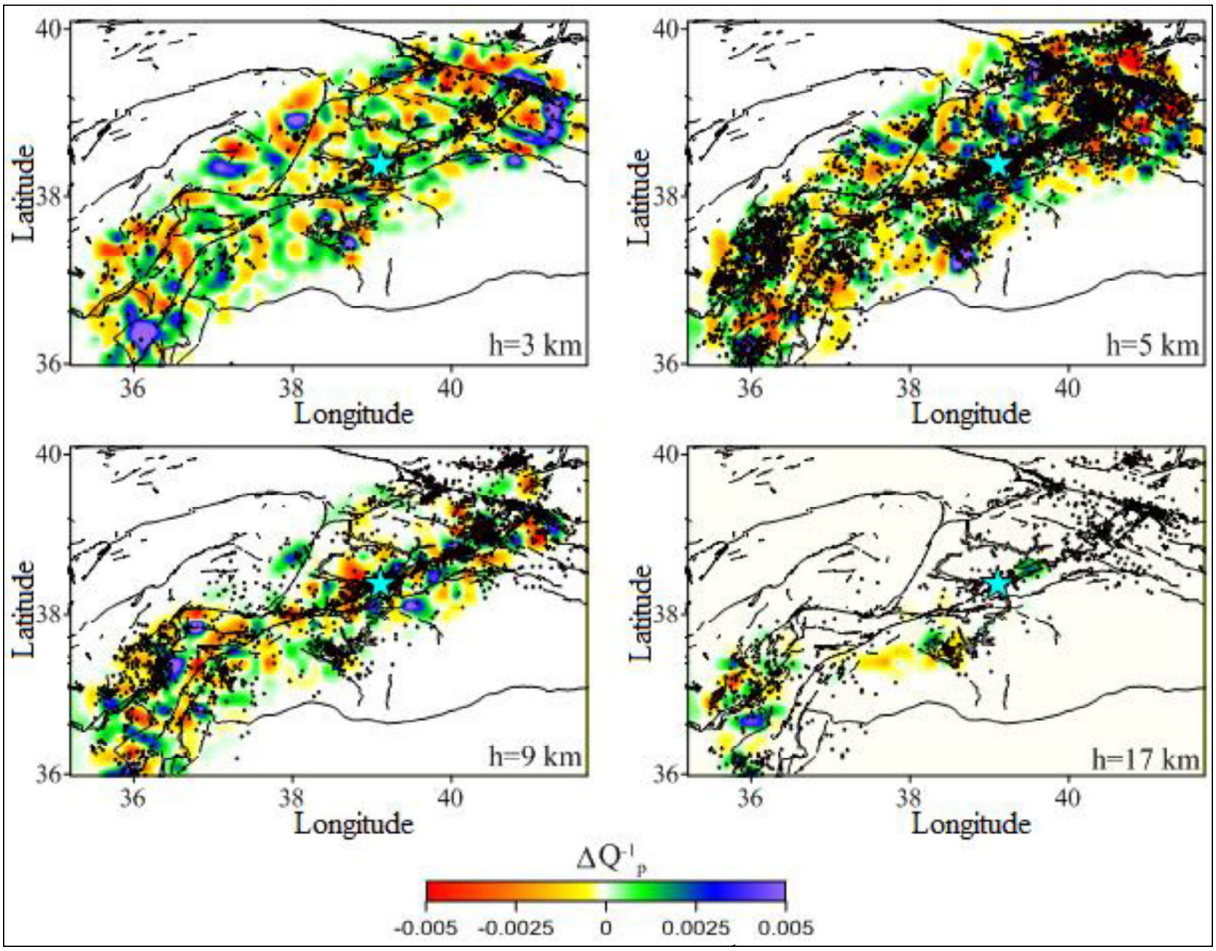

Figure 11- The spatial distribution of P wave attenuation (ΔQ_v^{-1}) values at 3, 5, 9 and 17 km depths and their relationship with the tectonic structure. The points here show the focal distribution of earthquakes at the depths given.

that they show a change due to faults as going deeper. The variation starts from the 5th kilometer depending on the fault planes. At this depth, the decrease in % Vp values (Figure 9) and the increase in Vp values (Figure 10) are particularly concentrated on the Hazar - Sincik fault. This situation continues down to 30 km depth (Figures 9 and 10). In the results obtained by geodetic studies too, it was suggested that the slip had reached a depth of 20 km (Melgar et al., 2020). However, there is observed an increase in % Vp and ΔQ_p^{-1} values in the NAFZ in the Karlıova region. In addition, the existence of similar situation was detected in Hatay, which is on the Türkoğlu - Antakya segment where two important earthquakes had occurred in 1822 and 1872, in the Adana Basin where the 1945 and 1998 earthquakes had occurred, in Gölbaşı - Türkoğlu, where the 1114 and 1513 earthquakes had occurred, and on Karlıova - Bingöl segments where the 1866 and 1971 earthquakes had occurred (İmamoğlu and Çetin, 2007; Yalçın et al., 2012; Demirtaş and Erkmen, 2019; Jamalreyhan et al., 2020). It was observed that the % Vp, Vp and ΔQ_p^{-1} values obtained were compatible with the heat flux values (Çırmık, 2018). It is possible to say that the mantle material approaches the surface in this region. It was determined that the slip velocity on the EAFZ was mostly over the Hazar - Sincik segment and the velocities obtained from the fault surround were concentrated in the Bingöl - Karlıova region (Bulut, 2017).

Two separate sections in two different directions along the EAFZ (Figure 12-17) as being perpendicular to the Hazar - Sincik segment (from the 24 January 2020 Sivrice earthquake epicentre) (Figure 18) were taken and the changes of % Vp, Vp, ΔQ_v^{-1} and frequency dependency degree (h) were determined**.** It was seen that the deep seated earthquakes that occurred along the EAFZ in the instrumental period concentrated on this segment. The increase of h up to 1.08 on this segment indicates that seismotectonic

activity is high here (Figure 16). In sections taken perpendicular to the EAFZ as given in Figure 17, it was observed that the effects of velocity and attenuation were on the Hazar - Sincik segment where the deepest Sivrice earthquake occurred on January 24, 2020. On the other hand, there is an earthquake clustering on Gölbaşı - Türkoğlu (segment number 2), Bingöl - Karlıova (segment number 6) and the unnamed segment number 7 on the EAFZ. However, it is possible to say that the cluster on segment number 7 is the Bingöl earthquake that occurred on May 1, 2003 and its aftershocks.

In addition, a 3 - dimensional cross - section was taken to determine the change of % Vp, (ΔQ_v^{-1}) and η along the EAFZ (Figures 19-21). The compatibility of %Vp with (ΔQ_v^{-1}) values in the horizontal cross - section maps and each other at the intersection points of the lines are noteworthy. Based on the cross - sections and examination of the earthquake focal

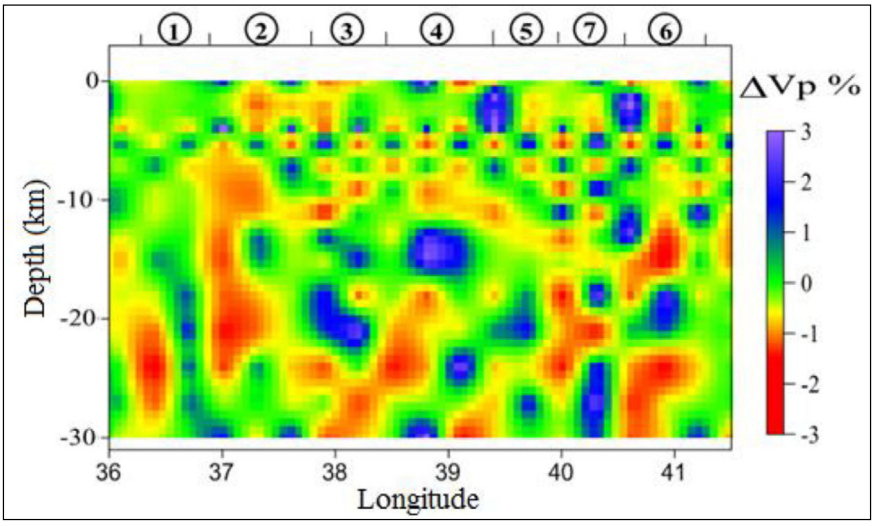

Figure 12- Checkerboard test result for P wave attenuation (ΔQ_v^{-1}) along the EAFZ. Segments on the cross section; 1) Türkoğlu-Antakya segment, 2) Gölbaşı-Türkoğlu segment, 3) Çelikhan-Gölbaşı segment, 4) Hazar-Sincik segment, 5) Palu-Hazar segment and 6) Karlıova-Bingöl segment. The number 7 here is not named, and it is one of the seismic gaps present in the region.

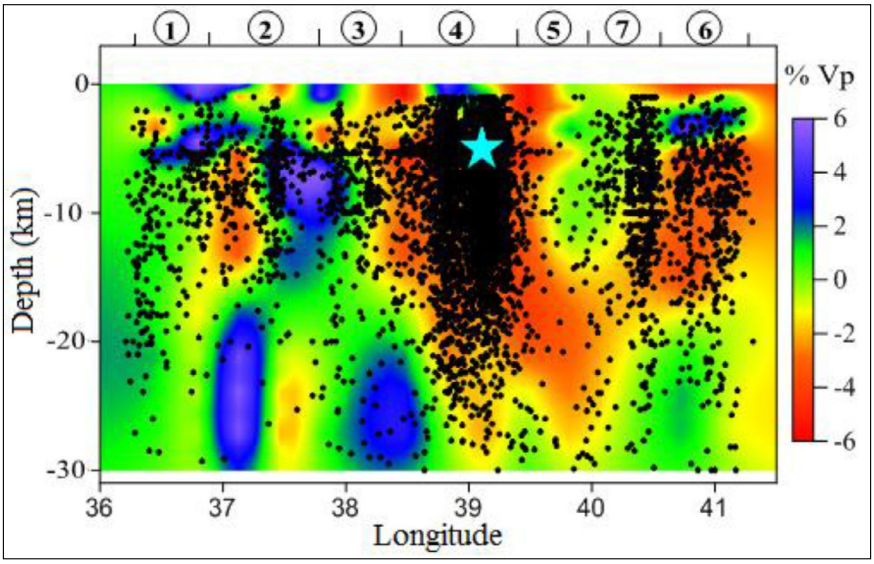

Figure 13- %Vp change along the EAFZ. Here, the black dots indicate the focal distribution of earthquakes along the zone, and the blue star indicates the focal depth of the January 24, 2020 Elazığ-Sivrice earthquake. Numbers on the cross section are the same as in Figure 12.

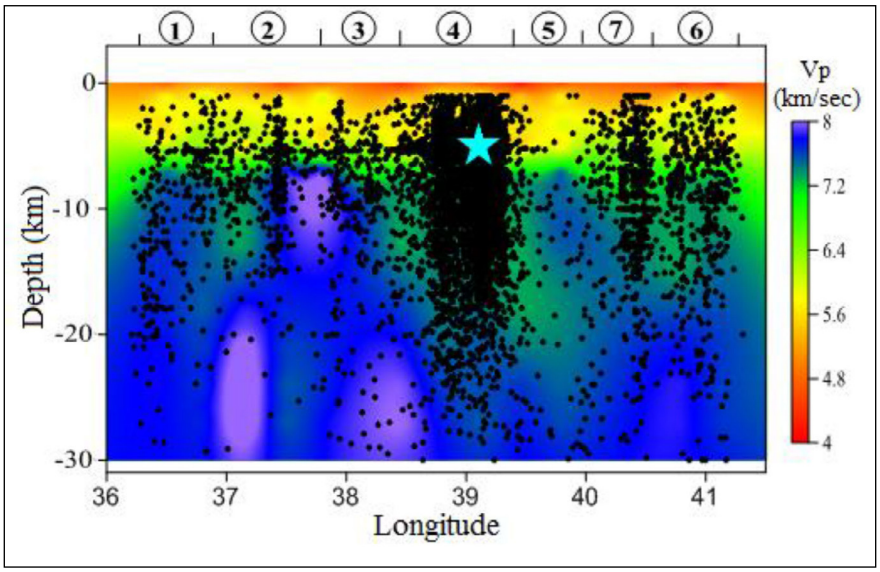

Figure 14- Vp (km/sec) change along the EAFZ. Here, the black dots indicate the focal distribution of the earthquakes occurring along the zone, while the blue star indicates the focal point of the January 24, 2020 Elazığ-Sivrice earthquake. Numbers on the cross section are the same as in Figure 12.

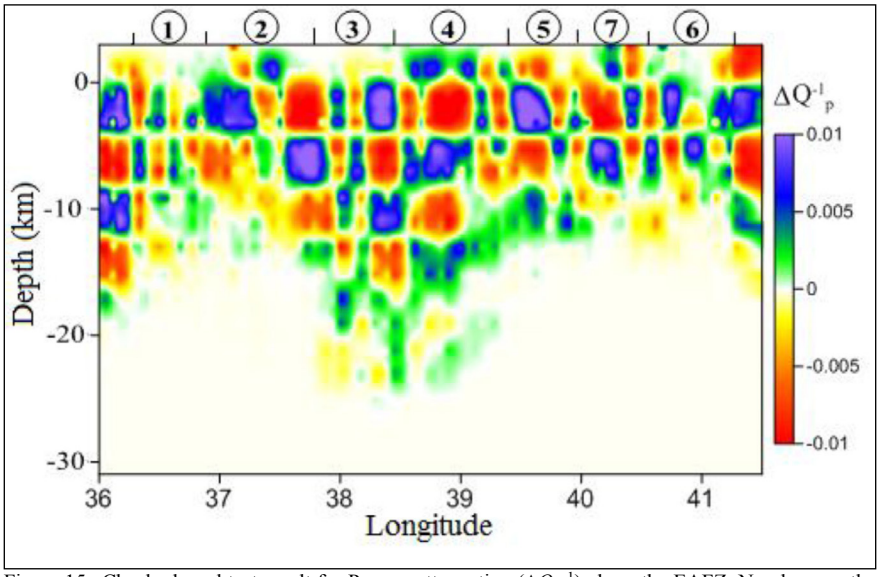

Figure 15- Checkerboard test result for P wave attenuation (ΔQ_v^{-1}) along the EAFZ. Numbers on the cross section are the same as in Figure 12.

depths, the EAFZ depth is estimated to be around 36 km. It was observed that the %Vp, Vp, **(ΔQ_v^{-1})** values obtained were compatible with seismogenic zones and crustal attenuation determined in the region (Turkelli et al., 2003; Zor et al., 2007).

It is observed that the %Vp change decreases to 30 km, ΔQ_v^{-1} value decreases to 17 km and the frequency - dependent change decreases down to 15 km in vertical sections obtained along the EAFZ. It is seen that all three values reach the deepest point in the Hazar - Sincik segment (Figures 12-17). On the other hand, the decrease of the %Vp and the increase of the Vp values were detected in the segment 6 and in the segment 2, close to the boundary of segment 1 (Figures 13 and 14). There was observed a change on the boundary region of the Dead Sea Fault and the EAFZ in ΔQ_v^{-1} values, and it is compatible with the change in velocity (Figure 16). A similar situation is also observed in the values of h (Figure 17). It was

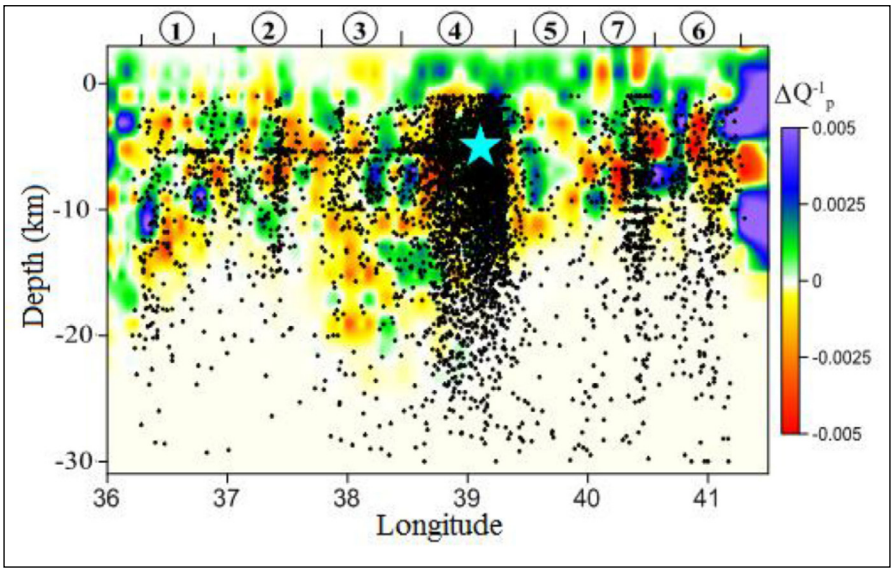

Figure 16- The variation of attenuation (ΔQ_v^{-1}) values along the EAFZ. Here, the black dots indicate the focal distribution of earthquakes along the zone, and the blue star shows the focal depth of the 24 January 2020 Elazığ-Sivrice earthquake. Numbers on the cross section are the same as in Figure 12.

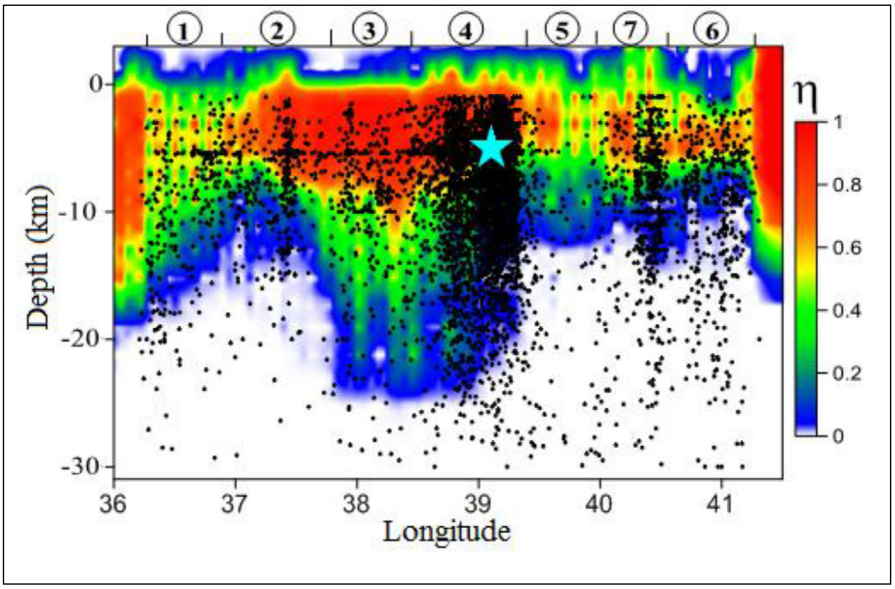

Figure 17- The change of frequency dependency degree (h) values along the EAFZ. Here, the black dots indicate the focal distribution of the earthquakes occurring along the zone, while the blue star indicates the focal point of the January 24, 2020 Elazığ-Sivrice earthquake. Numbers on the cross section are the same as in Figure 12.

revealed that the results obtained from the cross - sections given in Figure 18 were consistent with the results obtained along the EAFZ and Hazar - Sincik segment, which is the most important segment of EAFZ, and its slope was shown linearly. It is demonstrated that the change in %Vp, Vp, ΔQ_v^{-1} and h clearly continued along the fault.

All these determinations are given in three dimensions in figures 19, 20 and 21. The changes in %Vp, ΔQ_p^{-1} and h values are revealed more clearly. It is clearly seen that the decrease in the %Vp and the increase in Vp values are in the Hatay region, in segment number 2, in Hazar - Sincik and in Bingöl - Karlıova segment which is segment number 6 (Figure 19). Similarly, it is observed that the change in values

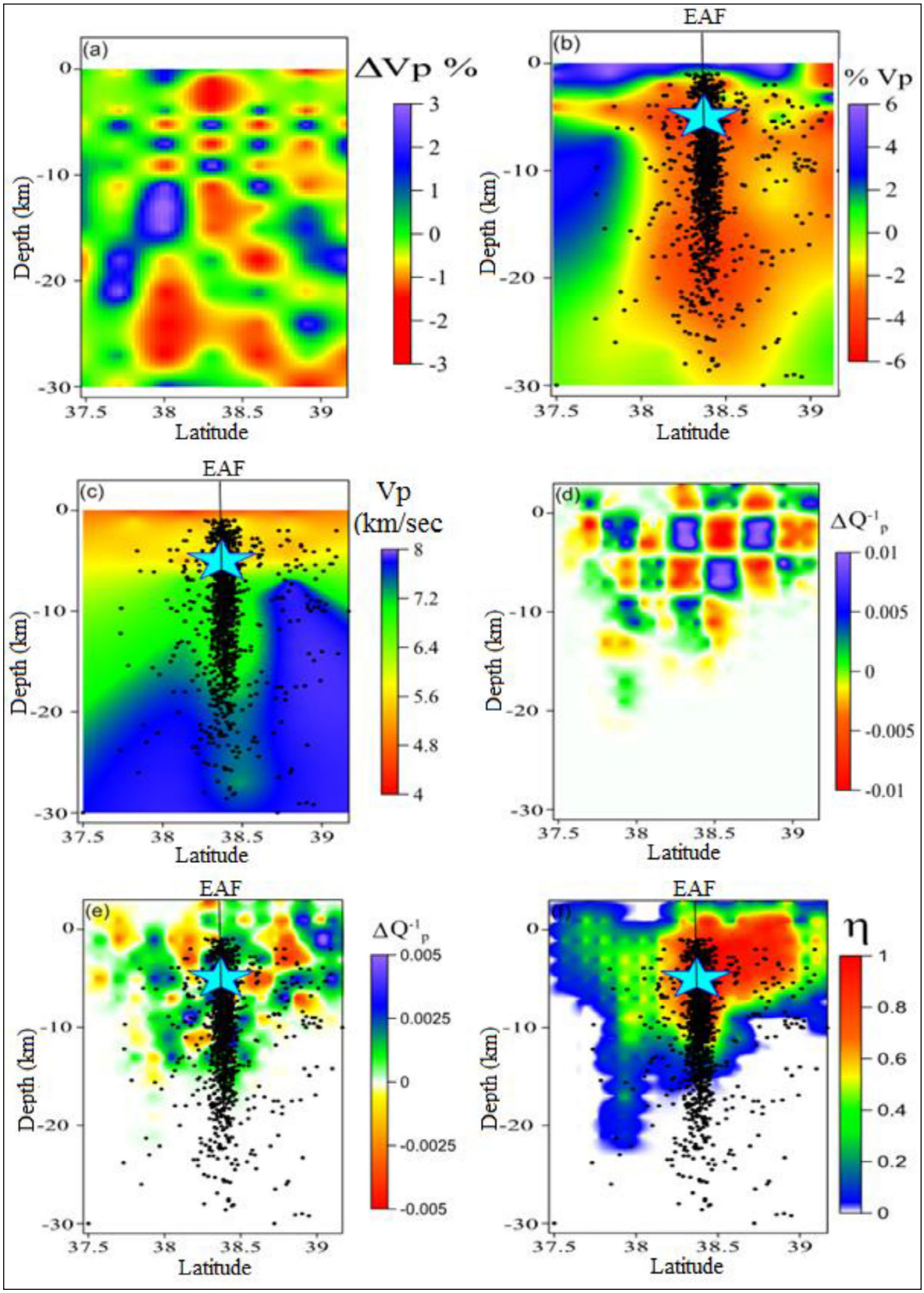

Figure 18- The change of a) DVp%, b) %Vp, c) Vp, d) ΔQ_v^{-1} checkerboard test, e) ΔQ_v^{-1} and f) η (Figure 1) along the section taken perpendicular to the Hazar-Sincik segment of the EAFZ shown as number 4 (Figure 1). Here, the black dots indicate the focal distribution of the earthquakes occurring along the section, and the blue star shows the focal point of the January 24, 2020 Elazığ-Sivrice earthquake.

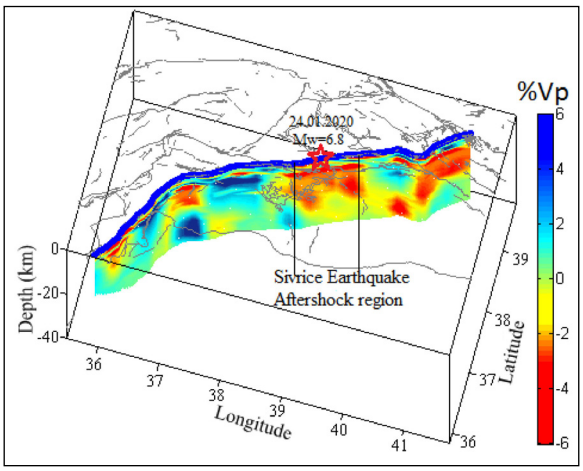

Figure 19- Three-dimensional view of %Vp change along the EAFZ. Here, the star refers to the epicenter of the January 24, 2020 Elazığ-Sivrice earthquake.

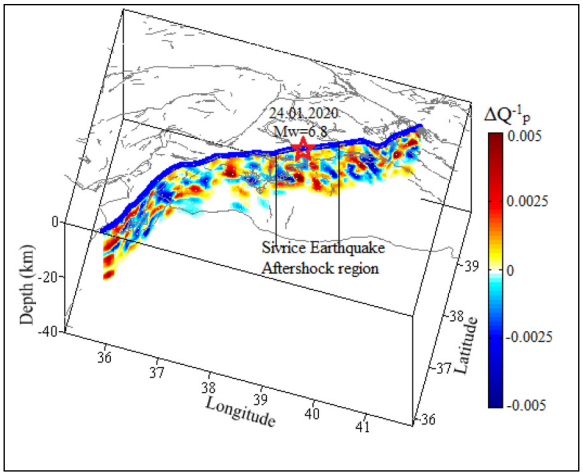

Figure 20- Three-dimensional view of the change in ΔQ_v^{-1} value along the EAFZ. The other information is the same as in Figure 19.

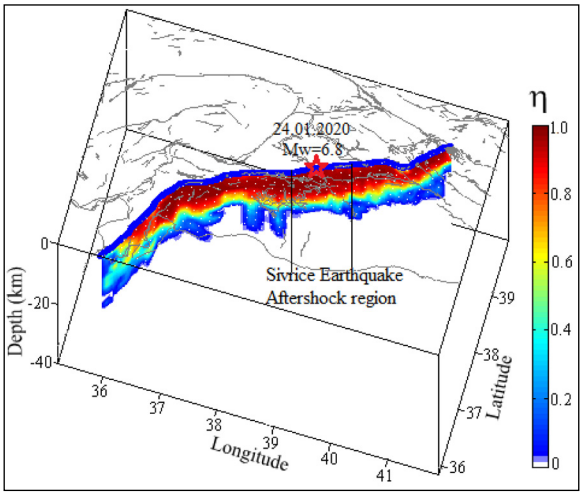

Figure 21- Three-dimensional view of the change in η value along the EAFZ. The other information is the same as in Figure 19.

of ΔQ_v^{-1} concentrates on the same segments, but differently, the value of ΔQ_p^{-1} decreases in the Yayla fault that cuts the EAFZ (MTA, 2013) (Figure 20). The fact that the maximum value in the frequency dependency level is in segment number 2 indicates that this region is in the character of an intersection, therefore it is a highly altered area. The value of h was observed in segment number 5 mostly at a depth of 15 km.

In this study, it was determined that the P wave velocity change increased up to 6% in areas near the surface and along the fault zone. While this change is higher in the fault segments as it goes deeper, it decreases in other areas. Similar results were also obtained in the studies conducted in the region. While the high P wave velocity anomalies are seen in areas close to the surface according to Salah et al. (2011), low seismic velocity anomalies are observed in deeper crustal layers. Aydın et al. (2020) stated that Vp was in the range of 6.13 - 6.49 km/sec in areas close to the surface in the region and the velocity increased towards deeper parts. It was stated by Çağlar (2019) that between 22 - 35 km depths in Hatay and its surroundings, Vp varied between 6.0 - 7.5 km/sec, and Vp greater than 7.5 km/sec was seen in areas close to the crust - mantle boundary.

It was determined that the P wave attenuation (ΔQ_p^{-1}) value varied within the range of ± 0.005 along the EAFZ. On the other hand, the degree of frequency dependency ranges from 0.1 to 1.08. Both values indicate that the region is seismotectonically active. Aydın and Kadirov (2008) determined the P wave quality factor as 28.5 where Vp was 6.25 km/sec in the region. Aydın et al. (2020) and Sertçelik (2012) examined the Coda wave attenuation pattern in the region and determined the seismic wave frequency dependency degrees as 1.25 and 0.93, respectively. These values show that the region has a high heterogeneity and is seismotectonically active.

When all these results and the 2020 Sivrice earthquake coulomb stress change (Jamalreyhani et al., 2020) are examined, the seismicity on the EAFZ should be expected to be in the Palu - Hazar segment. The change in %Vp, Vp, ΔQ_p^{-1} and h is in that direction. This situation is clearly seen in depth sections. In addition, the changes on the EAFZ will be followed with new data in order to make this study sustainable.

5. Conclusion

The three dimensional %Vp and Vp, ΔQ_v^{-1} and h values belonging to the local earthquakes recorded by 26 stations along the EAFZ were calculated by using the tomographic method to the multiple P wave arrival time inverse solution belonging to the local earthquakes recorded by 40 stations affiliated to KOREI. The checkerboard resolution test results, beam number and beam path maps show that the velocity anomalies obtained give reliable results down to a depth of approximately 30 km. Accordingly, it was observed that velocity values were generally lower than the average in some segments along the EAFZ. Regions with low %Vp anomalies are clearly visible at almost all depths. These can be interpreted as the movement of the partial melt into the crust in the lower crust and the melting mantle. It is noteworthy that although some of the earthquakes occur in high - speed regions in the region, most of them are concentrated in regions with low velocity, but in areas earthquakes with small magnitudes, active faults and high heterogeneity. Along the EAFZ, there are many sedimentary basins and widespread fault zones. The existence of low - speed zones is due to such patterns.

Velocity variations in the region show a heterogeneous pattern. It was observed that earthquakes clustered at a depth of 0 - 10 km, where the velocity changes were the greatest. However, it was observed that there was a reduction in the decrease of P wave velocity after 20 km depth. Then, the speed directly increases as the depth increases. At approximately 20 km, the wave velocity generally increases and reaches its highest level at this depth. This suggests a formation change at around 40 km.

Cross - sections were taken in two different directions in the study area, and the compatibility of these sections with respect to each other, % Vp, Vp, ΔQ_v^{-1} and h change maps were observed at the intersection points of the sections. As a result of this study, it is observed that velocity and attenuation values vary according to seismogenic limits along the EAFZ. Low Vp, high ΔQ_v^{-1} and h indicate that the environment does not lose its heterogeneity with depth and that a complex structure or upper mantle material that increases the attenuation is close to the upper part of the crust. The Vp, ΔQ_v^{-1} and h frequency dependency degree show significant changes according to the heterogeneous structure in the upper crust. These heterogeneities are shaped depending on the tectonics of the region. The high h indicates that the heterogeneity is not lost with depth, and there is a complex structure that increases the attenuation.

The data used in this study covers the period until the end of 2019. In other words, it includes the earthquake data that occurred until a time close to the 24 January 2020 Sivrice earthquake. The results obtained show that the stress accumulation was formed on the Hazar - Sincik segment where the earthquake had occurred. While the Vp value changes between 4 - 8 km/sec along the EAFZ, it was detected that it increased up to 7.5 km/sec on this segment. While the values of ΔQ_v^{-1} change within the range of ± 0.005, it is seen that it falls on the boundaries of this segment.

By adding data for the year 2020 to the existing data, it can be traced in which segment the stress accumulation occurs on the EAFZ. This situation is important for the sustainability of the study. Knowing the earthquake behavior of the EAFZ in the near future is of vital importance for the reduction of earthquake damages in the regions where many cities with a significant population and very important facilities for the economy of our country are located.

Acknowledgements

The authors thank to Wessel and Smith (1998), who prepared the GMT (Generic Mapping Tools) software used in the preparation of the figures, Prof. Orhan Dede Polat (Dokuz Eylul University, Department of Geophysical Engineering) for his contributions in the use of software, Dr. Mohamed Farouk Abdelwahed who prepared TOMOTOOLS software used in determining Vp velocity variations and to Dr. Luca De Siena who prepared MuRATv.2 used in determining the attenuation pattern.

References

Abdel - Fattah, A. K., Morsy, M., El - Hady, S., Kim, K. Y., Sami, M. 2008. Intrinsic and scattering attenuation in the crust of the Abu Dabbab area in the eastern desert of Egypt. Physics of the Earth and Planetary Interiors 168, 103-112.

AFAD, 2020. Report on 24 January 2020 Sivrice (Elazığ) Mw 6.8 Earthquake, Disaster and Emergency Management Presidency of Turkey, Ministry of Interior, Ankara, Turkey, Open File Rep. 46.

Akıncı, A. 1994. Attenuative behaviors of Western Anatolia and Southern Spain using single and Multiple

scattering models, Ph.D.Thesis, Dokuz Eylül University, Grauate School of Natural and Applied Sciences 37-39.

Akıncı, A. Eyidoğan, H. 1996. Frequency-dependent attenuation of S and coda waves in Erzincan region (Turkey) Physics of the Earth and Planetary Interiors 97, 1, 109-119 (11).

Aki, K. 1980. Scattering and attenuation of shear waves in the litosphere. Journal of Geophysical Research 85, 6496-6504.

Aki, K., Chouet, B. 1975. Origin of Coda wave: Source, attenuation and scattering effects, Journal of Geophysical Research 80, 21, 3322-3342.

Aksoy, E., İncegöz, M., Koçyiğit, A. 2007. Lake Hazar Basin: a negative flower structure on the East Anatolian Fault System (EAFS), SE Turkey. Turk. J. Earth Sci. 16, 319-338.

Allen, M., Jackson, J., Walker, R. 2004. Late Cenozoic reorganization of the Arabia-Eurasia collision and the comparison of short - term and long - term deformation rates. Tectonics 23, 1, TC2008.

Arpat, E., Şaroğlu, F. 1972. Doğu Anadolu Fayı ile ilgili bazı gözlemler. Maden Tetkik ve Arama Dergisi 78, 44-50.

Aydın, U., Kadirov, A. 2008. Erzincan ve Çevresinde P Dalgası Soğurulması. SAÜ Fen Bilimleri Dergisi 12(1), 1-8.

Aydın, U., Şahin, Ş., Kalkan, E. 2012. Yarbaşı, N., Aksoy, G., Kemaliye çevresinde Pg, Sg Soğurulması ve yeni magnitüd fomülü, Fen Bilimleri Dergisi 16, 1, 13-23.

Aydın, U., Şahin, Ş., Salah, M.K. 2020. Upper crustal Poisson's ratio and coda-wave attenuation beneath Eastern Anatolia, Earthq Eng and Eng Vib. 19, 335-347.

Barka, A. A., Kadinsky - Cade, K. 1988. Strike - slip fault geometry in Turkey and its influence on earthquake activity. Tectonophysics 7, 663-684

Bianco, F., Del Pezzo, E., Castellamo, M., Ibanez, J., Diluccio, F. 2002. Separation of intrinsic and scattering seismic attenuation in the Southern Apennine zone, Italy. Journal of Geophysical Research 150, 10-22.

Bulut, F., Bohnhoff, M., Eken, T., Janssen, C., Kılıç, T., Dresen, G. 2012. The East Anatolian Fault Zone: Seismotectonic setting and spatiotemporal characteristics of seismicity based on precise earthquake locations. J. Geophys. Res. 117, B07304, https://doi.org/10.1029/2011JB008966.

Bulut, F. 2017. Doğu Anadolu Fayı boyunca Sismik ve A-sismik Tektonik Hareketler: Hazar Gölü Doğu'sunda Sismik Boşluk mu yoksa Krip mi? AKÜ FEMÜBİD 17 015803 (257-263).

Çağlar, Ö. 2019. Determination of 3-D crustal seismic velocity structure beneath Hatay and surroundings, Journal of the Faculty of Engineering and Architecture of Gazi University 34(4), 2215-2227.

Çırmık, A.Y. 2018. Examining the crustal structures of Eastern Anatolia, using thermal gradient, heat flow, radiogenic heat production and seismic velocities (Vp and Vs) derived from Curie Point depth, Examining the crustal structures of eastern Anatolia 59, 2, 117-134.

De Siena, L., Del Pezzo, E., Bianco, F., Tramelli, A. 2009. Multiple resolution seismic attenuation imaging at Mt. Vesuvius, Physics of the Earth and Planetary Interiors 173, 17-32.

De Siena, L., Calvet, M., Watson, K. J., Jonkers A. R. T., Thomas, C. 2016. Seismic scattering and absorption mapping of debris flows, feding paths, and tectonic units at Mount St. Helens volcano, Earth and Planetary Science Letters 442, 21-31.

De Siena, L., Amoruso, A., Del Pezzo, E., Wakeford, Z., Castellano, M., Crescentini, L. 2017. Space-weighted seismic attenuation mapping of the aseismic source of Campi Flegrei 1983-1984 unrest, Geophys. Res. Lett. 44, 1740-1748, doi:10.1002/2017GL072507.

Del Pezzo, E., Bianco, F., De Siena, L., Zollo, A. 2006. Small scale shallow attenuation structure at Mt. Vesuvius. Phys. Earth Planet. Inter. 157, 257-268.

Demirtaş, R. 2003. DAFZ'nda Deprem Üreten Diri Faylar; 1900-2003 Yılları Arasında Doğu Anadolu Fay Zonunda Olmuş Hasar Yapıcı Depremler. Deprem ve Kentleşme. 23-24-25 Eylül 2003, TMMOB Jeoloji Müh. Odası yayınları 78, Konferans serisi 3.

Demirtaş, R., Erkmen, C. 2019. Doğu Anadolu Fay Sistemi Deprem Etkinliği, Gelecek Deprem Potansiyeli, Researchgate DOI: 10.13140/RG.2.2.24235.49449.

Demirsıkan, İ. H., Şahin, Ş., Öksüm, E. 2019. Orta Anadolu'da kabuğa ait sismik P ve S dalga hızı yapısının belirlenmesi, Pamukkale Üniversitesi, Mühendislik Bilimleri Dergisi 25, 6, 775-784,

Dewey, J. F., Hempton, M. R., Kidd, W. S. F., Şaroğlu, F., Şengör, A. M. C. 1986. Shortening of continental lithosphere: the neotectonics of eastern Anatolia: a young collision zone. In: Coward, M. P., Ries, A. C. (Eds.), Collision Tectonics. Geological Society, London, Special Publications 19, 3-36.

Djamour, Y., Andrnant, P., Nankali, H. R., Tavakoli, F. 2011. NW Iran-Eastern Turkey present - day kinematics:

Results from the Iranian permanent GPS network. Earth and Planetary Science Letters 307, 27-34, doi:10.1016/j.epsl.2011.04.029.

Duman, T. Y., Emre, Ö. 2013. The East Anatolian Fault: geometry, segmentation and jog characteristics, Geological Society, London, Special Publications 372, 495-529. Doi:10.1144/SP372.14.

Eken, T., Mayeda, K., Hofstetter, A., Gök, R., Örgülü, G., Turkelli, N. 2004. An Application of the Coda Methodology for Moment - Rate Spectra Using Broadband Stations in Turkey, Geophysical Research Letters 31(11): L11609. doi: https://doi.org/10.1029/2004GL019627.

Farouk, M., Zhao, D. 2006. Tomo tools programme for Windows V 1.0. Geodynamics Research Center (GRC), Ehime University, Japan, Scientific Report 1. (unpublished).

Ford, S. R., Phillips, W.S., Walter, W. R., Pasyanos, M. E., Mayeda, K., Dreger, D. S. 2010. Attenuation Tomography of the Yellow Sea / Korean Peninsula from Coda - source normalized and direct Lg Amplitudes. Pure Appl. Geophys 167, 1163-1170.

Frenkal, A., Mcgarr, A., Bicknell, J., Mri, J., Seeber, L., Cranswick, E. 1990. Attenuation of high-frequency shear waves in the crust: measurements from New York State, South Africa and Southern California. Journal of Geophysical Research 95, 17441-17457.

Hempton, M.R. 1985. Structure and deformation history of the Bitlis sture near Lake Hazar, south eastern Turkey. Geol. Soc. Am. Bull. 96, 233-243.

Herece, E. 2003. Doğu Anadolu Fayı. Antakya ve Osmaniye'nin Depremselliği ve Kentleşmeye Etkileri. 26-27 Haziran 2003, TMMOB Jeoloji Müh. Odası yayınları 76, Konferans serisi 1.

Herece, E., Akay, E. 1992. Karlıova - Çelikhan arasında Doğu Anadolu Fayı, Türkiye 9. Petrol Kongresi, 361-372.

Horasan, G., Boztepe - Güney, A. 2004. S-wave attenuation in the Sea of Marmara, Turkey, Phys. Earth Planet. Interiors 142, 215-224.

Ibanez, J. M., Del Pezzo, E. D., Miguel, F., Herraiz, M., Alguacil, G., Morales, J. 1990. Depth - dependent seismic attenuation in the Granada zone (South Spain). Bull. Seismol. Soc. Am. 80, 1232-1244.

İmamoğlu, M. Ş., Çetin, E. 2007. Güneydoğu Anadolu Bölgesi ve yakın yöresinin depremselliği, D.Ü. Ziya Gökalp Eğitim Fakültesi Dergisi 9, 93-103.

Jamalreyhani, M., Büyükakpınar, P., Cesca, S., Dahm, T., Sudhaus, H., Rezapour, M., Isken, M. P., Asayesh, B. M., Heimann, S. 2020. Seismicity related to the eastern sector of Anatolian escape tectonic: the example of the 24 January 2020 Mw 6.77 Elazığ-Sivrice earthquake. Solid Earth, https://doi.org/10.5194/se-2020-55.

Jordan, T., Chen, Y., Gasparani, P., Madariaga, R., Main, I., Marzocchi, W., Papadopoulos, G., Sobolev, G., Yamaoka, K., Zcchau, J. 2011. Operational earthquake forecasting: State of knowledge and guidelines for utilization. Annals of Geophysics 54, 4. doi: 10.4401/ag-5350

Kalafat, D., Gürbüz, C., Üçer, S.B. 1987. Batı Türkiye'de Kabuk ve Üst Manto Yapısının Araştırılması. Deprem Araştırma Bülteni 59, 43-64.

Kartal, R. F., Kadiroğlu, F. T. 2013. Doğu Anadolu Fayının sismotektoniği ve bu fay üzerindeki son beş yıllık deprem aktivitesinin istatistiksel analizi, 66. Türkiye Jeoloji Kurultayı 01-05 Nisan 2013, ODTÜ Kültür ve Kongre Merkezi, Ankara.

KOERI, 2020. Kandilli Observatory and Earthquake Research Institute, Dataset / Seismic Network. doi: 10.7914/SN/KO, Çengelköy, İstanbul, http://www.koeri.boun.edu.tr. January 30, 2020.

Melgar, D., Ganas, A., Taymaz, T., Valkaniotis, S., Crowell, B.W., Kapetanidis, V., Tsironi, V., Yolsl-Çevikbilen, S., Öcalan, T. 2020. Rupture Kinematics of January 24, 2020 Mw 6.7 Doğanyol-Sivrice, Turkey Earthquake on the East Anatolian Fault Zone Imaged by Space Geodesy, Manuscript submitted to, Earth and Planetary Science Letters, DOI: 10.31223/osf.io/xzg9c.

Mc Kenzie, D. P. 1976. The East Anatolian Fault, a major structure in Eastern Turkey. Earth and Planetory Sciences 29, 189-193.

Mohanty, W. K., Prakash, R., Suresh, G., Shukla, A. K., Walling, M. Y., Srivastava, J. P. 2009. Estimation of Coda wave attenuation for the National Capital Region, Delhi, India, using local earthquakes, Pure and Applied Geophysics 166(3), 429-449.

MTA. 2013. Türkiye Diri Fay Haritası. Maden Tetkik Arama Genel Müdürlüğü, Ankara.

Mukhopadhyay, S., Sharma, J. 2010. Attenuation characteristics of Garwhal-Kumaun Himalayas from analysis of coda of local earthquakes, Journal of Seismology 14, 693-713.

Nalbant, S., McCloskey, J., Steacy, S., Barka, A. 2002. Stree accumulation and increased seismic risk in Eastern Turkey. Earth and Planetary Science Letters 195, 291-298.

Özer, C., Gök, E,. Polat, O. 2018. Three - Dimensional Seismic Velocity Structure of the Aegean Region of Turkey from Local Earthquake Tomography, Annals of Geophysics 21(61), 2018.

Pulli, J.J. 1984. Attenuation of coda waves in New England, Bulletin of the Seismological Society of America 74, 4, 1149-1166

Reilinger, R., McClusky, S., Andrnant, P., Lawrence, S., Ergintav, S., Çakmak, R., Özener, H., Kadirov, F., Guliev, I., Stepanyan, R. 2006. GPS constraints on continental deformation in the Africa - Arabia Eurasia continental collision zone and implications for the dynamics of plate interactions. Journal of Geophysical Research: Solid Earth (1978-2012) 111, doi:10.1029/2005JB004051.

Salah, M. K., Şahin, Ş. 2019. 3D crustal velocity and *VP* / *VS* structures beneath Southeast Anatolia and their geodynamic implications, Geofizicheskiy Zhurnal 2(41), 122-140.

Salah, M. K., Şahin, Ş., Destici, C. 2007. Seismic Velocity and Poisson's Ratio Tomography of the Crust Beneath Southwest Anatolia: an Insight into the Occurrence of Large Earthquakes, Journal of Seismology 11: 415-432. DOI 10.1007/s10950-007- 9062-2.

Salah, M. K., Şahin, Ş., Aydın, U. 2011. Seismic Velocity and Poisson's Ratio Tomography of the Crust Beneath East Anatolia, Journal of Asia Earth Sciences 40, 3, 746-761.

Sato, H. 1977. Energy propagation including scattering effects single isotropic scattering approximation. Journal of Geophysical Research 25, 27-41.

Sato, H., Fehler, M.C. 1998. Seismic Wave Propagation and Scattering in the Heterogenous Earth. Springer.

Sharma, B., Kumar, D., Teotia, S. S., Rastogi, B. K., Gupta, A. K., Prajapati, S. 2011. Attenuation of Coda Waves in the Saurashtra Region, Gujarat (India) Pure Appl. Geophys. doi:10.1007/s00024-011-0295-1.

Sertçelik, F. 2012. Estimation of Coda Wave Attenuation in the East Anatolia Fault Zone, Turkey. Pure Appl. Geophys. 169, 1189-1204, https://doi.org/10.1007/s00024-011-0368-1

Şahin, Ş., Alptekin, Ö. 2003. Güneybatı Anadolu'da kabuk ve üst mantoda sismik dalgaların frekans bağımlı soğurulması. Yerbilimleri 27(2), 53-62

Şahin, Ş., Öksüm, E. 2020. Determination of Volcanic Structures in andaround Nevşehir by Seismic Attenuation Method. Journal of the Faculty of Engineering and Architecture of Gazi University 35:1, 181-191.

Şaroğlu, F., Emre, Ö., Kuşçu, İ. 1992. The East Anatolian Fault Zone of Turkey. Annal. Tecn. 6, 99-125.

Toker, M., Şahin, Ş. 2019. Crustal Poisson's ratio tomography and velocity modeling across tectono-magmatic lake regions of Eastern Anatolia (Turkey): New geophysical constraints for crustal tectonics, Journal of Geodynamics 131, 101651, 1-28.

Taymaz, T., Eyidoğan, H., Jackson, J.A. 1991. Source Parameters of large earthquakes in the East Anatolian Fault Zone (Turkey). Geophysical Journal International - Oxford 106, 537-550.

Thurber, C. H. 1987. Seismic structure and tectonics of Kilauea volcano Hawaii. In: Decker, R. W., Wright, T. L., Stau§er, P. H. (Eds.), Volcanism in Hawaii. US Geological Survey, 919ñ934.

Turkelli, N., Sandvol, E., Zor, E., Gök, R., Bekler, T., Al-Lazki, A., Karabulut, H., Kuleli, S., Eken, T., Gürbüz, C., Bayraktutan, S., Seber, D., Barazangi, M. 2003. Seismogenic Zones in Eastern Turkey, Geophysical Research Letters 30(24), 8039. doi:10.1029/2003GL018023.

Um, J., Thurber, C. H. 1987. A fast algorithm for two-point seismic ray tracing. Bull. Seism. Soc. Am. 77, 972-986.

Wessel, P., Smith, W. H. F. 1998. New improved version of Generic Mapping Tools released. EOS Trans Am Geophys U 79, 579.

Yalçın, H., Gülen, L., Çağnan, Z., Kalafat, D. 2012. Kıbrıs ve Yakın Çevresinin Depremselliği. 65. Jeoloji Kurultayı, Bildiri Özetleri Kitabı, 4-5. Ankara.

Zhao, D., Hasegawa, A., Horiuchi, S. 1992. Tomographic imaging of P- and S- wave velocity structure beneath north eastern Japan. Journal of Geophysical Research 97, 19909-19928.

Zhao, D., Hasegawa, A., Kanamori, H., 1994. Deep structure of Japan subduction zone as derived from local, regional and teleseismic events. Journal of Geophysical Research 99, 22313-22329.

Zor, E., Sandvol, E., Xie, J., Türkelli, N., Mitchell, B., Gasanov, A.H., Yetirmishli, G. 2007. Crustal Attenuation Within the Turkish Plateau and Surrounding Regions, Bulletin of the Seismological Society of America 97, 1B, 151–161.

Bulletin of the Mineral Research and Exploration

http://bulletin.mta.gov.tr

Geological characteristics of the boundary between Bolkardağı-Bozkır Units and the Ulukışla Basin and the structural evolution of the region, Central Taurides, Turkey

Tolga ESİRTGEN[a*] and Veysel IŞIK[b]

[a]*General Directorate of Mineral Research and Exploration (MTA), Department of Geological Researches, 06800, Ankara, Turkey*
[b]*Ankara University, Department of Geological Engineering, Tectonical Research Group, Gölbaşı, Ankara, Turkey*

Research Article

Keywords:
Tectonic contact, Structural analysis, Paleostress, Taurus Unit, Ulukışla Basin, Central Taurides.

ABSTRACT

The character of the boundary between the tectonic units in the Central Taurides and the Ulukışla Basin is controversial. The contact has been accepted as discordant or tectonic contact by different researchers. The deformation data of the units in the study area provide important information about the Mesozoic - Cenozoic period geological developments of the region. Regional compression in NW - SE direction has caused the development of fold, foliation and reverse fault type structures in the units in the study area. Similar structural deformations are observed in the rock units defined in the Ulukışla Basin as well. In this study, structural data were collected from the field in order to determine the deformation pattern and contact relations of the units in the region. Field data and structural analysis reveal that the contact between the Ulukışla Basin deposits and the Bolkardağı Unit in the study area is of 70° - 80° southeast dipping reverse fault character. These structural data in the region were interpreted as the product of a movement from southeast to northwest.

Received Date: 09.06.2020
Accepted Date: 22.01.2021

1. Introduction

Taurides extending from west to east along the southern boundary of Turkey, the western, central and eastern parts to be examined in three geographically. Accordingly, Kırkkavak Fault separates the Western Taurides and Central Taurides, while Ecemiş Fault separates the Central Taurides from the Eastern Taurides (Figure 1). The first division in the Taurides according to the definition of union was made by Özgül (1976).

The Central Taurides are the areas where the tectono - stratigraphy of the unions outcropping in the Taurides are best seen and followed. The Geyikdağı Unit is relatively autochthonous and located at the lowest part of the tectono - stratigraphy. While the Unit is overlain by Bozkır, Bolkardağı and Aladağ thrusts from the north, the Alanya and Antalya units thrust over the Geyikdağı Unit from the south (Figure 1).

The study area is located in the eastern part of the Central Taurides and includes the Bozkır, Bolkardağı and Aladağ units and the units forming the Ulukışla Basin (Figure 2). The Ulukışla Basin forms a contact with the lithologies of the Niğde Massif in the north. There are opinions that the basin sediments overlie the Niğde Massif unconformably or by tectonic contacts (Blumenthal, 1941, 1952; Whitney and Dilek, 1997; Gautier et al., 2002, Demircioğlu and Eren, 2000, 2003, 2017). The contact character of the basin with the tectonic units outcropping in the Taurides in the south is also controversial. In the discussions, the

Citation Info: Esirtgen, T., Işık, V. 2021. Geological characteristics of the boundary between Bolkardağı-Bozkır Units and the Ulukışla Basin and the structural evolution of the region, Central Taurides, Turkey. Bulletin of the Mineral Research and Exploration 165, 163-190. https://doi.org/10.19111/bulletinofmre.868515

**Corresponding author: Tolga ESİRTGEN, tolga.esirtgen@mta.gov.tr*

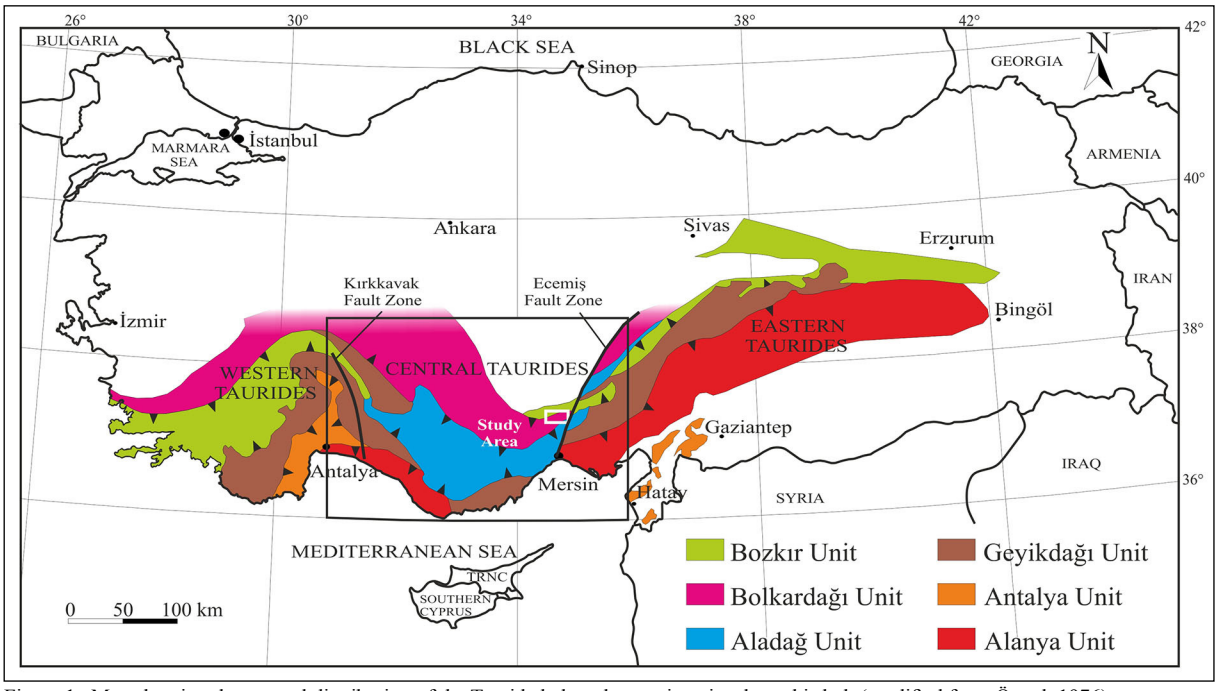

Figure 1- Map showing the general distribution of the Tauride belt and tectonic units along this belt (modified from Özgül, 1976).

character of the Ulukışla Basin's contact relationship with the units comes out. Some researchers argue that the Ulukışla Basin unconformably overlies the Bolkardağı Unit (Çevikbaş and Öztunalı, 1992; Dilek and Whitney, 1997; Clark and Robertson, 2002; Alan et al., 2007, 2011). However, the other researchers define the contact relationship tectonically (Blumenthal, 1956; Demirtaşlı et al., 1973, 1986; Ulu, 2002; Zorlu et al., 2011).

The apparent differences in opinions in studies indicating that the contact relationship between the two units is tectonic are also remarkable. Demirtaşlı et al. (1986) mapped the Bolkar Group formations corresponding to the Bolkardağı Unit as overlapping the Upper Cretaceous - lower - middle Eocene formations of the Ereğli - Ulukışla Basin along the Bolkar thrust. On the 1 / 500,000 scale geological map of the region prepared by MTA (Ulu, 2002), the contact relationship between the Bolkardağı Unit and the Ulukışla Basin is shown as thrust in some parts and as unconformable in other parts it is shown. Zorlu et al. (2011), on the other hand, showed the Bozkır Unit as thrusting over the Bolkardağı Unit, and the units belonging to the Ulukışla Basin as unconformable on the units in their maps.

However, according to Dilek et al. (1999*a*), Gautier et al. (2008), Sarıfakıoğlu et al. (2012) and Karaoğlan (2015), the boundary between the basin units and the units is tectonic contact represented by normal faulting. Gürer et al. (2016*a*, 2017) interpreted that the Ulukışla Basin thrusted over the Bolkardağı Unit and then the same fault plane worked as normal faulting. Seyitoğlu et al. (2017) stated that the basin units were deposited under the control of the İvriz Detachment Fault, and that the basin units were overlain by the Bolkardağı Unit in the following periods. Işık et al. (2018) showed that the primary contact of the Ulukışla Basin with the basement rocks (Bozkır, Bolkardağı units) in the Central Taurides had been significantly destroyed, and the lithologies of Bozkır and Bolkardağı Units in mapping areas thrusted over the Paleogene units of the basin with reverse/thrust faults from south to north after Middle Eocene.

Apart from reverse / thrust and normal fault contact relationship, the different fault characteristics are also included in the literature. According to Engin (2013), the Ulukışla Basin and the Bolkardağı Unit took to their current positions with a strike - slip fault. Similarly, Gürer et al. (2014) interprets the Ulukışla Basin as the continuation of the Sivas Basin and states that their current positions are associated with the strike - slip faulting. The contact relationship of the Ulukışla Basin with tectonic units outcropping in Taurides is important in terms of determining the

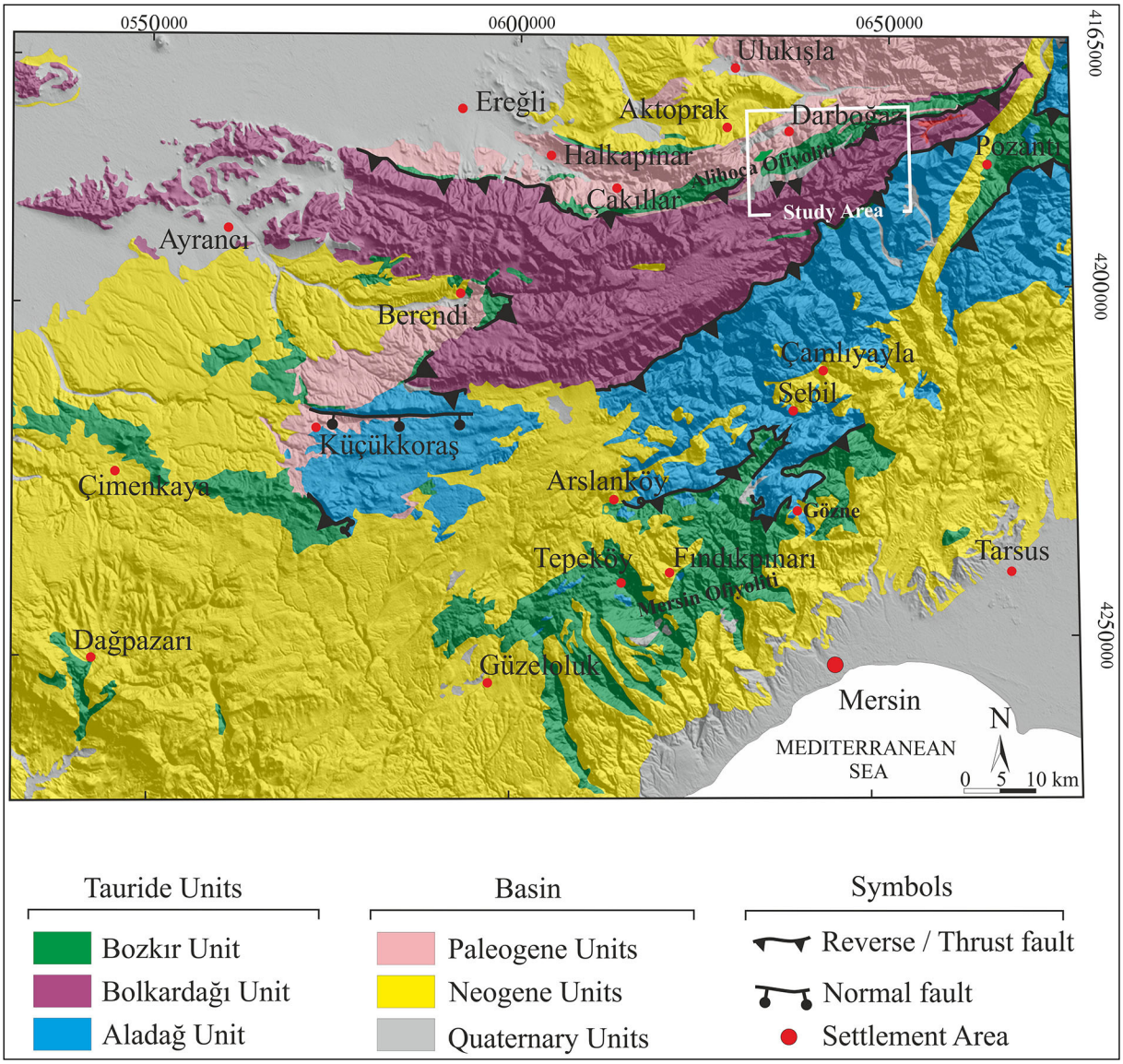

Figure 2- Geological map showing tectonic units and basin units outcropping in the eastern part of the Central Taurides (modified from Ulu, 2002).

geological development of both the Taurus orogenic belt and the Ulukışla Basin. The purpose of this study is to determine the contact relationship character of the Ulukışla Basin with the tectonic units cropping out in Taurides and to reveal the geological evolution of the study area.

2. Method

The eastern part of the Central Taurides (Figure 2), in which the study area is located, has been mapped for different purposes (Blumenthal, 1941, 1956; Özgül, 1971, 1976; Demirtaşlı et al., 1973, 1986, Alan et al., 2007, 2011). In this study 1/25.000 scale N33 - a1 and N33 - a2 sheets, in which the contact relationship of the Bolkardağı and Bozkır units and the Ulukışla Basin are evident, were selected as the study area (Figure 3). In this context, the rock units located in the study area were examined in order to reveal whether the basin contact relationship with the units was stratigraphic or tectonic, and if so, with what kind of faults the units came together. In the study area, the units forming the tectonic units outcropping in Taurides were determined and mapped as unit. The abbreviations were used to distinguish the mapped units (e.g., Kk: Kalkankaya formation).

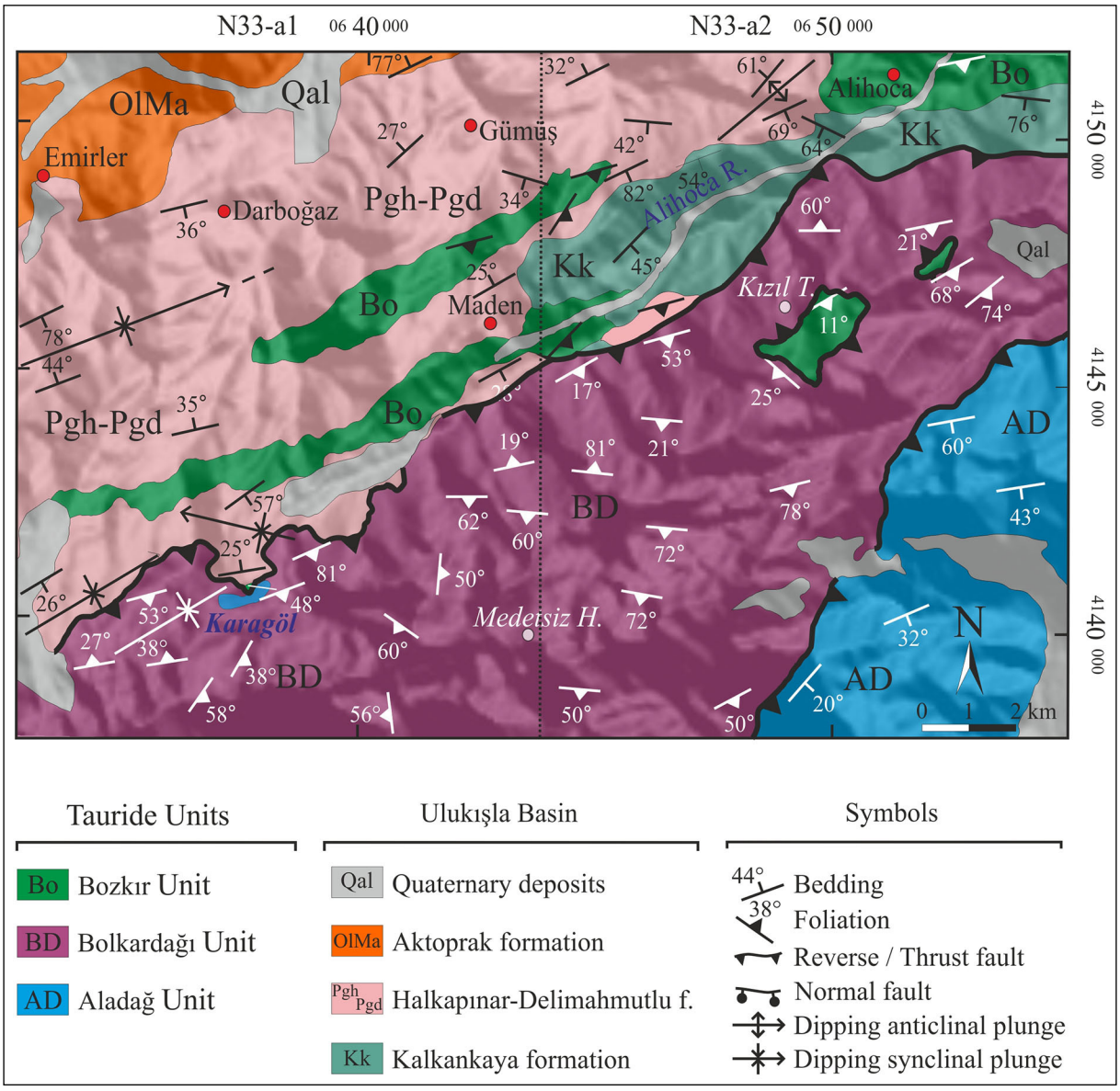

Figure 3- Geological map of the study area.

This abbreviation was also included in the text. The paleontological - petrographic samples were taken from all units representing the mapping area, the contact relationship of the units was examined, and all primary and secondary structural elements (bedding, foliation, fold, joint, fault) were determined. Total of 82 from the Bolkardağı Unit, 52 from the Bozkır Unit and 110 measurements from the Ulukışla Basin units (e.g. bedding, foliation, joint, reverse fault) were taken. The positions of these structural elements were evaluated in Stereonet v.11.2.2 (Allmendinger et al., 2013) and Win Tensor 5.9.0 software. The age, type of lithology, the formation environment and conditions of formations of rock units outcropping in the area were determined from thin section studies of samples taken for petrographic and paleontological purposes. By evaluating the field observations, structural measurements and sample analysis data together, the stratigraphy, deformation characteristic and geological evolution of the region were determined.

3. Regional Geology

The study area and its surroundings are located in the eastern part of the Central Taurides (Figure 2). The Ulukışla Basin is located in the northwest of the Bozkır and Bolkardağı units and in the south of the

Niğde Massif. The basin includes the units between the late Campanian - Quaternary age ranges. The basin is represented by carbonate, clastic and evaporitic lithologies. The fan delta, deep sea and lacustrine environment deposits overlying the shallow marine units at the basin floor reveal that the basin, which once was a shallow environment, gradually deepens then the basin depth decreases again over time and terrestrial environmental conditions prevail.

Tauride units, which limit the southern part of the basin, show arc geometry with an approximately east - west trending and southward bending. The Bozkır Unit is represented by oceanic crust rocks in the study area and its close vicinity, and it is defined as Alihoca Ophiolite and Ophiolitic Mélange, Kızıltepe Ophiolite, Pozantı - Karsantı Ophiolite, Mersin Ophiolite and Ophiolitic Mélange (Figure 2). The general acceptance is that these rocks began to overthrust the Tauride platform in the late Cretaceous. The Bolkardağı Unit, which is in contact with the basin sediments in the study area, includes Middle Devonian - Late Cretaceous units. The unit consists of rocks that has undergone metamorphism in greenschist and blueschist facies depending on the depth of burial. The widespread rock lithology of the study area is composed of marbles of which their primary sedimentation is Triassic. The contact relationship of the Bolkardağı Unit with the Bozkır Unit is tectonic. Similarly, it has a tectonic relationship with the Ulukışla Basin in the study area (Figure 3). Aladağ Unit consists of carbonates and clastics in the Late Devonian - Late Cretaceous age ranges (Figure 2). Mostly the Permian limestones crop out in the study area. The contact of this unit with other tectonic units (Bolkardağ, Bozkır) is tectonic. It is unconformably overlain by Miocene basin units in large areas outside the study area (Figure 2). Aladağ Unit has again unconformity contact with Oligocene and Miocene basin units along the Ecemiş Fault Zone.

4. Stratigraphy

The lithologies of Aladağ, Bolkardağı, Bozkır Units and the Ulukışla Basin constitute the rock units of the study area (Figures 3 and 4). Aladağ Unit is located in the southeastern part of the mapping area. In the northern and northwestern parts of the mapping area the rock units of Bolkardağı, Bozkır, Ulukışla Basins are located. The Bozkır Unit approximately strikes in NE - SW and outcrops in limited areas.

4.1. Aladağ Unit

The unit presents a sequence consisting of the late Permian recrystallized limestones and dolomite in the

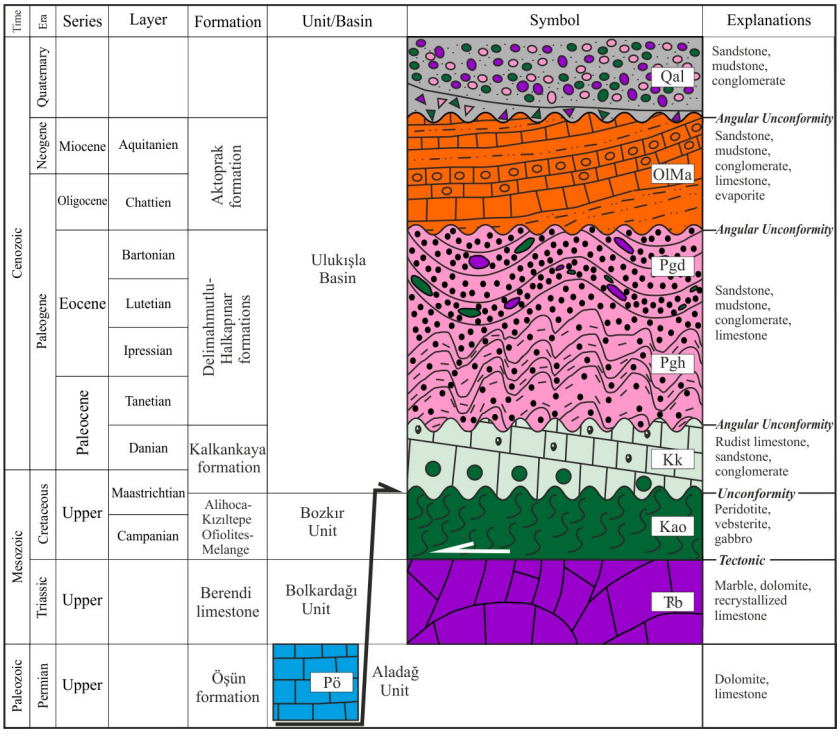

Figure 4- Stratigraphic section of the study area.

study area (Figure 5a). The weathering and fresh joint surfaces of limestones and dolomites are yellow, gray, smoky colored. The unit is occasionally thick - bedded and massive. Apart from folding, it has a broken structure in places. These limestones belonging to the Aladağ Unit have been described by Demirtaşlı et al. (1986) as the "Öşün formation" (Pö). The Aladağ Unit tectonically overlies the Bolkardağ Unit on the map. The upper contact of the unit is not visible in the study area. However, it is tectonically overlain by the ophiolite related Mersin Mélange of the Bozkır Unit between Arslanköy and Mersin in the south, outside the study area (Figure 2).

4.2. Bolkardağı Unit

Bolkardağı Unit located in the northeast of the Aladağ Unit in the study area has mostly marble and recrystallized limestone lithology (Figure 5b). In previous studies, this unit was named as the "Berendi Limestone" (Demirtaşlı, 1975) (TRb). Dolomite and calcschist constitute the other rock types of the Bolkardağı Unit within the mapping area. Metacarbonates are gray - white and widely folded. The foliation planes are prominent in calcschists and show different degrees of folding. Calcite and dolomite are commonly found as major minerals in thin section studies of these rocks (Figure 6a, b).

Although the granoblastic texture is typical, the orientation of the grains is clear. In some samples, the carbonate minerals are accompanied by glaucophane and chlorite minerals. The lithologies formed by plagioclase (albite), quartz, glaucophane, muscovite and chlorite minerals in samples taken from different levels of calcchists were defined as glaucophane schists. Some calcschists also contain fine glaucophane minerals in addition to the common calcite minerals. Hand sample and thin section studies indicate that the rocks forming the Bolkardağ Unit are affected by greenschist and blueschist facies metamorphisms. The metamorphism of the greenschist facies of the Unit has been emphasized by previous researchers (Özgül, 1976; Okay, 1985; Demirtaşlı et al., 1986; Çevikbaş, 1991; Whitney and Dilek; 1997; Okay and Tüysüz, 1999; Candan et al., 2005; Ulu, 2006; Robertson et al., 2009; Pourteau et al., 2010, 2013; Parlak et al., 2014; Van Hinsbergen et al., 2016). Kaaden (1966) and Çalapkulu (1980) stated that the unit contained rocks with glaucophane, while Göncüoğlu (2011) reported that some parts of the Kütahya - Bolkardağ belt has undergone metamorphism in the blueschist facies. Candan et al. (2005), Pourteau et al. (2010, 2014), Rimmelé et al. (2005), Parlak et al. (2014), Gürer et al. (2016*b*) stated that the Tauride microcontinent has undergone metamorphism under HP - LT conditions. Özgül (1976) stated that the youngest unit of the Bolkardağı Unit, which has undergone metamorphism, was of Paleocene age. Okay (1985), on the other hand, stated that the metamorphism of the Unit due to the ophiolitic thrust occurred in the latest Cretaceous period. Demirtaşlı et al. (1986) pointed out that the units in the Bolkardağı group showed a distinct metamorphism when moving towards the north and this situation was most evident in the increase of recrystallization in limestones and a decrease in the possibility of detecting fossils. According to Ulu (2006), the degree of metamorphism is more distinctive in the northern part and its age is Maastrichtian - Selandian.

4.3. Bozkır Unit

The Bozkır Unit is represented by the Alihoca Ophiolite, Ophiolitic Mélange and the Kızıltepe Ophiolite in the study area (Figure 5c, d). Ophiolite and mélange units in the region were named as the "Alihoca Ophiolite Massif" by Blumenthal (1956). These lithologies are found as NE - SW trending outcrops in the northern part of the mapping area (Figure 3). The Alihoca Ophiolite (Kao) consists of serpentinized peridotites, websterite, radiolarite, cumulate and isotropic gabbro.

Beneath this ophiolitic mass there is a mélange section. The Alihoca Ophiolite Mélange consists of blocky and red - brown clastic matrix. Blocky lithologies of mélange are ophiolite, recrystallized limestone, marble, dolomite and calcschist. The Kızıltepe Ophiolite (Kko) has limited outcrops in the study area. The lower parts of the unit, of which the upper parts are represented by serpentinized peridotites, are composed of rock assemblages dominated by the metamorphism. Thin section studies of hand samples taken from this section reveal that they have metagabbro, amphibolite and glaucophane albite schist lithology.

Plagioclase and glaucophane constitute the major mineral composition of some rocks (Figure 6c, d). The partial argillization and sericitization are evident in subhedral plagioclase phenocrysts. Glaucophane

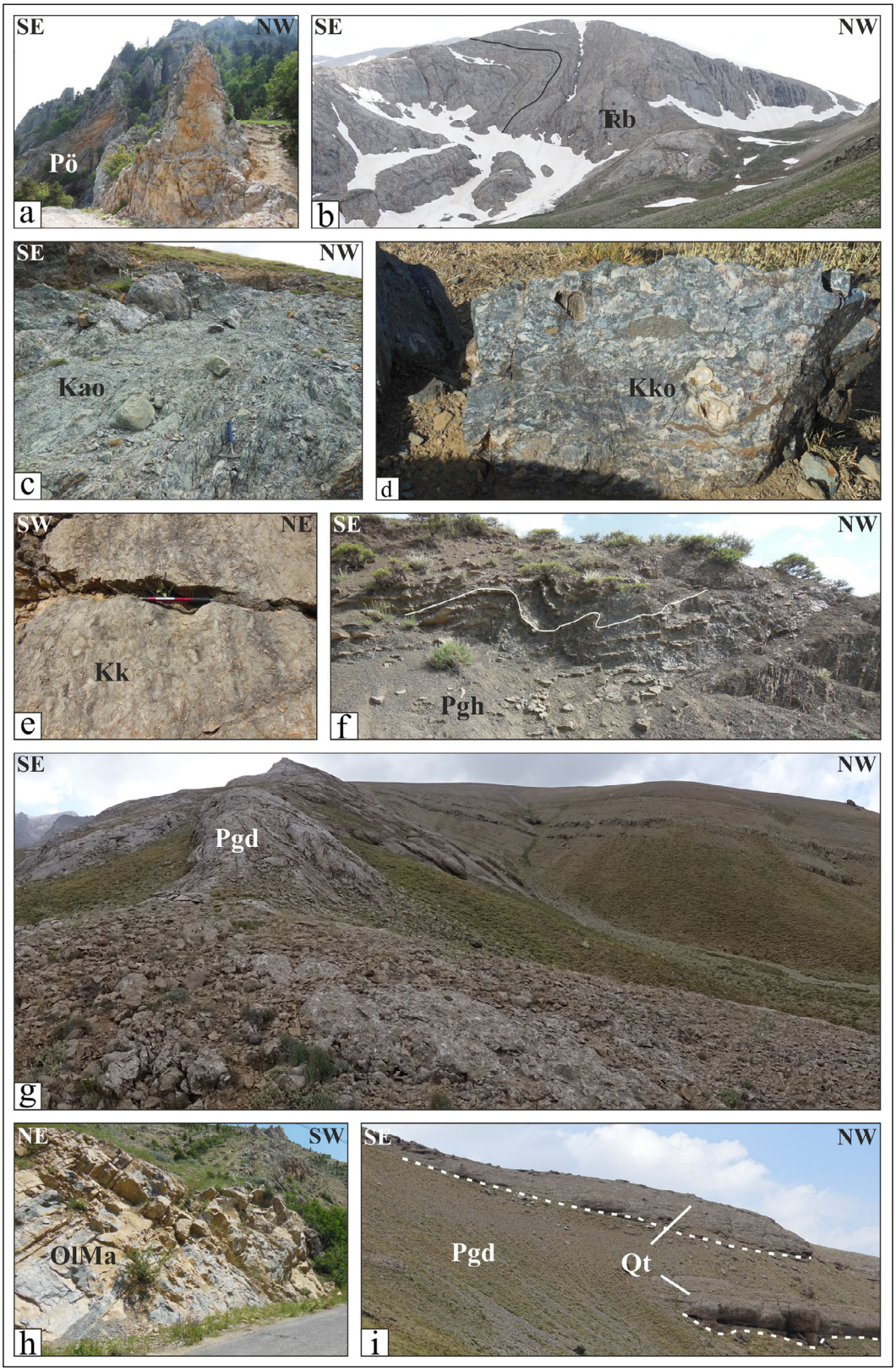

Figure 5- Field views of the units in the study area: a) Öşün formation limestones (Pö), b) Berendi limestone (TRb), c) Alihoca Ophiolite serpentinites (Kao), d) Kızıltepe Ophiolite metaperidotite (Kko), e) Kalkankaya formation limestones (Kk), f) Halkapınar formation sandstone-mudstone alternation (Pgh), g) Delimahmutlu formation calcarenites (Pgd), h) Aktoprak formation limestones (OlMa), i) Quaternary conglomerates (Qal).

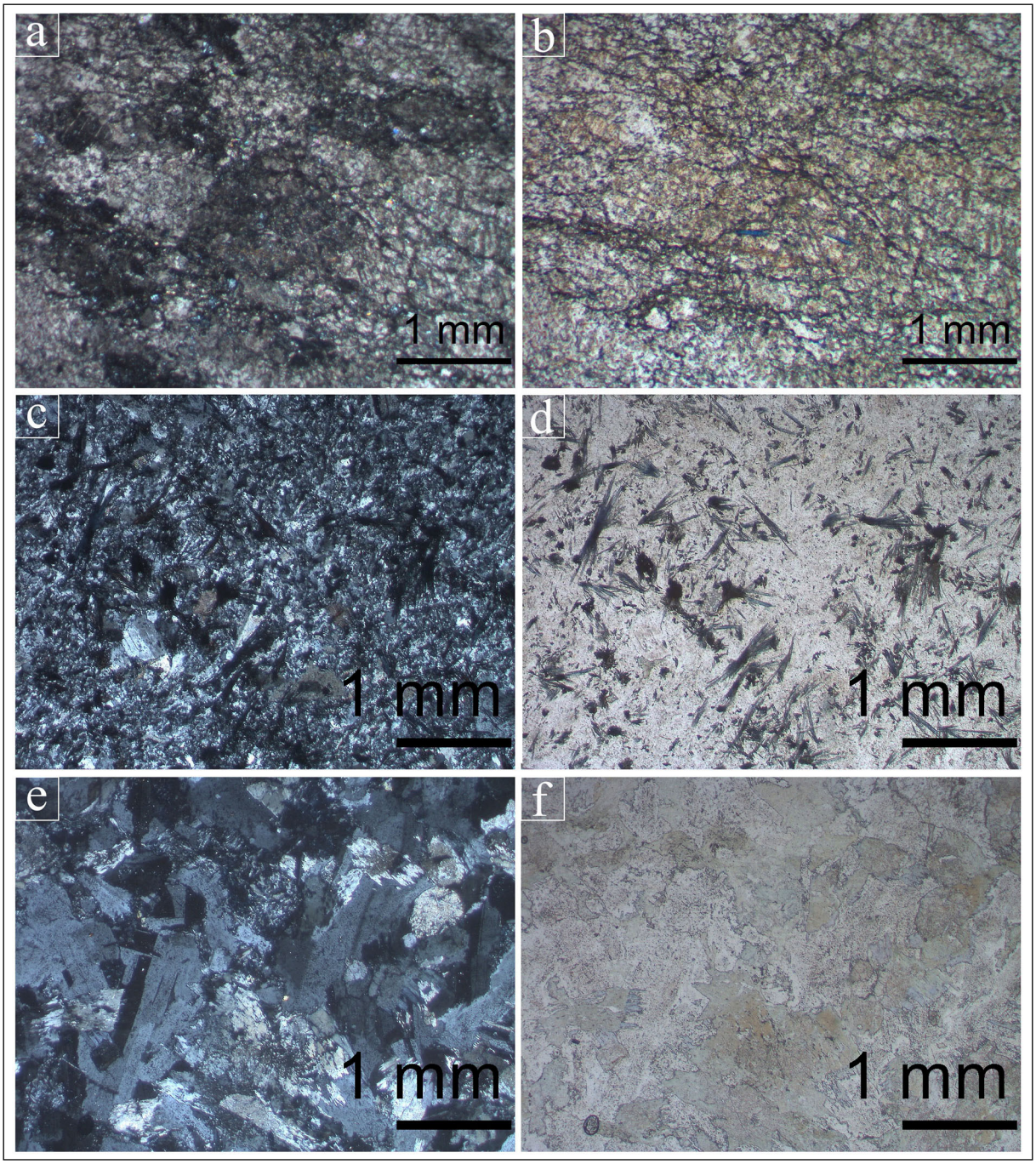

Figure 6- Microscopic views of the samples taken from the Bolkardağı Unit, which have undergone metamorphism in blueschist facies in the study area; a) cross nicols, b) parallel nicols; c, e) cross nicols and d, f) parallel nicols.

minerals, on the other hand, have acicular and thin rod - like grains; and it is distinctive with its typical bluish purple color. It is in disseminated grain and mineral clusters in the rock. This mineral composition is accompanied by local quartz. The plagioclase and clinopyroxene minerals constitute the major mineral composition of some rocks (Figure 6e, f). Plagioclases are subhedral grained that show local sericitization. The clinopyroxenes show full or partial uralitization. The clinopyroxene is seen as residue in areas where the alteration is weak. The actinolites are common minerals developed as a result of uralitization. These fringe - shaped minerals are accompanied by fine glaucophane and chlorite grains (Figure 6e, f).

Dilek and Whitney (1997) stated that the Kızıltepe Ophiolite was affected by metamorphism ranging from greenschist to blueschist facies.

4.4. Ulukışla Basin

In the northern part of the study area is the Ulukışla Basin, which is represented by Cenozoic units (Figures 2 and 3). The basin units defined on the basis of formation in previous studies show rejuvenation towards the northern part. The Kalkankaya formation (Kk), which is the oldest unit of the Ulukışla Basin, was first defined by Blumenthal (1956). The formation, which outcrops in the southern part of the basin, has outcrops trending approximately in E - W and NE - SW in the study area. The formation, whose dominant lithology is limestone, begins to deposit with red clastic (conglomerate, sandstone) rocks at the bottom then continues with limestones containing abundant rudist and loftusia fossils (Figure 5e) in upper parts. The formation also includes calcarenite levels in places. The formation is medium - thick bedded and has a thickness of approximately 100 m in the study area. Çevikbaş and Öztunalı (1992) dated the Kalkankaya formation as late Maastrichtian - early Paleocene. Its boundaries with the Bolkardağı Unit have a tectonical relationship within the mapping area (Figure 3). Its contact with the Bozkır Unit (Alihoca Ophiolite and Ophiolitic Mélange) is unconformable. Paleocene - Eocene Halkapınar (Pgh) and Delimahmutlu (Pgd) formations, which widely spread in the basin, unconformably overlie the Kalkankaya formation.

The Paleogene Halkapınar and Delimahmutlu formations have lateral and vertical relationships with each other. In this study, it was mapped together without discrimination. The formations were first defined by Demirtaşlı et al. (1973). Thin to medium thick bedded sandstone and mudstone constitute the main rock type of the Halkapınar formation (Figure 5f). Thick bedded limestones also accompany these units as interlayers. The formation with a thickness of 600 m in the study area is represented by the deep sea deposits. However, the thickness of the formation throughout the basin is 1,000 m (Demirtaşlı et al., 1984) or 2,000 m (Clark and Robertson, 2005) and shows different depositional environment characteristics from terrestrial to the deep sea environment (alluvial fan, fan delta, turbiditic sequence). According to Alan et al. (2007), the Halkapınar formation is Thanetian - Lutetian. The fossil assemblage (benthic foraminifera, algae and macro shell) of the samples collected within the scope of the study indicates that the formation is Thanetian. The Halkapınar formation does not have any contact with the Bolkardağ Unit within the study area; however, it unconformably overlies the Bozkır Units in limited areas. The primary boundary outside the study area was defined as a detachment fault (İvriz Detachment Fault) between the Halkapınar formation and Bolkardağı Unit in the western part (Seyitoğlu et al., 2017). In some other studies, the contact relationship between the Tauride units and Halkapınar formation is described as discordant (Demirtaşlı et al., 1986; Dilek and Whitney, 1997; Clark and Robertson, 2005; Gürer et al., 2016*a*). The Halkapınar formation in the study area transits into the Delimahmutlu formation at the top. The dominant lithology of the Delimahmutlu formation is constituted by conglomerate, sandstone and limestone (Figure 5g). The grains of the pebbles that form the basement levels are largely derived from the rocks of the Bolkardağ Unit. The pebble sizes are variable and sometimes in blocky size. They are badly sorted and rounded. The formation, which has a thickness of approximately 250 m, represents the fan delta depositional environment. It consists of rich macro fossil of which its certain levels are easily traced. Alan et al. (2007) determined the age of the formation as Lutetian - Bartonian (Middle - Late Eocene). The fossil assemblages (benthic foraminifera, algae) of the samples taken from the Delimahmutlu formation outcropping in the study area give the age of the formation as Late Ipressian (Early Eocene).

The Delimahmutlu formation is overlain by the Aktoprak formation, which is represented by terrestrial deposits. The Aktoprak formation crops out in a limited area in northwest part of the map. The formation was first defined by Demirtaşlı et al. (1973). The formation with evaporite, marl, lacustrine limestone lithology (Figure 5h) has a thickness of 450 m in the Ulukışla Basin. Blumenthal (1956) stated the age of the formation as Chattian - Aquitanian (Late Oligocene - Early Miocene). The Aktoprak formation has unconformable contact relationships with the upper and lower units in the mapping area. However, the formation presents a normal fault contact relationship in the western part with the underlying units (Seyitoğlu et al., 2017). Quaternary deposits are the youngest units in the mapping area. Quaternary sediments, which unconformably overlie the Unit rocks and basin units, represent colluviums, incised

valley deposits and terraces (Figure 5i) on the foothills of high regions, and the fluvial deposits in areas where horizontal topography is dominant.

5. Structural Geology

The deformations in different densities are observed in the units outcropping in the study area and its close vicinity. The units, which form the Aladağ, Bolkardağı and Bozkır units, show folding in varying sizes (e.g. tight, closed, harmonic folds) and reverse faulting. The development of foliation almost parallel to the bedding and oblique foliation is also characteristic especially in the rocks forming the Bolkardağı Unit. The joint growth is common in these rocks. Foldings and faultings are observed in limited outcrops in units belonging to the Ulukışla Basin in the study area. Open folds are the common type of folds. The local tight folds are also common in Paleogene sequences of the basin. Reverse faults have also developed in areas close to the contacts of the basin with the unit rocks.

Structural measurements (bedding, foliation, fault, joint) obtained from the mapping area were grouped under three lithological groups. These are Bozkır and Bolkardağı units and the Ulukışla Basin.

5.1. Structures of the Bolkardağı Unit

The lithologies of the Bolkardağı Unit show folding varying from outcrop scale to megascopic scale. Demirtaşlı et al. (1986) assessed this structural feature of the Bolkar Unit as a large anticlinorium in the Bolkar Mountains and evaluated that the folds in the Ereğli - Ulukışla Basin and the folds in the Bolkar group were more or less parallel.

Our field observations reveal that the units forming the Bolkar Unit are mostly represented by asymmetric and overturned folds according to the axial planes and position of the fold limbs. Considering Fleuty (1964)'s fold classification, the angular relationship between the fold limbs indicate tight, narrow and open fold development of the Bolkardağı Unit lithologies. The bedding measurements obtained from sections where the stratification is significant reveal that the beds strike NE - SW and dip NW or SE. The analysis of these measurements determined the condition of the fold axis as N40°E, 14° (Figure 7a). The axis plane of the folding is determined as N50°W, 76°SW. The data obtained from the bedding measurements revealed that the folds in the Bolkardağı Unit cropping out in the study area are semi perpendicular to perpendicular axis planes and have low plunging fold axis as fold geometry. The folds in the foliation planes have also similar features. Analysis of the measurements obtained from these planes gives the condition of the fold axis as N74°E, 11° (Figure 7b), and the state of the axis plane as N14°W, 79° NE. Field observations show that the orientation of the folds is NW in direction.

There are reverse faults affecting the Bolkardağı Unit in the study area. Especially, the fault plane and slip plane developments are observed in places along the contacts of the unit with Paleogene units of the Ulukışla Basin. In some of these planes the shear lineation is evident. Figure 7c shows the distribution of measurements taken from reverse faults on the equal area net. The Froclich diagram shows that the faults are concentrated in the reverse fault zone (Figure 7d). The paleostress analyses of the planes in which the shear lineaments are characteristic reveal the position of the main paleostress axes ($\sigma1$, $\sigma2$, $\sigma3$) forming the faulting (Figure 7c). As can be seen in Table 1, the largest ($\sigma1$) and the intermediate main paleostress ($\sigma2$) axes forming the faults affecting the Bolkardağı Unit lithologies are close to horizontal, and the smallest main paleostress ($\sigma3$) axis is close to vertical. The ratios of R and R' obtained from the analysis are 0.89 and 2.50, respectively. When all the data are evaluated together, the reverse faulting affecting the Bolkardağı Unit points to the radial compressive tectonic regime (Table 1).

The Bolkardağı Unit offers metamorphism in addition to its prominent deformation. Our hand sample and microscopic examinations reveal that the rocks are affected by metamorphism in greenschist and blueschist facies. This metamorphism demonstrated by the Bolkardağı Unit in the Central Taurides has been evaluated in some studies. Accordingly, Ulu (2006) dated the greenschist metamorphism of the Bolkardağı Unit as Maastrichtian - Selandian (Upper Cretaceous - lower Paleocene). Robertson et al. (2009) stated that the unit was deep buried and underwent high pressure/low temperature metamorphism (blueschist). According to the researchers, the dating of this metamorphism is 80 my. However, Parlak et al. (2014) dated the high pressure/low temperature metamorphism as Turonian, which is much older.

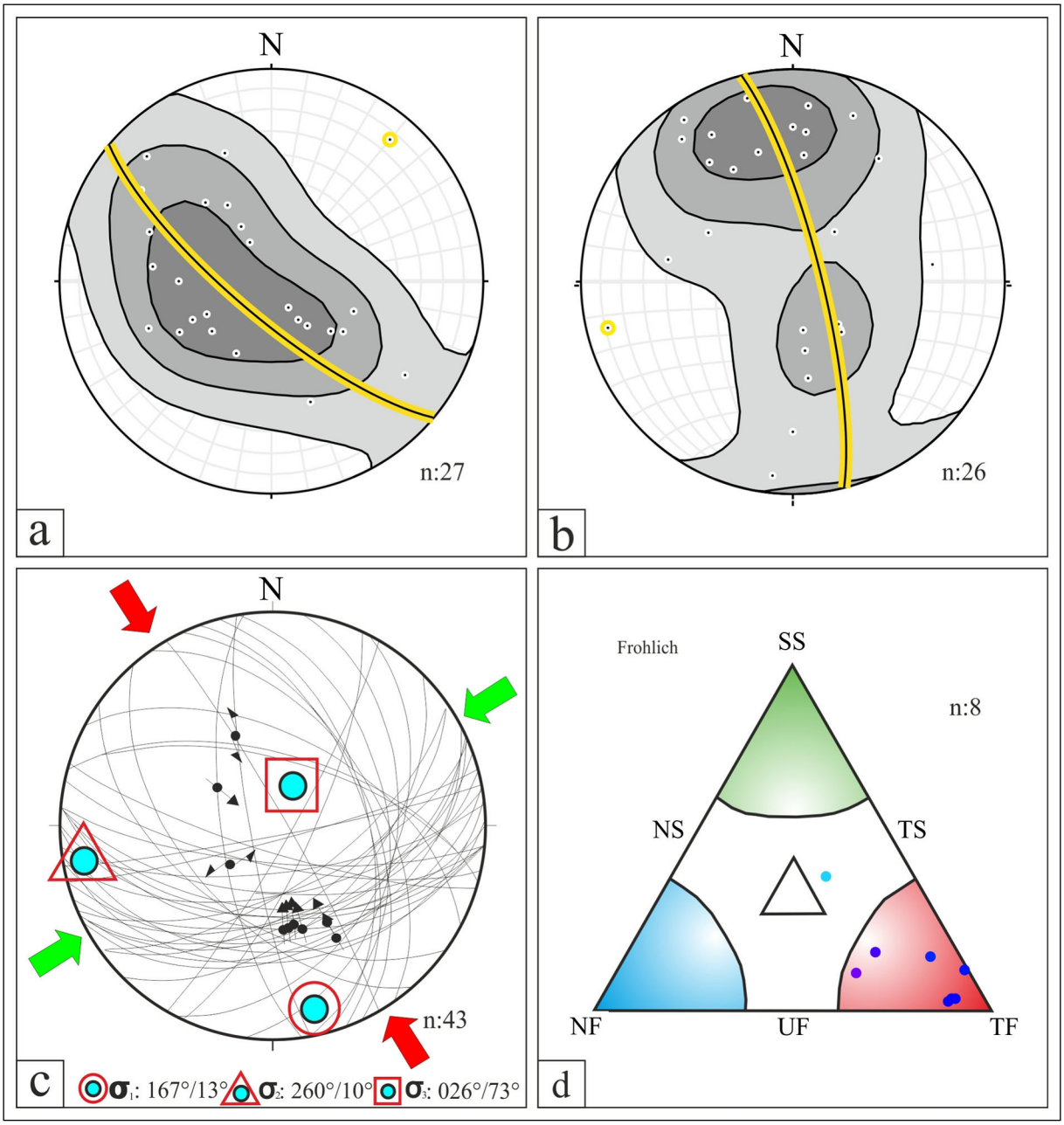

Figure 7- a) Point-contour diagram of the layer planes, b) point-contour diagram of the planes of foliations, c) diagram showing the reverse fault planes and compression directions, d) Froclich diagram showing the character of the faults (SF: Strike-slip fault, NF: Normal fault, RF: Reverse fault) of the Bolkardağı Unit in the study area.

Table 1- Table showing the results paleostress analysis of reverse faultings in the study area.

Area	Method	Fault Plain	σ_1	σ_2	σ_3	R Index	R' ndex	Misfit(α)	Tectonic Regime
Bolkardağı Unit	F5	43	167°/13°	260°/10°	023°/73°	0,89	2,50	6,2	Radial Compressive
Bozkır Unit	F5	20	173°/25°	290°/43°	063°/36°	0,64	1,36	14,6	Oblique Transpressive
Ulukışla Basin	F5	19	146°/21°	237°/04°	337°/68°	0,34	2,34	2,8	Pure Compressive

When we evaluate our findings and results of analysis together with the literature data, the Bolkardağı Unit should probably be located in the north of Tauride Platform and deeply buried due to the high pressure/low temperature metamorphism.

The thrust of the ophiolitic units representing the Bozkır Unit and the compression in regional scale caused the development of widely developed folds and reverse faults together. The character of the tectonic contact between the Bolkardağı Unit and the Ulukışla Basin reveals that, unlike its primary development, it has a reverse faulting character and that the faulting has developed due to the compression in NW - SE direction. The situation of reverse faults and dominant NW trend of folds do not support the previous north to south movement. On the contrary, it shows the existence of a development from south to north movement.

5.2. Deformation Structures of the Bozkır Unit

The lithologies belonging to the Alihoca Ophiolite, melange and Kızıltepe Ophiolite belonging to the Bozkır Unit are seen as folded in the study area, similar to the Bolkardağı Unit.

During our field studies, it was seen that folds on the foliation planes of the units that make up the Bozkır Unit revealed that the units were mostly represented by asymmetric and overturned folds according to the axial planes and position of fold limbs. The lithologies of the unit generally indicate the open fold developments.

The analysis of measurements obtained from the foliation planes gives the condition of fold axis as N84°E, 18°, and state of the axis plane as N6°W, 72°SW (Figure 8a). Field observations show that the orientation of the folds is NW.

There are observed reverse faults affecting the Bozkır Unit within the study area. In some parts of the reverse fault planes the slip lineaments are evident. Figure 8b shows the distribution of measurements taken from reverse faults on the equal area net. The Froclich diagram shows that the faults are concentrated in the reverse fault zone (Figure 8c). The paleostress analysis of the planes in which shear lineaments are characteristic reveal the position of the main paleostress axes (σ1, σ2, σ3) forming the faulting (Figure 8b). As can be seen in Table 1, the largest paleostress (σ1) axis that forms the faults affecting the Bozkır Unit lithologies is horizontal, and the smallest major paleostress (σ3) axis is close to the vertical. The ratios of R and R' obtained from the analysis are 0.64 and 1.36, respectively. When all the data are evaluated together, the reverse faulting affecting the Bozkır Unit points out an oblique transpressive tectonic regime (Table 1).

The analysis of measurements obtained from foliation planes seen in the Alihoca Ophiolite outcropping at the Karagöl location gives the condition of fold axis as N77°E, 7°, and the state of axis plane as N13°W, 83°SW (Figure 8d). The field observations show that the orientation of the folds is NW.

5.3. Deformation Structures of the Ulukışla Basin

Ulukışla Basin deposits are located at the northern boundary of Bolkardağı and Bozkır Units. The sequence in the basin includes Kalkankaya, Halkapınar, Delimahmutlu, Aktoprak Formations and Quaternary deposits. During our field studies, it was revealed that the units deposited in the Ulukışla Basin from basin deposits were mostly represented by asymmetric and overturned folds according to the position of the axial planes and fold limbs.

Considering Fleuty (1964)'s fold classification, the angular relations among the fold limbs indicate open fold development of the Ulukışla Basin units. The bedding measurements reveal that the beds strike NE - SW, dip NW or SE and strike NW - SE, and dip NE indicating two fold axes. Analysis of these measurements gives the position of the first fold axis as N63°D, 2°, the axis plane of the first folding that occurred was determined as N27°W, 88°NE, the state of the second axis as N13°W, 2°, and the axis plane as N77°E, 88°SW (Figure 9a). The data obtained from the bedding measurements reveal that the folds in the Ulukışla Basin units outcropping in the study area are semi perpendicular to perpendicular axis planes, low plunging fold axis as fold geometry.

The dominant orientation of the joints formed in the Ulukışla Basin units is N77°E (Figure 9b).

In the study area, there are reverse faults affecting the Ulukışla Basin deposits. In some parts of the reverse fault planes the slip lineaments are evident. Figure 9c shows the distribution of measurements taken from the reverse faults on the equal - area

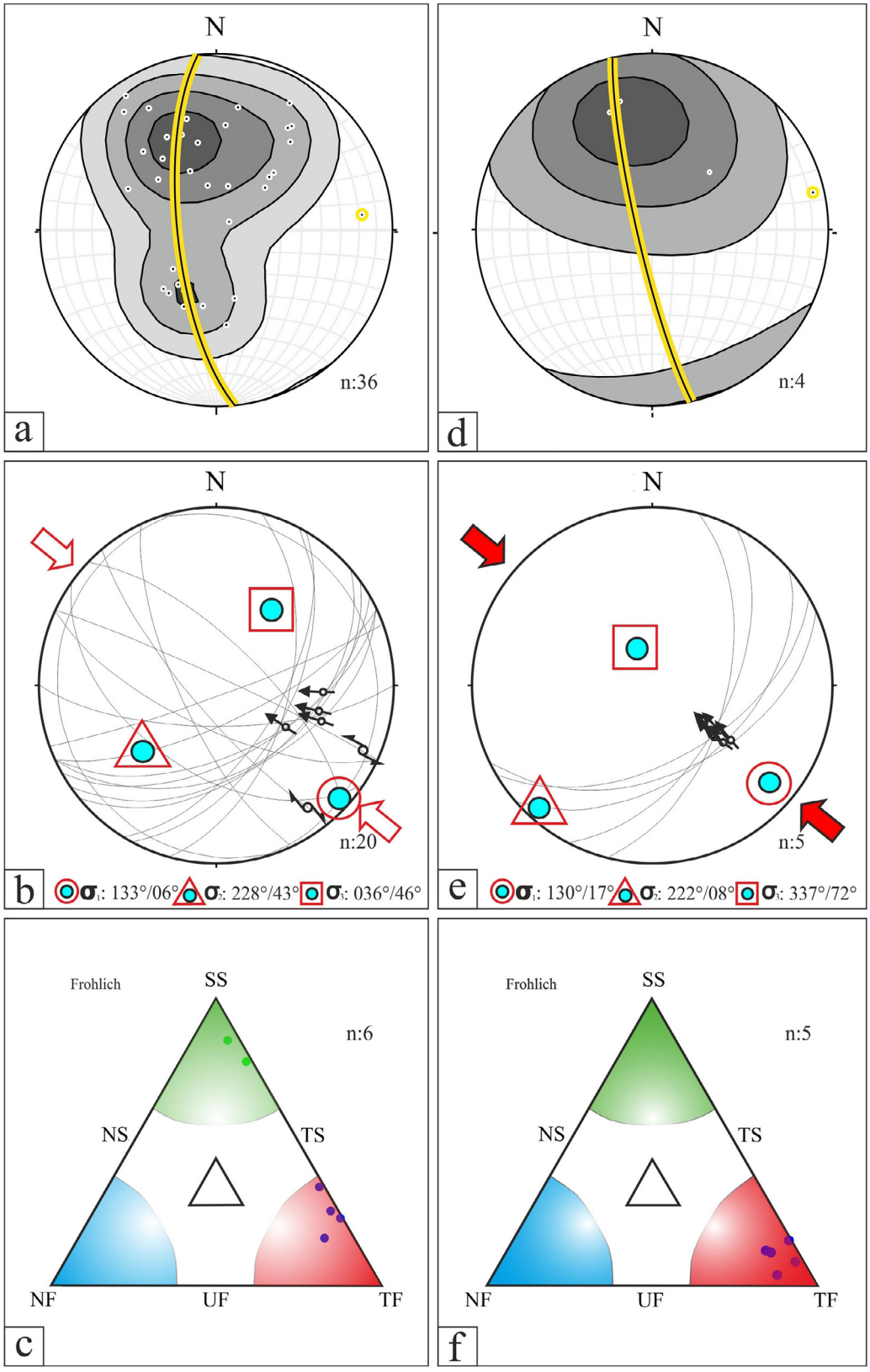

Figure 8- Point-contour diagram showing the reverse fault planes and compression directions and the Froclich diagram displaying the characteristics of the faults of units of the Bozkır Unit in the study area (a, b, c), and the ophiolites in the Karagöl location (d, e, f) (SF: Strike-slip fault, NF: Normal fault, RF: Reverse fault).

net. The Froclich diagram shows that the faults are concentrated in the reverse fault zone (Figure 9d). The paleostress analysis of the planes in which the shear lineaments are characteristic reveal the position of the main paleostress axes (σ1, σ2, σ3) forming the faulting (Figure 9c). As can be seen in Table 1, the largest (σ1) and intermediate main paleostress (σ2) axes forming the faults that affect the Ulukışla Basin lithologies are horizontal, and the smallest main paleostress (σ3) axis is close to the vertical. The ratios of R and R' obtained from the analysis are 0.34 and 2.34, respectively. When all the data are evaluated together, the reverse faulting that affect the Ulukışla Basin indicates a pure compressive tectonic regime (Table 1).

There are closed folds close to the border of Bolkardağı Unit (Figure 10c). The foliations were formed as dipping to the southeast. The reverse faults

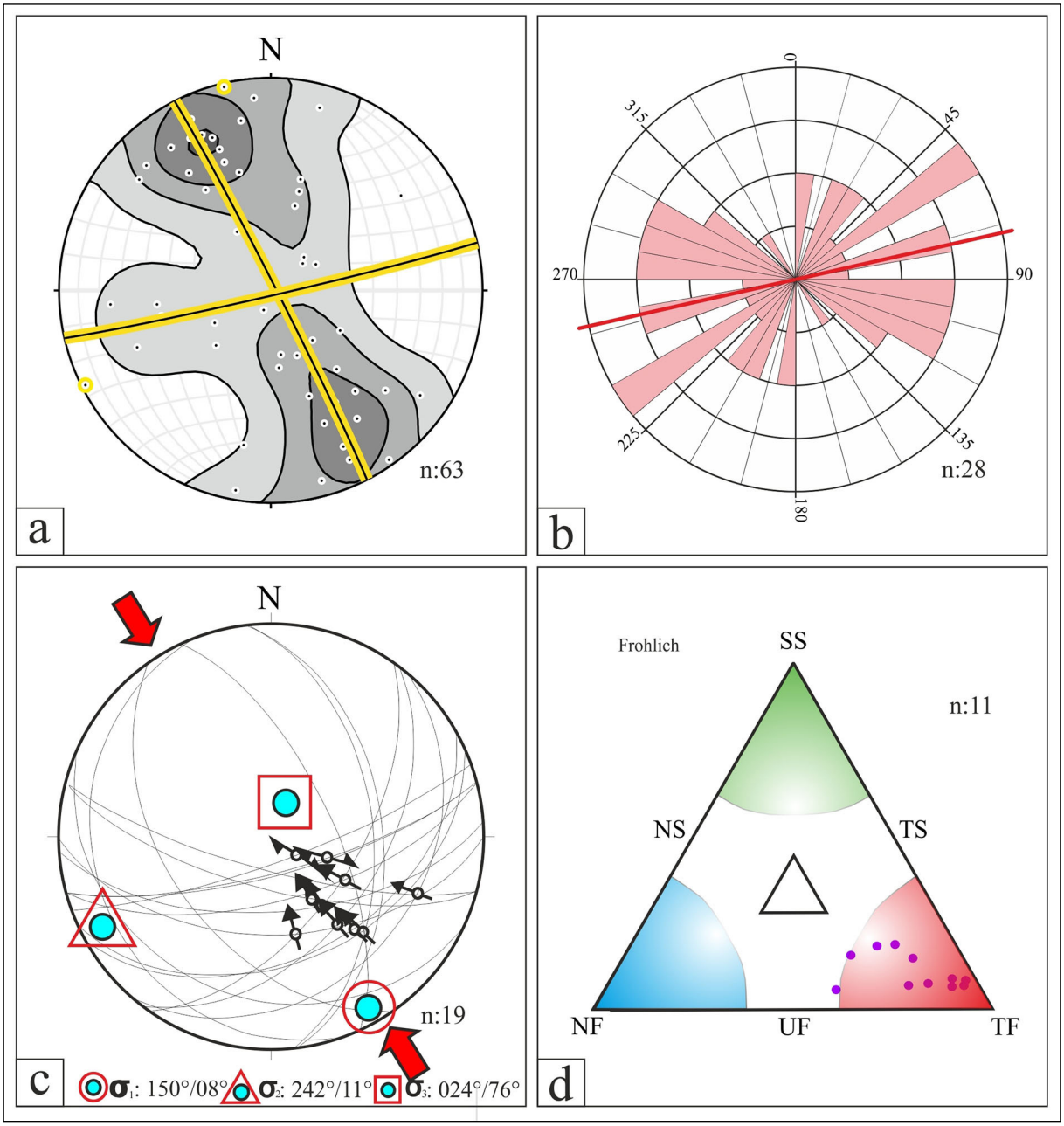

Figure 9- a) Point contour diagram of the bedding planes, b) rose diagram showing joint lineations, c) diagram showing the reverse fault planes and direction of compressions, d) Froclich diagram showing the characteristics of faults of units belonging to the Ulukışla Basin in the study area (SF: strike-slip , NF: Normal fault, RF: Reverse fault).

also dip accordingly to the southeast and the whole sequence is located in NW direction, indicating a thrust from SE to NW.

Demirtaşlı et al. (1986) state that the Bolkar group thrusts over the units of Ereğli - Ulukışla Basin from south to north along the Bolkar thrust. In east of the Horoz Village, they also state that the Bolkar group is thrusted over the Kalkankaya formation from south to north. The researchers claim that the Bolkar Group formations thrusted over the Upper Cretaceous - Paleocene sediments of the Ereğli - Ulukışla Basin along the Bolkar thrust in the late Paleocene - early Eocene from south to north. During the Oligocene and Miocene period, the Ereğli - Ulukışla Basin was completely closed, and the lacustrine limestones and marls (Kurtulmuş Tepe member of the Aktoprak formation) were deposited in local and small - scale lakes that replaced the retreated sea (Demirtaşlı et al., 1986).

Gürer et al. (2016*a*) stated that the Ulukışla Basin and Bolkardağı Unit were under a compression in NW - SE direction in their studies on deformation of the Ulukışla Basin. They claimed that due to this compression effect, the Ulukışla Basin thrusted towards the Bolkardağı Unit from northwest to southeast. Afterwards, they also stated that the Bolkardağı Unit back - thrusted the Ulukışla Basin which overlian it. They emphasized that due to this movement, the Cretaceous - Paleogene strata gained a subvertical slope and attributed this interpretation to Blumenthal (1956) and Demirtaşlı et al. (1973). Blumenthal (1956) and Demirtaşlı et al. (1973) stated that the Bolkardağı Unit thrusted over the Ulukışla Basin, but they did not make any comments on the fact that this thrust was a back thrust.

The contact of the Bolkardağı Unit with the Delimahmutlu formation just in the west of Karagöl is a reverse fault that moved from southeast to northwest. All of the folds and reverse faults in the internal structure of the Bolkardağı Unit also orient NW. Except for the Quaternary units, the Ulukışla Basin deposits also contain folds in NW direction.

Gürer et al. (2016*a*) indicate that there are southward orienting faults showing the movement from north to south on the slope in the north of Karagöl. The researchers who attribute the southward movement of the Ulukışla Basin to these faults state that this is the result of compression in NW - SE direction. However, these faults do not exist in the mentioned outcrop. The discontinuities shown as faults in the study are the boundary of Quaternary conglomerates (Figure 5i) and terraces deposited on the Delimahmutlu formation.

Since the discontinuity planes show movement from southeast to northwest, the thrust of the Bolkardağı Unit towards northwest over the Ulukışla Basin is a thrust but not a back thrust. That is, not the secondary but the primary movement of the unit is towards NW.

5.4. The Contact Relationship of the Central Taurides with the Ulukışla Basin

Numerous structural data on the boundaries of Bozkır, Bolkardağı units and the Ulukışla Basin were collected and analyzed in the study area and its vicinity. When structural analysis and field data were evaluated together, it was determined that the Bolkardağı Unit overthrust the Alihoca Ophiolite and melange with tectonic contacts along the boundary with Bozkır Unit.

As continental parts, which contain tectonic units outcropping in the Taurides, plunged under the Anatolian microcontinent towards the north, it was considered that the oceanic plate settled on top of these units and remained in this position. As stated in previous studies, the Bolkardağı Unit is in the form of a northward - overturned asymmetric anticline (Blumenthal, 1956). In addition, the unit is heavily folded in itself. Özgül (1976) showed the Bozkır Unit as overlying the other units in his studies in the Taurides, and following studies. Dilek and Whitney (1997) stated that the Kızıltepe Ophiolite overthrusts the Bolkardağı Unit in their studies in the region. In this study carried out in the region, it was seen that the Alihoca and Kızıltepe Ophiolites were found as clips not above the Bolkardağı Unit, but below the unit as a tectonic contact. The data regarding this contact relationship are explained in detail in the structural geology section. The ophiolites overthrusts the Bolkardağı Unit at the time of the closure of the ocean are below the Bolkardağı Unit today, after the closure of ocean. In the maps of studies carried out in the Ulukışla Basin (Clark and Robertson, 2002; Demirtaşlı et al., 1986; Robertson et al., 2009; Alan et

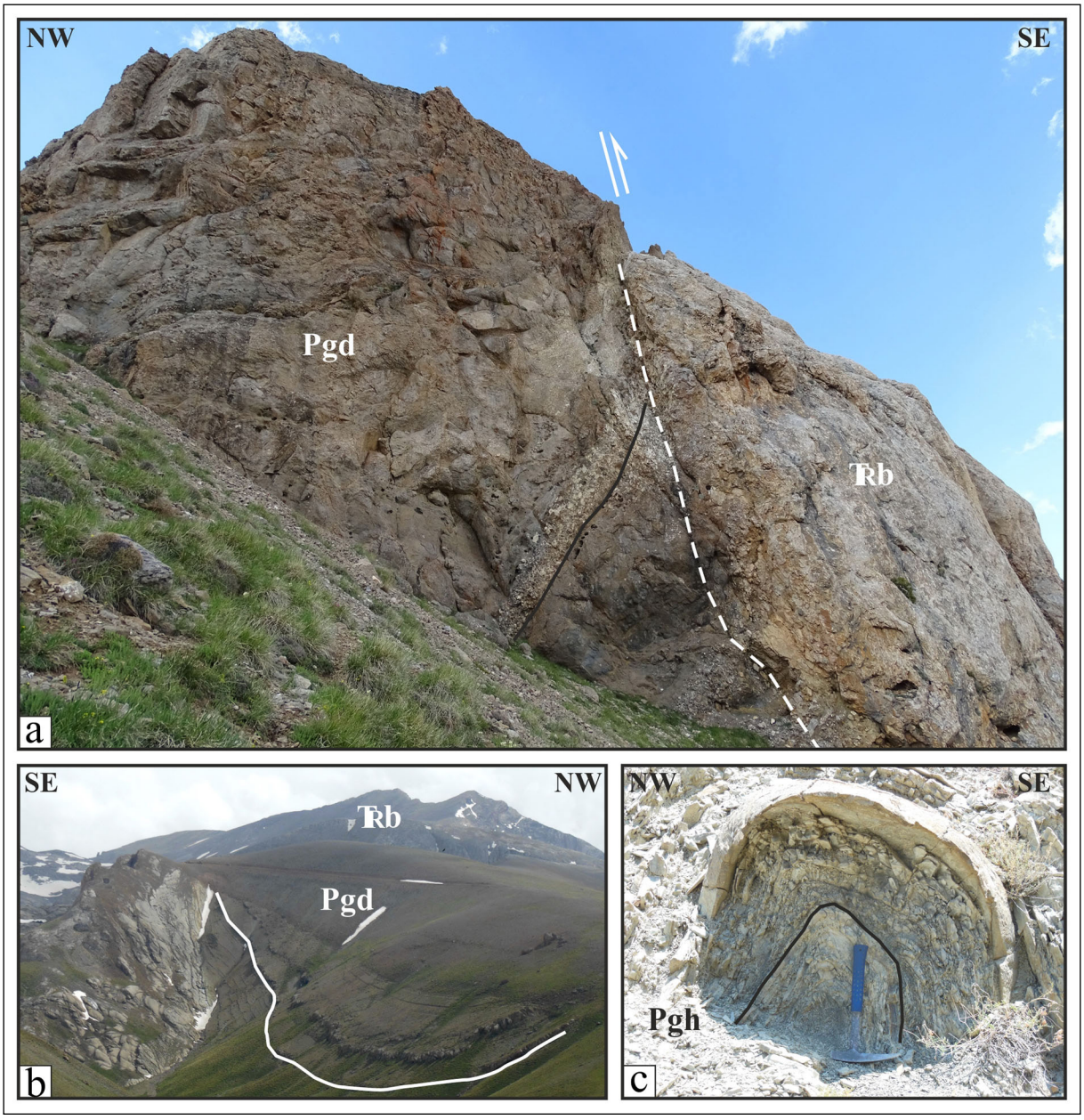

Figure 10- Deformations formed in units in the study area: a) unconformity and reverse fault inclined between the Delimahmutlu formation and Berendi limestone, b) megascopic syncline in the Delimahmutlu formation, c) narrow folds in the Delimahmutlu formation.

al., 2011), the Bolkardağı unit thrusts over it towards the northwest within itself.

Alihoca ophiolite and mélange belonging to the Bozkır Unit overlies the Ulukışla Basin units with a thrust towards the northwest. The units within the Ulukışla Basin are also seen as folded in accordance with this direction.

Gürer et al. (2016*a*), on the other hand, state that the ophiolites shifted backward, (ie. towards the north) after overthrusting the Bolkardağı Unit. However, the ophiolites are thrusted by the Bolkardağı Unit towards the northwest. Zorlu et al. (2011) evaluated the Late Cretaceous - late Paleocene period as the extensional phase and the late Paleocene - early Eocene period as the compressional phase in their studies on the geological evolution of Ulukışla Basin.

The Karagöl location in the south of Darboğaz Village is a location where the contact relationship of Bolkardağı Unit marbles, Alihoca Ophiolite and the Ulukışla Basin deposits can be clearly seen.

The reverse fault plane in northeast of the Karagöl locality, which cuts the Late Triassic marbles and pushes them onto the ophiolitic slice, strikes N89°E and dips 40°SE. The reverse fault in marbles on the western edge of Çiniligöl also strikes N55°W and dips 53°SW. Another reverse fault plane located between the Karagöl and Çiniligöl strikes N55°E and dips 58°SE. Bolkardağı marbles meet the basal conglomerates of the Delimahmutlu formation with a reverse fault plane which strikes N25°E and dips 75°SE just in north of Karagöl.

Another reverse fault, which cuts the marbles in Karagöl, strikes N73°W and dips 80°SW. The main vector of the polar points of the reverse faults cutting the unit is 349.4°/34.4°. The main strike of the reverse fault planes is N79.4°E and the dip direction is 55.6°SE. The reverse fault plane cutting the northern slope of Bolkar Mountains located in the west of Karagöl strikes N60°E and dips 77°SE. The fold axis plane of the megascopic scale recumbent anticline on the hanging block of this fault plane is also N60°E in direction, dips 34°SE. These reverse faults in and around Karagöl caused the unit to propagate, to be folded and get shorten from southeast to northwest.

The foliation found in marbles in contact with the Delimahmutlu formation in the north of Karagöl, on the other hand, strikes N55°E and dips 58°SE. These planes also show that the sequence remain under the effect of stress from southeast to northwest.

The conglomerates at the bottom of the Delimahmutlu formation, which face with marbles of the Bolkardağı Unit close to vertical strikes N35°E and dips 75°NW (Figure 10a). The bedding of the sandstone layers forming the deltaic sequence towards the top of the sequence turns to N75°W/78°NE. One of the reasons for this change in the direction of the beds is the thrust of Bolkardağı Unit over the Paleogene sequence while the deposition continues and the sequence to be folded during the "fault propagation deformation" process. The other reason is that the Paleogene sequence to consist of fan delta deposits and the charging channels to change direction to fill different depositional areas during the formation of these deposits.

Quaternary pebbles in the study area have a distinctive unconformable contact relationship with underlying delta deposits. The incised valley deposits with distinctive contact, which contain the pebbles of all units in the region were deposited in the Delimahmutlu formation. Due to the rapid uplift of the region, the section, which was a depositional area for the Delimahmutlu formation a while ago then turned into an erosional area. During this erosion, the incised valleys were formed in the formation and the pebbles, which fed by the lithologies in the source area formed the incised valley sediments, were deposited. The bottom contact of the incised valley deposits is eroded due to the sudden uplift and has a ditinctive unconformable contact. Gürer et al (2016*a*), who worked around Karagöl, stated that there was a fault at the contact between the Delimahmutlu formation and the overlying Quaternary incised valley deposits. They stated that the incised valley deposits thrusted over the Delimahmutlu formation deposits dipping towards north and moving from north to south.

At the aforementioned point, there is no deformation structure in the Quaternary deposits that can be formed by compression. There are no reverse faults thrusting from north to south within or in the north of delta deposits of the Late Ipressian Delimahmutlu formation.

The Delimahmutlu formation unconformably overlies the Bolkardağı Unit and the Alihoca Ophiolite with its basal conglomerate. The Bolkardağı Unit was subjected to NW - oriented folds due to the NW - SE compression effective in the region and propagated to the northwest by NE - SW trending and SE dipping reverse faults. Due to this propagation, the contact of the Delimahmutlu formation with the unit was inclined towards the northwest and became steep, and the sequence was folded to form a syncline in megascopic scale (Figure 10b). In all units, except for the Quaternary incised valley deposits and terraces in this location, NW - SE trending fold axis planes (Figure 10c) and reverse faults subjected to NW - SE compression were formed. These reverse faults have moved all the units in the region in NW direction. When structural data in the whole study area are examined together, it is seen that they are conformable with the data around Karagöl.

The units in the whole study area was deformed due to NW - SE compression in a way to contain NE - SW striking, NW orienting, SE dipping layer and discontinuity planes. In other words, the allochthonous

rocks and basin deposits in the region was thrusted from southeast to northwest.

6. Geological Evolution

Stratigraphic, paleontological, structural and petrographical data were obtained through field and laboratory studies carried out in and around the study area. There are many previous studies on Bozkır and Bolkardağı Units and the Ulukışla Basin (Blumenthal, 1956; Demirtaşlı et al., 1984, 1986; Clark and Robertson, 2002, 2005). In these studies, especially the stratigraphic, sedimentological and metamorphic features in some units have been revealed in different details. In order to interpret data obtained together with the findings of previous study for the study area and its immediate surroundings the following geological evolution was proposed (Figure 11).

6.1. Late Cretaceous Period

6.1.1. Turonian Period (Subduction)

Before Turonian period, the Inner Tauride Ocean has existed between the Anatolia and the Tauride Mountains (Çalapkulu, 1978; Şengör and Yılmaz, 1981; Oktay, 1982; Demirtaşlı et al., 1984; Özgül, 1984; Okay, 1985; Şengör, 1987; Şengör et al., 1988; Dilek and Moores, 1990; Koçyiğit, 1990; Robertson et al., 1996; Dilek and Whitney, 1997; Whitney and Dilek, 1997; Görür et al., 1998; Dilek et al., 1999b; Okay and Tüysüz, 1999; Robertson, 2000; Kadıoğlu et al., 2003, 2006; Rimmele, 2003; Garfunkel, 2004; Parlak and Robertson, 2004; Dilek, 2006; Parlak et al., 2006; Işık et al., 2008; Mackintosh and Robertson, 2009; Gans et al., 2009; Kadıoğlu and Dilek, 2009; Robertson and Parlak, 2009; Pourteau et al., 2010; Pourteau, 2011; Koç et al., 2012; Jolivet et al., 2013; Warren et al., 2013; Esirtgen, 2014).

In the subduction zone formed in this ocean, the subduction processes started in the Turonian period (Okay et al., 2001). Studies related to the beginning of subduction are generally the studies related to petrography, mapping and dating of ophiolites. In these studies, it is stated that the Bozkır Unit, which contains ophiolites, overlain the Tauride platform from north to south as the ocean has begun to subduct northward during the closure process. This ocean, in some studies (Göncüoğlu, 1986; Göncüoğlu et al., 1992, 1997; Alan et al., 2007) is referred to as the northern branch of Neotethys (İzmir - Ankara - Erzincan Ocean) and in some studies (Özgül, 1976; Şengör et al., 1980; Şengör and Yılmaz, 1981; Koçyiğit, 1983; Demirtaşlı et al., 1984; Görür et al., 1984; Robertson and Dixon, 1984; Okay, 1985; Dilek and Moores, 1990; Dilek and Tekeli, 1992; Parlak et al., 1996; Robertson, 1998; Pourteau et al., 2010) as the Inner Tauride Ocean. In studies related to the basic units in the Tauride Mountains, it is stated that Bolkardağı and Aladağ Units also overlain the Geyikdağı Unit from north to south (Özgül, 1976; Ulu, 2006; Alan et al., 2007).

The subduction in the Neotethys Ocean started in the Turonian period 92 - 90 Ma years ago (Dilek and Whitney, 1997). The oceanic plate during this subduction process started to overlie the carbonate platform forming the Taurides (Figure 11a). Kızıltepe Ophiolite, Alihoca Ophiolite and melange, which are parts of this plate, are found as tectonic clips on the Bolkar Mountains according to this study. Dilek et al. (1999*a*), who emphasized that the Alihoca's ophiolite was very close to trench, states that the ages obtained from basement metamorphics or plagiogranites related to the time of formation of ophiolites range from 89 - 94 Ma (Dilek et al., 1999*a*; Parlak and Delaloye, 1999; Önen and Hall, 2000; Çelik et al., 2006, 2011; Van Hinsbergen et al., 2016). Robertson et al. (2009) stated that the subduction in the Inner Tauride Ocean had occurred between 95 - 85 ma, (Cenomanian - Santonian) in their studies investigating the ophiolites and mélange related to the northern boundary of the Tauride - Anatolide continent. Sarıfakıoğlu et al. (2012) stated that subduction in the Inner Tauride Ocean started in the Late Cretaceous, and that the Central Anatolian Crystalline Complex collided with the Tauride platform in Eocene.

6.1.2. Coniacian - Campanian Period (Metamorphism)

Towards the end of the Mesozoic period, the Bolkar platform and oceanic plate have subducted below the overlying oceanic plate due to the oceanic subduction and undergone regional metamorphism (Figure 11b). There are various studies about the stratigraphic position and the age of settlement of the Alihoca Ophiolite and melange, which was emplaced on the Bolkardağı Unit after subduction and metamorphism. Çevikbaş (1991), in his study in the Ulukışla - Çamardı Basin, stated that the Bolkar group had been subjected to metamorphism before

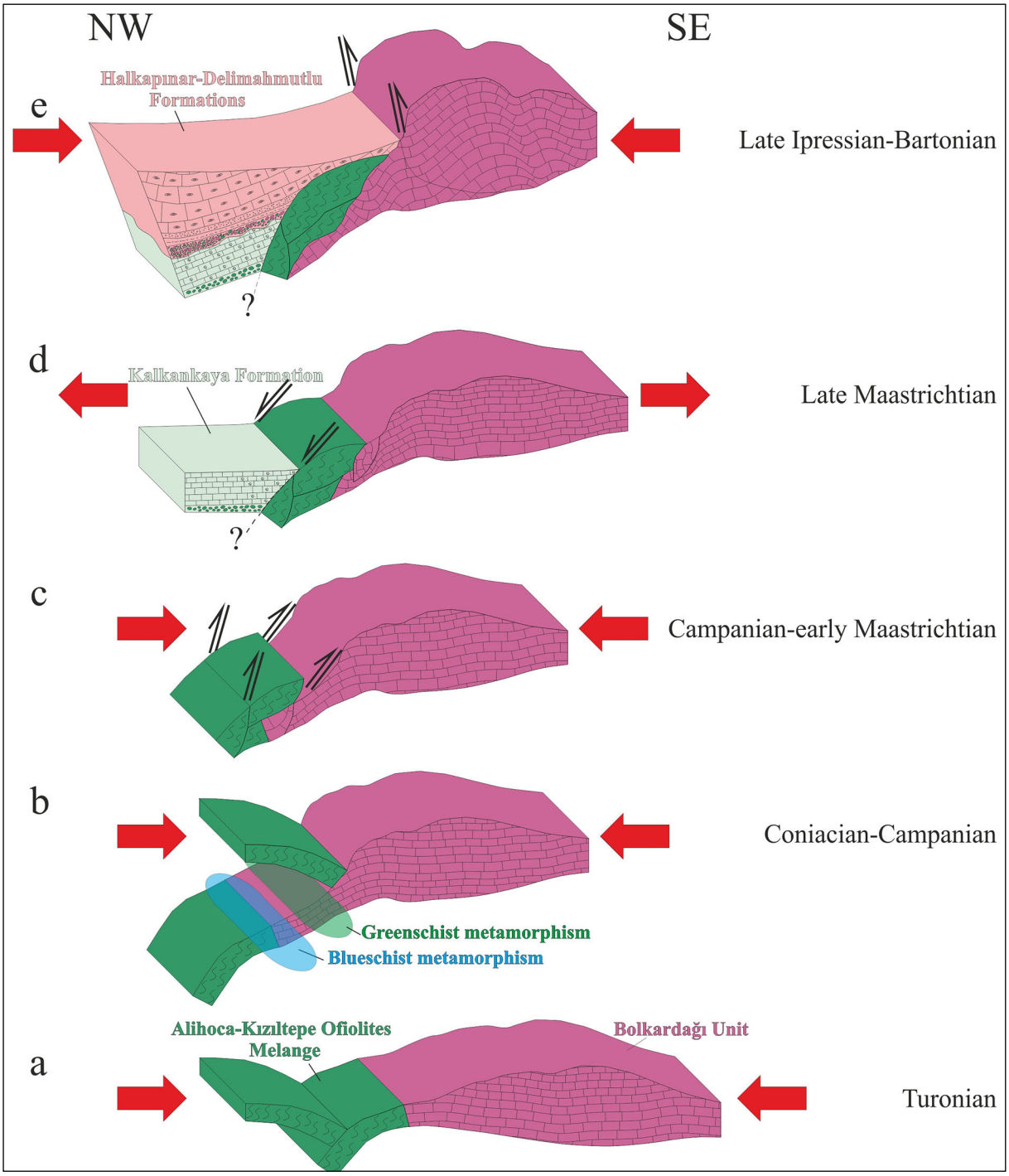

Figure 11- Tectonic development of the Bozkır Unit, Bolkardağı Unit and the Ulukışla Basin deposits over time.

the late Maastrichtian, and the Alihoca Ophiolitic Complex and Madenköy Ophiolite Melange probably had exhumed during this period, and interpreted the terrestrialization as the beginning of collision of the Bolkardağı Unit with the Niğde continental crusts. In their work on the exhumation of Niğde complex, Whitney and Dilek (1997) stated that the basement unit and ophiolites in the Bolkar Mountains region contained lithologies in the blueschist facies. They emphasized that this situation indicates the subduction of the northern edge of the Taurus carbonate platform partially beneath the Central Anatolian Crystalline Complex. The northern part of the Anatolide - Tauride continent has undergone HP - LT metamorphism

according to the studies of Candan et al. (2005) and Pourteau et al. (2010, 2013). In the studies of Okay and Tüysüz (1999), Ulu (2006) and Van Hinsbergen et al. (2016), it was stated that there occured low grade metamorphism in the Taurus Mountains and the age of metamorphism became younger as moving from north to south. The sediments of the Bolkardağı Unit have been subjected to HP - LT metamorphism in many places. This metamorphism is described by Candan et al. (2005) and Pourteau et al. (2010, 2014) as 6 - 9 kbar and ~350°C, and by Rimmelé et al. (2005) as 13 - 14 kbar, and ~400°C. In his work on the metamorphism of the Bolkardağı Unit, Parlak et al. (2014) stated that during the collision of the submerged trench and the passive margin, the Taurus microcontinent had been deeply submerged and metamorphism under HP - LT conditions and these rocks had been exposed in the Maastrichtian. Gürer et al. (2016*b*) stated that the Taurus passive continental margin had propagated towards the subduction zone in the north in Cretaceous - Paleocene period at the latest and had been subjected to HP - LT metamorphism.

During the subduction process, Bolkardağı Unit and Alihoca Ophiolite has undergone metamorphism in greenschist and blueschist facies due to the different metamorphism conditions. The metamorphism of the Bolkardağı Unit is a regional metamorphism that occurred approximately 80 my ago in subduction processes (Robertson et al., 2009). While the northernmost parts of the Bolkardağı Unit submerged very deep with ophiolites and exposed to HP - LT conditions, the southern parts was subjected to metamorphism in the greenschist facies. The Bolkardağı Unit, which was risen later, had been overlain by the Alihoca Ophiolite.

During the field studies, the lithologies showing different metamorphic facies were determined in thin section studies of mineralogical - petrographic samples taken from Bozkır and Bolkardağı units. Considering the results of the petrographic examination, the carbonates in the Bolkardağı Unit and the ophiolitic rocks belonging to the Bozkır Unit have undergone metamorphism under varying depth and temperature conditions from greenschist to blueschist facies.

At the basement of the region there is a sequence belonging to the Bolkardağı Unit representing the northernmost end of the Tauride platform. This basement has submerged under the northern oceanic lithosphere together with ophiolites related to the subduction in the Inner Tauride Ocean and undergone different degrees of metamorphism in the greenschist - blueschist facies. Considering these data, the age of metamorphism of the Bolkardağı Unit must be Coniacian - Campanian, the time interval after the subduction in Turonian but before the early Maastrichtian when it turned into a land.

6.1.3. Campanian - early Maastrichtian Period (Exhumation - Ophiolite Obduction)

The submerged lithosphere during the closure process of the Inner Tauride Ocean has been ruptured between 76 - 67 Ma, (Parlak et al., 2013*a*). The Bolkardağı Unit and ophiolites, which had been undergone metamorphism due to the subduction, was exhumed rapidly after rupture. Therefore, the micrites with globotruncana unconformably overly all the units in the Bolkardağı Unit sequence (Özgül, 1997). After this exhumation, the Alihoca Ophiolite - melange and Kızıltepe Ophiolite have overlain the Bolkardağı Unit due to the continuation of the closure process (Figure 11c).

There are many opinions about ophiolite obduction. The Bolkar group had been exposed before the late Maastrichtian by Çevikbaş (1991) and in the early Maastrichtian by Çevikbaş and Öztunalı (1992). According to Özgül (1997), the Bozkır Unit overlain the Bolkardağı Unit in the late Senonian. Dilek et al. (1999*b*) stated in their studies in the Tauride Mountains that the ophiolites in the Paleocene had overlain the carbonate platform during the closure process in the Inner Taurus Ocean. Jaffey and Robertson (2005) mentioned that ophiolitic rocks settled southward on the Bolkar platform in the Late Cretaceous period. Robertson et al. (2009) admit that this settlement of the melange occurred in the Santonian - Maastrichtian period 85 - 65 ma ago.

The metamorphism of the unit took place in the Coniacian - Campanian period. The basement age of the Kalkankaya formation, which is the first unit to be deposited on ophiolites in the study area, is the late Maastrichtian. The formation is underlain by ophiolites and metamorphics belonging to the Bolkardağı Unit.

Before the deposition of the unit, the ophiolites have overlain and settled on the Bolkardağı Unit.

Considering this stratigraphic data, the Bolkardağı Unit must have been exposed in Campanian - early Maastrichtian period and overlain by ophiolites.

6.1.4. Late Maastrichtian Period (Deposition)

After the settlement of the Alihoca Ophiolite on the Bolkardağı Unit, Seyitoğlu et al. (2017) mentioned in his works in the region, that there was material inflow from Bolkardağı and Bozkır units to the basin with the activity of the main fault. The first unit deposited in the basin is the Kalkankaya formation defined by Blumenthal (1956). Before the deposition of the formation, the region was a continent in the early Maastrichtian (Çevikbaş and Öztunalı, 1992). The Kalkankaya formation, which forms the previous deposits of the Ulukışla Basin, overlies the Bolkardağı marbles and the Alihoca Ophiolite with an angular unconformity. The deposition of formation starts with red colored, mostly ophiolitic pebbles at the bottom. Limestones in the upper parts contain abundant loftusia and rudist.

The Kalkankaya formation, which contains the oldest sediments of the Ulukışla Basin, is of late Maastrichtian - early Paleocene age (Çevikbaş and Öztunalı, 1992).

Gürer et al. (2014), in their studies on the Ulukışla Basin, stated that the sediments had been deposited in the basin between the Central Anatolian Crystalline Complex and the Taurides during the Late Cretaceous - Paleocene period due to the activity of E - W trending listric faults. Gürer et al. (2016*a*), in their study on the deformation of the Ulukışla Basin, also emphasized that the basin had been subjected to N - S and E - W extensions up to 56 my, during latest Cretaceous - Paleocene period. They stated that the N - S directing extensions in Campanian - Maastrichtian were E - W in Paleocene. Seyitoğlu et al. (2017) defined the İvriz fault on the border of the Ulukışla Basin and the Bolkar group. They stated that this fault was a high angle detachment fault in the Late Cretaceous - Paleocene, but later transformed into a low angle normal fault and played an important role in the exhumation of the Central Anatolian Crystalline Complex.

Following the metamorphism, the Bolkardağı Unit was overthrusted by ophiolites, uplifted relative to the basin and formed a feeding area for the basin. During the Late Maastrichtian - early Paleocene period, the limestones of the Kalkankaya formation have been deposited in the depositional area located to the north of the Bolkardağı Unit and the Alihoca Ophiolite (Figure 11d). The Maastrichtian age was dated from the determination of samples taken from the Kalkankaya formation in the study area for paleontological purposes. Paleontological data show that the formation was deposited in Maastrichtian and that the basin had a shallow sea and transitional environment.

6.2. Early - Middle Eocene Period

6.2.1. Late Ipressian - Bartonian Period (Deposition and Compression)

Demirtaşlı et al. (1984) noted that the Bolkar thrust affected the Eocene deposits in the Ulukışla Basin and formed narrow - closed folds in their studies on the geology of the Bolkar Mountains. Since the Oligocene deposits unconformably overlie the boundary they accept the age of thrust as Eocene for the Bolkar Mountains. Dilek et al. (1999*b*) stated that the ophiolites shifted northward over the Bolkar Mountains in Eocene, and that the Bolkar Mountains rose vertically in the Oligo - Miocene relative to the Ulukışla Basin. Alan et al. (2007) stated that the nappe movements had continued during the Late Cretaceous - Eocene period in their work on the main units in the Central Taurides. Robertson et al. (2009) mentioned that the continental collision and crustal thickening phases occurred in the approaching phase between Lutetian and Bartonian. Engin (2013), in his study on the tectonic evolution of the Ulukışla Basin, mentioned that the opening in the region should have started in the middle Eocene after the continental collision and detachment of submerged plate. Gürer et al. (2014), stated that the Ulukışla Basin deposits were folded due to N - S compression in the post - Paleocene. Gürer et al. (2014) also emphasized that the Tauride fault - fold belt was south oriented and accepted a tectonic line cutting the Tauride belt as a back thrust. The researchers stated that this thrust propagated northward compressing the region. In their studies on the Ulukışla Basin, Gürer et al. (2016*a*) stated that there had been a short period of tectonic stagnation after the Late Cretaceous - Paleocene stress, and N - S orienting compression forming the fold structure of Bolkar Mountains between 49 - 20 Ma had also affected the Ulukışla Basin. They stated that Eocene sequence in the Karagöl region was affected by a

south orienting thrust. Gürer et al. (2017) argue that in the Ulukışla Basin normal faults with strikes of E - W due to N - S compression since Lutetian were formed, and the region was folded.

The effects of compression in the region are seen as folding, development of reverse faults and vertical uplift. On the northern border of the Bolkardağı Unit, several folds and reverse faults are observed in the Ulukışla Basin deposits. The axes of the folds are asymmetrical and overturned. The angle between the fold limbs is mostly narrow and sometimes folds are seen as in closed fold geometry.

When folding caused by the compression of the region could not compensate the amount of compression, ESE - WNW trending SE dipping and N - NW oriented reverse faults developed in all units in the region and at the contacts of the units. The Bolkardağı Unit in this period overthrusted the overlying Alihoca Ophiolite with NW trending SE dipping reverse faults. Regional uplift also occurred as a result of folding and faulting. This uplift shows itself with the entrance of materials varying from blocks in few decimeters to silt - clay size into the Ulukışla Basin. During Thanetian - Lutetian period, the Halkapınar and Delimahmutlu Formations have been formed by the material entrance into the basin from Bolkardağı and the Bozkır Unit, which is the source area (Figure 11e). The Halkapınar formation located in the near west of the study area is the first product of this deposition. The fact that the thickness of the formation is between 1.000 - 2.000 m, contains deep sea sediments and debris flow deposits show that the basin deepens with the periodic activity of faults and that the continuous sedimentation takes place according to the source area. The deep sea sediments of the Halkapınar formation are seen below the conglomerates of the Delimahmutlu formation. The facies of the Halkapınar formation represents all the environments ranging from basin margin to the deep sea. The unit is Thanetian - Lutetian in age (Alan et al., 2007).

The thrust of the Bolkardağı Unit over the basin and the uplift caused the basin margin to rise and the deposition of the Delimahmutlu formation consisting of abundant nummulitic fan delta deposits in a shallow marine environment. In studies carried out in the region, Alan et al. (2007) state that the Delimahmutlu formation is Lutetian - Bartonian in age. During the studies, the late Ipressian age was obtained from the benthic foraminifera in samples taken from the contact of Bolkardağı marbles of the Delimahmutlu formation, and the middle Eocene age was taken from the areas at 800 m north of the same sequence at elevation of 100 m lower of the sequence.

Delimahmutlu formation was unconformably deposited on the Bolkardağı Unit marbles. The unit, which overlies the marbles with conglomerates, was inclined and folded with the effect of compression and vertical uplift. Both the structural and sedimantological data such as debris flows and brecciated levels in deltaic sequence show that the region continues to compress and the Bolkardağı Unit continues to rise, thrusts over the basin and deforms the units, and that the fault propagation folds develop. It is accepted that all the structural elements in the Bolkardağı Unit in the Central Taurides from north to south are south oriented in accordance with the ophiolite obduction. However, it was observed that the orientation of the structural elements in all units in the region were towards NW in field studies. In other words, the units contain structural elements that show movement from southeast to northwest, but not from north to south.

Gürer et al. (2016*a*) interpreted the faults at the contact of the Bolkardağı Unit and the Ulukışla Basin as folded or reversed normal faults. However, the faults at this contact are reverse faults. The orientation of fold axes within the Bolkardağı Unit and Ulukışla Basin deposits is towards NW and NE. The foliation planes strike ENE - WSW and dip SE. The faults in the region are of reverse fault character. The fault planes mostly strike NE - SW and dip SE.

All these structural elements clearly show that the region was thrusted from southeast to northwest in NW direction on planes striking NE - SW, dipping SE as a result of compression in NW - SE direction.

In the Early - Middle Eocene period, the Halkapınar and Delimahmutlu formation were unconformably deposited on the Bolkardağı Unit in the depositional area in the north of the Bolkardağı Unit. During the deposition of the Delimahmutlu formation, the unit was affected by regional tectonics and deformed together with the Halkapınar formation. These deformation products are seen as bending, folding and reverse faulting in the units. Işık et al. (2014), in their

studies on the Savcılı fault zone, stated that faulting occurred at approximately 40 my and 23 my by Rb - Sr analysis, and the region had been compressed during this period. This compression to be observed in the area in the same period also supports this study.

7. Results

By evaluating stratigraphic, petrographic and structural data in this study, the following results were obtained:

1. In the study area, the oceanic lithosphere and the northern part of the Tauride belt have been subducted into different depths during the sub - oceanic subduction processes. The ophiolites belonging to the pre Campanian Bozkır Unit and the Bolkardağı Unit have undergone metamorphism in the greenschist and blueschist facies.

2. The ophiolites belonging to the Bozkır Unit have overthrust the Bolkardağı Unit during the Campanian - early Maastrichtian period.

3. The extensional regime effective in the region in the Late Maastrichtian - Bartonian period have enabled the Ulukışla Basin units to be deposited unconformably on the basin units in shallow and gradually deepening environments.

4. Starting from the Late Ipressian, the region began to be recompressed; the basement and basin units have been subjected to deformation. The structures developed in connection with this event revealed that the Bolkardağı Unit overthrusted the Alihoca Ophiolite / Mélange representing the Bozkır Unit, Kızıltepe Ophiolite and Ulukışla Basin deposits with reverse / thrust faults from southeast to northwest.

5. The initial unconformable contact between the Ulukışla Basin deposits and the Bolkardağı Unit was thrusted over the Ulukışla Basin of the Bolkardağı Unit, and then it turned into a 70° - 80° reverse fault in the study area. This structural development in the region was interpreted as the product of a movement from southeast to northwest.

Acknowledgements

This study was carried out within the scope of "Orta Toroslar'daki Tektonik Hatların Kinematiği - Yaşlandırılması ve Evrimi" (so called the "Kinematics - Dating and Evolution of Tectonic Lines in the Central Taurides") conducted by the Department of Geological Researches, MTA General Directorate, Ankara, Turkey and TÜBİTAK - 115Y140 project in 2016 - 2017. The authors are thankful to Assoc. Prof. Ayhan Ilgar, Assoc. Prof. Levent Karadenizli, Dr. Ayşe Çağlayan, Reza Saber and to Aycan Günay as they shared their opinions during field studies. Petrographic and paleontological examinations of the samples were carried out by Aylin Paçala and Fatma Gedik, respectively. The authors would also like to thank them for their assistance.

The authors also appreciate to Prof. Dr. Yaşar Eren and two unknown referees for their supportive contributions and suggestions to make the article better.

References

Alan, İ., Şahin, Ş., Keskin, H., Altun, İ., Bakırhan, Balcı, V. B., Böke, N., Saçlı, L., Pehlivan, Ş., Kop, A., Hanilçi, N., Çelik, Ö. F. 2007. Maden Tetkik ve Arama Genel Müdürlüğü Jeoloji Etütleri Dairesi Orta Torosların Jeodinamik Evrimi Ereğli (Konya) - Ulukışla (Niğde) - Karsantı (Adana) - Namrun (İçel) Yöresi. Maden Tetkik ve Arama Genel Müdürlüğü Rapor No: 11006, Ankara (unpublished).

Alan, İ., Şahin, Ş., Bakırhan, B. 2011. 1:100.000 ölçekli Türkiye Jeoloji Haritaları, Adana N-33 Paftası. Maden Tetkik ve Arama Genel Müdürlüğü Jeoloji Etütleri Dairesi, No: 166.

Allmendinger, R. W., Cardozo, N. C., Fisher, D. 2013. Structural Geology Algorithms: Vectors & Tensors: Cambridge, England, Cambridge University Press 289.

Blumenthal, M. M. 1941. Un aperçu de la géologie du Taurus dans les vilayets de Niğde et d'Adana. Mineral Research and Exploration Institute of Turkey (MTA) Publication B-6, 49-95.

Blumenthal, M. M. 1952. Das Taurische Hochgebirge Aladag, neuere forschungen zu seiner Geographie, Stratigraphie und Tektonik. Mineral Research and Exploration Institute of Turkey (MTA) Publication D-6.

Blumenthal, M. M. 1956. Yüksek Bolkardağ'ın kuzey kenar bölgelerinin ve batı uzantılarının jeolojisi. Maden Tetkik ve Arama Genel Müdürlüğü Yayını Seri D, No: 7, 153, Ankara.

Candan, O., Çetinkaplan, M., Oberhänsli, R., Rimmelé, G., Akal, C. 2005. Alpine high - P/low-T metamorphism of the Afyon Zone and implications for the metamorphic evolution of Western Anatolia, Turkey. Lithos 84(1-2), 102-124.

Clark, M., Robertson, A.H.F. 2002. The role of the Early Tertiary Ulukışla Basin, Southern Turkey, in suturing of the Mesozoic Tethys ocean. Journal of Geological Society, London 159, 673-690.

Clark, M., Robertson, A. H. F. 2005. Uppermost Cretaceous-Lower Tertiary Ulukışla Basin, south - central Turkey: sedimentary evolution of part of a unified basin complex within an evolving Neotethyan suture zone. Sedimentary Geology 173, 15-51.

Çalapkulu, F. 1978. Bolkardağ bölgesinin jeolojik evrimi. Türk. Jeol. Kurumu, 32. Bilimsel ve Teknik Kurul. Bildiri özetleri, 7-8.

Çalapkulu, F. 1980. Horoz Granodiyoritinin Jeolojik İncelemesi. Türk. Jeol. Kurumu 23, 59-68.

Çelik, Ö. F., Delaloye, M., Feraud, G. 2006. Precise 40Ar - 39Ar ages from the metamorphic sole rocks of the Tauride Belt Ophiolites, southern Turkey: implications for the rapid cooling history. Geol. Mag. 143(02), 213.

Çelik, Ö. F., Marzoli, A., Marschik, R,. Chiaradia, M., Neubauer, F., Öz, I. 2011. Early - Middle Jurassic intra-oceanic subduction in the İzmir - Ankara - Erzincan Ocean, Northern Turkey. Tectonophysics 509 (1-2), 120–134.

Çevikbaş, A. 1991. Ulukışla - Çamardı (Niğde) Tersiyer havzasının jeodinamik evrimi ve maden yatakları yönünden önemi: Doktora tezi İ.Ü. Mühendislik Fakültesi, Jeoloji Mühendisliği Bölümü, 235, İstanbul (unpublished).

Çevikbaş, A., Öztunalı, Ö. 1992. Ulukışla - Çamardı (Niğde) Mestrihtiyen Sonrası Çökel Havzasının Jeolojisi. Bulletin of the Mineral Research and Exploration 114, 155-172.

Demircioğlu, R., Eren, Y. 2000. Çamardı (Niğde) civarında Niğde Masifi örtü birimlerinin yapısal özellikleri, N.Ü. Aksaray Mühendislik Fakültesi, Haymana-Tuzgölü-Ulukışla basenleri uygulamalı çalışma (Workshop), Bildiri özleri, 6.

Demircioğlu, R., Eren,Y. 2003. Niğde Masifi (Çamardı-Niğde) Tersiyer yaşlı örtü kayaçlarındaki Oligosen öncesi paleogerilme konumu, SDÜ Mühendislik ve Mimarlık Fakültesi 20. Yıl Jeoloji Sempozyum, Bildiriler, 37.

Demircioğlu, R., Eren, Y. 2017. Çamardı (Niğde Yöresinde Niğde Masifinin Yapısal Özellikleri. Bulletin of the Mineral Research and Exploration 154, 15-26.

Demirtaşlı, E. 1975. İran, Pakistan ve Türkiye'deki Alt Paleozoyik Yaşlı Kayaçların Stratigrafik Korelasyonu. Cumhuriyetin 50. Yılı Yerbilimleri Kongresi, Maden Tetkik ve Arama Genel Müdürlüğü Özel Yayını, Ankara, 204-222.

Demirtaşlı, E., Bilgin, A. Z., Erenler, F., Işıklar, S., Sanlı, D. Y., Selim, M., Turhan, N. 1973. Bolkardağları'nın Jeolojisi. Cumhuriyetin 50. Yılı Yerbilimleri Kongresi, Maden Tetkik ve Arama Genel Müdürlüğü Özel Yayını 42-57, Ankara.

Demirtaşlı, E., Turhan, N., Bilgin, A. Z., Selim, M. 1984. Geology of the Bolkar Mountains: In: Tekeli, O. and Göncüoğlu, M.C (eds), Geology of the Taurus Belt. 125-142.

Demirtaşlı, E., Turhan, N., Bilgin, A. Z. 1986. Bolkar Dağları ile Ereğli - Ulukışla havzasının genel jeolojisi. Maden Tetkik ve Arama Genel Müdürlüğü Rapor no: 8097, Ankara (unpublished).

Dilek, Y. 2006. Collision tectonics of the Mediterranean region: Causes and consequences. Geological Society of America Special Paper 409.

Dilek, Y., Moores, E. 1990. Regional tectonics of the eastern Mediterranean ophiolites. In: Malpas, J., Moores, E., Panayiotou, A., Xenophontos, C. (Ed.), Ophiolites - Oceanic Crustal Analogues. Troodos Ophiolite Symposium Proceedings 295-309.

Dilek, Y., Tekeli, O. 1992. Ophiolite geology of the Inner-Tauride belt, S. Turkey, and implications for Mesozoic tectonics of the eastern Mediterranean region. Geological Society of America Abstracts with Programs 24, A280.

Dilek, Y., Whitney, D. L. 1997. Counterclockwise P-T-t trajectory from the metamorphic sole of a Neo-Tethyan ophiolite (Turkey). Tectonophysics 280, 295-310.

Dilek, Y., Thy, P., Hacker, B., Grundvig, S. 1999*a*. Structure and Petrology of Tauride ophiolites and mafic dike intrusions (Turkey) Implications for the Neotethyan ocean. GSA Bulletin 1999(111), 8, 1192-1216.

Dilek, Y., Whitney, D. L., Tekeli, O. 1999*b*. Links Between Tectonic Processes and Landscape Morphology in an Alpine Collision Zone, South - Central Turkey. Z. Geomorph. N.E. 118, 147-164.

Engin, C. 2013. Structural architecture and tectonıc evolutıon of the Ulukışla sedimentary basin in South - Central Turkey. PhD thesis, Miami University Oxford, Ohio.

Esirtgen, T. 2014. Orta Toroslarda Bucakkışla Bölgesinin (GB Karaman) Tektono - Sedimanter Gelişimi, Tectono-Sedimantery Evolution of Bucakkışla

Region (SW Karaman) In Central Taurides, Bulletin of the Mineral Research and Exploration 148, 19-42, Ankara.

Fleuty, M. J. 1964. The description of folds. Proceedings of the Geologists' Association 75(4), 461-492.

Gans, C. R., Beck, S. L., Zandt, G., Biryol, C. B., Özacar, A. A. 2009. Detecting the limit of slab break-off in central Turkey: New high - resolution Pn tomography results. Geophysical Journal International 179, 1566–1577.

Garfunkel, Z. 2004. Origin of the Eastern Mediterranean basin: a reevluation. Tectonophysics 391, 11-34.

Gautier, P., Bozkurt, E., Hallot, E., Dirik, K. 2002. Dating the exhumation of a metamorphic dome: geological evidence for pre - Eocene unroofing of the Niğde Massif (central Anatolia, Turkey). Geol. Mag. 139 (5), 559-576.

Gautier, P., Bozkurt, E., Bosse, V., Hallot, E., Dirik, K. 2008. Coeval extensional shearing and lateral underflow during Late Cretaceous core complex development in the Niğde Massif, Central Anatolia, Turkey. Tectonics 27, TC 1003.

Göncüoğlu, M. C. 1986. Geochronological data from the southern part (Niğde area) of the Central Anatolian massif. Mineral Research and Exploration Institute of Turkey (Maden Tetkik ve Arama) Bulletin 105/106, 111-124.

Göncüoğlu, M. C. 2011. Kütahya - Bolkardağ Kuşağının Jeolojisi. Bulletin of the Mineral Research and Exploration 142, 227-282.

Göncüoğlu, M. C., Erler, A., Toprak, V., Yalınız, K., Olgun, E. Rojay, B. 1992. Orta Anadolu Masifin Batı Kesiminin Jeolojisi. Vol. 2. Orta Kesim. Turkish Petroleum Corporation (TPAO) Reports, 3155.

Göncüoğlu, M. C., Dirik, K., Kozlu, H. 1997. Pre - Alpine and Alpine terranes in Turkey: explanatory notes to the terrane map of Turkey. In: Papanikolaou, D., Sassi, F.P . (Ed.), IGCP Project no: 276; Paleozoic domains and their alpidic evolution in the Tethys. Annales Géologiques des Pays Helléniques, 515-536.

Görür, N., Oktay, F. Y., Seymen, İ., Şengör, A. M. C. 1984. Paleotectonic evolution of the Tuzgölü basin complex, central Turkey: Sedimentary record of a Neo-Tethyan closure. In: The geological evolution of the eastern Mediterranean.(Ed. by Dixon, J. E. and Robertson, A. H. F.), Geol. Soc. London Spec. Paper 17; 467-482.

Görür, N., Tüysüz, O., Şengör, A. M. C. 1998. Tectonic Evolution of the central Anatolian Basins. International Geology Review 40, 831-850.

Gürer, D., Van Hinsbergen, D., Matenco, L., Kaymakçı, N., Corfu, F. 2014. Late Cretaceous to recent tectonic evolution of the Ulukışla Basin (Southern Central Anatolia). Geophysical Research Abstracts 16, EGU2014-12854.

Gürer, D., Van Hinsbergen, D., Matenco, L., Kaymakci, N., Corfu, F., Cascella, A. 2016*a*. Kinematics of a former oceanic plate of the Neotethys revealed by deformation in the Ulukışla basin (Turkey). Tectonics.

Gürer, D., Plunder, A., Kirst, F., Corfu, F., Schmid, S. F., Van Hinsbergen, D.J.J. 2016*b*. A long - lived extensional back - arc in Anatolia? AGU Fall Meeting, 12-16 December 2016.

Gürer, D., Harin, M. D., Van Hinsbergen, D. J. J., Umhoefer, P. J. 2017. Cenozoic Structural and Stratigraphic Evolution of the Ulukışla and Sivas Basins (Central and Eastern Turkey). Geophysical Research Abstracts 19, EGU2017-18332.

Işık, V., Lo, C. H., Göncüoğlu, C., Demirel, S. 2008. $^{39}Ar/^{40}Ar$ Ages from the Yozgat Batolith: Preliminary Data on the Timing of Late Cretaceous Extension in the Central Anatolian Crystalline Complex, Turkey. The Journal of Geology 116 (5), 520-526.

Işık, V., Uysal, I. T., Çağlayan, A., Seyitoğlu, G. 2014. The evolution of intraplate fault systems in central Turkey: Structural evidence and Ar - Ar and Rb-Sr age constraints for the Savcili Fault Zone. Tectonics 33, 1875-1899.

Işık, V., Çağlayan, A., Saber, R., Esirtgen, T., Seyitoğlu, G., Ilgar, A., Zhao, J., Bolhar, R., Cenki-Tok, B., Günay, A. 2018. Orta Toroslar'da Bindirme Sisteminin Yapısal Analizi, Jeokronolojisi ve Bunların Tektonik Anlamları. TÜBİTAK 115Y140 Numaralı Proje 291.

Jaffey, N., Robertson, A. 2005. Non - marine sedimentation associated with Oligocene-Recent exhumation and uplift of the Central Taurus Mountains, S. Turkey. Sedimentary Geology 173, 53-89.

Jolivet, L., Faccenna, C., Huet, B., Labrousse, L., Le Pourhiet, L., Lacombe, O., Lecomte, E., Burov, E., Denèle, Y., Brun, J. P., Philippon, M., Paul, A., Salaün, G., Karabulut, H., Piromallo, C., Monié, P., Gueydan, F., Okay, A. I., Oberhänsli, R., Pourteau, A., Augier, R., Gadenne, L., Driussi, O. 2013. Aegean tectonics: Strain localisation, slab tearing and trench retreat. Tectonophysics 597-598, 1-33.

Kaaden, G., van der, 1966. Türkiye'deki Glokofan Kayaçlarının Önemi ve Dağılışı. Maden Tetkik ve Arama Dergisi 67, 36-67, Ankara.

Kadıoğlu, Y. K., Dilek, Y. 2009. Structure and geochemistry of the adakitic Horoz granitoid, Bolkar Mountains South central Turkey and its tectonomagmatic evolution. International Geology Review, 1-31.

Kadıoğlu, Y. K., Dilek, Y., Güleç, N., Foland, K. A. 2003. Tectonomagmatic evolution of bimodal plutons in the Central Anatolian Crystalline Complex, Turkey. Journal of Geology 111, 671–690.

Kadıoğlu, Y. K., Dilek, Y., Foland, K. A. 2006. Slab break - off and syncollisional origin of the Late Cretaceous magmatism in the Central Anatolian crystalline complex Turkey. Geological Society of America, Special Paper, 409, 381-415.

Karaoğlan, F. 2016. Tracking the uplift of the Bolkar Mountains (South - central Turkey): evidence from apatite fission track thermochronology. Turkish Journal of Earth Science 25, 64-80.

Koç, A., Kaymakcı, N., van Hinsbergen, D. J. J., Kuiper, K. F., Vissers, R. L. M. 2012. Tectono - sedimentary evolution and geochronology of the Middle Miocene Altınapa Basin, and implications for the Late Cenozoic uplift history of the Taurides, southern Turkey. Tectonophysics 532–535, 134-155.

Koçyiğit, A. 1983. Hoyran Gölü (Isparta Büklümü) Dolayının Tektoniği. Türkiye Jeoloji Kurumu Bülteni 26-1, 1-10.

Koçyiğit, A. 1990. Üç Kent Kuşağı'nın Erzincan batısındaki (KD Türkiye) yapısal ilişkileri: Karakaya, İç Toros ve Erzincan Kenetleri. In: 8th Petrol Congress of Turkey, Proceedings, Ankara, 152-160.

Mackintosh, P. W., Robertson, A. H. F. 2009. Structural and sedimentary evidence from the northern margin of the Tauride platform: testing models of Late Triassic 'Cimmerian' uplift and deformation in southern Turkey. Tectonophysics 473, 203–215.

Okay, A. I. 1985. Distribution and characteristics of the north - west Turkish blueschists: Dixon, J.E. and Robertson, A. H. F., The Geological Evaluation of the Eastern Mediterranean, Spec. Pub. of the Geo. Soc. 17, Blackwell Sci. Publ., Oxford, 848.

Okay, A. I., Tüysüz, O. 1999. Tethyan sutures of northern Turkey. In: Durand, B., Jolivet, L., Horvath, F., Seranne, M. (Ed.), Mediterranean Basins: Tertiary extension within the Alpine Orogen. Geological Society of London Special Publication, 156, 475–515.

Okay, A. I., Tansel, I., Tüysüz, O. 2001. Obduction, subduction and collision as reflected in the Upper Cretaceous-Lower Eocene sedimentary record of western Turkey. Geological Magazine 138, 117-142.

Oktay, F. T. 1982. Ulukışla ve çevresinin stratigrafisi ve jeolojik evrimi. Türkiye Jeoloji Kurumu Bülteni 25, 15-23.

Önen, P., Hall, R. 2000. Sub-ophiolite metamorphic rocks from NW Anatolia, Turkey. J. Metamorph. Geol. 18(5), 483-495.

Özgül, N. 1971. Toroslar'ın kuzey kesiminin yapısal gelişiminde blok hareketlerinin önemi. Türkiye Jeoloji Kurumu Bülteni 14-1, 85-101.

Özgül, N. 1976. Torosların Bazı Temel Jeoloji Özellikleri. Türkiye Jeoloji Kurumu Bülteni 19, 5-78.

Özgül, N. 1984. Stratigraphy and tectonic evolution of the Central Taurides, Geology of the Taurus belt. International Symposium, 77-90.

Özgül, N. 1997. Bozkır - Hadim - Taşkent (Orta Torosların Kuzey Kesimi) Dolayında Yer Alan Tektono-Stratigrafik Birliklerin Stratigrafisi. Maden Tetkik ve Arama Dergisi 119, 113-174.

Parlak, O., Delaloye, M. 1999. Precise $^{40}Ar/^{39}Ar$ ages from the metamorphic sole of the Mersin ophiolite (southern Turkey). Tectonophysics 301, 145-158.

Parlak, O., Robertson, A. H. F. 2004. The ophiolite - related Mersin Melange, southern Turkey: its role in the tectonic - sedimentary setting of Tethys in the Eastern Mediterranean region. Geol. Mag. 141 (3), 257-286.

Parlak, O., Delaloye, E., Bingöl, E. 1996. Mineral chemistry of ultramafic and mafic cumulates as an indicator of the arc-related origin of the Mersin ophiolite (southern Turkey). Geol Rundsch 85, 647-661.

Parlak, O., Yılmaz, H., Boztuğ, D. 2006. Origin and Tectonic Significance of the Metamorphic Sole and Isolated Dykes of the Divriği Ophiolite (Sivas, Turkey): Evidence for Slab Break - off prior to Ophiolite Emplacement. Turkish Journal of Earth Sciences 15, 2006, 25-45.

Parlak, O., Kop, A., Robertson, A., Karaoğlan, F., Neubauer, F., Koepke, J. 2014. Upper Cretaceous HP - LT metamorphism along the leading edge of the Mesozoic Bolkardağ platform, southern Turkey. Geophysical Research Abstracts 16, EGU2014-3665-2.

Pourteau, A. 2011. Closure of the Neotethys Ocean in Anatolia: structural, petrologic and

geochronologic insights from low - grade high-pressure metasediments, Afyon Zone, Institutional Repository of the University of Potsdam, PhD thesis.

Pourteau, A., Candan, O., Oberhanslı, R. 2010. High-pressure metasediments in central Turkey: Constraints on the Neotethyan closure history. Tectonics 29, 1-18.

Pourteau, A., Sudo, M., Candan, O., Lanari, P., Vidal, O., Oberhänsli, R. 2013. Neotethys closure history of Anatolia: insights from 40 Ar- 39 Ar geochronology and P-T estimation in high-pressure metasedimentary rocks. J. Metamorph. Geol., 31, 585–606.

Pourteau, A., Bousquet, R., Vidal, O., Plunder, A., Duesterhoeft, E., Candan, O., Oberhänsli, R. 2014. Multistage growth of Fe - Mg - carpholite and Fe - Mg - chloritoid, from field evidence to thermodynamic modelling, Contrib. to Mineral. Petrol., 168(6), 1090.

Rimmele, G., 2003. Structural and Metamorphic Evolution of the Lycian Nappes and the Menderes Massif (Southweat Turkey): Geodynamic Implications and Correlations with the Aegean Domain. PhD Thesis, Universität Potsdam, Deutschland.

Rimmelé, G., Parra, T., Goffé, B., Oberhänsli, R., Jolivet, L., Candan, O. 2005. Exhumation Paths of High - Pressure - Low - Temperature Metamorphic Rocks from the Lycian Nappes and the Menderes Massif (SW Turkey): a Multi - Equilibrium Approach, J. Petrol., 46(3), 641–669, doi:10.1093/petrology/egh092.

Robertson, A. H. F. 1998. Mesozoic - Tertiary tectonic evolution of the East Mediterranean area: integration of marine and land evidence. In: Robertson, A. H. F., Emeis, K. C., Richter, C., Camerlenghi, A. (Ed.), Proceedings of the Ocean Drilling Program, Scientific Results 160, 723-782.

Robertson, A. H. F. 2000. Mesozoic–Tertiary tectonic-sedimentary evolution of a south Tethyan oceanic basin and its margins in Southern Turkey. In: Bozkurt, E., Winchester, J.A., Piper, J.D.A. (Eds.), Tectonics and Magmatism in Turkey and the Surrounding Area. Spec. Publ. - Geol. Soc. Lond. 173, 97-138.

Robertson, A. H. F., Dixon, J. D. 1984. Introduction: Aspects of the Geological Evolution of the Eastern Mediterranean. In: Dixon, J. E. & Robertson, A. H. F. (eds) The Geological Evolution of the Eastern Mediterranean. Geological Society, London, Special Publications, 17, 1–74.

Robertson, A. H. F., Parlak, O. 2009. Overview of the Tectonic Setting of Genesis and Emplacement of Cretaceous Ophiolites in Turkey and the Adjacent Eastern Mediterranean region. 62nd Geological Kurultai of Turkey, 13−17 April 2009, MTA–Ankara, Turkey, 826-827.

Robertson, A. H. F., Dixon, J. E., Brown, S. 1996. Alternative models for the Late Palaeozoic - Early Tertiary development of Tethys in the eastern Mediterranean region. In: Morris, A. & Tarling, D. H. (eds) Palaeomagnetism and Tectonics of the Mediterranean Region. Geological Society, London, Special Publications 105, 239-263.

Robertson, A. H. F., Parlak, O., Ustaömer, T. 2009. Melange genesis and ophiolite emplacement related to subduction of the northern margin of the Tauride-Anatolide continent, Central and Western Turkey. Geological Society, London, Special Publications 311, 9-66.

Sarıfakıoğlu, E., Dilek, Y., Winchester, J. A. 2012. Late Cretaceous subduction initiation and Palaeocene - Eocene slab breakoff magmatism in South - Central Anatolia, Turkey. International Geology Review 2012, 1-22.

Seyitoğlu, G., Işık, V., Gürbüz, E., Gürbüz, A. 2017. The discovery of a low - angle normal fault in the Taurus Mountains the İvriz detachment and implications concerning the Cenozoic geology of southern Turkey. Turkish Journal of Earth Sciences 26, 189-205.

Şengör, A. M. C. 1987. Tectonics of the Tethysides: orogenic collage development in a collisional setting. Ann. Rev. Earth Planet. Sci. 15, 213-244.

Şengör, A. M. C., Yılmaz, Y. 1981. Tethyan evolution of Turkey: a plate tectonic approach. Tectonophysics, 75, 181-241.

Şengör, A. M. C., Yılmaz, Y., Ketin, İ. 1980. Remnants of a pre-Late Jurassic ocean in Northern Turkey: fragments of Permo-Triassic Paleo-Tethys?: Reply. Geological Society of America Bulletin, 93, 932-936.

Şengör, A.M.C., Altıner, D., Cin, A., Ustaömer, T., Hsü, K.J. 1988. Origin and assembly of the Tethyside orogenic collage at the expense of Gondwana Land. Geological Society, London, Special Publications 1988, 37, 119-181.

Ulu, Ü. 2002. 1/500.000 ölçekli Türkiye jeoloji haritaları, No: 15 / Adana. Maden Tetkik ve Arama Genel Müdürlüğü, Ankara.

Ulu, Ü, 2006. Bolkar Dağları'nın Jeolojisi: Maden Tetkik ve Arama Genel Müdürlüğü Raporu, No: 10776, 88 sayfa, Ankara (unpublished).

Van Hinsbergen, D. J. J., Maffione, M., Plunder, A., Kaymakcı, N., Ganerød, M., Hendriks, B. W. H., Corfu, F., Gürer, D., de Gelder, G. I. N. O, Peters, K., McPhee, P.J., Brouwer, F. M., Advokaat, E. L., Vissers, R. L. M. 2016. Tectonic evolution and paleogeography of the Kırşehir Block and the Central Anatolian Ophiolites, Turkey. Tectonics 35(4), 983–1014.

Warren, L. M., Beck, S. L., Biryol, C. B., Zandt, G., Özacar, A. A., Yang, Y. 2013. Crustal velocity structure of Central and Eastern Turkey from ambient noise tomography. Geophysical Journal International 1-14.

Whitney, D. L., Dilek, Y. 1997. Core complex development in central Anatolia, Turkey. Geology 25, 11, 1023-1026.

Zorlu, K., İnan, S., Gül, M., İnan, M., Kurt, M. A., Alpaslan, M. 2011. Geological Evolution of the Ulukışla Basin (Late Cretaceous - Eocene) Central Anatolia, Turkey. Hacettepe Üniversitesi Yerbilimleri Uygulama ve Araştırma Merkezi Bülteni, Yerbilimleri 32 (2), 151-170.

Bulletin of the Mineral Research and Exploration

http://bulletin.mta.gov.tr

Natural and cultural heritage integration and geoconservation recommendatory of the Nemrut - Süphan proposed geopark area, Bitlis - Turkey

Yahya ÇİFTÇİ[a*] and Yıldırım GÜNGÖR[b]

[a]*General Directorate of Mineral Research and Exploration (MTA), Department of Mineral Researches, Ankara, Turkey (retired)*
[b]*İstanbul University - Cerrahpaşa, Faculty of Engineering, Department of Geological Engineering, Büyükçekmece Campus-İstanbul, Turkey*

Research Article

Keywords:
Nemrut, Süphan, Geopark, Geo-Conservation, Bitlis, Lake Van.

ABSTRACT

Nemrut-Süphan proposed geopark area located in Eastern Anatolia, Bitlis County, between the Bitlis City Center and Tatvan-Ahlat-Adilcevaz Villages which covers total of 5.300 square km. Two strato - volcano of Turkey, the Nemrut (2.948 meters) and Süphan (4.058 meters) mountains, are located in this area. The southern part of the area consists of metamorphic rocks meters, which are the oldest strata of Turkey. The biggest soda lake of the World, Lake Van, consist the eastern side, of the geopark area. Ophiolitic rocks also exist in this area, representing the remnant of the ancient Neo - Tethys ocean. Total 44 geosite were proposed and determined in the geopark area, most of them are located on five proposed geo - routes. These proposed geosites and several cultural heritage elements are amalgamated within the scope of the geopark management system. This plan also includes the geo - conservation table of these proposed geosites. This area is ready for announcing as a second "International Geopark" (UNESCO) of Turkey in terms of unique geodiversity, cultural heritages, bio - diversity and different kinds of summer and winter outdoor activity potential, in the light of the performed inventory studies.

Received Date 15.06.2020
Accepted Date: 05.01.2021

1. Introduction

During field considering, the main concept of the geopark was determined by first considering the geodiversity of it. The main concept of Nemrut - Süphan geopark is "volcanic geopark". However, there are also very valuable formations representing magmatic - metamorphic processes and oceanic crust in this geopark which lies on one of the oldest massives of Turkey from south. In northern areas, Nemrut caldera is obsreved, which is the best preserved calderas of Turkey and still holds the status of "National Park" and products of volcanic flow - eruption - pyroclastic fall deposits around it (Figure 1). The youngest lava flows in Turkey are also within the same volcanic system. Further to the north, Turkey's third highest peak (4.058 m) is located as the Süphan Stratovolcano. It also has characteristic recent lake sedimentary formations in its northern areas. The Lake Van, which limits the geopark from east, is a "geological heritage" subject on its own, with recent stramatolite formations at the bottom.

In addition to this rich geodiversity, the region has a very rich accumulation in terms of cultural assets (archeology, ethnography, gastronomy, history) and the inventory studies carried out by different people and institutions over time on these cultural values have been combined in a suitable format and processed on the geopark map. The geopark area also has a wide

Citation Info: Çiftçi, Y., Güngör, Y. 2021. Natural and cultural heritage integration and geoconservation recommendatory of the Nemrut-Süphan proposed geopark area, Bitlis-Turkey. Bulletin of the Mineral Research and Exploration 165, 191-215. https://doi.org/10.19111/bulletinofmre.860092

**Corresponding author: Yahya ÇİFTÇİ, yahyaciftci@gmail.com*

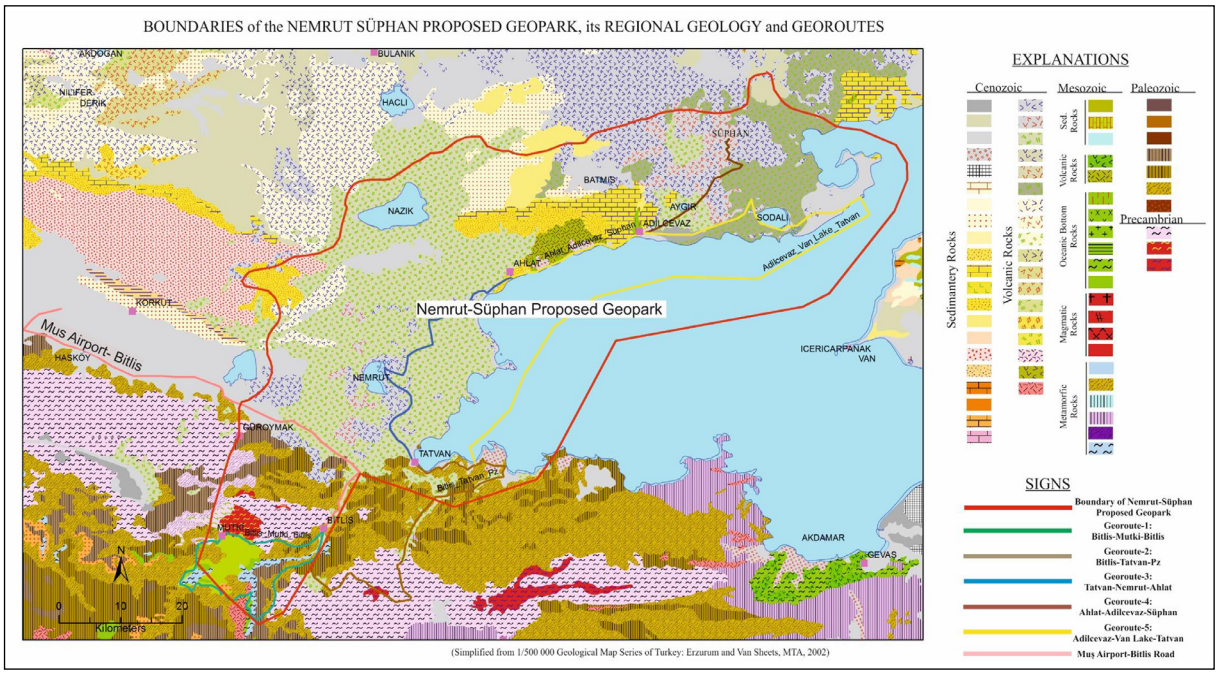

Figure 1- Geological map of Nemrut-Süphan proposed geopark area with a scale of 1: 500.000, boundaries and georoutes (modified from MTA, 2002).

variety of opportunities in terms of "Outdoor Sports" and within the scope of this study, an "inventory study" on outdoor sports has been carried out and processed on the geopark map.

Although there are international examples for the operation / management model of the geopark, it is not easy to develop a consistent and continuous model in this regard, given the unique conditions of the region. However, when the above - mentioned extraordinary possibilities come together, a rare "UNESCO Geopark" candidate comes out. With this work, this area has been re - projected as a geopark for socio - economic purposes, defined and programmed with all the necessary components in the context of being an international geopark.

1.1. Cultural Geology Terms Used in the Article

Geosite: In its broadest concept, it defines rock, mineral, fossil assemblage, structure, succession, landform or piece of land that expresses any current or old geological process, event or feature (Jemirko).

Jeopark: It is the area where the same or different types of geosites are found collectively and not smaller than the pedestrian walking distance (Jemirko).

Geoturism: It is the tourism activities whose subject is geological assets. All of the periodic outdoor activities and nature promotion activities organized in accordance with scientific, social and economic purposes are included in this wide group.

Geological Heritage: It is the geosite that has significant scientific or visual value which is threatened by natural or man - made extinction (Jemirko).

Georoof (Roof List): It is the type of grouping or listing for geosite or geological heritage separately, according to a specific feature (Jemirko).

Geoinventory: It is the total representation of geosite or geological heritage without any discrimination (Jemirko).

Geoprotection: It is a social concept related to the protection of natural resources of the Earth (Henriques et al., 2011). Beyond this general definition, the aforementioned conservation concept focuses especially on the protection of geosites that have; 1) high scientific value, 2) educational value and 3) touristic and cultural values. It is evaluated under three headings as; 1) Basic Geoprotection, 2) Applied Geoprotection and 3) Technical applications in geoprotection.

Georoute: It is a travel route that passes through locations that carries the value of being a geosite on any piece of land or in a geopark and serves a specific scientific / educational / touristic purpose, and whose starting and ending points are determined.

Jeotravers: Georoute arranged according to a geological cross section that clearly reflects a certain period of the Earth's formation.

Geotravel: It is an educational / touristic "nature walk" aiming to introduce any geological feature of the world. This trekking can be in the form of normal trekking and can also be carried out by tour skiing, bicycle, canoe, paragliding etc.

Cultural Heritage: All kinds of archaeological and ethnographic values created by human.

Natural Heritage: Any kind of geological formation that is not declared as "Geological Heritage" or defined and classified as "geosite" in all aspects, but located in and around a geopark and expresses a value in itself. It is a social definition rather than a scientific one. Areas such as lakes, waterfalls, cliffs, fault mirrors, wetlands / reeds, caves, private living / breeding areas are within this scope. Such areas can be registered as geosite or geological heritage through scientific studies to be conducted.

2. Geographical Location of the Proposed Geopark Area

Nemrut - Süphan proposed geopark area is located in the province of Bitlis, in east of Turkey. The geopark area, which covers a total area of 5300 km^2, consists of Tatvan, Ahlat, Adilcevaz, Güroymak, Mutki and Hizan districts. The study area has been surrounded by Lake Van in the east and high mountainous areas in the west. Süphan Mountain (4.058 m), Nemrut Mountain (2.916 m), Kirkor Mountain (2.428 m) Kırmızıtaş Hill (2.607 m) and Yıldız Mountains (3.002 m) are important heights of the geopark. Bitlis river, Kocaçay and Karasu river are among the important rivers. There are two airports for transportation to Nemrut - Süphan proposed geopark. One of them is the Muş Airport, which is 93 kilometers away from the Nemrut Kaldera, the geopark center, and the other is the Ferit Melen (Van) Airport, which is 154 kilometers away from the Nemrut Kaldera. The Lake Van, which is a soda lake that covers more than half of the geopark border, has an area of 2.755 km^2 and a max. depth of 490 m. It is also possible to reach the geopark by a nostalgic train journey with the Van Lake Express, which travels between İstanbul and Van. This train boards on the ferry in Tatvan, passes the Lake and reaches Van. In addition, daily shuttle bus services to the area of the geopark are held all over Turkey. Access to all geosites located on the determined georoutes is very easy.

3. Geology and Geological Evolution of the Proposed Geopark Area and its Vicinity

The southern part of the proposed geopark area consists of old metamorphic rocks belonging probably to Pan - African basement and overlying autochthonous rocks, which are defined as the "Bitlis Massif" in the literature and located on the collision zone of the Laurasia and Gondwana continents. This region has attracted attention for various reasons, but mostly because it remains on the Bitlis - Zağros Suture Zone, in the continent - continent collision zone mentioned above, and the old rocks of the massif have been the subject of many scientific studies. Some of these pioneering studies are referred to as Arni (1940), Tolun (1953; 1960), Kranck (1954; 1957), Altınlı (1963; 1966*a*, 1966*b*), Ketin (1966). With the spread of the concept of plate tectonics, especially the studies aimed at understanding the tectonic evolution of the region have come to the fore, some of them are; Dewey (1973), Boray (1973), Özkaya (1974; 1975; 1978*a, b;* 1982*a, b, c*). In Turkey, the hydrocarbon and mineral explorations in Anatolia have been condensed in 60's and 70's especially in SE Anatolia. The stratigraphical and tectonic studies carried out within this context that come to mind first are Kellog (1960), Ibbotson (1969), Sungurlu (1974), Açıkbaş and Baştuğ (1975), Yılmaz (1978), Açıkbaş (1979), Perinçek (1980) and Helvacı (1983a). Yılmaz (1971), Baştuğ (1976), Yılmaz et al. (1981), Tolluoğlu and Erkan (1982), Göncüoğlu and Turhan (1983a, b), Helvacı (1983b), Yazgan (1983) and Yazgan and Chessex (1991). can be given as examples to comprehensive and regional geology, magmatism / metamorphism studies. Especially after the 2000s, the scientific studies focused on volcanism and tectonic evolution in the region has gained importance. Among them, Elmas and Yılmaz (2003), Keskin (2003; 2007), Yılmaz (2005), Karaoğlu et al. (2005), Özdemir et al. (2006), Lebedev et al. (2010), Özdemir (2011), Oberhansli et al. (2011), Özdemir et al. (2011), Keskin et al. (2012), Özdemir and Güleç

(2014), Schmincke et al. (2014), Hisarlı et al. (2015), Özdemir et al. (2016) and Karaoğlu and Kılıç (2017) have very comprehensive studies. Very detailed geological maps with a scale of 1 / 100.000 in the region have been systematically prepared by MTA for many years. The exploratory studies, which are at the closest disclosure to the regions worked within the scope of this publication, were carried out by Akay et al. (1988), Göncüoğlu and Turhan (1992) and Çağlayan and Şengün (2002). In this study, the last study mentioned in the definition of the tectonostratigraphic relations of the core and cover rocks of the Bitlis Massif has been accepted as the basis.

The age of metamorphism of amphibolite, biotitic gneiss, muscovitic gneiss and mica schists defined as "Yolcular Group" in the core of the massif is 570 million years (Yılmaz et al., 1971; Helvacı and Griffin, 1983). These rocks were cut by Cadomian metagranites (540 my) (Ustaömer et al., 2009). These metamorphic core rocks are covered transgressively by metaclastic rocks belonging to Paleozoic Bitlis Group and the rocks belonging to carbonate rocks assemblage intercalating with volcanics of Permo - Mesozoic Çadırdağı group (Çağlayan and Şengün, 2002). The Bitlis Group consists of brown, greenish brown, dirty white quartzite, quartz schist, mica schist, phyllite and slate assemblages occassionally with marble interlayers (Şengün, 1984; Şengün et al., 1991). The carbonate rock assemblage with volcanic intercalations that transgressively come in northward direction and cover the Yolcular Group, which consist of the core rocks and Bitlis Group metaclastics, were distinguished as the Çadırdağ Group by Boray (1973). This group from bottom to top consists of possibly Permian Gelintaş formation, Nallıkaya formation formed by coarse foliated metabasite, Upper Permian Kerzevil formation, Lower - Middle (?) Triassic Benekli formation, Upper Triassic (?) - Jurassic - Lower Cretaceous Bacavan formation that has the characteristics of comprehensive series, Lahtandere formation alternating with limestone and volcanite, Sit formation with pillow lava structure and Campanian Tilkikaya formation (Çağlayan and Şengün, 2002).

All these metamorphic series were overlain by samples of which are commonly found in southern sections of Mutki county in south that represent the closure of the ocean in Upper Cretaceous (Late Campanian - Early Maastrichtian) (southern branch of Neotethys) and by ultrabasic and epi - ophiolitic successions which are widely found between Ahlat and Adilcevaz districts in the north. The regional compressional regime that had started in the Upper Cretaceous has continued until today and still continues (Elmas and Yılmaz, 2003). The current trace of the ocean, which started to close in the Upper Cretaceous, is called the "Bitlis - Zağros Suture Zone", and this zone starts roughly from east of Adana Province and leaves our country from east of Hakkari drawing a convex arc. Then it reaches the SE Iran and traced until the northern end of the Gulf of Oman (Figure 2). Continent - continent collision has started along the Bitlis Suture Belt since the Middle Miocene. The collision caused the rise of the East Anatolian region continuously, which still continues today. This region, which is 220 km long and 1.600 - 2.000 m high, is called the "Eastern Anatolian High Plateau" (Figure 3). Due to the tectonic regime that developed after the collision, it is known that the volcanic material emerged from the N - S oriented opening cracks in the Eastern Anatolia and formed recent volcanic rocks (Yılmaz et al., 1987). These volcanic centers in the Eastern Anatolia are mainly Nemrut (2.916 m), Süphan (4.058 m), Tendürek (3.584 m) and Ağrı Mountains (5.137 m) (Figure 4).

The Nemrut and Süphan stratovolcanoes, from mentioned volcanic centers above, remain within the proposed geopark area (Özdemir et al., 2006). In the north of Nemrut Volcano, which is considered active in the volcanic literature, the lava outflow occurred in AD 1443 from the crack opened in the area known today as Kantaşı (Figure 4) (Karaoğlu et al., 2005). The traces of this outflow are clearly seen when the parasite cone is climbed where this volcanic exit begins. In addition, hot water and steam outlets continue in and around the caldera today. The characteristic lava and eruption products emitted by these volcanic centers were found on the georoutes and proposed as geosites.

Carbonate rocks, which remain in the proposed geopark area, is the Adilcevaz Limestone rich in carbonate rocks and characteristic life forms. This sequence, which widely outcrops in the western and northern areas of Adilcevaz district (Figure 1), is an occassionally massive bedded carbonate sequence deposited in a shallow marine environment and contains bioherm / biostrome packs and contains abundant coral fossils (Yeşilova and Yakupoğlu, 2007).

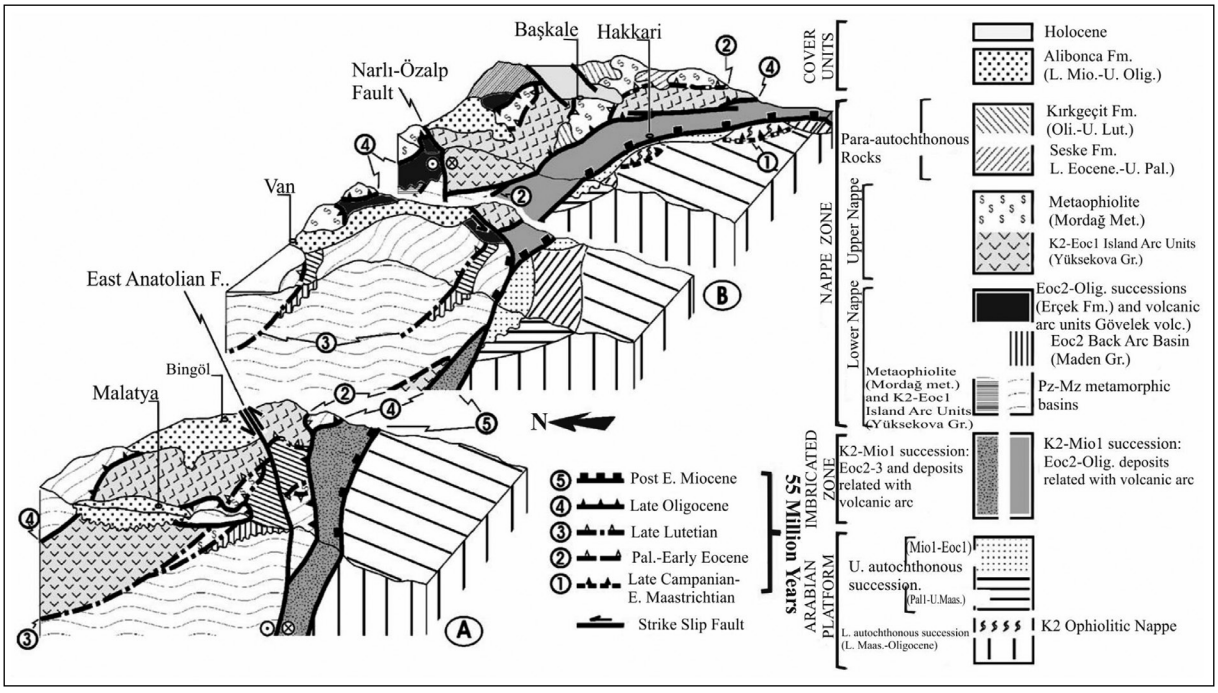

Figure 2- Schematic section showing the regional geotectonic environments, their products and general structural elements (modified from Elmas and Yılmaz, 2003).

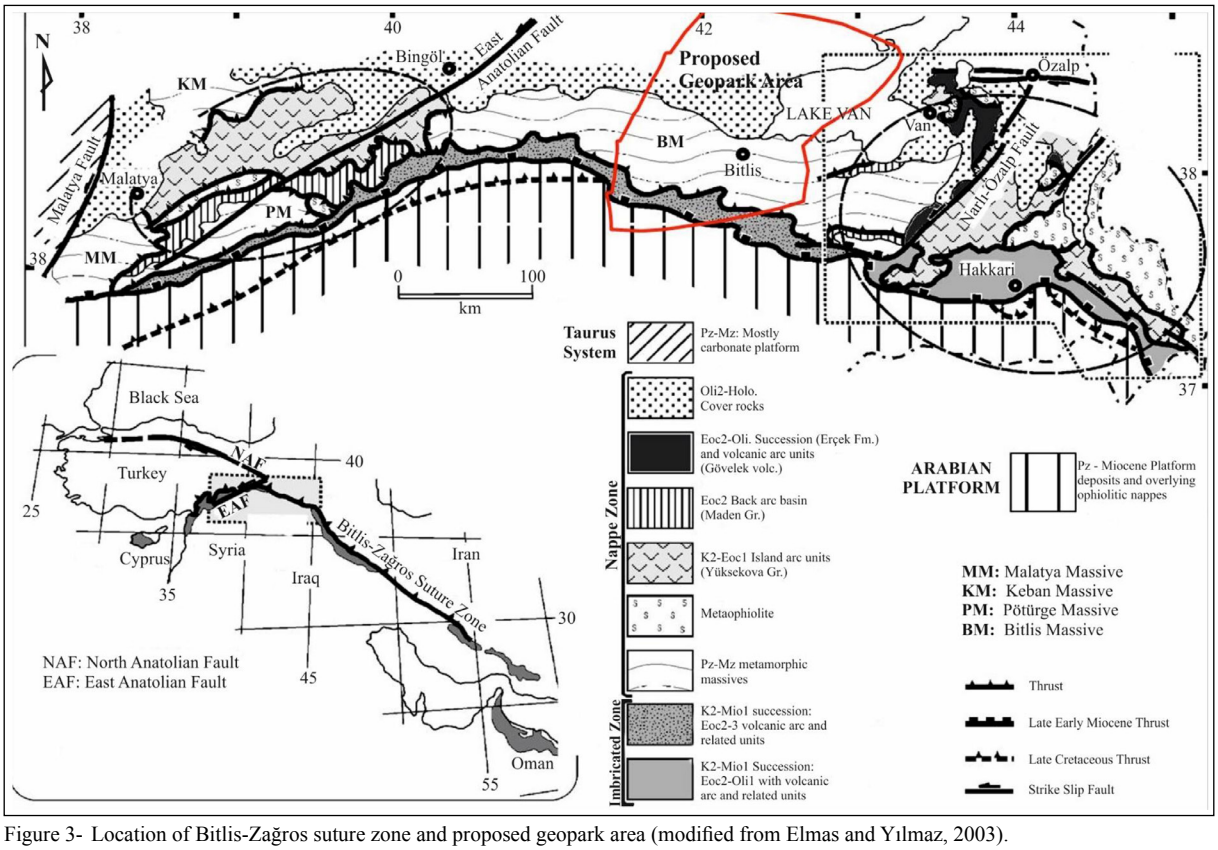

Figure 3- Location of Bitlis-Zağros suture zone and proposed geopark area (modified from Elmas and Yılmaz, 2003).

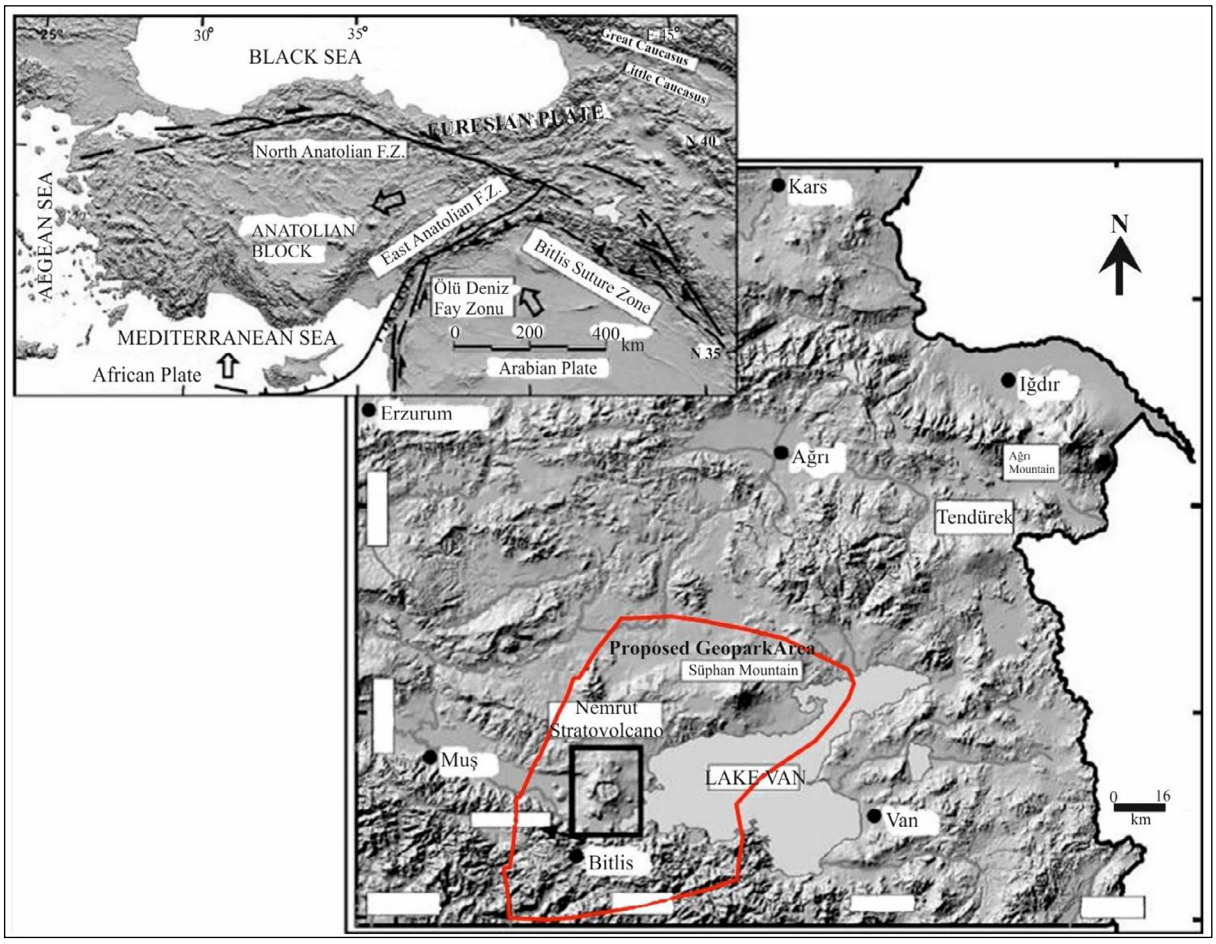

Figure 4- Regional tectonic location of Nemrut and Süphan Stratovolcanoes, their surroundings and the proposed geopark area (modified from Özdemir et al., 2006).

The proposed geopark area is in the region of an ocean called the Neotethys that existed here 200 million years ago. Neotethys Ocean was squeezed and disappeared between the Arabian Plate moving northward and the relatively stable Eurasian Plate. One part of this oceanic crust was disappeared by subducting into the mantle, and some crust fragments were settled on the continental crust in both directions by thrusting and met the continent to continent collision. The hypothetical model of this geological evolution was shown by Oberhansli et al. (2011) in Figure 5. In addition, the hypothetical model about the geological evolution of the region prepared by Keskin (2007; 2012), who carried out detailed studies on volcanism in the region, is given in Figure 6.

4. Geopark Inventory Studies

Before starting the Nemrut - Süphan inventory of geosites in the geopark, the purpose of this study has been clearly demonstrated in terms of topic, scope / value, scale and use. Considering the attitudes in studies of Lima et al. (2010), the geosites determined in this field have been defined and determined for use in the Nemrut - Süphan geopark project, some of which have scientific value and some have aesthetic value. According to this:

Subject: Formations that have the characteristics of Geosite in Nemrut - Süphan Geopark

Scope / Value: Geosites remaining in the specified area have features that can be used for both scientific/ educational and touristic purposes. Some of the determined geosites are unique geological structures representing a very characteristic period in the formation process of the earth's crust and they have the potential to be registered as a "geological heritage" in this respect. Some of these have features that can serve educational and touristic purposes more.

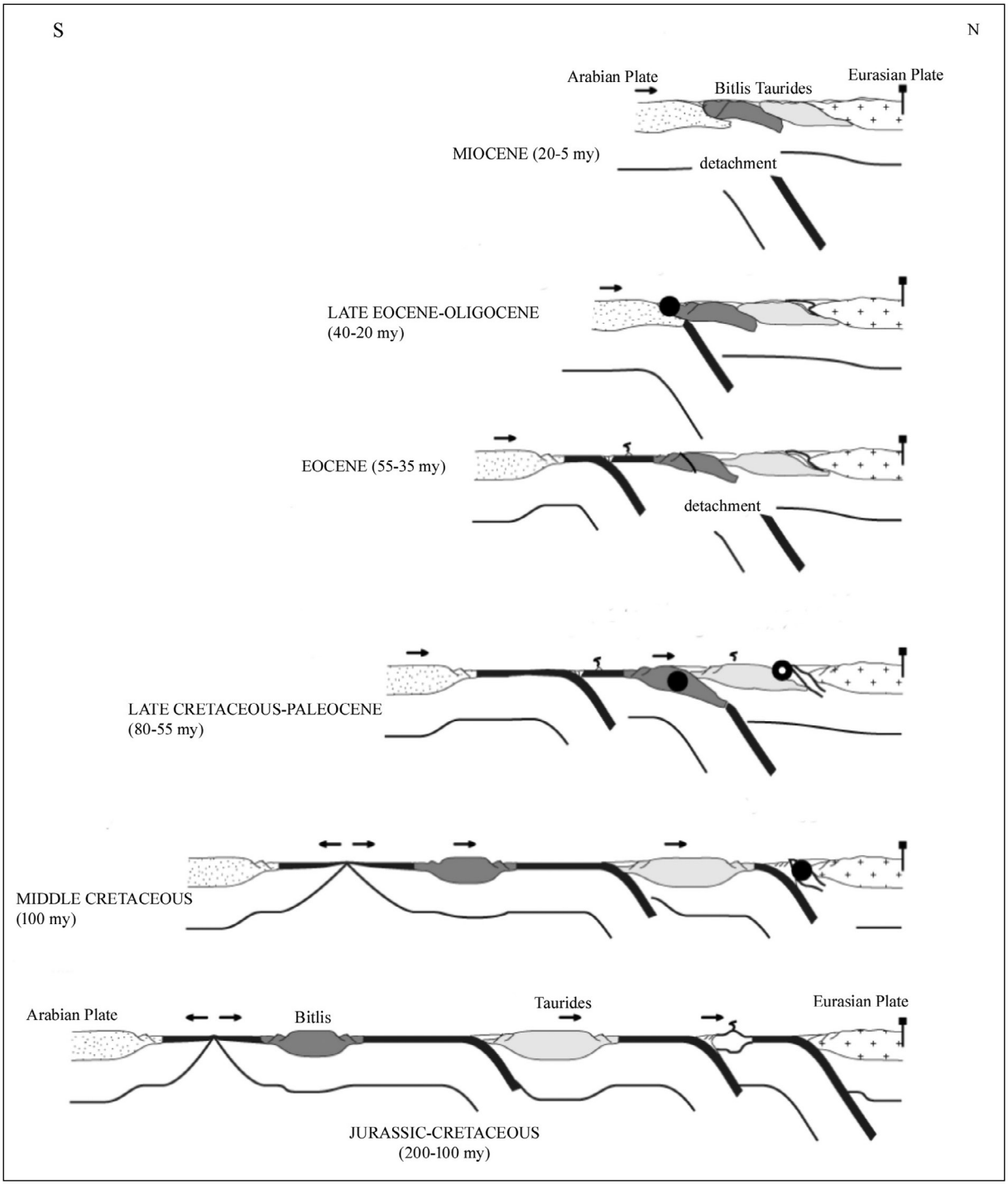

Figure 5- Jurassic-Miocene geological evolution of the SE Anatolia (modified from Oberhansli et al., 2011).

Scale: The boundaries of the inventory study area are shown in Figure 1. Besides, Nemrut and Süphan volcanoes, which are the two largest stratovolcanoes of Turkey, are located in an area of approximately 5300 km^2 within the boundaries of Bitlis Province, in Güroymak, Tatvan, Adilcevaz and Ahlat districts and in the geopark area constituting the western part of the Lake Van in addition to Bitlis city center.

Purpose of Use: The primary purpose of the inventory studies is to serve the geotourism activities to be carried out within the scope of the geopark to be

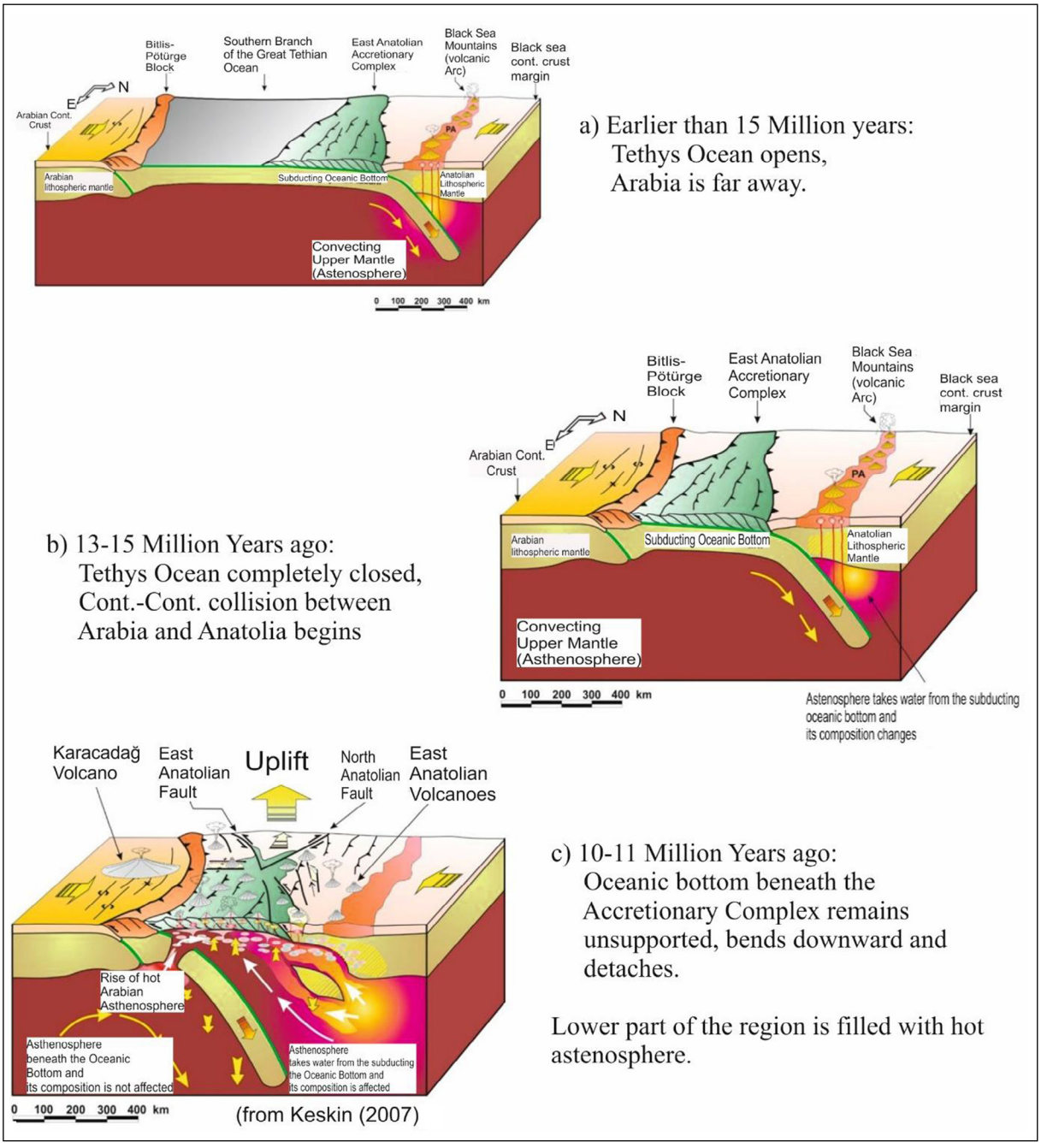

Figure 6- Geological evolution of the SE Anatolia Region in Miocene: Earlier than 15 Million Years: Lower Miocene; 13-15 Million Years: Middle Miocene; 10-11 Million Years: Upper Miocene (from Keskin, 2012).

defined in the area described above. In addition, some geosites have a special importance with their "high scientific value". Therefore, it has been suggested that they should be evaluated for this purpose. In addition, the determined geosites are also a potential geological heritage element and they are also an application object for geoconservation strategies to be established in this context.

Geosites in this context were evaluated under the provisions of the "Regulation on Procedures and Principles Regarding the Determination, Registration and Approval of Protected Areas" published in the Official Newspaper No.28358 in 19.07.2012 with the article 13/A of Decree Law (KHK) number 644 and the Law number 2863. Thus, the process of registering these geosites as elements of "geological heritage"

will be initiated. In the defined geopark area, the proposals were developed for the "geo - conservation" strategies necessary for the "geological heritage" value formations identified among the geological assets that have witnessed the evolution of the earth's crust for the last 550 million years, to participate in sustainable development processes.

4.1. Method

For the display format of geosites considered within the scope of this study, the standard display recommendations in Çiftçi and Güngör (2016) were adopted. For the geosite classes, a combined chart containing the classification codes proposed in the same publication and determined by Pro Geo (1998) was applied (Çiftçi and Güngör, 2016; Table 1). In this display proposal, it was aimed at defining the main geographical location for geosites, definition of geosite, geological heritage features, physical environment - security - logistics, protection / conservation features, geosite inventory features, appearance at the time of preparation of the inventory and all kinds of scientific and visual features (if any) under representational sections in the geopark museum (Figure 7). As a matter of fact, Kazancı et al. (2015) and Brilha (2016) suggested a similar casting form. However, the forms suggested in this study will be meaningful and useful documents when they are turned into a catalog, independent of the report. The mentioned form was reconstituted and developed according to the regulations in Turkey (Figure 7).

4.2. Georoute Studies

The proposed geopark area is very large and has an extremely wide geodiversity. This wide areal spread was presented to the service of the geopark with georoutes created in different concepts (Figure 1). A sufficient number of geosites were identified on each georoute, as far as possible, in accordance with the "**accessibility**" and "**protection**" criteria. Some of these geosites are also among the geological heritage items in the region. However, the main criterion has been the determination of geosites, which are easily accessible for visitors at all ages, whose visual features are in the foreground and can also be used for educational purposes, in accordance with the purpose of the geopark management. In this study, a total of 44 geosites were determined and their list is given in Table 1.

In the area defined on Figure 1, firstly; five (5) georoutes have been defined and care has been taken to keep the geosites that will represent the regional geology on these routes. Likewise, taking into account some geosite locations that are important in terms of "**scientific value**", the routes of these georoutes were determined. The georoutes defined on Figure 1 were arranged in a way that allows visitors to visit the geopark to make a "time travel" from past to present in the context of geological history. While doing this, the care was taken to find logistical facilities on each georoute considering the advantage of the transportation infrastructure as much as possible. The 5 georoutes determined in this study, were introduced separately together with the geosites on and/or around them, below.

Georoute - 1: Georoute - 1, marked as "Bitlis - Mutki - Bitlis" on Figure 1, were determined in a way that it would represent ultrabasic and basic rocks belonging to the ophiolitic sequences that were deposited on these basement rocks during the closure of Neotethys, together with the core and cover rocks of the Bitlis Massif. There are also flow products of quaternary volcanism in the Baykan Valley and the travertine formations left by the geothermal waters that exit along the faults controlling this valley on this route. However, since the general context of this route is the "**Journey from Precambrian to Present**", the geosite location was not determined among the young formations on the route. The geosites belonging to these young formations were determined on the Georoute - 2.

Georoute - 2: Georoute - 2, marked as "Bitlis - Tatvan - Pz" on Figure 1, together with the core and cover rocks of the Bitlis Massif, was determined in a way that it would traverse unconformably overlying these basement rocks, the travertine deposits developed in Quaternary and the volcanic products of the Nemrut Volcanism. It was determined to traverse volcanic products. Representative ones belonging to geosites on Georoute 1 and 2, whose features are given in Table 1, are shown in Figure 8.

Georoute - 3: Georoute - 3, marked as "Tatvan - Nemrut - Ahlat" on Figure 1, was created to introduce each stage of the formation of the Nemrut Stratovolcano. Each of the geosites given in Table 1 represents one stage in the formation of the Nemrut Stratovolcano. These locations to be carefully

NATURAL HERITAGE TYPE: GEOLOGICAL HERITAGE (GEOSITE)

GEOGRAPHIC LOCATION				GEOSITE DEFINITION	
X:		Y:	Z:	GEOSITE NAME	
COORDINATE SYSTEM: PROJECTION (REF): ZONE: 1:25000 SHEET NO:				GEOSITE CLASS GEOSITE CODE: GEOSITE SCORE	(Based on Pro Geo (1998)
PROVINCE	DISTRICT	VILLAGE		DIMENSIONS:	
				GEOLOGIC NAME: GROUP: FM: MBR.	
LOCALITY				GEOLOGICAL AGE	
DESCRIPTION of TRANSPORTATION:				LITHOLOGY	

FEATURES of GEOLOGICAL HERITAGE	PHYSICAL ENV., SECURITY, LOGISTICS	
DESCRIPTION	DIST. to MUSEUM	
	ROUTE NAME, NO:	
SCIENTIFIC VALUE and LIKE WISE FORMATIONS	CLOSEST WATER SOURCE	
	CLOSEST LOGISTIC STATION	
BEST OBSERVATION/SIGHT SEEING POINT	RISKS of NATURAL DISASTER	
RECOMMENDED MATERIALS for INVESTIGATION/OBSERVATION	**EMERGENCY CALL:**	

GEOSITE CLASSIFICATION (Gen. Dir. for Protection of Natural Assets)

Chart 20.1					Chart 20.2			
Natural Aesthetics	Infrequency	Sensitivity	Scienticity	Ave. Score	Regional Importance	National Importance	International Importance	Importance Score

TOTAL SCORE (Charts 20.1and 20.2)

PROPOSAL for PROTECTION AREA

A ABSOLUTE PROTECTION AREA (>10 points)	B QUALIFIED NATURAL PROTECTION AREA (6-9 points)	C SUSTAINABLE PROTECTION and CONTROLLED USE AREA (3-5 points)

GEOSITE INV. NO of TURKEY TR-00/0000	
FEATURES of GEOSITE INVENTORY	
GEOPARK NAME	
PREPARED BY	
DATE of PREPERATION	
SUGGESTED AS GEOSITE BY:	
RELATED ARTICLES	
ADDRESS for ADDITIONAL INFO	

ITS VIEW in INVENTORY HISTORY	ITS LOCALITY in the GEOPARK/GEOROUTE

Figure 7- Geosite Inventory Form (Çiftçi and Güngör, 2016).

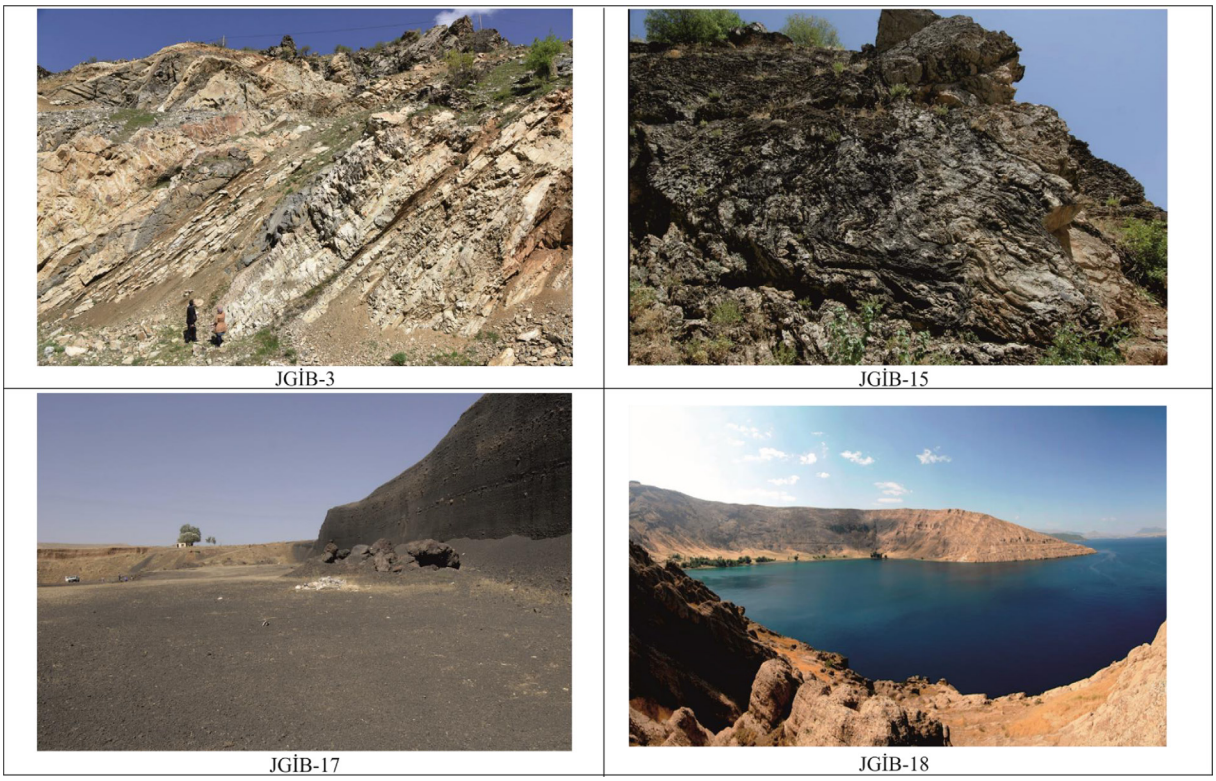

Figure 8- Some geosites on Georoute-1 and Georoute-2.

preserved and to introduce them to visitors in a predetermined order will make it easier to understand the geological formation of the Nemrut Stratovolcano. Representative ones belonging to these geosites whose properties are given in Table 1 are in Figure 9.

Georoute - 4: Georoute - 4, marked as "Ahlat - Adilcevaz - Süphan" on Figure 1, was created to introduce the formation of the Süphan Stratovolcano. Some geosites in this area are not located on the said georoute. However, the route in question has been determined as the safest route since it is also a climbing route to Mount Süphan. Visitors who will make investigation on this route should act with a professional mountaineer. Representative ones belonging to these geosites whose properties are given in Table 1 are on Figure 10.

Georoute - 5: The destination of the fifth georoute determined in the Nemrut - Süphan geopark and geological observation stations on this route are shown on Figure 1 with the sign "Adilcevaz - Lake Van - Tatvan". The purpose of determining this route is to exhibit the sedimentary rock presence of the Geopark and the young sedimentary formations of the region. There are young lake deposits of the Lake Van and very special "Tufa Deposits" on the route. When you come to the shore of the Lake Van, the boat journey starts towards Tatvan. The purpose of this georoute is to allow the observation of stratomatolitic biological formations, which remain on the route and develop at the bottom of the Lake Van. Diving on this route is only possible for visitors with a "high altitude diving" certificate. When viewing condition is suitable, the Tuff Cone from the Lake İncekaya will create an extremely interesting visual feast. Representative ones belonging to these geosites whose properties are given in Table 1 are on Figure 11.

The locations and routes of georoutes in the geopark are given in Figure 12.

4.3. Cultural Heritage Inventory

There is a wide range of cultural heritage elements with archaeological and ethnographic features, from obsidian workshops, which are thought to belong to the Neolithic period, to recent ethnographic values in the Nemrut - Süphan geopark and its immediate surroundings. The carved shelters that enabled traces of human life in Ahlat to be traced back thousands of years are intertwined with the İlhanlı - Seljuk

Table 1- Georoutes determined in Nemrut-Süphan geopark and the geosites identified on / around them, their ages and lithologies.

Geouroute	Geosite Name	Geological Age	Explanations
Georoute-1: Bitlis-Mutki-Bitlis	JGİB-1	Precambrian	Gneiss, Schist
	JGİB-2	U. Paleozoic	Metagranite
	JGİB-3	Precambrian	Schist
	JGİB-4	U. Cretaceous	Peridotite
	JGİB-5	Trias.-L. Juras.	Metavolcanite
	JGİB-6	U. Senonian	Flysch
	JGİB-7	Eocene	Continental clastic
	JGİB-8	L-M. Eocene	Volcanite/Sed. rocks
	JGİB-9	L. Permian	Limestone, marble
	JGİB-10	U. Permian	Limestone
	JGİB-11	Precambrian	Biotitic metagranite
Georoute -2: Bitlis-Tatvan-Pz	JGİB-12	Quaternary	Basalt, ignimbrite
	JGİB-13	Paleozoic	Gneiss, Schist
	JGİB-14	Precambrian	Metagranite
	JGİB-15	Paleozoic	Amphibolite
	JGİB-16	Quaternary	Travertine
	JGİB-17	Quaternary	Scorian deposits
	JGİB-18	Quaternary	İncekaya tuff cone
Georoute -3: Tatvan-Nemrut-Ahlat	JİGN-1	Quaternary	Nemrut Camels
	JİGN-2	Quaternary	Pyroclastic debris
	JİGN-3	Quaternary	Rhyolitic lava flow
	JİGN-4	Quaternary	Nemrut Caldera
	JİGN-5	Quaternary	Post-caldera freatom. deposits
	JİGN-6	Quaternary	Post-caldera rhyolitic lava
	JİGN-7	Quaternary	Maar crater
	JİGN-8	Quaternary	Steam pipe
	JİGN-9	Quaternary	Ilığ Lake
	JİGN-10	Quaternary	Nemrut Crater Lake
	JİGN-11	Quaternary	Kantaşı (Bloodstone)
	JİGN-12	Quaternary	Nemrut Opening Crack-1
	JİGN-13	Quaternary	Nemrut Opening Crack-2
Georoute -4: Ahlat-Adilcevaz-Süphan	JGİS-1	Quaternary	Baking Zone
	JGİS-2	Quaternary	Rhyolitic Obsidian
	JGİS-3	Quaternary	Aygır Maar
	JGİS-4	Quaternary	Blocky Ash Flow
	JGİS-5	Quaternary	Dacitic Dome
	JGİS-6	Quaternary	Süphan crater
	JGİS-7	Quaternary	Trachytic lava
Georoute -5: Adilcevaz- Van Lake-Tatvan	JGİA-1	Quaternary	Recent Lake Dep.
	JGİA-2	L. Miocene	Fossil cemetery
	JGİA-3	U. Cretaceous	Peridotite
	JGİA-4	Quaternary	Tufa deposits
	JGİA-5	Quaternary	Travertine channel
	JGİA-6	Quaternary	Microbialitic formations
	Stromatolite and microbialitic occurrences at the bottom of the Lake Van. These represent the oxygen-producing cyanobacteria activities that formed the first atmosphere in the early phase of life on Earth. Guided diving can be done with high altitude diving certificate and equipment.		

JGİN-1

JGİN-5

JGİN-10

JGİN-11

Figure 9- Some geosites on Georoute-3.

JGİS-1

JGİS-2

JGİS-3

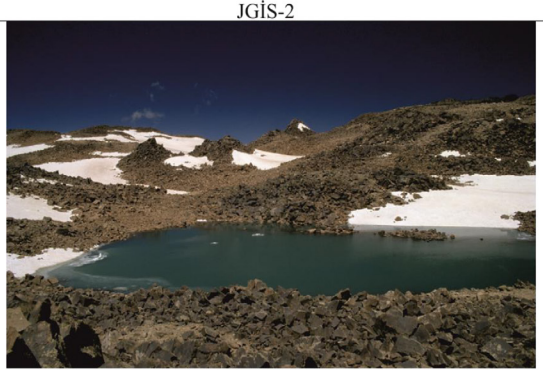

JGİS-6

Figure 10- Some geosites on Georoute-4.

Figure 11- Some geosites on Georoute-5.

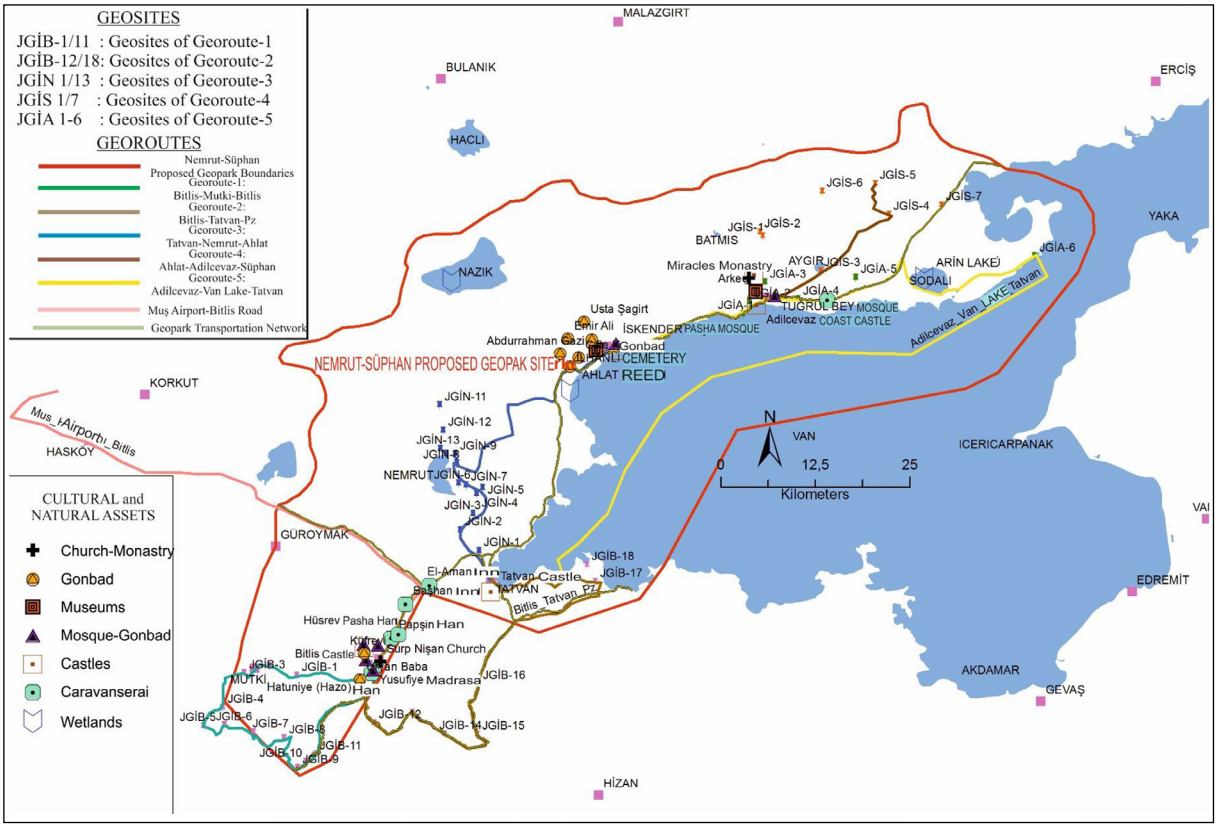

Figure 12- Proposed Nemrut-Süphan geopark routes, natural and cultural assets (the geosite numbers also indicate the order of visits).

cemetery (Figure 12). It is understood that the region is a center of attraction due to the shelter / feeding opportunities it offers to Paleolithic and Neolithic people. Its proximity to the Mesopotamian region and the richness of natural resources (obsidian, metallic mineral) also fed the Urartian civilization in the later period. After the Roman - Byzantine civilizations, the Malazgirt victory in 1071, which is located in the near northern part of the geopark area, initiated the settlement and spread of the Turks in the region. In addition to structures such as; Han, Bath, Madrasa, Gonbad and Mansion the Ahlat Seljuk cemetery, the Seljuk Gonbads, which fascinates people with their unique stone workmanship and is included in the UNESCO World Cultural Heritage Temporary list form the most important elements of the cultural heritage of the geopark area. The cultural heritage elements in the region, which is very rich in terms of cuisine culture and handicrafts, are given in Table 2. Representatives of these cultural heritage elements whose characteristics are given in Table 2 are given in Figure 13.

Many plants that are consumed starting from the spring and grow in nature are among the important nutritional habits of the region. Çiriş plant (gullik), cağ, uşkın, various mushroom and kenger species are among the important natural food resources of the region, which date back thousands of years. Representatives of these ethnographic elements whose features are given in Table 2 are given in Figure 14.

4.4. Natural Life

Lakes, lake shores and especially the delta areas where fresh waters meet lakes are the most important wetlands in the basin (Adızel et al., 1995). Many plant and animal species live in different habitats from the plains on the basin bottom to the peaks of high mountains. In addition to sweet, salty, bitter and sparkling habitats, the endemic species specific to the basin have been formed as a result of the influence of many environmental factors such as altitude and climate (Çetinkaya, 1999; Çetinkaya et al., 1995). The natural assets and biodiversity elements other than the geosites in the Geopark area are given in Table 3. The necessary information about these natural assets has been compiled and is excluded from the content of this article. However, these natural assets have been effective in determining the georoutes.

4.5. Outdoor Sports

In the Nemrut - Süphan proposed geopark, there are eight trekking (DY - 1/8), four bicycles (B - 1/4), four tour skis (TK - 1/4), three canoes (K - 1/3) and two climbing routes were determined and shown on the geopark map.

The general characteristics of all routes and the associated geosites are given in Table 4.

5. Geopark Workshop and Trainings

Two geopark workshops were held during the study period. These workshops were implemented by creating common ideas. In addition, three "Geopark Training Studies" were conducted. Educational activities were carried out separately at Primary, High School and University levels and field trips were organized. In these studies, very warm feedback was received from the students.

6. Results

Nemrut - Süphan proposed geopark is an internationally qualified geopark candidate with its unique geological, biological and cultural heritage elements. Table 5 was created by evaluating the geosites determined in the geoprak area in accordance with the criteria of the General Directorate for Protection of Natural Assets. When this table is analyzed, 18 of the 44 (+1) proposed geosites "Definitely Protected Areas" (A); 18 of them "Qualified Natural Protection Areas" (B) and 9 of them have been proposed to be declared as “Sustainable Protection and Controlled Use Areas” (C).

All other geopark values, especially the geosite locations, are defined in easily accessible, promoted and protected locations. Thus, it is ensured that the geopark is more suitable for sustainable management conditions. Of course, the more detailed studies can be carried out for the proposed geosite areas in the geopark area or the formations that have the characteristics of "geoheritage" from geological assets in other locations, and even these can be added to the natural assets of the geopark during the operation process, the geodiversity can be enriched and the UNESCO criteria of the geopark can be developed.

Table 2- Elements of Cultural Heritage of the Nemrut-Süphan Geopark.

Cultural Heritage		NAME	PERIOD	EXPLANATION
CULTURAL HERITAGE (ARCHEOLOGY)	ARCHEOLOGICAL MUSEUMS	**Ahlat Archeological Museum**	**Urartian, Roman, Byzantian, Seljuk, Ottoman**	It is adjacent to the historical Seljuk Cemetery, which is established on an area of approximately 200 decares in Ahlat.
		Adilcevaz Archeological Exhibition Area	**Urartu**	It is a small exhibition area where the findings from the Kef Castle excavations are displayed behind the Adilcevaz Bus Terminal.
	TOMBS	**Küfrevi Tomb (Bitlis)**		The tomb, which was built in 1898 in a completely different style from the Bitlis architectural structure, is a visiting place in the garden of Küfrevi Mansion.
		Emir Bayındır Tomb (Ahlat)		It is located in Taht-ı Süleyman district. The name of Melik Bayındır İbn-i Rüstem Bey, who died in 886 in Hijri, is written in the inscription that surrounds the gonbad all around.
		Çifte Tomb (Ahlat)		Two gonbads are next to each other. The big gonbad belongs to Bugatay Aka and Şirin Hatun (Lady) from Akkoyunlu, and the small gonbad belongs to Esen Tekin Hatun. It is written in the inscriptions on the south and west sides that the tomb was built in 1280.
		Emir Ali Tomb (Ahlat)		This gonbad is located on the (Harabe Şehir) ruined city road. Since its inscription was broken during the Russian war, the exact date of its construction is not known. Based on its architectural features, it is thought to belong to the 14th century.
		Usta Şagirt Tomb (Ahlat)		It is located in the south of Meydanlık cemetery, very close to the Lake Van. It is called "Ulu Kumbet (Gonbad)" because it is the biggest gonbad of Ahlat.
		Şeyh Babo (Üryan Baba) Tomb (Bitlis)		There is no inscription of the tomb located on a hill in İnönü district. However, the date 1834 is written on the tombstone inside.
		Abdurrahman Gazi Tomb (Ahlat)		This person is from Sahabe-i Kiram and he was under the command of Al-Jazeera Commander Iyaz Bin Ganem, who was assigned to conquer the region in 641 during the time of Hazrat Omar and was martyred here during the conquest of Ahlat.
		Ahlat İlhanlı Cemetery		In the cemetery, apart from the cist graves with and without witnesses, each of which has a monumental structure, there are also chamber-style underground tombs, which are the Central Asian Turkish Tomb types.
	CASTLES	**Bitlis Castles (Bitlis)**		Bitlis Castle, located on the steep slope of the bazaar in the city center, was built in 312 by one of their commanders, Leys Bedlis, on the order of Alexander the Great.
		Tatvan Castles (Tatvan)		It was built by Zal Pasha, one of the viziers of Suleiman the Magnificent, in the Tuğ quarter of Tatvan.
		Ahlat Coast Castles (Ahlat)		The castle, which belongs to the Urartu period, was destroyed in 1224 as a result of a severe earthquake. It was rebuilt by Suleiman Magnificent in 1556.
		Adilcevaz Coast Castles (Adilcevaz)		It is an Ottoman period castle built on steep rocks on the shore of the Lake Van.
		Kef Castles (Adilcevaz)		Kef Castle, which is located at 6 km from Adilcevaz on a hill to the north of it and estimated to be Arzaşkun City, is a settlement where the Urartians lived.
	MOSQUES and GONBADS	**Ulu Mosque (Bitlis)**		The mosque located in the city center of Bitlis, was built by Ebu'l Muzaffer Muhammed in 1150 AD according to its inscription.
		Gökmeydan Mosque (Bitlis)		The dates of 1801 are recorded on the inscription and 1924 in the inscription of the minaret of the mosque in the central Gökmeydan district.
		Adilcevaz Tuğrul Bey (Zal Pasha) Mosque		It is on the Adilcevaz-Ahlat road by the lake. It was built in the 16th century.
		Ahlat İskender Pasha Mosque		It is in the old Ahlat castle. According to its inscription, it was built by Iskender Pasha, probably by the architechture Mimar Sinan, on the date of 992 (AD.1584).

Table 2- Continue[n].

CULTURAL HERITAGE (ARCHEOLOGY)	MADRASAS and BATHS (HAMMAMS)	**İhlasiye Madrasa (Bitlis)**	The madrasa located in the city center was built by the Seljuks in 1216.
		Yusufiye Madrasa (Bitlis)	This madrasa located in the central Girik Düzü locality is thought to have been built in the 17th-19th century.
		Han Palace Hammam	On the castle
		Palace Hammam	Zeydan District
		El Aman Hammam	In the El Aman Caravanserai
		Ahlat and Adilcevaz Castle Hammams	Only the remnants
	HANS and CARAVANSERAIS	**Hatuniye (Hazo) Han**	It was built in 1626-1627, according to the inscription of the Hazo Han, which is located in the south of Bitlis, near the Bitlis River, in the vicinity of Alemdar Bridge. It is said to have been built in the 11st century by Hamu Hatun, the daughter of Sultan Evhadullah Han from the Abbasids.
		Papşin (Hüsrev Pasha) Han	Located on the Bitlis-Tatvan highway. It is rumored that it was built by Beylerbeyi Hüsrev Pasha in the 16th century.
		Başhan Han	Located on the Bitlis-Tatvan highway. It is rumored that it was built by Beylerbeyi Hüsrev Pasha in the 16th century.
		El-Aman Han	El Aman Han, one of the largest caravanserais in Anatolia, constitutes a gonbad with its shops, mosque and bath. It was built by Hüsrev Pasha in the 16th century.
		Şerefiye, Arasa, Yusufiye, Duhan and Kokoz Zal Pasha Hans	
	BRIDGE, SPA	**Narlıdere (Kasrik) Bridge**	This magnificent structure located in Narlıdere Village on the Bitlis-Baykan road was approximately constructed in 16th -17th centuries.
		Ahlat Emir Bayındır Bridge	It is estimated that it was probably built in the 13th century and was repaired or renovated in the Akkoyunlu period in the 15th century.
		Güroymak (Çukur) Spa, Ilıcak (Germav) Spa, Nemrut Mountain Spa, Alemdar, Köprü Altı, Çim Çölmüğü, Arap Bridge, Yılan Dirilten, Acı Su spa and etc.	
	CHURCH, MONASTRY	**Miracles Monastry and Church**	Adilcevaz is on the opposite slope of the Kef castle.
		Surp Nişan Church	It is in the Kurubulak locality of Herzan District in the city center of Bitlis.
	HANDICRAFTS	**Weaving**	The handicrafts woven on hand looms are mainly gej (local fabric), prayer rug and saddlebag, cacım, aba and Bitlis Belt, carpet and rug.
		Harik	Local shoe
		Pottery, needle and bead lace, stonework and walking stick making	
		Stone work	These rocks, which are called as Ahlat stone and are one of the erupted breccias of Nemrut Volcano, are used as traditional building stones in the region. This material was used in most archaeological and ethnographic works in the region.
		Wood carving	Ahlat stick is the most important wood carving product unique to the region.
		Local architecture	Bitlis Houses
	CUISINE CULTURE	Local dishes cooked in the region are; Stuffed Meatballs, Şekalok Meal, Tutmanç Aşı (food), Çorti Meatballs, Büryan Kebab, Stuffed Dolma, Gari Aşı, Ayran Aşı, Glorik, Gebol, Çireş Beet, Kengerli Rice, Halim Aşı, Keşkek, Çorti Aşı, Keledoş and so on.	
	NATURAL and ENDEMIC NUTRITION SOURCES	Cağ plant, gullik (çiriş weed), kenger and ışgın plants are consumed in different ways.	

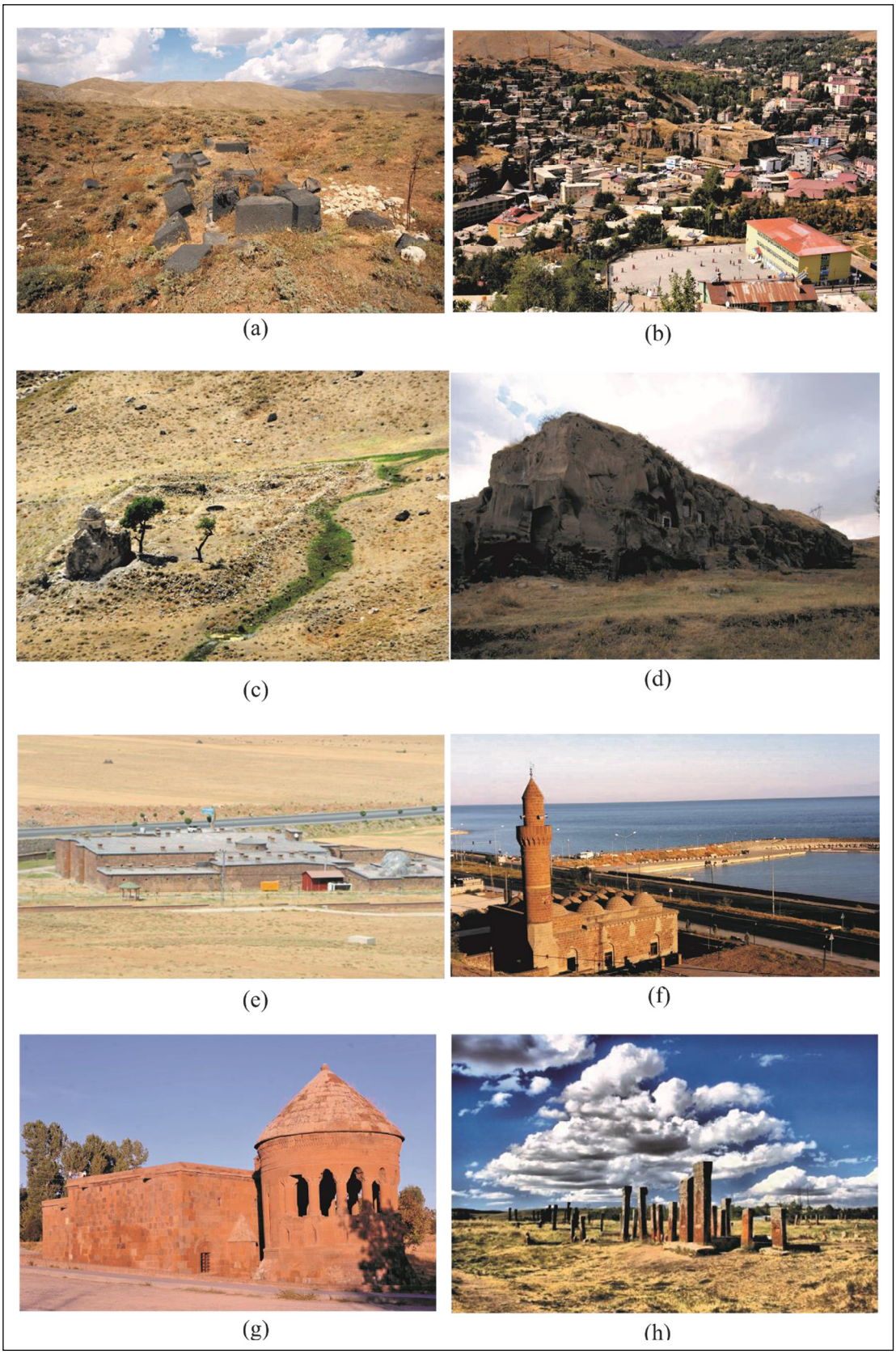

Figure 13- Some cultural heritage elements found in the Nemrut-Süphan proposed geopark: a) Kef Castle, b) Bitlis Castle, c) Miracles Monastery, d) Neolithic cave houses, e) El-Aman Han, f) Adilcevaz Zal Pasha Mosque, g) Emir Bayındır Gonbad, h) Ahlat-İlhanlı Cemetery.

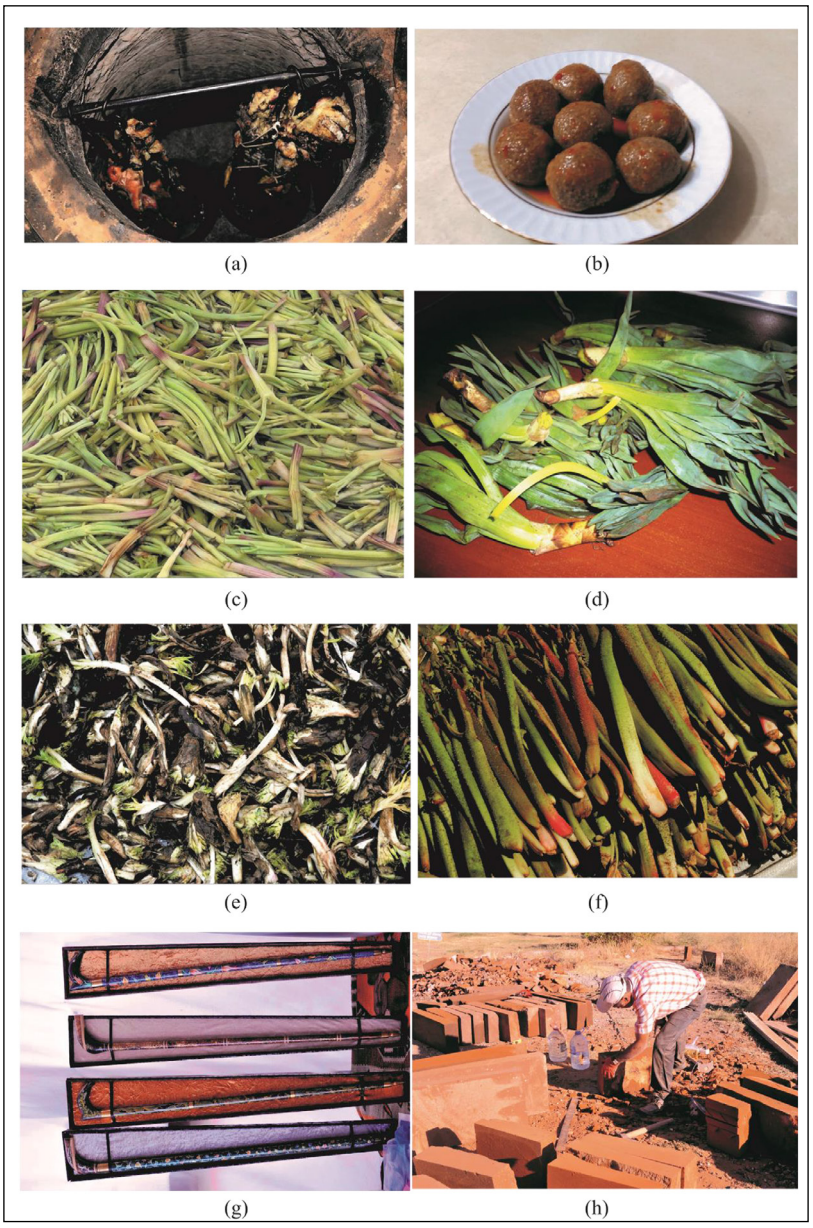

Figure 14- Some ethnographic values found in the Nemrut-Süphan proposed geopark: a) Büryan Kebab, b) Bitlis Meatball, c) Cağ plant, d) Gulik (green grass) plant, e) Kenger plant, f) Uçkun plant, g) Ahlat stick, h) Ahlat Stone (ignimbrite).

Table 3- Other natural heritage elements / natural assets, protected areas, biodiversity elements in the Nemrut-Süphan geopark area and its surroundings.

Natural Assets	Lake Van (with soda)	Lake Van is a soda lake with an average water surface of 1,646 m^2, the southern coast deepening rapidly and the deepest point of which is approximately 460 m, spreading over an area of approximately 390,000 ha.
	Arin Lake (with soda)	It is one of the most important points in terms of bird presence in the basin. It is classified as class B wetland in the literature.
	Nazik Lake	As a result of the drastic decrease in the water level in recent years, the reeds on the coasts have been significantly damaged. Fishing is done in the lake.
	Nemrut Crater Lake	It is the highest altitude volcanic wetland in the basin. It is located in the crater pit of Mount Nemrut. It consists of two lakes, one hot and the other cold.
	Aygır Maar Lake	Aygır Maar has a circular crater about 1.5 km in diameter on the SE slope of Süphan Volcano (Figure 1). Maar products have reached a distance of approximately 2.5 km from the crater.
	Ahlat Reed	Ahlat Reed is a very rich natural asset with its 101 bird species.

Table 4- Outdoor sport routes in the Nemrut-Süphan Geopark: T: Trekking; B: Bicycle; C: Canoe; TS: Tour Skiing routes.

ROUTE NAME	START-END POINTS	GEOSITES on ROUTES	LENGTH (m)
Kışkılı Climbing Route	Adilcevaz-Kışkılı Locality-Süphan Summit	JGİS-6	9,2
Harmantepe Climbing Route	Adilcevaz-Harmantepe Village-Süphan Summit	JGİS-6	10,5
T-1	Tatvan-İncekaya Village -Bamya Hill	JGİB-18	3,4
T -2	Tatvan-İncekaya Village -Deşte Hill	JGİB-18	4
T -3	Tatvan-Çataltaş Village -Deşte Hill	JGİB-17, 18	3
T -4	Nemrut Caldera-Around the Hill	JGİN-4, 5, 13	20
T -5	Nemrut-Derinbayır Village – Kantaşı	JGİN-11, 12	19
T -6	Aygır Maar Lake Surround	JGİS-3	5,6
T -7	Kirkor Dome	-	10
T -8	Adilcevaz-Kef Castle	JGİA-3	10
B-1	Between Tatvan-İncekaya Village, Coast of Lake Van	JGİB-18	20
B-2	Ahlat-Nemrut Caldera-Tatvan	JGİN-1, 2,3, 4, 5, 8	50
B-3	Adilcevaz-Aygır Maar Lake Surround-Adilcevaz	JGİA-4; JGİS-3	23
B-4	Adilcevaz-Arin Lake Surround-Adilcevaz	JGİA-4, 5	58
C-1	Tatvan-İncekaya Cove-Çataltaş	JGİB-18	24,5
C-2	Nemrut Crater Lake Surround	JGİN-10	19
C-3	Nazik Lake Surround	-	31,6
TS-1	Harmantepe Village -Süphan Crater-Kışkılı Locality	JGİS-6	17
TS-2	Boryan Village - Kirkor Dome – Çilhur Village	-	8
TS-3	Boryan Village -Kirkor Dome-Cankurtaran	-	9
TS-4	Taşharman (Ahlat)-Nemrut Crater-Tatvan	JGİN-1, 2, 3, 4, 5	37,4

7. General Assessment and Proposals

By conducting field studies within the framework of the main context in the Nemrut - Süphan proposed geopark area and its surroundings, the geosite inventory, literature studies, cultural heritage and natural asset inventory studies were completed, geopark and geological maps were prepared and all geopark inventories were indicated on these maps and made available to use. The things to be done in the next step are given below. When these studies are completed, the Nemrut–Süphan proposal geopark will be opened to visitors as an approved geopark.

1. Studies continue for a "Geopark Management System" and "Implementation Program".

2. El - Aman Han, one of the largest caravanserais of the Anatolia, built in the 16th Century, is considered for the "Geopark Visitor Center" and "Geopark Museum".

3. The design of the introductory signs of the determined geosites has been made and the preparation step has started. The ignimbrites, one of the natural building stones in the region, should be used for the signs.

4. Studies on the production of brochures, books, booklets and maps describing the Nemrut – Süphan proposed geopark have been completed and introductory documents (with English, French and German translations) will be prepared for all geopark elements before the operational step.

5. Works have started for the production of local souvenirs, especially the Ahlat stick.

6. Works continue for resting and logistic stations to be established at "Observation Points" in certain locations within the geopark.

7. "Continuous Education Programs" have been prepared within the geopark. These trainings have been started and will continue in a certain order after the geopark is opened to the visitors.

8. The procedure for informing all local government elements on the subject has been implemented, but this has been limited. In the next stages of the work, the

Table 5- The scoring and geoconservation proposal table of the proposed geosites (designed according to the Regulation of the General Directorate for Protection of Natural Assets).

PROPOSED GEOSITES			GEOSITE CODE AND CLASS*										CHART 20.1**					CHART 20.2**				TOTAL SCORE***	PROPOSAL of PROTECTION AREA**		
CODE	AGE	LITHOLOGY	Sedimantology/ Stratigraphy	Environment (Lake, Waterfall, etc.)	Volcanism/ magmatism	Economical Geology (gemology, etc.)	Structural Geology (fault, fold, etc.)	Erosive Shapes (Geomorphology)	Meteoric Events	Continent/Ocean scale Structures	Bathymetric Env. (shelf, ect.)	History and Culture (Archeo., Etnog.)	Natural Aesthetics	Infrequency	Sensitivity	Scientificity	AVERAGE SCORE/4	Regional Importance	National Importance	International Importance	IMPORTANCE SCORE	Chart 20.1 + Chart 20.2	Sustainable Protection and Controlled Use Area (C)	Qualified Natural Protection Area (B)	DEFINITELY PROTECTION AREA (A)
JGİB-1	Precambrian	Gneiss, Schist			X		X						6	6	6	8	6	1	2		3	**9**		B	
JGİB-2	U.Paleozoic	Metagranite			X		X						8	10	8	10	9	1	2	3	6	**15**			A
JGİB-3	Precambrian	Schist			X		X						6	6	6	8	6	1	2		3	**9**		B	
JGİB-4	U. Cretaceous	Peridotite			X								6	5	5	4	5	1			1	**6**	C		
JGİB-5	Trias.-L. Juras.	Metavolcanite	X										6	5	5	4	5	1			1	**6**	C		
JGİB-6	U. Senonian	Flysch	X										6	5	5	4	5	1			1	**6**	C		
JGİB-7	Eocene	Continental clastic	X										6	5	5	4	5	1			1	**6**	C		
JGİB-8	L-M. Eocene	Volcanite/Sed. rocks	X										6	5	5	4	5	1			1	**6**	C		
JGİB-9	L. Permian	Limestone, marble	X										6	5	5	4	5	1			1	**6**	C		
JGİB-10	U. Permian	Limestones	X										6	5	5	4	5	1			1	**6**	C		
JGİB-11	Precambrian	Biotitic metagranite			X								6	5	5	4	6	1	2		3	**9**		B	
JGİB-12	Quaternary	Basalt, ignimbrite	X										6	5	5	4	4	1			1	**6**	C		
JGİB-13	Paleozoic	Gneiss, Schist			X								6	5	5	8	6	1	2		3	**9**		B	
JGİB-14	Precambrian	Metagranite			X								8	10	8	10	9	1	2	3	6	**15**			A
JGİB-15	Paleozoic	Amphibolite			X		X						8	10	8	10	9	1	2	3	6	**15**			A
JGİB-16	Quaternary	Travertine	X										6	5	5	4	5	1			1	**6**	C		
JGİB-17	Quaternary	Scorian deposits	X										6	6	6	8	6	1	2		3	**9**		B	
JGİB-18	Quaternary	İncekaya Tuff cone	X					X					10	10	10	10	10	1	2	3	6	**16**			A
JGİN-1	Quaternary	Nemrut Camels	X					X					8	10	8	10	9	1	2	3	6	**15**			A
JGİN-2	Quaternary	Pyroclastic debris	X										6	6	6	8	6	1	2		3	**9**		B	
JGİN-3	Quaternary	Rhyolitic lava flow			X								6	6	6	8	6	1	2		3	**9**		B	
JGİN-4	Quaternary	Nemrut Caldera			X								10	10	10	10	10	1	2	3	6	**16**			A
JGİN-5	Quaternary	Post-caldera freatom. deposits	X										6	6	6	8	6	1	2		3	**9**		B	
JGİN-6	Quaternary	Post-caldera rhyolitic lava			X								6	6	6	8	6	1	2		3	**9**		B	
JGİN-7	Quaternary	Maar crater			X								6	6	6	8	6	1	2		3	**9**		B	
JGİN-8	Quaternary	Steam pipe			X								6	6	6	8	6	1	2		3	**9**		B	
JGİN-9	Quaternary	Ilığ Lake		X									6	6	6	8	6	1	2		3	**9**		B	
JGİN-10	Quaternary	Nemrut Crater Lake		X									10	10	10	10	10	1	2	3	6	**16**			A
JGİN-11	Quaternary	Kantaşı (Bloodstone)			X								10	10	10	10	10	1	2	3	6	**16**			A
JGİN-12	Quaternary	Nemrut Opening Crack-1			X								10	10	10	10	10	1	2	3	6	**16**			A
JGİN-13	Quaternary	Nemrut Opening Crack-2			X								10	10	10	10	10	1	2	3	6	**16**			A
JGİS-1	Quaternary	Baking Zone			X								8	10	8	10	9	1	2		3	**12**			A
JGİS-2	Quaternary	Rhyolitic Obsidian			X								6	6	6	8	6	1	2		3	**9**		B	
JGİS-3	Quaternary	Aygır Maar		X									10	10	10	10	10	1	2		3	**13**			A
JGİS-4	Quaternary	Blocky Ash Flow	X										6	6	6	8	6	1	2		3	**9**		B	
JGİS-5	Quaternary	Dacitic Dome			X								6	6	6	8	6	1	2		3	**9**		B	
JGİS-6	Quaternary	Süphan crater			X								10	10	10	10	10	1	2	3	6	**16**			A
JGİS-7	Quaternary	Trachytic lava			X								6	6	6	8	6	1	2		3	**9**		B	
JGİA-1	Quaternary	Recent Lake Dep.	X										6	6	6	8	6	1	2		3	**9**		B	
JGİA-2	L. Miocene	Fossil cemetery	X										8	10	8	10	9	1	2		3	**12**			A
JGİA-3	U. Cretaceous	Peridotite			X								6	6	6	8	6	1	2		3	**9**		B	
JGİA-4	Quaternary	Tufa deposits	X										10	10	10	10	10	1	2	3	6	**16**			A
JGİA-5	Quaternary	Travertine channel			X			X					10	10	10	10	10	1	2	3	6	**16**			A
JGİA-6	Quaternary	Microbialitic formations									X		10	10	10	10	10	1	2	3	6	**16**			A
DELİKTAŞ	Quaternary	Travertine	X					X					10	10	10	10	10	1	2	3	6	**16**			A

*ProGeo (1998) Geosite Classification Chart

** "Regulation on Procedures and Principles Regarding the Determination, Registration and Approval of Protected Areas" published in the Official Newspaper No.28358 in 19.07.2012 with the article 13/A of Decree Law (KHK) number 644 and the Law Number 2863.

appropriate information and training will be provided for each of the local stakeholders.

9. The efforts will be made to educate and train the guides who will work in the geopark.

10. Considering the determined georoutes of geosites in the geopark, the security and logistics protocols will be prepared, geoprotection conditions will be determined and necessary documents will be provided to local institutions that will follow this.

11. The participation of Tour Operators operating in the region in the geopark management processes will be ensured, and the geopark will be declared as national and then as international destination without losing time.

12. The transportation - accommodation opportunities of the geopark visitors have been clearly revealed and the accommodation opportunities have been increased by local investors, especially in Tatvan.

13. In order to ensure the participation of the actors that produce ethnographic value within the scope of the local economy in the geopark management processes, the relevant expert groups will be provided for training.

14. It is recommended to certify local and authentic flavors, carry out patent studies, determine the hygiene standards at provincial level, discuss the standards to be used in flavor stations to be established in the medium and long term, and provide training, and communicate with some organizations such as the "Slow City".

As a result, the Nemrut - Süphan proposed geopark is ready to be declared as a "National Geopark" as soon as the above suggestions are fulfilled based on the completed inventory studies with a wide variety of geosite assets, rich natural and cultural heritage elements. During the management stage, when the application preparation processes are followed, the deficiencies are eliminated and the standard studies foreseen by UNESCO are carried out, it will be possible to apply for participation in the Global Geopark Network (GGN).

Acknowledgements

This study covers one part of the field studies carried out within the framework of the "Nemrut - Süphan Geopark Protocol" signed between the Bitlis Governorship and Istanbul University. These studies were carried out through several field studies, workshops, training and promotional activities in the region. We would like to thank to the Bitlis Governorship for their assistance and support at every stage of these works. In addition, the General Secretary of the Governorship Special Provincial Administration Adem Aydoğdu, the Vice Secretary General Halil Avkan, our colleague Geology Engineer Evrim Çelik and the Bitlis Provincial Directorate of Culture supported and contributed at every stage during the inventory work. We sincerely thank them all.

References

Açıkbaş, D. 1979. Geology and hydrocarbon possibilities of Baykan - Şirvan-Pervari region. TPAO Raporu (unpublished).

Açıkbaş, D., Baştuğ, C. 1975. Geological report and petroleum posibilities of northern areas of Cacas-Hani region. TPAO Raporu 971 (unpublished).

Adızel, Ö., Tepe, I., Alp, Ş., Kul, A. R. 1995. Van Gölü havzası sulak alanları, önemi ve karşılaştıkları problemler. Sulak Alanların Korunması Uluslar Arası Toplantısı, 27 Eylül - 01 Ekim 1995, Nevşehir, 10.

Akay, E., Göncüoğlu, M. C., Turan, N. 1988. 1/100.000 ölçekli, Açınsama Nitelikli Türkiye Jeoloji Haritaları Serisi, No: 17. Muş K47 Paftası. Maden Tetkik ve Arama Genel Müdürlüğü Jeoloji Etütleri Dairesi Yayını.

Altınlı, İ. E. 1963. 1/500.000 Ölçekli Türkiye Jeoloji Haritası. Van Paftası İzahnamesi, Maden Tetkik ve Arama Enstitüsü, Ankara.

Altınlı, İ. E. 1966*a*. Doğu ve Güneydoğu Anadolu'nun Jeolojisi, 1. Kısım. Maden Tetkik ve Arama Dergisi 66, 35-74.

Altınlı, İ. E. 1966*b*. Doğu ve Güneydoğu Anadolu'nun Jeolojisi, 2. Kısım. Maden Tetkik ve Arama Dergisi 67, 1-22.

Arni, P. 1940. Siirt garbında, Başor Çayı mıntıkasında Bitlis Dağları cenubi silsilelerinin jeolojik müşahedeleri. Maden Tetkik ve Arama Dergisi 4, 527-528.

Baştuğ, C. 1976. Bitlis napının stratigrafisi ve GD Anadolu Sütur Zonu'nun evrimi. Yeryuvarı ve İnsan 1, 55-61.

Boray, A. 1973. The structure and metamorphism of the Bitlis area. SE Turkey. Ph. Thesis, Univ. Of

London, 233. (unpublished).

Brilha, J. 2016. Inventory and QuantitativeAssessment of Geosites and Geodiversity Sites: a Review. Geoheritage 8, 119-134. https://doi.org/10.1007/s12371-014-0139-3

Çağlayan, M. A., Şengün, M. 2002. 1/100.000 ölçekli, açınsama nitelikli Türkiye jeoloji haritaları, No: 66. Van-L48 Paftası, Jeoloji Etütleri Dairesi, Maden Tetkik ve Arama Genel Müdürlüğü, Ankara.

Çetinkaya, O. 1999. Van Gölü Havzası Su Kaynakları ve Balıkçılık Potansiyeli, X. Ulusal Su Ürünleri Sempozyumu, Adana.

Çetinkaya, O., Sarı, M., Arabacı, Şen, F., M., Duyar, H.A. 1995. Van Gölü Havzası Karasu Çayı Balık Populasyonları Üzerinde Araştırmalar. Yüzüncü Yıl Üniv., Ziraat Fakültesi Dergisi 5 (2), 189-202. ISSN 1018-9424 Van.

Çiftçi, Y., Güngör, Y. 2016. Jeopark projeleri kapsamındaki doğal ve kültürel miras unsurları için standart gösterim önerileri. Maden Tetkik ve Arama Dergisi 153, 223-238.

Dewey, J. F., Pitmann, W. C., Ryan, W. B. F. ve Bonnin, J. 1973. Plate tectonics and the evolution of the Alpine system. Bulletin of the Geological Society of America 84, 3137-3180.

Elmas, A., Yılmaz, Y. 2003. Development of an Oblique Subduction Zone - Tectonic Evolution of the Tethys Suture Zone in Southeast Turkey. International Geology Review 45, 2003, 827-840.

Göncüoğlu, M. C., Turhan, N. 1983*a*. Bitlis metamorfitlerinde yeni yaş bulguları. Maden Tetkik ve Arama Dergisi 95/96, 44-47.

Göncüoğlu, M. C., Turhan, N. 1983*b*. Bitlis metamorfit kuşağının jeolojisi. Geology of the Taurus Belt, TJUS Proceedings 374.

Göncüoğlu, M. C., Turhan, N. 1992. 1/100.000 ölçekli Açınsama Nitelikli Türkiye Jeoloji Haritaları Serisi, No: 38. Muş İ-33 (L47) Paftası. Maden Tetkik ve Arama Genel Müdürlüğü Jeoloji Etütleri Dairesi Yayını.

Helvacı, C. 1983*a*. Bitlis Masifi Avnik (Bingöl) yöresindeki apatitçe zengin demir yataklarının oluşumu. Geology of the Taurus Belt. TJUS Proceeding, 317-344.

Helvacı, C. 1983*b*. Bitlis Masifi Avnik (Bingöl) bölgesi metamorfik kayaçların petrojenezi. Türkiye Jeoloji Kurumu Bülteni 26, 117-132.

Helvacı, C., Griffin, W. L. 1983. Metamorphic feldspatization of metavolcanics and granitoids, Avnik area, Turkey. Contributions to Mineralogy and Petrology 83, 309-319.

Henriques, M. H., dos Reis, R. P., Brilha, J., Mota, T. 2011. Geoconservation as an Emerging Geoscience. Geoheritage 3, 117-128. DOI: 10.1007/s12371-011-0039-8

Hisarlı, Z. M., Çinku, M. C., Ustaömer, T., Keskin, M., Orbay, N. 2015. Neotectonic deformation in the Eurasia - Arabia collision zone, the East Anatolian Plateau, E Turkey: evidence from paleomagnetic study of Neogene - Quaternary volcanic rocks. Internetional Journal of Earth Sciences (Geologische Rundschau) 105, 139-165 (2016).

Ibbotson, P. 1969. Siirt - Bitlis regional mineral survey Project. 1/2225 First Annual Rep. (Robertson Res. Co. Ltd.). Maden Tetkik ve Arama Genel Müdürlüğü, Derleme Rapor No: 4101, Ankara (unpublished).

JEMIRKO. https://www.jemirko.org.tr/jeolojik-miras-terimleri/

Karaoğlu, Ö., Kılıç, S. 2017. Nemrut Volkanı ve Kral Nemrut'un Efsanesi. Mavi Gezegen Popüler Yerbilim Dergisi, JMO Yayını 22.

Karaoğlu, Ö., Özdemir, Y., Tolluoğlu, A. Ü., Karabıyıkoğlu, M., Köse, O., Froger, J. L. 2005. Stratigraphy of the volcanic products around Nemrut Caldera: implications for reconstruction of the caldera formation. Turkish Journal of Earth Science 14, 123-143.

Kazancı, N., Şaroğlu, F., Suludere, Y. 2015. Geological Heritage and Framework List of the Geosites in Turkey. Bulletin of the Mineral Research and Exploration 151, 263-272.

Kellog, H. E. 1960. Stratigraphic report, Bitlis - Siirt area, Petroleum district V, SE Turkey. Petrol İşleri Genel Müdürlüğü Teknik Arşivi, Ankara (unpublished).

Keskin, M. 2003. Magma generation by slab steepening and breakoff beneath a subduction - accretion complex: An alternative model for collisionrelated volcanism in Eastern Anatolia, Turkey. Geophysical Research Letters 30, 1-4.

Keskin, M. 2007. Eastern Anatolia: A hotspot in a collision zone without a mantle plume. Plates, Plumes And Planetary Processes 430, 693-722

Keskin, M., Chugaev, A. V., Lebedev, V. A., Sharakov, E. V., Oyan, V., Kavak, O. 2012. The geochronology and origin of mantle sources for late cenozoic intraplate volcanism in the frontal part of the Arabian plate in the Karacadag neovolcanic area of Turkey. Part 1. The results of isotopegeochronological studies. Journal of Volcanology and Seismology 6, 352-360.

Ketin, İ. 1966. Anadolu'nun Tektonik Birlikleri. Maden Tetkik ve Arama Dergisi 66, 20-34.

Kranck, E. H. 1954. Deep structures and metamorphism. Trans. The New York Academy of Sciences II. 16, 234-244.

Kranck, E. H. 1957. On folding movements in the zone of the basement. Geologische Rundschau 47, 261-282.

Lebedev, V. V., Sharakov, E. V., Keskin, M., Oyan, V. 2010. Geochronology of Late Cenozoic volcanism in the area of Van Lake, Turkey: An example of development dynamics for magmatic processes. Doklady Earth Sciences 433, 1031-1037.

Lima, F. F., Brilha, J. B., Salamuni, E. 2010. Inventorying geological heritage in large territories: a methodological proposal applied to Brazil. Geoheritage 2(3-4), 91-99.

MTA. 2002. 1/500.000 ölçekli Türkiye Jeoloji Haritası, Van Paftası. Maden Tetkik ve Arama Genel Müdürlüğü, Ankara.

Oberhänsli, R., Bousquet, R., Candan, O., Okay A.I. 2012. Dating subduction events in East Anatolia.Turkish Journal of Earth Sciences 21, 1-18.

Özdemir, Y. 2011. Volcanostratigraphy and petrogenesis of Süphan Stratovolcano. Yayınlanmamış Doktora Tezi, ODTÜ, 279.

Özdemir, Y., Güleç, N. 2014. Geological and geochemical evolution of the Quaternary Süphan stratovolcano, eastern Anatolia, Turkey: evidence for the lithosphere-asthenosphere interaction in post collisional volcanism. Journal of Petrology 55, 37-62.

Özdemir, Y., Karaoğlu, Ö., Tolluoğlu, A. Ü., Güleç, N. 2006. Volcano - stratigraphy and petrogenesis of the Nemrut stratovolcano (East Anatolian High Plateau): the most recent post-collisional volcanism in Turkey. Chemical Geology 226, 189-211.

Özdemir, Y., Blundy J. D., Güleç, N. 2011. The importance of fractionalcrystallization and magma mixing in controlling chemical differentiationat Süphan stratovolcano, eastern Anatolia, Turkey. Contributions to Mineralogy and Petrology 162, 573-597.

Özdemir, Y., Akkaya, İ., Oyan, V., Kelfoun, K. 2016. A Debris Avalanche at Süphan Stratovolcano (Turkey) and Implications for Hazard Evaluation. Bulletin of Volcanology 78(9).

Özkaya, İ. 1974. GD Anadolu Sason ve Baykan yöresinin stratigrafisi. Türkiye Jeoloji Kurumu Bülteni 17/1, 51-72.

Özkaya, İ. 1975. Sason yöresinin yapısal jeolojisi. Cumhuriyetin 50. Yılı Yerbilimleri Kongresi, Bildiriler 21-30.

Özkaya, İ. 1978*a*. Yüksekova Şemdinli yöresi Jeolojisi. Türkiye 4. Petrol Kongresi, Bildiriler, 63-82.

Özkaya, İ. 1978*b*. Ergani Maden yöresi stratigrafisi. Türkiye Jeoloji Kurumu Bülteni 21/2, 120-140.

Özkaya, İ. 1982*a*. Marginal basin ophiolites at Oramar and Karadağ, SE Turkey. Journal of the Geological Society of London 139, 203-210.

Özkaya, İ. 1982*b*. Origin and tectonic setting of some melange units in Turkey. Journal of the Geological Society of London 90, 269-278.

Özkaya, İ. 1982*c*. Upper Cretaceous plate rupture and development of leaky transcurrent fault ophiolites in SE Turkey. Tectonophysics 88, 103-116.

Perinçek, D. 1980. Bitlis metamorfitlerinde volkanitli Triyas. Türkiye Jeoloji Kurumu Bülteni 23/2, 101-118.

Pro Geo Group. 1998. A first attempt at a geosites framework for European lUGS initiative to Support recognition of World heritage and European geodiversity. Geologica Balcanica 28, 5-32.

Schmincke, H. U., Sumita, M. (Paleovan scientific team). 2014. Impact ofvolcanism on the evolution of Lake Van (eastern Anatolia) III:periodic (Nemrut) vs. episodic (Süphan) explosive eruptions andclimate forcing reflected in a tephra gap between ca. 14 ka and ca. 30 ka. Journal of Volcanology and Geothermal Research 285, 195-213.

Sungurlu, O. 1974. VI. Bölge kuzeyinin jeolojisi ve petrol imkanları. Türkiye 2. Petrol Kongresi Tebliğleri, 85-107.

Şengün, M. 1984. Tatvan güneyinin (Bitlis Masifi) jeolojik/petrografik incelemesi. Hacettepe Üniversitesi Doktora Tezi, 157 (unpublished).

Şengün, M., Çağlayan, M. A., Sevin, M. 1991. Bitlis masifi, Bitlis-Tatvan-Hizan-Şirvan dolayının jeolojisi. Maden Tetkik ve Arama Genel Müdürlüğü, Rapor No: 9105, 200. Ankara (unpublished).

Tolluoğlu, A. Ü., Erkan, Y. 1982. Mutki (Bitlis) yöresindeki bölgesel metamorfik kayaçların petrografik incelenmesi. Yerbilimleri 9, 73-89.

Tolun, N. 1953. Contribution a'le etude geologie des environs du S et SE du lac de Van. Maden Tetkik ve Arama Bülteni 44/45, 77-112.

Tolun, N. 1960. Stratigraphy and tectonics of southeastern University of İstanbul. Faculty of Science Journal 25, 203-264.

Ustaömer, P. A., Ustaömer, T., Collins A. S., Robertson, A. H. F. 2009. Cadomian (Ediacaran - Cambrian) arc magmatism in the Bitlis Massif, SE Turkey: Magmatism along the developing northern margin of Gondwana. Tectonophysics 473, 99-112.

Yazgan, E. 1983. Geodynamic evolution of Eastern Taurus. Geology of the Taurus Belt. Proceedings, 199-208.

Yazgan, E., Chessex, R. 1991. Geology and tectonic evolution of the SE Taurides in the Region of Malatya. TPJD Bul. 3/1, 1-42.

Yeşilova, Ç., Yakupoğlu, T. 2007. Adilcevaz Kireçtaşının (Van Gölü Kuzeyi) Mikrofasiyes Özellikleri. Türkiye Jeoloji Bülteni 50, 1, 27-39.

Yılmaz, O. 1971. Etüde petrographique et geochronologique de la region de Cacas: Univ. Grenoble, Doctora teheses (unpublished), 230.

Yılmaz, O., Michel, R., Vialette, Y., Bonhomme, M. G. 1981. Reinterpretation des donne es isotopipues Rb - Sr obtenues sur les metamorphites de la partie meridionale du massif de Bitlis (Turquie): Sciences geologiques, bulletins et memoires, 34/1,59-73.

Yılmaz, Y. 1978. Gevaş (Van) dolayında Bitlis Masifi – Ofiyolit ilişkisi. Türkiye 4. Petrol Kongresi Bildirileri, 83-94.

Yılmaz, Y. 2005. Doğu Anadolu'nun genç tektoniği ve morfotektonik gelişimi. Deprem Sempozyumu, 23-25 Mart, Kocaeli.

Yılmaz, Y., Şaroğlu, F., Güner, Y. 1987. Initiation of the neomagmatism in East Anatolia. Tectonophysics 134, 177-199.

Bulletin of the Mineral Research and Exploration

http://bulletin.mta.gov.tr

The effect of urban heat island on groundwater located in shallow aquifers of Kütahya city center and shallow geothermal energy potential of the region, Turkey

Ali Samet ÖNGEN[a*] and Zeynel Abidin ERGÜLER[a]

[a]*Kütahya Dumlupınar University, Faculty of Engineering, Department of Geological Engineering, Kütahya, Turkey*

Research Article

Keywords:
Urban heat island, Shallow geothermal energy, Renewable energy, Groundwater, Heat capacity.

ABSTRACT

As a result of urbanization, natural surfaces are replaced by artificial surfaces that trap heat such as buildings, pavements and asphalt, so residential areas have higher temperature values than rural areas. This effect, defined as the urban heat island, causes an increase not only in air temperature but also in the subsurface and groundwater. Groundwater temperature values were measured during one year in an area approximately 53 km^2 consisting of different types of settlement areas to determine the urban heat island effect on the subsurface of Kütahya. As a result of the measurements, urban heat island maps were prepared. It was observed that the groundwater temperature anomalies increased towards the urban/industrial areas. The difference of groundwater temperature in urban / rural areas reached up to 7°C by well. This heat energy increasing with the effect of urban heat island can be used in the heating processes of buildings by utilizing systems called "shallow geothermal energy". For this reason, the heat potential of the alluvial aquifer under Kütahya was calculated. The theoretical heat potential values of the this aquifer range between 1.64×10^{13} kJ K^{-1} and 5.55×10^{13} kJ K^{-1} with a mean value of 3.50×10^{13} kJ K^{-1}. It is thought that urban heat island maps and the heat potential calculations of the aquifers may be important parameters for applicability of shallow geothermal systems in the city center of Kütahya.

Received Date: 16.06.2020
Accepted Date: 26.10.2020

1. Introduction

Due to economic, social and cultural factors, the human population in cities is increasing and city centers are getting more crowded. Urbanization in cities is rapidly increasing worldwide as a result of the need for shelter due to the increasing population. As a result of urbanization, artificial surfaces replace natural vegetation. As a result, city centers have higher air temperature values compared to the surrounding rural areas. This situation was first expressed by Howard (1883) and defined as "urban heat island". In another study (Oke, 1973), the highest air temperature difference in urban and rural areas was defined as the urban heat island intensity, and it was stated that the intensity of the urban heat island can reach up to 12 °C in open and windless summer evenings. As a result of the urban heat island effect, the air temperature in city centers can be up to 10 °C higher than in rural areas (Oke, 1987; Klysik and Fortuniak, 1999). According to Menberg (2013*a*), the difference between the city center and rural areas increases up to 20 K due to artificial structures.

The most important reason for the urban heat island effect is that natural surfaces are replaced by artificial surfaces. It has been stated in previous studies that green areas are cooler than urban areas around

Citation Info: Öngen, A. S., Ergüler, Z. A. 2021. The effect of urban heat island on groundwater located in shallow aquifers of Kütahya city center and shallow geothermal energy potential of the region, Turkey. Bulletin of the Mineral Research and Exploration 165, 217-234.
https://doi.org/10.19111/bulletinofmre.820395

**Corresponding author: Ali Samet ÖNGEN, alisamet.ongen@dpu.edu.tr*

them (Gallo and Owen, 1999; Spronken - Smith and Oke, 1999). Artificial surfaces increasing due to urbanization in cities cause anthropogenic heat losses and changes in the radiation level in the atmosphere and the energy balance in cities. This situation causes change in the urban microclimate and increase in air temperature (Landsberg, 1956; Oke, 1988). Because during the day, plants emit the radiation coming from the sun back to the atmosphere through evaporation - transpiration (evapotranspiration). But; evapotranspiration decreases with the disappearance of natural surfaces, artificial surfaces such as buildings, asphalt, roads, sidewalks, bridges trap the sun's rays and cause the air temperature to increase during the day. As a result, the urban heat island effect emerges and higher air temperature values are observed in urban areas compared to rural areas with dense green areas. Filled areas, subway tunnels, electrical cables, district heating systems and sewage systems are other man - made structures that cause the urban heat island effect (Balke, 1977; Pollack et al., 1998; Menberg et al., 2013*b*).

It has been emphasized in previous studies (Oke, 1973) that the urban heat island effect is also a result of the city's size and population growth. Ezber et al. (2007) examined the effect of urban heat island in İstanbul and showed that the urban heat island factor is directly related to population and city size. However, according to some previous studies, it was stated that this effect was observed not only in big cities but also in medium - sized cities such as Granada (Spain) (Montavez et al., 2000) or in small cities such as Aveiro (Portugal) (Pinho and Manso Orgaz, 2000). According to Allen et al. (2003), the urban heat island effect may not be observed in every city. This effect depends on many factors such as regional weather, topography, density of streets, buildings and man - made structures, and the number of man - made areas such as parks and gardens. Landsberg (1981) pointed out that the urban heat island effect shows a heterogeneous distribution and is an area - specific concept, many microclimatic changes occur within the city, and the urban heat island is a summary of microclimatic changes in the city. In other words, the density of the urban heat island may vary within the city area depending on the urban characteristics.

Many studies and meteorological records show that in the last century there is a significant temperature increase trend in cities (Perrier et al., 2005; Ferguson and Woodbury, 2007; Taniguchi et al., 2007). This situation is a result of not only climatic factors, but also the urban heat island effect resulting from urbanization as mentioned above (Oke, 1973; Kataoka et al., 2009). For example, Karaca et al. (1995) examined the relationship between the population growth and the urban heat island effect in İstanbul and observed that the average temperature has decreased by 1.17 °C in the last 40 years in the northern part of İstanbul, where housing is less, and the average temperature has increased by 0.47 °C in the last 40 years in the southern part where housing is intense. This is a proof that the temperature increase in cities is not only a result of climatic factors but also of urbanization.

As in the previous studies mentioned above, the urban heat island effect that occurs in the atmosphere is widely known, and this change has been the focus of international studies for many years. However, the urban heat island effect causes an increase in temperature in and around the underground as well as in the atmosphere (Taniguchi et al., 2007). Underground temperature is controlled by the heat flux from the center of the earth and the surface temperature (Huang et al., 2009). Temperature changes that occur on the earth with the effect of urban heat island are transmitted underground by heat transfer and especially shallow aquifers located close to the surface are affected by atmospheric events occurring on the surface. Therefore, engineering structures such as buildings, parking lots, asphalt, subway tunnels that cause the urban heat island effect are responsible for the rise of the temperature of the ground and therefore the units located at shallow depths underground and the groundwater. It has been proven in various studies that the urban heat island effect has a strong effect on underground temperature and the urban heat island effect has been determined by many researchers using soil temperature and/or groundwater temperature values (Taniguchi et al., 1999; Changnon, 1999; Ferguson and Woodbury, 2004; Taniguchi, 2006; Taniguchi et al., 2007). Ferguson and Woodbury (2004) calculated heat loss from buildings in urban areas and stated that the underground environment is affected by previously ignored man - made activities such as subway networks or re - injected thermal waters. Ampofo et al. (2004) stated that 70% of the heat in the London subway can be vented out with

ventilation, and the remaining 30% is transmitted to the underground. Kottmeir et al. (2007), using the Berlin example, established a relationship between the percentage of covered surfaces and groundwater temperature values. According to the researcher; there is a direct proportion between covered surfaces and percentage of urbanization and groundwater temperature. Groundwater temperature decreases in rural areas where closed surfaces and the percentage of construction are decreasing. Taniguchi (2006) established a direct relationship between population density and underground temperature values in Bangkok. Also, the increase in underground soil temperature in rapidly growing Asian cities has been researched by many studies (Taniguchi and Uemura, 2005; Taniguchi et al., 2009). In similar studies, it was observed that the soil temperature increased between 2 and 3 K in tropical and temperate regions as a result of the destruction of forest areas (Murtha and Williams, 1986; Nitoiu and Beltrami, 2005). In Turkey, Yalçın and Yetemen (2009) measured the soil temperatures at shallow depths at different points located on both sides of İstanbul and found that the underground temperature difference increased up to 3.5 K in settlement areas. It has been observed that the underground temperature measured in urban areas is 5 K warmer than the surrounding areas (Taniguchi et al., 1999; Ferguson and Woodbury, 2004; Reiter, 2006). In the study conducted in Cologne, Germany by Zhu et al. (2010), the areal distribution of groundwater temperature was examined and it was stated that the highest groundwater temperature values were found in aquifers under the city center where urbanization is intense. In many similar studies, groundwater temperature values increasing with the urban heat island effect have led to the idea of using aquifers located in the shallow depths of the city center as a geothermal energy source. With the increase in groundwater temperatures due to the urban heat island effect, these aquifers will become geothermal reservoirs and an environmentally friendly and renewable energy source will be provided as an alternative to fossil fuels. Because; aquifer with high temperature values means high amount of stored energy, high amount of stored energy means high geothermal potential. In this sense, high - temperature urban aquifers may allow the applicability of systems that are important for the national economy and environmental health like shallow geothermal systems. There are many studies assessing the applicability of shallow geothermal energy systems in rural and denser residential areas (Lee et al., 2017; Casasso et al., 2017; Francisco Pinto and Graça, 2018). The system in question has been installed more than half a million in countries such as France, Germany, Austria, the Netherlands and Sweden (EGEC, 2018). This number is about one million units worldwide (Pophillat et al., 2020). The number of these systems will increase as the installation costs decrease (Soltani et al., 2019).

As a result of the urban heat island effect arising due to the increasing population and urbanization, city centers become warmer than the surrounding rural areas. It has been predicted that the urban heat island effect can be observed in Kütahya, a city where the population and urbanization are constantly increasing. For this reason, within the scope of the study, it is planned to measure the groundwater temperatures and create urban heat island maps in order to determine the urban heat island effect in Kütahya city center. It has been proven in previous studies that the urban heat island effect has a strong effect not only on air but also underground and groundwater temperature. The idea of using these aquifers located in the shallow depths of the city center as a geothermal energy source was born with the increase in the temperatures of the underground environment and groundwater with the effect of the urban heat island. In Turkey where fossil fuel consumption and energy imports are high, it is thought that this environmentally friendly renewable energy source will be a very important alternative. Accordingly, in addition to determining the existence of the urban heat island effect in Kütahya city center, it was aimed to determine the heat potential of the alluvial aquifer. In summary, the main objectives of this study are to examine the effect of the urban heat island effect on the groundwater temperature in shallow aquifers in the city center of Kütahya, to assess the mentioned temperature values in terms of shallow geothermal systems and to calculate the heat potential in the alluvial aquifer.

2. Study Site

Located in the Inner West Anatolia part of the Aegean Region, Kütahya was established at the foot of the Yellice Mountain, on the southern edge of the Kütahya Plain. It is located between 38° 70’ and 39° 80’ north latitudes and 29° 00’ and 30° 30’ east longitudes. Based on Turkish Statistical Institute

(TURKSTAT) data the city constitutes approximately 1.5% of Turkey's land with its 12.014 km^2 area.

Based on TURKSTAT 2019 data, the general population of Kütahya was determined as 579,257. Due to the stronger social and economic opportunities of the central district compared to other districts, approximately 50% of this population (272,367 people) live in the central district (Table 1). Therefore, population density and urbanization rate in the central district is higher than other districts. Again, based on TURKSTAT (2019) data, the annual population growth rate in Kütahya for 2019 is 2.3%, while this rate in the Central district is up to 20.7%. Depending on the increasing population, new areas are being opened to development, the rate of urbanization is increasing and the amount of agricultural lands and green areas is decreasing. This situation increases the potential for urban heat island effect to occur in the city center.

Kütahya Plain is a tectonic plain formed due to the Kütahya fault, and urbanization is intensely observed here. The plain has a generally flat topography and there are alluvial units in it. According to Özburan (2009), the alluvium that overlies the units in the region inharmoniously is the product of the Porsuk and Felent rivers and their branches. The highest place in the study area is Yellice Mountain located in the southern part of the city. Paleozoic, Mesozoic and Cenozoic units crop out in the city. There are metamorphic units consisting of schist and marble at the base and ophiolitic rocks overlie them. Above these units there is a sequence standing with discordance, reflecting the lake/stream environment, intrusive with volcanics, clastic and carbonated. Younger fluvial sediments developed during and after the formation of the Kütahya Graben are found as graben filling (Özburan, 2009). Quaternary aged Kirazpınar, Yakaca and Kütahya formations and alluvium are found as cover units in the region (Figure 1).

The Alluvium unit, which spreads 145 m^2 in the region, is observed in the agricultural lands forming the plains along the Felent and Porsuk River. Groundwater is especially included in these

Table 1 - Statistical information about Kütahya city center.

Elevation (m)	Population (Person) [a]	Population density (km^2)[b]	Area (km^2)	T_{ort} (°C)[c]	Number of wells studied	Survey area (km^2)	Well/Area (well/km^2)
970	272.367	110.27	2470	10.81	41	52.44	0.78

a. Turkey Statistical Institute (TURKSTAT) (2019). b. General Directorate of Mapping c. Kütahya Meteorology Directorate (1970-2019), T_{ort}: Annual average air temperature.

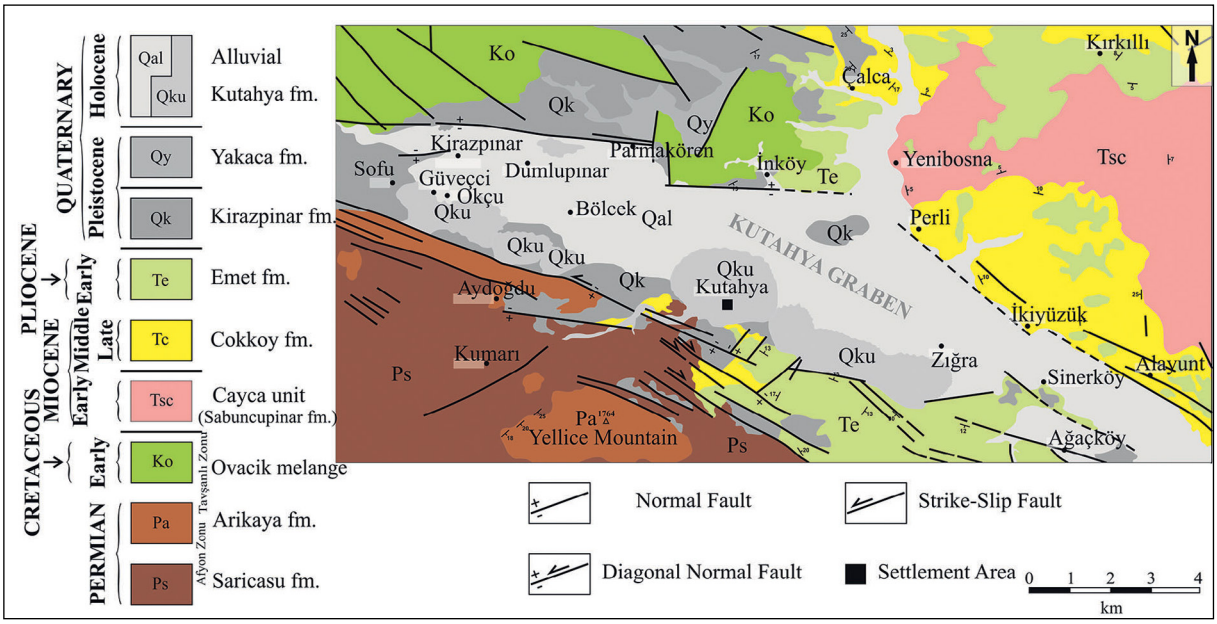

Figure 1 - General geological map of Kütahya and its surroundings (Özburan, 2009).

Quaternary aged sediments. This water is used by the people of the region for purposes such as agricultural irrigation. Based on the results of the drilling in the alluvium unit, the drilling flows are between 2 - 12 l/s and the specific flow values are between 0.04 - 0.22 l/s/m. Quaternary aged aquifer located in the shallow depths of the city has an average hydraulic conductivity of 44.2 m/day and a transmissivity of 213.48 m^2/day (DSİ, 2003). As a result of intense tectonic activity in the region, metamorphic rocks with high secondary permeability and sedimentary rocks with high porosity form permeable units. The streams with continuous flow in the study area are the Felent River, which runs from the northwest to the southeast, and the Porsuk Riverfrom the south to the north (DSİ, 2003).

3. Material and Method

In order to determine the areal distribution of groundwater temperature in urban and rural areas in Kütahya Central district and to determine the urban heat island effect by using these values, water wells suitable for measurement in areas with dense urbanization and rural areas were required. In this direction, the field study started in the Kütahya plain in January 2019 and 42 water wells suitable for the measurement of groundwater level and groundwater temperature in rural and urban areas were determined (Figure 2). Due to the collapse in the well numbered L36 in February, this well was canceled and the work continued with 41 wells in total. In order to fully determine the urban heat island effect, care has been taken to distribute the well locations to be measured in urban, rural and industrial areas (Figure 2). Groundwater level and temperature were measured periodically every month for 12 months from January to December 2019 in an area of approximately 53 km^2 where residences, commercial buildings, public buildings, factories, green areas and agricultural lands are located, using level and temperature measurement tool (Heron Conductivity Plus). Groundwater temperatures were measured 1 meter below the groundwater table, considering the contact of the water surface with the atmosphere. Measurement depths in the wells vary between 1.20 and 25.40 meters. Maps showing the areal distribution of the data were created using Internal Distance Weighting (IDW) geostatistics

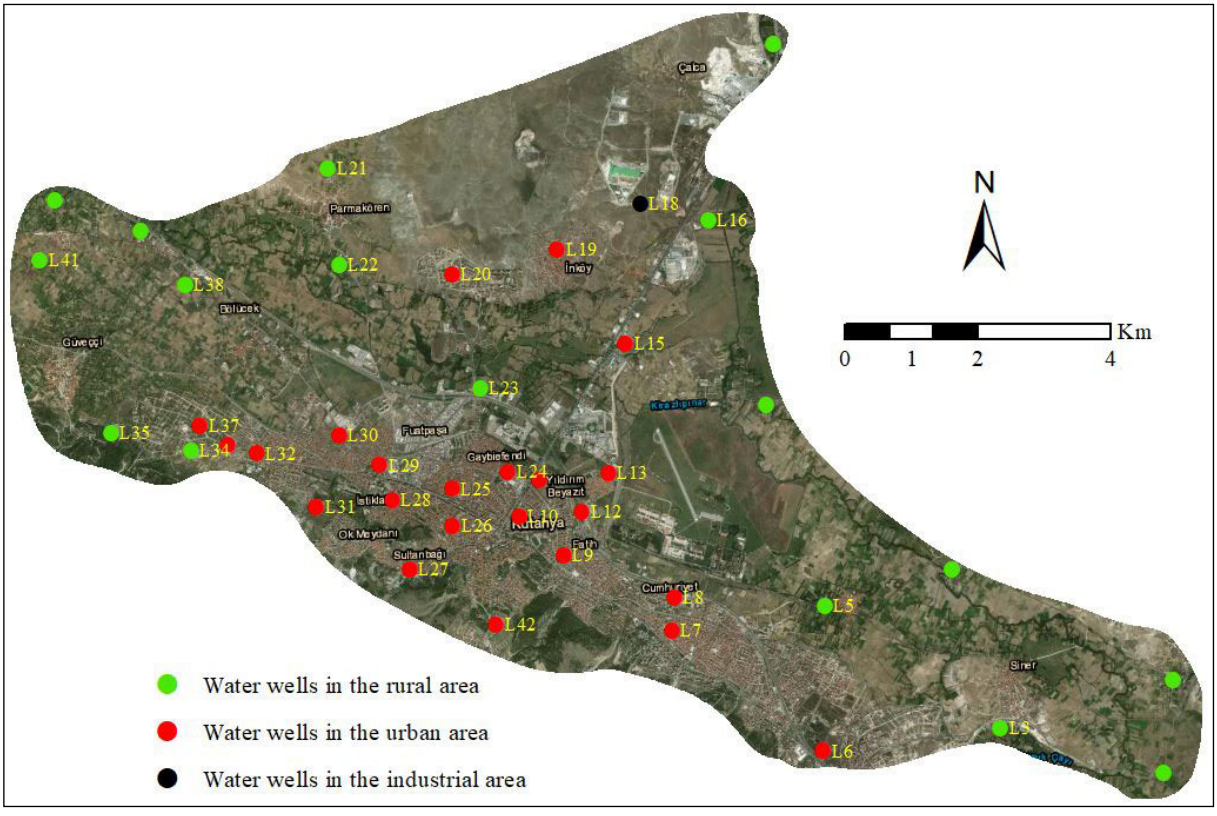

Figure 2- Locations of wells where measurements are made.

method in the ArcMap 10.7 software (ESRI, 2019) in order to observe the areal distribution of the obtained temperature values and to determine the effect of the urban heat island based on the areas, and the effect of urbanization on groundwater and its environment was examined. In addition, groundwater temperature values obtained in field studies were compared with air temperature and 100 cm soil temperature values obtained from Kütahya Meteorology Station.

In order to determine the volumetric heat capacity C_s (kJ m^{-3} K^{-1}) of the soil, which is one of the parameters required to calculate the heat potential of the alluvial aquifer located in shallow depths under the city center, ground samples were taken from the well places where the measurement was made and then in November 2019, the volumetric heat capacities of the ground samples were determined using the ISOMET 2114 device in the laboratories of Torino Technical University (Politecnico di Torino) Department of Land, Environment and Infrastructure Engineering in Torino (Italy).

4. Observations and Obtained Data

4.1. Meteorological Data

In Kütahya, where the continental climate prevails, summers are hot and dry, winters are cold and rainy. According to the Köppen - Geiger (1954) climate classification, the city is in the CSB (hot and dry summer, cool and rainy winter) climate class. Rainfall is generally observed in spring, autumn and winter. In order to determine the effect of increasing urbanization on air temperature over time, 50 years of monthly/annual air temperature and 100 cm soil temperature data between 1970 and 2019 were obtained from Kütahya Meteorology Station. The location of the meteorology station in an area where urbanization is concentrated is seen as an important advantage in terms of understanding the effects of the urban heat island effect on the air and soil temperature. Based on meteorological data; annual average air temperature and soil temperature values were assessed in 10 - year time intervals from 1970 to 2019 (Table 2). Accordingly, the annual average air temperature value, which was 10.26 °C between 1970 - 1979, has continuously increased over time, and this value reached 11.92 °C between 2010 - 2019. In other words, the average annual air temperature has increased by +1,66 °C in Kütahya city center in the last 50 years. Again, based on the data of the last 50 years, 100 cm soil temperature values have increased almost the same (+1.61 °C) since 1970. Based on TURKSTAT data; The population of Kütahya Central district, which was 129,056 people in 1970, increased by 111% in the last 50 years, reaching 272,367 people in 2019. This increase in the population caused the need for accommodation and urbanization in the city center increased from year to year. Based on the data obtained from the meteorology station located in the city center of Kütahya, between 1970 and 2019, the average air temperature increased by +1.66 °C and the average annual soil temperature increased by +1.61 °C. Since there is no meteorology station in rural areas in Kütahya, the average temperatures in urban and rural areas between these years cannot be compared. However, it is known that urbanization continuously increased depending on the population and green areas decreased between these years. Therefore, this increase in average air and soil temperatures between

Table 2 - Monthly and annual average air temperature and 100 cm soil temperature values between 1970 and 2019 in Kütahya city center.

Parameter	Time interval (year)	Month												Average	Diff.*
		1	2	3	4	5	6	7	8	9	10	11	12		
$T_{air\ (°C)}$	1970-1979	0.34	2.38	5.65	9.92	14.09	17.73	20.19	19.35	15.96	11.25	6.11	0.79	10.26	1.66
	1980-1989	0.64	0.76	4.32	10.21	13.90	17.89	20.21	20.26	16.80	10.95	5.53	2.24	10.31	
	1990-1999	0.13	1.09	4.22	9.47	14.42	17.95	20.38	20.46	16.28	12.17	5.96	2.39	10.41	
	2000-2009	0.19	1.53	6.12	10.07	14.85	19.06	21.97	21.86	16.91	12.41	6.69	1.97	11.14	
	2010-2019	1.17	3.93	6.86	11.07	15.57	19.23	22.25	22.19	18.39	12.19	7.57	2.57	11.92	
$T_{earth\ (°C)}$	1970-1979	5.56	5.03	6.26	9.12	12.35	15.46	18.45	19.72	18.42	15.32	11.21	7.89	12.07	1.61
	1980-1989	6.21	5.35	5.99	9.23	12.38	15.34	18.33	19.91	18.98	15.82	11.75	8.52	12.37	
	1990-1999	7.54	6.28	7.11	9.74	13.18	16.2	18.67	19.92	19.15	16.59	13.01	9.85	13.10	
	2000-2009	8.00	7.04	8.01	10.55	13.61	16.87	19.81	21.34	20.35	17.48	13.67	10.07	13.90	
	2010-2019	8.09	7.27	8.11	10.10	13.07	15.86	18.66	20.47	20.10	17.57	14.06	10.81	13.68	

T_{air}: Air temperature; $T_{earth:}$ Earth temperature * Refers to the annual average temperature difference between 1970-2019.

1970 and 2019 is thought to be a result of not only climatic factors but also urbanization. Based on the data, the air temperature is the highest in July with an average of 21 °C and the lowest in January with 0.36°C; soil temperature is highest in August with 20.27°C and lowest in February with 6.19°C.

4.2. Groundwater Temperature Distribution

Underground temperature is affected by physical factors such as ground type, thermal conductivity, specific heat capacity and density. In addition to these factors; climatic factors such as heat flux from underground, earth cover (natural/artificial) and air temperature, wind, sunlight and humidity are known as other factors affecting underground temperature (Landsberg, 1981; Krarti et al., 1995; Popiel et al., 2001). Popiel et al. (2001) divided the earth into three zones based on temperature distribution as surface zone, shallow zone and deep zone. Accordingly, the surface zone is the part of the ground up to a depth of 1 meter and this zone is affected by daily temperature changes. The zone in which the annual effect of the air temperature is observed is called the shallow zone. The shallow zone extends from 1 meter to 20 meters deep and depends on the type of ground and the water content. The deep zone is located under the shallow zone and is not affected by atmospheric changes. On the other hand, Oke (1987) defined the part up to 0.75 meter below ground as the surface zone, and the part up to 14 meters as shallow zone. Although researchers specify the depth limits for these zones, the depth of these zones depends on the type of cover of the surface. According to Landsberg (1981), daily and annual heat waves reach a depth of 4 to 8 meters on the grass - covered surface and deeper on concrete - covered surfaces and affect depths of 15 - 19 meters. Rybach and Sanner (2000) stated that this effect reaches a depth of 15 meters (Yalçın and Yetemen, 2009).

As stated in previous studies (Taniguchi et al., 1999; Ampofo et al., 2004; Ferguson and Woodbury, 2004; Taniguchi, 2006, 2007; Yalçın and Yetemen, 2009; Zhu et al., 2010) urban heat island effect causes an increase not only in air temperature, but also in ground temperature through thermal diffusivity and in groundwater temperature as a result of heat transfer between ground and groundwater. In order to determine the effect of the urban heat island factor on the groundwater temperature in the city center of Kütahya, the annual average values of the groundwater temperature measurements made monthly in 41 water wells are presented in Table 3 and the graph of the change of groundwater temperature values by months within the year is presented in Figure 3.

Based on the data obtained; the highest groundwater temperature was observed as 17.55 °C in August in location L26, which is in one of the regions where urbanization is most intense in the city center, while the lowest groundwater temperature was observed as 7.60 °C in March in location L40, where rural areas and cultivated agricultural lands are dense. The month when the groundwater temperature is the highest during the year is August with an average temperature of 14.43 °C, and the lowest month is March with an average temperature of 11.83 °C. Based on the data obtained from all wells examined; areal average annual temperature of groundwater in the city center of Kütahya is 13.02 °C. The difference in groundwater

Table 3- Annual average groundwater temperature (T_{sort}) values in wells in urban (U), rural (R) and industrial areas where the measurements were made.

Location	L1	L2	L3	L4	L5	L6	L7	L8	L9	L10	L11	L12	L13	L14
T_{sort} (°C)	11.22	12.72	12.28	12.69	12.95	13.96	14.88	15.92	14.76	16.63	13.89	12.11	12.44	10.90
Area	R	R	R	R	R	U	U	U	U	U	U	U	U	R
Location	L15	L16	L17	L18	L19	L20	L21	L22	L23	L24	L25	L26	L27	L28
T_{sort} (°C)	11.82	13.80	11.64	14.15	14.01	14.59	13.56	11.05	11.71	12.76	15.71	15.93	11.58	13.15
Area	U	R	R	I	U	U	R	R	U	U	U	U	U	U
Location	L29	L30	L31	L32	L33	L34	L35	L37	L38	L39	L40	L41	L42	
T_{sort} (°C)	14.12	13.38	12.35	11.92	12.95	11.66	12.46	13.47	12.77	12.34	9.73	12.80	11.23	
Area	U	U	U	U	U	R	R	U	R	R	R	R	U	

T_{sort} (°C): Annual average groundwater temperature values R: Wells located in rural areas, U: Wells located in urban areas, I: Wells located in industrial areas.

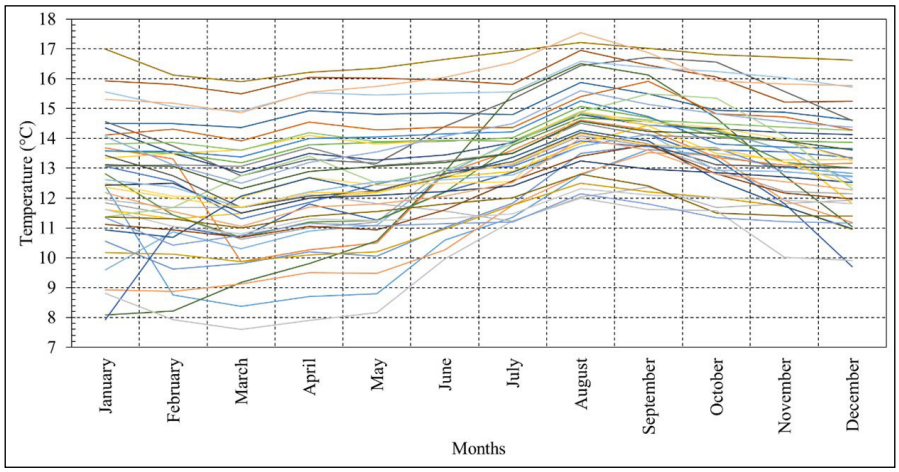

Figure 3- Groundwater temperature change by months in the wells measured in 2019.

temperature in rural areas, mostly consisting of green areas and agricultural lands and in the city center, where urbanization is intense, varies from month to month, and this difference increases up to 1.63 °C.

As a result of the measurements made to observe the areal distribution of these groundwater temperature values and to determine the areal distribution of the urban heat island effect; urban heat island maps were created with the Internal Distance Weighting (IDW) method in the ArcMap 10.7 software (ESRI, 2019) based on August with the highest average groundwater temperature, March with the lowest average groundwater temperature and 12 - month average groundwater temperature values and the effect of the urban heat island on groundwater and its environment has been studied (Figure 4).

When the annual and monthly urban heat island maps are examined, it is clearly observed that the groundwater temperatures in the city center of Kütahya vary greatly from region to region and there is a tendency to increase the temperature towards the regions where urbanization is concentrated. The lowest temperatures were observed in rural areas, and the highest temperatures were observed in residential areas. In the city region, the groundwater temperature rises up to 16.93 °C in August. In rural areas, this value was measured as 11.20 °C in the same month. While the groundwater temperature is 11.95 °C on average annually in the measurements made from the wells in rural areas, the groundwater temperature in urban areas reaches 13.58 °C by increasing this average +1.63 °C. When the comparison is made on the basis of wells one by one, the difference between the two wells in urban and rural areas increases up to about 7 °C. For example, while the average annual groundwater temperature is 16.63 °C in a location on Ataturk Boulevard where urbanization is most intense in Kütahya, this value is 9. 73°C with a difference of 6.90 °C in the well in Kirazpınar Quarter, an old village dominated by agricultural lands and green areas. This situation is considered as an important indicator in terms of the direct effect of human - made structures on groundwater temperature. Based on the prepared maps (Figure 4), the groundwater temperature values in the city center of Kütahya show heterogeneous distribution within the study area, and these temperature values are directly related to human origin factors such as urbanization.

Considering the changing air, soil and groundwater temperatures throughout the year; soil and groundwater temperature increases/decreases parallel to air temperature (Figure 5). The soil temperature is significantly affected by the air temperature and large increases and decreases are observed throughout the year. This is due to the fact that the data used is based on the soil temperature at 100 cm depth. Because; soil temperature values measured at the meteorology station are the values taken from the surface zone, which Popiel et al. (2001) refers to up to a depth of 1 meter, and this zone is affected by daily temperature changes. Since the groundwater temperature measurements are made within the shallow zone, not from the surface zone, temperature fluctuations in groundwater are observed less.

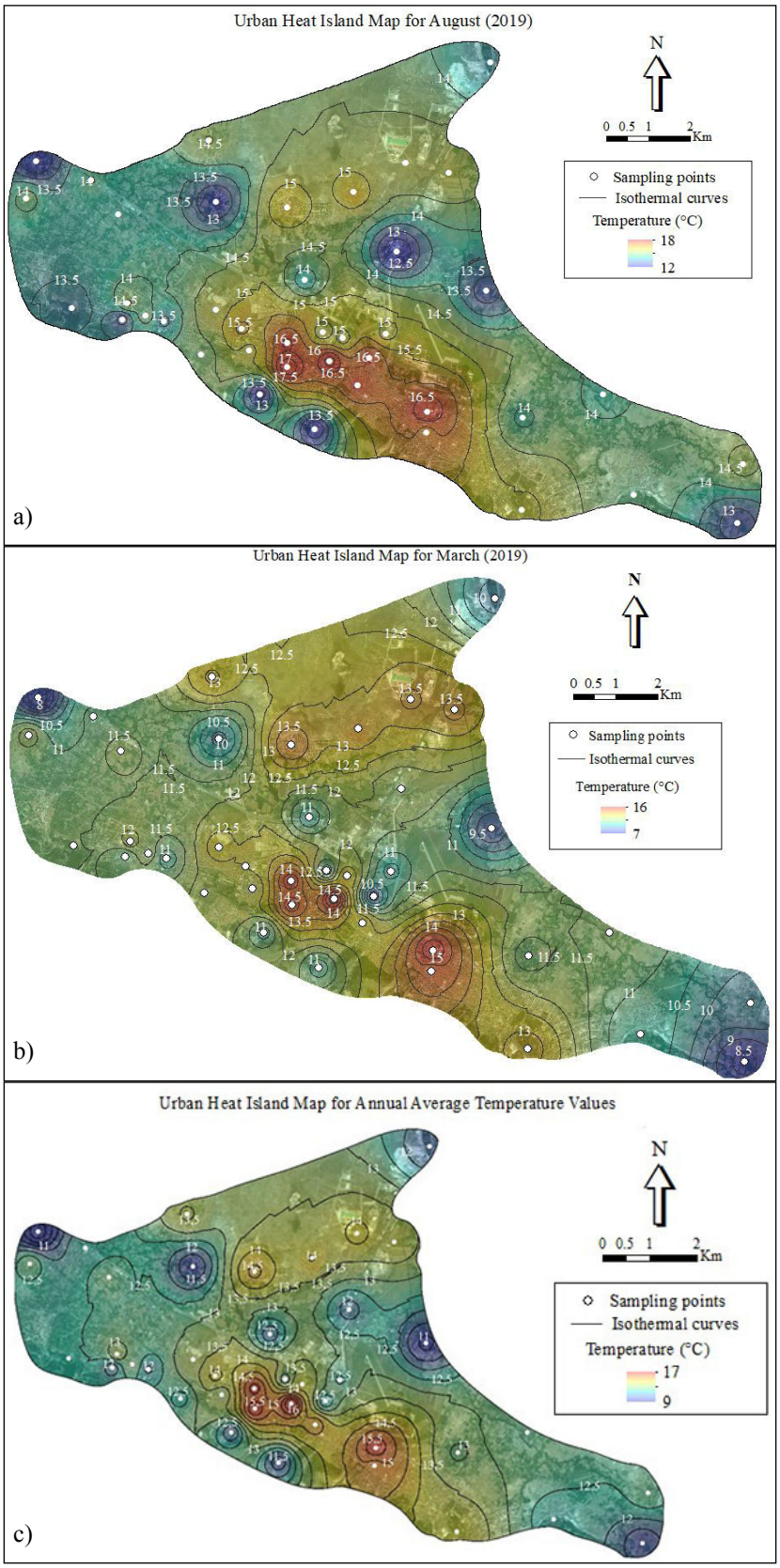

Figure 4- Urban heat island maps: a) August (2019) when the groundwater temperature values are the highest, b) March (2019) when the groundwater temperature values are the lowest, c) The annual average temperature values.

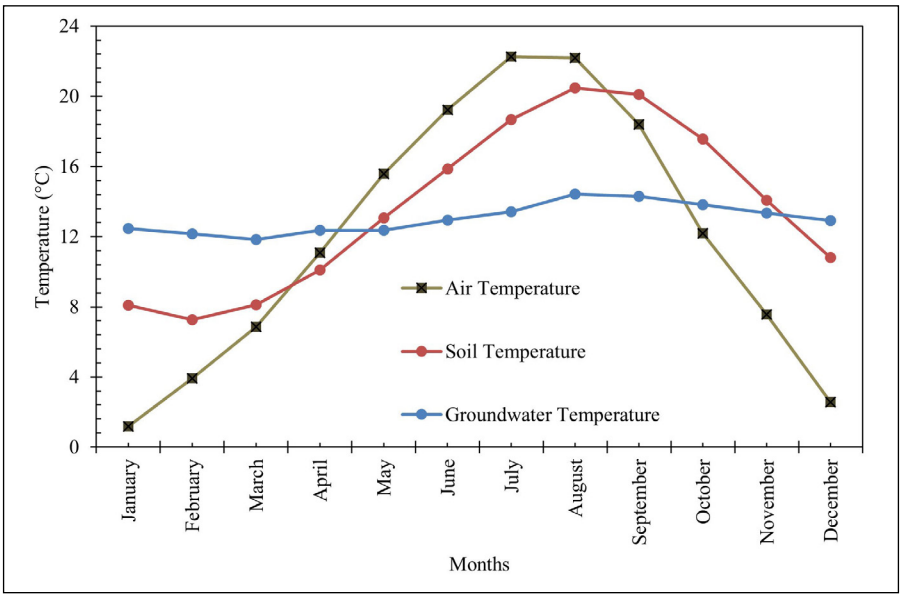

Figure 5- Temperature change graph of air, 100 cm soil and groundwater by months in 2019.

5. Shallow Geothermal Energy

The increase in the energy need due to the population growth in recent years has led researchers to focus on renewable and reliable energy sources. In this sense, shallow geothermal energy has become one of the popular renewable energy sources especially in Europe in recent years. The temperature increase in groundwater due to the urban heat island effect caused the heat potential of these waters to increase, this situation led to the idea of using groundwater in shallow regions as a low - enthalpy energy source, and the concept of shallow geothermal energy has passed to the energy literature. With shallow geothermal energy systems, it has become possible to use these groundwaters for heating. Turkey is a country where the population is constantly increasing and urbanization is increasing rapidly accordingly. Today, Turkey provides its energy needs mostly from non - renewable energy sources and fossil fuels. Most of these resources are imported from abroad. The dissemination of renewable energy sources such as shallow geothermal energy is important for the national economy and environmental health. Both heating and cooling needs of buildings can be provided with shallow geothermal systems.

Due to the climate of Kütahya and its vicinity being hot and dry in summers and quite rainy in winters, shallow aquifers in the region have an important potential in terms of groundwater resources. Hot summer months cause some of the sun rays to be absorbed by natural and artificial grounds, as a result of this, it causes an increase in groundwater temperatures and therefore shallow geothermal energy potential. When the climatic conditions and urbanization rate are considered, it is predicted that the shallow geothermal system will be an important alternative to energy resources in Kütahya. The most important advantages of the system are that shallow geothermal energy is renewable, environmentally friendly and sustainable. Today, energy production based on fossil fuels causes a significant amount of CO_2 emission, as a result, serious environmental problems occur. However, the shallow geothermal system using heat pumps causes much less CO_2 emission than other systems, making it an environmentally friendly system.

While geothermal energy is defined as the energy stored in the form of heat in the depths of the earth, shallow geothermal energy is defined as the system that allows the use of the low temperature groundwater in the shallow depths by increasing the temperature by heat pumps in the heating and cooling systems of the houses. Many studies up to now (Allen et al., 2003; Kerl et al., 2012; Zhu et al., 2010) have shown that shallow aquifers under cities can be an important energy source with low enthalpy. The earth serves as a collector for the storage of energy received from the sun under the earth. Likewise, the heat from the earth's

core is stored under the earth. These two sources are the two main factors affecting the shallow geothermal potential of a region. However, shallow geothermal energy is mostly derived from sun rays, and only a small proportion of the stored energy in shallow aquifers is due to the earth's internal heat or heat generated by plate tectonics (Banks, 2010). Shallow geothermal energy mostly covers the part of the ground up to 100 m depth. The system can be applied to deeper areas, but this increases the cost.

Heat pumps are tools that transfer heat from a heat source to a cooler (Aye and Charters, 2003). In shallow geothermal systems, heat pumps are essential as they are units where water/fluid enters and leaves and its temperature is increased/decreased. Shallow geothermal systems; based on the working principle and the way of establishment, are examined in two ways as open - loop and closed - loop (Figure 6) (Stauffer et al., 2013; Huang, 2012; Rees, 2016). Soil is used as heat source in the closed loop system, which has been used more widely until today. The soil temperature is taken from the ground with the help of fluid, and it is transmitted to the fluid named 'the thermal transfer fluid' circulated in the pipes. This fluid which is inside the pipes and consisting of water and antifreeze, circulates continuously in the closed loop system. The heat gained from the soil as a result of the heat exchange of the antifreeze fluid is increased by heat pumps and used in the heating processes of the buildings. In a closed loop system, the pipes are laid horizontally to a depth of 1 - 2 meters or vertically up to a depth of 100 meters, depending on the convenience of the application area and the purpose of heating/cooling. In the open loop system, which is observed to be less, the heat energy is taken directly from the groundwater, lake or river by means of pipes placed in the borehole, which is pumped and transferred to the heat exchanger and then to the heat

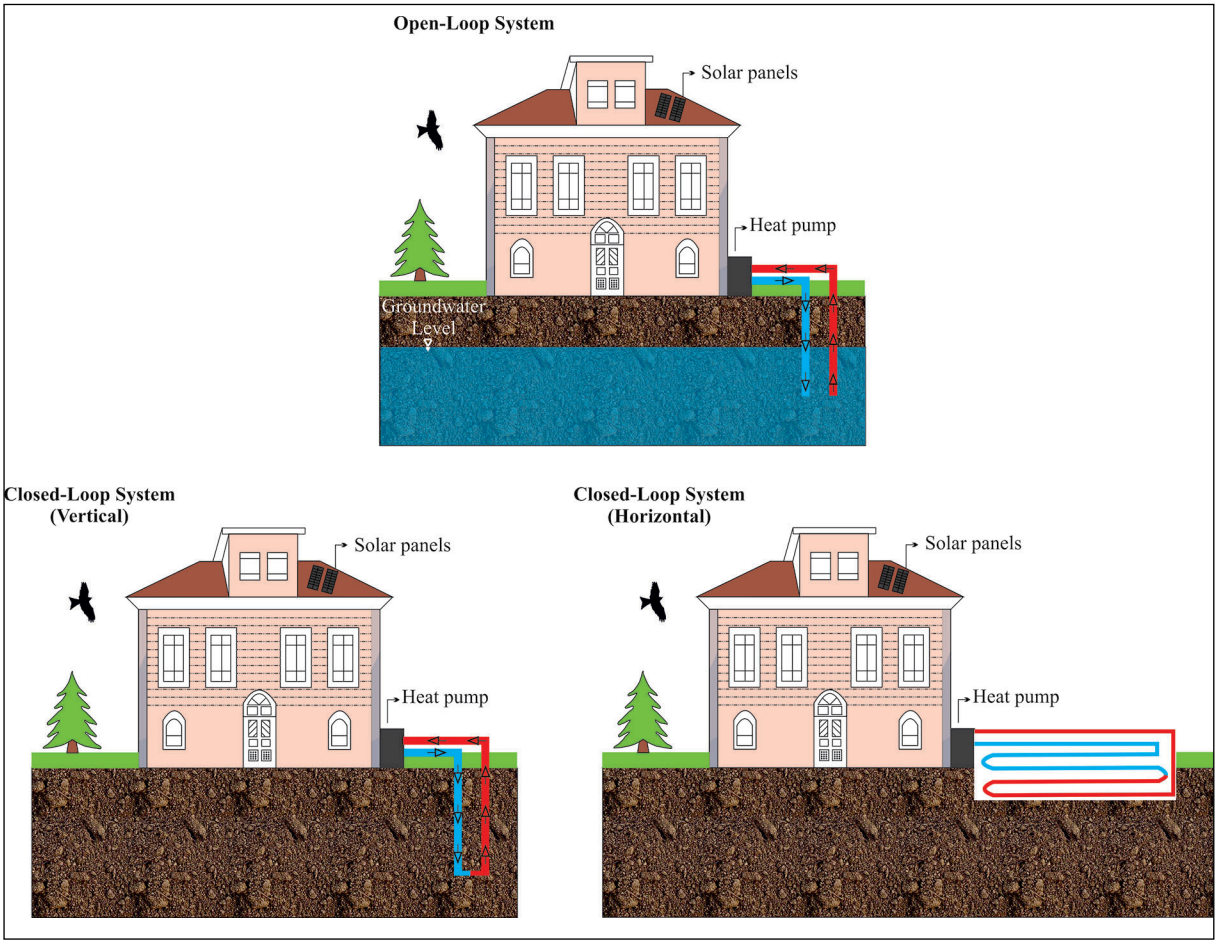

Figure 6- Schematic representation of shallow geothermal systems.

pump. In other words; the open - loops are systems in which the water to be used in heating and cooling is drawn from groundwater or water bodies such as lakes/rivers by pumping through the borehole. In an open loop system, water circulates between two or more groundwater wells. After this water is drawn from underground and used for heating/cooling, it is injected back into the same aquifer or any water body (lake, river, etc.) on the surface through a second borehole. When the required amount of water is extracted in the open loop system, the aquifer must have high permeability in order to minimize the drawdown (Rafferty, 2000; Sanner, 2001).

Coefficient of performance (*COP*) of the heat pump, which is an important factor in the system cost, is defined as the ratio of the energy obtained at the output of a heat pump system to the consumed electrical energy (Curtis et al., 2005). COP is calculated with the equation stated below.

$$COP = \frac{Q}{W}$$

Here Q: is the heat supplied or removed from the reservoir; W: is the work consumed by the heat pump. More clearly; this coefficient expresses the ratio between the electrical energy consumed by the system and the amount of heat it can produce. High COP value is preferred in heat pumps in order to lower system cost. For example, in a system with a COP value of 4, 4 units of heat are obtained for one unit of electrical energy consumed. COP varies depending on the thermal load, building type, temperature to be supplied, input water temperature, climatic conditions, size, material and type of heat exchanger (Sanner et al., 2003; Yalçın and Yetemen, 2009). Also; COP of the heat pump increases according to the temperature of the input water (Boyd and Lineau, 1995; Sanner et al., 2003). Therefore; high reservoir temperature will increase the COP value, which will reduce the system cost.

According to Allen et al. (2003), if a shallow geothermal system is used in a 1 - meter - thick gravel aquifer with 12°C groundwater temperature, an annual energy saving of 2 GWh is ensured. According to this study; a heat pump operated with a COP value of 4.5:1 in a well having a groundwater temperature of 12 °C and an efficiency of 20 l/s can generate 865 kW of heat. It has been stated that in Finland, where the annual average groundwater temperature varies between 3.5 and 6.6 °C (Mälkki and Soveri, 1986; Oikari, 1981), 55 to 60 MW energy can be provided for the need for heating through water - source heat pumps with a COP value of 3.5 (Arola et al., 2014). As stated in the previous section, Kütahya city center is a region where the urban heat island effect with a groundwater temperature difference of +1.63 °C between rural areas and urban areas is observed. Increasing groundwater temperatures in the city center of Kütahya due to the effect of the urban heat island, an annual average groundwater temperature of 13.02 °C and soil temperature of 13.68 °C according to the last 10 years' data, groundwater - carrying aquifers being located in shallow depths and the groundwater level being close to the surface are the factors that increase the applicability of shallow geothermal systems in Kütahya city center. In this sense, when the data obtained within the scope of the study are compared with the results of previous studies (Allen et al., 2003; Arola et al., 2014; Zhu et al., 2010), a very promising picture emerges at the point of installation of both open and closed shallow geothermal systems in Kütahya.

6. Energy Potential of Alluvial Aquifer in Kütahya City Center

The use of heat energy in shallow aquifers in residential heating and/or cooling processes through shallow geothermal systems has become increasingly widespread especially in Europe in recent years. Increasing groundwater and soil temperatures due to urban heat island effect, enables the use of shallow aquifers as geothermal reservoirs, and this heat is used in residential heating through shallow geothermal systems. Therefore; the theoretical heat capacity of the alluvial aquifer carrying groundwater in the city center of Kütahya is calculated using the data in Table 4 through the following equation after Balke (1977).

$$Q = Qw + Qs = V\ n\ Cw\ \Delta T + V\ (1 - n) Cs\ \Delta T$$

Here Q (kJ) is the theoretical total heat content of the aquifer, V (m^3) is the aquifer volume, n is the porosity, C_w and C_s ($kJm^{-3}K^{-1}$) are the theoretical heat content stored in the groundwater and soil, Q_w and Q_s (kJ) are the heat stored in groundwater and in the ground. According to the VDI 4640/1 (2010) guide published by The Association of German Engineers (Verein Deutscher Ingenieure, VDI), the C_w value for

Table 4- Calculation of the heat content in alluvial aquifer in Kütahya province.

Parameteres	Lowest	Highest	Average
Aquifer thickness (m)	10	64	28
Aquifer volume, V (m^3)	2.87×10^9		
Porosity, n	0.42	0.52	0.47
Volumetric heat capacity of water, C_w (kJ m^{-3} K^{-1})*	4.150		
Potential heat of groundwater, Q_w (kJ K^{-1})	1×10^{13}	3.72×10^{13}	2.24×10^{13}
Volumetric heat capacity of the ground, C_s (kJ m^{-3} K^{-1})	1.934	2.216	2.075
Potential heat of the ground, Q_s (kJ K^{-1})	6.44×10^{12}	1.83×10^{13}	1.26×10^{13}
Temperature difference, ΔT (°C)	2	6	4
Heat potential underground (kJ)	1.64×10^{13}	5.55×10^{13}	3.50×10^{13}

* Based on recommended value in VDI 4640/1 (2000) manual.

water is 4.150 $kJm^{-3}K^{-1}$. C_s value changes depending on the sediment type, and according to the results obtained from the experiments carried out in the laboratories of Turin Technical University (POLITO); it varies between 1.934 and 2.216 $kJm^{-3}K^{-1}$ in Kütahya city center. ΔT is the temperature decrease observed throughout the aquifer, ranging between 2 and 6 °C. Care has been taken to ensure that the ΔT values selected here are within the limits specified in the VDI 4640/4 (2004) manual published by The Association of German Engineers (Verein Deutscher Ingenieure, VDI). The thickness of the alluvial aquifer has been determined by using many borehole data obtained until today by The State Hydraulic Works (DSİ) and private engineering bureaus, and it varies between 10 and 64 m in Kütahya. Another parameter, the volume of the alluvial aquifer in the study area was calculated using the obtained borehole data using *Surfer 14 (Golden Software, LLC, 2017)* and *ArcMap 10.7 (ESRI, 2019)* software.

Based on the results obtained, alluvial aquifers in the city center of Kütahya theoretically have a serious heat potential between $1{,}64\times10^{13}$ kJ K^{-1} and $5{,}55\times10^{13}$ kJ K^{-1}, on average $3{,}50\times10^{13}$ kJ K^{-1}. It is predicted that the aquifer efficiency of this heat in the alluvium aquifer can be used in the heating processes of residential and/or commercial buildings after the factors such as hydraulic conductivity of the aquifer, annual groundwater budget, heat transfer models and its suitability in terms of shallow geothermal systems are fully revealed. It is predicted that a significant contribution to the environmental health can be made with reduction of fossil fuel consumption by uncovering this "hidden treasure", untouched until today, with the help of shallow geothermal systems, and to the national economy with the decrease in the amount of energy imported and returning to our renewable own resources.

7. Discussion

In various studies examining the effects of the urban heat island effect on the underground and its environment (Taniguchi et al., 1999; Changnon, 1999; Ferguson and Woodbury, 2004; Taniguchi, 2006, 2007), it has been proven that this effect has a strong effect on the ground temperature. In this study, using the groundwater temperature values measured for a year, the urban heat island effect in the city center of DSİT has been revealed. In the urban heat island maps created, it was clearly observed that the groundwater temperature values in Kütahya has increased towards urban and industrial areas.

The groundwater, whose temperature increases as a result of the urban heat island effect, can be used in the heating/cooling needs of the houses with shallow geothermal systems. These systems have been widespread in Europe since the early 2000s and have become increasingly popular. Based on the European Geothermal Congress report published by Sanner (2019) in 2019, there are approximately 1.9 million shallow geothermal systems currently in use in Europe. Based on the same report, shallow geothermal energy constitutes 66.5% of geothermal use in Europe and the energy obtained in European countries with these systems has reached a total capacity of 26,900 MWth (megawatt thermal) (Sanner, 2019). However, the fact that shallow geothermal energy systems are still not widespread in our country stands out as a

serious deficiency in this area. For this reason, within the scope of the study, it was aimed to determine the existence of the urban heat island effect in the city center of Kütahya, and therefore the temperature increase in aquifers located at shallow depths. As a result of the heat island maps created based on groundwater temperature measurements, the existence of the urban heat island effect in Kütahya city center was determined. Then, the heat potential of the alluvial aquifer whose temperature increased with the effect of the urban heat island was obtained. Based on the results, it has been revealed that this aquifer theoretically has an average heat potential of 3.50×10^{13} kJ K^{-1}. This result shows that large amounts of thermal energy are stored in city centers with high population density. In the study carried out by Zhu et al. (2010) in Cologne (Germany) and Winnipeg (Canada), this value is 2.90×10^{13} kJ for Cologne and 4.10×10^{13} kJ for Winnipeg. The researcher pointed out that this energy is a large amount corresponding to 2.5 times the annual heating need of the city of Cologne. The potential energy calculated in the alluvial aquifer in Kütahya city center is 1.2 times the energy in the city of Cologne. Bayer et al. (2019) divided the shallow geothermal potential of a city/region into three categories: "theoretical potential", "technical potential" and "economic potential". According to the researcher, the total physically energy available underground refers to the "theoretical potential". The next subcategory, the "technical potential", is the poriton of the theoretical potential that can be harnessed by available technologies. As only part of the technically extractable energy is economically reasonable, this other fraction is defined as "economic potential". The energy calculated within the scope of this study represents the theoretical potential.

Groundwater temperatures obtained within the scope of the study and soil temperature values obtained from Kütahya Meteorology Station are suitable values for the shallow geothermal system. Uncovering this hidden treasure located in the shallow depths of the ground is very important for both Kütahya and the economy of Turkey, where fossil fuel consumption and energy imports are high.

From now on, it is thought that the shallow geothermal energy potential of Kütahya should be determined theoretically and mapped on the basis of urban, industrial and rural regions by including other aquifers located at shallow depths under the alluvial aquifer. Urban heat island maps and heat potential calculations of aquifers can provide important data in assessing the applicability of shallow geothermal systems in the city center of Kütahya and/or throughout the country in the future. Depending on the geological, hydrogeological and areal conditions, open or closed systems may be preferred from shallow geothermal systems and some of the heating need of the city can be met with these systems. Thus, a contribution to the national economy by a national renewable energy resource and as well to environmental health by reducing fossil fuel consumption.

8. Results

In the city center of Kütahya, where the groundwater temperature distribution varies depending on the regions due to urbanization and industrialization, groundwater temperature anomalies show a clear increase towards the city center. In rural areas where the effect of man - made factors on groundwater temperature is minimal, groundwater temperature values are lower than in urban areas. In regions where urbanization and other man - made factors are intense, it has been observed that groundwater temperature values are 1.63 °C higher than rural areas. In this sense, the study results are consistent with previous studies focused on the urban heat island effect. The main reason for this situation is the intense construction in the city center, lack of green areas, underground car parks, closed surfaces that do not take air, sewage systems, thermal energy that has accumulated for years and still continues to accumulate due to the effects of the heat spread from the floor of the buildings to the underground. When the annual air temperature and the annual groundwater temperature values are compared, it was observed that these two parameters are related and that the air temperature controls the underground temperature.

The heat potential of the alluvial aquifer under the city center of Kütahya has been calculated numerically and it has been revealed that this aquifer theoretically has at least 1.64×10^{13} kJ K^{-1}, maximum 5.55×10^{13} kJ K^{-1}, average 3.50×10^{13} kJ K^{-1} heat potential.

When the temperature anomalies in the urban area are examined, it has been observed that the groundwater temperature in the urban area varies more than in the rural areas. In other words; while

the groundwater temperature in a rural area does not vary much in a well compared to another well, in an urban area, these values vary more from well to well. It is thought that this situation is caused by the size of the spaces between the buildings in the city center. While some buildings are built very closely to each other in the city center, other buildings have much more space between them. In urban areas where sparse distribution is observed, empty spaces between buildings consist of green areas or natural areas with soil surfaces. This causes the groundwater temperature to vary by area. From this situation, it can be concluded that groundwater temperature shows a homogeneous distribution in rural areas and a heterogeneous distribution in urban areas.

Except for the city center, groundwater temperature values are higher in industrial areas than in rural areas. It is thought that there may be hot wastewater discharge into the aquifer by the factories and this discharge may increase the groundwater temperature in addition to the factory structuring.

It has been proven that the urban heat island effect has an effect not only on the air temperature values but also on the underground and its surroundings. As a result of the thermal energy that man - made structures confine and spread to the underground, the groundwater and soil temperature values change and the urban heat island effect emerges.

Groundwater temperature values measured in the city center of Kütahya vary between 7.60 °C and 17.55 °C throughout the year when all rural and urban areas are included, and the annual average groundwater temperature is 13.02 °C. These are very promising values regarding the shallow geothermal system in Kütahya. But; the temperature values alone are not sufficient for the applicability of the system. In order to fully reveal the suitability of the system, factors such as aquifer efficiency, hydraulic conductivity of the aquifer, annual groundwater budget must also be determined. In addition, in case the system is implemented, it is very important to create heat transfer models that will occur within and between aquifers, system health and observing the thermal effect/pollution that may occur in aquifers over time, thus assessing the sustainability of the system.

Considering the urbanization rate and accordingly increasing need for energy whether in Kütahya or in Turkey, the dissemination of renewable energy sources such as shallow geothermal energy is very important for the national economy and environmental health. It is expected that the use of such renewable resources will play an important role in increasing the domestic energy potential and reducing the foreign dependence on energy.

Acknowledgments

We would like to thank Dr. Alessandro Casasso, who let us to use the Politecnico di Torino (POLITO) laboratories for thermal analysis within the scope of the study, Kütahya Meteorology Directorate for their support in providing some of the data used in the study, Geophysical Engineer Serkan Azdiken and Geological Senior Engineer Turgay Eser to the 3rd Regional Directorate of State Hydraulic Works (DSİ) and Zemin Mühendislik Company (Kütahya).

References

Allen, A., Milenic, D., Sikora, P. 2003. Shallow gravel aquifers and the urban 'heat island' effect: a source of low enthalpy geothermal energy. Geothermics 32, 569-578.

Ampofo, F., Maidment, G. G., Missenden, J. F. 2004. Underground railway environment in the UK Part 2: investigation of heat load. Applied Thermal Engineering 24, 633-645.

Arola, T., Korkka-Niemi, K. 2014. The effect of urban heat islands on geothermal potential: examples from Quaternary aquifers in Finland. Hydrogeology Journal 22, 1953-1967.

Aye, L., Charters, W. W. S. 2003. Electrical and engine-driven heat pumps for effective utilisation of renewable energy resources. Applied Thermal Engineering 23, 1295-1300.

Balke, K. D. 1977. Das Grundwasser als Energieträger. Brennstoff - Wärme - Kraft 29, 191-194.

Banks, D. 2010. An introduction to thermogeology: ground source heating and cooling. Blackwell, Oxford.

Bayer, P., Attard, G., Blum, P., Menberg, K. 2019. The geothermal potential of cities. Renewable and Sustainable Energy Reviews 106, 17-30.

Boyd, L. T., Lienau, P. J. 1995. Geothermal heat pump performance. Geothermal Resources Council Annual 1995, 8-11 October, Reno, NV, USA.

Casasso, A., Pestotnik, S., Rajver, D., Jez, J., Prestor, J., Sethi, R. 2017. Assessment and mapping of the closed-loop shallow geothermal potential of Cerkno (Slovenia). Energy Procedia 125, 335-344.

Changnon, S. A. 1999. A rare long record of deep soil temperatures defines temporal temperature changes and an urban heat island, Climatic Change 42, 531- 538.

Curtis, R., Lund, J., Banner, B., Rybach, L., Hellstrom, G. 2005. Ground source heat pumps - geothermal energy for anyone, anywhere: current worldwide activity. Proceedings of the World Geothermal Congress-2005, 24-29 April 2005, Antalya, Turkey.

Devlet Su İşleri Genel Müdürlüğü (DSİ), 2003. Kütahya Ovası Karst Hidrojeolojisi Ara Raporu.

EGEC, 2018. 2018 EGEC Geothermal Market Report. Dumas, P., Garabetian, T., Serrano, C., Pinzuti, V. (editors). European Geothermal Energy Council (EGEC), Brussels.

ESRI, 2019. ArcGIS Desktop 10.7. Redlands, CA: Environmental Systems Research Institute.

Ezber, Y., Sen, O.L., Kindap, T., Karaca, M. 2007. Climatic effects of urbanization in Istanbul: a statistical and modeling analysis. International Journal of Climatology 27, 667-679.

Ferguson, G., Woodbury, A. D. 2004. Subsurface heat flow in an urban environment, Journal of Geophysical Research 109, B02402, doi:10.1029/2003JB002715.

Ferguson, G., Woodbury, A. D. 2007. Urban heat island in the subsurface. Geophysical Research Letters 34 (23).

Francisco, Pinto, J., Carrilho, da Graça, G. 2018. Comparison between geothermal district heating and deep energy refurbishment of residential building districts. Sustainable Cities and Society 38, 309-324.

Gallo, K. P., Owen, T. P. 1999. Satellite-based adjustments for the urban heat island bias. Journal of Applied Meteorology and Climatology 38, 806-813.

Howard, L. 1883. Climate of London. 3rd Edition, Harvey and Darton, London.

Huang, S. 2012. Geothermal energy in China. Nature Climate Change 2, 557-560.

Huang, S., Taniguchi, M., Yamano, M., Wang, C. 2009. Detecting urbanization effects on surface and subsurface thermal environment - a case study of Osaka. Science of the Total Environment 407, 3142-3152.

Karaca, M., Anteplioğlu, U., Karsan, H. 1995. Detection of urban heat island in İstanbul, Turkey. Nuovo Cimento 18C (N1), 49-55.

Kataoka, K., Matsumoto, F., Ichinose, T. , Taniguchi, M. 2009. Urban warming trends in several large Asian cities over the last 100 years. Science of the Total Environment 407, 3112-3119.

Kerl, M., Runge, N., Tauchmann, H., Goldscheider, N. 2012. Hydrogeologisches Konzeptmodell von München: Grundlage für die thermische Grundwassernutzung (Conceptual hydrogeological model of the City of Munich, Germany, as a basis for geothermal groundwater utilisation). Grundwasser 17, 127-135.

Klysik, K., Fortuniak, K. 1999. Temporal and spatial characteristics of the urban heat island of Lodz, Poland. Atmospheric Environment 33, 3885-3995.

Krarti, M., Lopez-Alonzo, C., Claridge, D. E., Kreider, J. F. 1995. Analytical model to predict annual soil surface temperature variation. Journal of Solar Energy Engineering 117, 91-99.

Kottmeier, C., Bieger,t C., Corsmeier, U. 2007. Effects of urban land use on surface temperature in Berlin. Journal of Urban Planning and Development 133, 128-137.

Köppen, W., Geiger, R. 1954. Klima der erde (Climate of the earth). Wall Map 1:16 Mill. Klett-Perthes, Gotha.

Kütahya Meteoroloji Müdürlüğü. 1970-2019 yılları arasında Kütahya Meteoroloji İstasyonu'ndan ölçülen Kütahya ili şehir merkezine ait aylık/yıllık hava sıcaklığı, 100 cm toprak sıcaklığı değerleri.

Landsberg, H. 1956. The climate of towns. In Man's Role in Changing the Face of the Earth, Edited by W. L. Thomas Jr., pp. 584-603, University of Chicago Press, Chicago, III.

Landsberg, H. E. 1981. The urban climate. Academic Press, New York.

Lee, J. S., Kim, H. C., Im, S. Y. 2017. Comparative analysis between district heating and geothermal heat pump system. Energy Procedia 116, 403-406.

Mälkki, E., Soveri, J. 1986. Pohjavesi (Groundwater). In: Mustonen S (ed) Sovellettu hydrologia (Applied hydrology). Vesiyhdistys ry (Water Association). Mäntän kirjapaino (Mäntän printing house), Mänttä.

Menberg, K., Bayer, P., Zosseder, K., Rumohr, S., Blum, P. 2013*a*. Subsurface urban heat islands in German cities. Science of the Total Environment 442, 123-133.

Menberg, K., Blum, P., Schaffitel A., Bayer, A. 2013*b*. Long-term evolution of anthropogenic heat fluxes into a subsurface urban heat island. Environmental Science and Technology 47, 9747-9455.

Montavez, J. P, Rodriguez, A., Himenez, J. I. 2000. A study of the urban heat island of Granada. International Journal of Climatalogy 20, 899-911.

Murtha, G. G., Williams, J. 1986. Measurement, prediction and interpolation of soil temperature for use in soil taxonomy: Tropical Australian experience, Geoderma 37, 189-206.

Nitoiu, D., Beltrami, H. 2005. Subsurface thermal effects of land use changes. Journal of Geophysical Research 110, F01005, doi:10.1029/2004JF000151.

Oikari, H. 1981. Pohjaveden lämpötila Etelä - ja Keski-Suomessa vuosina 1975-1978 (Groundwater temperature in southern and central Finland in 1975 - 1978). Vesihallituksen lähde-ja pohjavesiputkihavaintoihin perustuva selvitys (Report based on the Water Board's spring and groundwater pipe observations), Pro gradu-tutkielma (Master's thesis). Maantieteen Laitos (Department of Geography), Luonnonmaantiede (Natural Geography), Helsingin Yliopisto (University of Helsinki), Helsinki, 65.

Oke, T. R. 1973. City size and the urban heat island. Atmospheric Environment 7, 769- 779.

Oke, T. R. 1987. Boundary layer climates. Routhledge, London.

Oke, T. R. 1988. The urban energy balance. Progress Physical Geography 12, 471-508.

Özburan, M. 2009. Kütahya ve çevresinin neotektonik incelenmesi. Doktora Tezi, Kocaeli Üniversitesi Fen Bilimleri Enstitüsü, 227.

Perrier, F., Le Mouel, J.L., Poirier, J.P., Shnirman, M.G. 2005. Long-term climate change and surface versus underground temperature measurements in Paris. International Journal of Climatology 25**,** 1619-1631.

Pinho, O. S., Manso Orgaz, M. D. 2000. The urban heat island in a small city in coastal Portugal. International Journal of Biometeorology 44, 198-203.

Pollack, H. N., Huang, S. P., Shen, P. Y. 1998. Climate change record in subsurface temperatures: a global perspective. Science 282, 279-281.

Pophillat, W., Bayer, P., Teyssier, E., Blum, P., Attard, G. 2020. Impact of groundwater heat pump systems on subsurface temperature under variable advection, conduction and dispersion. Geothermics 83.

Popiel, C. O., Wojtkowiak, J., Biernacka, B. 2001. Measurements of temperature distribution in ground. Experimental Thermal and Fluid Science 25, 301-309.

Rafferty, K. 2000. Scaling in geothermal heat pump systems. Geo - Heat Center Quart Bull. 21(1), 11-15.

Rees, S. 2016. Advances in ground - source heat pump systems. Amsterdam: Woodhead Publishing.

Reiter, M. 2006. Vadose zone temperature measurements at a site in the northern Albuquerque Basin indicate ground-surface warming due to urbanization, Environmental and Engineering Geoscience 12, 353-360.

Rybach, L., Sanner, B. 2000. Ground - source heat pump systems: the European experience. Geo-Heat Center Quart Bull 21(1), 16-26.

Sanner, B. 2019. Summary of EGC 2019 Country Update Reports on Geothermal Energy in Europe, European Geothermal Congress 11-14 June 2019, Den Haag, The Netherlands.

Sanner, B. 2001. Shallow geothermal energy. Geo-Heat Center Quart Bull 22(2), 19-25.

Sanner, B., Karytsas, C., Mendrinos, D., Rybach, L. 2003. Current status of ground source heat pumps and underground thermal energy storage in Europe. Geothermics 32, 579-588.

Soltani, M., Kashkooli, F. M., Dehghani-Sanij, A. R., Kazemi, A. R., Bordbar, N., Farschi, M. J., Elmi, M., Gharali, K., Dusseault, M. B. 2019. A comprehensive study of geothermal heating and cooling systems. Sustainable Cities and Society 44, 793-818.

Spronken-Smith, R. A., Oke, T. R. 1999. The thermal regime of urban parks in two cities with different summer climates. International Journal of Remote Sensing 19, 2085- 2104.

Stauffer, F., Bayer, P., Blum, P., Giraldo, N. M., Kinzelbach, W. 2013. Thermal use of shallow groundwater. CRC Press.

Taniguchi, M. 2006. Anthropogenic effects on subsurface temperature in Bangkok. Climate of Past Discussions 2, 831-846.

Taniguchi, M., Uemura, T. 2005. Effects of urbanization and groundwater flow on the subsurface temperature in Osaka, Japan. Physics of the Earth and Planetary Interiors 305-313.

Taniguchi, M., Shimada J., Tanaka, T., Kayane, I., Sakura, Y., Shimano, Y., Kawashima, S. 1999. Disturbances of temperature-depth profiles due to climate change and subsurface water flow: 1. An effect of linear increase in surface temperature caused by global warming and urbanization in the Tokyo metropolitan area, Water Resour. Res. 35, 137-152.

Taniguchi, M., Uemura, T., Jago-on, K. 2007. Combined effects of urbanization and global warming on

subsurface temperature in four Asian cities, Vadose Zone Journal 6, 591-596.

Taniguchi, M., Shimada, J., Fukuda, Y., Yamano, M., Onodera, S., Kaneko, S., Yoshikoshi, A. 2009. Anthropogenic effects on the subsurface thermal and groundwater environments in Osaka, Japan and Bangkok, Thailand. Science of Total Environment 407, 3153-3164.

Türkiye İstatistik Kurumu (TÜİK), 2019. İl ve ilçelere göre il/ilçe merkezi, belde/köy nüfusu ve yıllık nüfus artış hızı verileri.

VDI (Verein Deutscher Igneieure), 2004. VDI 4640/4 Thermal Use of the Underground-Direct Uses.

VDI (Verein Deutscher Igneieure), 2010. VDI 4640 Thermal Use of Underground, Blatt 1: Fundamentals, Approvals, Environmental Aspects.

Yalçın, T., Yetemen, O. 2009. Local warming of groundwaters caused by the urban heat island effect in İstanbul, Turkey. Hydrogeology Journal 17, 1247-1255.

Zhu, K., Blum, P, Ferguson, G., Balke, K-D., Bayer, P. 2010. The geothermal potential of urban heat islands. Environmental Research Letters 5, 6.

Bulletin of the Mineral Research and Exploration

http://bulletin.mta.gov.tr

Beneficiation and flowsheet development of a low grade iron ore: A case study

Özgür ÖZCAN[a*], Ahad AGHLMANDI HARZANAGH[a], Eren Caner ORHAN[a] and Şevket Levent ERGÜN[a]

[a] *Hacettepe University, Faculty of Engineering, Mining Engineering, Ankara, Turkey*

Research Article

Keywords:
Low grade iron ore, Gravity concentration, Magnetic separation, Flowsheet development.

ABSTRACT

In the present study a detailed characterization followed by beneficiation of low grade iron ore was studied. The Run of Mine (R.O.M) sample assayed 21.91 % Fe, which is very low grade in nature. The impurities are SiO_2 26.25%, MgO 20.48%, CaO 5.85%, Al_2O_3 1.86% and loss on ignition (LOI) 12.71%. A Davis Tube test was performed for the assessment of the separability of magnetic ores by low intensity magnetic separators. The heavy liquid test was carried out to evaluate the possible response of the sample by the gravity concentration technique. The samples were subjected to jigging, dry low intensity magnetic separation (DLIMS) and shaking table tests. Thus a sufficient concentrate could not be obtained in +1 mm by using jigging and DLIMS. The obtained results show that the a high grade iron concentrate (>65% Fe) with lower recoveries was obtained from shaking table tests by using -1 mm fraction. According to the results a flowsheet was developed. From the developed flowsheet, it is possible to obtain pellet grade concentrate with 65.41% Fe, 2.54% SiO_2, 2.79% MgO, 0.70% CaO and 0.32% Al_2O_3. with 21.42% weight recovery. The overall gangue rejection recovery of the circuit is over 95%.

Received Date: 16.06.2020
Accepted Date: 28.11.2020

1. Introduction

Basic raw material for iron and steel industry is iron ore which leads to world growing economy. With increasing global demand of iron ores due to the huge requirement of steel all over the world, countries have increased their production by initiating steps to utilize the low - grade iron ores, fines and slimes. Upgrading these low grade ores is becoming an attractive proposition today.

The high grade iron ore is depleting due to the increasing global demand of iron. In Turkey, a substantial quantity of low grade iron ore deposits is present. Hence, to increase the iron ore resources to meet the ever increasing demand of iron and steel, the use of the abundant low grade iron ore is inevitable.

Processing of iron ores generally depend on the size and the nature of impurities present in the ore body. Depending upon the origin and mineralogical characteristics of the ore, different beneficiation methods are being adopted for iron ore from simple crushing and screening to complex concentration processes (Singh and Mehrotra, 2007; Rath and Singh, 2007; Rath et al., 2010; Jyoti et al., 2010; Gundewar, 2011; Özcan and Çelik, 2016; Das and Sarkar, 2018). Therefore, it is essential to identify suitable beneficiation methods and develop flowsheets for different origin iron ores.

The most commonly used beneficiation methods for iron ores are the gravity and magnetic separation techniques (Seifelnassr et al., 2012; Wills and Finch, 2016). In addition to this, a lot of developments in

Citation Info: Özcan, Ö., Aghlmandi Harzanagh, A., Orhan, E. C., Ergün, Ş. L. 2021. Beneficiation and flowsheet development of a low grade iron ore: A case study. Bulletin of the Mineral Research and Exploration 165, 235-251. https://doi.org/10.19111/bulletinofmre.834182

**Corresponding author: Özgür ÖZCAN, ozgurozcan@hacettepe.edu.tr*

iron ore processing have been taken place in recent years. The emphasis was on the development of a cost effective flowsheet to beneficiate the low - grade iron ores to produce concentrates suitable for blast furnace, sinter or pellet making. Some of the development features in the processing side are jigging, innovations in spiral concentrator, autogenous grinding, column flotation, high gradient magnetic separators (HGMS), fine screening, shaking table separation etc. (Rath et al., 2013). Physicochemical method i.e. agglomeration and selective flocculation has been taken for further utilization of the tailings and slimes (Panda et al., 2017).

Normally iron ores with 65 % Fe content and above are desirable to achieve better productivity either through blast furnace or direct reduction for the metal iron production. Iron ore with low Fe content and high Al:Si ratio cannot be used directly in any of the processes. The alumina to silica ratio that is typically greater than one possesses serious operational problems during sintering and subsequent smelting in the blast furnace (Srivastava et al., 2001; Muwanguzi et al., 2012). This has been mainly due to the presence of high levels of impurities such as silica and alumina in the raw materials (Dwari et al., 2014). Therefore, research on beneficiation and utilization of low grade iron ore to produce quality raw material is highly essential.

Iron ores usually contain a huge amount of silicates and its presence has been found to have a negative effect on the quality of the iron and also it complicates the process for the production of iron. Thus, it is important that the silicate content of the enriched iron mineral can be reduced as much as possible (Rath et al., 2013).

Detailed initial characterization of the samples were required before developing a suitable beneficiation flowsheet. Limited studies have been carried out based on earlier experience to develop conceptual flowsheet.

In the present work, an iron ore sample which has very low iron grade and high silica content was taken up for detailed material characterization and subsequent physical beneficiation studies. Iron ore is processed for production of a concentrate of an economic grade and recovery suitable for the sinter/ pellet. Different physical beneficiation methods were performed to ore in different size fractions. Effect of particle size and operational parameters on the performance was also evaluated.

2. Raw Material

The low - grade iron ore sample was taken from an iron ore mine, in Central Anatolia Region, Turkey. The representative samples were obtained from the open pit mine area (Figure 1). Approximately 10 tons of mine excavated and crushed down to 6 mm in the plant crushing circuit. Then, representative sample were transported to laboratory to perform detailed characterization and beneficiation tests.

3. Material Characterization and Previous Tests

The as - received iron ore sample was subjected to material characterization in terms of particle size analysis, XRD analysis, size wise chemical analysis. In addition, Davis tube test and heavy liquid test for were performed to evaluate the behavior of iron ore sample in magnetic separation, jigging and shaking table. These steps are described in detail in the following sections and corresponding observations are presented. A simplified flowsheet of experimental procedure is shown in Figure 2.

3.1. Particle Size Analysis

The particle size distribution of the iron ore was determined by using the Vibratory Laboratory Sieve Shaker (RETSCH AS 200 basic). According to results, the 80% of the sample (d_{80}) is finer than 3.44 mm and the d_{50} value is 1.64 mm. Particle size distribution of iron ore sample is represented in Figure 3.

3.2. Qualitative Mineralogical Analysis and Ore Microscopy

Qualitative mineralogical analysis of the ore sample was performed to identify its mineralogical composition and textural properties. Qualitatively, the iron ore sample revealed a mineralogy composed carbonate minerals, mica minerals, silicate minerals, opaque minerals and trace amount of sphen.

Microscopic analysis was performed to identify the ore minerals in the sample. Analysis was performed by using optical microscope and thin sections of the representative ore sample. Analysis results was revealed that the ore contains mainly magnetite, minor amount of limonite, chromite, pyrite and trace amount of hematite as ore minerals.

Figure 1- Excavation of iron ore sample from open pit area.

3.3. Chemical Analysis

Chemical analysis of samples was conducted by using XRF method. Size wise chemical analysis of iron ore sample is presented in Table 1. The sample contains 21.91 % Fe, which is very low grade in nature. The impurities are SiO_2 26.25%, MgO 20.48%, CaO 5.85%, Al_2O_3 1.86% and loss on ignition (LOI) 12.71%.

It can be observed from Table 1 that the main impurities are silica and magnesia in the ore. According to results, total iron and silica grades of size fractions are close to each other. Increase in fineness increases the total iron grade and decreases the silica grade marginally. The finest size fraction of feed has the highest total iron grade. From the Table 1 and size - analysis data, it can be found that +0.212 mm fraction contains more than 80% of total iron and 85% of silica and magnesia All impurities are concentrated in the coarser size fractions. This ore cannot be used either in blast furnace or sponge iron making without a physical beneficiation.

3.4. Davis Tube Tests

A Davis tube (DT) is a laboratory instrument designed to separate small samples of magnetic ores into strongly magnetic and weakly magnetic fractions. It has become standard laboratory equipment used for the assessment of the separability of magnetic ores by low - intensity magnetic separators (Schulz, 1964; Svoboda, 1987). The Davis tube comprises a 25 mm glass tube that is gyrated at an angle between the poles of a high - intensity electromagnet. The magnetic intensity between the poles is controlled by means of an adjustable autotransformer. The tube is gyrated between the poles in a reciprocating motion at a frequency controlled by an adjustable driving motor.

A number of tests were conducted to determine the impact of magnetic field strength and effect of particle size. Tests at 425, 600, and 732 Gauss were conducted for a grinding size of -500 µm, -300 µm, -150 µm, -75 µm and -45 µm separately. The pulp sample is fed to the top of the Davis tube after which the oscillation motor and wash water are turned on.

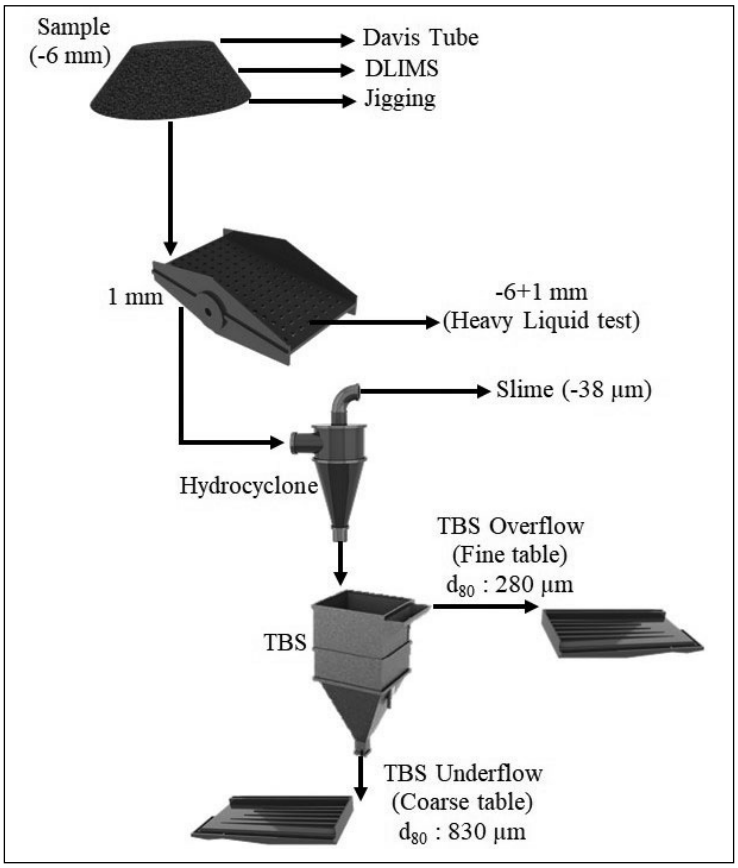

Figure 2- Simplified flowsheet of test procedure.

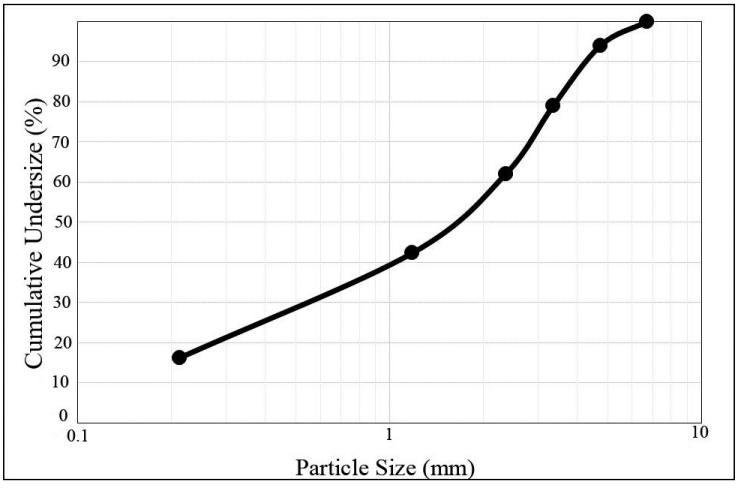

Figure 3- Particle size distribution of iron ore sample.

Nonmagnetic sample collection then commences from the tube outlet. The magnetic concentrate is removed from the tube at the end of each test by turning off the current to the magnets. Chemical analysis of the feed, magnetic and non - magnetic samples of each test was performed. Effect of magnetic field strength and particle size on the total iron grade of magnetic samples are shown in Figure 4.

Davis tube test results revealed that total iron grade of magnetic product can be increased from 21.91% to 65.33% at -75 µm grinding size. Also,

Table 1- Fractional chemical analysis of iron ore sample.

		GRADE (%)					
Size fraction (mm)	Weight (%)	Fe	SiO_2	MgO	CaO	Al_2O_3	LOI
-6+3.35	21.00	22.30	26.40	20.60	5.91	1.18	12.88
-3.35+1.18	36.69	21.28	26.80	20.90	5.94	1.64	12.93
-1.18+0.212	26.06	20.27	26.70	20.70	5.87	2.56	13.04
-0.212	16.25	25.45	24.10	19.05	5.51	2.12	11.45
Feed	100.00	21.91	26.25	20.48	5.85	1.86	12.71
		DISTRIBUTION (%)					
Size fraction (mm)	Weight (%)	Fe	SiO_2	MgO	CaO	Al_2O_3	LOI
-6+3.35	21.00	21.37	21.12	21.12	21.23	13.31	-
-3.35+1.18	36.69	35.64	37.46	37.44	37.29	32.33	-
-1.18+0.212	26.06	24.11	26.50	26.33	26.17	35.84	-
-0.212	16.25	18.88	14.92	15.11	15.32	18.51	-
Feed	100.00	100.00	100.00	100.00	100.00	100.00	-

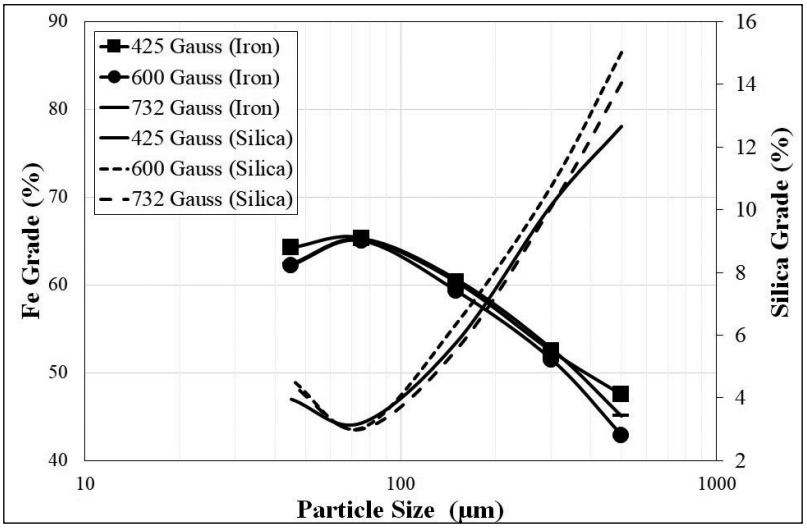

Figure 4- Effect of magnetic field strength and particle size on the total iron and silica grade of magnetic products.

silica grade of the magnetic product can be decreased from 26.25% to 3.20%. Increase in fineness increases the total iron grade of magnetic product significantly. However, magnetic strength field has a marginal effect on product quality. Liberation of iron ore particles is quite acceptable below 100 µm size fractions. According to Davis tube test results 26.33% of the feed material can be concentrated as a magnetic product with an 81.25% Fe recovery. Total iron content in the magnetic product decreasing from 65.33% Fe to 62% Fe with increasing fineness from -75 µm to -45 µm. As stated before, in this sample magnetite is the main iron - bearing phase. However, iron ore consists a portion of weakly magnetic minerals which are hematite and goethite. According to results, it can be concluded that the recovery of these weakly magnetic minerals decreases and can report to non - magnetic product at -45 µm size fraction. According to Davis tube test results the grades of the magnetic concentrates are quite acceptable between -100+45 µm. This may indicate that magnetite can be liberated from gangue sufficiently below 100 µm. It is indicating the suitability of the magnetic separation process only below 100 µm for the studied iron ore sample.

3.5. Heavy Liquid Test

Heavy liquid separation is also known as "sink and float separation" and commercial adaptations of the common laboratory procedure used for separating a mixture of two products having difference in specific gravity (Wills and Napier - Mun, 2006). Laboratory testing may be performed on ores to assess the suitability of dense medium separation (and other gravity methods) and to determine the economic separating density (Angadi et al., 2017). The sink and float studies of -6+1.18 mm fraction at two specific gravities viz. 2.85 g/cm^3, and 3.30 g/cm^3 were carried out to evaluate the liberation characteristics of iron and gangue particles in coarser size fractions.

Pure tungsten carbide and sodium polytungstate mixture was used to obtain high densities as described in the study of Aghlmandi (Aghlmandi et al., 2017). Then, sample was introduced into the liquid of highest density. The float product was removed and washed and placed in the liquid of next lower density. All the products were finally drained, washed, dried, weighed and analyzed, to assess the performance of the heavy liquid test. Results of heavy liquid test are tabulated in Table 2.

The high - weight percentage (89.03%) and low total iron grade of the float fractions (18.47%) of 3.30 g/cm^3 indicate the presence of liberated gangue in this density class. Approximately 95% of the silica can be rejected in float products. Even so, the silica grade of 3.30 g/cm^3 sink product is 11.20% SiO_2. This indicates that there is some locked gangue material associated with the sink product.

The results of the study at 3.30 g/cm^3 density indicated that a total iron of 47.46% Fe could be obtained at a recovery of 24.04%. Silica grade can be decreased from 26.65% SiO_2 to 11.20% SiO_2. However, total iron recovery in the sink product is quite low. Approximately 76% of the total iron rejects in the float products. The results obtained from the heavy liquid test indicate that the ore is not suitable for obtain a sinter/pellet grade concentrate in coarser size fractions. These results also show that liberation degree of +1 mm is quite insufficient. Coarse size gravity separation is not suitable for this ore.

4. Beneficiation Studies, Results and Discussion

It is evident from the detailed characterization of the low grade iron ore that liberation of the ore is insufficient in coarser size fractions (+1 mm). A high grade concentrate can be obtained below 75 μm with a low silica content. According to characterization, different beneficiation tests were designed and performed to obtain concentrates in different size fractions separately. Effect of operational parameters also evaluated.

4.1. Dry Low Intensity Magnetic Separation (DLIMS) Studies

It is well known from the characterization tests that liberation of the ore is insufficient in coarser size fractions. To obtain different concentrates, a number

Table 2- Heavy liquid test results.

		GRADE (%)				
Size fraction (mm)	Weight (%)	Fe	SiO_2	MgO	CaO	Al_2O_3
2.85 g/cm^3 Float	76.25	16.49	29.80	23.10	6.46	1.51
3.30 g/cm^3 Float	12.78	30.31	21.12	16.65	4.96	1.45
3.30 g/cm^3 Sink	10.97	47.46	11.20	9.56	3.37	1.21
Feed (-6+1.18 mm)	100.00	21.65	26.65	20.79	5.93	1.47
		DISTRIBUTION (%)				
Size fraction (mm)	Weight (%)	Fe	SiO_2	MgO	CaO	Al_2O_3
2.85 g/cm^3 Float	76.25	58.07	85.26	84.72	83.07	78.42
3.30 g/cm^3 Float	12.78	17.89	10.12	10.23	10.69	12.54
3.30 g/cm^3 Sink	10.97	24.04	4.61	5.04	6.23	9.04
Feed (-6+1.18 mm)	100.00	100.00	100.00	100.00	100.00	100.00

of tests were conducted with variable current by using -6 mm sample. In the experiments, the feed rate was kept constant to create a mono particle layer. While the current was set to obtain a clean tail, magnetic field variation (732, 885 and 1200 Gauss) was examined whether it has an effect on grade and recovery. Test results are tabulated in Table 3 and Table 4 for magnetic and non - magnetic products respectively.

It can be seen from Table 3 that total iron grade of the magnetic concentrates decreases with increasing magnetic field intensity. The high recovery of impurities is due to the fact that a large portion of the locked particles reported to the magnetic fraction. The obtained results show that the DLIMS of the -6 mm sample reveals poor separation performance as the magnetic products still has high silica content (>22%) and iron losses in the non - magnetic product. This may be related to the low degree of liberation. Thus, a sufficient concentrate could not be obtained in +1 mm by using DLIMS.

4.2. Jigging

A laboratory scale mineral jig fitted with screen was used for the jigging studies. The cross sectional area of the jig is 10.5x10.5 cm. It has constant stroke lengths with a hutch which convincingly maintains pulsation of water flow for effective separation of light and heavies. The effects of water velocity on jigging was studied by using -6 mm iron ore sample. Two jigging tests were carried out in a batch mode. Each test was performed for 15 minutes. The samples were collected after allowing the jig to stabilize for a period of 5 minutes. The jig pressure varied from 0.1 to 0.2 bar. The effect of pressure on concentrate weight, grade and recovery was evaluated. The concentrates and tailings in jigging operations were collected, dried, weighed and analyzed. The chemical analysis results are tabulated in Table 5 and Table 6 for 0.1 and 0.2 bar respectively.

Jigging results shows that a higher grade concentrate can be obtained by using higher pressure.

Table 3- Magnetic products of DLIMS test.

		GRADE (%)				
Magnetic Field (Gauss)	Weight (%)	Fe	SiO_2	MgO	CaO	Al_2O_3
732	58.57	30.29	22.37	18.54	4.00	1.18
885	68.77	28.11	23.56	19.08	4.33	1.28
1200	76.85	25.98	24.71	19.90	4.86	1.41
		RECOVERY (%)				
Magnetic Field (Gauss)	Weight (%)	Fe	SiO_2	MgO	CaO	Al_2O_3
732	58.57	80.97	49.91	53.00	40.04	37.27
885	68.77	88.25	61.71	64.04	50.98	47.21
1200	76.85	91.14	72.35	74.65	63.95	58.03

Table 4- Non-magnetic products of DLIMS test.

		GRADE (%)				
Magnetic Field (Gauss)	Weight (%)	Fe	SiO_2	MgO	CaO	Al_2O_3
732	41.43	10.06	31.74	23.24	8.46	2.82
885	31.23	8.24	32.19	23.59	9.18	3.15
1200	23.15	8.38	31.36	22.43	9.10	3.37
		RECOVERY (%)				
Magnetic Field (Gauss)	Weight (%)	Fe	SiO_2	MgO	CaO	Al_2O_3
732	41.43	19.03	50.09	47.00	59.96	62.73
885	31.23	11.75	38.29	35.96	49.02	52.79
1200	23.15	8.86	27.65	25.35	36.05	41.97

Table 5- Jigging results of 0.1 bar test condition.

		GRADE (%)				
Product	Weight (%)	Fe	SiO_2	MgO	CaO	Al_2O_3
Feed	100.00	21.91	26.25	20.48	5.85	1.86
Concentrate	33.59	27.38	22.7	18.15	5.38	1.74
Tail	66.41	19.14	28.05	21.66	6.08	1.92
		RECOVERY (%)				
Product	Weight (%)	Fe	SiO_2	MgO	CaO	Al_2O_3
Feed	100.00	100.00	100.00	100.00	100.00	100.00
Concentrate	33.59	41.98	29.05	29.76	30.92	31.40
Tail	66.41	58.02	70.95	70.24	69.08	68.60

Table 6- Jigging results of 0.2 bar test condition.

		GRADE (%)				
Product	Weight (%)	Fe	SiO_2	MgO	CaO	Al_2O_3
Feed	100.00	21.91	26.25	20.48	5.85	1.86
Concentrate	10.45	33.10	19.20	15.60	4.96	1.60
Tail	89.55	20.60	27.07	21.05	5.95	1.89
		RECOVERY (%)				
Product	Weight (%)	Fe	SiO2	MgO	CaO	Al_2O_3
Feed	100.00	100.00	100.00	100.00	100.00	100.00
Concentrate	10.45	15.78	7.64	7.95	8.86	8.98
Tail	89.55	84.22	92.36	92.05	91.14	91.02

It is possible to obtain an iron concentrate of 33.10% Fe with 15.78% recovery. The jig tail contains 20.60% Fe, which is quite high. Thus a sufficient concentrate could not be obtained in +1 mm by using jigging as predicted by the results of the sink - float tests. Jig tail samples of 0.1 bar and 0.2 bar test conditions were subjected to fractional chemical analysis to know the distribution of iron in the fractions (Table 7 and Table 8).

It is observed from Table 7 and Table 8 that total iron grades of size fractions are close to each other in both tailing samples. The distributions of total iron, silica and magnesia in the tailings are also very similar. These results show that the total iron losses in both jig pressures is caused by locked particles.

4.3. Shaking Table Test

Shaking table tests were performed on the -1 mm size fraction by using laboratory scale hydrocyclone, 100x100 mm teetered bed separator (TBS), and shaking table (500×1200 mm). The -1 mm sample was first classified in a 50 mm hydrocyclone to remove the ultra - fines. A number of tests were conducted by varying spigot and inlet pressure. Desliming tests were aimed to rejecting ultrafine particles and obtaining a highest iron recovery in the hydrocyclone underflow. Then, the best sample was fed to TBS to obtain narrow size fractions for shaking table tests (Figure 2). To obtain a high grade final concentrate, wash water rate adjusted 15 liters per minute (lpm) for coarse table test and 10 lpm for fine table test. Tilt angle (5°) was kept at maximum during the shaking table tests. Feed solid content was 25%. Approximately 200 kg of sample were used during shaking table tests. During the tests a large number of samples were taken to obtain grade recovery relationship and to determine table performance. The view of shaking table test is given in Figure 5. All samples obtained in each step of shaking table tests were dried, weighed and analyzed, to assess the performance of the beneficiation. Desliming test results are tabulated in Table 9.

The best result was obtained by using a 1 mm spigot opening and 0.5 bar cyclone feed pressure. As

Table 7- Fractional chemical analysis of jig tail (0.1 bar).

		TENNÖR (%)				
Size Fraction (mm)	Weight (%)	Fe	SiO_2	MgO	CaO	Al_2O_3
-6+3.35	12.58	19.82	28.55	21.52	5.83	1.46
-3.35+1.18	31.48	18.57	28.82	22.33	6.14	1.69
-1.18	55.94	19.31	27.50	21.32	6.11	2.16
		DISTRIBUTION (%))				
Size Fraction (mm)	Weight (%)	Fe	SiO_2	MgO	CaO	Al_2O_3
-6+3.35	12.58	13.03	12.81	12.50	12.06	9.59
-3.35+1.18	31.48	30.54	32.34	32.44	31.78	27.66
-1.18	55.94	56.43	54.85	55.06	56.16	62.75

Table 8- Fractional chemical analysis of jig tail (0.2 bar).

		GRADE (%)				
Size Fraction (mm)	Weight (%)	Fe	SiO_2	MgO	CaO	Al_2O_3
-6+3.35	16.07	18.70	28.41	22.11	6.28	1.25
-3.35+1.18	33.98	19.43	28.01	21.81	6.23	1.51
-1.18	49.94	22.01	26.00	20.20	5.65	2.36
		DISTRIBUTION (%))				
Size Fraction (mm)	Weight (%)	Fe	SiO2	MgO	CaO	Al_2O_3
-6+3.35	16.07	14.59	16.87	16.88	16.96	10.59
-3.35+1.18	33.98	32.05	35.16	35.20	35.57	27.22
-1.18	49.94	53.36	47.97	47.92	47.48	62.20

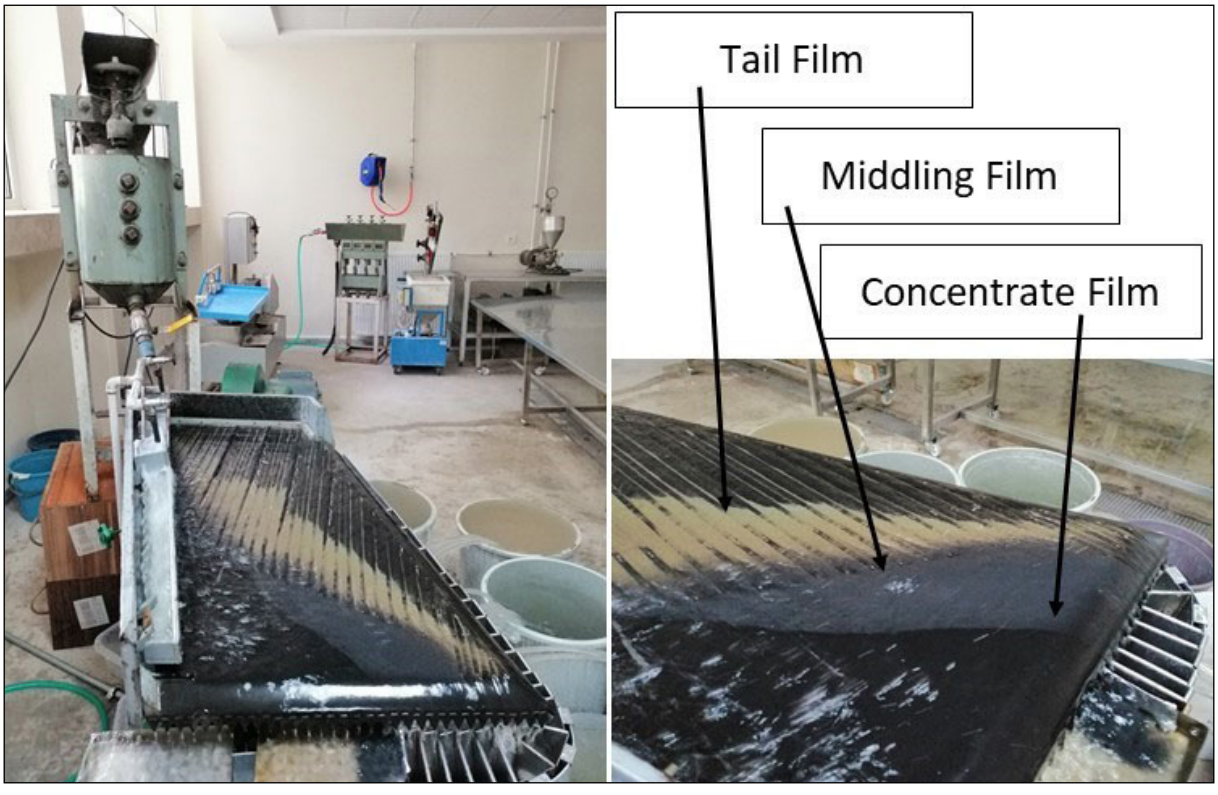

Figure 5- Shaking table test and sampling apparatus.

Table 9- Desliming test results (Best condition).

		GRADE (%)				
Product	Weight (%)	Fe	SiO_2	MgO	CaO	Al_2O_3
Cyclone Feed (-1 mm)	100.00	22.26	25.70	20.07	5.73	2.39
Cyclone Overflow	12.13	7.97	34.40	25.50	7.60	1.85
Cyclone Underflow	87.87	24.23	24.50	19.32	5.47	2.47
		DISTRIBUTION (%))				
Size Fraction (mm)	Weight (%)	Fe	SiO2	MgO	CaO	Al_2O_3
Cyclone Feed (-1 mm)	100.00	100.00	100.00	100.00	100.00	100.00
Cyclone Overflow	12.13	4.34	16.23	15.41	16.08	9.38
Cyclone Underflow	87.87	95.66	83.77	84.59	83.92	90.62

seen from Table 9, 87.87% of the feed material by weight was collected as an underflow a total iron grade of 24.23% Fe and a total iron recovery of 95.66%. Only 4.34% of the total iron in the hydrocyclone feed was rejected in slime fraction. According to particle size analysis 100% of the slime fraction was finer than 38 μm.

It is well known that ultrafine entrainment to the gravity concentration processes results in relatively lower efficiency value. The alumina bearing minerals particularly, the clay containing impurities are very finely disseminated in the iron ore matrix. Therefore, it can be concluded that an efficient desliming positively effects the shaking table performance.

In addition to this, if particles are fed to a shaking table in narrow sizes, the effect of size over density is eliminated, and besides beneficiation will also be enhanced (Das et al., 2009). Hydrocyclone underflow sample was divided to two narrow size fractions by using TBS. The effect of size on the shaking table performance was also evaluated. TBS test results are tabulated in Table 10.

It can be seen in Table 10 that approximately 60% of the TBS feed material was reported to underflow (coarse) fraction. In terms of chemical analyses of TBS product, no significant difference can be determined. TBS products were used in shaking table tests separately. Shaking table test results of TBS underflow and TBS overflow are tabulated in Table 11 and Table 12 respectively.

According to Table 11 a high grade concentrate can be obtained from coarse table test. As it can be seen in Table 11 that only 7.37% of the feed material can be obtained as a concentrate with a total iron grade of 65.72% Fe and 2.46% SiO_2. Approximately 19% of the total iron in the feed can be recovered in the

Table 10- TBS test results.

			GRADE (%)				
Product	Weight (%)	d_{80} (mm)	Fe	SiO_2	MgO	CaO	Al_2O_3
TBS Feed	100.00	0.70	24.23	24.50	19.32	5.47	2.47
TBS Underflow	60.02	0.83	25.49	23.49	18.29	5.32	2.34
TBS Overflow	39.98	0.28	22.34	26.02	20.86	5.71	2.66
			DISTRIBUTION (%))				
Product	Weight (%)	d_{80} (mm)	Fe	SiO_2	MgO	CaO	Al_2O_3
TBS Feed	100.00	0.70	100.00	100.00	100.00	100.00	100.00
TBS Underflow	60.02	0.83	63.14	57.54	56.83	58.31	56.90
TBS Overflow	39.98	0.28	36.86	42.46	43.17	41.69	43.10

Table 11- Shaking table test results of TBS underflow (Coarse fraction).

		GRADE (%)				
Product	Weight (%)	Fe	SiO_2	MgO	CaO	Al_2O_3
Table Feed	100.00	25.49	23.49	18.29	5.32	2.34
Concentrate 1	3.37	67.64	1.52	2.01	0.35	0.31
Concentrate 2	2.00	66.46	2.36	2.69	0.65	0.39
Concentrate 3	1.99	61.71	4.16	4.14	1.41	0.52
Middling 1	46.86	28.18	21.30	16.80	5.51	2.00
Middling 2	26.75	19.17	27.20	21.00	6.23	2.43
Tail 1	13.45	13.61	30.50	23.30	5.81	3.08
Tail 2	5.58	8.71	34.90	26.20	4.21	5.51
		RECOVERY (%)				
Product	Weight (%)	Fe	SiO_2	MgO	CaO	Al_2O_3
Table Feed	100.00	100.00	100.00	100.00	100.00	100.00
Concentrate 1	3.37	8.96	0.22	0.37	0.22	0.45
Concentrate 2	2.00	5.21	0.20	0.29	0.24	0.33
Concentrate 3	1.99	4.82	0.35	0.45	0.53	0.44
Middling 1	46.86	51.80	42.49	43.04	48.55	40.09
Middling 2	26.75	20.12	30.98	30.72	31.34	27.81
Tail 1	13.45	7.18	17.46	17.13	14.69	17.72
Tail 2	5.58	1.91	8.29	7.99	4.42	13.15

Table 12- Shaking table test results of TBS overflow (Fine fraction).

		GRADE (%)				
Product	Weight (%)	Fe	SiO_2	MgO	CaO	Al_2O_3
Table Feed	100.00	22.34	26.02	20.86	5.71	2.66
Concentrate 1	3.74	65.72	1.68	2.23	0.34	0.17
Concentrate 2	8.59	64.18	2.37	2.82	0.77	0.22
Concentrate 3	9.27	48.86	8.91	8.14	3.65	0.81
Middling 1	7.92	19.73	24.18	20.16	8.54	2.10
Middling 2	17.35	13.27	29.68	24.08	7.42	2.93
Tail 1	35.85	11.30	33.57	26.52	6.58	3.34
Tail 2	17.28	11.18	33.73	26.01	5.61	3.96
		RECOVERY (%)				
Product	Weight (%)	Fe	SiO_2	MgO	CaO	Al_2O_3
Table Feed	100.00	100.00	100.00	100.00	100.00	100.00
Concentrate 1	3.74	10.99	0.24	0.40	0.22	0.24
Concentrate 2	8.59	24.66	0.78	1.16	1.16	0.71
Concentrate 3	9.27	20.27	3.18	3.62	5.93	2.84
Middling 1	7.92	6.99	7.36	7.65	11.85	6.25
Middling 2	17.35	10.30	19.79	20.03	22.55	19.12
Tail 1	35.85	18.13	46.25	45.59	41.31	45.06
Tail 2	17.28	8.65	22.40	21.55	16.97	25.78

concentrate. However, approximately 75% of the feed material by weight reports to middling. 71.92% of the total iron in the feed losses in the middling stream. Total iron losses in the tail stream is quite low (9.09%) for coarse fraction.

A high grade concentrate can be obtained from fine table test as well. According to results, 12.32% of the feed material can be obtained as a concentrate with a total iron grade of 64.65% Fe and 2.16% SiO_2. Approximately 35% of the total iron in the feed can be recovered in the concentrate. In the fine table test approximately 35% of the feed material by weight reports to middling. 37.57% of the total iron in the feed losses in the middling stream which is lower than coarse table test. Total iron losses in the tail stream is 26.78% for fine fraction.

Construction of grade/recovery curves is one of the well - accepted methods of assessing performance of separation units in mineral processing. Grade/recovery curves were constructed to evaluate the effect of size on the table performances (Figure 6).

It can be observed from Figure 6 that shaking table can produce a high grade iron concentrate (>65% Fe) with lower recoveries independent to feed size. The grade/recovery curve obtained from coarse table was truncated and flat in appearance as it generated concentrates with marginal total iron recoveries. Figure 6 shows that there are high grade products in the range of 20 - 70% recovery for the fine shaking table, while there is no data in the same range for the coarse shaking table. These data show that there are no possibilities to produce a high or intermediate grade product (middling) on coarse shaking table. This result can be explained by insufficient liberation of coarser size fractions. The grade/recovery relationship for the fine table followed a characteristic curve extending the arc along the ordinate, which indicates the ability of this size fraction to generate high - grade concentrates with higher recovery of total iron values than coarse table. The grade/recovery curve method presented in Figure 6 indicates that the performance of fine table was better than the coarse table. It can be concluded that the higher liberation degree of finer fraction can result in a better separation efficiency on the fine table test.

5. Flowsheet Development Studies

It is evident from the beneficiation studies of the low grade iron ore that a sinter/pellet grade product cannot be produced in coarser size fraction (+1 mm) by using gravity and/or magnetic separation methods. Therefore, a flowsheet for -1 mm has been considered. A 80 tph grinding and concentration circuit was developed. Flowrates of each stream were calculated by using experimental data. JKSimmet software was used to flowsheet development, mass balance and simulation of circuit. The developed flowsheet

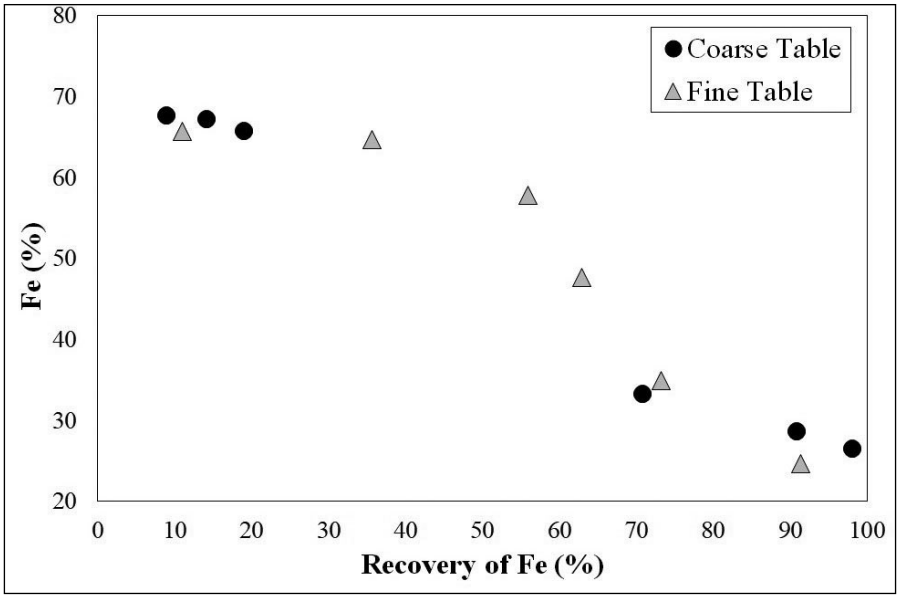

Figure 6- Grade/recovery curves of shaking table tests.

includes a crushing - grinding circuit and two stages of gravity concentration circuit to obtain a high grade concentrate. The middling of the gravity circuit regrinds and concentrated in the three stage magnetic separation. Figure 7 shows the simplified view of developed flowsheet.

A rod mill and a 1 mm aperture screen were used in grinding circuit. Plant feed fed to 1 mm aperture screen. The screen oversize reports to the rod mill. Rod mill discharge and screen undersize streams are fed to desliming cyclone. Cyclone overflow stream reject as slime and cyclone underflow stream fed to spiral concentration circuit. Spiral concentration circuit includes rougher and scavenger stages. Spiral concentration circuit aims to obtain a pre concentrate by using small number of equipment. In the spiral circuit design, the weight, grade and efficiency values obtained from the desliming studies were used. The amount of concentrate to be obtained from the spiral circuit is the amount of TBS feed obtained from experimental studies. For the concentrates to be obtained from the rougher and scavenger stages, possible grade values were predicted and the grade and recovery calculations were completed. The performance of the spiral circuit has been determined based on these values.

In the spiral circuit rougher tail fed to scavenger spiral. Concentrates of rougher and scavenger spirals

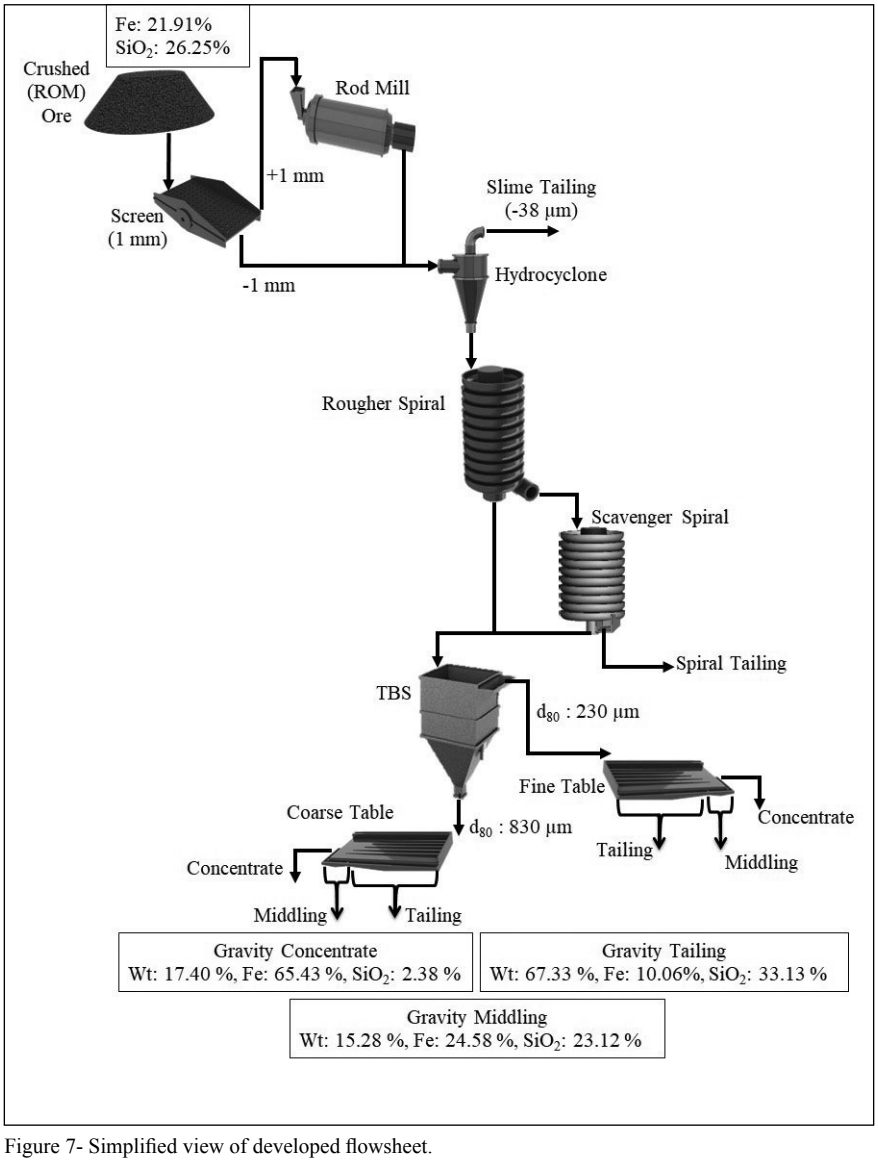

Figure 7- Simplified view of developed flowsheet.

are fed to TBS. TBS separates the stream into two size fractions as coarse and fine. Final concentrate is obtained in shaking tables. Mass balance, water balance and solid content of the beneficiation circuit is tabulated in Table 13.

Table 13- Flowrates of developed flowsheet after mass balance.

STREAM	Solid Tonnage (tph)	Water Tonnage (tph)	Solid Content (%)
Feed	80	80	50
Rod Mill Discharge	51.70	17.23	75.00
Water 1 (rod mill feed)	-	15.63	-
Water 2 (cyclone feed)	-	0.00	-
1mm Screen Undersize	28.30	78.40	26.52
1mm Screen Oversize	51.70	1.60	97.00
Cyclone Feed	80.00	95.63	45.55
Cyclone Overflow (slime)	12.38	72.68	14.56
Cyclone Underflow	67.62	22.95	74.66
Rougher Spiral Concentrate	24.96	10.14	71.10
Rougher Spiral Tail	42.66	91.28	31.85
Water 3 (Cyclone Underflow)	-	78.47	-
Scavenger Spiral Concentrate	15.14	9.13	62.39
Scavenger Spiral Tail	27.51	82.15	25.09
TBS Feed	40.10	32.81	55.00
TBS Underflow (coarse)	22.38	4.92	81.97
TBS Overflow (fine)	17.72	27.89	38.86
Coarse Table Concentrate	10.23	8.37	55.00
Coarse Table Middling	5.59	6.83	45.00
Coarse Table Tail	6.56	37.01	11.16
Fine Table Concentrate	3.69	3.41	52.00
Fine Table Middling	6.63	9.16	42.00
Fine Table Tail	7.41	40.62	12.23
Water 4 (TBS Feed)	-	95.00	-
Water 5 (coarse table)	-	47.29	-
Water 5 (fine table)	-	-	-

It can be revealed from Table 13. that approximately 50% of the feed reports to shaking table circuit. According to grade/recovery calculations, 86% of the total iron can be pre concentrated by spiral circuit. The calculated product specifications of gravity concentration circuit are tabulated in Table 14.

From the gravity concentration flowsheet, it is possible to obtain a concentrate containing 65.43% Fe, 2.38% SiO_2, 2.74% MgO, 0.70% CaO and 0.34% Al_2O_3. Total iron recovery of gravity concentration circuit is 51.96%. Impurity rejection values for the gangue contents in this flowsheet were higher than 80%. According to calculations approximately 17% of the total feed can be obtained as middling. Total iron recovery of middling is 17.13%. As for the middling, re - grind or middling beneficiation options can be considered because of the particularly high grade and high weight percent of this product. It is well known from the Davis tube test that liberation degree was quite high below 75 µm. In this condition a high grade iron concentrate can be obtained by using magnetic separation. According to results, a middling beneficiation circuits including a regrind mill and three stages of magnetic separation was developed (Figure 8).

Middling concentration circuit includes a regrind ball mill closed circuit with a hydrocyclone. Cyclone underflow fed to regrind mill and cyclone overflow fed to three stages low intensity magnetic separation. Performance of three stage magnetic separation circuit as calculated by using experimental and mass balance results (Table 15).

Table 14- Product specifications of gravity concentration circuit.

		GRADE (%)				
Product	Weight (%)	Fe	SiO_2	MgO	CaO	Al_2O_3
R.O.M Ore	100.00	21.91	26.25	20.48	5.85	1.86
Gravity Concentrate	17.40	65.43	2.38	2.74	0.70	0.34
Gravity Middling	15.28	24.58	23.12	18.64	6.26	2.16
Gravity Tail	67.32	10.06	33.13	25.48	7.09	2.18
		RECOVERY (%)				
Product	Weight (%)	Fe	SiO_2	MgO	CaO	Al_2O_3
R.O.M Ore	100.00	100.00	100.00	100.00	100.00	100.00
Gravity Concentrate	17.40	51.96	1.58	2.32	2.08	3.18
Gravity Middling	15.28	17.13	13.45	13.90	16.34	17.78
Gravity Tail	67.33	30.90	84.97	83.77	81.59	79.05

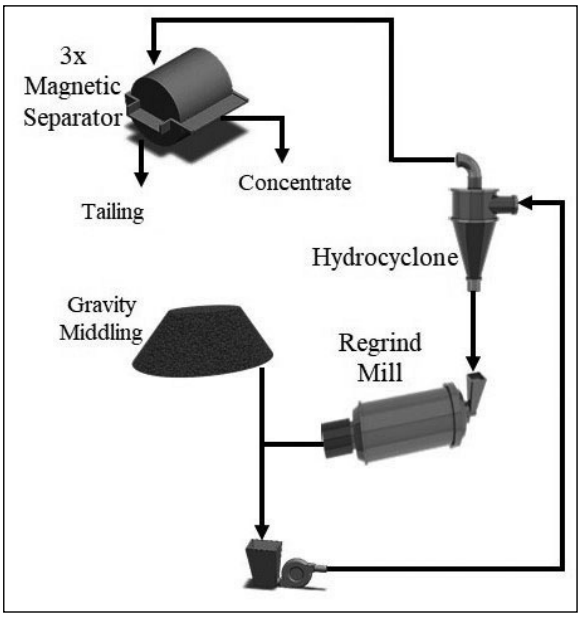

Figure 8- Middling regrind and concentration circuit.

After regrinding and three stages of magnetic separation, middling of tables can be concentrated up to 65.33% Fe, 3.20% SiO_2, 3.05% MgO, 0.69% CaO and 0.24% Al_2O_3. Total iron recovery of magnetic separation circuit is 70.00%. Impurity rejection values for the gangue contents in this flowsheet were higher than 95%. As a conclusion the overall performance of circuit and product specifications was calculated. The overall product specifications of circuit are listed in Table 16.

It can be observed from Table 16 that specifications of final concentrate are suitable for the pellet/sinter making (Roy et al., 2007; Shobhana et al., 2012; Harman, 2012; Mark and Henry, 2016). Silica content of R.O.M. ore could be reduced down to 2.54% SiO_2. Impurity rejection values for the gangue contents were higher than 95% in the overall. In industry the general acceptance limit of SiO_2 for sinter/pellet feed is given as in the range of 1%–5% in the references (Roy et al., 2007; Shobhana et al., 2012; Harman, 2012; Mark and Henry, 2016). It is also reported that SiO_2 content

Table 15- Product specifications of magnetic separation circuit.

		GRADE (%)				
Product	Weight (%)	Fe	SiO_2	MgO	CaO	Al_2O_3
Gravity Middling	100.00	24.58	23.12	18.64	6.26	2.16
Magnetic Concentrate	26.33	65.33	3.20	3.05	0.69	0.24
Magnetic Tail	73.67	10.01	30.24	24.21	8.25	2.85
		RECOVERY (%)				
Product	Weight (%)	Fe	SiO_2	MgO	CaO	Al_2O_3
Gravity Middling	100.00	100.00	100.00	100.00	100.00	100.00
Magnetic Concentrate	26.33	70.00	3.64	4.31	2.90	2.92
Magnetic Tail	73.67	30.00	96.36	95.69	97.10	97.08

Table 16- Product specifications of final products.

		GRADE (%)				
Product	Weight (%)	Fe	SiO_2	MgO	CaO	Al_2O_3
R.O.M Ore	100.00	21.91	26.25	20.48	5.85	1.86
Final Concentrate	21.42	65.41	2.54	2.79	0.70	0.32
Final Tail	78.58	10.05	32.72	25.30	7.26	2.28
		RECOVERY (%)				
Product	Weight (%)	Fe	SiO_2	MgO	CaO	Al_2O_3
R.O.M Ore	100.00	100.00	100.00	100.00	100.00	100.00
Final Concentrate	21.42	63.96	2.07	2.92	2.55	3.70
Final Tail	78.58	36.04	97.93	97.08	97.45	96.30

can be as high as 9.5% in some cases (Harman, 2012). Based on the analysis of SiO_2 and Al_2O_3 contents, the alumina to silica ratio of final concentrate can be calculated as 0.12 which is below acceptable limits. According to results it may be concluded that the final concentrate can be used for iron production.

6. Conclusion

In this study, possibilities for beneficiation and flowsheet development of a low grade iron ore were evaluated. Detailed material characterization studies were performed to developing the optimum flowsheet for the iron ore sample.

Different physical beneficiation methods were performed to ore to obtain a high grade iron concentrate including jigging, low intensity magnetic separation, and shaking table. Desliming and hydraulic classification also performed to ore to prepare an optimum feed to shaking table test.

A high grade iron concentrate could not be obtained above 1 mm by using DLIMS or jigging methods. This may be related to the low liberation degree of iron ore sample Gravity concentration method can produce a high grade concentrate below 1 mm while an acceptable magnetic concentrate can be obtainable only below 100 µm. The main advantage of the gravity concentration method can be seen as producing a pre concentrate by using spiral concentration. A coarse size pre - concentration below 1 mm has various advantages. An important amount of gangue material can be discarded early in the process. It decreases the amount of material that needs to be treated in downstream process. This significantly reduces the energy and water consumption and operating cost per ton of concentrate. Spiral concentration can be used a pre - concentration method below 1 mm. Spiral concentration can be beneficial to decreasing the numbers of shaking tables and increasing the feed grade of shaking table circuit.

According to results, a high grade iron concentrate can be obtained from shaking table. However, approximately 75% of the feed material by weight reports to middling in coarse table. It shows that liberation degree of -1 mm size fraction is better than +1 mm but also poor. The grade/recovery curve method indicates that the performance of fine table was better than the coarse table. It can be concluded that the higher liberation degree of fine table feed can resulted a better separation efficiency on the test.

The lower recovery values of gravity separation can be increases by using a wet low intensity magnetic separation (WLIMS). Feed size of the WLIMS should be below 100 µm according to Davis Tube tests. A small diameter of regrind mill can be suitable for grinding of table middling stream.

As a conclusion the overall performance of the proposed circuit and product specifications was calculated. According to calculations a final concentrate containing 65.41% Fe, 2.54% SiO_2, 2.79% MgO, 0.70% CaO and 0.32% Al_2O_3 can be obtained. Overall iron recovery of circuit is 63.96% shows that complex mineralogical composition and liberation characteristics of iron ore sample can limit the recovery and prevents to obtain higher recovery values. Overall gangue rejection recovery of circuit was over 95%. These specifications show that specifications of final concentrate are suitable for the pellet/sinter making.

A grinding size below 100 µm followed by magnetic separation with cleaner and scavenger stages can be discussed as an alternative beneficiation circuit. A decrease of grinding size increases the both grinding costs and total recovery. However, operational costs must be accurately calculated for this situation.

An efficient, low cost and environmentally friendly concentration processes by gravity and magnetic separation were developed for beneficiation of low grade iron ore sample. Through the process, 67.33% of the feed is directly discarded, greatly reducing the ore processing capacity of the magnetic separation circuit. The main benefit of preconcentration is the selective discard of waste from the feed stream, thus improving project economics while reducing the power and amount of material which reports to downstream process.

It should be noted that if the proposed flow sheets are considered for operation, they should be re - evaluated in terms of the number of required equipment, amount of water, and some other operational parameters considering market prices.

References

Aghlmandi, A., Ergun, L., Gülcan, E. 2017. Beneficiation of oxide ores using dense medium cyclones. A simulation study. Physicochemical Problems in Mineral Processing 53(1), 379-393.

Angadi, S. I., Eswaraiah, C., Jeon, H. S., Mishra, B. K., Jan, D., Miller, J. D. 2017. Selection of Gravity Separators for the Beneficiation of the Uljin Tin Ore. Mineral Processing and Extractive Metallurgy Review 38, 54-61.

Das, A., Sarkar, B., Mehraotra, S. P. 2009. Prediction ofseparation performance of Floatex Density Separatorfor processing of fine coal particles. International Journal of Mineral Processing 91, 41-49.

Das., A., Sarkar, B. 2018. Advanced Gravity Concentration of Fine Particles: A Review. Mineral Processing and Extractive Metallurgy Review 39, 1-36.

Dwari, R. K., Rao, D. S., Reddy, P. S. R. 2014. Mineralogical and Beneficiation Studies of a Low Grade Iron Ore Sample. Journal of The Institution of Engineers (India): Series D 95, 115-123.

Gundewar, J. S. 2011. Iron and steel vision 2020. (Sumesh, M., Ed.), Nagpur: Aqua Process, 36-87.

Harman, J. 2012. Anglo American Iron Ore Quality and Volume, http://www.angloamerican.com/~/media/Files/A/Anglo-American-PLC-V2/presentations/2012pres/global_iron_ore.pdf.

Jyoti, D., Rath, R. K., Mohanty, S., Singh, R., Bhattacharyya, K. K. 2010. Beneficiation of a finely disseminated low - grade iron ore by froth flotation. Proceedings of the XI International Mineral Processing Techno, MPT 15-17 December, 2010, New Delhi, 590-596.

Mark Wren, M., Henry, D. 2016. Iron ore 64.5 % Fe specification: website;http://www.ipccaustralia.com /downloads/ipcc-iron-ore-64-specifications-brazil-web.pdf

Muwanguzi, J. B. A., Karasev, V. A., Byaruhanga, K. J., Par G. J. 2012. Characterization of Chemical Composition and Microstructure of Natural Iron Ore from Muko Deposits. International Scholarly Research Network ISRN Materials Science 2012, 1-9.

Özcan, Ö., Çelik, İ. B. 2016. Beneficiation Routes for Upgrading Iron Ore Tailings with Teetered Bed Separator. Separation Science and Technology 51, 2844-2855.

Panda, L., Biswal, S. Venugopal, R., Mandre, N. R. 2017. Recovery of Ultra - Fine Iron Ore from Iron Ore Tailings. Transactions of the Indian Institute of Metals 71, 463-468.

Rath, R. K., Singh, R. 2007. Gravity concentration of iron ores, in: Advanced Gravity Separation, Jamshedpur: NML Publication, 74-88.

Rath, R. K., Mohanty, S., Singh, R., Nayak, B., Bhattacharyya, K. K. 2010. Beneficiation response of a low grade iron ore from eastern India for the production of sinter and pellet feed. in: Proceedings of the XI International Mineral Processing Technology, NML 15-17 December, 2010, Jamshedpur, New Delhi, 179-185.

Rath, R. K., Mohanty, S., Nayak, B., Ratnakar Singh, R., Bhattacharyya, K. K. 2013. A Comparative Study on Processing of High Alumina Hematite Iron Ore by Gravity, Magnetic and Flotation Methods. Journal of Materials Science and Engineering 3, 349-354

Roy, S., Das, A., Mohanty, M. K. 2007. Feasibility of producing pellet grade concentrate by beneficiation of iron ore slime. Separation Science and Technology 42, 3271-3287.

Schulz, N. F. 1964. Determination of the magnetic separation characteristics with the Davis Magnetic Tube. Trans. SME-AIME 229, 211-216.

Seifelnassr, A., Moslim, E., Abouzeid, A. Z. 2012. Effective processing of low-grade iron ore through gravity and magnetic separation techniques. Physicochemical Problems of Mineral Processing 48, 567-578.

Shobhana, D., Santosh, P., Mohanta, M. K., Singh, R. 2012. Utilization of iron ore slimes: a future prospective. Separation Science and Technology 47, 769-776.

Singh, R., Mehrotra, S.P. 2007. Beneficiation of iron ores for iron and steelmaking. Steel Tech 1, 17-32.

Srivastava, M. P., Pan, S. K., Prasad, N., Mishra, B. K. 2001. Characterization and processing of iron ore fines of Kiruburu deposit of India. International Journal of Mineral Processing 61, 93-107.

Svoboda, J. 1987. Magnetic Methods for the Treatment of Minerals. Amsterdam: Elsevier, 223.

Wills, B. A., Napier-Munn, T. J. 2006. Mineral Processing Technology, Elsevier Science & Technology Books, 261-265.

Wills, B. A., Finch, J. A. 2016. Wills' Mineral Processing Technology (Eighth Edition), Oxford: Elsevier Science and Technology.

Bulletin of the Mineral Research and Exploration

http://bulletin.mta.gov.tr

Petrography and geochemical decomposition parameters of crystalline rocks; Demirköy intrusive body (DIB), *NW Turkey*

Ezgi ULUSOY[a*] and Yusuf Kağan KADIOĞLU[b,c]

[a]*General Directorate of Mineral Research and Exploration (MTA), Department of Geological Research, Ankara, Turkey*
[b]*Ankara University, Faculty of Engineering, Department of Geological Engineering, Ankara, Turkey*
[c]*Earth Sciences Application and Research Centre (YEBIM) of Ankara University, Ankara, Turkey*

Research Article

Keywords:
Weathering, Hydrothermal alteration, Crystalline rocks, Demirköy Intrusive Body (DIB), Strandja Massif.

ABSTRACT

The crystalline rocks represent the most weathering rock groups due to their textural and mineralogical decomposition. This study, focused on the petrographic properties and geochemical variation of the altered rocks from Demirköy Intrusive Body (DIB) located at NW Turkey were examined based on the location of structural and morphological properties. DIB consists of intrusive rocks in the composition of ranging from granite to gabbro. The sampling made from the dominant rock units composing of granodiorite and quartz diorite, within the DIB a cross weathering section divided into three levels as regolit, saprolite and saprock. For each level of all the section Ruxton ratio (Ro), chemical alteration index (CIA), chemical weathering index (CIW), plagioclase alteration index (PIA) were determined. The results show a linear decrease from the surface to the core of the host rock. The chlorite-carbonate-pyrite index (CCPI) versus Ishikawa alteration index (AI) variation diagram shows that decomposition in profiles occurred in diagenetic alteration and where the hydrothermal alteration effect is not observed. On the other hand, Mg, Fe, Ti, Ca decreased remarkably while the ratio of the elements such as Si, Na, K, Al increased. The increasing and decreasing of geochemical elements are related to their physical strength and chemical behavior. The chemical variation diagrams of all the levels revealed that the regolites exhibit chemical compounds from hydrothermal fluids in the immediate vicinity of the source rocks.

Received Date: 26.06.2020
Accepted Date: 11.09.2020

1. Introduction

Apart from tectonic events, the main processes that shape surface morphology are rock weathering, soil formation and sediment deposition. Weathering is the physical - mechanical changes of rock masses, which occurs due to atmospheric and hydrospheric conditions, are compositional and consolidation changes that can be observed chemically and mineralogically - petrographically. Chemical - mineralogical and physical transformations occurring in all rock types associated with weathering processes that occur under various climatic conditions (Whalley and Turkington, 2001; Borrelli et al., 2007; Ietto et al., 2013).

Weathering begins in crystalline rocks along the boundaries of foliation planes, the compositional discontinuities and boundries of rock forming crystals and occur in situ decomposition. As a result of decomposition, regolith (A soil horizon), saprolite (grus, B soil horizon) and saprock (C soil horizon) zones are formed from the surface to depth (Bates and Jackson, 1987; Nahon, 1991; Power and Smith, 1994;

Citation Info: Ulusoy, E., Kadıoğlu, Y. K. 2021. Petrography and geochemical decomposition parameters of crystalline rocks; Demirköy intrusive body (DIB), NW Turkey. Bulletin of the Mineral Research and Exploration 165, 253-265. https://doi.org/10.19111/bulletinofmre.793795

**Corresponding author: Ezgi ULUSOY, ezgi.ulusoy@mta.gov.tr*

Delvigne, 1998; Hillel, 1998; Sharma and Rajmani, 2000; Taylor and Eggleton, 2001; Meunier, 2005; Velde and Meunier, 2008; Graham and O'Geen, 2010). The products of the rock, which is between the fresh rock and atmospheric conditions, in - situ weathered, and do not change volumetrically are defined as saprolites (Ollier et al., 2007; Ollier, 2010; Arias et al., 2016). Due to the weathering effect, depending on the mineralogical and chemical composition of the bedrock, the grain size of the rocks decreases and new minerals are formed. Depending on these changes, the weathering process accelerates or slows down. Decomposition of feldspar and mica minerals like biotite - muscovite play an important role in the weathering process of acidic - intermediate crystalline rocks. As a result of the process, the term 'gruss' (earthy crystals) is used for the medium - coarse grained material, which exhibits less mineralogical and chemical differences compared to the bedrock, and consists of clayey and poorly sorted quartz grains (Migoń and Thomas, 2002). Under the conditions of burial, uplift, erosion, paleoclimate, fracture development associated with weathering processes, can occur at a depth of a few meters to tens or even hundreds of meters depth from the surface related to chemical decomposition (primarily hydrolysis) and the effect of groundwater.

In the Late Cretaceous DIB granitoids in the Istranca Massif, which is covered with heavy vegetation called North Forests; spheroidal (rindlet) weathering and arenization (gruss) as weathering products, are clearly observed. In this study, the mineralogical - petrographic and chemical alteration parameters of DIB granodiorite and quartz diorite compositional crystalline rocks, due to weathering, and the mineralogical and chemical properties of the final products resulting from the weathering are examined for the first time. With the obtained data of different compositional intrusive rocks; The processes and properties of decomposition in the same environment were compared. This study can also be used to evaluate the suitability and productivity of the regolith in terms of agricultural activities according to its mineralogical and chemical properties.

2. Geographical Features and Geology of the Study Area

The study area is located around Demirköy district, in the east of Kırklareli province, NW Turkey. The region is located in the mid - altitude mountain range, has important water resources and high - density drainage networks consisting of many dry and wet streams. For this reason, the weathering process has developed faster in rocks. The region with typical climatic conditions of the Thrace Peninsula; winters are quite cold and rainy; summers are warm and rainy. Consequently, above a certain height and especially on the northern slopes of the mountains, broad - leafed woodlands, mostly made of beech and hornbeam are abundant. Coniferous and oak forests are observed on the south facing slopes where the altitude decreases. In the Istranca (Yıldız) Mountains, where the total annual precipitation is over 1000 mm, lime - free forest soil cover is common due to the dominance of magmatic rocks (Boyraz and Cangir, 2009). While there is enrichment in organic matter due to the heavy forest cover, heavy rainfall has caused the soil to wash in places and podsolic soil formation.

As one of the Turkey's tectonic units, The Strandja Massif (Zone) located in the west of the Pontide belt is separated from the Pontides by the West Black Sea fault and extends towards Eastern Europe (Okay and Tüysüz, 1999). The Strandja Massif, outcropped in the Strandja (Yıldız) Mountain range, basically consists of crystalline core complex and an overlying Triassic - Jurassic low - grade metamorphic clastic and carbonate cover (Aydın, 1982; Çağlayan and Yurtsever, 1998). The units belonging to the Massif are cut by Late Cretaceous - aged, different compositional intrusions and are covered by Late Cretaceous sedimentary - volcanosedimentary units, which no metamorphic effect is observed. DIB, which is the most widespread, Late Cretaceous intrusions, outcropped in an area of approximately 120 km^2 in east of the Massif with WNW - SSE trending ellipsoidal shape (Figure 1) (Ulusoy, 2012).

The intrusive rocks of the DIB are in sharp contact with the metacarbonate and metaclastics of the Strandja Massif. The İkiztepe Granitoid is probably tectonic contact, which is covered with forest and vegetation to the west of the intrusive body (Üşümezsoy, 1982; Ulusoy and Kadıoğlu, 2015). DIB generally consists of granitic, granodioritic, monzodioritic, dioritic and gabbroic assemblages. Felsic and intermediate members are fine - grained, phaneritic textured and consist of roundish - ellipsoidal, from a few to 50 cm in diameters, mafic enclaves. Granite and granodiorites

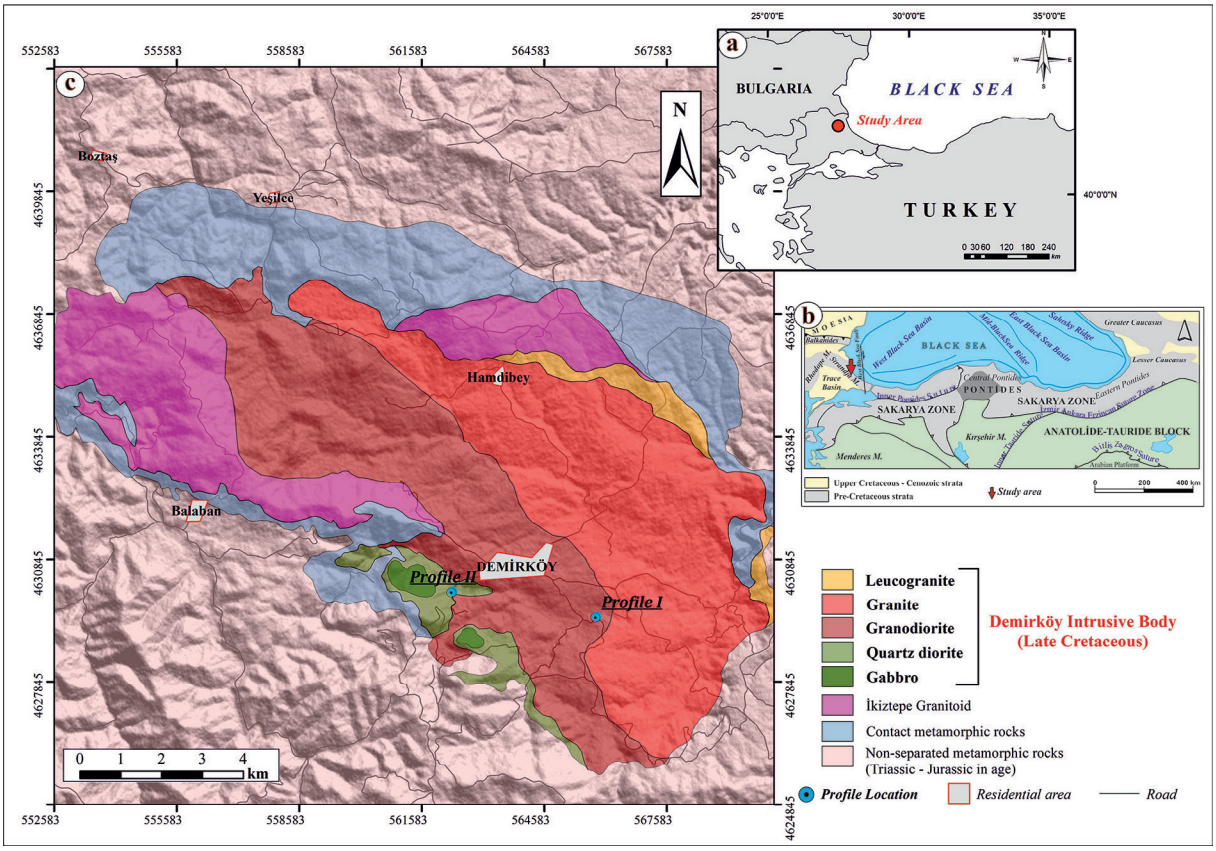

Figure 1- a) Location map of study area, b) tectonic units of Turkey with location of study area (from Okay and Nikishin, 2015) and c) detailed geological map of DIB.

of DIB are calc - alkaline, peraluminous and has medium K content. The mafic rocks of the intrusion are in gabbroic and dioritic composition and generally have calc - alkalen - tholeiitic characteristics. Cooling age of DIB is determined as Late Cretaceous (80 Ma; K - Ar, Moore et al., 1980), and in the light of petrological findings, it is stated that it may be mantle - enriched crustal contaminated H - type granite intruded due to closure of Srednogorie Arc (Aykol and Tokel, 1991; Karacık and Tüysüz, 2010). Apatite fission track studies carried out in the Strandja Massif indicate that after Late Jurassic metamorphism, slow cooling during the Cretaceous - Early Eocene time, and then fast uplift - exhumation and erosion events took place in the region (Catto et al., 2018).

3. Material and Method

Rock units are sampled to reveal the mineralogical composition, textural properties and types of weathering. Thin sections are prepared from these samples and they are selected for X - ray diffraction (XRD) and chemical analysis. Selected samples were crushed in a jaw crusher and then ground using a tungsten carbide mill in Ankara University Earth Sciences Application and Research Center (YEBİM) Laboratories. 4gr of grinded sample was mixed with 0.9 gr of cemented material (wachs), compressed under hydraulic pressure and turned into powder pellets, and major element oxide analyses were performed on the Spectro X - LAB 2000 Polarized Energy Dispersive X - Ray Fluorescence Spectrometer (PEDXRF). The major oxide composition analysis was performed using the GEO - 7220 method, and the device was calibrated by using the K02–GSR–09 and 01–GS–N–Granite standards created by USGS for plutonic rocks (granite, granodiorite, etc.). On the other hand, X - ray diffraction (XRD) analysis was made with a Bruker D8 Advance X - Ray diffractometer at shooting speed of 0.0390º2θ, under 40 mA, 40 kV, with a copper (Cu) X - ray tube and a device with a wavelength of 1.540604 Å in General Directorate of Mineral Research and Exploration (MTA), Mineral Analysis Technology Department Laboratories. The qualitative mineralogical composition of whole rock

and normal (between 2º and 30º, N), ethylene glycol - treated (between 2º and 30º, EG), 550ºC baked (2º - 30º) detailed clay XRD diffractograms were measured from oriented clay samples.

4. Research Findings

4.1. Field Observations

The crystalline rocks belonging to the DIB, outcropped in the study area with heavy forest and vegetation where the altitude is partially increased, covers large areas that are weathered and turned into sand (arena, gruss, saprolite). In the region, outcrops, in which weathering effect is macroscopically weak or not observed at all, are generally observed in stream valleys within groundwater level. As the elevation increases, the weathering continues to increase significantly along the jointed and fractured surfaces. Granodioritic and quartz dioritic rocks are sampled along the significant profiles to investigate weathering processes (Figures 2b and c). As a result of systematic sampling, there are four zones observed in both sections. Accordingly, the top level is about 30 cm thick, red - brown colored, humus - rich soil (regolith - A soil horizon) layer, which is enriched by plant roots and fringes. Below this, there is 1 - 1.5 m - thick saprolite level belonging to the crystalline rock which is texturally sandy (B soil horizon). Saprolite contains small amounts of bedrock fragments and blocks (saprock) in the first levels. Towards deeper saprolite levels, the rate of saprock is gradually increasing. Samples taken from saprock are divided into two subgroups as dispersible - brittle and compact rock (C soil horizon). In dispersible - brittle samples, the rock is highly weathered and can be easily broken by hand, while in compact samples the textural integrity is preserved and consists mostly of solid rock.

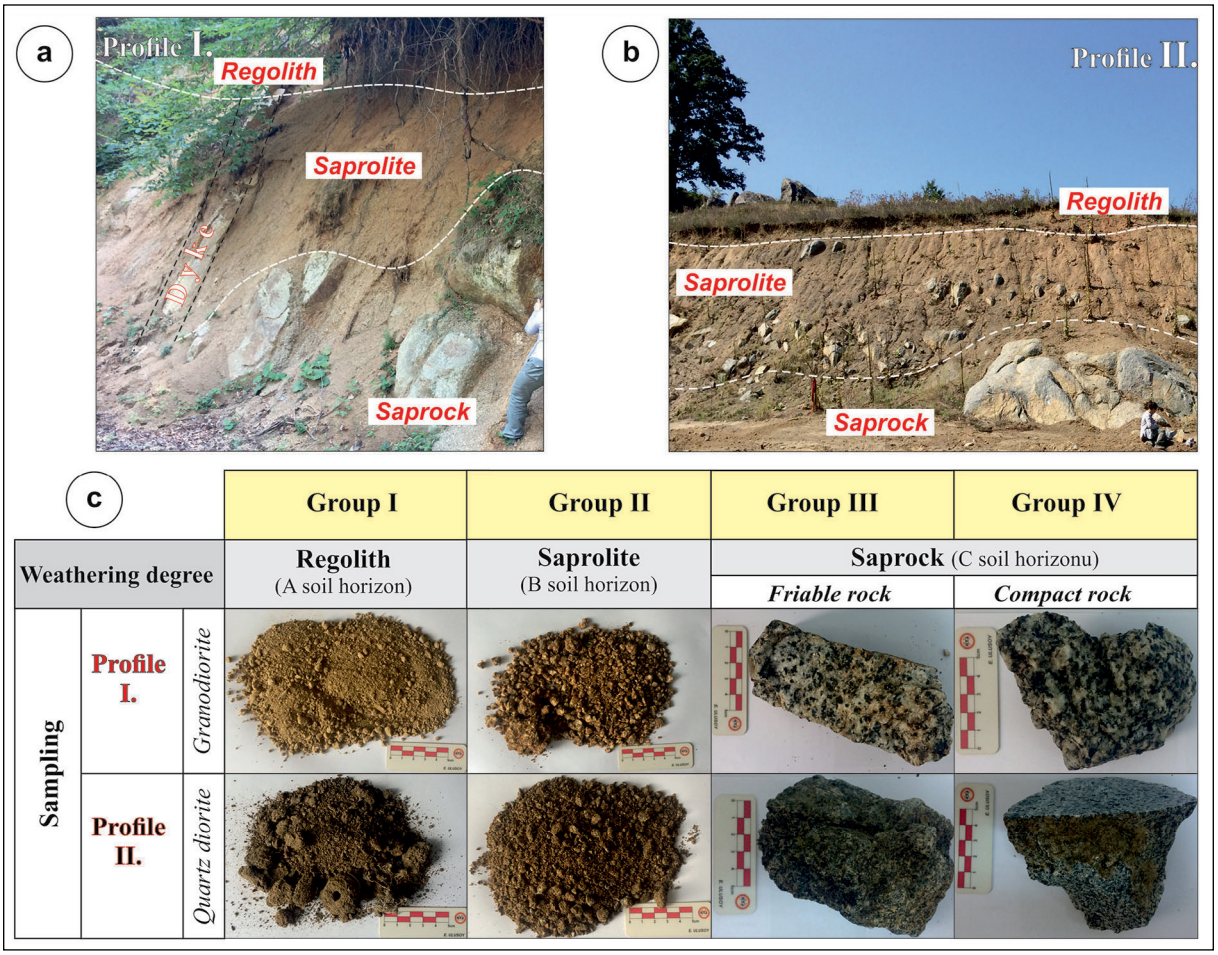

Figure 2- a) General view of regolith, saprolite and saprock levels in granodiorite profile I, b) General view of regolith, saprolite and saprock levels in quartz diorite profile II, c) Macroscopic views of the weathered samples from both sections.

4.2. Mineralogy - Petrography

Profile I is in granodioritic composition with phaneritic texture. The main composition of the rock is medium - grained, subhedral plagioclase, orthoclase and anhedral quartz crystals. Mafic mineral content of the rock is 35% with large - small subhedral - euhedral amphibole and subhedral brown biotite crystals. Fine - grained titanite and zircon crystals with very fine - grained apatite minerals are observed accessory minerals. Disseminated, fine - grained semi - euhedral opaque mineral crystals are observed in the rock. Poikilitic texture is common in partially coarse - grained quartz, orthoclase and amphibole crystals. Argillization is observed. Feldspars turn to sericite, mafic minerals, on the other hand, altered to chlorite (amphibole, biotite), biotite (amphibole) and opacitized (Figure 3a-c). Dispersible - brittle minerals (quartz and feldspars) are fractured - cracked, and iron hydroxide staining is observed along the discontinuities (Figure 3a-b).

Profile II is quartz dioritic in composition and displays phaneritic texture. The main composition of medium grained rock is subhedral plagioclase, subhedral - euhedral amphibole, clinopyroxene and biotite. Mafic mineral content of the rock is generally more than 50%. Less amount of anhedral quartz is observed in the rock. It contains small amounts of fine - grained, subhedral titanite as accessory mineral. Disseminated, fine - grained, semi - euhedral opaque mineral crystals are observed in the rock. Plagioclase crystals intensely turn to epidote, sericite and clay. Intense uralitization is observed in clinopyroxene, and pyroxene can only be observed as residues from place to place. In amphibole crystals; Chloritization, epidotization and biotitization are observed along cleavage surfaces. Opacitization and opacification are

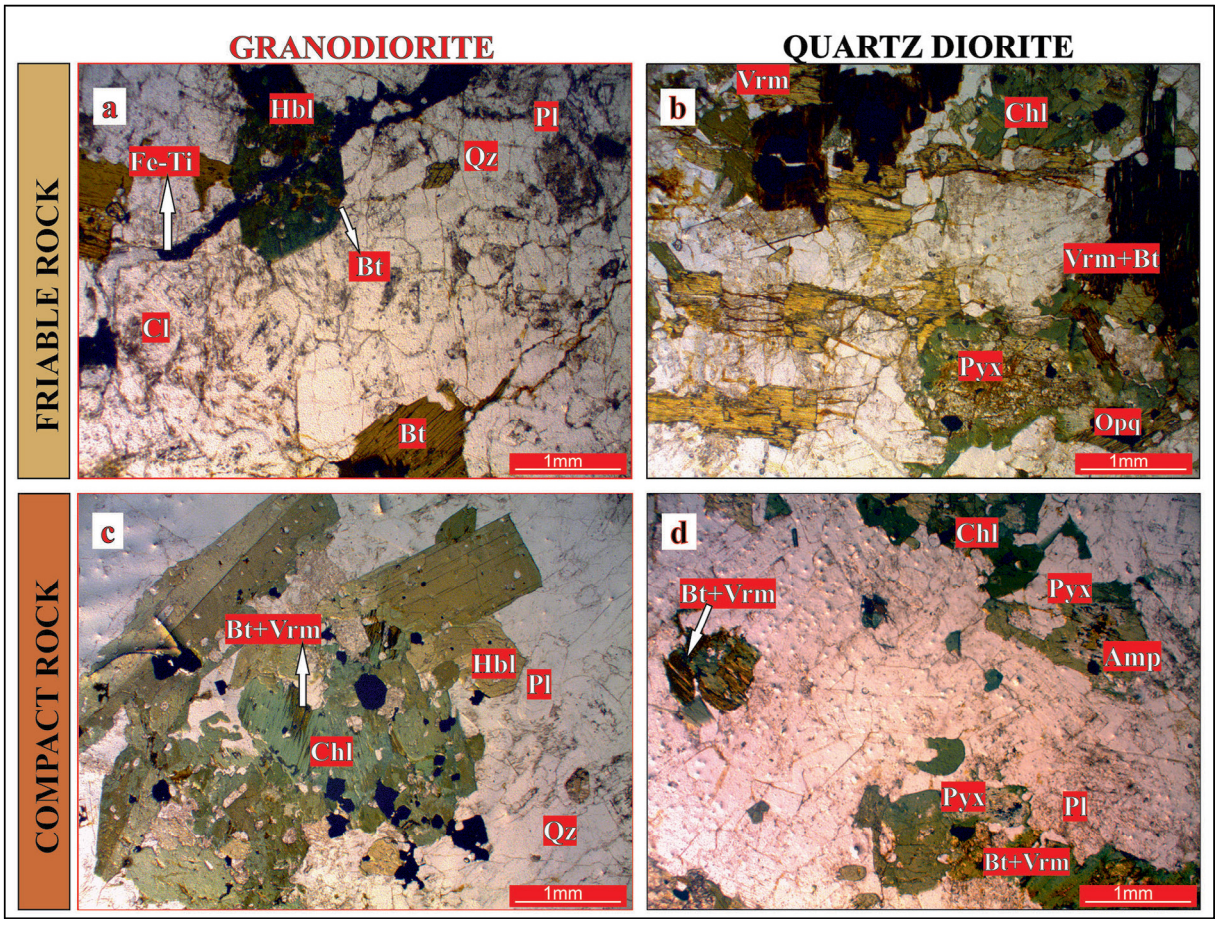

Figure 3- Microphotographs along profile lines; a) friable granodiorite, b) friable quartz diorite, c) compact rock of granodiorite, d) compact rock of quartz diorite in thin section (Qz: quartz, Bt: biotite, Hbl: hornblende, Amp: amphibole, Pyx: Pyroxene, Vrm: vermiculitization, Fe-Ti: iron-titanium oxidation, Cl: clay, Chl: chloritization).

common in mafic minerals (Figure 3b-d). Similar to profile I, iron hydroxide staining is clearly observed along the discontinuities.

4.3. XRD Results and Clay Mineralogy

The result of qualitative mineralogical analysis performed by X - Ray Diffraction (XRD) method of samples from the surface to deep levels in the study area is shown in Figure 4. In all zones for both rock profiles, besides primary minerals, it is observed that secondary minerals are developed as the result of decomposition. Besides in some of the samples belonging to the regolith (soil) and saprolite zone, a proportional decrease can be observed in the minerals studied with the effect of dispersion and washing by surface water.

Profile I, along to the granodioritic rock, consists of quartz, K - feldspar, plagioclase, hornblende, biotite and magnetite (Figure 4a). Depending on the main composition, chlorite and illite are observed as the dominant clay minerals. Besides, kaoline is observed at some levels in regolith and saprock (Figure 5a).

Profile II, along to quartz dioritic composition, consists of plagioclase, alkali feldspar, hornblende, tremolite - actinolite and clinopyroxene (Figure 4b). There is diversity in minerals released as a result of weathering in the mafic mineral - riched quartz dioritic profile II. Secondary vermiculite and chlorite formation are observed in mafic minerals (Figure 5b). In the saprolites of both rocks, depending on the weathering of calcium - rich plagioclases, smectite is formed at different rates. It is possible to observe illite developed from chlorite and feldspars developed from mafic minerals in both profiles of saprock level.

4.4. Whole Rock Geochemistry

From the profiles in the study area, major oxide element concentrations and the major oxide values and calculated weathering parameters of 17 samples of soil, saprolite, saprock and fresh rock were determined and are given in Table 2. For each group of rock, major oxide values indicate similar composition but significantly differ proportionally from the fresh rock. Loss on ignition (LOI) rates were calculated in order to determine whether the samples were affected by alteration and the volatile component ratio. While loss on ignition values are ≤0.5 in fresh rock, it was observed that this ratio reached up to 13.83 in regoliths towards the upper levels of the profile where the weathering is denser (Table 1).

The weathering and alteration parameters given in Table 2 were calculated in order to follow the chemical

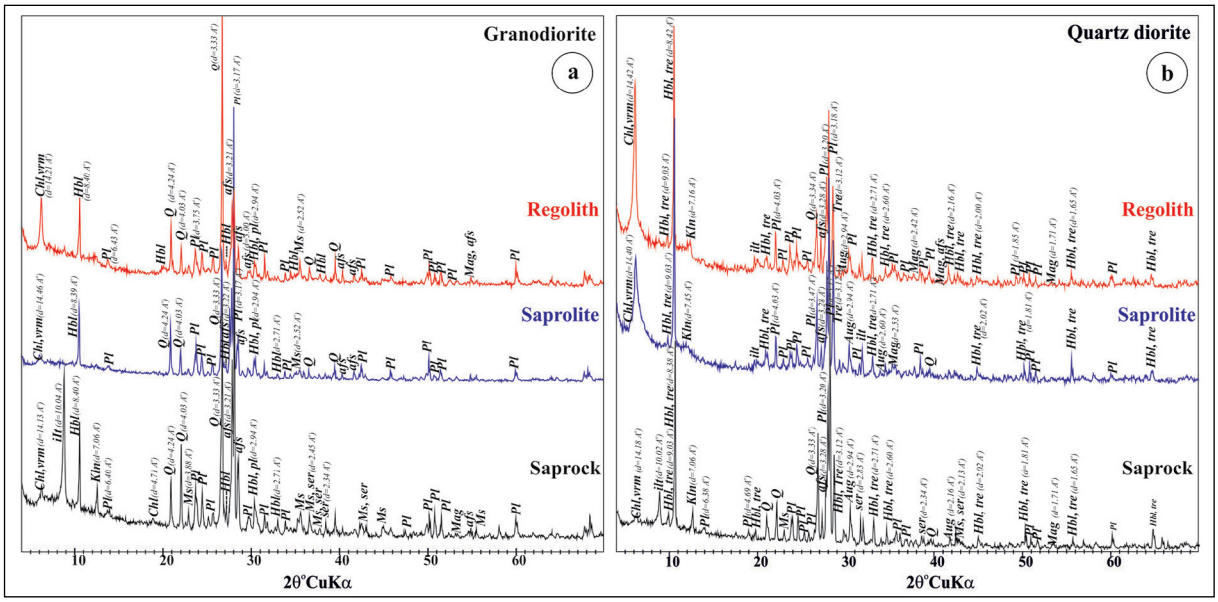

Figure 4- Qualitative mineralogical composition of whole rock analyzed by X-ray diffraction method; a) granodiorite, b) quartz diorite (Q: quartz, aph: alkali feldspar, pl: plagioclase, ms: muscovite, ser: sericite, mag: magnetite, hbl: hornblende, tre: tremolite, aug: augite / clinopyroxene, chl: chlorite, vrm: vermiculite, ilt: illite, sme: smectite (montmorrilonite), kln: kaoline)

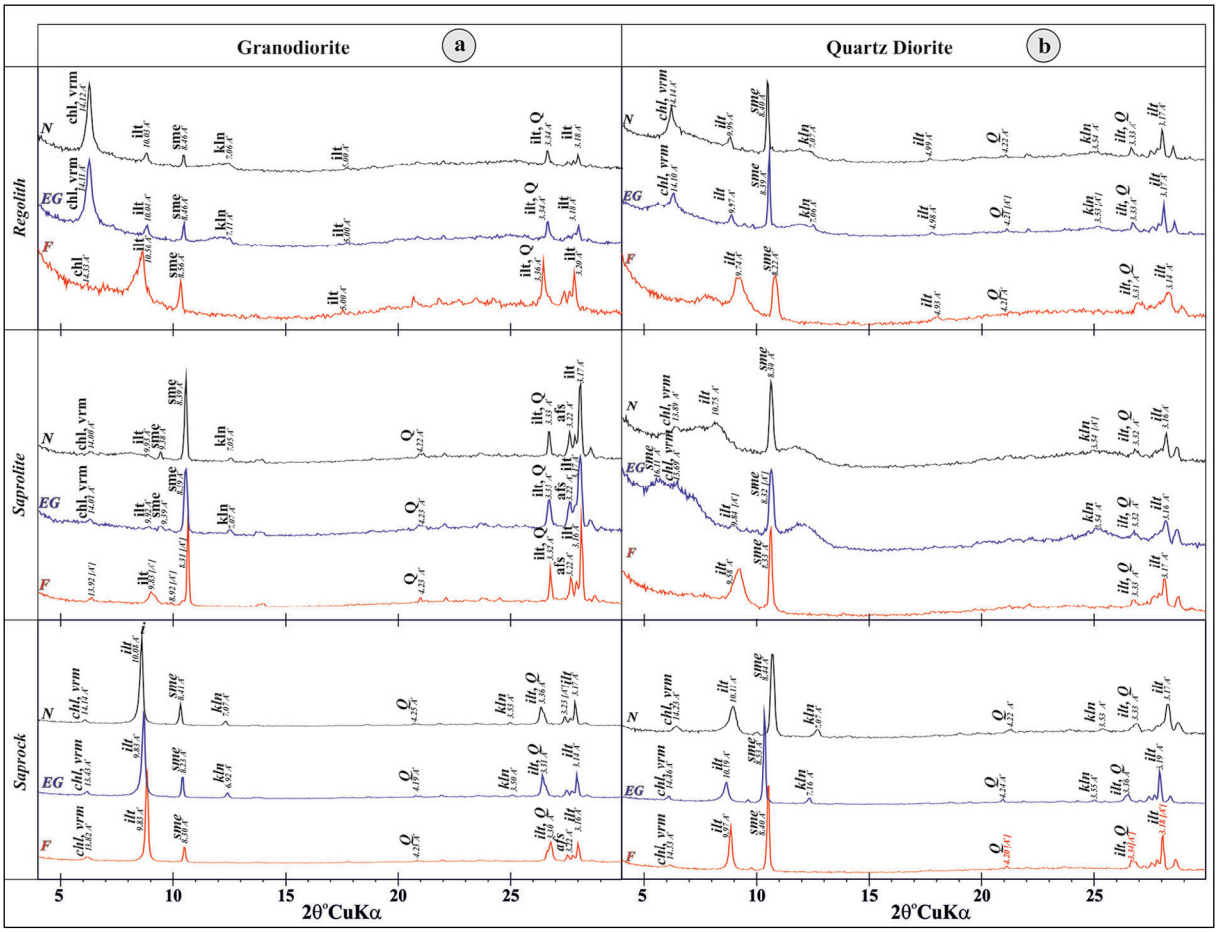

Figure 5- Detailed clay XRD diffractograms of granodiorite and quartz diorite profiles in the study area; a) granodiorite, b) quartz diorite (N: normal, EG: after treatment with ethylene glycol, F: 550ºC dried peaks; chl: chlorite, vrm: vermiculite, ilt: illite, sme: smectite, kln: kaoline, Q: quartz, afs: alkali feldspar)

changes of the zones in the weathering sections. Ruxton (Ro) ratio refers to silicification and argillization in acidic and intermediate rocks (Ruxton, 1968; Fiantis et al., 2010). In all samples in the study area, the Ruxton ratio (Ro) varies between 2.40 and 3.93, indicating that the rocks are not fresh. Chemical index of alteration (CIA) and chemical index of weathering (CIW) are the measure of the transformation of feldspars to clay (kaolinite) in the rock (Nesbitt and Young, 1982; Harnois, 1988). In the samples in the study area, the chemical index of alteration (CIA) is between 54.72 - 77.23 and the chemical index of weathering (CIW) is between 58.11 - 82.91, and depending on the alteration and weathering processes, argillization occurs as a result of the alteration of feldspar minerals in all samples. Palgioclase index of alteration (PIA) expresses the weathering degree of plagioclase crystals that show the fastest weathering in silicate rocks (Fedo et al., 1995). The ratio of PIA in the collected samples is between 55.34 - 79.75, indicating that plagioclases, one of the main minerals, are generally weathered. Ishikawa alteration index (AI), Chlorite - carbonate - pyrite index (CCPI) and advanced argillic alteration index (AAAI) values refer to the chemical and mineralogical changes that occur due to hydrothermal alteration during the weathering process and the density of alteration (Ishikawa et al., 1976; Large et al., 2001; Williams and Davidson, 2004).

In order to determine the effect of hydrothermal alteration on the weathering of the samples in the study area; Ishikawa alteration index (AI, between 27.03 - 57.63); The chlorite - carbonate - pyrite index (CCP between 33.42 - 88.07) and Advanced Argillic Alteration Index (AAAI, between 24.95 - 60.15) were calculated.

Table 1-Major oxide values and weathering parameters of samples from the study area.

			Na_2O	MgO	Al_2O_3	SiO_2	P_2O_5	K_2O	CaO	TiO_2	MnO	Fe_2O_3	LOI	*Sum*	Ro	CIA	CIW	PIA	AI	CCPI	AAAI
I. Profile: Granodiorite	***Regolith***	KW-23A	1.04	0.96	19.31	57.20	0.03	3.36	3.53	0.13	0.01	2.41	11.25	*99.23*	2.96	70.89	80.86	77.73	48.59	43.40	50.83
	Regolith	KW-23B	1.53	0.92	18.17	57.84	0.24	4.32	2.45	0.11	0.13	2.62	11.94	*100.26*	3.18	68.66	82.05	77.70	56.84	37.65	60.15
	Regolith	KW-23C	1.05	0.24	17.13	56.88	0.08	4.56	2.48	0.43	0.05	2.58	13.83	*99.31*	3.32	67.91	82.91	78.07	57.63	33.42	54.18
	Saprolite	KW-24	2.64	3.14	17.68	53.62	0.08	1.10	2.90	0.20	0.27	13.55	1.40	*96.58*	3.03	72.68	76.13	74.94	43.33	81.68	38.17
	Saprolite	KW-25	2.82	1.67	17.61	63.95	0.14	2.08	5.30	0.29	0.08	3.99	1.88	*99.81*	3.63	63.32	68.43	65.66	31.57	53.61	39.50
	Saprolite	KW-30	3.09	1.98	16.47	63.24	0.14	1.73	6.92	0.32	0.09	4.30	1.56	*99.84*	3.84	58.38	62.19	59.55	27.03	56.58	34.52
	Saprolite	KW-31	3.20	1.51	16.98	65.26	0.11	2.12	5.36	0.24	0.08	3.56	1.38	*99.81*	3.84	61.38	66.48	63.44	29.80	48.81	39.31
	Saprolite	KW-27	2.78	1.83	16.93	65.03	0.13	1.85	5.19	0.29	0.08	4.17	1.49	*99.78*	3.84	63.29	68.00	65.43	31.64	56.47	39.89
	Saprolite	KW-33	2.25	3.13	17.00	60.62	0.18	1.82	6.04	0.59	0.14	5.86	1.96	*99.59*	3.57	62.71	67.22	64.68	37.40	68.87	34.67
	Saprock	KW-26	2.68	3.43	15.91	62.32	0.16	2.65	5.71	0.51	0.13	5.54	0.75	*99.78*	3.92	59.04	65.49	61.26	42.03	62.70	34.54
	Saprock	KW-29	2.31	3.68	15.96	61.37	0.14	2.46	5.82	0.61	0.14	6.19	0.98	*99.66*	3.85	60.12	66.27	62.43	43.05	67.42	34.22
	Fresh rock	KW-28	3.25	2.43	16.47	64.73	0.12	2.32	5.57	0.39	0.09	4.05	0.44	*99.86*	3.93	59.64	65.12	61.59	35.04	35.04	36.51
II. Profile: Quartz diorite	***Regolith***	KW-41	0.73	3.62	21.09	50.67	0.17	1.12	5.47	0.65	0.15	8.56	7.07	*99.30*	2.40	74.26	77.30	76.33	43.32	86.85	34.06
	Regolith	KW-42A	1.34	3.90	19.59	50.31	0.17	1.18	6.12	0.57	0.14	8.05	8.54	*99.91*	2.57	69.39	72.42	71.16	40.53	82.61	30.69
	Regolith	KW-42B	0.04	1.89	18.50	53.02	0.17	1.02	4.39	1.20	0.08	5.94	12.83	*99.08*	2.87	77.23	80.65	79.75	39.59	88.07	45.59
	Regolith	KW-42C	0.77	2.24	18.01	51.90	0.08	1.20	4.04	0.91	0.06	6.72	13.63	*99.57*	2.88	74.99	78.93	77.76	41.73	81.99	42.40
	Saprolite	KW-46	0.77	4.35	19.77	52.69	0.16	1.03	6.80	0.69	0.16	8.74	4.36	*99.50*	2.67	69.69	72.32	71.23	41.54	87.93	30.66
	Saprolite	KW-38	1.35	4.57	18.15	54.09	0.21	1.18	7.90	0.71	0.15	8.55	2.66	*99.52*	2.98	63.50	66.23	64.72	38.32	83.84	28.13
	Saprolite	KW-36	1.94	4.79	17.01	56.08	0.19	1.41	8.46	0.39	0.16	7.94	1.46	*99.83*	3.30	59.03	62.06	60.00	37.34	79.21	26.96
	Saprock	KW-35	2.51	4.58	16.75	56.42	0.21	1.39	7.18	0.56	0.14	8.00	2.13	*99.87*	3.37	60.19	63.35	61.32	38.12	76.34	28.33
	Saprock	KW-37	1.54	6.20	15.30	56.26	0.21	1.73	7.77	0.69	0.17	8.51	1.42	*99.79*	3.68	58.10	62.18	59.33	46.00	81.84	26.62
	Saprock	KW-40	2.02	5.77	15.30	55.44	0.19	1.56	8.89	0.62	0.15	8.23	1.65	*99.81*	3.62	55.11	58.38	55.76	40.16	79.66	24.95
	Saprock	KW-45	1.98	4.70	16.26	56.14	0.20	1.30	9.29	0.47	0.15	8.16	1.19	*99.85*	3.45	56.38	59.05	57.02	34.73	79.64	26.01
	Saprock	KW-44	2.26	5.08	16.03	55.86	0.22	1.47	8.88	0.65	0.15	8.51	0.70	*99.83*	3.49	55.96	58.98	56.64	37.03	78.46	25.61
	Fresh rock	KW-43	2.04	5.16	15.95	56.64	0.23	1.58	8.72	0.57	0.15	8.31	0.55	*99.89*	3.55	56.39	59.73	57.20	38.53	38.53	26.25
	Fresh rock	KW-39	2.40	5.56	15.32	56.45	0.20	1.63	8.64	0.66	0.15	8.31	0.56	*99.87*	3.69	54.72	58.11	55.34	39.44	39.44	25.38

LOI: Loss on ignition (%), **Ro:** Ruxton rate, **CIA:** Chemical index of alteration, **CIW:** Chemical index of weathering, **PIA:** Plagioclase index of alteration, **AI:** Ishikawa Alteration index, **CCPI:** Chlorite- Carbonate-Pyrite index, **AAAI:** Advance argillic alteration index.

Table 2- Weathering parameters and optimum values used in this study.

		Optimum values		
Parameters	**Formula**	**F**	**W**	**Reference**
Ruxton rate (Ro)	SiO_2/Al_2O_3	10	0	*Ruxton (1986)*
Chemical index of alteration (CIA)	$100*[Al_2O_3 / (Al_2O_3 + CaO + Na_2O + K_2O)]$	≤50	100	*Nesbitt and Young (1982)*
Chemical index of weathering (CIW)	$100*[Al_2O_3 / (Al_2O_3 + CaO + Na_2O)]$	≤50	100	*Harnois (1988)*
Plagioclase index of alteration (PIA)	$100*[(Al_2O_3-K_2O)/(Al_2O_3+CaO+Na_2O-K_2O)]$	≤50	100	*Fedo et al (1995)*
Ishikawa Alteration index (AI)	$100*[K_2O+MgO)/(K_2O+MgO+Na_2O+CaO)]$	20-65	>60	*Ishikawa et al (1976)*
Chlorite- Carbonate-Pyrite index (CCPI)	$100*[(MgO+FeO)/(MgO+FeO+Na_2O+K_2O)]$	15-85	>65	*Large et al (2001)*
Advance argillic alteration index (AAAI)	$100*[(SiO_2)/(SiO_2+10MgO+10CaO+10Na_2O)]$	20-60	>60	*Willians and Davidson (2004)*

F: Fresh rock, **W:** weathered rock.

5. Discussion

Strandja (Yıldız) Mountain, is one of Turkey's most heavily forested region, is an important area to examine the alteration characteristics of crystalline rocks. In this study, the Late Cretaceous - aged granodiorite and diorite of the DIB were distinctively selected, the weathering products, differences of same - aged rocks and two different compositions derived from the same source were tried to be determined. For this purpose, detailed mineralogical, petrographic and chemical analyzes of the sections selected from the areas where both rock units weathered and altered (Figure 2). As a result of the analysis, it is seen that the chemical index of alteration (CIA) and chemical index of weathering (CIW) values increase from depth to surface. Likewise, it is seen that the loss on ignition (LOI) values increase at different rates in all levels of both rock units from depth to surface. Since granodiorite compositional rock contains more K - feldspar, it can be concluded that it is more decomposed than quartz diorite and has a higher LOI value (Table 1 and Figure 6). Samples were collected

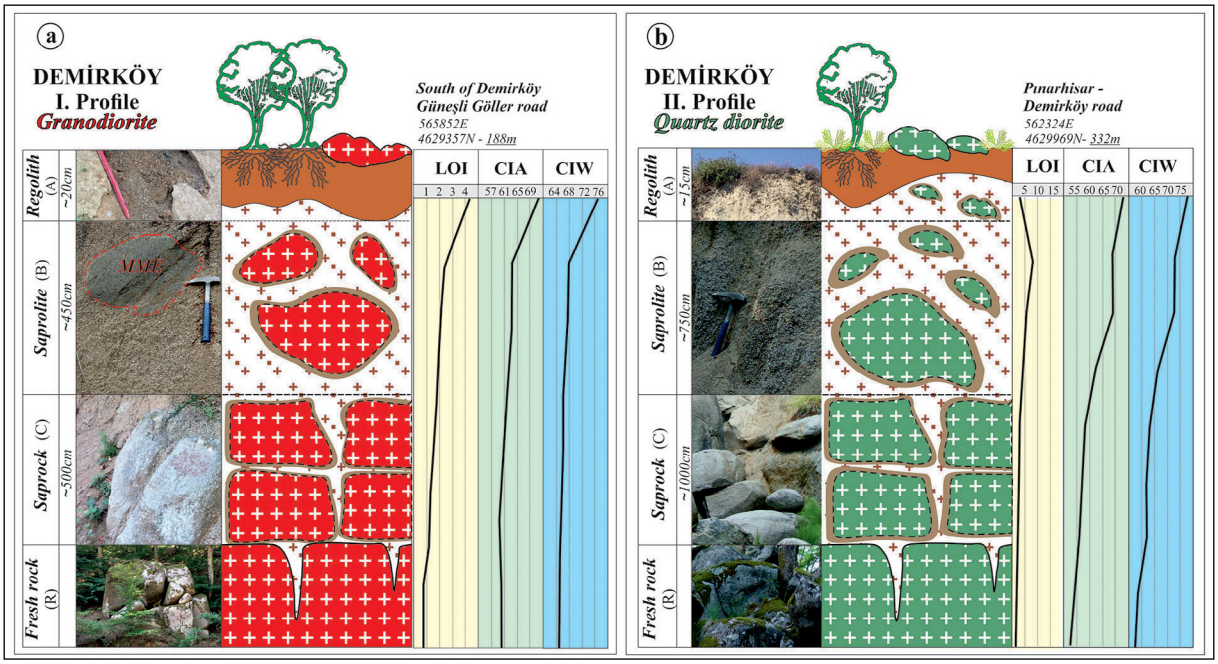

Figure 6- Samples were collected from: a) The vertical profile line of the granodiorite and the change in loss on ignition (LOI), chemical index of alteration (CIA), chemical index of weathering (CIW) parameters from the surface to the fresh rock; b) Vertical profile line of quartz diorite and change in loss on ignition (LOI), chemical index of alteration (CIA), chemical index of weathering (CIW) parameters from the surface to fresh rock. (A, B, C, R soil horizons, Hillel, 1998).

from regolith, saprolite and saprock, respectively, along both profiles, and XRD analyzes were performed and compared (Figures 4 and 5).

According to the detailed clay analysis (XRD) results; clay mineral association observed in profiles belonging to both rock groups are illite±kaoline+smectite+chlorite+chlorite/vermiculite. From this point of view, vermiculite and smectite are formed because of textural breakdown of the rock (Figure 5). Illite and chlorite are predominant in the weathering products of the granodiorite profile I, whereas in the weathering products of the quartz diorite profile II, there is a proportional increase in the amount of smectite - vermiculite in addition to illite and chlorite (Figure 5).

Multi element variation diagrams were drawn by dividing the main element analysis results of each unit into fresh rock values in order to reveal the behavioral and compositional differences of regolith, saprolite and saprock units formed as a result of weathering according to source rocks (host rock) (Figure 7). Regolith products in the granodiorite profile are depleted in terms of CaO%, MgO% and MnO% elements as a result of washing, and on the other hand, an increase in clay content and an enrichment in Al_2O_3% is observed. As a result of the decomposition in saprolite and saprock products of the same rock, it is seen that there is a decrease in Fe_2O_3%, MgO%, P_2O_5%, TiO_2% and MnO% values. On the other hand, regolith products in the quartz diorite profile become depleted in terms of Na_2O%, CaO%, MgO%, P_2O_5% and MnO% elements as a result of washing, and the Al_2O_3% value is enriched due to the increase in the clay content ratio. When the weathering rates of both units are compared, it can be said that the quartz diorite undergoes less alteration and weathering compared to the granodiorite (Figure 6). As a result of the decomposition of both rock units, a significant change was observed in the total Al_2O_3% and % LOI values (Table 1). Variation diagrams were drawn separately (SiO_2 + Na_2O + K_2O + CaO)% versus % LOI and Al_2O_3% values to reveal the alteration boundaries based on the change rates of these elements (Figures 8a and b).

Accordingly, in regolith, saprolite and saprock, it is possible to show the discrimination areas in which loss on ignition rates show a significant change with a clear line interval depending on the LOI% values (Figure 8a). Thus, it is possible to separate

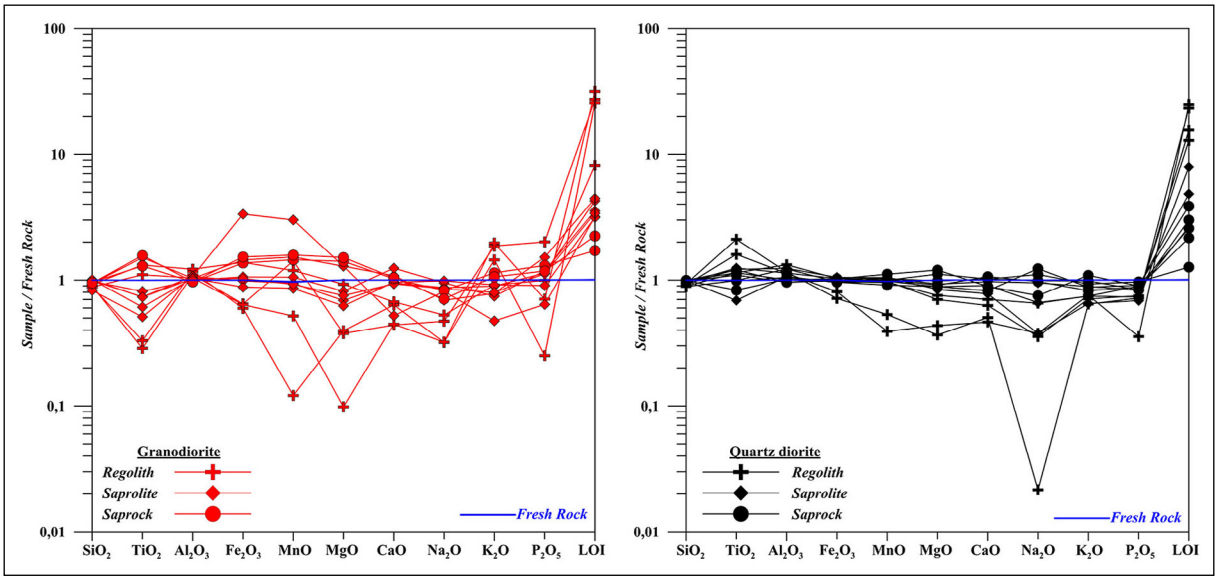

Figure 7- % Major oxide change diagram normalized to fresh rock values of weathering zones of granodiorite and quartz diorite sections.

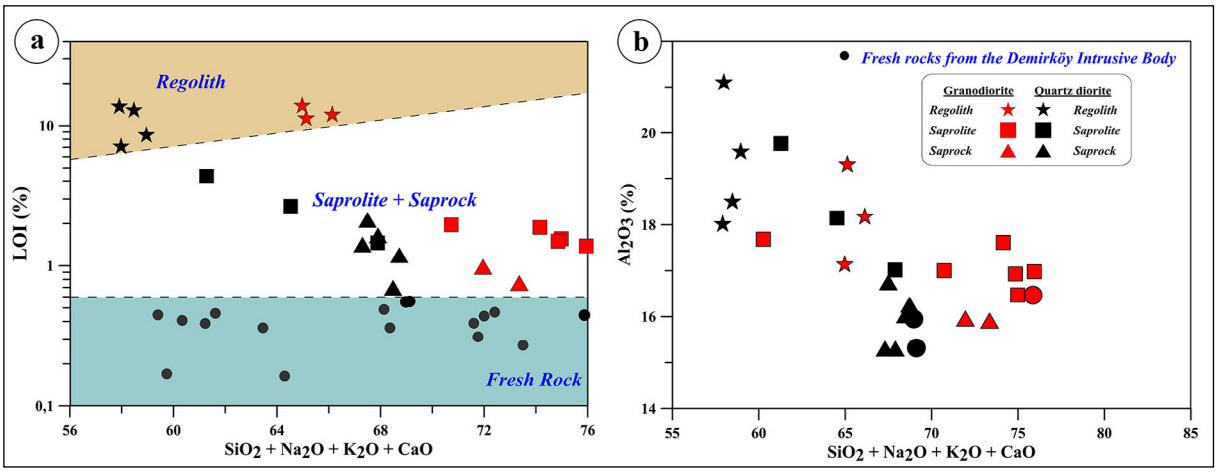

Figure 8- In the rock groups belonging to the study area; a) The change of the (SiO_2+Na_2O+K_2O+CaO)% major oxide total according to the LOI% value, b) The change of the sum of the (SiO_2+Na_2O+K_2O+CaO)% major oxide elements according to the Al_2O_3 value.

the boundaries of regolith and saprolite - saprock from fresh rock by using (SiO_2+Na_2O+K_2O+CaO)% values against LOI%. On the other hand, since both rock groups contain different amounts of clay due to weathering, a distinct boundary of differentiation was not determined in the Al_2O_3% variation diagram (SiO_2+Na_2O+K_2O+CaO) (Figure 8b).

In order to determine the alteration degree of the rocks, they were evaluated according to the chemical analysis results on the ACNK diagram (Figure 9a). According to the ACNK diagram, saprock samples belonging to granodiorite and quartz diorite profiles are observed in transition to slightly and medium altered rock area. Regolith samples that are assumed to fall into the highly altered rock area, fall into the moderately altered rock area, probably due to washing. In the change of the rate of loss on ignition versus the plagioclase weathering index; It is observed that the arenization tendency of the samples increased parallel to the increasing segregation (Figure 9b).

In order to distinguish whether alteration is diagenetic or hydrothermal (Large et al., 2001), alteration index variation diagrams versus CCP (chlorite - carbonate - pyrite) index were drawn

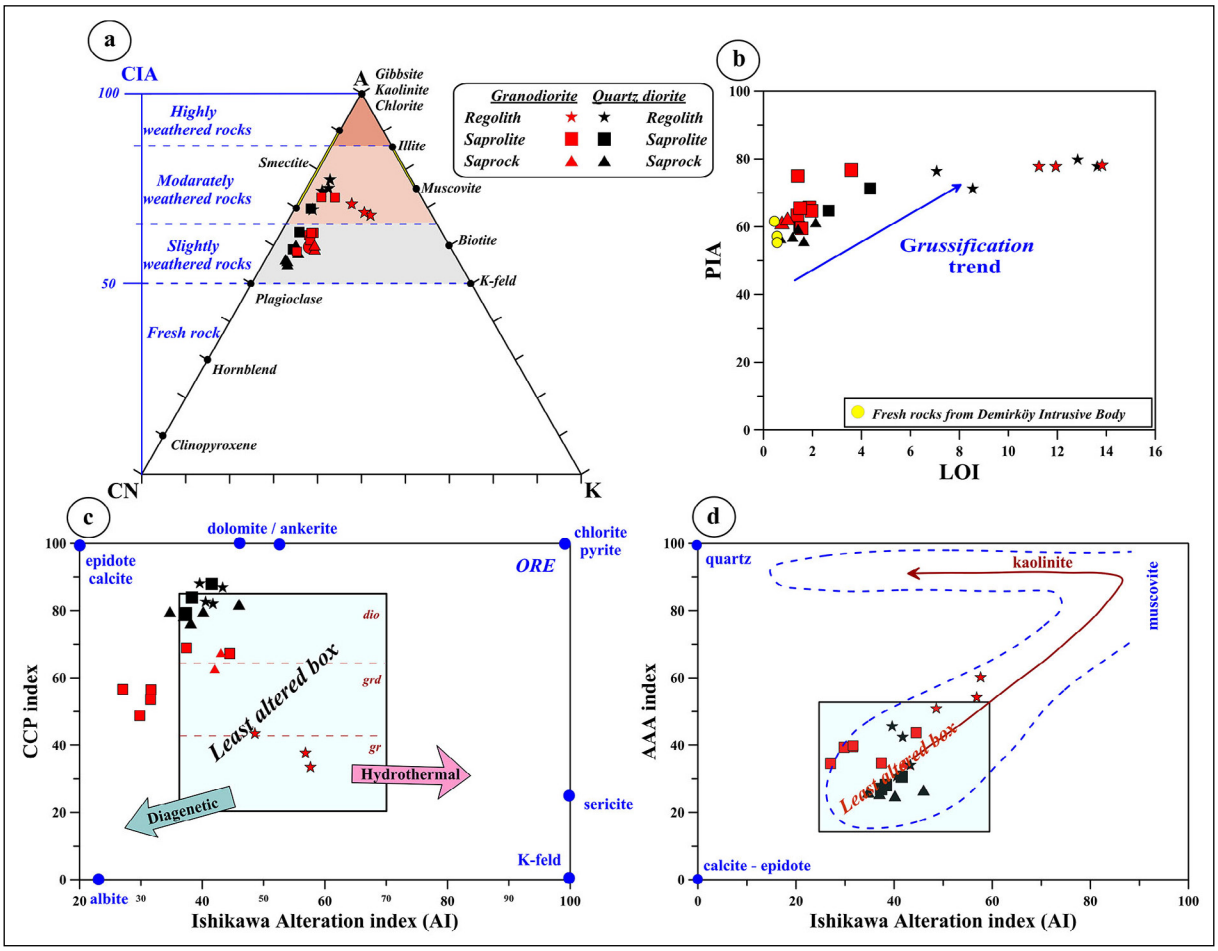

Figure 9- a) The distribution of samples in the ACNK diagram and their classification according to the CIA value (Nesbitt and Young, 1982), b) the variation diagram according to the loss on ignition value versus the plagioclase decomposition index (Fedo et al, 1995), c) Distribution of the samples relative to the box plot in the CCP (calcite-chlorite-pyrite) index versus alteration index (Large et al., 2001), d) Distribution of the samples relative to the box plot in the alteration index change versus the advanced argillic alteration index (AAAI) (Williams and Davidson, 2004).

(Figure 9c). According to this diagram; It has been demonstrated that the alteration properties of the samples collected from the DIB are not hydrothermal in general, but tend towards albite, calcite - epidote and are due to diagenetic alteration. Alteration index (AI) is accepted between 20 - 60 for fresh rocks, and when it is more than 50, it is accepted that the effect of hydrothermal alteration begins. In field observations, metasomatic effect and hot fluid - relatedmalachite - azurite - pyrite formations (Fe, Cu enrichments) are observed at the contact and close to the contact of granitic and granodioritic rocks. In Figure 9c, the discordant position of the granodiorite in regoliths was formed as a result of the metasomatic effects. Figure 9d shows that the distinct tendency of rock groups to become clay at the regolith level may be related to the increase in the Al_2O_3 ratio. This relationship has emerged as a result of the increase in the ratio of clay content at these levels and the decrease in quartz and other mineral ratios in the rocks.

6. Conclusion

Crystalline rocks can undergo significant changes due to atmospheric and hydrothermal factors. These changes are significantly related to the primary composition of the rocks as well as the degree of weathering. Strandja Massif, is part of Turkey's tectonic units which lies through the East Europe, separated from Pontides with West Black Sea Fault. Alteration may caused due to faulting and magmatic intrusions within the tectonic unit. At the same time, weathering occurs depending on the changes

in climatic conditions. In this study, granodioritic and quartz dioritic rocks in the DIB within the Stranja Massif, outcropped in the Strandja (Yıldız) mountain range. The alteration of two different rock units from the surface to the depth was investigated mineralogically, petrographically and geochemically, and their weathering features and genesis were determined. The alteration degrees of two different rock units belonging to the same intrusive body and the different weathering products were determined. The weathering lithologies of both rock units are divided into 3 different levels as regolith, saprolite and saprock, they were mineralogically and chemically investigated. Regolith, saprolite - saprock and fresh rock boundaries are determined based on LOI% versus (SiO_2+Na_2O+K_2O+CaO)% values of both rock units. While the weathering products of the granodiorite mostly are illite and chlorite - type clay, smectite and vermiculite - type clay are also observed in quartz diorite. It was determined that both rock units were generally altered as a result of diagenetic alteration, and did not show any metal - bearing alteration due to hydrothermal alteration. There is a weak hydrothermal effect at the regolith levels, and it is thought that this may occur as a result of the combination of the transported products with the advanced alteration due to effects of metasomatism and hydrothermal fluids. Agriculturally, it has been determined that the regolith products formed by the weathering of the granodiorite are richer in K_2O% content and quartz compared to quartz diorite and are efficient due to their sandy texture.

Ackowledgement

This study, was carried out within the scope of 'Turkey's Pluton Database' conducted by MTA Geological Research in 2016 - 2017. The authors thank to Ayşegül Aydın (MTA) for supporting field works, Dr. Kıymet Deniz (Ankara University) for her support in the analysis process, Dr. Ebru Kavukçu (MTA) and Arif Talay (MTA) for their contribution in conducting the analyses. The authors also thank to two anonymous referees especially with their suggestions and critics on XRD results and Dr. Hafize Akıllı (MTA) to contribute to the development of the article with their constructive critics.

References

Arias, D., Pando, L., López-Fernández, C., Díaz-Díaz, L. M., Rubio-Ordóñez, Á. 2016. Deep weathering of granitic rocks: A case of tunnelling in NW Spain. Catena 137, 572-580.

Aydın, Y. 1982. Geology of the Yıldız mountains (Strandja). (Doctoral dissertation, Habilitation thesis, Istanbul Technical University).

Aykol, A., Tokel, S. 1991. The geochemistry and tectonic setting of the Demirköy pluton of the Srednogorie - Istranca granitoid chain, NW Turkey. Mineralogical Magazine 55(379), 249-256.

Bates, R.L., Jackson, J.A. 1987. Glossary of geology (3rd edition) American Geological Institute, Alexandria, Virginia.

Borrelli, L., Greco, R., Gullà, G. 2007. Weathering grade of rock masses as a predisposing factor to slope instabilities: reconnaissance and control procedures. Geomorphology 87(3), 158-175.

Boyraz, D., Cangir, C. 2009. Yıldız Orman Ekosisteminde Yer Alan Tipik Toprakların Sınıflandırılması ve Amenajmanları. Journal of Tekirdag Agricultural Faculty 6(1).

Catto, S., Cavazza, W., Zattin, M., Okay, A. I. 2018. No significant Alpine tectonic overprint on the Cimmerian Strandja Massif (SE Bulgaria and NW Turkey). International Geology Review 60(4), 513-529.

Çağlayan, M. A., Yurtsever, A. 1998. Burgaz-A3, Edirne B-2 ve B-3; Burgaz A-4 ve Kırklareli B-4; Kırklareli B-5 ve B-6; Kırklareli C-6 paftaları, 1: 100.000 ölçekli açınsama nitelikli Türkiye Jeoloji haritaları No: 20, 21, 22, 23. Maden Tetkik ve Arama Genel Müdürlüğü, Ankara.

Delvigne, J. 1998. Atlas of micromorphology of mineral alteration and weathering: Ontario Canada Mineralogical Association of Canada and Orstom editions.

Fedo, C. M., Wayne Nesbitt, H., Young, G. M. 1995. Unraveling the effects of potassium metasomatism in sedimentary rocks and paleosols, with implications for paleoweathering conditions and provenance. Geology 23(10), 921-924.

Fiantis, D., Nelson, M., Shamshuddin, J., Goh, T. B., Van Ranst, E. 2010. Determination of the geochemical weathering indices and trace elements content of new volcanic ash deposits from Mt. Talang (West Sumatra) Indonesia. Eurasian Soil Science 43(13), 1477-1485.

Graham, R. C., O'Geen, A. T. 2010. Soil mineralogy trends in California landscapes. Geoderma 154(3-4), 418-437.

Harnois, L. 1988. The CIW index: a new chemical index of weathering. SedG, 55(3), 319-322.

Hillel, D. 1998. Environmental Soil Physics, Academic Press, San Diego.

Ietto, F., Le Pera, E., Perri, F. 2013. Weathering of the 'Rupe di Tropea' (southern Calabria): consolidation criteria and erosion - rate estimate. Rend Online Soc Geol Ital 24, 178-180.

Ishikawa, Y., Sawaguchi, T., Iwaya, S., Hariuchi, M. 1976. Delineation of prospecting targets for Kuroko deposits based on modes of volcanism underlying dacite and alteration halos. Mining Geology 26, 105-117.

Karacık, Z., Tüysüz, O. 2010. Petrogenesis of the Late Cretaceous Demirköy Igneous Complex in the NW Turkey: implications for magma genesis in the Strandja Zone. Lithos 114(3-4), 369-384.

Large, R. R., Gemmell, J. B., Paulick, H., Huston, D. L. 2001. The alteration box plot: A simple approach to understanding the relationship between alteration mineralogy and lithogeochemistry associated with volcanic-hosted massive sulfide deposits. Economic Geology 96(5), 957-971.

Meunier, A. 2005. Clays in soils and weathered rocks. Clays 231-293.

Migon, P., Thomas, M. F. 2002. Grus weathering mantles - problems of interpretation. Catena 49(1-2), 5-24.

Moore, W. J., McKee, E. H., Akıncı, Ö. 1980. Chemistry and chronology of the plutonic rocks in the Pontid Mountains, Northern Turkey. Belgrade: Europe Copper Deposits 209-216.

Nahon, D. B. 1991. Introduction to the petrology of soils and chemical weathering. John Wiley and Sons, Inc.

Nesbitt, H., Young, G. M. 1982. Early Proterozoic climates and plate motions inferred from major element chemistry of lutites. Nature 299(5885), 715-717.

Okay, A. I., Tüysüz, O. 1999. Tethyan sutures of northern Turkey. Geological Society, London, Special Publications 156(1), 475-515.

Okay, A. I., Nikishin, A. M. 2015. Tectonic evolution of the southern margin of Laurasia in the Black Sea region. International Geology Review 57, 5-8, 1051-1076.

Ollier, C. D. 2010. Very deep weathering and related landslides. Geological Society, London, Engineering Geology Special Publications 23(1), 5-14.

Ollier, C., Calcaterra, D., Parise, M. 2007. Studies in weathering and slope movements - an introduction. Geomorphology 3(87), 101-103.

Power, E. T., Smith, B. J. 1994. A comparative study of deep weathering and weathering products: case studies from Ireland, Corsica and Southeast Brazil. In "Rock weathering and landform evolution", 21-40.

Ruxton, B. P. 1968. Measures of the Degree of Chemical Weathering of Rocks," J. Geol 76, 518-527.

Sharma, A., Rajamani, V. 2000. Weathering of gneissic rocks in the upper reaches of Cauvery river, south India: implications to neotectonics of the region. Chemical Geology 166(3-4), 203-223.

Taylor, G., Eggleton, R. A. 2001. Regolith geology and geomorphology. John Wiley and Sons.

Ulusoy, E. 2012. Demirköy (Kırklareli) intrüzif kayaçlarının jeolojisi ve petrolojisi (Msc thesis, University of Ankara).

Ulusoy, E., Kadıoğlu, Y. K. 2015. Temporal and Spatial Position of Magmatic Rocks within Eastern part of Strandja Massif: Demirköy, Kırklareli, NW Turkey. İstanbul Üniversitesi'nde Jeoloji'nin 100. Yılı Sempozyumu Bildiri Özleri Kitabı, 53-54.

Üşümezsoy, Ş. 1982. Istranca masifinin petrojenetik evrimi (Doctoral dissertation, PhD Thesis, İstanbul University, Eathsciences Faculty).

Velde, B. B., Meunier, A. 2008. The origin of clay minerals in soils and weathered rocks. Springer Science and Business Media.

Whalley, W. B., Turkington, A. V. 2001. Weathering and geomorphology. Geomorphology (Amsterdam) 41(1).

Williams, N. C., Davidson, G. J. 2004. Possible submarine advanced argillic alteration at the Basin Lake prospect, Western Tasmania, Australia. Economic Geology 99(5), 987-1002.

Bulletin of the Mineral Research and Exploration

http://bulletin.mta.gov.tr

Systematic and biostratigraphic evaluation of the Late Cretaceous benthic foraminiferal assemblages of southeastern Batman

Derya SİNANOĞLU[a*]

[a]*Batman University, Petroleum and Natural Gas Engineering Department, Batman, Turkey*

Research Article

Keywords:
Benthic Foraminifera, Systematic Paleontology, Garzan formation, Maastrichtian.

ABSTRACT

The study area is located in 15 km west of Gercüş town (southeast of Batman) at the northern margin of the Arabian Plate. This region is the only place where Garzan formation, one of the important petroleum reservoir of the Southeastern Anatolia, outcrops and detailed scientific studies have been carried out. The unit, mainly of beige - yellowish, thin - thick bedded, benthic foraminifera and algae bearing limestones, has a rich fossil content and high diversity. This diversity in the benthic foraminifera is noteworthy. These assemblages contains *Vandenbroekia munieri* Marie, *Coskinolina* sp., *Cyclogyra* sp. with porcellaneous test; *Biconcava bentori* Hamaoui, *Nezzazata simplex* Omara, *Nezzazatinella picardi* (Henson), *Trochospira avnimelechi* Hamaoui, *Antalyna korayi* Farinacci and Köylüoğlu, *Moncharmontia apenninica* (De Castro), *Moncharmontia compressa* (De Castro), *Fleuryana adriatica* (De Castro), *Pseudocyclammina sphaeroidea* Gendrot, *Broeckinella arabica* Henson, *Cuneolina pavonia* d'Orbigny, *Cuneolina ketini* Inan, *Dicyclina schlumbergeri* Munier - Chalmas, *Pseudolituonella reicheli* Marie, *Dictyoconella complanata* Henson, *Minouxia lobata* Gendrot, *Minouxia gümbelitrioides* Marie, *Arenobulimina* sp. with microgranular and agglutinated tests and *Fissoelphidium operculiferum* Smout, *Orbitoides medius* (d'Archiac), *Orbitoides megaloformis* Papp and Küpper, *Omphalocyclus anatoliensis* Özcan, *Sirtina orbitoidiformis* Brönnimann and Wirtz, *Goupillaudina* sp. with hyaline test. In this study, the age of Garzan formation has been determined as Maastrichtian based on benthic foraminifera.

Received Date: 07.07.2020
Accepted Date: 13.10.2020

1. Introduction

Southeastern Anatolia is the region where almost 99% of Turkey's petroleum production is produced. Batman region is the place where the most of this production is carried out. The study area is located in the southeast of Batman, about 15 km west of the town of Gercüş. Detailed paleontological researches could not be carried out due to the security issues in the region that has been lasting for years. The present studies are limited with the information obtained mostly from drillings done by of Turkish Petroleum Corporation (TPAO). The main geological structure of the Southeastern Anatolia Region is linked to the relative relations of the Arabian and Anatolian continents over time. The units formed in the North during the subduction of the oceanic crust between Eurasian and Arabian continents towards the Eurasian continent, thrusted over the Arabian Plate in early Miocene (Yılmaz, 1993; Robertson, 2000). In the vicinity of Batman, where the study area is located, the main structural elements formed during the Cenozoic nappe emplacement caused the Cretaceous aged reservoirs to be folded and fractured as well, due

Citation Info: Sinanoğlu, D. 2021. Systematic and biostratigraphic evaluation of the Late Cretaceous benthic foraminifera assemblages of southeastern Batman. Bulletin of the Mineral Research and Exploration 165, 267-293. https://doi.org/10.19111/bulletinofmre.809914

**Corresponding author: Derya SİNANOĞLU, derya.sinanoglu@batman.edu.tr*

to the fact that the Cretaceous allochthons remain in the north. For this reason, Cenozoic structures, which can be defined very well, are important in terms of hydrocarbon exploration (Siyako et al., 2013). Most of the subsequent studies are unpublished and in the form of reports, which aimed at revealing the stratigraphy and the tectonic structure of the basin in order to determine the hydrocarbon possibilities of the region. Paleontological studies are also very limited. The aim of this study is to reveal the micropaleontological data of the Garzan formation from which some of the petroleum in Batman region are obtained. For this purpose; this purpose; detailed investigations were carried out on the benthic foraminifera determined in the formation, and systematic studies of larger benthic foraminifera based on the biometrical analysis were yada have been performed. The detailed age data obtained, provided a better understanding of the biostratigraphic features of the formation (Figure 1).

2. Material and Method

Measured section, isolated specimens and washing samples were taken from the outcrops which is the only locality of the Garzan formation in the area studied. Most of the isolated specimens are orbitoid forms. Equatorial sections have importance particularly in the determination of these forms (*Orbitoides*, *Omphalacyclus*). For this reason, before preparing thin sections, external views of the individuals were noted and their thickness was measured. Samples were soaked in diluted HCl (17%) in order to see their external view more clearly. The way followed in thin section preparation is as follows; in the preparation of equatorial sections, the specimen is abraded on the glass plate via grinding powders. This process is continued until the first chamber appears. When the first chamber appears, grinded surface of the specimen is adhered on the grinded slide, with Canada balsam by using a heater. In order to set the thin section to proper thickness for the examination under a microscope, grinding process repeated with grinding powders. The axial sections of the mentioned forms are prepared in following similar ways. Weathered sandy - clayey soft rock samples taken from the field were prepared and the soil samples were washed and dried well first. Then, the samples were kept in 17% diluted hydrogen peroxide solution for 24 hours. After the waiting period, they were filtered and dried in a drying - oven or in a hot environment. Finally, foraminifers were extracted under binocular microscope by using 0.125 - 0.250 mesh sieves. Hard rocks are first cut a few mm thick in the Petrocat machine. The surface to be adhered on the slide is smoothed on a glass plate with grinding powders. Similarly, the surface of the slide to be adhered is abraded by iron powders. The sample is adhered on to the glass with Canada balsam, that no air - bubble void should be remained. After cooling down for a while, the samples are thinned. In order to set the sample on the slide to proper thickness for the examination under a microscope, fine grinding powders are used. Thus, the required thickness is ensured. In addition, the Knitter Method was used to extract calcareous fossil forms from hard limestone samples. For this, approximately 100 grams of sample was ground coarsely and put into a deep bottle. 65% acetic acid and 100 ml of chloroform were added, enough to cover 0.5 cm more on it, the bottle was shaken and closed in a way that it would not take air. After waiting 15 hours, the samples were washed and dried. The above - mentioned oriented thin section preparation methods were carried out on the obtained individuals.

The samples taken from Garzan formation constitute 130 m of the section which is approximately 155 m along the section line. 20 samples were taken from the Garzan formation and most of these samples are hard limestone. In addition, isolated samples of orbitoids were obtained from unconsolidated levels. systematic descriptions and classification of foraminifera is in accordance with the studies of Loeblich and Tappan (1987).

3. Regional Geology and Stratigraphy

Distinct geological units ranging form Precambrian to recent are exposed in the Southeastern Anatolia Region. Due to the presence of representative outcrops in the Southeastern Anatolia, many geologists (predominantly the geologists from oil companies) have concentrated on in Amanos Mountains, in Adıyaman - Pendeği - Tut regions, in Karababa and Korudağ in the Hazro region, around Mardin - Derik, in the Harbol Hermis basins and in Hakkari (Yılmaz and Duran, 1997).

The main geological structure of the Southeastern Anatolia Region was controlled by the relative movements of the Arabian and Anatolian continents over time. Uplift and subsidence on the Arabian continent due to these movements controlled the

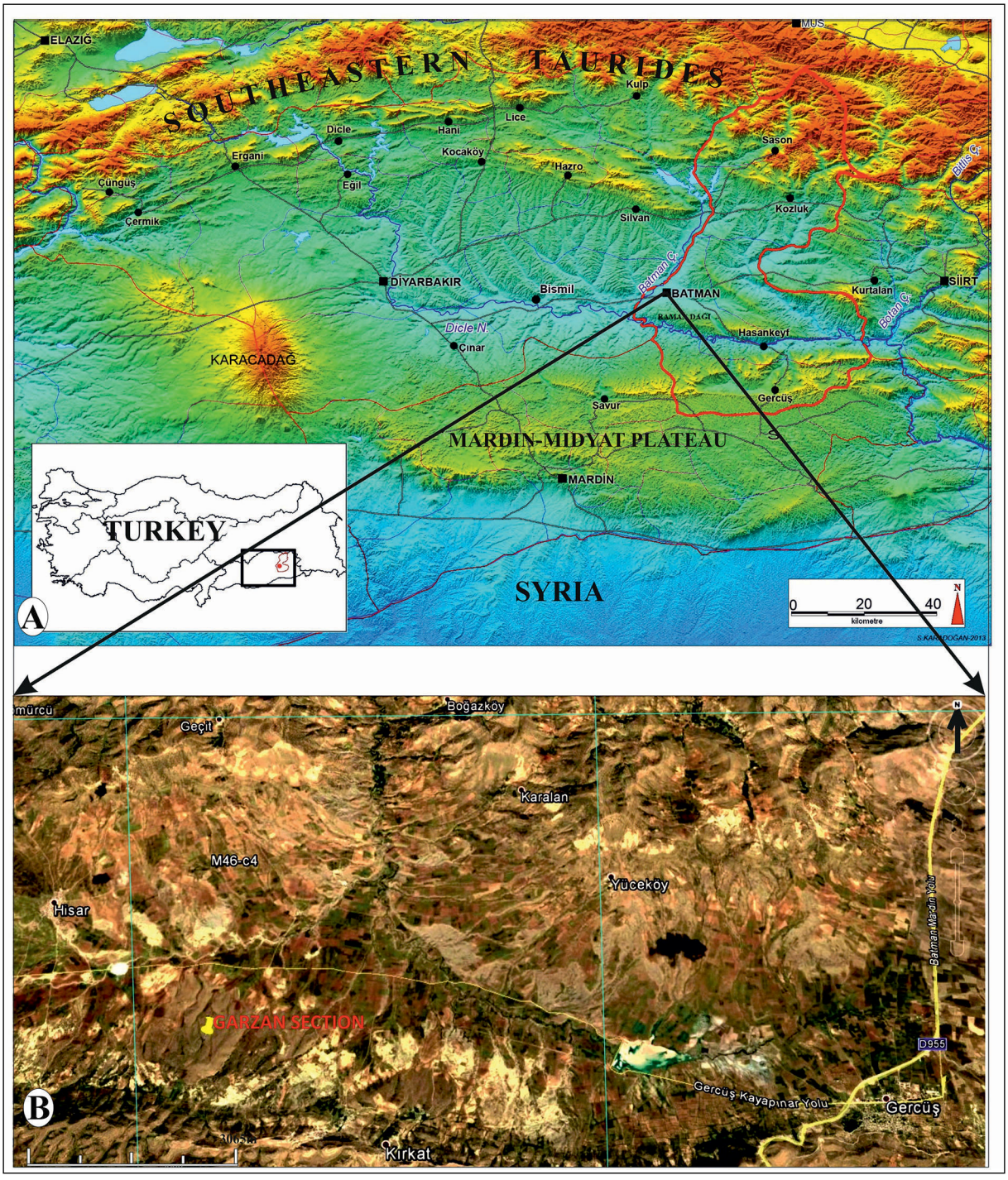

Figure 1- Location of the study area A) Geographical location of the province Batman -modified after Sinanoğlu et al., 2017; B) Google Earth view of the study area).

sedimentation. The units in the study area start with the Kıradağ formation, which is not observed on the surface, and continues with the Garzan formation represented by shallow marine carbonates that are exposed in the core of the Gercüş Anticline. The oldest formation outcropping in the study area is the Garzan formation of Şırnak Group which consists of beige - yellowish colored algal limestones with abundant foraminiferal content. Due to ongoing deepening, Garzan carbonates are conformably covered by Lower Germav formation consisting of alternation of light grey colored, fossiliferous carbonated siltstone,

clayey limestone, marl. This formation, with a conformable contact, is followed by Paleocene aged Upper Germav formation which is characterized by dark grey marls, greenish grey sandstones and clays. The formation gains a regressive character towards the top, and passes to limestones and sandstones. With the regression, terrestrial Antak formation was deposited. Paleocene Antak formation consisting of fluvial - originated conglomerate, sandstone and mudstones, and the other units of this period were defined in the Şırnak Group. As the last stage, Hoya formation consisting of shallow marine limestones was deposited with the transgression that developed in the middle Eocene. Hoya formations which overlies the Şırnak Group with an angular unconformity was defined in the Midyat Group (Siyako et al., 2013; Figures 2 and 3).

3.1. Garzan Formation

The formation, consisting of shallow marine limestones, is defined as reservoir rocks in the Garzan oil field and was named after the Garzan (Yanarsu) River that flows in the south of the area (Kellog, 1960; 1961; Salem et al., 1986). It was first described by Kellog (1960) in the literature. Garzan formation, which was deposited in a widespread area in the region and has known to be operated for oil production in many fields, is accepted as the lateral equivalent of the Besni formation in the west and, in the east, Üçkiraz formation defined in Hakkari (Güven et al., 1991). The formation forms a high and flat hill in the study area, compared to the surrounding Germav shales (Figure 2). Bioclastic limestones deposited in shallow marine environments such as reefs, near reefs and lagoons constitute the main lithology of the unit. It is one of the levels where oil is produced and has very good reservoir characteristics in Western Raman, Garzan and Germik fields, which are some of the largest fields in the Batman Region (Figures 4 and 5).

There are also clayey limestone and marl levels in the formation. The formation consists of cream - grey - light grey - beige colored, hard to very hard, thin - bedded to massive, fractured rocks with abundant fossils and karstic cavities. Bedding in the formation is distinct and discontinuous. Asphaltite and heavy oil residues are seen in the upper levels.

4. Benthic Foraminiferal Systematics

In this study, systematic descriptions of the important benthic foraminifera determined in the Late Cretaceous Garzan formation outcropping around

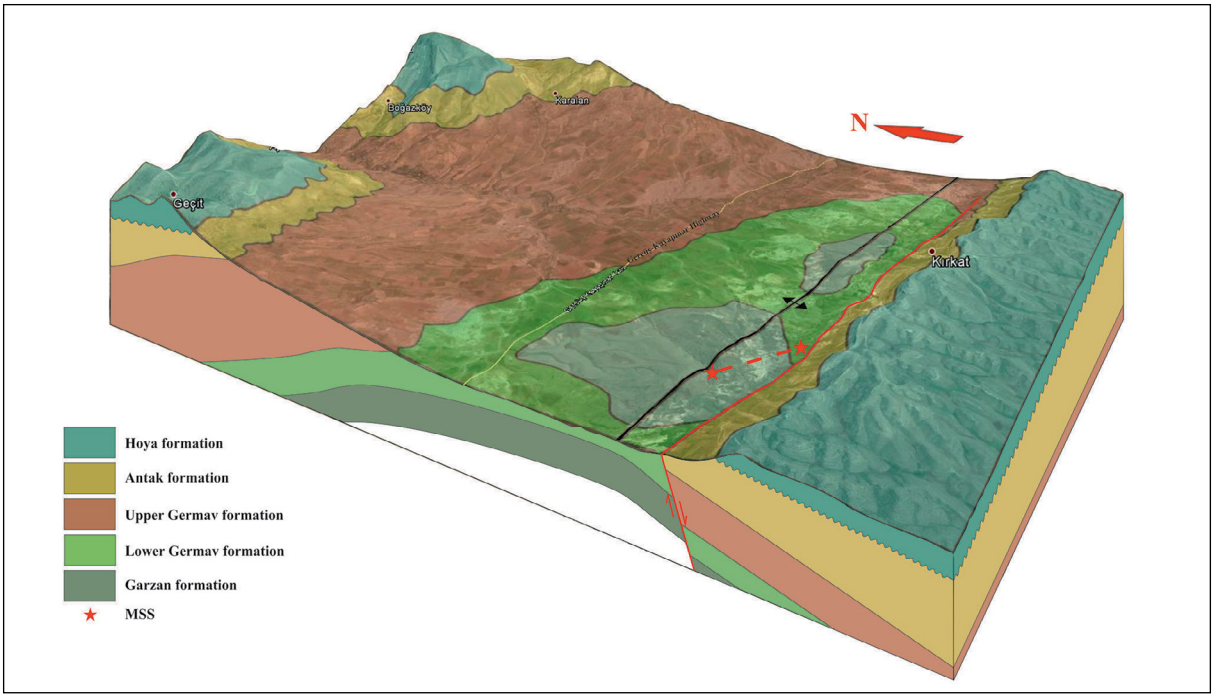

Figure 2- Garzan measured stratigraphic section line and 3D geological relief map of the study area (Section was measured between the coordinates N:4161 300 / E: 700 200 and N:4160 574 / E:700 308).

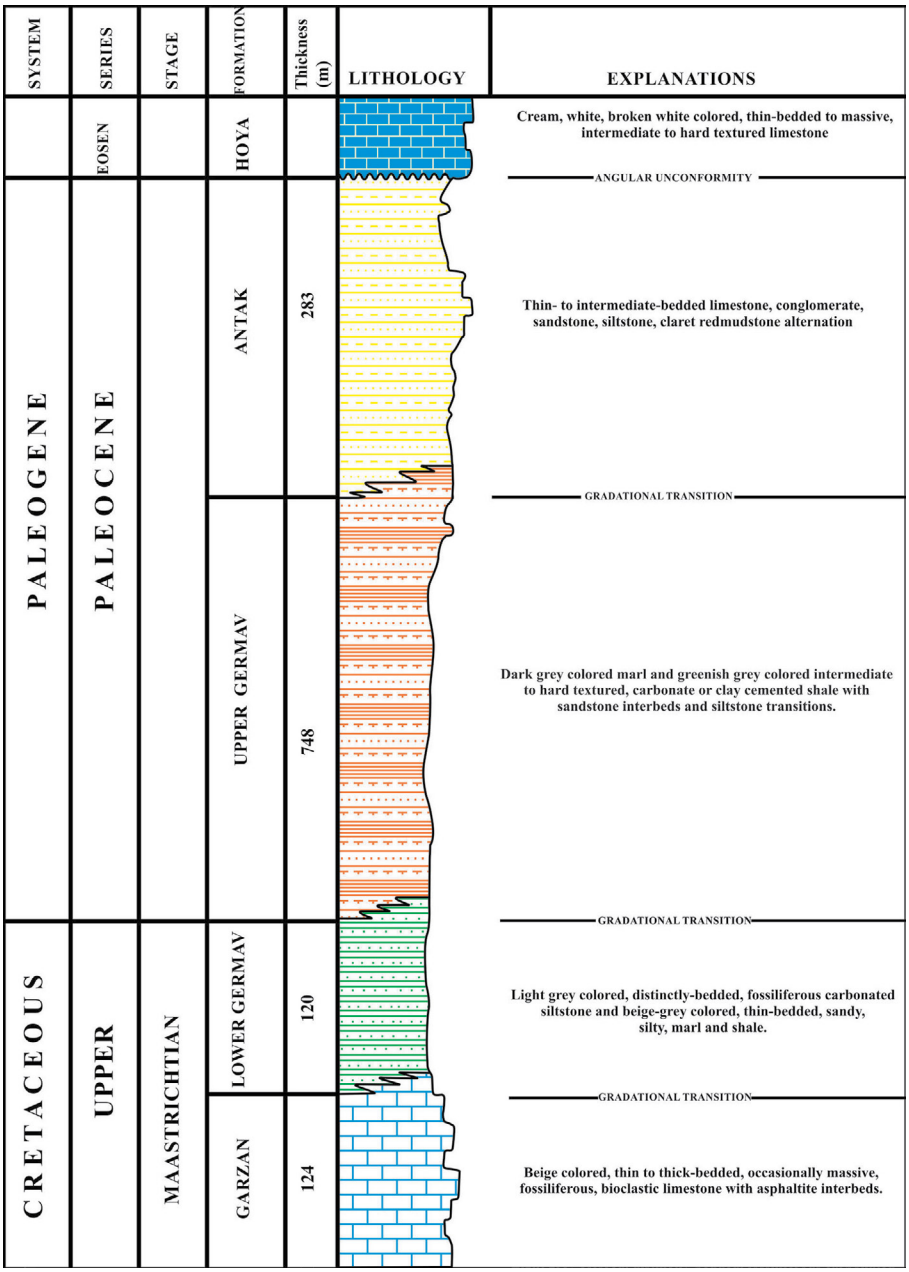

Figure 3- Generalized stratigraphic section of the study area (Modified after Siyako et al., 2013).

Gerçüş - Batman are given. Systematic descriptions are here presented based on fundamentally Loeblich and Tappan (1997). Figures of the determined foraminifers are presented in Plates 1-3.

Order: Foraminiferidae Eichwald, 1830

Suborder: Textulariina Delage and Herouard,1896

Superfamily: Lituolacea de Blainville, 1827

Family: Mayncinidae Loeblich and Tappan, 1985

Genus: *Biconcava* Hamaoui, 1965

Biconcava bentori Hamaoui, 1965

(Plate I, Figures. 1,2)

1965 *Biconcava bentori* Hamaoui; p. 14, pl. 1, figs. 12a-b; pl. 5, fig. 14; pl. 14, fig. 7.

1966 *Biconcava bentori* Hamaoui; De Castro, p. 7, 27.

1968 *Biconcava bentori* Hamaoui; Sgrosso, p. 164, fig. 3.

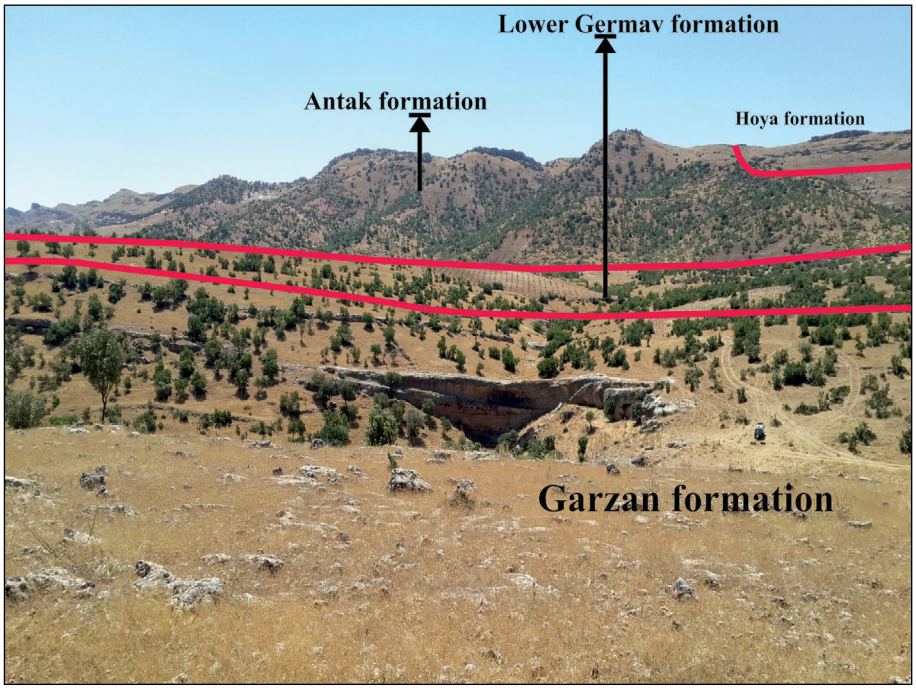

Figure 4- The stratigraphic position of the formations along the section line (M46-c4) (View to SE).

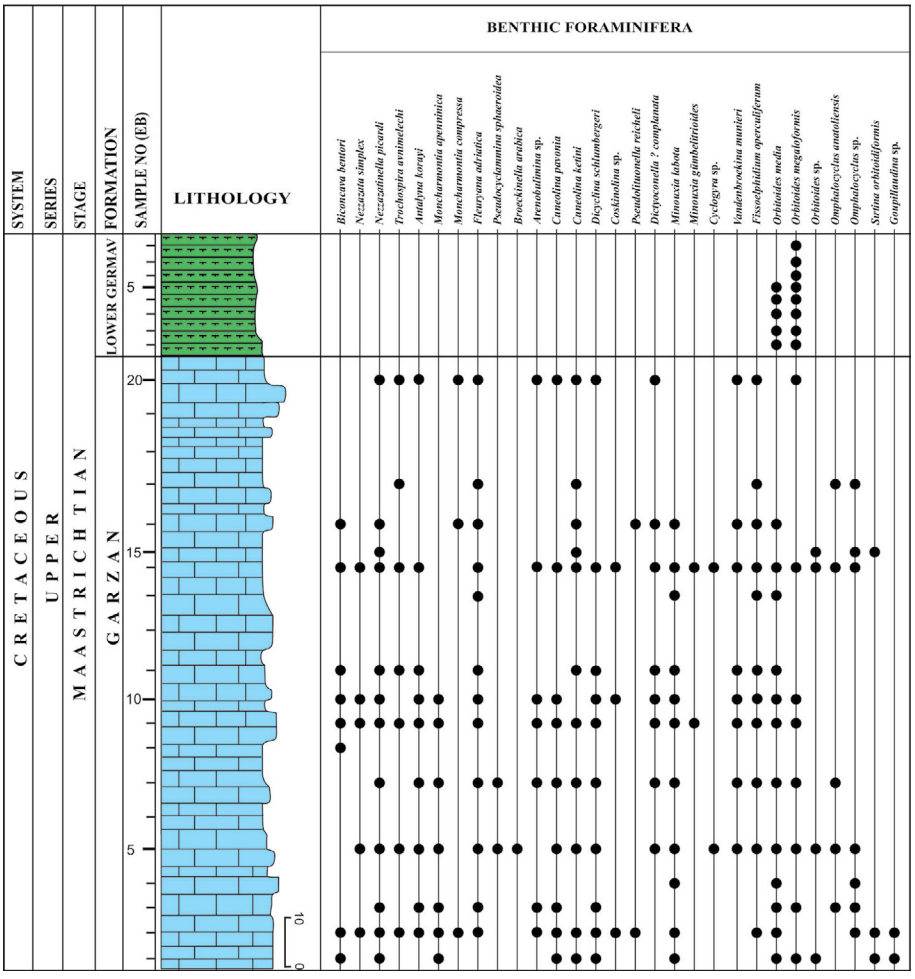

Figure 5- Benthic foraminiferal distribution of Garzan measured section.

1971 *Biconcava bentori* Hamaoui; Fleury, p. 185, pl. 3, figs. 15, 16.

Description: Test is lenticular, not rounded at the poles and has a partly angular appearance. Diameter and the thickness range between 0.30 - 0.55 mm and 0.09 - 0.15 mm, respectively. It is planispirally coiled and partly evolute. Proloculus is generally spherical and large in size. Its diameter is about 0.05 mm.

Stratigraphic and Geographical Distribution: *B. Bentori* was first described in the Cenomanian levels in the Hazera formation which is the type locality in Israel (Hamaoui, 1965; Luperto-Sinni, 1976). This species was found in Turkey (Bey Dağları) within the Late Cretaceous levels with *Chrysalidina gradata* d'Orbigny, *Trochospira avnimelechi* Hamaoui and Saint - Marc, *Nummoloculina regularis* (Philipson), *Dicyclina schlumbergeri* Munier - Chalmas, *Nezzazatinella picardi* (Henson), *Pseudolituonella reicheli* Marie, *Cuneolina pavonia* d'Orbigny, *Biplanata peneropliformis* Hamaoui and Saint - Marc (Sarı, 2006). It was reported from the late Cenomanian - early Turonian levels of the Eastern Desert/Egypt by İsmail et al. (2009) with *Daxia cenomana* Cuvillier and Szakal, *Flabellammina aegyptiaca* Said and Barakat, *F. alexanderi* Cushman, *Nezzazata gyra conica* (Smout), *N. simplex* Omara, *Dicyclina sampoi* Cherchi and Schroeder and *Nakkadyia awadi*. *B. bentori* was observed in the lower - middle levels of the Garzan section (Figure 5: 1 to16 meters).

Family: Nezzazatidae Hamaoui and Saint-Marc, 1970

Subfamily: Nezzazatinae Hamaoui and Saint-Marc, 1970

Genus: *Nezzazata* Omara, 1956

Nezzazata simplex Omara, 1956

(Plate I, Figures 3,4)

1956 *Nezzazata simplex* Omara, p. 889, pl. 102, figs. 7-13.

1965 *Nezzazata simplex* Omara; Omara and Strauch, p. 551, pl. 65, figs. 1-7.

2000 *Nezzazata simplex* Omara; İsmail, p. 250, figs. 7, 11, 12.

2009 *Nezzazata simplex* Omara; İsmail et al., pl. 4, fig. 1.

Description: Test is small and slightly conical. Diameter of the test varies between 0.175 - 0.50 mm. Proloculus is spherical shaped and tiny. Its diameter is about 0.01 mm. Coiling is in trochospiral manner. Size of the chambers slowly increase from the center towards the periphery. In the axial sections, marginal parts of the test show an angular appearance.

Stratigraphic and Geographical Distribution: This species was found in Cenomanian aged levels in its type locality in Egypt (Omara, 1956). İsmail (2000) reported this species from the Cenomanian - Turonian levels of Umm Khaysar Southern Galala, Eastern Desert (Egypt) with *Biconcava bentori, Nezzazata simplex, N. gyra conica, Dicyclina sampoi*. The same species, was later reported again in the Eastern Desert (Egypt) from the late Cenomanian - early Turonian aged levels with *Daxia cenomana, Flabellammina aegyptiaca, F. alexanderi, Nezzazata gyra conica, Biconcava bentori, Dicyclina sampoi* and *Nakkadyia awadi* (İsmail et al., 2009). *N. simplex* was observed at rare levels in the Garzan section in the study area (Figure 5: 2 to 4 meters).

Genus: *Nezzazatinella* Darmoian, 1976

Nezzazatinella picardi (Henson), 1948

(Plate I, Figure 5)

1947 *Valvulammina picardi* n. sp., Henson, p. 613, pl. 15, figs. 1, 3, pl. 18, figs. 3-6.

1981 *Nezzazatinella picardi* (Henson); Tronchetti, p. 49, pl. 11, figs. 1-10.

1985 *Nezzazatinella picardi* (Henson); Bilotte, pl. 15, figs. 3.

1992 *Nezzazatinella picardi* (Henson); Schlagintweit, pl. 1, figs. 9.

Description: Test is rounded or sharp at the poles, sutures are slightly curved and conical in shape. Diameter of the test ranges between 0.4 - 1.5 mm. Proloculus is spherical, and its diameter ranges between 0.07 - 0.25 mm. While the chambers are low in the early stage, they rapidly broaden in the adult stage. Coiling is in low trochospiral manner and asymmetrical (Table 1).

Stratigraphic and Geographical Distribution: Type locality of the species is the Middle East (Henson, 1948). Schlagintweit (1992) reported this species

Table 1- Biometrical data of *Nezzazatinella picardi*.

Sample	Diameter (mm)	Proloculus (mm)	Height-width of the chambers in the first whorl	Height-width of the chambers in the last whorl
GA1A2	1.125	0.25	-	0.275-0.275
GA1A3	0.625 0.5	0.075 0.25	0.1-0.1 0.1-0.1	0.125-0.25 0.125-0.375
GA2A1	0.975	0.05	0.15-0.075	0.125-0.375
GA2A2	0.375	0.075	0.1-0.1	0.175-0.1
GA2a	0.8 0.5	0.125 0.1	- 0.1-0.075	0.375-0.25 0.25-0.175
GA3A2	0.7	0.1	0.125-0.075	0.25-0.125
GA5A3	1.425	0.1	0.15-0.2	0.2-0.75
GA5a	1.025	0.15	0.075-0.075	0.35-0.15
GA10a	0.825 0.775	0.075 0.175	0.125-0.125 0.125-0.075	0.5-0.125 0.375-0.15
GA14A3	1.075	-	0.1-0.05	0.5-0.125
GA14a	1	0.125	0.125-0.75	0.525-0.225
GA16A1	0.575	0.2	0.125-0.1	0.325-0.125
GA20A3***	1.3	0.1	0.05-0.05	0.15-0.65

from the Cenomanian levels of Tyrol Mountains - Austria. This species was found in the Upper Cretaceous levels of Bey Dağları with *Nezzazatinella picardi* (Henson), *Dicyclina schlumbergeri* Munier, *Pseudonummoloculina heimi* (Bonet), *Scandonea* sp. and *Spiroloculina* sp. (Sarı, 2006). In this study, it has been determined from lower - middle - upper levels of the Garzan section (Figure 5: 1 to 20 meters).

Genus: *Trochospira* Hamaoui, 1965

Trochospira avnimelechi Hamaoui, 1965

(Plate I, Figure 6)

1965 *Trochospira avnimelechi* Hamaoui, p. 21, pl. 4, fig. 3.

1970 *Trochospira avnimelechi* Hamaoui; Hamaoui and Saint-Marc, p. 294, pls. 12-17.

1997 *Trochospira avnimelechi* Hamaoui; Çoruh et al., p. 417-418, pl. 75, figs. 1, 2.

Description: Test is lenticular or unequally biconvex. It shows a distinct angular appearance at the poles. Wall is microgranular calcareous and imperforate. Diameter and the thickness of the test range between 0.5 - 1.75 mm and 0.3 - 0.85, respectively. Coiling is in trochospiral manner, however, in the last whorl coiling may not be observed (Table 2).

Table 2- Biometrical data of *Trochospira avnimelechi*.

Sample	Diameter (mm)	Thickness (mm)	Height-width of the ultimate chamber
GA1d	1.125	0.5	0.25-0.125
GA3A1	1.55	0.85	0.8-0.25
GA5A1	1.55	0.6	0.6-0.2
GA5A3	1.625	0.7	0.625-0.55
GA5c	1.175	0.5	0.375-0.4
GA7b	0.5	0.275	0.25-0.275
GA10A2	0.5	0.35	0.125-0.35
GA10a	0.75	0.475	0.425-0.275
GA11b	0.775	0.35	0.25-0.125
GA11c	0.8	0.325	0.25-0.125
GA14A1	1.125	0.625	0.5-0.275
GA14A3	0.825	0.375	-
GA17d	0.9	0.425	0.35-0.2
GA20A2	1.75	0.625	0.625-0.375

Stratigraphic and Geographical Distribution: This species which was described (Hamoui, 1965) in the Cenomanian levels of its type locality in Israel, was determined also in the Cenomanian levels of Grecia Occidentale (Greece) region (Fleury, 1971). This species was found in the Upper Cretaceous levels of the Bey Dağları with *Biconcava bentori* Hamaoui, *Chrysalidina gradata* d'Orbigny, *Nummoloculina regularis* (Philipson) (Sarı, 2006). In this study, it has been determined in the lower - middle - upper levels of the Garzan section (Figure 5: 2 to 20 meters).

Subfamily: Coxitinae Hamaoui and Saint-Marc, 1970

Genus: *Antalyna* Farinacci and Köylüoğlu, 1985

Antalyna korayi Farinacci and Köylüoğlu, 1985

(Plate I, Figure 7)

1985 *Antalyna korayi* Farinacci and Köylüoğlu, p. 103-108, pls. 1-2, figs. 1-6.

2010 *Antalyna korayi* Farinacci and Köylüoğlu; Afghah, p. 74. 75, figs. 5, 3, 24.

2012 *Antalyna korayi* Farinacci and Köylüoğlu; Afghah and Farhoudi, p. 338, pl. 3, fig. 4.

Description: Test is convex in the dorsal side, and concave in the ventral side. Its basal view is ovoid. Wall is calcareous, microgranular, imperforate, subepidermal mesh is developed. Septal wall is simple mesh. Diameter and the height of the test range between 0.7 - 1.6 mm and 0.6 - 1.5 mm, respectively. Coiling is in milioline manner in in the early stage, and later on it becomes trochospiral. In the last whorl, height rapidly increases and no coiling is observed (Table 3).

Stratigraphic and Geographical Distribution: This species was described in the Late Maastrichtian from its type locality in Antalya with *Rhapydionina liburnica (*Stache), *Laffiteina mengaudi* (Astre), *Dictyoconella complanata* Henson (Farinacci and Köylüoğlu, 1985). This species was found in the Upper Cretaceous of Iran, accompanied by *Omphalocyclus macroporus, Lepidorbitoides minor, L. socialis, Loftusia minor, Orbitoides triangularis, O. apiculata, Siderolites calcitrapoides* (Afghah, 2010; Afghah and Farhoudi, 2012). It was observed at almost all levels in the Garzan section (Figure 5: 1 to 20 meters).

Table 3- Biometrical data of *Antalyna korayi*.

Sample	Diameter (mm)	Height (mm)
GA3c	0.75	0.625
GA10A2	1.625	1.5
GA14A3	0.8	1.025
GA14a	1.25 1.5 0.95	0.95 0.75 0.7
GA14b	1.25	0.625
GA14A2	1	0.625
GA14A3	1.425	0.75
GA20c	1.125	0.625

Superfamily: Biokovinacea Gusic, 1977

Family: Charentiidae Leoblich and Tappan, 1985

Genus: *Moncharmontia* De Castro, 1967

Moncharmontia apenninica (De Castro), 1967

(Plate I, Figure 8)

1966 *Neoendothyra apenninica* De Castro, p. 317-347, pl. 5.

1967 *Moncharmontia apenninica* (De Castro); De Castro, pl. 2.

1986 *Moncharmontia apenninica* (De Castro); Bilotte, pl. 369.

1994 *Moncharmontia apenninica* (De Castro); Chiocchini et al., pl. 22, figs. 16-18.

2001 *Moncharmontia apenninica* (De Castro); Tesovic et al., pl. 2, figs. G-I.

Description: Test is quite small, slightly inflated, lenticular or ovoid in shape. It is coiled in planispiral - evolute manner. Diameter and the thickness of the test vary between 0.20 - 0.50 mm and 0.2 - 0.3 mm, respectively. It has an elongation index of 1.5. Chambers are subspherical in the axial section, and their sizes increase towards the outer whorls (Table 4).

Stratigraphic and Geographical Distribution: It was described in Senonian in its type locality, Italy (De Castro, 1967). This species was found in the Pusica formation and the Upper Cretaceous carbonates of Brač Island (Croatia's Dalmatian Coast), accompanied by *Cuneolina pavonia, Discyclina schlumbergeri, Moncharmontia compressa, Orbitoides tissoti, O. media* (Tesovic et al., 2001). It generally occurs in the lower levels of Garzan section (Figure 5: 2 m).

Table 4- Biometrical data and features of the species *Moncharmontia apenninica* and *Moncharmontia compressa*.

Features	*Moncharmontia apenninica*	*Moncharmontia compressa*
Test shape in the axial parts	Umbilical area is smooth	Umbilical area is intermediate
Equatorial diameter (D)	0.20-0.50 mm	0.30-0.50 mm
Thickness (d)	0.20-0.30 mm	0.15-0.20 mm
Proloculus diameter	0.09-0.1 mm	0.05-0.08 mm

Moncharmontia compressa (De Castro), 1966

(Plate I, Figure 9)

1966 *Neoendothyra apenninica compressa* De Castro, p. 20-24, pl. 3, figs. 4-8.

1994 *Moncharmontia compressa* (De Castro); Chiocchini et al., pl. 23, figs. 2, 3, 10.

2001 *Moncharmontia compressa* (De Castro); Tesovic et al., pl. 2, figs. M-N.

Description: Test is quite small and flattened lenticular in umbilical area. Its wall structure is identical to that in *M. apenninica*. Diameter and the thickness range between 0.30 - 0.50 mm and 0.15 - 0.2 mm, respectively. It is coiled in planispiral - evolute manner. Chambers are heart - shaped in the axial section, and their sizes increase towards the outer whorls.

Stratigraphic and Geographical Distribution: It was described in Senonian in its type locality, Italy (De Castro, 1966). This species was reported from the Pusica formation in Brač Island (Croatia). It occurs in Upper Cretaceous carbonates with *Cuneolina pavonia, Discyclina schlumbergeri, Moncharmontia apenninica, Orbitoides tissoti, O. media* (Tesovic et al., 2001). It was generally observed in the lower and upper levels of the Garzan section (Figure 5: 1 and 16 to 20 meters).

Fleuryana adriatica (De Castro), 1972

(Plate I, Figures 10-11)

1972 *Moncharmontia apenninica compressa* De Castro-Bignot, pl. 16, figs. 6, 7, 8.

1988 *Moncharmontia apenninica* (De Castro); Drobne et al., pl. 24, figs. 6, 7.

1989 *Moncharmontia apenninica* (De Castro); Drobne et al., pl. 3, figs. 10, 11, 12.

1994 *Fleuryana adriatica* (De Castro); De Castro et al., p. 129-149, pl. 1, figs. 1-15; pl. 2, figs. 1-14; pl. 3, figs. 1-16; pl. 4, figs. 1-8.

Description: Test is quite small and lenticular. It is planispirally - evolute coiled and has 2.5 - 3.5 whorls. Diameter of the test ranges between 0.30 - 0.60 mm. In first whorls, wall is involute, so leading to the chamber lumina to be triangular - shaped. Size of the chambers slightly increase towards the end, and they become higher and longer (Table 5).

Stratigraphic and Geographical Distribution: This species was found in the Upper Cretaceous levels in its type locality, Brač Island (Croatia) (De Castro et al., 1994). It was reported from the Maastrichtian of Austria (Sanders et al., 2004). Velic (2007) stated the presence of this species in the Maastrichtian of Southeastern Europe. It was observed in the lower - middle - upper levels of Garzan section (Figure 5: 2 to 20 meters).

Genus: Pseudocyclammina Yabe and Hanzawa, 1926

Superfamily: Ataxophragmiacea Schwager, 1877

Family: Cuneolinidae Saidova, 1981

Subfamily: Cuneolininae Saidova, 1981

Genus: *Cuneolina* d'Orbigny, 1839

Cuneolina pavonia d'Orbigny, 1839

(Plate I, Figures 15-16)

1839 *Cuneolina pavonia* d'Orbigny, p. 150, figs. 6B, C.

1993 *Cuneolina pavonia* d'Orbigny; Grotsch et al., figs. 5B-E.

2001 *Cuneolina pavonia* d'Orbigny; Tesovic et al., pl. 1, figs. B-C.

Description: Test is conical with a large basal diameter. Height of the biserial test ranges between 0.75 - 1.2 mm. In the basal sections, diameter and the thickness range between 0.825 - 1.375 and 0.04 - 0.003 mm, respectively. Large proloculus is ovoid, and its diameter is 0.026. Proloculus is followed by subepidermic zone with small chambers. Chambers are subdivided by vertical partitions. Chamberlets are rectangular - shaped (Table 6).

Table 5- Numbers of chambers of the species *M. apenninica* and *F. adriatica* in each whorl.

Species	1st whorl	2nd whorl	3rd whorl
M. apenninica	7-8	9-10.5	13 (rarely)
F. adriatica	10.5-11	13	14-16

Table 6- Biometrical data of *Cuneolina pavonia*.

Sample	Basal diameter (mm)	Height (mm)	Height-width of the chamberlets in first stage	Height-width of the chamberlets in last stage
GA1A3	1.375	1.2	0.025-0.025	0.05-0.05
GA1a	0.825	1	0.1-0.025	0.15-0.05
GA9A1	0.955	1.625	0.075-0.025	0.125-0.025
GA11c	0.875	0.775	0.075-0.05	0.125-0.075
GA14A3	0.755	0.85	0.05-0.025	0.125-0.05
GA16a	0.875	0.75	0.025-0.025	0.125-0.075
GA20A1	0.850 1.175	0.75 0.875	0.075-0.05 0.05-0.05	0.125-0.075 0.125-0.05

Stratigraphic and Geographical Distribution: This species was described from its type locality Cuba (d'Orbigny, 1839). Dilley (1973) reported this species from the Albian and Maastrichtian of Northern and Central America, Southern Europe, Northern and Western Africa, Middle East. It was determined in the Santonian of Spain (Hofker, 1967; Caus and Cornella, 1983; Caus, 1988; Gischler et al., 1994) and of Turkey (Sarı and Özer, 2002). It was also found in the Campanian of the Line Islands in the Pacific (Premoli Silva and Brusa, 1981) and in the Maastrichtian of Iraq (Al - Omari and Sadek, 1976). It was observed in the lower and middle parts of Garzan section (Figure 5: 2 to 20 meters).

Cuneolina ketini İnan, 1988

(Plate I, Figures 17-18)

1988 *Cuneolina ketini* İnan, pl. 1, figs. 1-8; pl. 2, figs. 1-8

2004 *Cuneolina ketini* İnan; Sanders et al., pl. 4, figs. 1, 2 and 7.

Description: Test is high conical with a small and narrow basal diameter. Height of the biserial test is 2.5 mm. In the basal sections, diameter and the thickness range between 0.4 - 1 and 0.2 - 0.5 mm, respectively. Proloculus is tiny and spherical. Proloculus is followed by a spiral stage. Rectangular chambers are subdivided by vertical partitions. Their heights and widths vary between 0.06 - 0.14 and 0.03 - 0.05, respectively Table 7).

Stratigraphic and Geographical Distribution: This species was found in the Upper Cretaceous levels in its type locality Sivas (Turkey) with *Orbitoides medius, O. apiculatus, Omphalocyclus macroporus, Pseudomphalocyclus blumenthali* and *Loftusia minor* (İnan, 1988). Sanders et al. (2004) stated its presence in Campanian levels of the Austrian Alps. Tewari et al. (2007) reported the presence of this species in Maastrichtian aged levels in the Northern Italy - Northwestern Adriatic Platform. It was observed in the lower - middle - upper levels of Garzan section (Figure 5: 1 to 20 meters).

Family: Dicyclinidae Loeblich and Tappan, 1964

Genus: *Dicyclina* Munier-Chalmas, 1887

Dicyclina schlumbergeri Munier-Chalmas, 1887

(Plate I, Figure 19)

1887 *Dicyclina schlumbergeri* Munier-Chalmas, p. 362, pl. 1; p.363, pl. 2.

1978 *Dicyclina schlumbergeri* Munier-Chalmas;

Table 7- Comparison of the genera *Dicyclina* and *Cuneolina*.

FEATURES	*Dicyclina*	*Cuneolina*
Test shape	Discoidal, slightly undulated and flattened	Compressed, flabelliform, conical.
Growth stage	Slightly inflated in the early stage	Trochospiral in the early stage, with about five chambers
Chambers and chamberlets	Chambers annular, added on the two sides of the test	Very broad and low biserally arranged
Internal part	Subdivided by numerous thin radial partitions	Subdivided into nearly rectangular chamberlets by radial partitions arising perpendicular to the outer wall
Aperture	Numerous pores at the periphery	At the internal margins, biserial

Luperto Sinni and Ricchetti, p. 47, figs. 1-7; p. 48, figs. 1-6.

1990 *Dicyclina schlumbergeri* Munier-Chalmas; Cherchi and Schroeder, p. 333, figs. 5-11.

2001 *Dicyclina schlumbergeri* Munier-Chalmas; Tesovic et al., pl. 1, figs. D-H.

Description: Test is discoidal, smooth or undulated on the surface. It more inflated in early stage comparing to the adult stage. Wall is agglutinated calcareous, and consists of imperforate epiderm and subepidermal mesh. Diameter and the thickness vary between 7.625 - 1.375 mm and 0.175 - 0.525 mm, respectively. Large proloculus is ovoid, and has a diameter of 1.1 mm. Alternating chambers on each side of the test developed as circle. Internal part is subdivided by numerous thin, radial partitions which are perpendicular to the wall and extending from chamber to chamber. Number of the secondary partitions located between the main partitions, varies between 3 to 5 (Table 8).

Stratigraphic and Geographical Distribution: This species was reported from the Upper Cretaceous levels in its type locality France (Munier - Chalmas, 1887). This species was found in the Pusica formation in Brač Island (Croatia's Dalmatian Coast) and in the Upper Cretaceous carbonates. It was accompanied by *Cuneolina pavonia, Moncharmontia apeninica, M. compressa, Orbitoides tissoti, O. media* (Tesovic et al., 2001). It was recorded in the Upper Cretaceous limestones of Murge/Altamura (Southern Italy) with the assemblage containing *Cuneolina pavonia, Moncharmontia apenninica, Minouxia conica, Pseudolituonella* sp. (Checconi et al., 2008). It was observed at almost all levels in the Garzan section (Figure 5: 1 to 20 meters).

Superfamily: Orbitolinacea Martin, 1980

Family: Orbitolinidae Martin, 1980

Subfamily: Dictyoconinae Moullade, 1965

Genus: Dictyoconella Henson, 1948

Dictyoconella ? *complanata* Henson, 1948

(Plate II, Figure 2)

1948 *Dictyoconella complanata* Henson, p. 25, pl. 6, figs. 2, 3, 16; pl. 10, figs. 14.

1985 *Dictyoconella complanata* Henson; Farinacci and Köylüoğlu, p. 106

2012 *Dictyoconella complanata* Henson; Afghah and Farhoudi, pl. 2, figs. 2.

Description: Test is quiet large, and bilaterally flattened peneropliform. A subepidermal mesh formed by intersecting primary and secondary horizontal extensions is observed interior. Early planispiral stage consists of numerous large, flattened and slightly arched chambers, while the adult stage consists of uncoiled, uniserially arranged chambers. Beams which connect with radial extensions, are present in the central zone (Table 9).

Table 8- Biometrical data of *Dicyclina schlumbergeri*.

Sample	Diameter (mm)	Thickness (mm)	Numbers of secondary partitions
GA5A1	1.87 4.62	0.175 0.275	3
GA5A2	1.375	0.325	-
GA5a	5.125 3.125	0.325 0.3	3-4, width of the proloculus: 0.875 3-4, height of the proloculus: 0.3
GA5d	6.625	0.375	-
GA7b	3.175	0.35	-
GA7c	5.375 2	0.5 0.3	- 4
GA7d	3.675	0.375	-
GA9A2	2.95	0.425	-
GA9A3	2.125 2	0.375 0.3	- -
GA9d	2.25	0.425	3
GA10A3	5.25 7.625	0.5 0.525	5 5

Table 9- Biometrical data of *Dictyoconella* ? *complanata*.

Sample	Basal diameter (mm)	Basal thickness (mm)
GA3a	1.1	0.375
GA5A1	1.05	0.3
GA5A3	1	0.725
GA7a	0.75	0.475
GA7c	1	0.325
GA9d	0.875	0.5
GA10A1	0.975 0.825	0.525 0.525
GA14A3	0.675	0.4
GA14a	1.375 1.125	0.825 0.6
GA14b	2 1.05	1 0.575
GA16A2	1	0.525
GA16A3	0.75	0.625
GA20A1	1.05 1.175 1.225	0.75 0.575 0.5
GA20A2	1.7	0.85
GA20a	1.625	0.6
GA20b	1.2 1.15	0.675 0.45
GA20c	1.125	0.525

Stratigraphic and Geographical Distribution: This species was described in the Upper Cretaceous aged levels from its type locality Qatar accompanying with *Omphalocyclus macropora* and *Loftusia* spp. (Henson, 1948). It was found in the Late Maastrichtian of Southwestern Turkey with *Rhapydionina liburnica, Laffiteina mengaudi, Antalyna korayi* (Farinacci and Köylüoğlu, 1985). In Zagros Mountains (Iran), it was reported from the Upper Cretaceous - Masstrichtian sediments of the Tarbur formation (Afghah and Farhoudi, 2012). It was observed at almost all levels in the Garzan section (Figure 5: 1 to 20 meters).

Vandenbroekia munieri Marie, 1958

(Plate II, Figures 4,5)

1958 *Vandenbroekia munieri* Marie, p. 135, pl. 1, figs. 1-8.

Description: Test is discoidal and slightly conical. Test diameter ranges approximately between 2.5 - 5.85 mm. Proloculus is spherical. In the megalospheric generations, it is followed by peneroplid type spiral chambers. Annular whorls are present after this stage. Chambers are peneropliform in the juvenile stage, while they are annular in the adult stage. Height of the chambers increase towards the outer whorls. Diameters of the test and proloculus varies between 2.5 - 6 mm and 0.425 - 0.475 mm, respectively. In the axial sections, proloculi are subspherical, and the ultimate chambers are elongated subspherical (Table 10).

Stratigraphic and Geographical Distribution: It was found in the Campanian levels of its type locality in France (Marie, 1958). It was observed at almost all levels in the Garzan section (Figure 5: 1 to 20 meters).

Superfamily: Orbitoidacea Schwager, 1876

Family: Orbitoididae Schwager, 1876

Table 10- Biometrical data of *Vandenbroekia munieri* (Pr= Proloculus).

Sample	Diameter (mm)	Thickness (Periphery-central) mm	Height-width of the chambers in the first and last whorls	Whorl numbers
GA5A1	4.75 5 4.875	0.225-0.1 0.175-0.1 0.15-0.125	0.075/0.1-0.15/0.15 - 0.075/0.1-0.125/0.1	19 12 17
GA5A2	3.25 4.5 5.125	0.15-0.1 0.15-0.05 0.1-0.05	- 0.05/0.05-0.125/0.125 -	- 17 11
GA5A3	5	0.1-0.05	-	13
GA5c	5.25	0.175-0.025	-	15
GA5d	5.375	0.2-0.05	-	12
GA7b	6	0.125-0.1	-	-
GA20A3	2.5; Pr=0.425 4.8; Pr=0.475	0.125-0.225 0.25-0.2	0.125/0.15-0.125-0.1 0.125/0.125-0.125/0.15	11 19
GA20a	5.85	0.2-0.2	0.125/0.125-0.125/0.15	14
GA20b	5.425	0.15-0.225	0.05/0.025-0.1/0.2	25

Subfamily: Orbitoidinae Schwager, 1876

Genus: *Orbitoides* d'Orbigny, 1848

Orbitoides media (d'Archiac), 1837

(Plate III, Figures 1,2)

1823 *Lycophris faujasi* Defrance, c. 24

1837 *Orbitoides media* (d' Archiac), pl. 3, figs. 1-6, pl. 5, figs. 3-4, pl. 35, figs. 2

1916 *Orbitoides media* (d'Archiac); Douville, pl. 12, figs. l a, b, c.

1935 *Orbitoides media* (d'Archiac); Florida, pl. 14, figs. l -2.

1958 *Orbitoides media* (d'Archiac); Neumann, pl. 3, figs. l -6; pl. 5, figs. 3-4.

1965 *Orbitoides media* (d'Archiac); Meriç, pl. 15. figs. 6-12; pl. 16, figs. l -4.

Description: Test is large, discoidal, generally biconvex and asymmetrical. Concavo - convex or planoconvex tests are rarely observed. Embryonic chambers of the megalospheric generation can be seen as three - or four - chambered depending on the level of the partitions in the horizontal sections. It has a subspherical protoconch and a reniform deuteroconch. There is a wall surrounding the embryon from the outside. Equatorial chambers surrounding the embryon are arcuate. Their heights and widths increase towards the edges. In the axial sections, lateral chambers enlarge towards the periphery. Beams are present at the margins. Many arcuate equatorial chambers and basic stolons, adjacent to each other, develop within successive cycles following the embryon. Equatorial layers are surrounded by many lateral chambers and pillars on both sides of the test. Limits in this species which were first accepted by Van Gorsel (1978) as $500<Li+li<600$ and $4<E<5.5$ followed in this study as well (Figure 6).

Stratigraphic and Geographical Distribution: The species was found in the Campanian levels of its type locality in France (d'Archiac, 1837). This species has also been observed in Spain, North Africa, Italy, Greece, Syria, Turkey and India. Baumfalk (1986) reported this species from the Upper Campanian sediments of France accompanying with *Orbitoides tissoti* and *Orbitoides medius megaloformis*. *Orbitoides medius* and *O. megaloformis* were recorded in the samples from Darende (probably in lower - middle Maastrichtian; Meriç and Görmüş, 1997) and Pazarcık regions (middle - upper Maastrichtian; Görmüş et al., 1994). In the Hekimhan region, the presence of *Orbitoides*

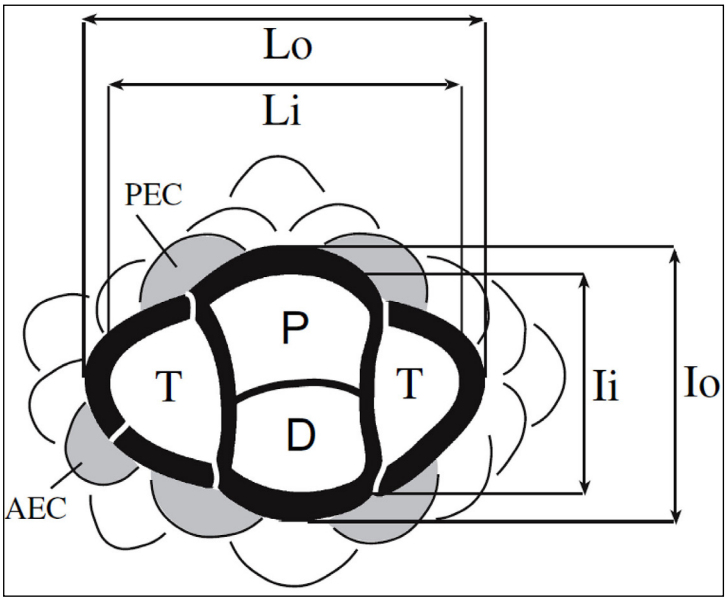

Figure 6- The first chamber and its parameters used in orbitoid identification criteria (AEC+PEC: Auxiliary chambers; Li: Largest diameter of embryon excluding the thickness of the wall; li: Diameter of embryon excluding the thickness of the wall and perpendicular to Li; Li+li: Size of embryon; after Özcan, 2007).

medius was mentioned in the mudstones (probably upper Campanian - lower Maastrichtian; Görmüş, 1992) associated with the reef framework. It was determined in the Pusica formation and in the Upper Cretaceous carbonates of the Brač Island (Croatia's Dalmatian Coast) accompanied by *Cuneolina pavonia, Discyclina schlumbergeri, Moncharmontia apeninica, M. compressa, Orbitoides tissoti, O. media* (Tesovic et al., 2001). In the Zagros Mountains (Iran), an assemblage which contains *Dicyclina schlumbergeri, Antalyna korayi, Dictyoconella complanata, Omphalocyclus macroporus, Orbitoides media, O. tissoti, Goupilloidina shirazensis, Minouxia* sp., *Trochospira* sp., *Nezzatinella* sp., *Nezzazata* sp. in the Upper Cretaceous - Maastrichtian sediments of the Tarbur formation was reported (Afghah and Farhoudi, 2012). Abyat et al. (2014) determined that species in the Upper Cretaceous levels of Southwestern Iran. In the Garzan section, it was found at the all levels of the Garzan formation, and in the lower levels of the Germav formation (Figure 5: 1 to 25 meters).

Orbitoides megaloformis Papp and Küpper, 1953

(Plate III, Figures 3,4)

1953 *Obitoides media megaloformis* n. ssp. Papp and Küpper, s. 74-75, pl. 1, figs. 9.

1956 *Obitoides media megaloformis* Papp and Küpper; Papp, p. 138, pl. 1, figs. 9.

1985 *Orbitoides megaloformis* Papp and Küpper; Drooger and Klerk, p. 115, pls. 3-4

1993 *Orbitoides megaloformis* Papp and Küpper; Neumman, p. 319-324, pl. 1, figs. 16-18; pl. 2, figs. 1-8, pl. 4, figs. 1, 3, 6

Description: Test is large, discoidal and generally biconvex. The megalospheric individuals with thin - walled embryon appear as having 3 or 4 partitions depending on the level of the parts in the horizontal sections and have a thick wall. Limits in this species which were first accepted by Van Gorsel (1978) as 600<Li+li<750 and 5.5<E<10 followed in this study as well (Figure 6). While the Equatorial chambers are constantly adjacent to the basic stolons in the peripheral parts of the test, they are curved in other horizontal parts. Thick - walled lateral chambers are developed on both sides of the equatorial chambers. There are many pillars between the lateral chambers (Table 11).

Table 11- Biometrical data of *Orbitoides* determined in the Garzan formation.

Sample	Li + li (µm)	E	Determination
Or-2	600	5	*O. media*
Or-3	620	8	*O. megaloformis*
Or-4	500	5	*O. media*
Or-5	550		*O. media*
Or-7	630		*O. media*
Or-9	690	8	*O. megaloformis*
Or-10	620	7	*O. megaloformis*
Or-13	670		*O. megaloformis*
Or-14	670		*O. megaloformis*
Or-15	660	7	*O. megaloformis*
Or-18	490	5	*O. media?*
Or-20	500	6	*O. media?*
Or-22	740	4	*O. media?*
Or-24	600	4	*O. media?*
Or-25	520		*O. media*
Or-27	720	4	*O. megaloformis?*
Or-28	590		*O. media*
Or-29	700		*O. media*
Or-30	580		*O. media*
GAY-1	670	7	*O. megaloformis*
GAY-2	700		*O. megaloformis*
GAY-4	630	4	*O. megaloformis*
GAY-5	700	7	*O. megaloformis*
GAY-8	500	5	*O. media*

Stratigraphic and Geographical Distribution: This species was found in the Upper Campanian levels of the Pemberger sandstones in its type locality in Austria (Papp and Küpper, 1953). Caus et al. (1996), reported this species accompanying with *O. medius* in the Pyrenees. In the Garzan section, it was found at the all levels of the Garzan formation, and in the lower levels of the Germav formation (Figure 5: 1 to 28 meters).

Subfamily: Omphalocyclinae Vaughan, 1928

Genus: Omphalocyclus Bronn, 1853

Omphalocyclus anatoliensis Özcan, 2007

(Plate III, Figures 5,6)

2007 *Omphalocyclus anatoliensis* sp. nov., Özcan, figs. 8, 9 A-G, I-P, 13 P, U

Description: Test is quite small (diameter<3 mm), flattened, depressed in the center, biconcave. It is seen as in form of bowtie in the axial sections due to its shape. Very small embryon of the species typically has three partitions. Depending on the size, levels of the partitions and asymmetrical conditions with respect to the equatorial layers, it may have double, triple and quadruplet partitions. Li+li values range between 164 µm and 575 µm (Figure 6). E value is between 3 - 4 on average. Equatorial chamberlets are generally narrow, and mostly curved in the early stage, then they broaden towards the outwards. Embryon, at first, is followed by orbitoid type (arcuate) chambers. Towards the periphery, the equatorial chambers increase in width and decrease in height. Therefore, the equatorial chambers take a rectangular shape towards the periphery of the test. It does not contain a real lateral chamber (Table 12).

Table 12- Biometrical data of *Omphalocyclus anatoliensis* determined in the Garzan formation.

Sample	Li + li (µm)	E	Determination
Om-3	390	-	*O. anatoliensis*
Om-5	270	-	*O. anatoliensis*
Om-7	430	4	*O. anatoliensis*
GA-14	420	3	*O. anatoliensis*
GA17A2	270	4	*O. anatoliensis*
GA17b	290	3	*O. anatoliensis*

Stratigraphic and Geographical Distribution: This species was found in the late Campanian levels of its type locality in Kahta - Adıyaman accompanied by *L. bisambergensis, O. media, O. megaloformis, S. calcitrapoides* and *Loftusia* spp. (Özcan, 2007). It was observed in the lower and upper levels of the Garzan section (Figure 5: 3 to 16 meters).

5. Discussion and Conclusions

The forms determined in the Garzan measured stratigraphic section, are common in the Upper Cretaceous shallow marine sediments of Tethyan Belt.

Fleuryana adriatica which was obtained at almost all levels of the Garzan section, was observed in Maastrichtian in Austria and Southeastern Europe (Sanders et al., 2004; Velic, 2007). Likewise, the *Cuneolina ketini* found in the Garzan section, was described in the Maastrichtian levels in Sivas, which is the type locality of the species (İnan, 1988).

Cuneolina pavonia was recorded by Dilley (1973) in the Albian and the Maastrichtian in Northern and Central America, Southern Europe, Northern and Western Africa and Middle East. It was determined in the Santonian in Spain (Hofker, 1967; Caus and Cornella, 1983; Caus, 1988; Gischler et al., 1994) and in Turkey (Sarı and Özer, 2002). This species was mentioned in the Coniacian - early Campanian by Checconi et al. (2008) in southern Italy, in the Cenomanian - early Turonian by Robertson et al. (2015) in Adıyaman, in the middle - late Cenomanian by Taslı et al. (2006) in the Bolkar Mountains, in the late Cenomanian - Maastrichtian by Tesovic et al. (2001) in Croatia, in the Campanian - Maastrichtian by Vaziri et al. (2005) and Vaziri (2011) in Iran.

Dicyclina schlumbergeri (Munier - Chalmas, 1887) reported in Upper Cretaceous levels in France, which is its type locality, was observed in the measured section at all levels. This species was found in the Coniacian - Campanian carbonate sediments in Croatia, accompanied by the species *Cuneolina pavonia, Moncharmontia apeninica, M. compressa, Orbitoides tissoti, O. media* (Tesovic et al., 2001). It was mentioned in the Coniacian - Campanian aged limestones of Murge/Altamura (Southern Italy) with the assemblage containing *Cuneolina pavonia, Moncharmontia apenninica, Minouxia conica, Pseudolituonella* sp. (Checconi et al., 2008). Taslı et al. (2006) reported *Moncharmontia compressa* and *Dicyclina schlumbergeri* in Coniacian - Santonian from the Bolkar Mountains. Schlüter et al. (2008) stated the presence of *M. apenninica* and *D. schlumbergeri* in Coniacian - Maastrichtian in the southern Italy. Boix et al. (2011) recorded *D. schlumbergeri* in Coniacian - Santonian in the Spanish Pyrenees. *C. pavonia, N. simplex, N. picardi, D. schlumbergeri* was determined in the Cenomanian - Coniacian levels of the Bey Dağları by Sarı et al. (2009). This species was reported in the Campanian - Maastrichtian levels of Iran by several researchers (Vaziri et al., 2005; Afghah, 2009; Vaziri, 2011; Afghah and Farhoudi, 2012; Abyat et al., 2014), accompanied by the assemblage of *A. korayi, O. medius, D. complanata, M. apenninica, N. picardi*. Sanders et al. (2004) determined this species in the Cenomanian - Maastrichtian of Austria.

Biconcava bentori was observed in the Cenomanian levels in the Bolkar Mountains (Taslı et al., 2006; Sarı et al., 2009), Southern Italy (Frija et al., 2015) and Egypt (İsmail et al., 2009).

The genus *Vandenbroekia* whose type locality is the Campanian aged levels in France, has not been observed in the previous studies. The presence of *Vandenbroekia*, which offers a limited spread, has been reported for the first time with this study both in Turkey and in the Maastrichtian.

Nezzazatinella picardi, which was observed in the lower - middle - upper levels of the Garzan section, was found in the Cenomanian - Turonian aged levels in Adıyaman by Robertson et al. (2015). This species was also reported in the middle - upper Cenomanian of the Bolkar Mountains by Taslı et al. (2006), in the Cenomanian - Coniacian of the Bey Dağları by Sarı et al. (2009), in the Campanian - Maastrichtian of Iran by Vaziri et al. (2005) and Vaziri (2011), in the Cenomanian - Santonian of Austria by Schlagintweit (1992).

Antalyna korayi was described in the late Maastrichtian in its type locality in Antalya, accompanied by *Rhapydionina liburnica* (Stache), *Laffiteina mengaudi* (Astre), *Dictyoconella complanata* Henson (Farinacci and Köylüoğlu, 1985). This species was found in the Campanian - Maastrichtian levels of Iran, with *Omphalocyclus macroporus, Lepidorbitoides minor, L. socialis, Loftusia minor, Orbitoides triangularis, O. apiculata, Siderolites calcitrapoides* (Afghah, 2010; Afghah and Farhoudi, 2012; Abyat et al., 2014).

Orbitoides media was first described in the Campanian levels of its type locality in France (d'Archiac, 1837). It was determined in the Pusica formation and the Upper Cretaceous carbonates in Croatia, accompanied by *Cuneolina pavonia, Discyclina schlumbergeri, Moncharmontia apeninica, M. compressa, Orbitoides tissoti* (Tesovic et al., 2001). This species was also reported from the Maastrichtian levels of Iran (Afghah and Farhoudi, 2012; Abyat et al., 2014).

Orbitoides megaloformis was found in the Pemberger Sandstone in Austria which the type locality of the species (Papp and Küpper, 1953). Caus et al., (1996) reported this species in the Campanian aged levels from the Pyrenees.

Omphalocyclus anatoliensis was found in the Upper Campanian levels of Kahta - Adıyaman, the type locality, accompanied by *L. bisambergensis, O. media, O. megaloformis, S. calcitrapoides* and *Loftusia* spp. (Özcan, 2007). In the Garzan section, it was observed that this species was not occurred with forms characterizing the late Campanian, but with forms in the Maastrichtian.

Garzan formation, which contains mainly beige - yellowish colored, thin - thick bedded shallow marine limestones, is remarkable with high diversity and abundance in terms of larger benthic foraminifera. Porcellaneous, microgranular and agglutinated genera and species such as *Vandenbroekia munieri* Marie, *Biconcava bentori* Hamaoui, *Nezzazatinella picardi* (Henson), *Trochospira avnimelechi* Hamaoui, *Antalyna korayi* Farinacci and Köylüoğlu, *Moncharmontia apenninica* (De Castro), *Moncharmontia compressa* (De Castro), *Fleuryana adriatica* (De Castro), *Cuneolina pavonia* d'Orbigny, *Cuneolina ketini* İnan, *Dicyclina schlumbergeri* Munier - Chalmas, *Dictyoconella complanata* Henson starts appearing from the lower levels of the unit, however, they become abundant or poor at different levels.

In this study, supported also by biometric data, in the light of all individuals identified and the paleontological data, it was determined that the age of the Garzan formation is Maastrichtian (Upper Cretaceous).

Acknowledgements

First of all, I would like to express my appreciation to my advisor Prof. Dr. Nazire Özgen Erdem who made a great contribution to this study. Fields geologists Muzaffer Siyako, Halil Şeker and İsmail Bahtiyar from the Turkish Petroleum Corporation (TPAO) are also thanked. This study is a part of Author's PhD thesis, and supported within the scope of Project CÜBAP M - 604.

References

Abyat, A., Afghah, M., Feghhi, A. 2014. Biostratigraphy and lithostratigraphy of Tarbur Formation (Upper Cretaceous) in southwest of Khorram Abad (southwest Iran). Carbonates Evaporites DOI 10.1007/s13146-014-0218-1, Springer - Verlag Berlin Heidelberg.

Afghah, M. 2009. New investigations of the Tarbur Formation lithostratigraphy in the review of type section and its correlation with Kuh - e Tir section.

Journal of Sciences Islamic Azad University 19, 183-196.

Afghah, M. 2010. Biozonation and biostratigraphic limits of the Tarbur Formation around Shiraz (SW of Iran). PhD Thesis University of Münster, 171 p.

Afghah, M., Farhoudi, G. 2012. Boundary Between Upper Cretaceous and Lower Paleocene in the Zagros Mountain Ranges of Southwestern Iran, Acta Geologica Sinica 86, 2, 325-338.

Al-Omari, F.S., Sadek, A. 1976. *Loftusia* from northern Iraq: Revista Española de Micropaleontología 8, 57-67.

Baumfalk, A. Y. 1986. The Evolution of "*Orbitoides media*" (Foraminiferida) in the Late Campanian. Journal of Foraminiferal Research 16(4), 293-312.

Boix, C., Frijia, G., Vicedo, V., Bernaus, J.M., Di Lucia, M., Parante, M., Caus, E. 2011. Larger foraminifera distribution and strontiom isotope stratigraphy of the La Cova limestones (Coniaciane Santonia, "Serra del Montsec", Pyrenees, NE Spain). Cretaceous Research 32, 806-822.

Caus, E. 1988. Upper Cretaceous larger foraminifera: paleoecological distribution. Revue de Pale´obiologie vol. spe´c. 2, 417- 419.

Caus, E., Cornella, A. 1983. Macroforaminifères du Crétacé supérieur du bassin sud - pyrénéen. Géologie Méditerranéenne 10, 137-142.

Caus, E., Bernaus, J. M., Gomez-Garrido, A. 1996. Biostratigraphic utility of species of the genus Orbitoides. Journal of Foraminiferal Research 26(2), 124-136.

Checconi, A., Retorri, R., Spalluto, L. 2008. Biostratigrafia a foraminiferi del Cretaceo Superiore della successione di Parco Priore (Calcare di Altamura, Piattaforma Apula, Italia Meridionale). Annali dell'Università degli Studi di Ferrara Museologia Scientifica e Naturalistica, 4: 1-9.

Cherchi, A., Schroeder, R. 1990. Revision de Dicyclina schlumbergeri Munier - Chalmas, grand Foraminife`re du Cretace´ mesoge´en. Comptes Rendus de l'Acade´mie des Sciences, Paris, Se´rie II 310, 329-334.

Chiocchini, M., Farinacci, A., Mancinelli, A., Molinari, V., Potetti, M. 1994. Biostratigrafia a foraminiferi, dasicladali e calpionelle delle successioni carbonatiche mesozoiche dell'Appennino centrale (Italia). Studi Geologici Camerti, Volume Speciale 1994 (Biostratigrafia dell'Italia centrale), 9-129.

Çoruh, T., Yakar, H., Ediger, V. Ş. 1997. Güneydoğu Anadolu Bölgesi otokton istifinin biyostratigrafi atlası. Türkiye Petrolleri Anonim Ortaklığı, Araştırma Merkezi Grubu Başkanlığı Eğitim Yayınları, No: 30, 510.

De Castro, P. 1966. Sulla presenza di un nuovo genere di Endothyridae ne Cretacico superiore della Campania. Boll. Soc. Nat. Napoli, 75, 1-33, 7, şek. 1, Napoli.

De Castro, P. 1967. *Moncharmontia apenninica*, nuovo nome per *Neoendothyra apenninica* De Castro, 1966, Bolletino della Societa` dei Naturalisti in Napoli 76, 2.

De Castro, P., Drobne, K., Gušić, I. 1994. *Fleuryana adriatica* n.gen., n.sp. (Foraminiferida) from the Uppermost Maastrichtian of the Brač island (Croatia) and some other localities on the Adriatic carbonate platform. Razprave IV razreda SAZU Ljubljana 35/8, 129-149.

Dilley, F. C. 1973. Cretaceous Larger Foraminifera, in Hallam, A., ed., Atlas of Palaeobiogeography: Amsterdam, Elsevier Scientific Publishing Company, 403-419.

Douville, H. 1916. Le Crétacé et l'Éocène du Tibet central. Palaeont. Indica (V) 3, 1-52.

Drobne. K. 1984. *Periloculina slovenica*, B Form, from the Paleocene of Majevica Mt. (Yugoslavia) and the new family Fabulariidae. Razprave, (4 razred), Slovenska Akademija Znanosti in Umetnosti 25, 1-32.

Drooger, C. W., de Klerk, J. C. 1985. The Punctuation in the Evolution of "*Orbitoides*" in the Campanian of South - West France. Bull. Utrecht Micropaleontology 33, 1-143.

d'Archiac, A. 1837. Mémoire sur la formation Crétacé du sud - ouest de la France. Mémoires de la Société Géologique de France 2(7), 157-192.

d'Orbigny, A. 1839. Foraminife`res. In De la Sagra, R. Histoire physique, politique et naturelle delile de Cuba (ed. Bertrand, A.), Paris, 1, 224.

Farinacci, A., Köylüoğlu, M. 1985. *Antalyna korayi* n. sp. in the phyletic lineage of the Nczzazatidae (Foraminifera): Revue de Micropaleontologie 28(2), 103-108, Paris.

Fleury, J. J. 1971. Le Cénomanien a Foraminifères benthoniques du massif du Varassova (zone du Gavrovo, Akarnanie, Grèce continentale), Revue de Micropaléontologie 14 (3), 181-194.

Florida, B. G. 1935. Sul rinvenimento di Orbitoidi non rimaneggiate nel flysch Lombardo: Bull. Soc. Geol. Ital. Roma. 54. L 14. 253-262, XIV.

Frijia, G., Parente, M., Di Lucia, M. and Mutti, M. 2015. Carbon and strontium isotope stratigraphy of the Upper Cretaceous (Cenomanian - Campanian) shallow - water carbonates of southern Italy: Chronostratigraphic calibration of larger foraminifera biostratigraphy. Cretaceous Research 53: 110-139.

Gischler, E., Gräfe, K. U., Wiedmann, J. 1994. The Upper Cretaceous *Lacazina* limestone in the Basco-Cantabrian and Iberian Basins of northern Spain:

Cold-water grain associations in warm - water environments: Facies 30, 209-246.

Görmüş, M. 1992. Quantitative Data on the Relationship between the Orbitoides genus and its Environment. Revista Espanola de Micropaleontologia Madrid XXIV (3), 13-6.

Görmüş, M., Meriç, E., Avşar, N. 1994. Pazarcık (K.Maraş) ve Darende (B Malatya) - Hekimhan (KB Malatya) Yörelerindeki Orbitoides Parametrelerinin Karşılaştırılması. Türkiye Jeoloji Kurultayı Bülteni 9, 109-125, Ankara.

Grotsch, J., Schroeder, R., Noe, S., Flu gel, E. 1993. Carbonate platforms as recorders of high - amplitude eustatic sea - level fluctuation: the late Albian appenninica - event. Basin Research 5, 197-212.

Güven, A., Dinçer, A., Tuna. M. E., Çoruh, T. 1991. Güneydoğu Anadolu Kampaniyen - Paleosen otokton istifinin stratigrafisi. Türkiye Petrolleri Anonim Ortaklığı (TPAO) Arama Grubu, Rapor no. 2828, 133.

Hamoui, M. 1965. Biostratigraphy of the Cenomanian type Hazera Formation. Geology Israel, Stratigraphy Section 124, 15, Jerusalem.

Henson, F. 1948. Larger imperforate Foraminifera of South - West Asia. Families Lituolidae, Orbitolinidae, and Meandropsinidae: British Museum (Natural History), London, 127.

Hofker, J. Jr. 1967. Primitive *Orbitoides* from Spain: Micropaleontology, 13, 243-249.

İnan, N. 1988. *Cuneolina ketini* (Foraminifere) n.sp.du Maastrichtian d'Anatolie Centrale (Turquie): Revue de Paleobiologie 7, 2, Geneve, 327-333.

İsmail, A. A. 2000. Biostratigraphy of the Maastrichtian chalks in west central Sinai, Egypt. Revue de Paléobiologie 19: 319-337.

İsmail, A. A., Hussein-Kamel, Y. F., Boukhary, M., Ghandour, A. A. 2009. Late Cenomanian - Early Turonian foraminifera from Eastern Desert, Egypt, Micropaleontology 55, 4, 396-412.

Kellog, H. E. 1960. Stratigraphic report, Bitlis Siirt area, Petroleum District V, Southeast Turkey, Petrol İşleri Genel Müdürlüğü Teknik Arşivi, Rapor no. 2, 25.

Kellog, H. E. 1961. Regional stratigraphy and petroleum possibilities of Sotheast Turkey: AMOSEAS (American Overseas Petroleum) report, Türkiye Petrolleri Anonim Ortaklığı (TPAO) Arama Grubu Rapor no.767, 29.

Loeblich, A. R., Tappan, H. 1964. Sarcodina - chiefly "The camoebians" and Foraminiferida. In Moore, R.C. (ed.), Treatise on Invertebrate Paleontology Part C, Protista 2 (2 volumes.), University of Kansas Press, 1-900.

Loeblich, A. R., Tappan, H. 1987. Foraminiferal Genera and their Classification. Van Nostrand Reinhold Company, New York, 970.

Luperto Sinni, E. 1976. Microfossili senoniani delle Murge. Riv Ital Paleont Stratigraphy 82, 293-416.

Luperto-Sinni, E., Ricchetti, G. 1978. Studio micropaleontologico - stratigrafico di una successione carbonatica del Cretaceo superiore rilevata nel sottosuolo delle Murge sud - orientali. Riv. Ital. Paleontology 84/3, 561-666.

Marie, P. 1958. Peneroplidae du Crétacé supérieur à faciès récifal. I-. A propos des genres Broekina et Praesorites et sur le nouveau genre Vandenbroekia. Revue de Micropaleontology 1, 125-140, Pl. I.

Meriç, E. 1965. Kahta-Nemrut dağı arasındaki bölgenin jeolojik ve paleontolojik etüdü. İstanbul Üniv. Fen Fak. Mecmuası 30 (1-2), 55-107.

Meriç, E., Görmüş, M.1997. About an unusual schizogonic reproduction in Simplorbites and Orbitoidesgenera. Geology Society Bulletin of Turkey 40 (2), 75-83.

Munier-Chalmas, E. 1887. Sur la Cyclolinna et Rois Nouveaux Genres de Foraminiferes de Couches a Rudistes; Cyclopsina, Dicyclina, et Spirocyclina. Soc. Geol. France, C.R.Somm. Paris (7), 30-31.

Neumann, M. 1958. Revision des *Orbitoides* du Cretace et de l'Eocene en Aquitaine Occidentale. Memoire de la Societe Geologique de France. Nouvelle Serie, tome 37, fasc. 2-3, no. 83, 174p. and 36pls.

Omara, S. 1956. New foraminifera from the Cenomanian of Sinai, Egypt. Journal of Paleontology 30, 883-890.

Omara, S., Strauch, F. 1965. The foraminiferal genus *Nezzazata* Omara. Rivista Italiana di Paleontolgia e Stratigrafia 71, 547-562.

Özcan, E. 2007. Morphometric analysis of the genus *Omphalocyclus* from the Late Cretaceous of Turkey: new data on its stratigraphic distribution in Mediterranean Tethys and description of two new taxa. Cretaceous Research 28, 621-641.

Papp, A., Küpper, K. 1953. Die foraminiferen faun von Guttaring und Klein St. Paul II. Orbitoiden aus Sandsteinen von Pemberger bei Klein St Paul. Sitzber. Österr. Akad. Wiss., Math. Naturw., Kl. I (162), 65-82.

Premoli Silva, I., Brusa, C. 1981. Shallow - water skeletal debris and larger foraminifers from Deep Sea Drilling Project Site 462, Nauru Basin, western equatorial Pacific. In Larson, R.L., Schlanger, S.O., et al., Init. Repts. DSDP, 61: Washington (U.S. Govt. Printing Office), 439-73.

Robertson, A. H. F. 2000. Mesozoic - Tertiary Tectonic - Sedimentary Evolution of a South Tethyan Oceanic Basin and its Margins in Southern Turkey, Geological Society, London, Special Publications 173, 97-138.

Robertson, A. H. F., Boulton, S. J., Taslı, K., İnan, N., Yıldız, A., Parlak, O. 2015. Late Cretaceous - Miocene sedimentary development of the Arabian continental margin in SE Turkey (Adıyaman Region): Implications for regional palaeogeography and the closure history of Southern Neotethys. Journal of Asian Earth Sciences 115, 571-616.

Salem, R., Eren, A., Özbahçeci, H., Araç, M., Öncü, H., İşbilir, M., Üngör, A., Biçer Z., Yılmaz, Z., Yılmaz E. 1986. Geologic and hydrocarbon evaluation of Maasrichtian sediments in central district X, Southeast Turkey: Türkiye Petrolleri Anonim Ortaklığı (TPAO) Arama Grubu Rapor no. 2202, 53 s.

Sanders, D., Pons, J. M., Caus, E. 2004. Shallow - water limestone clasts in a Campanian deep - water debrite (Krappfeld, Central Alps, Austria): implications for carbonate platform history, Ann. Naturhist. Mus. Wien, s. 139-165.

Sarı, B. 2006. Upper Cretaceous planktonic foraminiferal biostratigraphy of the Bey Dağları autochthon in the Korkuteli Area, Western Taurides, Turkey. Journal of Foraminiferal Research 36, 241-261.

Sarı, B., Özer, S. 2002. Upper Cretaceous stratigraphy of the Beydağları carbonate platform, Korkuteli area (Western Taurides, Turkey). Turkish Journal of Earth Sciences 11, 39-59.

Sarı, B., Taslı, K., Özer, S. 2009. Benthonic foraminiferal biostratigraphy of the Upper Cretaceous (Middle Cenomanian - Coniacian) sequences of the Bey Dağları Carbonate Platform, Western Taurides, Turkey. Turkish Journal of Earth Sciences 18 (3), 393-425.

Schlagintweit, F. 1992. Benthonische Foraminiferen aus Flachwasserkarbonaten der Oberkreide der Nördlichen Kalkalpen (Gosauschichtgruppe, Österreich), Mitt, österr. Geology 84, 327-353.

Schlüter, M., Steuber, T., Parente, M. 2008. Chronostratigraphy of Campanian - Maastrichtian platform carbonates and rudist associations of Salento (Apulia, Italy). Cretaceous Research 29, 100e114.

Sinanoğlu, D., Siyako, M., Karadoğan, S., Özgen-Erdem, N. 2017. Kültürel Jeoloji Açısından Hasankeyf (Batman) Yerleşmesi. 35 Türkiye Jeoloji Bülteni Geological Bulletin of Turkey 60-1.

Siyako, M, Bahtiyar, İ., Özdoğan, T., Açıkbaş, İ., Kaya, Ö. Ç. 2013. Türkiye Petrolleri Anonim Ortaklığı (TPAO) Araştırma Merkezi, Rapor no. 5463, 154. (unpublished).

Taslı, K., Özer, E., Koç, H. 2006. Benthic foraminiferal assemblages of the Cretaceous platform carbonate succession in the Yavca area (Bolkar Mountains, S Turkey): biostratigraphy and paleoenvironments. Géobios 39 (4), 521-533.

Tesovic, B. C., Gusic, I., Jeleska, V., Buckovic, D. 2001. Stratigraphy and microfacies of the Upper Cretaceous Pucisca Formation, Island of Brac, Croatia, Cretaceous Research 22, 591-613

Tewari, V. C., Stenni, B., Pugliese, N., Drobne, K., Riccamboni, R., Dolenec, T. 2007. Peritidal sedimentary depositional facies and carbon isote variation across K/T boundary carbonates from NW Adriatic platform. Palaeogeography, Palaeoclimatology 255, 77-86.

Tronchetti, G. 1981. Les Foraminiferes cretaces de Provence (Aptien - Santonien). Systematique, Biostratigraphie, Paleoecologie, Paleogeographie. Trav. Lab, Geol. Hist. Paleontology 12 (3 Bände), 1-559, Marseille.

van Gorsel, J. T. 1978. Late Cretaceous orbitoidal foraminifera. In: Hedley RH, Adams CG (eds) Foraminifera 3. Academic, London, 1-109.

Vaziri, S. H. 2011. Microbiostratigraphy of the Upper Cretaceous rocks (Sadr unit) in the Nakhlak area, Central Iran, *6th International Conference EMMM-2011*, A.A. Borissiak Paleontological Institute RAS, Russia, September 19-22.

Vaziri, S. H., Senowbari-Daryan, B., Kohansal Ghadimvand, N. 2005. Lithofacies and microbiofacies of the Upper Cretaceous rocks (Sadr unit) of Nakhlak area in northeastern Nain, Central Iran. J. Geoscience Osaka City University 48, 71-80.

Velic, I. 2007. Stratigraphy and paleobiogeography of Mesozoic benthic foraminifera of the Karst Dinarides (SE Europe). Geologia Croatica 60 (1), 1-113.

Yılmaz, Y. 1993. New evidence and model on the evolution of the Southeast Anatolian orogen. Geological Society of American Bulletin 105, 251-271.

Yılmaz, E., Duran, O. 1997. Güneydoğu Anadolu Bölgesi otokton ve allokton birimler stratigrafi adlama sözlüğü (Lexicon). TPAO Genel Müdürlüğü, Eğitim Yayınları No.31.

PLATES

PLATE I

1. *Biconcava bentori* Hamaoui, equatorial section, X100 (GA11A1-k)

2. *Biconcava bentori* Hamaoui, axial section, X100 (GA14a-k)

3,4. *Nezzazata simplex* Omara, equatorial sections, X60 (GA9b-k, GA14b-d)

5. *Nezzazatinella picardi* (Henson), axial section, X60 (GA14a-d)

6. *Trochospira avnimelechi* Hamaoui, oblique section, X60 (GA14A2-d)

7. *Antalyna korayi* Farinacci ve Köylüoğlu, oblique section, X60 (GA14a-b)

8. *Moncharmontia apenninica* (De Castro), axial section, X100 (GA9A1-h)

9. *Moncharmontia compressa* (De Castro), axial section, X100 (GA9A2-c)

10. *Fleuryana adriatica* (De Castro), oblique section, X100 (GA9d-e)

11. *Fleuryana adriatica* (De Castro), equatorial section, X100 (GA9c-b)

12. *Pseudocyclammina sphaeroidea* Gendrot, axial section, X60 (GA5A1-6)

13. *Arenobulimina* sp., axial section, X60 (GA10a-k)

14. *Broeckinella arabica* Henson, axial section, X60 (GA5A2-f)

15. *Cuneolina pavonia* d'Orbigny, axial section, X60 (GA9c-a)

16. *Cuneolina pavonia* d'Orbigny, basal section, X60 (GA9A1-3)

17. *Cuneolina ketini* İnan, vertical section, X60 (GA11c-a)

18. *Cuneolina ketini* İnan, basal section, X60 (GA16d-1)

19. *Dicyclina schlumbergeri* Munier-Chalmas, axial sections, X30 (GA5a-10)

20. *Coskinolina* sp., oblique section, X60 (GA2a-ı)

21. *Minouxia gümbelitrioides* Marie, equatorial section, X60 (GA5A2-3)

PLATE-I

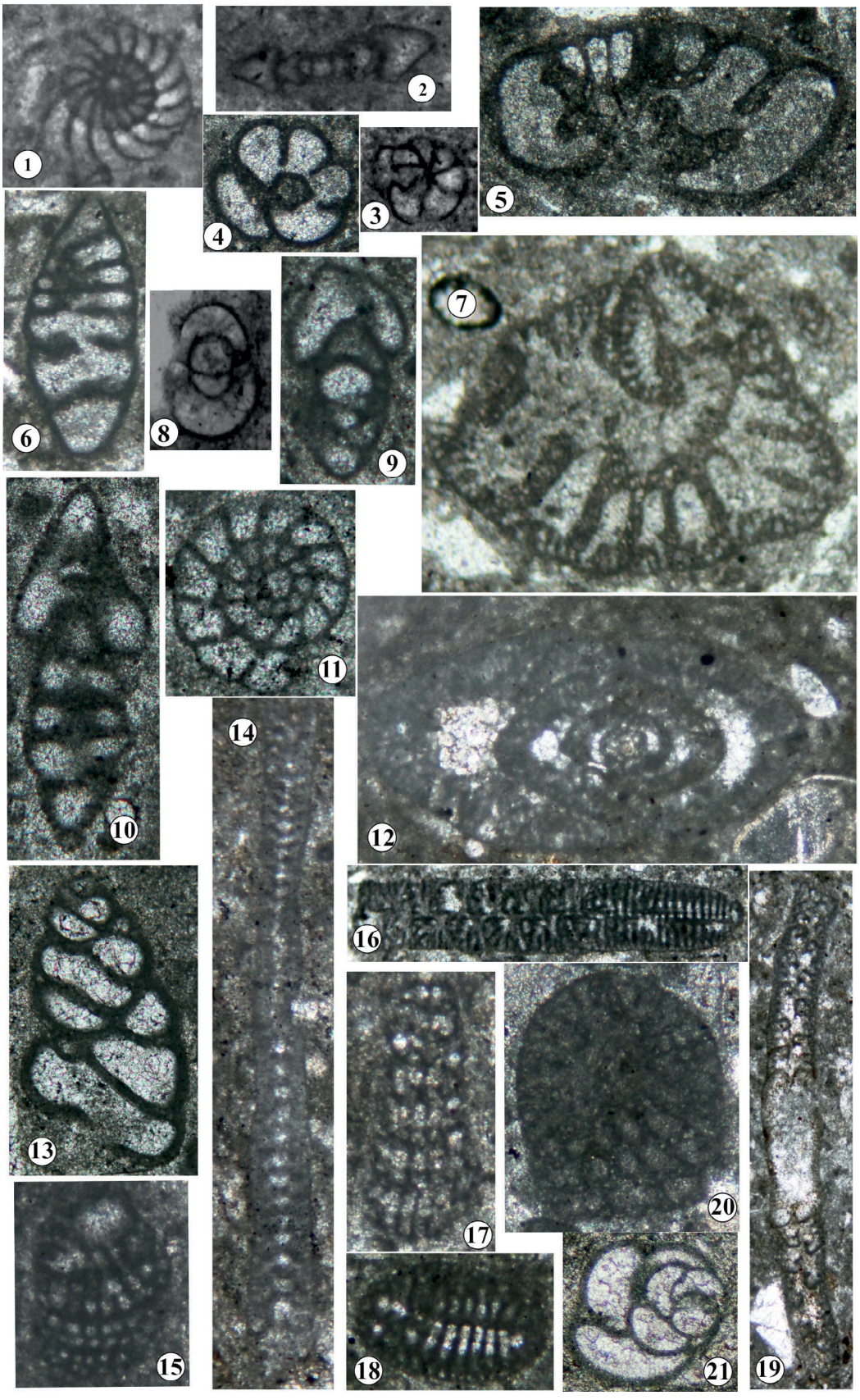

PLATE II

1. *Pseudolituonella reicheli* Marie, longitudinal section, X60 (GA2d-3)

2. *Dictyoconella* ? *complanata* Henson, basal section, X60 (GA14a-a)

3. *Minouxia lobata* Gendrot, equatorial section, X60 (GA9c-3)

4,5. *Vandenbroekia munieri* Marie, axial sections, X30 (GA20b-2, GA5A3-13)

6. *Cyclogyra* sp., axial section, X60 (GA5d-7)

7. *Fissoelphidium operculiferum* Smout, axial section, X60 (GA14a-f)

8. *Fissoelphidium operculiferum* Smout, equatorial section, X60 (GA5A2-1)

9. *Sırtina orbitoidiformis* Brönnimann ve Wirtz, axial section, X60 (GA2b-1)

10. *Goupillaudina* sp., axial section, X100 (GA1b-f)

11. *Goupillaudina* sp., equatorial section, X100 (GA2A1-c)

12. *Omphalocyclus* sp., axial section, X20 (GA5A3-1)

PLATE-II

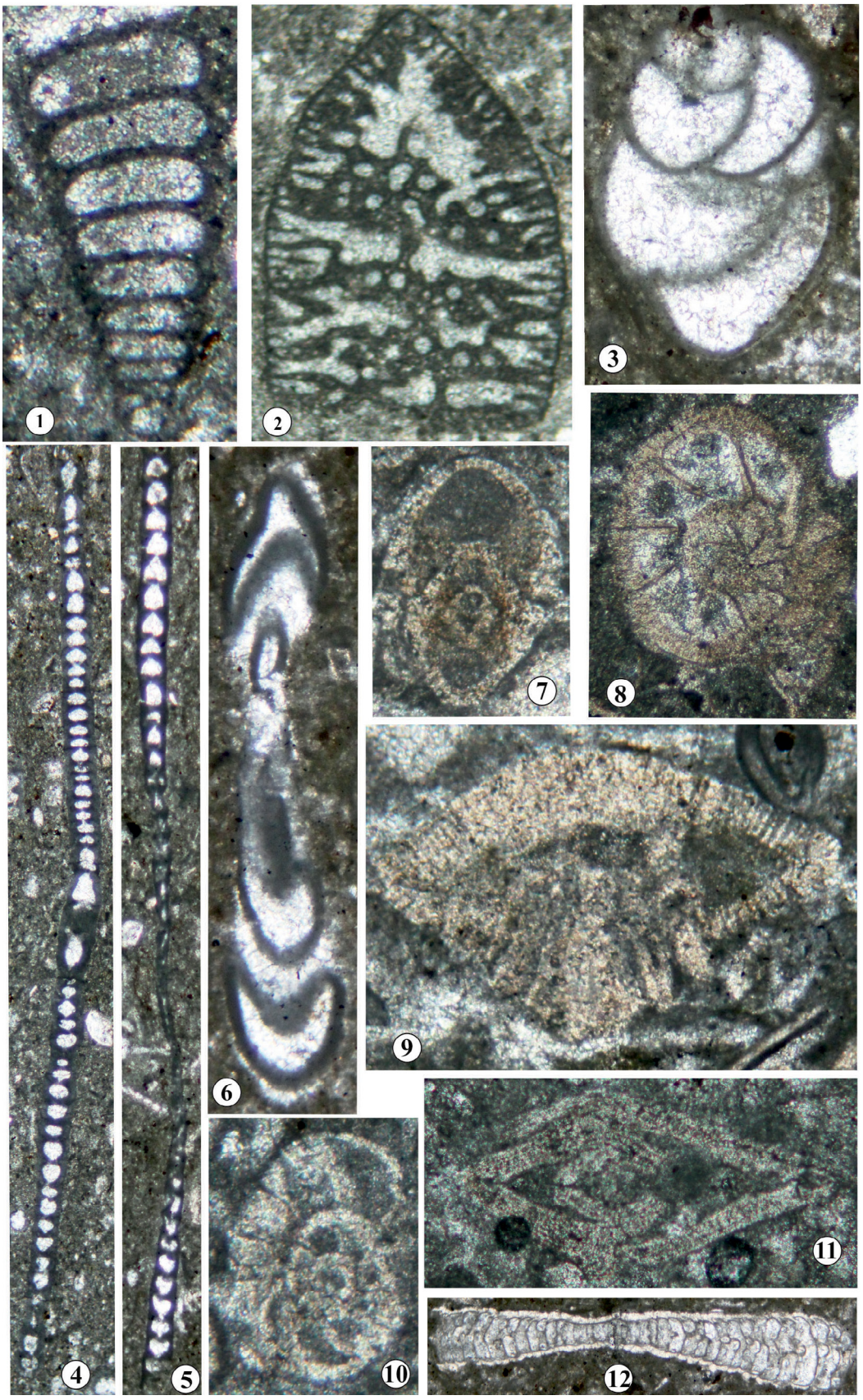

PLATE III

1,2. *Orbitoides media* (d'Archiac), equatorial sections, X20 (GA-Or-2)

3,4. *Orbitoides megaloformis* Papp ve Küpper, equatorial sections, X20 (GA-Or-9, GA-Or-15)

5,6. *Omphalocyclus anatoliensis* Özcan, equatorial sections, X20 (GA-Om-7, GA17b)

7. *Omphalocyclus* sp., axial section, X20 (GA5A3-11)

8,9. *Orbitoides* sp., axial sections, X20 (GA14b-b)

PLATE-III

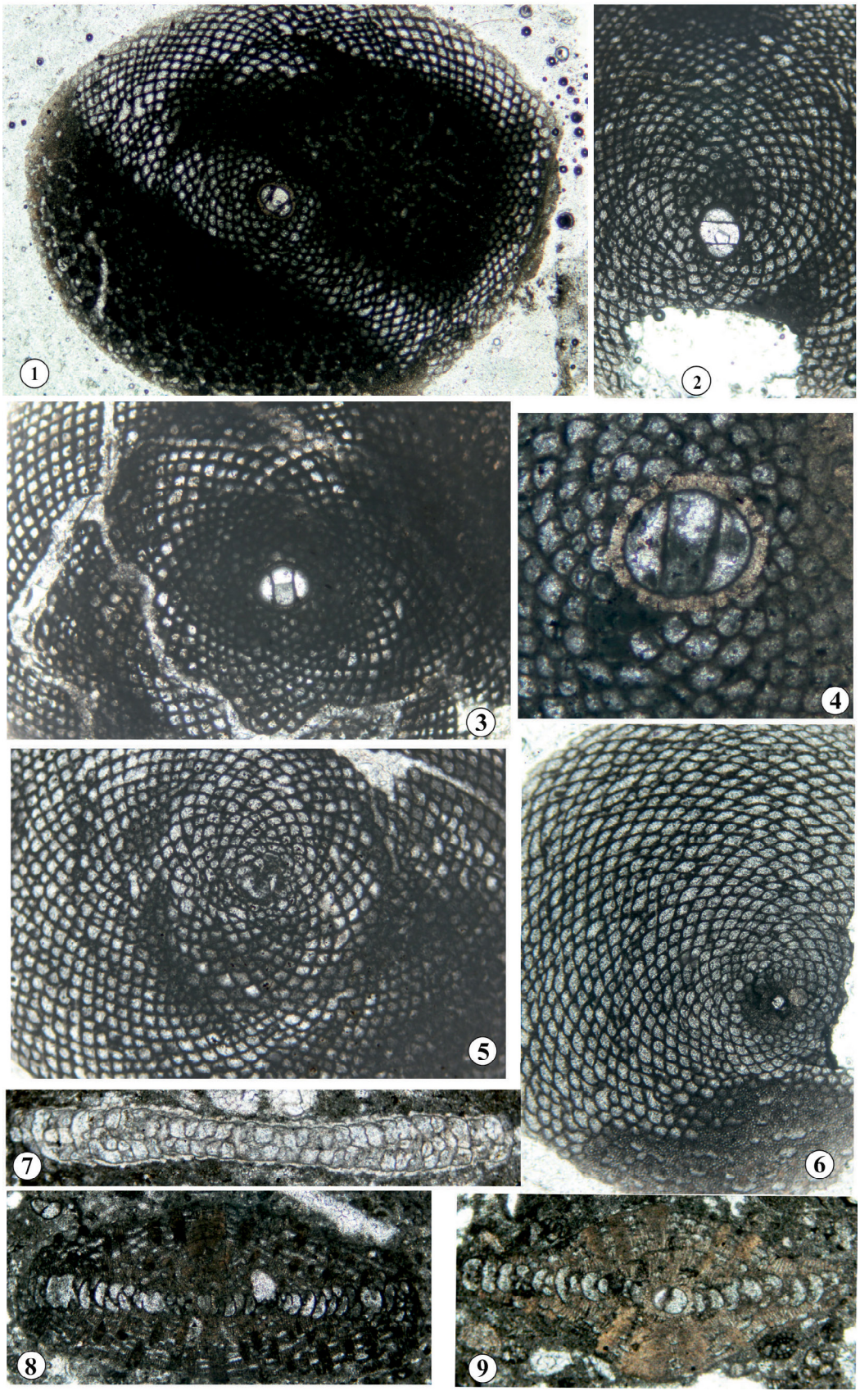

Publication Rules for the "Bulletin of the Mineral Research and Exploration"

1. Purposes

- To contribute to the establishment of scientific communication issues in earth sciences both in Turkey and internationally.
- To contribute to economic (mining, oil and gas, geothermal etc.), environmental and social (geoheritage etc.) studies in Turkey and in the World.
- To make the earth science scientific research and applications made by the MTA on publicly known,
- To use the bulletin as an effective tool in the international publication exchange by keeping it at a high level in terms of quality, scope and format,
- To contribute to the efforts of developing Turkish as a language of science and removing foreign words.

2. Scope-Attribute

In order for manuscripts to be published in the Bulletin of the Mineral Research and Exploration, they must have at least one of the following qualifications:

2.1. Research Articles and Reviews

2.1.1. Original Scientific Researches

- Such articles cover original scientific research and its results that contribute to the fundamental issues of earth sciences, research and evaluation of underground resources, and examine the environmental problems in terms of earth sciences,
- It covers research that apply new approaches and methods in solving problems related to earth sciences.

2.1.2. Review Articles

- They cover studies that compile previous research on subjects of earth sciences with a critical approach and put forward a new opinion on that subject.

2.2. Criticism and Response Articles

- Articles that criticize all or part of an article of the bulletin in the latest issue are published in the following first issue, if submitted within six months at the latest from the date of publication digitally.
- Before the publication, review articles are sent to the responsible author of the criticized article to make a response.
- If the criticism is not responded within foreseen time, the criticism letter is published alone, subsequent replies are not published. Replies are not allowed to be re-criticized.
- In criticizing and replying, scientific discussion and ethical rules should be followed. Criticism and response manuscripts should not exceed four pages, including figures, if available.

2.3. Brief Notes

- In "Brief Notes" section of the Bulletin of the Mineral Research and Exploration, the brief, objective and concise articles reflecting the data obtained from scientific researches and applications carried out in the area of earth sciences or new findings related to previously unknown geosciences in Turkey are given place.
- The articles arranged in the "Brief Notes" section are published without waiting in the first or in the second issue the latest, after the date they are sent to the Chair of the Editorial Board in order to ensure rapid communication.
- Articles requested to be published in the "Brief Notes" section should not exceed four pages, including all figures and tables.

3. Submission and Acceptance for Manuscripts

- The manuscripts submitted to be published in the Bulletin of the Mineral Research and Exploration should be prepared in TURKISH and / or ENGLISH in accordance with the Publishing Rules of the Bulletin of the Mineral Research and Exploration, and submitted via electronic application at http://dergi.mta.gov.tr/index.php.
- The manuscript must not have been previously published partially or completely elsewhere (except in abstract form).
- Manuscripts submitted with the request for publication in the Bulletin of the Mineral Research and Exploration should not exceed 30 pages, including all illustrations. The articles exceeding 30 pages can be published if deemed appropriate by referees and editors.
- In the submitted manuscript, the number of figures and tables should be given in proportion to the main text in a ratio of 1/3.

- Corresponding author is asked to suggest at least three referees for the evaluation of the manuscript. (The proposed referees and the authors should not have any joint work within the last two years).
- Manuscripts that do not comply with the Publishing Rules for the Bulletin of the Mineral Research and Exploration in terms of quality and form are directly returned without being examined in terms of content.
- Manuscripts deemed appropriate in terms of format are sent to at least two expert referees for review by the Editorial Board of the Bulletin of the Mineral Research and Exploration.
- Authors should make the referee corrections and suggestions sent to them within 20 days and upload to the system.
- Comments from referees are evaluated by the Editors and associated editors. Manuscripts deemed necessary to be corrected are sent back to the authors with a request for correction. Whether the suggested corrections have been made or not is checked by the Editorial Board.
- In the revision proposals given by the editors and referees, if there are suggestions that are not accepted by the author and have not been corrected, a report explaining the reason for rejecting these suggestions by the author should be sent to the Editorial Board together with the corrected copies.
- After the last control at the printing stage, the pre-print of the manuscript is sent to the authors in pdf format and the printing control is requested.
- Articles, not accepted for publication are not returned to the authors, for the unpublished articles, a letter is written to the responsible author indicating the reason for rejection.

4. Language and Period of Publication

- The Bulletin of the Mineral Research and Exploration is published three times a year, each issue as being in Turkish and the other in English languages.
- The spelling rules of the Turkish Language Association are valid for the spelling rules for the Turkish issue. However, in spelling of the words related to earth sciences, the spelling forms of technical terms are used in accordance with the decision of the Editorial Board (For example; underground, ground, earth's crust, etc.).

5. Spelling Draft

- The text of the manuscripts to be sent for the first review with the request to be published in the Bulletin of the Mineral Research and Exploration should be written in A4 (29.7 x 21 cm) size, word format, Times New Roman 10 pt., normal with 2.0 line spacing.
- At the bottom, top, left and right of the page 2.5 cm indent must be left. Formulas that require the use of special letters and symbols should be presented in computer media.
- In all subtitles, the initials of all words must be capital. First degree headings to be used in the article should be written in Times New Roman, 10 pt., bold and left aligned by giving numbers. Secondary headings should be written in Times New Roman, 10 pt., normal font and left aligned by giving numbers. Third-degree headings should be written in Times New Roman, 10 pt., italic font and left-aligned by giving numbers. Fourth-order headings should be written in Times New Roman, 10 pt., italic, aligned to the left, without giving numbers, and the text should continue after the title without a colon and a paragraph (see example article: www.dergi.mta.gov.tr).
- One blank line should be left after paragraphs in the text.
- Paragraph headings should be written 0.5 mm indentation.
- One article should respectively contain;

  -Title

  -Author's Name and Surname and * sign

  - Abstract

  - Key words

  - Introduction

  - Main Text

  - Discussion

  - Results

  - Acknowledgements

  - Reference sections.
- Line and page numbers must be added to the article text.

5.1. Title of the Article

- The title should reflect the subject of the article as briefly, clearly and adequately as possible. Subjects that are not sufficiently covered in the article should not be included in the title. The first letter of the title should be capitalized and the other words should be in lowercase letters (except for proper names) in Times New Roman, 10 pt. and bolded.

5.2. Author Name, Address and E-Mail Address

- The first name of the authors should be in lowercase (except the first letter), and the surname should be in capital letter and without any title.
- Only the name of the organization should be specified in the occupational address after the name and surname of the authors (position should not be specified).
- ORCID number should be taken from www.orcid.org and placed under the address.
- In articles written by more than one author, numbers should be placed on surnames of the authors, the address information should be included in the bottom line with a single line spacing. In this section, the corresponding author of the article should be indicated by using an asterisk (*) and the corresponding author's e-mail, telephone and other contact information must be provided.
- Abbreviations should not be used in writing the author's name and address. Addresses should be given in Turkish in Turkish publication and in English in English publication.

5.3. Abstract

- Abstract should be written at a level that can be understood without referring to the other parts of the article.
- The abstract should be organized as a brief presentation of the sections in the article, reflect the purpose of the article, be informative, and should be written in a way to emphasize new data and results on the subject.
- Short and simple sentences should be used in writing the abstract.
- In the abstract, there should not be any reference to other parts and illustrations of the article or to other articles.
- Information not mentioned in the main text should not be included in the abstract.
- The abstract should not exceed approximately 200 words and should be written as a single paragraph.
- Abstract should be written in Times New Roman, 10 pt., normal text with single line spacing.
- "ABSTRACT" should not be placed for the articles to be included in "Brief Notes" section.
- The English abstract should be given under the heading "ABSTRACT".

5.4. Key words

In order to facilitate searches, five keywords that will indicate the general content of the article should be selected and specified in this section. Words used in the title should not be repeated.

5.5. Introduction

- In this section, the necessary information for preparatory and facilitative to understand the article such as the purpose of the study, its location, methods of study and previous reviews on the subject should be given.
- If an unusual way is followed in naming, classification and abbreviations within the text of the manuscript, its reason should be stated in this section.
- Each of the topics to be included in this section can create a separate paragraph or a subtitle can be given for each of them when necessary (e.g. method, material, terminology and etc.).
- This section can again be used when reminder information is needed to facilitate the understanding of the article (e.g. statistical information, formulas, experimental or application methods and etc.).

5.6. Main Body of Article

- Constitutes the main body of the article.
- In this section, the data, findings and opinions that are intended to be transferred to the reader on the subject are mentioned.
- The data used in other parts of the article such as "Abstract", "Discussions", "Results" originate from this part.
- Care should be taken not to deviate from the purpose stressed in the "Introduction" section of the article when dealing the topics. Information that does not

contribute to the achievement of the purpose of the article or that is not used to reach the conclusion should not be included.

- All data used in this section and all opinions put forward should be proven by the findings obtained from the studies or based on a source by reference.
- The way and method to be followed in handling the topics vary according to the characteristics of the topics covered.
- Subject headings in necessary numbers with different stages should be used in this section.

5.7. Discussions

- The data and findings objectively conveyed in the "Main Text" section of the article should be discussed by the author in this section. Discussions should be separate from the "Results" section.

5.8. Results

- New data and findings obtained from the review that constitutes the subject of the article should be stated concisely and concretely in this section.
- Subjects that are not adequately addressed and / or covered in the main text should not be included in this section.
- The results can be given as items in order to emphasize the research results and make the expression understandable.

5.9. Acknowledgements

- In this section, important contributions in the realization of the study, which is the subject of the article, are indicated. An attitude that will distract this section from its main purpose should not be taken in the Acknowledgements.

Contribution should be stated as short and concise as possible to the persons and/or organizations that provided assistance (reading, writing, language assistance, etc.) during the research, and should not take an attitude that would distract this section from its main purpose.

5.10. References

- In this section, only the documents mentioned in the article should be included in complete.
- Abbreviations should be avoided in naming the publications and journals.
- The mentioned documents should be written in Times New Roman and 9 pt.
- The first line of the references should be written as justified to the left margin of the page, and the other lines should be written by giving a hanging indent value of 1.25.
- The references should be listed in alphabetical order, taking into account the surnames of the authors.
- If one author has more than one work in the same year, lowercase alphabet letters should be used right after the year of publication and the letters should be italic (e.g. Saklar, 2011*a, b*).
- If more than one document of the same author is cited, first his / her single-name publications in chronological order, then double-names according to the second author's surname in chronological order, and then multi-names according to the alphabetical order of the authors' surnames and publication year should be given.

For example:

Corradini, C., 2007. The conodont genus Pseudooneotodus Drygant from the Silurian and Lower Devonian of Sardinia and the Carnic Alps (Italy). Bollettino-Societa Paleontologica Italiana 46 (2/3), 139-148.

Corradini, C., Corriga, M. G., 2010. Silurian and lowermost Devonian conodonts from the Passo Volaia area (Carnic Alps, Italy), Bollettino della Società Paleontologica Italiana 49 (3), 237-253.

Corradini, C., Corriga, M. G., A 2012. Pridoli – Lochkovian conodont zonation in Sardinia and the Carnic Alps: implications for a global zonation scheme, Bulletin of Geosciences 87 (4), 635-650.

Corradini, C., Serpagli E., 1999. A Silurian conodont biozonation from late Llandovery to end Pridoli in Sardinia (Italy), In Serpagli (Ed.), Studies on conodonts: Proceedings of the 7th European Conodont Symposium, Bollettino della Società Paleontologica Italiana 37 (2-3) (1998), 255-273.

Corradini, C., Corriga, M. G., Männik, P., Schönlaub, H. P., 2015. Revised conodont stratigraphy of the Cellon section (Silurian, Carnic Alps), Lethaia 48 (1), 56-71.

Corradini, C., Leone, F., Loi, A., Serpagli, E., 2001.Conodont Stratigraphy of A Highly

Tectonised Silurian-Devonian Section in The San Basilio Area (Se Sardinia, Italy), Bollettino Della Societa Paleontologica Italiana 40 (3), 315-323, 1 Pl.

Corradini, C., Pondrelli, M., Serventi, P., Simonetto, L., 2003. The Silurian cephalopod limestone in the Monte Cocco area (Carnic Alps, Italy): conodont biostratigraphy, Revista Española de Micropaleontologia 35 (3), 285-294.

- If documents of different authors with the same surname are mentioned, they should be written in alphabetical order, considering their first names.
- If the document is in a periodical publication (if it is an article), information about the document is given in the following order: Authors ' surname, first letters of the authors' first names. Year of publication. The name of the article. The name of the publication in which the article was published, volume number and / or issue number with the first letters in capital, the numbers of the first and last page of the document. Punctuation marks like comma and etc. after journal names should not be used.
- In the examples below, the information about the mentioned documents is organized according to different document types, taking into account the punctuation marks.

For example:

Gürsoy, M. 2017. Munzur Dağları Alt Miyosen çökelleri mollusk topluluğu ve paleoekolojisi (Doğu Anadolu, Türkiye). Maden Tetkik ve Arama Dergisi 155, 75-99.

Pamir, H. N. 1953. Türkiye'de kurulacak bir Hidrojeoloji Enstitüsü hakkında rapor. Türkiye Jeoloji Bülteni 4, 1, 63-68.

Robertson, A. H. F. 2002. Overview of the genesis and emplacement of Mesozoic ophiolites in the Eastern Mediterranean Tethyan region. Lithos 65, 1-67.

- If the document is a book: authors' surnames, authors' first names. Year of publication. Title of the book with capital letters. The name of the publishing organization or the name of the publication in which the document was published, the volume and / or issue number, and the total number of pages of the book should be specified, respectively.

For example:

Einsele, G. 1992. Sedimentary Basins. Springer Verlag, 628.

Ketin, İ., Canıtez, N. 1956. Yapısal Jeoloji. İTÜ, 308.

Meriç, E. 1983. Foraminiferler. Maden Tetkik ve Arama Genel Müdürlüğü Eğitim Serisi, 26, 280.

- If the document is published in a book containing the articles of various authors, the usual order for the document included in a periodical publication is followed until the end of the document title. Then the editors' surnames and initials and the abbreviation of the editor word "Ed." is written in parentheses. Then, the title of the book in which the document is located is written with the first letters in capital letters. Name of publishing organization. The place of publication, the volume number of the publication in which the document was published, and the numbers of the first and last pages of the document should be written.

For example:

Anderson, L. 1967. Latest information from seismic observations. Gaskell, T. F. (Ed.). The Earth's Mantle. Academic Press. London, 335-420.

Göncüoğlu, M. C., Turhan, N., Şentürk, K., Özcan, A., Uysal, S., Yalınız, K. 2000. A geotraverse across northwestern Turkey. Bozkurt, E., Winchester, J. A., Piper, J. D. A. (Ed.). Tectonics and Magmatism in Turkey and the Surrounding Area. Geological Society of London. Special Publication, 173, 139-162.

- If it is desired to specify the name of a book in which the writings of various authors are collected as a document; following the surnames and names of the book's editors, in parentheses the "Ed." statement is written. Year of publication. Title of the book with capital letters. The name of the publishing organization or the name of the publication in which the document was published, the volume and / or issue number and the total number of pages of the book should be specified.

For example:

Gaskel, T. F. (Ed.). 1967. The Earth's Mantle. Academic Press, 520.

- If the document is "published abstract", information about the document is given in the following order:

Authors' surnames, authors' first names. Year of publication. Name of the document (paper). The name, date and place of the meeting where the paper is published, and the first and last page numbers in the book containing the abstract should be written.

For example:

Öztunalı, Ö., Yeniyol, M. 1980. Yunak (Konya) yöresi kayaçlarının petrojenezi. Türkiye Jeoloji Kurumu 34. Bilim Teknik Kurultayı, Ankara, 36.

Yılmaz, Y. 2001. Some striking features of the Anatolian geology. 4. International Turkish Geology Symposium, 24-28 Eylül 2001, Adana, 13-14.

- If the mentioned document has not been published like report, lecture notes and etc., the word "unpublished" should be written at the end of the information about the document in parentheses after the information about the document is given in the usual order for the document in a periodical publication.

For example:

Akyol, E. 1978. Palinoloji ders notları. EÜ Fen Fakültesi Yerbilimleri Bölümü, 45, İzmir (unpublished).

Özdemir, C., Biçen, C. 1971. Erzincan ili, İliç ilçesi ve civarı demir etütleri raporu. Maden Tetkik Arama Genel Müdürlüğü, Rapor No: 4461, 21, Ankara (unpublished).

- For unpublished courses, seminars and similar notes, the course organizer after document name. The place of the meeting. Title of the book and relevant page numbers should be given.

For example:

Walker, G.R., Mutti, E. 1973. Turbidity facies and facies associations. Society for Sedimentary Geology Pacific Section Short Course. Annaheim. Turbitides and Deep Water Sedimentation, 119-157.

- If the document is a thesis; author's surname, initial of the author's first name. Year of publication. Name of the thesis. The type of the thesis, the university where it was given, the total number of pages, its province and the word "unpublished" are written in parentheses.

For example:

Akıllı, H. 2019. Polatlı-Haymana (Ankara) civarı sıcak sularının izotop jeokimyası (δ18O, δD, 3H, δ13C, δ34S, 87Sr/86Sr) ve ana iz element bileşimleri ile incelenmesi. PhD Thesis, Ankara University, 255, Ankara (unpublished).

Argun Aktan, Ö. 2019. Marmara Denizi Batı Kıta Sahanlığı Yüzeysel Çökellerinde Jeojenik ve Antropojenik Ağır Metal Zenginleşmesine Yönelik Araştırmalar (Şarköy Kanyonu, KB Türkiye). MSc Thesis, Ankara University, 179, Ankara.

- Anonymous works should be arranged according to the publishing institution.

For example:

MTA. 1964. 1/500.000 ölçekli Türkiye Jeoloji Haritası, İstanbul Paftası. Maden Tetkik ve Arama Genel Müdürlüğü, Ankara.

- For the documents that are in print, no date is put after the name of the author, the name of the article and the source to be published should be specified and the word "in print" and / or "in review" should be written at the end (in parentheses).

For example:

Ishihara, S. The granitoid and mineralization. Economic Geology 75th Anniversary (in press).

- Information downloaded from the Internet should be given in the form of the name of the institution, its web address, and the date on which the web address was accessed. Turkish references should be given directly in Turkish and should be written in Turkish characters.

For example:

ERD (Earthquake Research Department of Turkey). http://www.afad.gov.tr. 3 March 2013.

- While citing the source, the original language should be adhered to, and the title of the article should not be translated.

6. Illustrations

- All of the drawings, photographs, plates and tables used in the article are referred to as "illustrating".

- Illustrations should be used when their use is unavoidable or when they make the subject easier to understand.
- In the selection and arrangement of the format and size of the illustrations, an attitude should be made to prevent loss of space as much as possible considering the page length and layout of the bulletin.
- The number of illustrations used should be proportional to the size of the text.
- All illustrations should be submitted in separate files regardless of the text.
- Abbreviations should not be used in illustration explanations in the text and should be numbered in the order of mention within the text.
- Photographs and plates must be submitted as a computer file in which all details can be seen for the examination of the article, with EPS, TIFF or JPEG extension and at least 300 dpi resolution.

6.1. Figures

- Drawings and photographs other than the plate to be included in the article are evaluated together as "Figure" and numbered in the order of mention in the text.
- The figures should be prepared in computer considering the dimensions ofa single column width as 7.4 cm or double column width as 15.8 cm. The figure area with its caption should not exceed 15.8x21 cm.
- While preparing the figures, unnecessary details should not be included and care should be taken not to use more space than necessary for the transfer of information.
- In figure descriptions, a space should be left after the word "Figure" is written, and the number is given in the usual sequence number, followed by a hyphen (-) and a space again, and a description of the relevant figure should be written. If the figure legend exceeds the bottom lines, the following lines should to be written after the "Figure 1-" statement alignment. Figure descriptions should be created as follows, without exceeding the edges of the figure and justified on both sides.

For example:

Figure 1- The district of Sandıklı (Afyon); a) geological map of the southwest, b) the general vertical section of the study area (Seymen, 1981), c) Turkey's most important neotectonic structures (modified from Koçyiğit, 1994).

- Drawings should be drawn in computer properly, clean and with care.
- The use of thin lines that may disappear when minimized in figures should be avoided.
- Symbols or letters used in all drawings should not be less than 2 mm (7 pt.) in Times New Roman.
- All standardized symbols used in the drawings should preferably be explained in the drawing, if they are too long then they should be explained in the figure below.
- Bar scale should be used in all drawings and the north direction should be indicated on all maps.
- The name of the author, description of the figure, figure number should not be included in the drawing.
- Photographs should reflect the aims of the subject and should be in adequate numbers.
- Figures should be framed.

6.2. Plates

- Plates should be used in cases where multiple photographs are required to be printed together on a special paper.
- Plate dimensions must be equal to the size of the bulletin's usable area of the page.
- Figure numbers should be written under each of the figures on the plate and bar scale should be used.
- Original plates must be attached to the final copy to be submitted in the case of acceptance of the manuscript.
- Figures and plates should be numbered among themselves and independently. Figures should be numbered with Latin numerals and plates with Roman numerals (eg Figure 1, Plate I).
- There should be no explanation text on the figures inside the plate.

6.3. Tables

- All tables should be arranged in word format and should be prepared in Times New Roman.
- Tables should not exceed the size of 15x8 cm together with the table caption.

• Table explanations should be created without exceeding the edges of the figure and justified as in the example below.

For example:

Table 1- Hydrogeochemical analysis results of geothermal waters in the study area.

7. Nomenclature and Abbreviation

• Abbreviations must be in the accepted international or national form. Unusual nomenclature and abbreviations that are not standardized in the article should be avoided. In cases where it is deemed necessary to use such nomenclature and abbreviations, the way and method followed should be explained.

• There should not be a dot between the words initials used in standard abbreviations (such as MTA, DSİ).

• Abbreviations of geography aspects should be made in English (N, S, E, W, NE and etc.).

The word group to be abbreviated should be written clearly where it is mentioned first time and the abbreviation should be given in parentheses, then only the abbreviated form should be written throughout the article.

• Systems with international validity (m, inch, etc.) should be used as the unit of measure. Decimals should be separated with commas in Turkish articles and with a period in English articles.

• The names of figures, plates and tables in the article should not be abbreviated. For example, "As seen in the generalized stratigraphic section of the region (Figure 1) …….".

7.1. Stratigraphic Nomenclature

• Stratigraphic nomenclature should be done in accordance with the Stratigraphical Classification and Nomenclature Rules prepared by Turkey Stratigraphy Committee (TSC).

(https://www.mta.gov.tr/v3.0/sayfalar/birimler/belgeler/Stratigrafi_adlama_kurallari.pdf)

• Attention should be paid to the use of formation names accepted (formalized) by the TSC. If the formation name used is official, the letter "F" should be capitalized, and if it is informal and plural, the letter "f" should be written in lowercase. For example; Bostancı Formation (formal), Kaynarca formation (unofficial), Baltalimanı, Trakya and Tarlaağızı formations (plural).

7.2. Chronostatigraphic and Geochronologic Nomenclature

• "International Chronostratigraphic Chart" (https://stratigraphy.org/chart), which is updated annually by the International Stratigraphic Committee, should be taken into consideration in chronostratigraphic and geochronological nomenclature.

• Position within a chronostratigraphic unit can be expressed in adjectives indicating the position, for example: lower, middle, upper and etc. When using these adjectives, it should be decided whether the lower, middle and upper distinction is formal / informal in the International Chronostratigraphic Chart.

For example:

lower Miocene, Upper Holocene and etc.

• When stating the time where a geochronological unit is, temporal adjectives such as; early, middle, late and etc. are used. When using these adjectives, the International Chronostratigraphic Chart should be taken into consideration to decide whether the adjectives begin with capital or lowercase letters.

For example:

early Miocene, Late Holocene etc.

7.3. Paleontological Nomenclature and Spelling of Fossil Names

• Original names of fossils should be used.

For example:

Nummulites with limestone

• Fossil genus and species names are written in italics, cf., aff. and gr. etc. expressions are written as normal (perpendicular). When writing fossil names for the first time, the surnames of the people who identify them and the year in which they were first defined should be written. In later uses, the surnames and the year in which they are defined may not be written. The surnames and dates of identifiers coming at the end of the fossil names are not references, they should not be included in the mentioned documents.

For example:

Alveolina aragonensis Hottinger, 1960 not a reference.

Alveolina cf. *aragonensis* Hottinger, 1960 not a reference.

Alveolina aff. *aragonensis* Hottinger, 1960 not a reference.

Alveolina gr. *aragonensis* Hottinger, 1960 not a reference.

- After the first use of the same genus in the text is written clearly, it can be abbreviated as in the example so that it will not be confused with another genus in later use.

For example:

Alveolina aragonensis, A. polathensis, A. ellipsoidalis etc.

- If the date is in parentheses after the person describing it after the name of the fossil in the text, this is a reference and should be included in the mentioned documents.

For example:

Alveolina aragonensis Hottinger (1960) is a reference.

- The following rules should be taken into account when writing the systematic paleontologic section.

a. First of all, genus, species and subspecies to be identified should be written in hierarchical order like the order, upper family, family type species and so on. Later, the species to be described should be written together with the surnames and date of the people who defined the subspecies name. If there is a photograph of the described fossil, the plate or figure with the photograph should be added under the fossil name. The names of the authors listed here are not references, so they are not included in the reference.

For example:

Order: Foraminiferida Eichwald, 1830

Superfamily: Alveolinacea Ehrenberg, 1839

Family: Alveolinidae Ehrenberg, 1839

Type Genus: *Borelis* de Montfort, 1808

Type Species: *Borelis melenoides* de Montfort, 1808
= *Nautilus melo* Fichtel and Moll, 1798

Borelis vonderschmitti (Schweighauser, 1951)

(Plate II, Figure 3-5 or Figure 3A-H).

b. Similar or synonyms (synonym) list should be left-aligned in chronological order. The page and figure number of the synonymous fossil in the relevant study should be included in the synonymous list. Authors in the synonymous list are references and must be included in the references.

For example:

1951 *Neoalveolina vonderschmitti* **Schweighauser**, page 468, figures 1-4.

1974 *Borelis vonderschmitti* (Schweighauser), **Hottinger**, page 67, plate 98, figures 1-7.

c. After the synonymous list is given, the definition, explanations (similarities and differences), dimensions, material, stratigraphic distribution (according to the characteristics of the fossil) should be written.

d. If the fossil is defined for the first time (new species) in the systematic paleontology section, the origin of the name, holotype, type locality, material, description, explanation (similarity and differences), age and geographical distribution, dimensions (according to the features that define the fossil) should be written. Photographs of the fossil identified for the first time by the authors must necessarily be placed in plates or figures.

e. Bar scale indicating the size of fossils must be used definitely in plates / figures.

8. References

- In the references to be made in the Main Text, only the surnames of the authors and the publication year of the mentioned article should be specified. Referencing should be arranged according to one of the following examples:
- Referring to a publication with a single author (in chronological order):
  - Altınlı (1972, 1976) defined the Bilecik sandstone in detail.

  It is known that the fold axes of the Devonian and Carboniferous units around İstanbul are N-S trending (Ketin, 1953, 1956; Altınlı, 1999).
- Referring to a publication with two authors:
  - The upper parts of the unit include Ilerdian fossils (Sirel and Gündüz, 1976; Keskin and Turhan, 1987, 1989).
- Referring to a publication with more than two authors:
  - According to Caner et al. (1975), the Alıcı formation reflects the conditions of fluvial environment.

- Unit disappears by wedging towards E (Tokay et al., 1984).

• Referring to a reference in another publication:

  It is known that Lebling mentioned about the existence of Liassic around Çakraz (Lebling, 1932; Charles, 1933).

• When referring to the works of the authors with the same surname in the same year, referring the authors' first names by writing their initials:

  - Many studies have been done in the field of structural geology in the study area (Gutnic et al., 1979; Yılmaz A., 1983; Yılmaz, İ., 1983; Poisson et al., 1984 etc.).

9. Prints Sent to Authors

Two copies of the relevant issue published in the Bulletin of the Mineral Research and Exploration are sent to the authors.

10. Terms of Publication and Copyrights

• Some or all of the articles to be published in the Bulletin of the Mineral Research and Exploration should not have been published before.

• Authors who submit a publication to the Bulletin of the Mineral Research and Exploration are deemed to have accepted the bulletin's publication rules in advance.

• The copyright of the manuscripts accepted for publication and converted into publications belongs to the General Directorate of Mineral Research and Exploration (MTA).

The authors of the study sign the relevant forms within the scope of the provisions specified in the Regulation of the Editorial Board regarding the transfer of copyright and submit them to the Editorial Board. After the publication of the article, MTA may pay royalty fees to the authors of the article for their declarations within the scope of the "Regulation on the Editorial and Processing Fees to be paid by the Public Organizations and Institutions".

NOTE: Information and forms about Bulletin of the Mineral Research and Exploration can be accessed from the website: http://dergi.mta.gov.tr/index.php